

Dmitry V. Chalikov

---

# Numerical Modeling of Sea Waves

# Numerical Modeling of Sea Waves

Dmitry V. Chalikov

# Numerical Modeling of Sea Waves



Springer

Dmitry V. Chalikov  
P.P. Shirshov Institute of Oceanography  
Russian Academy of Sciences  
Saint-Petersburg  
Russia

ISBN 978-3-319-32914-7                    ISBN 978-3-319-32916-1 (eBook)  
DOI 10.1007/978-3-319-32916-1

Library of Congress Control Number: 2016942526

© Springer International Publishing Switzerland 2016

This work is subject to copyright. All rights are reserved by the Publisher, whether the whole or part of the material is concerned, specifically the rights of translation, reprinting, reuse of illustrations, recitation, broadcasting, reproduction on microfilms or in any other physical way, and transmission or information storage and retrieval, electronic adaptation, computer software, or by similar or dissimilar methodology now known or hereafter developed.

The use of general descriptive names, registered names, trademarks, service marks, etc. in this publication does not imply, even in the absence of a specific statement, that such names are exempt from the relevant protective laws and regulations and therefore free for general use.

The publisher, the authors and the editors are safe to assume that the advice and information in this book are believed to be true and accurate at the date of publication. Neither the publisher nor the authors or the editors give a warranty, express or implied, with respect to the material contained herein or for any errors or omissions that may have been made.

Printed on acid-free paper

This Springer imprint is published by Springer Nature  
The registered company is Springer International Publishing AG Switzerland

*To my wife Olga*

# Preface

The work on sea wave problem I started many years ago when I had graduated from the university. It was the time when all specialists in the earth sciences were impressed by the progress in application of computers in the geophysical fluid dynamics and, particularly, by a great success in the numerical modeling of three-dimensional atmosphere launched by Prof. Josef Smagorinsky. Being not quite well prepared for a purely analytical investigation, I felt a strong doubt about such methods since I believed that all the results obtained analytically are based on severe simplifications; therefore, they cannot be a perfect reflection of nature (my present feeling is about the same). This is why the author of this book began to meditate on the possible application of the computer modeling for sea waves. The problem of boundary layer was more familiar to me, so the first series of works was devoted to a wind–wave interaction problem. The work on mathematical modeling of sea waves was started in the 1970s, when a model for investigation of wind–wave interaction was completed. Actually, it was an attempt to construct a coupled windwave model, but the wave counterpart (despite the fact that it was based on the full equations) was able to generate only monochromatic linear waves. I was inspired by the publication of my first paper on this topic by Journal of Fluid Mechanics (1978). Now, I realize that the paper was quite imperfect, but the publication gave me a strong momentum for moving in this direction. The following numerous papers (see review in Chalikov 1986) considered the structure of the wave boundary layer (WBL) above 1-D wave surface assigned as a superposition of linear waves with random phases and the prescribed empirical spectrum. Gradually, I distanced myself from this activity because of growing dissatisfaction with the formulation of the problem. The model of WBL as well as its modifications was based on a finite-difference scheme with poor resolution and could not be used for investigation of a thin structure of boundary layer. Besides, the model did not use the advantages of Fourier presentation. Finally, I left my model to colleagues and students and continued working on the problems which had nothing to do with wave problems, such as the theory of ice ages, super-rotation of Venus atmosphere, and global ocean–atmosphere interaction.

A real breakthrough in the numerical wave modeling happened in 1989 when the conformal transformation of 1-D potential equation was first applied. In 1991, I was invited for work at the National Center for Environment Prediction (NCEP/NOAA) where excellent conditions due to the support of then Director of NCEP Eugenia Kalnay gave me a good possibility to continue my study. One of the directions of my work at NCEP was construction of the parameterization schemes for the input and dissipation of energy in the WAVEWATCH wave prediction model jointly with Hendrik Tolman. The experiments on application of the neural network (NN) technique, carried out by Vladimir Krasnopol'sky with my participation, can be also referred to this direction. The construction of the first numerical model for surface waves was accelerated due to collaboration with Dmitry Sheinin. A discussion of the problem with Vladimir Zakharov was also quite useful. The extended results of simulation of the wave dynamics were first shown at Conference (Arizona University) organized by V. Zakharov (Chalikov and Sheinin 1994). It is funny that neither I nor Sheinin knew that conformal mapping had been used before in many other works (see references in Chap. 1).

The model allowed us to obtain a lot of new results which we believe are true. After investigation of different types of wave processes, we came to the conclusion that wave motion is a more complicated phenomenon than it was assumed before. Generally speaking, wave motion should be defined as a liquid motion with free surface in a physical space. Most of the wave specialists seem to overestimate the role of presentation of natural wave field as a set of almost independent wave modes whose energy defines the continuous wave spectrum. In reality, spectrum is not continuous, and wave surface in a statistical sense is not a physical image of spectrum because the statistical properties of surface depend on the resolution of spectrum. A spectrum of strongly nonlinear processes (e.g., the breaking spectrum) cannot be treated as a physical reality because the nonlinearity can shift the spectral density far away from its true location in the wave number space. For example, the breaking process happens at sharp crests of more or less large waves in the narrow intervals of physical space. The Fourier image of such  $\delta$ -like behavior turns out to be distributed over many wave numbers, while in reality, the breaking makes lower the heights of nonlinear waves.

Some of the facts discovered with the 2-D conformal model are confirmed by our 3-D model. The three-dimensional modeling is not as elegant as the two-dimensional one; besides, it takes a lot of computer time. Another property of 3-D wave simulation is that it sensitive to the initial conditions. Fortunately, this sensitivity refers to the individual solution, and to the less extent, it concerns its statistical characteristics. Anyway, for obtaining the smooth, statistically significant results, it is necessary to use the ensemble modeling, which is convenient to carry out using multiprocessor computers. The speed of the calculations remains low, which makes the entire problem quite uncomfortable. The most striking result obtained with the 3-D model is irregularity of the 2-D wave spectrum and sensitivity of its shape to the initial phases. The results obtained allow us to suggest that the Hasselmann's theory is not as universal as it was considered before. The separation of nonlinear interactions into reversible and irreversible interactions cannot

be universal. For example, the reversible interactions can initiate the wave breaking which makes them finally irreversible. Wave breaking not only decreases the wave energy but also redistributes the energy between wave components.

A thoughtful reader can find some contradictions in different parts of this book. Some of these contradictions appear as a result of transformation of author's views. I prefer to leave in the book some of the contradictory points of view, since until now I have not been sure which of them are true. The physics of waves is too complicated; therefore, this book can be just considered as a first look at this marvelous phenomenon, using no sophisticated mathematics or complicated tools and sensors, except for computer.

Saint-Petersburg, Russia  
Melbourne, Australia

Dmitry V. Chalikov

## Acknowledgments

I would like to acknowledge the many people that have contributed to this book in different ways. This book is devoted mostly to the author's results partly obtained in collaboration with colleagues. I am especially grateful to Dmitry Sheinin who took part in construction of the first version of conformal model and developed the codes for calculations of the stationary solutions. I also enjoyed collaboration with Hendrik Tolman (National Meteorological Center, USA) who introduced me to the problem of sea wave forecast. Many problems described in this book would never have been completed without collaboration with Alexander Babanin (Swinburne University of Technology, Australia) who supported me over the last 10 years. I am also thankful to my colleagues Sergey Suslov and Elena Sanina for their helpful collaboration. Also, I wish to express sincere gratitude to Director of Institute of Oceanography RAS R.I. Nigmatulin and Director of St.-Petersburg Branch of the Institute A.A. Rodionov for their permanent understanding and support. My wife Olga with her kind assistance in smoothing my English deserves special gratitude. Without her meticulous corrections, this book would have never been accomplished. Also, I would like to thank my numerous colleagues from different countries and institutes, who made up a comfort environment for my scientific growth. Special thanks deserve all my anonymous reviewers whose constructive critics helped me improve my results and strengthen my fortitude.

The work was supported by Russian Science Foundation (RSF), Grant #16-17-00124.

# Contents

<b>1</b>	<b>Introduction: Different Approaches to Numerical Modeling of Sea Waves—Specifics of Current Approach . . . . .</b>	<b>1</b>
<b>2</b>	<b>Two-Dimensional Wave Model . . . . .</b>	<b>7</b>
2.1	2-D Equations of Potential Motion with Free Surface . . . . .	7
2.2	Conformal Coordinates and Equations in the Conformal Coordinates . . . . .	9
2.3	Numerical Solution of Potential Equations . . . . .	15
2.4	Conclusion . . . . .	17
<b>3</b>	<b>Stationary Solutions of Potential Equations . . . . .</b>	<b>19</b>
3.1	The Stationary Form of Equations . . . . .	20
3.2	Pure Gravity Waves . . . . .	21
3.3	Gravity-Capillary Waves . . . . .	29
3.4	Pure Capillary Waves . . . . .	32
3.5	Conclusion . . . . .	33
<b>4</b>	<b>Two-Dimensional Wave Modeling Based on Conformal Mapping . . . . .</b>	<b>35</b>
4.1	Validation of Two-Dimensional Model by Comparison with the Stationary Solutions . . . . .	35
4.2	Examples on Non-stationary Solutions . . . . .	38
4.3	Simulation of Steep Waves . . . . .	43
4.4	Interaction of Surface Waves at Very Close Wave Numbers . . . . .	53
4.5	Conclusion . . . . .	56
<b>5</b>	<b>Statistical Properties of One-Dimensional Waves . . . . .</b>	<b>59</b>
5.1	‘Lifetime’ of Wave Components . . . . .	59
5.2	Statistical Characteristics of a Multi-mode Wave Field . . . . .	61
5.3	Mysterious Properties of ‘Upper’ Conformal Coordinates . . . . .	68
5.4	Conclusions . . . . .	71

<b>6 Nonlinear Interaction in One-Dimensional Wave Field . . . . .</b>	75
6.1 Adiabatic Transformation of Stokes Waves . . . . .	76
6.2 Quasi-Stationary Regime. . . . .	90
6.3 Transformation of Harmonic Wave on Deep Water . . . . .	94
6.4 On Nonlinear Energy Transfer in Unidirected Adiabatic Surface Waves. . . . .	98
6.5 Conclusions . . . . .	103
<b>7 Modeling of Extreme Waves. . . . .</b>	107
7.1 Extreme Wave Phenomenon . . . . .	107
7.2 Description of the Numerical Experiments. . . . .	111
7.3 The Breaking and Surviving Extreme Waves. . . . .	116
7.4 The Properties of Extreme Waves . . . . .	122
7.5 Statistics of Extreme Waves . . . . .	130
7.6 Conclusion . . . . .	134
<b>8 Numerical Investigation of Wave Breaking . . . . .</b>	137
8.1 Wave-Breaking Phenomenon. . . . .	137
8.2 Description of the Numerical Experiments. . . . .	140
8.3 Results of the Numerical Experiments . . . . .	141
8.4 Nonlinear Sharpening of Waves as a Possible Cause of Breaking. . . . .	165
8.5 Conclusions . . . . .	172
<b>9 Numerical Modeling of Wind-Wave Interaction . . . . .</b>	175
9.1 Wave Boundary Layer (WBL). . . . .	175
9.2 Equations of WBL . . . . .	181
9.3 The Numerical Scheme for WBL Equations . . . . .	185
9.4 The Coupling of Wave Models with the Model of WBL. . . . .	187
9.5 The Structure of Surface Pressure Above Solid Waves . . . . .	188
9.6 Description of the Numerical Experiments with the Coupled Model . . . . .	192
9.7 Evolution of Waves . . . . .	193
9.8 Wave-Produced Momentum Flux (WPMF) . . . . .	197
9.9 Evaluation of $\beta$ -Function . . . . .	202
9.10 Conclusions . . . . .	211
<b>10 One-Dimensional Modeling of the WBL . . . . .</b>	213
10.1 The One-Dimensional Model of WBL . . . . .	214
10.2 Vertical Structure of WBL . . . . .	217
10.3 Drag Coefficient at High Wind Speed. . . . .	221
10.4 Evolution of Wave Field. . . . .	223
10.5 Wind Input . . . . .	224
10.6 Wave Dissipation. . . . .	226
10.7 Simulation of One-Dimensional Wave Field Evolution . . . . .	231
10.8 Conclusions . . . . .	238

<b>11 Numerical Investigation of Turbulence Generation in Non-breaking Potential Waves . . . . .</b>	243
11.1 Turbulence Generation by Potential Waves. Theoretical Background . . . . .	244
11.2 Cylindrical Conformal Coordinates . . . . .	247
11.3 Equation for Vortical Motion . . . . .	248
11.4 Large-Eddy Simulation Approach . . . . .	253
11.5 Modeling of Waves . . . . .	254
11.6 Results of Simulations . . . . .	255
11.7 Coupling Between Waves and Upper-Ocean Layer . . . . .	264
11.8 Conclusion . . . . .	265
<b>12 Three-Dimensional Modeling of Potential Waves . . . . .</b>	267
12.1 Existing Approaches to Modeling of 3-D Waves, Their Advantages, and Disadvantages . . . . .	267
12.2 Equations and Transformation of Coordinates . . . . .	269
12.3 Three-Dimensional Deepwater Wave Model . . . . .	271
12.4 Linear (Analytic) and Nonlinear Components of Velocity Potential. Numerical Solution of 3-D Equation for Velocity Potential . . . . .	272
12.5 Validation of the 3-D Deepwater Model . . . . .	277
12.6 Simulation of a Multi-Mode Wave Field . . . . .	284
12.7 Ensemble Modeling of 3-D Waves . . . . .	292
12.8 Comparison of Linear and Nonlinear Extreme Wave Statistics . . . . .	296
12.9 Conclusions . . . . .	304
<b>Afterword: What Has Been Done . . . . .</b>	307
<b>References . . . . .</b>	321

# Abbreviations

1-D	One-dimensional
2-D	Two-dimensional
B.-F.	Benjamin–Feir (instability theory)
FFT	Fast Fourier transform
HOS	High-order scheme
JONSWAP	JOint North Sea WAve Project
Ku	Kurtosis
LES	Large-eddy simulation
MNLS	Modified nonlinear Schrödinger (equation)
NCEP	National Center for Environmental Prediction
NLS	Nonlinear Schrödinger (equation)
NN	Neural network
NOAA	National Ocean Atmosphere Administration
Sk	Skewness
TDMA	Three-diagonal matrix algorithm
WAVEWATCH	NCEP windwave model (NCEP NOAA)
WBL	Wave boundary layer
WM	Wave model

# Chapter 1

## Introduction: Different Approaches to Numerical Modeling of Sea Waves—Specifics of Current Approach

**Abstract** Development of the mathematical modeling of wave processes and the advantages of the conformal coordinates for investigation of a two-dimensional flow with free surface are discussed. Different approaches to the numerical modeling of a three-dimensional flow are briefly analyzed.

Very often the term *mathematical modeling* is applied to any theoretical scheme describing the object in terms of mathematics and aimed to obtain the numerical results, which characterizes somehow the real process. On our opinion it is incorrect, since such methods are often based on very simple formulations, which is able to describe correctly only one side of real phenomenon. The essence of mathematical modeling is complete replacing of real object by mathematical construction like it used in physical laboratory modeling. It is better to define the mathematical modeling as a method of investigation of complicated processes based on a full mathematical formulation of a problem. One of the typical examples of mathematical modeling is the simulation of natural liquid objects on a basis of fluid mechanics equations, i.e., the Navier–Stokes (or the Euler) equations.

Computational techniques for numerical solution of the Navier–Stokes equation have brought new development to geophysical fluid dynamics. Using modern numerical models, the structure, and evolution of many complicated dynamical phenomenon in different fluids, including the atmosphere and ocean, can be successfully simulated. Unfortunately, the applications of these methods to the problem of surface wave were on unknown reasons greatly delayed. Even now, the authors developing the numerical modeling of surface waves often meet fierce resistance of reviewers, who probably prefer the traditional analytical and semi-analytical methods. However, the number of works devoted to mathematical modeling of waves is quickly growing.

The subject of this book is describing the application of mathematical modeling to sea waves. We limit the scope of review to those works, which is devoted to free periodic waves and based on the principal equation for potential waves.

The problem of numerical simulation of surface waves has a long history. The most general approach to simulate a motion with a free surface is based on some sort of

Lagrangian approach (Harlow and Welch 1965) which assumes the tracing of variable surface in a fixed grid with different order accuracy (see, e.g., Noh and Woodward 1976; Hirt and Nichols 1981; Prosperiti and Jacobs 1983; Miyata 1986). At present, the applicability of this method is restricted by simulation over relatively short-term periods. However, accuracy of this method will increase significantly when very high resolution become possible. An advantage of this method is that it can be used for simulation of 3-D rotational motion of viscous fluid even for non-single-value interface. The simulation of nonlinear unsteady potential flow with a free surface began with the development of the Eulerian–Lagrangian boundary integral equations approach by Longuet-Higgins and Cokelet (1976) for steep overturning waves. The instability of waves was generated by asymmetric pressure applied on a surface. This method, in principle, may be generalized for 3-D motion, but it needs the considerable computational resources. A motion with a single-value 1-D and 2-D interface is readily simulated using simplest surface-following coordinates  $(x, y, z - \eta(x, y, t))$  where  $(x, y, z)$  are Cartesian coordinates and  $\eta$  is a surface elevation (Chalikov 1978). This system of coordinates is unsteady and non-orthogonal, so equations of motion become complicated. Still, this method was effectively applied for simulation of interaction of waves with a shear flow by Dimas and Triantafyllou (1994). Evidently, this approach may be joined with the MAC method applied locally in the intervals with large steepness. Waves on finite depth have been investigated by transforming the volume occupied by fluid into a rectangular domain (Dommermuth 1993). Much more complicated surface-following transformations have been constructed even for the case of a multiple-valued surface (Thompson and Warsi 1982). Grid method was generalized with adaptive grids (e.g., Fritts et al. 1988) and in finite-volume approach (Farmer et al. 1993).

The long-term simulations of a nonlinear multi-mode wave field is difficult to perform, since the numerical schemes based on the initial Euler equations fails to provide sufficient accuracy for treating the nonlinearity of wave motion. The main source of errors is primarily due to finite-difference presentation of the vertical structure of the flow when waves with different wave numbers are present. Thus, the theoretical and numerical investigations of surface gravity waves are usually based on the equations for potential flow with a free surface. In this case, the flow is fully determined by the form of the surface and three-dimensional velocity potential. The potentiality assumption idealizes, of course, the phenomenon, since actual wave motion is both rotational and turbulent.

However, many observed properties of surface waves are reproduced well on a basis of a potential approach. For example, it is well known that even linear wave theory gives the estimation of phase velocity with accuracy of the order of 1 %. The numerical methods for inviscid free-surface flow have been reviewed by Mei (1978), Yeung (1982), and Hyman (1984), and for viscous flows by Floryan and Rasmussen (1989). The review of numerical methods for incompressible nonlinear free-surface flow was presented by Tsai and Yue (1996).

The main advantage of potential motion is that the system of Euler equations is reduced to Laplace equation with two nonlinear boundary conditions. However, the solution of the problem if surface wave motion is complicated by the requirement to

apply the kinematic and dynamic boundary conditions (both nonlinear) on the free surface, the location of which is unknown at any given moment. Some attempts have been made previously to reproduce the evolution of waves in Cartesian coordinate system (e.g., Prosperetti and Jacobs 1983), but such technique is inapplicable to long-term simulation of waves. Note that applying of this approach is unavoidable when surface loses its non-single-value properties (when wave breaks), but in his case, the simulation can be done only over very short interval less than one wave period (e.g., Iafrati 2009). A more feasible approach is based on a formulation of the governing equation in a surface-following coordinate system; the simplest technique uses the ‘height’ accounted from surface along with Cartesian coordinates in the horizontal. However, this does not eliminate all the problems since the Laplace equation is transformed into a general elliptic equation. This equation was solved in 2-D case by Chalikov and Liberman (1991) by iteration method. Another approach is based on expansion of velocity potential was developed by Watson and West (1975) and Dommermuth and Yue (1987).

All above-cited works considered the 2-D flow with a free surface. Here is appropriate to make clear some terminology. We will call the flow and model as 2-D flow or model when we consider the motion in vertical plane ( $x, z$ ); the waves taken as surface phenomenon are reasonable to call 1-D or unidirected waves. The unidirected waves often can be considered as a good approximation of wave field with very narrow angle distribution. In some cases when 2-D model is reduced to 1D model, it is also possible to call such model as one-dimensional. Consequently, the 3-D model describes the 3-D stricture of flow and 2-D surface waves.

The complexity of wave modeling depends on additional assumptions. The conditions of periodicity simplifies significantly the construction of model since in such case is possibly to use the Fourier presentation for construction of numerical scheme. This assumption works well when the domain can be considered as a small part of large domain with slowly changing over space integral characteristics. Periodic modes usually use the precise Fourier transform method, so they are well suited for long-term numerical simulation of wave field transformation due to nonlinearity, input, and dissipation of energy. For non-periodic processes, such as waves in restricted domain or waves above non-periodic bottom topography, the Fourier presentation is inapplicable and numerical schemed should be based on finite-difference presentations. Generally, such models are not exact compared with models based on Fourier presentation, but in most cases the finite-difference models consider the short-lasting processes when high accuracy is not needed.

The book devoted to investigation of periodic wave field only. At present, two different models use the principal 2-D fully nonlinear equations for potential flow with a free surface: a numerical model based on a boundary integral formulation for 2-D problem was developed by Vinje and Brevig (1981), Baker et al. (1982), and Roberts (1983). This method was used by Tanaka et al. (1987), who studied the instability and breaking of a solitary wave. Dommermuth and Yue (1987) compared the solution based on Cauchy integral method with precise measurements in the experimental wave tank and obtained good agreement. The boundary integral method was extended by Dold and Peregrine (1986), described in detail by Dold

(1992), and a model based on conformal mapping. Actually, Dold's model was one of the first models for surface waves simulation based on fluid mechanics equations, opposite to numerous approaches using simplified, severely truncated, or crippled 1-D equations (see information in reviews by Tsai and Yue (1996), and Kharif and Pelinovsky (2003). It is interesting that the sophisticated numerical analysis was often used also for solution of substitute 1-D equations. It remains unclear, what those efforts have been undertaken for, since the tiny initial 1-D equations could be solved easily with the highest accuracy at least 25 years ago? The Dold's (1992) approach has been successfully used for simulation of nonlinear group effects (Henderson et al. 1999), for investigation of many problems including wave breaking (Song and Banner 2002). However, later it was found that a simpler and more precise scheme could be constructed on a basis of conformal mapping. For the *stationary problem*, the mapping represents a classical complex variable method (e.g., Crapper 1957, 1984), originally developed by Stokes (1847). For the stationary problem, the method employs the velocity potential  $\Phi$  and the stream function  $\Psi$  as independent variables. In fact, the approach based on *non-stationary* conformal mapping had been formulated even before it was used for numerical integration. It had been introduced by Whitney (1971) and Ovsyannikov (1973), and later, it was considered by Kano and Nishida (1979), Fornberg (1980). Tanveer (1991, 1993) used that approach for investigation of Rayleigh–Taylor instability and generation of surface singularities. However, no authors of those works used conformal transformation for simulation of long-term multi-mode periodic wave dynamics. Such 2-D model was completed in 1992, when a systematic use of the new approach to different problems was initiated. A numerical scheme based on conformal mapping (and its validation), as well as the results of long-term simulations, were presented at the ONR meeting held in Arizona in 1994a (see also Chalikov and Sheinin 1994b, c). The scheme for arbitrary depth was described in detail by Chalikov and Sheinin 1996, 1998, hereafter ChSh). More details for the case of shallow water were given by Sheinin and Chalikov (2001). Later, the method developed was used with some minor modifications by Zakharov et al. (2002, 2006), to demonstrate certain nonlinear properties of steep waves.

The non-stationary conformal mapping for finite depth allows rewriting of the principal equations of potential flow with a free surface in a surface-following coordinate system. The Laplace equation retains its form, while the boundaries of the flow domain (i.e., the free surface and, in the case of finite depth, the bottom) are coordinate surfaces in the new coordinate system. Accordingly, the velocity potential in the entire domain receives a standard representation based on its Fourier expansion on the free surface. As a result, the hydrodynamic system of equations (not simplified) is represented by two simple evolutionary equations which can be solved numerically in a straightforward way and used for theoretical investigations. The assumption of potentiality simplifies the approach so significantly that the numerical scheme does not require any finite-difference approximations since the derivatives can be calculated precisely using the Fourier presentations, while nonlinearities can be approximated on a dense grid with the well-estimated accuracy. For restricted order of nonlinearity, this method is also precise and depends on

a number of digits assigned for calculations. The model represents a rarity in geophysical fluid dynamics (though the potential one), when a real process can be simulated with nearly computer accuracy. This statement can be fully correct if surface steepness is not too high. Increase of local steepness often results in developing of instability and even overturning of sharp crests. Formally, conformal mapping exists up to the moment when an overturning volume of water touches the surface. In such an imaginary evolution, the number of Fourier modes required increases up to infinity. If some special measures (smoothing, see, e.g., Dold 1992) are not taken, the calculations normally terminate much earlier, due to strong crest instability (Longuet-Higgins and Tanaka 1997) shortly manifesting itself by separation of the falling volume into two phases. This phenomenon is obviously non-potential. Hence, as in many branches of geophysical fluid dynamics, some special measures (which are probably arrogant from the point of view of potential theory) must be taken to prevent numerical instabilities, at the same time considering the physical consequences of such events.

Naturally, the method of conformal variables cannot be extended for a case of three-dimensional waves. Majority of the models designed for investigation of the three-dimensional wave dynamics are based on simplified equations. Overall, it is unclear which effects are missing in such simplified models. The most developed methods are based on the full three-dimensional equations and surface integral formulations (Clamond and Grue 2001; Clamond et al. 2005; Fochesato et al. 2006). These methods can be applied both to periodic and non-periodic flows. The main advantage of such methods is their high accuracy. The methods do not impose any restrictions on wave steepness, so they can be used for simulations of the waves that even approach the breaking (Grilli et al. 2001). However, these methods seem to be quite complicated. The application of method was illustrated by simulations of relatively simple wave fields, and it is unlikely that it can be applied to simulation of a long-term evolution of a large-scale multi-mode wave field. Implementation of a multi-pole technique for a general problem of the sea wave simulations obviously leads to considerable algorithmic difficulties.

Another method for 3-D waves includes an elliptic boundary layer problem solved by the finite-difference methods. Such approaches to simulation of the unsteady free-surface flows based on the full equations have been under development for at least three decades (see, e.g., Asaithambi 1987; Haussling and Van Eseltine 1975; Yeung 1982). Related applications were later described by Bingham and Zhang (2007). The main advantage of these methods is that it is based on initial equations being transformed into the surface-following coordinate system. The Laplace-type equation obtained by transformation into the sigma-coordinate system was solved in Cai et al. (1998) by the iterative conjugate gradient method, using the three-dimensional finite element discretization. The finite-difference multi-grid model for a 3-D flow was developed in Engsig-Karup et al. (2009). All of the papers of this group were mostly dedicated to technical applications of the water wave theory, for example, to calculations of a dynamic load on submerged bodies, or to simulation of wave dynamics in a domain with a complicated shape. A long-term evolution of such flows was not simulated; this is why the exact

conservation of energy was not the main priority of such models. Applicability of these models to investigations of the nonlinear properties of sea waves is also uncertain.

This book is devoted to numerical modeling of 1-D and 2-D periodic surface waves and different application of models. Main attention is given to nonlinear properties of waves: statistical characteristics of waves, Benjamin–Feir instability, formation of extreme (freak) waves, the process of wind–wave interaction, and wave–turbulence interaction. The attempts of numerical modeling of wave field development have been made.

# Chapter 2

## Two-Dimensional Wave Model

**Abstract** A method for numerical investigation of the nonlinear wave dynamics based on direct hydrodynamical modeling of the 1-D potential periodic surface waves is described. The model is a part of an interactive windwave model. Using non-stationary conformal mapping, the principal equations are rewritten in a surface-following coordinate system and reduced to two simple evolutionary equations for elevation and velocity potential of surface. Fourier expansion is used to approximate these equations.

### 2.1 2-D Equations of Potential Motion with Free Surface

The 1-D model is based on a non-dimensional form of the principal 2-D equations for potential waves written in the Cartesian coordinates, i.e., the Laplace equation for the velocity potential  $\Phi$  (Table 2.1)

$$\Phi_{xx} + \Phi_{zz} = 0 \quad (2.1.1)$$

and two boundary conditions at free surface  $h = h(x, t)$  the kinematic condition

$$h_t + h_x \Phi_x - \Phi_z = 0 \quad (2.1.2)$$

and the Lagrange integral

$$\Phi_t + \frac{1}{2} (\Phi_x^2 + \Phi_z^2) + h + p_0 - \sigma h_{xx} (1 + h_x^2)^{-3/2} = 0, \quad (2.1.3)$$

where  $p_0$  is external pressure (the independent variables in subscripts denote partial differentiation with respect to these variables). The equations are solved in the domain

$$-\infty < x < \infty, \quad -H \leq z \leq h(x, t), \quad (2.1.4)$$

**Table 2.1** Characteristics of numerical experiments

Run no.	1	2	3	4	5	6
Initial conditions	$h = 0.5 \cos x$	$h = 0.3 \sin x$	$h = 0.28 \cos x$	$h = 0.27 \cos x$	$h = 0.01(\cos 1.0x + \cos 11x)$	$h = 0.04 \cos(5x + \sin x)$
Resolution	$M = 3072,$ $N = 13824$	$M = 6144,$ $N = 27648$	$M = 3072,$ $N = 13824$	$M = 1536,$ $N = 6912$	$M = 12288, N = 55296$	$M = 3072, N = 13824$
Time step	$\Delta t = 5 \times 10^{-4}$	$\Delta t = 2.5 \times 10^{-4}$	$\Delta t = 5 \times 10^{-4}$	$\Delta t = 10^{-3}$	$\Delta t = 5 \times 10^{-4}$	$\Delta t = 10^{-3}$
Integration time	$T = 3.15$	$T = 5.58$	$T = 7.11$	$T = 500$	$T = 51.01$	$T = 37.44$

where  $H$  is either a finite depth or infinity. The variables  $\Phi$  and  $h$  are considered to be periodic with respect to  $x$ :

$$\Phi(x + 2\pi, z, t) = \Phi(x, z, t), \quad h(x + 2\pi, t) = h(x, t), \quad (2.1.5)$$

and normal velocity at the bottom is assumed to be zero:

$$\Phi_z(x, z = -H, t) = 0. \quad (2.1.6)$$

Equations (2.1.1)–(2.1.3) are written in a non-dimensional form with the following scales: length  $L$ , where  $2\pi L$  is dimensional period in the horizontal, time  $L^{1/2}g^{-1/2}$ , and the velocity potential  $L^{3/2}g^{1/2}$  ( $g$  is acceleration of gravity). Pressure is normalized by water density (so the pressure scale is  $Lg$ ). The last term in Eq. (2.1.3) describes the effect of surface tension, and

$$\sigma = \frac{\Gamma}{gL^2} \quad (2.1.7)$$

is a non-dimensional parameter ( $\Gamma = 8 \times 10^{-5} \text{ m}^3\text{s}^{-2}$  is the kinematic coefficient of surface tension for water).

## 2.2 Conformal Coordinates and Equations in the Conformal Coordinates

System (2.1.1)–(2.1.3.) should be solved as an initial value problem for the unknown functions  $\Phi$  and  $h$  with the given initial conditions  $\Phi(x, z = h(x, t = 0))$  and  $h(x, t = 0)$ . Note that though Eqs. (2.1.2) and (2.1.3) are written for a free surface, there are no straightforward ways to reduce the problem to a 1-D problem, since, to evaluate  $\Phi_z$  the Laplace Eq. (2.1.1) should be solved in the domain (2.1.4) with a curvilinear upper boundary that can be an arbitrary function of  $x$ . This difficulty makes integration of the system in the Cartesian coordinates either not sufficiently accurate or too expensive computationally. So, for the time periods much greater than the timescale, this way of solution is not efficient. [It is perhaps even more problematic to design an efficient numerical scheme for the stationary version of system (2.1.1)–(2.1.3)].

To make a numerical solution feasible, we introduce a time-dependent surface-following coordinate system that conformally maps the original domain (2.1.4) onto the strip

$$-\infty < \xi < \infty, \quad -\tilde{H} \leq \zeta < 0 \quad (2.2.1)$$

with the periodicity conditions given as

$$x(\xi + 2\pi, \zeta, \tau) = x(\xi, \zeta, \tau) + 2\pi, \quad z(\xi + 2\pi, \zeta, \tau) = z(\xi, \zeta, \tau) \quad (2.2.2)$$

where  $\tau$  is the new time coordinate,  $\tau = t$ .

According to a complex variable calculus, the conformal mapping exists and is unique up to an additive constant for  $x$ . Note that for the stationary problem this mapping represents a classic complex variable method (e.g., Crapper 1957, 1984) originally developed by Stokes (1847) who employed the velocity potential  $\Phi$  and the stream function  $\Psi$  as independent variables. In this case, it can be shown that  $\Phi = -c_b \zeta + \Phi_0$  and  $\Psi = -c_b \zeta + \Psi_0$  where  $-c$  is the mean velocity at the bottom, while  $\Phi_0, \Psi_0$  are constants. In a non-stationary case, the mapping is clearly time-dependent, and no analog of the last relations holds.

It is easy to show that, due to the periodicity condition (2.2.2), the required conformal mapping can be represented by Fourier series:

$$x = \xi + x_0(\tau) + \sum_{-M \leq k < M, k \neq 0} \eta_{-k}(\tau) \frac{\cos k(\zeta + \tilde{H})}{\sin kH} \vartheta_k(\xi), \quad (2.2.3)$$

$$z = \zeta + \eta_0(\tau) + \sum_{-M \leq k < M, k \neq 0} \eta_k(\tau) \frac{\sinh k(\zeta + \tilde{H})}{\sinh k\tilde{H}} \vartheta_k(\xi), \quad (2.2.4)$$

where  $\eta_k$  are the coefficients of Fourier expansion of free surface  $\eta(\xi, \tau)$  with respect to the new horizontal coordinate

$$\eta(\xi, \tau) = h(x(\xi, \zeta = 0, \tau)) = \sum_{-M \leq k < M} \eta_k(\tau) \vartheta_k(\xi), \quad (2.2.5)$$

$\vartheta_k$  denotes the function

$$\vartheta_k(\xi) = \begin{cases} \cos k\xi, & k \geq 0 \\ \sin k\xi, & k < 0 \end{cases}. \quad (2.2.6)$$

$M$  is a truncation number. The non-traditional presentation of Fourier coefficients with definition (2.2.6) is, in fact, convenient for calculations, since

$$(\vartheta_k)_\xi = k\vartheta_{-k}, \quad \frac{\partial}{\partial \xi} \sum (a_k \vartheta_k) = - \sum k a_{-k} \vartheta_k. \quad (2.2.7)$$

Note that in presentation (2.2.6) the indices  $k \geq 0$  refer to the real part of the complex presentation (i.e., coefficients at COS), while  $k > 0$  refer to the imaginary part (i.e., the coefficients at SIN with an opposite sign). The Fourier coefficients  $a_k$  form an array  $a(-M : M)$ , which makes convenient compact programming.

The time-dependent  $x_0(\tau)$  can be chosen arbitrarily, though it is convenient to assume

$$x_0(\tau) = 0 \quad (2.2.8)$$

The lower boundary condition cannot be chosen arbitrarily, since the relation

$$z(\xi, \zeta = -\tilde{H}, \tau) = -H \quad (2.2.9)$$

must hold, which yields after substituting expansion (2.2.4)

$$\tilde{H} = H + \eta_0(\tau). \quad (2.2.10)$$

Since  $\eta_0$  is determined by the Fourier expansion (2.2.5) and is generally an unknown function of time,  $\tilde{H}$  is also time-dependent. The conformal coordinates yield the Cauchy–Riemann conditions

$$x_\xi = z_\xi, \quad x_\zeta = -z_\xi. \quad (2.2.11)$$

Simple derivations show that Laplace equation retains its form

$$\Phi_{\xi\xi} + \Phi_{\zeta\zeta} = 0. \quad (2.2.12)$$

From conditions  $x_x = 1, x_z = 0, z_x = 0, z_z = 1$ , it follows that

$$\begin{aligned} \zeta_z &= J^{-1}x_\zeta = J^{-1}z_\xi = \xi_x, \\ -\zeta_x &= -J^{-1}x_\xi = J^{-1}z_\zeta = \xi_z, \end{aligned} \quad (2.2.13)$$

where

$$J = x_\xi^2 + z_\xi^2 = x_\zeta^2 + z_\zeta^2 \quad (2.2.14)$$

is the Jacobian of the transformation.

Since  $\eta$  does not change along  $z$ , i.e.,  $\partial\eta/\partial z = 0$ , it follows that

$$\eta_\xi \xi_z + \eta_\zeta \zeta_z = \eta_\xi \xi_z + \eta_\zeta \xi_x = 0. \quad (2.2.15)$$

So

$$\eta_\zeta = -\eta_\xi \xi_z \xi_z^{-1} = z_\xi^2 x_\xi^{-1}, \quad (2.2.16)$$

Note that if the differentiation is taken over  $\xi$  or  $\tau$ , we can replace functions  $\eta_\tau$  and  $\eta_\zeta$  by  $z_\tau$  and  $z_\xi$ , respectively, since both  $\eta$  and  $z(\zeta = 0)$  represent the elevation of surface  $\zeta = 0$ . Consider the terms  $\eta_t$  and  $\eta_x$  in the left-hand side of Eq. (2.1.2)

$$\eta_t = z_\tau + z_\xi \xi_t + \eta_\zeta \zeta_t = z_\tau + z_\xi \xi_t - z_\xi^2 x_\xi^{-1} \zeta_t, \quad (2.2.17)$$

$$\eta_x = \eta_\xi \xi_x + \eta_\zeta \zeta_x = z_\xi J^{-1}(x_\xi + z_\xi^2 x_\xi^{-1}) = z_\xi x_\xi^{-1} \quad (2.2.18)$$

Then, considering that

$$\begin{aligned} x_t &= x_\tau + x_\xi \xi_t + x_\zeta \zeta_t = x_\tau + x_\xi \xi_t - z_\xi \zeta_t \\ z_t &= z_\tau + z_\xi \xi_t + z_\zeta \zeta_t = z_\tau + z_\xi \xi_t + x_\xi \zeta_t \end{aligned} \quad (2.2.19)$$

and  $x_t = 0, z_t = 0$  we obtain the equations to define  $\xi_t$  and  $\zeta_t$ :

$$-x_\xi \xi_t + z_\xi \zeta_t = x_\tau, \quad (2.2.20)$$

$$-z_\xi \xi_t - x_\xi \zeta_t = z_\tau. \quad (2.2.21)$$

Finally, we obtain

$$\xi_t = J^{-1}(-x_\xi x_\tau - z_\xi z_\tau), \quad (2.2.22)$$

$$\zeta_t = J^{-1}(-x_\xi z_\tau - z_\xi x_\tau). \quad (2.2.23)$$

The derivatives of the velocity potential  $\Phi_x$  and  $\Phi_z$  take the following form

$$\Phi_x = J^{-1}(x_\xi \Phi_\xi - z_\xi \Phi_\zeta), \quad (2.2.24)$$

$$\Phi_z = J^{-1}(z_\xi \Phi_\xi - x_\xi \Phi_\zeta). \quad (2.2.25)$$

Inserting (2.2.17), (2.2.18), (2.2.22), (2.2.23), and (2.2.24) in (2.1.2) following some elementary calculations, we obtain the simple kinematic condition written in conformal variables

$$x_\xi z_\tau - z_\xi x_\tau = \Phi_\zeta, \quad (2.2.26)$$

After inserting the expressions for  $x_\tau$  and  $z_\tau$  into Eq. (2.2.23), we obtain

$$\zeta_t = J^{-1} \Phi_\zeta. \quad (2.2.27)$$

Further simplification can be done taking into account that functions  $x_\tau$  and  $z_\tau$  at  $k \neq 0$  satisfy the Cauchy–Riemann conditions. Considering the connections between two pairs of the coefficients (2.2.22) and (2.2.23), it can be shown that the functions  $\xi_t$  and  $\zeta_t$  for  $k \neq 0$  are connected by the Cauchy–Riemann relations (see ChSh, Chalikov and Sheinin 2005),

$$(\xi_t)_\xi = (\zeta_t)_\zeta, \quad (\xi_t)_\zeta = -(\zeta_t)_\xi, \quad (2.2.28)$$

while the Fourier coefficients  $(\xi_t)_k$  and  $(\zeta_t)_k$  for functions  $\xi_t$  and  $\zeta_t$  for  $k \neq 0$  are connected by the relation (which is called the Hilbert transform)

$$(\xi_t)_k = (\zeta_t)_{-k} \coth k\tilde{H}. \quad (2.2.29)$$

and the Fourier coefficient for  $(\xi_t)_0$  is equal to

$$(\xi_t)_0 = \frac{1}{2} \sum_{-M \leq k \leq M, k \neq 0} k \eta_{-k} \sinh^{-2} k\tilde{H} \quad (2.2.30)$$

Actually, the relation (2.2.29) follows from the fact that definition of the new coordinates is based on the same function  $\eta(\xi)$ . So, the second of the Eq. (2.2.20) can be considered as an equation for calculation of evolution of surface  $z(\tau)$  where variable  $\zeta_t$  is calculated using Eq. (2.2.24), while variable  $\xi_t$  is calculated with (2.2.26) and (2.2.27).

After transformation to the conformal coordinates, the time derivative  $\Phi_t$  in dynamic condition (2.1.3) takes the form

$$\Phi_t = \Phi_\tau + \xi_t \Phi_\xi + \zeta_t \Phi_\zeta, \quad (2.2.31)$$

then using (2.2.21), we obtain

$$\Phi_t = \Phi_\tau + J^{-1} \Phi_\xi (-x_\xi z_\tau - z_\xi x_\tau) + J^{-1} \Phi_\zeta (-x_\zeta z_\tau + z_\zeta x_\tau) \quad (2.2.32)$$

The last term describing an effect of surface tension takes the form  $\sigma J^{-3/2} (-x_{\xi\xi} z_\xi + z_{\xi\xi} x_\xi)$ .

According to (2.2.24) and (2.2.25),

$$\Phi_x^2 + \Phi_y^2 = \Phi_\xi^2 + \Phi_\zeta^2 \quad (2.2.33)$$

Finally, after use of (2.2.32), (2.2.33), (2.2.23), (2.2.26), and (2.2.27) we obtain the system of evolutionary equations in the conformal coordinates

$$z_\tau = x_\xi \xi_t + z_\xi \zeta_t, \quad (2.2.34)$$

$$\varphi_\tau = \xi_t \varphi_\xi - \frac{1}{2} J^{-1} (\varphi_\xi^2 - \Phi_\xi^2) - z - p_0 + \sigma J^{-3/2} (-x_{\xi\xi} z_\xi + z_{\xi\xi} x_\xi), \quad (2.2.35)$$

where  $\varphi$ (lower case) denotes the velocity potential on the surface  $z = \eta$ .

The boundary condition (2.1.6) is rewritten as

$$\Phi_\zeta(\xi, \zeta = -\tilde{H}, \tau) = 0 \quad (2.2.36)$$

The solution of Laplace equations (2.2.33) with the boundary condition (2.2.36) is yielded by Fourier expansion

$$\Phi(\xi, \zeta, \tau) = \sum_{-M \leq k \leq M} \varphi_k(\tau) \frac{\cosh k(\zeta + \tilde{H})}{\cosh k\tilde{H}} \vartheta_k(\xi) \quad (2.2.37)$$

where  $\varphi_k(\tau)$  are the Fourier coefficients for the surface potential  $\varphi$ . Strictly speaking, the values of  $\varphi$  cannot be considered as a boundary condition for the Laplace Eq. (2.2.34) which must use the instantaneous conditions (2.2.35) and (2.2.36). However, we use some sort of a time-splitting method, assuming that the vertical derivative  $\Phi_\zeta$

$$\Phi_\zeta(\xi, 0, \tau) = \sum_{-M \leq k \leq M} k \varphi_k(\tau) \tanh k\tilde{H} \vartheta_k(\xi) \quad (2.2.38)$$

can be taken from the previous time step. In this case, we can consider Eqs. (2.2.34) and (2.2.35) as the evolutionary equations for variables  $z(\xi, \tau)$  and  $\varphi(\xi, \tau)$ . Indeed, this assumption dramatically simplifies the problem.

Thus, the original system of equations is transformed into two simple 1-D Eqs. (2.2.34) and (2.2.35) and diagnostic relations (2.2.27), (2.2.29), (2.2.30). Both spatial derivatives of  $\Phi$  are obtained by differentiating the series (2.2.37) and can be solved using the Fourier transform method. These equations allow a precise investigation of the 1-D periodic potential waves in broad ranges of the two non-dimensional parameters such as depth  $H$  and capillarity  $\sigma$ .

For deep water ( $H = -\infty$ ), the coefficients in expansions (2.2.37) and (2.2.38) become simpler. The domain (2.2.1) turns into semi-plane  $\zeta < 0$  ( $\zeta \rightarrow -\infty$ ), the condition which replaces (2.2.36). The conformal mapping (2.2.3) and (2.2.4) acquires the form

$$x = \xi + \sum_{-M \leq k \leq M, k \neq 0} \text{sign}(k) \eta_{-k}(\tau) \exp(|k|\zeta) \vartheta_k(\xi), \quad (2.2.39)$$

$$z = \zeta + \sum_{-M \leq k \leq M, k \neq 0} \eta_k(\tau) \exp(|k|\zeta) \vartheta_k(\xi), \quad (2.2.40)$$

the solution of Laplace equations (2.2.12) becomes

$$\Phi(\xi, \zeta, \tau) = - \sum_{-M \leq k \leq M} \phi_k(\tau) \exp(|k|\zeta) \vartheta_k(\xi), \quad (2.2.41)$$

and operator (2.2.29) takes the form

$$(\zeta_t)_k = \text{sign}(k)(\zeta_t)_{-k} \quad (2.2.42)$$

## 2.3 Numerical Solution of Potential Equations

For spatial approximation of the system (2.2.34) and (2.2.35), we use a Galerkin-type (or ‘spectral’) method based on Fourier expansion of the prognostic variables with the finite truncation number  $M$ . The problem is thus reduced to a system of ordinary differential equations for the Fourier coefficients  $\eta_k(\tau), \phi_k(\tau), -M \leq k \leq M$ :

$$(\eta_k)_t = H_k(\eta_{-M}, \eta_{-M+1}, \dots, \eta_M, \phi_{-M}, \phi_{-M+1}, \dots, \phi_M), \quad (2.3.1)$$

$$(\phi_k)_t = F_k(\eta_{-M}, \eta_{-M+1}, \dots, \eta_M, \phi_{-M}, \phi_{-M+1}, \dots, \phi_M), \quad (2.3.2)$$

where  $H_k, F_k$  are the Fourier expansion coefficients, respectively, for the right-hand sides of Eqs. (2.2.34) and (2.2.35) as functions of  $\xi$ .

All the calculations described in this book use the so-called Fourier transform method. To calculate  $H_k$  and  $F_k$  as functions of the prognostic variables  $\eta_k$  and  $\phi_k$ , differentiation of the Fourier series is used (spatial derivatives are thus calculated exactly) and the nonlinearities are calculated (Orszag 1970; Eliassen et al. 1970) on a spatial grid. If  $Y(u(\xi), v(\xi), w(\xi))$  is a nonlinear function of its arguments which are represented by their Fourier expansion, the grid point values  $u(\xi_i), v(\xi_i), w(\xi_i)$  are first calculated, i.e., the inverse Fourier transforms are performed; after that  $Y_i(u(\xi_i), v(\xi_i), w(\xi_i))$  are calculated at each grid point. Finally, the Fourier coefficients  $Y_k$  of the function  $Y$  are found by direct Fourier transform. Here,  $\xi_i = 2\pi(j-1)/N$  where  $N$  is a number of grid points. This approach is exploited extensively in the geophysical fluid dynamics, particularly, in the global atmospheric modeling.

For the method to be a purely Galerkin one, i.e., to ensure the minimum mean square approximation error, the Fourier coefficients  $H_k, F_k$  must be calculated exactly for  $-M \leq k \leq M$ . For this purpose, we must choose

$$N > (v+1)M \quad (2.3.3)$$

where  $v$  is the maximum order of nonlinearity. Since the right-hand sides of Eqs. (2.2.34) and (2.2.35) include division by the Jacobian  $J$ , the nonlinearity is of infinite order so that the above condition for  $N$  cannot be met. However, the numerical integration shows that if to choose a value of  $N$  providing exact evaluation of the cubic nonlinearities [ $v = 3$  in (2.3.3)], a further increase of  $N$  (with fixed  $M$ ) does not affect the numerical solution. For the results presented in this book,  $N = 4M$  was taken.

Potential waves in absence of the input energy and non-potential disturbances are theoretically conservative, i.e., the sum of the potential and kinetic energies calculated by integration over the whole domain should remain constant. This property cannot be observed in a numerical model because of formation of the nonlinear flux of energy from the low to high wave numbers and partly because of the errors of time integration scheme. The total energy in a numerical model remains constant on condition that the spectral domain is very broad; hence, the flux of energy into a high wave number part of the spectrum is not restricted. For a finite size of the domain, the flux of energy into the truncated part of the spectrum always occurs. A corresponding decrease of the total energy can be considered as dissipation. Such dissipation also exists at natural conditions, i.e., the nonlinear interactions generate a flux of energy to the high-frequency waves which, in turn, quickly dissipate. However, high the spectral resolution might be, for the long-term simulations of strongly nonlinear waves an energy flux into the severed part of the spectrum ( $|k| > M$ ) must be parameterized; otherwise, the spurious energy accumulation at large wave numbers can corrupt the numerical solution. To achieve stability, simple dissipation terms were added to the right-hand sides of Eqs. (2.2.34) and (2.2.35) in Fourier domain:

$$\frac{\partial \eta_k}{\partial \tau} = E_k - \mu_k \eta_k, \quad (2.3.4)$$

$$\frac{\partial \varphi_k}{\partial \tau} = F_k - \mu_k \varphi_k \quad (2.3.5)$$

( $E_k$  and  $F_k$  are the Fourier components of the right-hand sides of the equations) and

$$\mu_k = \begin{cases} rM \left( \frac{|k|-k_d}{M-k_d} \right)^2 & \text{if } |k| > k_d, \\ 0 & \text{if } |k| \leq k_d \end{cases} \quad (2.3.6)$$

where  $k_d$  varies within the range of  $M/2 < K_d < 9M/10$  (depending on the model resolution), and  $r = 0.25$ . The algorithm (2.3.5)–(2.3.7) was suggested and validated in ChSh. The sensitivity of the results to the reasonable variations of  $r$  is low. This sort of dissipation (which we call ‘tail dissipation’) effectively absorbs the energy if wave numbers are close to the truncation number  $M$ , the longer waves being virtually intact. This is why the total effect of ‘tail dissipation’ is very small. However, this algorithm provides stability. Note that parameterization (2.3.5)–(2.3.7) describes the real process. To avoid smoothing, a similar model (Zakharov et al. 2002) uses the number of modes  $M = 1,000,000$ , which can be hardly considered as a rational solution of the problem. The spectrum in a finite domain cannot be conservative, since the flux of energy into a high wave number part of the spectrum always exists due to the nonlinear interactions. If we wish to reproduce the quasi-stationary regime, such loss of energy should be compensated by the corresponding energy input. We call this regime ‘quasi-adiabatic.’

For time integration, the fourth-order Runge–Kutta scheme was used. The choice of time step requires special consideration. For any time integration scheme, the stability criterion has the form:  $\Delta\tau \leq C\omega_{\max}^{-1}$  (if dissipation does not play a major role) where  $\Delta\tau$  is a time step, and  $\omega_{\max}$  is the maximum frequency of waves. The linear frequency can be found from the linear dispersion relation

$$\omega_{\max} = c_k k = \sqrt{(k + \sigma k^3) \tanh kH} \quad (2.3.7)$$

where  $\omega_{\max} = \omega_M$ . However, this approach works only for the essentially linear waves (i.e., for the waves with very small amplitudes). In most cases, strong nonlinear effects produce quite a chaotic movement of high-frequency waves, and thus, the dispersion relation (2.3.7) becomes inapplicable. Sometimes, the time step is restricted directly by the growing right sizes of Eqs. (2.2.34) and (2.2.35). This is why in most cases the time step  $\Delta\tau$  must be chosen empirically on the basis of stability considerations and the accuracy of energy conservation. For example, for the number of modes  $M = 1000$ , the time step  $\Delta\tau$  equals 0.001.

The main difficulty in construction of a numerical method for non-stationary potential waves is how to deal with the vertical dimension which, in order to simplify the problem, must be eliminated from the prognostic equations which are to be solved by numerical time integration. This problem was avoided in the numerical scheme by Chalikov and Liberman (1991), where the iterative algorithm calculation of Fourier coefficients for the velocity potential in the fixed coordinate system was developed. Such model allowed obtaining some important results, but the scheme turned out to be too complicated and numerically non-effective. The non-stationary surface-following conformal mapping used for construction of the numerical scheme for 1-D full equations is probably the most effective way to resolve this problem and make the model capable for long-term multi-mode simulations.

## 2.4 Conclusion

The method of conformal mapping developed by Stokes (1847) for stationary potential waves was extended to the non-stationary case where the conformal transformation becomes time-dependent and the surface-following coordinates are no longer the velocity potential and stream function. The method proved to be efficient because the original system consisting of Laplace equation and two non-linear boundary conditions on curvilinear surface is reduced without any simplifications to a system of two one-dimensional non-stationary equations. Like in the Cartesian coordinates, the dependent variables are the elevation and velocity potential on the surface; however, their dependence on the Cartesian horizontal coordinate  $x$  is represented parametrically via the new coordinate  $\xi$ . The Eq. (2.2.26) contains both derivatives over time  $z_\tau$  and  $x_\tau$ , but this inconvenience

can be easily eliminated due to the fact that the coordinate transformation is based on the same function  $\eta$ . The transformed system may be solved by numerical integration which is done efficiently by calculation of nonlinearities via the Fourier transform method. The system can be also used for analytical investigations based on various methods developed for the original system (see references in Chap. 1), an important advantage being that the problem of extrapolation for the velocity potential in the vertical does not exist. The 2-D model for periodic surface waves is probably the most exact model of the geophysical fluid dynamics describing real processes.

# **Chapter 3**

## **Stationary Solutions of Potential Equations**

**Abstract** For stationary equations, the proposed approach coincides with the conventional complex variable method. For this case, the numerical algorithms for solution of gravity (Stokes) and gravity-capillary wave equations are proposed, and the examples of numerical solutions are given. The results suggest that gravity-capillary waves do not approach Stokes waves as the capillarity coefficient decreases. Both stationary and non-stationary schemes use Fourier series representation for spatial approximation and the Fourier transform method to calculate the nonlinearities. The main properties of Stokes, gravity-capillary, and capillary waves for infinite depth are discussed. The properties of Stokes waves for finite depth are investigated.

The behavior of nonlinear waves is difficult to investigate analytically on the basis of full (non-simplified) potential equations. Even for the stationary equations exact solutions are known only for a specific case of pure capillary waves at deep water (Crapper's waves, Crapper 1957, 1984). For the case of stationary gravity deep water (Stokes) waves, the construction of analytical expansions for consecutive Fourier coefficients provides only an approximation for the truncated Fourier series and is, actually, a numerical procedure in which an amount of calculations increases sharply with increase of truncation number. As for the general non-stationary wave fields, the analytical investigation is clearly impossible without drastic simplifications which may lead to unpredictable consequences.

The stationary solution of potential equations is interesting not only as a mathematical object. The main role of such equations is that they can serve as a tool for validation of non-stationary models, when used as initial conditions for a non-stationary problem.

### 3.1 The Stationary Form of Equations

For a stationary problem, the method of conformal mapping is a well-known approach based on using the velocity potential  $\Phi$  and stream function  $\Psi$  as the independent variables (e.g., Crapper 1984). It is easy to show that in this case

$$\Phi = -c\xi + \Phi_0, \quad \Psi = c\xi + \Psi_0 \quad (3.1.1)$$

where  $-c$  is the velocity of mean flow,  $\Phi_x = -\Psi_z$  while  $\Phi_z = \Psi_x$  are the horizontal and vertical Cartesian velocity components, respectively, and  $\Phi_0$  and  $\Psi_0$  are constants.

For the stationary version of the system (2.2.34) and (2.2.35), the periodicity condition for  $\Phi$  (which suggests a zero mean flow velocity) must be replaced by a weaker condition of periodicity for velocity components, i.e., the spatial derivatives of  $\Phi$ . In the coordinate system moving with the wave's phase velocity, the mean flow velocity is equal to  $-c$ , and the velocity potential  $\Phi$  is given by the relations (3.1.1) where  $\Phi_0$  can depend on time (since the stationarity is assumed rather for the velocity field than for the velocity potential). Consequently, if the external pressure  $p = 0$ , the system (2.2.34) and (2.2.35) is reduced to one equation written for the surface  $\zeta = 0$ :

$$\frac{1}{2}c^2J^{-1} + z - \sigma J^{-3/2}(-x_{\xi\xi}z_{\xi} + z_{\xi\xi}x_{\xi}) = \alpha, \quad (3.1.2)$$

where  $\alpha = -d\Phi_0/d\tau$ ; and, since the left-hand side of (3.1.2) does not depend on time,  $\alpha$  is a constant (thus, the dependence of  $\Phi_0$  on  $\tau$  can only be linear).

To solve the Eq. (3.1.2) means to find the conformal mapping

$$x(\xi, \zeta) = \xi + \sum_{-M \leq k < M} \eta_k \frac{\cosh k(\zeta + H + \eta_0)}{\sin k(H + \eta_0)} \vartheta_k(\xi) \quad (3.1.3)$$

$$z(\xi, \zeta) = \zeta + \eta_0 + \sum_{-M \leq k < M} \eta_k \frac{\sinh k(\zeta + H + \eta_0)}{\sin k(H + \eta_0)} \vartheta_k(\xi) \quad (3.1.4)$$

for which the upper boundary condition is  $\zeta = 0$ . The lower boundary condition is  $\zeta = \text{const}$  (which is denoted below as  $\tilde{H}$  and which is not preliminarily known). If  $H = \infty$ , then the horizontal derivative of  $\zeta$  tends to zero at  $z \rightarrow -\infty$  which is equivalent to condition  $\lim(z_{\xi}) = 0$ , and is ensured by replacement of the fraction in (3.1.3) and (3.1.4) by  $\exp(k\xi)$ . The horizontal boundary conditions are  $2\pi$ -periodicity.

Since the “mapping depth”  $\tilde{H}$  replaced in (2.2.34) and (2.2.35) according to (2.2.10) is not known, the problem is not yet formally closed. As  $H$  is to be the “true depth,” the mean value over  $x$  of the surface elevation must be zero:

$$\frac{1}{2\pi} \int_0^{2\pi} h(x) dx = \frac{1}{2\pi} \int_0^{2\pi} z(\xi, \zeta = 0) x_\xi(\xi, \zeta = 0) d\xi = 0, \quad (3.1.5)$$

which, in Fourier space, means that

$$\eta_0 + \frac{1}{2} \sum_{-M \leq k \leq M, k \neq 0} k \coth(k(H + \eta_0)) \eta_k^2 = 0. \quad (3.1.6)$$

Similarly,  $\alpha$  in the right-hand side of (3.1.2) is not a prescribed parameter but yet another unknown value to be determined. For the case of deep water, there is a simple expression for  $\alpha$  (see below) that, however, does not hold in a general case. Finding this value should be a part of the numerical procedure. The phase velocity  $c$  is also calculated by the algorithm.

The Eq. (3.1.2) is solved numerically using the Fourier expansions (3.1.3) and (3.1.4) for  $x$  and  $z$  and the corresponding expressions—for their derivatives. Thus, the values to be determined by scheme are the Fourier coefficients  $\eta_k$  and the phase velocity  $c$ .

Note that because  $\sigma$  is a factor in the term of the highest differential order, we may face an effect of singularity for the small  $\sigma$ . Indeed, we should develop two different schemes for the case of pure gravity and gravity-capillary waves. It can be seen that in the latter case the numerical solution does not approach a pure gravity wave as  $\sigma$  decreases. Similarly, the Navier–Stokes equation does not approach the Euler equations when viscosity is going to zero.

## 3.2 Pure Gravity Waves

At  $\sigma = 0$ , the solution of Eq. (3.1.2) describes the pure gravity wave. For the case of infinite depth (Stokes wave), the method based on expansion of the Fourier coefficient for the surface height in power series of wave amplitude was originally proposed by Stokes (1847, 1880) who in his latter work obtained a fifth-order approximation. In recent studies, the method has been further developed into a computer-oriented recursive scheme which produces the consecutive power expansion coefficients; Drennan et al. (1988) carried out the power series calculations up to 170 terms. Later this record was beaten by Dallaston and McCue SW (2010) who calculated 846 terms.

A far more effective method of calculation of the Stokes waves, for both infinite and finite depths, was developed by D. Sheinin (see Sect. 3.1 in Chalikov and Sheinin (1998) for the case of infinite depth; and Sect. 3.1 in Sheinin and Chalikov (2001) for the case of finite depth). The solution in a form of the Fourier expansion coefficients for surface height is found numerically with an iterative algorithm valid for both the cases of infinite and finite depths.

For pure gravity waves, Eq. (3.1.2) can be rewritten in the form

$$\log\left(\frac{1}{2}c^2\right) - \log J = \log(a - z) \quad (3.2.1)$$

Introducing complex variables  $\rho = \xi + i\zeta$  and  $r(\rho, \tau) = x(\xi, \zeta, \tau) + iz(\xi, \zeta, \tau)$  and denoting  $w = \log\left(\frac{dr}{d\rho}\right)$ , we can see that

$$\log J = 2\operatorname{Re} w, \quad z_\xi = \operatorname{Im}(\exp w). \quad (3.2.2)$$

Thus, if the Fourier expansion for  $\log J$  is known,  $\operatorname{Im} w$  can be calculated with

$$(\operatorname{Im} w)_k = (\log J)_{-k} \coth k\tilde{H} \quad (3.2.3)$$

After that  $w$  and  $\exp w$  can be evaluated at the grid points (i.e., by inverse Fourier transform). This yields  $z_\xi$ , and upon finding the corresponding Fourier coefficients by direct Fourier transform,  $z$  can be obtained by integration in Fourier space. Thus,  $z$  can be easily found, if  $\log J$  is known. This allows us to reduce the differential relationship (3.1.6) to the equation with integral operator, which can be solved by a simple iterative procedure.

Assuming that  $z$  is an even function of  $\xi$ , it is convenient to choose

$$s = \frac{1}{4}(\log J(\xi = 0, \zeta = 0) - \log J(\xi = \pi, \zeta = 0)) \tanh \tilde{H} \quad (3.2.4)$$

The determining parameter  $s$  is the amplitude of wave (in linear approximation  $s$  is equal to the amplitude for wavenumber  $k = 1$ ). With  $\chi^{[n]}$  denoting the value of any variable  $\chi$  on  $n$ th iteration, the scheme can be rewritten as follows (all of the calculations are performed for surface  $\zeta = 0$ , unless it is indicated otherwise).

- Step 1. Assume that  $n = 0, \log J^0 = 2s \coth H \cos \xi$  (this is the solution of the linearized problem,  $\eta_0 = 0, H^{[0]} = H$ ).
- Step 2. For the given  $\log J^{[n]}$ , use Hilbert transform (2.2.29) (with the given  $\tilde{H}^{[n]}$ ) for complex calculation and integration in Fourier space to find  $z^{[n]}$  (i.e., the Fourier coefficients  $\eta_k^{[n]}$  for  $k \neq 0$ ;  $\eta_0^{[n]}$  are already determined), as described above. If the maximum surface grid point value of  $|z^{[n]} - z^{[n-1]}|$  is less than the prescribed accuracy  $\varepsilon$  (usually taken  $\sim 10^{-10}$ ), then the iterations are completed,  $z^{[n]}$  being an approximate solution within the accuracy given.
- Step 3. Calculate

$$\overline{J^{-1}} = \frac{1}{2\pi} \int_0^{2\pi} J^{-1} dx = \frac{1}{2\pi} \int_0^{2\pi} J^{-1} x_\xi d\xi \quad (3.2.5)$$

which is a mean value over  $x$  of the inverse Jacobian. This can be done using the relation

$$\overline{J^{-1}} = \frac{1}{2\pi} \int_0^{2\pi} \frac{d\xi}{x_\xi(\xi, \zeta = -\tilde{H})}, \quad (3.2.6)$$

$$x_\xi(\xi, \zeta = -\tilde{H}) = 1 + \sum_{-M \leq k \leq M, k \neq 0} k \sinh^{-1}(k\tilde{H}) \eta_k \vartheta_k(\xi) \quad (3.2.7)$$

(since in our case surface is an even function,  $\eta_k = 0$  for  $k < 0$ , i.e., the actual summation in (3.2.7) is over positive  $k$ ). The denominator in (3.2.6) is determined in Fourier space according to (3.2.7) with the obtained values  $\eta_k = \eta_k^{[n]}$  and  $\tilde{H} = \tilde{H}^{[n]}$ , then it is evaluated at the grid points (inverse Fourier transform) to calculate  $\overline{J^{-1}} = \overline{J^{-1}}^{[n]}$  by (3.2.6).

Step 4. Obtain [see (3.1.6)]

$$\eta_0^{[n+1]} = \frac{1}{2} \sum_{1 \leq k \leq M} k \coth(k(\tilde{H} + \eta_0^{[n]})) (\eta_0^{[n]})^2, \quad (3.2.8)$$

Let [according to (2.2.10)]

$$\tilde{H}^{[n+1]} = \tilde{H} + \eta_0^{n+1}. \quad (3.2.9)$$

Step 5. Calculate

$$a = a^{[n+1]} = \frac{\exp(4s \coth \tilde{H}^{[n+1]}) z^n(\xi = 0) - z^{[n]}(\xi = \pi)}{\exp(4s \coth \tilde{H}^{[n+1]}) - 1} \quad (3.2.10)$$

This will ensure relation (3.2.4) for the next iteration. Since from (3.1.2) it follows that  $\frac{1}{2} c^2 \overline{J^{-1}} = a$ , let  $\frac{1}{2} (c^{n+1})^2 = J a^{[n+1]}$ . Calculate grid point values of

$$\log J^{[n+1]} = -\log \frac{a^{[n+1]} - z^n}{\frac{1}{2} (c^{[n+1]})^2} \quad (3.2.11)$$

Step 6. Find the Fourier expansion of  $\log J^{[n+1]}$  (direct Fourier Transform); let  $n = n + 1$  and return to Step 2.

Relation (3.2.11) follows from the observation that the expression in the latter integral in (3.2.5) is the real part of an analytic function:  $J^{-1} x_\xi = \operatorname{Re} \left( \frac{dr}{d\rho} \right)^{-1}$ ; hence, according to Cauchy theorem, its contour integrals are zero; so, from the periodicity

condition it follows that all its integrals over  $\xi$  with the different constants  $\zeta$  are of the same value: In particular, the latter integral in (3.2.5) (where  $\zeta = 0$ ) is equal to the integral over the bottom  $(\zeta = -\tilde{H})$ , which is the right-hand side of (3.2.5), since at the bottom  $z_\xi = 0$  and thus  $J = x_\xi^2$ . The expansion (3.2.10) is obvious from (3.1.3).

For the infinite depth (Chalikov and Sheinin 1998), the algorithm becomes simpler; in particular,  $\frac{1}{2}c^2 = a$ , since the mean over  $x$  of the inverse Jacobian tends to 1 at  $\zeta \rightarrow -\infty$  and thus is equal to 1 at any  $\zeta$ -level including surface. This eliminates the calculations at *Step 3* and *Step 4*.

This algorithm turns out to be the simplest and fastest as compared to all the schemes for calculations of exact Stokes waves, which were developed before. The accuracy of the method is, in principle, infinite and restricted only by the length of word in computer. For the case of deep water, the algorithm converges up to the steepness  $ak = 0.44$ . Such wave is very unstable and being taken as the initial condition for a non-stationary problem quickly breaks (Chalikov and Sheinin 2005). The wave with steepness  $ak = 0.43$  exhibits the periodic regime, i.e., all modes of Stokes wave fluctuate, while the amplitudes of fluctuations slowly increase in time with development of crest instability (Longuet-Higgins 1978; Longuet-Higgins and Tanaka 1997). Finally such a wave also breaks. If Stokes wave is disturbed by noise, the Benjamin–Feir (B.–F.) instability starts to develop (Benjamin and Feir 1967). This type of instability was discussed in many works and numerically investigated by Chalikov (2007). The B.–F. instability under the pseudonym “modulation instability” is considered as a mechanism of the freak wave generation (see Chap. 6).

The calculation of the most steep Stokes wave with  $AK = 0.44$  and the number of modes  $M = 3200$  was done on a Dell PC (speed 3.11 GHz) with 550 iterations performed for 4.17 s. The number of modes with the amplitudes larger than  $\varepsilon$  in this case is equal to 1932 (Fig. 3.1, panel 1). The calculations for  $AK = 0.30$  took 52 iterations and 0.37 s. In this case, the number of modes required was 28. The phase speed (panel 2) reaches the maximum value  $c = 1.0926$  at  $AK = 0.44$ . The total volume  $V$ , the horizontal momentum  $M_h$ , the potential  $E_p$ , and kinetic  $E_k$  energies of waves were calculated with the exact relations:

$$\begin{aligned} V &= (2\pi)^{-1} \int_0^{2\pi} z z_\xi d\xi, \quad M_h = (2\pi)^{-1} \int_0^{2\pi} \varphi z_\xi z d\xi, \quad E_p = (2\pi)^{-1} \int_0^{2\pi} z^2 x_\xi d\xi, \\ E_k &= -(2\pi)^{-1} \int_0^{2\pi} \varphi \Phi_\xi d\xi, \end{aligned} \tag{3.2.12}$$

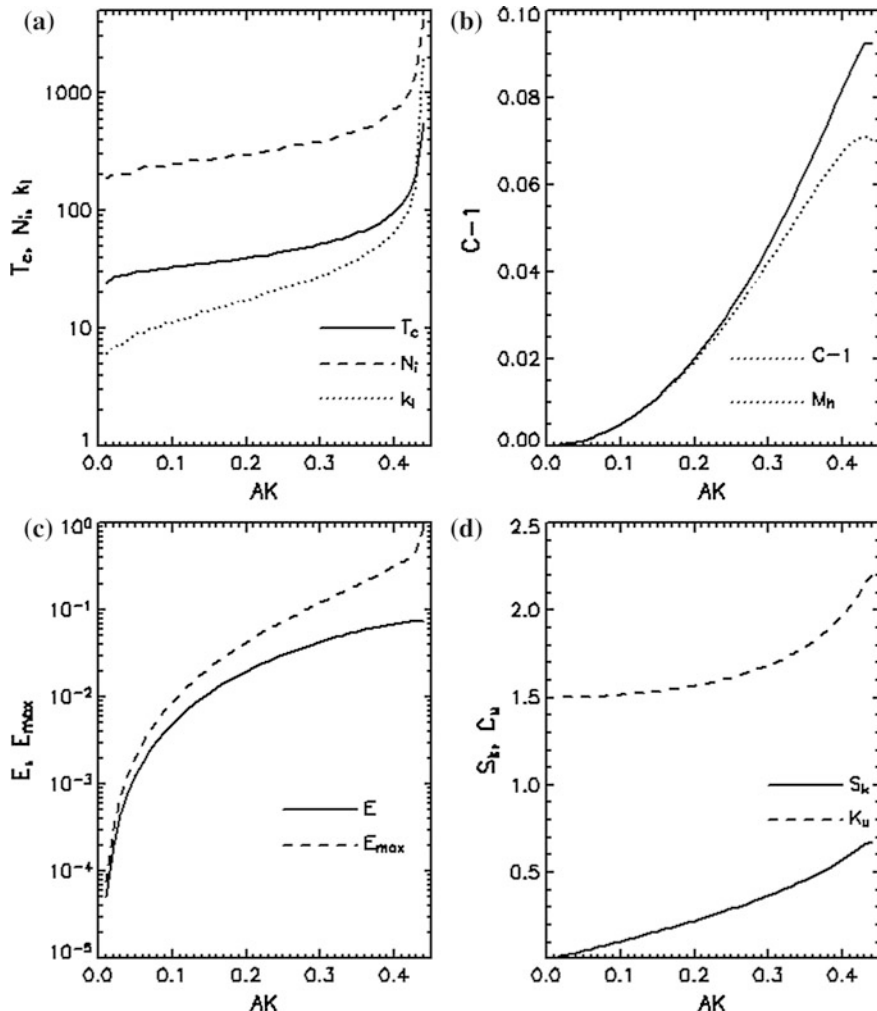


**Fig. 3.1** Characteristics of stationary solutions for Stokes waves as functions of steepness  $AK = (0.01–0.44)$ : **a**  $T_c$ —time of calculation in milliseconds,  $N_i$ —number of iterations,  $k_i$ —number of Fourier mode with amplitude less than  $10^{-11}$ ; **b**  $C - 1$  ( $C$  is a phase velocity),  $M_h$ —horizontal momentum; **c**  $E = E_p + E_k$ —total energy, averaged over period ( $E_p$ —potential energy,  $E_k$ —kinetic energy);  $E_{\max}$ —maximum value of total energy; **d** skewness  $sk$ , kurtosis  $ku$  (Reproduced with the permission from Chalikov (2007). © 2007 AIP Publishing LLC)

The dependence of  $M_h$  and exceeding of phase velocity over the linear value  $C - 1$  on steepness  $AK$  is shown in Fig. 3.1, panel 2. The dependence of sum of the kinetic and potential energies

$E = E_p + E_k$  on  $AK$  is shown in panel 3 (Fig. 3.1, solid line). Naturally, the energy is growing with steepness, though faster than  $(AK)^2$  because of the increase of crest sharpness and vertical asymmetry of surface (see dependence of skewness

$S_k$  and kurtosis  $K_u$  for Stokes waves on steepness  $AK$  in panel 4, Fig. 3.1). The examples of profiles of Stokes waves are shown in Fig. 3.2 along with the profiles of columnar potential  $e_p$  and kinetic  $e_k$  energies calculated by the relations:

$$e_p(x) = \frac{z^2}{2}, \quad e_k(x) = \int_{-H}^z (u^2 + w^2) dz \quad (3.2.13)$$

where  $u$  and  $w$  are the velocity components calculated through the two-dimensional velocity potential  $\varphi$ . The integral in (3.2.13) was calculated on a stretched vertical

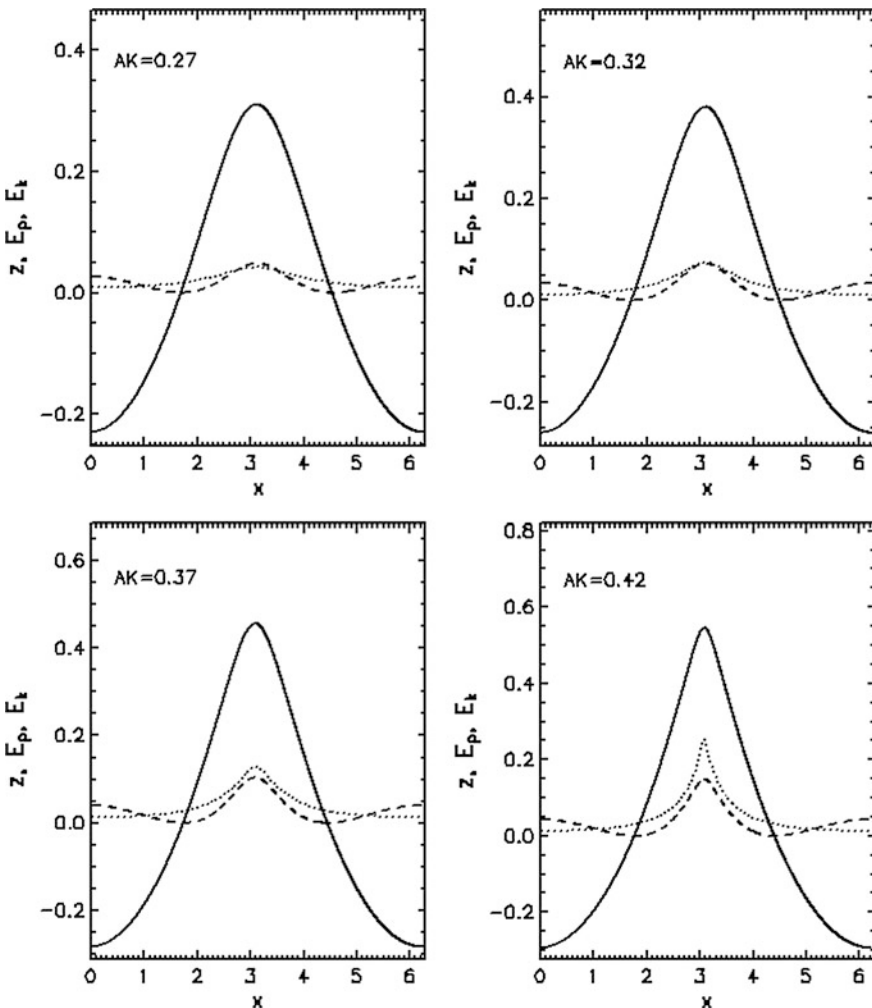


**Fig. 3.2** Profiles of Stokes waves of different steepness, profiles of potential (dashed curve) and kinetic (dotted curve) energy

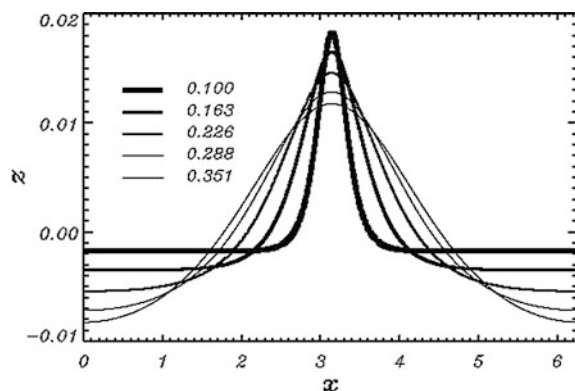
grid, the lower limit being  $z = 6\pi$ . The most interesting feature of Stokes waves is the concentration of total energy in the crest column with increase of steepness. As it follows from Fig. 3.1 (panel 4), for Stokes waves with  $AK = 0.25$  the ratio of maximum value of energy  $e = e_p + e_k$  to the averaged energy  $E$  is about 2.5, but for Stokes waves with  $AK = 0.42$  this ratio is 12.6 (see last panel in Fig. 3.2).

Such focusing of energy for the critical steepness can explain a destroying power of very large and steep breaking waves (freak waves). The problem of freak waves is discussed in details by Kharif and Pelinovsky (2003). The numerical modeling of freak waves is described in Chalikov 2009 (see Chap. 6).

The properties of Stokes wave at finite depth were investigated by Chalikov and Bulgakov (2015) for  $M = 1000$  and the number of grid points  $M = 4000$  within the steepness range  $0 < ak \leq 0.43$  and depth range  $0 < d \leq 2\pi$ . The most specific feature of a stationary gravity wave at finite depth is the sharpening of wave with decrease of depth (Fig. 3.3). All of the results in Fig. 3.3 refer to the steepness  $ak = 0.01$ . As shown, the length of positive values shrinks, and wave tends to become periodic  $\delta$ -function. The phase velocity of wave with the steepness  $ak = 0.01$  at depth  $d = 0.1$  is equal to 0.338.

The dependence of phase velocity on  $ak$  and  $d$  is given in Fig. 3.4. Note that the phase speed of linear wave ( $ak \rightarrow 0$ ) is equal to 1. The curve in the bottom of the picture shows the area of existence of the solution obtained with the algorithm described above. It would be reasonable to suppose that stationary waves in this domain do not exist or are highly unstable. The absence of solution is confirmed by the fact that upon approaching the area of instability the second derivative quickly grows, which means violation of continuity of the first derivative. For Stokes wave at deep water, the sharpening of wave occurs at  $ak = 0.443$ . However, this effect takes place at finite depth at smaller steepness. In upper domain stationary waves evidently exist, but they probably are unstable in the presence of disturbances similar to the Stokes wave at deep water. The line separating instability domain can be approximated by

**Fig. 3.3** Wave profile for different depths (see legend) for steepness  $ak = 0.01$



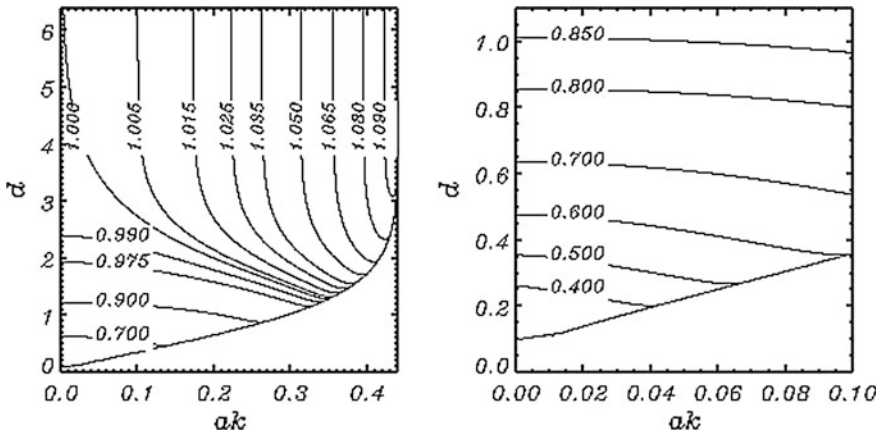


**Fig. 3.4** Phase speed of wave as function of depth  $d$  and steepness  $ak$ . Right panel corresponds to lower left corner of left panel

$$\frac{d}{2\pi} = \frac{-0.0021 + 0.2013ak - 0.03755(ak)^2}{0.47 - ak} \quad (3.2.14)$$

As shown, for depth  $d > \pi$  the solution is close to that for the Stokes wave; that is, the phase velocity with increase of steepness grows from 1 for a nearly linear wave up to 1.0922 for the steepness  $ak = 0.443$ . At smaller depth, the situation changes: The phase velocity decreases together with shrinking of the stability area (see right panel in Fig. 3.5). The smallest phase velocity  $c = 0.0412$  was obtained at  $ak = 0.0001$  and  $d = 0.0015$ . Probably, the phase velocity goes to zero simultaneously with  $d$  and  $ak$ . This hypothetic behavior is not taken into account in approximation (3.2.14).

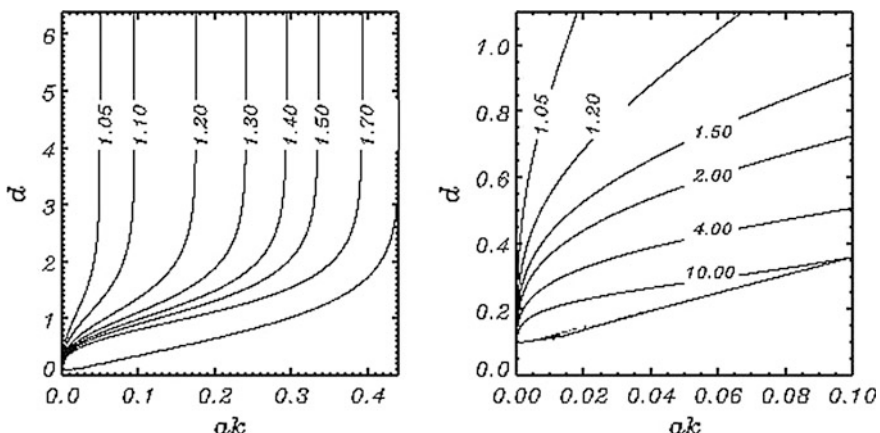


**Fig. 3.5** Ratio of crest height  $H_c$  to trough depth  $H_t$

The vertical asymmetry of stationary wave at finite depth is shown in Fig. 3.5 where the ratio of wave height  $H_c$  in crest and trough depth  $H_t$  is represented. For the linear wave, the ratio is equal to 1, while for the steepest Stokes wave this ratio is equal to 2.056. When depth and steepness become smaller, the ratio  $H_c/H_t$  increases. For example,  $H_c/H_t$  is equal to 633.19 for  $ak = 0.0001$  and  $d = 0.0015$ . Probably, this characteristic goes to infinity; hence, its limit value does not exist. The maximum value of the local steepness  $\max(\partial\eta/\partial x) = 1.971$  is reached at  $ak = 0.443$  for Stokes wave. The behavior of the second derivative characterizing sharpness of wave is more complicated. The absolute value of  $\partial^2\eta/\partial^2x$  in wave peak exceeds  $\partial^2\eta/\partial^2x$  in trough many times. At  $ak = 0.0001$  and  $d = 0.0002$ , the value  $\partial^2\eta/\partial^2x$  has extremes  $-20.1$  and  $6.1$ ; and at  $ak = 0.44$  and  $d = 2\pi$ , the extremes are equal to  $-287.5$  and  $0.3$ .

### 3.3 Gravity-Capillary Waves

An iterative algorithm similar to that described above has been worked out to obtain a numerical solution of (3.1.2) with  $\sigma > 0$ . Here again we assume that surface elevation is an even function of  $x$  and, hence, of  $\xi$ . To describe the algorithm, it is convenient to rewrite (3.1.2) in the form

$$\frac{1}{2}c_*^2 J^{-1/2} + J^{1/2} \left( \frac{\alpha}{\alpha+1} z - a_* \right) - \frac{1}{\alpha+1} J^{-1} (-x_{\xi\xi} z_{\xi} + z_{\xi\xi} x_{\xi}) = 0, \quad (3.3.1)$$

where  $\alpha = 1/\sigma$ ,  $a_* = a\alpha/(\alpha+1)$ ,  $c_*^2 = c^2\alpha/(\alpha+1) = c^2/(1+\sigma)$ . Note that  $c_*$  is the ratio of the actual phase speed to the phase speed of the linearized problem

$$c_l = \left( \frac{1}{k} + \sigma k \right)^{1/2} = \left( \frac{1}{k} + \frac{k}{\alpha} \right)^{1/2} \quad (3.3.2)$$

for the wave number  $k = 1$ ; the convenience of representing the results in terms of this ratio is that it does not depend on the choice of time scale.

Considering the last term on the left-hand side of (3.3.1), it can be seen that

$$J^{-1} (-x_{\xi\xi} z_{\xi} + z_{\xi\xi} x_{\xi}) = \text{Im} \left( \frac{dw}{d\rho} \right) = \text{Im}(w_{\xi}) = (\text{Im } w)_{\xi} \quad (3.3.2)$$

where  $w$  and  $\rho$  have the same meaning as in (3.2.2). Also, if we assume that the mean of the surface height over  $x$  coordinate is zero, we come to the following choice of the 0th Fourier coefficient:

$$\eta_0 = \frac{1}{2} \sum_{1 \leq k < M} k \eta_k^2, \quad (3.3.3)$$

Then, parameters  $a_*$  and  $c_*$  are connected by the relation

$$a_* = \frac{1}{2} c_*^2. \quad (3.3.4)$$

For pure gravity wave, this property directly follows from the results by Longuet-Higgins (1975); for a general case of gravity-capillary waves, the relation (3.3.3) still holds, as it can be deduced from the observation that the mean of the capillarity term in (2.1.3) over  $x$  is zero.

Relations (3.2.2), (3.3.2), and (3.3.4) allow us to rewrite (3.3.1) as follows:

$$-2(\alpha + 1)a_* \sinh(\operatorname{Re} w) + a \exp(\operatorname{Re} w)z = (\operatorname{Im} w)_\xi. \quad (3.3.5)$$

$$S = -\frac{1}{2}(\operatorname{Im} w_\xi(\xi = 0, \zeta = 0) - \operatorname{Im} w_\xi(\xi = \pi, \zeta = 0)) \quad (3.3.6)$$

As for the parameter determining wave amplitude [like  $s$  in (3.2.4), it is equal to the amplitude for the linearized problem], we can now formulate an iteration scheme as follows:

- Step 1. Assume  $n = 0$ ,  $(\operatorname{Im} w)_\xi^{[0]} = -Se^\zeta \cos \xi$  (solution of the linearized problem).
- Step 2. For given  $(\operatorname{Im} w)_\xi^{[n]}$ , find  $w^{[n]}$  in Fourier space by integration and a Hilbert transform [as in the equality (2.2.29)] at each grid point, then find  $z^{[n]}$  by a Fourier transform and integration according to the second relation (3.2.2), with the integration constant defined by (3.3.3). If the maximum surface grid point value of  $z^{[n]} = z^{[n-1]}$  is less than the prescribed accuracy  $\varepsilon$ , the iterations are completed, and  $z^{[n]}$  is an approximate solution within the accuracy given.
- Step 3. Calculate surface values of  $(\operatorname{Im} w)_\xi^{[n+1]}$  as the right-hand side of (3.3.5) by substituting  $w = w^{[n]}$ ,  $z = z^{[n]}$  into the left-hand side. Similarly to Step 3 (in the scheme for gravity waves)  $a_* = a_*^{[n+1]}$  must be chosen so that (3.3.6) holds for  $w = w^{[n+1]}$ :

$$a_\xi^{[n+1]} = \frac{\alpha}{2(\alpha + 1)} \frac{\eta^{[n]}(0) \exp(R^{[n]}(0)) - \eta^{[n]}(\pi) \exp(R^{[n]}(\pi))}{\sinh(R^{[n]}(0)) - \sinh(R^{[n]}(\pi))}, \quad (3.3.7)$$

**Table 3.1** Number of iterations  $N_{\text{it}}$  for gravity-capillary waves calculated for different  $\alpha$  I S

	0.001	0.1	0.2	0.4	0.6	0.8	1
0	4	16	18	20	21	21	20
0.5	22	41	41	39	39	43	43
1	37	61	48	47	44	43	42
1.5	79	93	58	48	43	41	39
2	7966	157	81	44	41	40	
3	152	106	88	62	54		
4	161	134	122	97			
5	212	178	157	138			
6	2,771,779	2051					

Blank entries mean that the scheme failed to converge

where

$$\eta^{[n]}(\xi) = z^{[n]}(\xi, \zeta = 0), \quad R^{[n]}(\xi) = \operatorname{Re} w^{[n]}(\xi, \zeta = 0). \quad (3.3.8)$$

Step 4. Find the Fourier expansion of  $(\operatorname{Im} w)^{[n+1]}_\xi$  by a Fourier transform; let  $n = n + 1$  and return to Step 2.

Convergence of the algorithm and dependence of wave amplitude on the parameter  $s$  for a different  $\alpha$  are characterized by Table 3.1. Since the wave profile obtained for a large  $\alpha$  has two maxima, the values of  $\hat{A}$

$$\hat{A} = \frac{1}{2} (\max(\eta(\xi)) - \min(\eta(\xi))) \quad (3.3.9)$$

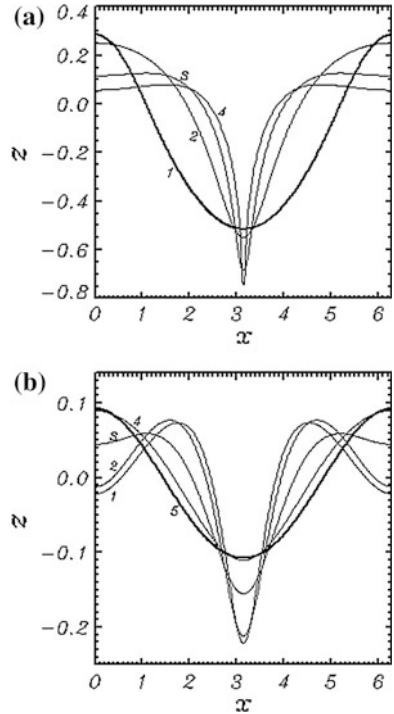
are indicated along with A

$$A = \frac{1}{2} (\eta(\xi = 0) - \eta(\xi = \pi)) = \frac{1}{2} (h(x = 0) - h(x = \pi)) \quad (3.3.10)$$

For  $\hat{A} = 0.4$  and  $\hat{A} = 0.1$ , the samples of the calculated wave profile with the different  $\alpha$  are given in Fig. 3.6 in panels *a* and *b*. It can be seen that with the increase of  $\alpha$  (i.e., with the capillarity coefficient  $\sigma$  decreasing), the wave profiles do not approach those of pure gravity waves, but rather shift the energy to the smaller scales where capillarity effects are more pronounced. Starting from  $\alpha = 2$  the two maxima emerge; thus,  $x = 0$  becomes a local minimum (the absolute minimum being always at  $x = \pi$ ); at the same time, the speed of convergence decreases rapidly, especially for small amplitudes. The values of  $\alpha$  which ensure equal phase velocities (3.1.21) for two neighboring wave numbers  $k, k + 1$ , are  $\alpha = 2(k = 1)$  and  $\alpha = 6(k = 2)$ .

The scheme for calculation of capillary-gravity waves does not converge for the values  $\alpha > 6$ ; ( $\sigma = 1/6$ ). When capillarity decreases, the phase velocity decreases and does not approach its value at  $\sigma = 0$ . This effect is explained by the structure of

**Fig. 3.6** Profiles of gravity-capillary waves,  $\hat{A} = 0.4$ . **a** Curve (1)  $\alpha = 0$  (Crapper's wave), (2)  $\alpha = 1$ , (3)  $\alpha = 2$ , (4)  $\alpha = 3$ ; **b**  $\hat{A} = 0.1$ . (1) 0, (2)  $\alpha = 4$ , (3)  $\alpha = 3$ , (4)  $\alpha = 2$ , (5)  $\alpha = 0$  (Crapper's wave)



the capillary term in Eq. (2.1.3) since the effect of capillarity is described by the high-order differential terms. Though the scheme may fail to reproduce some existing stationary solutions, the behavior of the profiles and phase velocities, as described above, suggests that for a small  $\sigma$  the solution may be unstable or simply nonexistent.

### 3.4 Pure Capillary Waves

Pure capillary waves are described by (3.1.20) if we formally set  $\alpha = 0$ . In this case, the solution is represented by a simple formula (Crapper 1957, 1984). In our notations, it can be written as follows:

$$x(\xi, \zeta) = \xi + \frac{4q \sin \xi}{1 - 2q \cos \xi + q^2} \quad (3.4.1)$$

$$z(\xi, \zeta) = \xi + \frac{4q(\cos \xi - q)}{1 - 2q \cos \xi + q^2} - \frac{1}{2}A \quad (3.4.2)$$

where

$$q = be^\zeta, \quad b = \frac{-2 + \sqrt{4 + A^2}}{A} \quad (3.4.3)$$

and  $A, S$  are defined by the expression:

$$A = S = \frac{4b}{1 - b^2}, \quad (3.4.4)$$

and phase speed  $c_*$  is defined as

$$c^2 = \frac{2(1 + \sigma)}{\sqrt{4 + A^2}}. \quad (3.4.5)$$

The last term in (3.4.2) may be any constant but here it is chosen to satisfy condition (3.3.4).

The exact solution (3.4.1)–(3.4.5) was used as another means to validate the scheme for the calculation of gravity-capillary waves with  $\sigma = 0$ . For all the amplitudes tested, up to the maximum possible amplitude (e.g., Crapper 1957, 1984), the maximum rms difference between the numerical ( $M = 96$ ) and exact solution was less than  $5 \times 10^{-12}$ . The phase velocity coincides with the theoretical values with the accuracy of 6 digits.

## 3.5 Conclusion

The exact and fast numerical methods for solution of stationary equations for gravity and gravity-capillary waves have been developed. The method allows us to obtain the solutions with computer accuracy. The method is based on the representation of differential equations for surface height, written in the new coordinates (which in this case are proportional to the velocity potential and stream functions) via operator of integration and (generalized) Hilbert transformation calculated in Fourier space. Again, the use of Fourier transform method to calculate nonlinearities allows a highly efficient implementation of the method. It should be noted that two separate algorithms for pure gravity and gravity-capillary waves were developed, and that in the latter case our algorithm fails to converge when the non-dimensional capillarity coefficient becomes small. This problem requires further investigations. It was shown that with decrease of values of the capillary coefficient the phase velocities of gravity-capillary waves decrease rather than approach the values of the Stokes phase velocity. Thus, the Stokes waves do not

appear to be an asymptotic form of gravity-capillary waves as the capillarity goes to zero. This, together with the non-convergence of the algorithm (and its various modifications) for small capillarity can be an indication that stationary gravity-capillary waves which are only slightly affected by the capillary forces are unstable or just nonexistent.

# Chapter 4

## Two-Dimensional Wave Modeling Based on Conformal Mapping

**Abstract** High accuracy was confirmed by validation of a non-stationary model against known solutions and by comparison between the results obtained with different resolutions in the horizontal. The method developed is applied for simulation of wave evolution with different initial conditions. The numerical experiments with the initially monochromatic waves of different steepness show that the model is able to simulate the breaking conditions when the surface becomes a multi-valued function of the horizontal coordinate. An estimate of the critical initial wave height that separates non-breaking and eventually breaking waves is obtained. Simulation of nonlinear evolution of a wave field represented initially by two modes with close wave numbers (amplitude modulation) and a wave field with a phase modulation is given. Both runs result in appearance of large and very steep waves. Both of them also break if the initial amplitudes are sufficiently large. The interaction of two monochromatic waves at water surface enters a different dynamic regime if their wave numbers become very close. In the course of evolution of two waves, downshifting of the initial wave energy and growth of the first mode occur depending on wave steepness and a relative distance between modes in Fourier space.

### 4.1 Validation of Two-Dimensional Model by Comparison with the Stationary Solutions

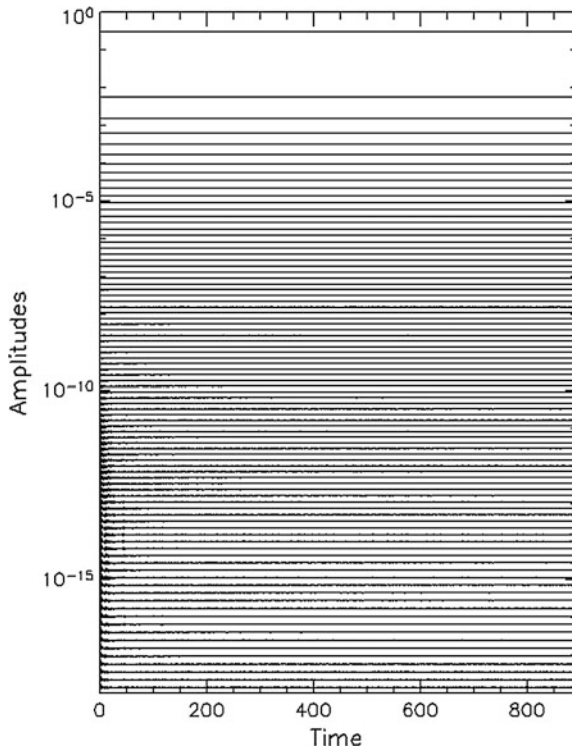
The stationary solutions described in Eqs. (3.1.2, 3.1.3, and 3.1.4) were used for validation of the non-stationary model (2.2.34), (2.2.35). The wave generated in a moving with phase velocity coordinate system was used as initial conditions for calculation of a progressive wave on the basis of non-stationary equations. If such a wave is stable with respect to the truncation errors, it should propagate with the specific phase velocity without changing its shape. Note that such validation is not always accurate. Let us, for example, place the components of Stokes wave at wave number  $k = n, 2n, 3n, \dots$ . In this case, the solution can be disturbed by the intermediate modes growing as the results of B-F (Benjamin and Feir 1967) instability. If these modes are assigned as noise in the initial conditions, we can observe a

selective enhancement of their amplitudes (Chalikov 2007, see Chap. 6). If the initial disturbances are not introduced, the solution will finally be distorted by the modes initiated by the truncations errors, and development of B-F instability will take place anyway. In both cases, validation of the model will be unsuccessful. The only way to avoid development of such scenario is dense assigning of the initial solution at wave numbers  $k = 1, 2, 3, \dots$ . In this case, we leave no room for development of unstable modes. The same consideration is valid for capillary-gravity waves and for capillary waves.

The model was validated against all the three types of waves: pure capillary deepwater (Crapper's) waves (which are analytical solutions), pure gravity, and gravity-capillary waves obtained numerically with the algorithm described above. The calculations were done for  $M = 96$  and  $N = 432$ . For all the test cases, a visual comparison of instantaneous wave profiles obtained during the simulations showed that the wave profiles moved without any perturbations. To estimate ‘steadiness’ of the numerical solution quantitatively, we calculated the phase velocities and amplitudes of the Fourier components for consecutive moments of time and obtained their temporal means and standard deviations over the period of integration. The Crapper wave was assigned with amplitude  $A_c = 0.7$ . The exact phase velocity  $c_c$  was equal to 0.971524, which exactly coincides with the phase velocity calculated by the results of the non-stationary solution. For Stokes wave with amplitude  $A_s = 0.3$ , the exact and calculated phase velocities were 1.046040 and 1.045997, respectively. For gravity-capillary wave, both of these values were equal to 1.160514. Hence, even for the cases of steep waves, the calculated phase velocities were very close to their exact values (i.e., those obtained for the stationary solutions) for all the three types of waves (pure gravity, gravity-capillary, and pure capillary waves). Since conservation of the amplitudes was also very accurate (deviation of their values from their initial values during the simulations was always less than  $10^{-7}$  for Stokes wave and less than  $10^{-11}$  for capillary and gravity-capillary waves), the modes retained their initial energies and remained consistent in phase; consequently, the simulated waves did not change their shapes during the integration. This result confirms that these waves are stable with respect to the truncation errors and that the numerical solutions yielded by the model, approximate the solutions of the original differential equations with high accuracy. For all model simulations described in (Chalikov and Sheinin 2005), a difference between the solutions presented and their versions obtained with  $M$  twice as large was practically absent, which confirms convergence of the numerical scheme.

An additional validation (Chalikov 2005) was performed by simulation of very steep Stokes waves for  $ak = 0.42$  for better resolution ( $M = 1000$ ,  $N = 4000$ ,  $\Delta\tau = 0.0025$ ). The evolution of the first 880 amplitudes is given in Fig. 4.1. It is shown that the amplitudes and, consequently, the shape of Stokes wave remained unchanged with a very high accuracy. These integrations can be continued much longer without noticeable changes of amplitudes. After 2,686,500 time steps (932 periods), the total energy for  $ak = 0.42$  and  $M = 1000$  decreased only at  $3 \cdot 10^{-8}\%$ . The calculations for  $ak = 0.42$  performed by Dold (1992) were quickly terminated

**Fig. 4.1** Long-term evolution of amplitudes of first 880 constituents of stokes waves: ( $ak = 0.42$ , each 10th constituents is shown) during 2,686,500 time steps (932 periods). (Reproduced with permission from Chalikov (2007) © 2007 AIP Publishing LLC)



due to the numerical instability. The exact phase velocity of Stokes wave obtained for the stationary solution for  $ak = 0.42$  was 1.089578. A direct calculation of phase velocity of the simulated Stokes wave gave value  $1.089579 \pm 10^{-6}$ .

Note that the validation based on simulation of running Stokes waves is full and not trivial, because the non-stationary equations ‘do not know’ the stationary solution obtained in a moving coordinate system with a different method.

Now, it becomes clear that solution for Stokes wave is not just an interesting mathematical result; i.e., the Stokes waves themselves begin to play an important role in investigation of the physics of surface waves. The traditional approach to investigation of nonlinear properties of waves was based on suggestion that wave field can be represented as a superposition of linear waves, so interaction of the linear objects was considered. Hence, such approach can be referred to as a quasi-linear approach. Of course, the spectral presentation can be introduced for nonlinear waves, but the information on phases is missing. However, the phase distribution in nonlinear waves is not random, since some part of shortwaves moves with the phase velocity of long waves, so, strictly speaking, they are not the waves but just auxiliary modes taking part in construction of shape of nonlinear waves (this is why the term ‘bound waves’ is misleading). The simple visual observing of sea surface shows that large wave has mostly sharp crests and smooth troughs. The

Fourier analysis of exact solution shows that the field of gravity waves is rather a superposition of Stokes waves than that of the linear waves (Chalikov 2005). These properties have a deep physical background; i.e., Stokes wave is an exact solution of principal equations, while the linear waves are unstable and quickly transform, turning into... Stokes waves (Chalikov 2010, see Chap. 6).

## 4.2 Examples on Non-stationary Solutions

The progressive gravity, capillary, and gravity-capillary waves represent a very specific case of nonlinear interactions; they consist of Fourier modes which, rather than obeying the linear dispersion relation, propagate with one and the same phase speed. It is evident that this effect can also be observed in more general situations: Due to the impact of nonlinearity, a multi-mode wave motion cannot be represented as a superposition of the Fourier modes propagating with their own phase speed; moreover, a certain wave number is not strictly associated with any single-phase speed. Perhaps, the most striking manifestation of nonlinearity is that some shorter waves propagate with the phase speed close to that of the long waves. The instantaneous phase velocity of  $k$ th mode can be calculated with the relation:

$$c_k = \frac{\eta_{-k} \frac{\partial \eta_k}{\partial \tau} - z_k \frac{\partial \eta_{-k}}{\partial \tau}}{k(\eta_k^2 + \eta_{-k}^2)} \quad (4.2.1)$$

An existence of such forced ('bound') components was clearly demonstrated in many laboratory and observational studies (see, e.g., Yuen and Lake 1982). Various explanations have been proposed for this phenomenon including the wind–wave and wave–current coupling, but in the works cited, it was found that this effect is mainly due to the nonlinearity of waves themselves. A realistic wave field contains both types of modes, i.e., free and 'bound' for the same wave number; thus, the 'observed' phase velocities reflect a combined effect of these two types. The partition of the energy between these types of waves depends on their density in wave spectrum. This phenomenon was reproduced in the 1-D potential model by Chalikov and Liberman (1991) who pointed out that each wave component with the wave number higher than that of a carrying wave turns out to have phase speed much greater than that predicted by the linear theory. They also found that phase velocity varies in time and that its standard deviation increases with wave number.

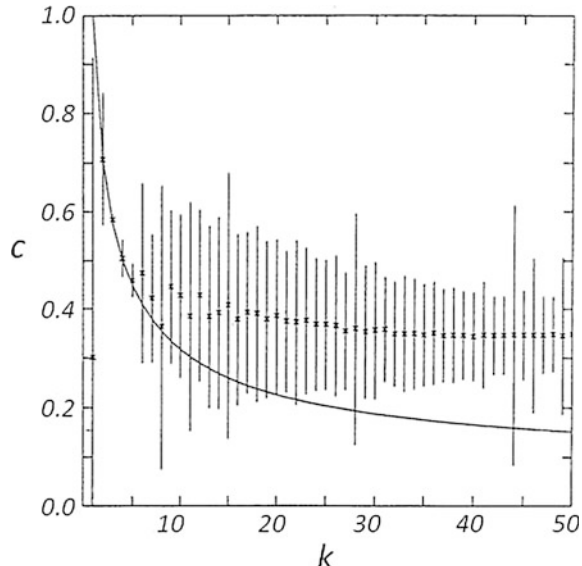
Another numerical experiment we consider as a simulation of Lake and Yuen (1978) laboratory experiment where the nonlinear interaction of two gravity waves with the wave numbers close to each other was investigated. The above authors evaluated phase velocities of different modes by calculating the coherence of the surface elevation values in two sections of wave and found out that the phase velocities of the waves not produced by wave maker were close to those of the primary waves. It is hardly possible to exactly reproduce their experiment since the

amplitudes of waves were not reported, and there are uncertainties as to modeling of the forcing. In the model, to obtain the flow which is qualitatively similar to the experimental one, we use a superposition of the 3rd and the 5th modes with equal amplitudes of 0.04 as the initial conditions for surface elevation. The corresponding surface velocity potential was assigned by the formula of small-amplitude waves. The simulation was performed with time step 0.01 up to  $t = 1000$ . It was found that the energy of 3rd mode is nearly conserved, while the energy of 5th mode became considerably less.

In Fig. 4.2, the temporal means and standard deviations of the instantaneous phase velocities are shown. It is seen that the linear dispersion relation is observed only for the wave numbers  $2 \leq k \leq 5$ . For  $k > 5$ , waves propagate significantly faster than the corresponding linear waves though slower than the primary waves. This effect is clearly pronounced only for the temporal means of phase velocities; the instantaneous values vary highly (as pointed out by Chalikov and Liberman 1991), which is reflected by a large standard deviation for the wave numbers  $k > 5$ . This scattering is caused by the presence of both ‘bound’ and free waves.

More information on free and ‘bound waves’ and their phase velocities is provided by the wave number–frequency spectrum  $S(k, \omega)$  shown in Fig. 4.3 along with the logarithms of the time-averaged wave number  $\bar{S}_k^\omega$  and frequency  $\bar{\omega}_k^\omega$  spectra. The picture of  $S$  looks as if it consists of patches; this effect is achieved by use of high density of contour lines. To calculate  $S$  for each  $k$ , the instantaneous Fourier expansions with respect to the  $x$  coordinate were stored during the entire period of simulation  $0 < t > 1000$  with the time interval of 0.08, and Fourier transform with respect to time was used. In this and other runs, the length of simulation ensured a sufficient frequency resolution  $\delta\omega = 2\pi/1000$ , which is essential for the analyses of

**Fig. 4.2** Simulation of Lake and Yuen (1978) experiment. Time-averaged phase velocity (asterisks) and its standard deviation (vertical bars) as function of wave number. Curve corresponds to linear dispersion relation



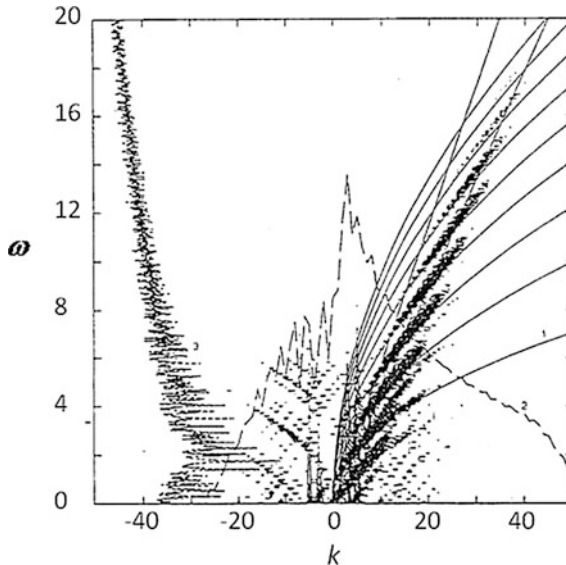


**Fig. 4.3** Simulation of Lake and Yuen (1978) experiment. Time-averaged spectral characteristics for the period  $\delta t = 1000$  (about 160 peak wave period). *Curve 1*—linear dispersion relation  $\omega^2 = k$ , the other parabolas correspond to dependence  $\omega^2 = nk$  ( $k = 1, 2, 3, \dots, 9$ ). The contour lines of  $\log_{10} S(k, \omega)$  (wave number–frequency spectrum) are seen as concatenated in patches. *Curve 2* is  $\log_{10} S^k(k)$  (wave number spectrum, right axis) and *curve 3* is  $\log_{10} S^\omega(\omega)$  (frequency spectrum, top axis)

the spectra; the maximum resolved frequency  $\omega = \pi/0.08$  far exceeded any possible ‘physical’ values of  $\omega$  and thus rendered the transforms aliasing error negligible.

The most remarkable feature of the wave number–frequency spectrum is that it is split into a set of branches in a regular way. This effect is well pronounced for the waves propagating in the direction prescribed for  $k > 0$  domain, but it is also noticeable for the waves moving in the opposite direction which were not presented in the initial conditions at  $k < 0$ . Note that the sign of  $k$  is determined by the sign of the component’s phase velocity, while  $\omega$  is assumed positive. The considerable part of energy belongs to the components which nearly obey the linear dispersion relation (curve 1 in Fig. 4.3). The remaining energy mostly belongs to what is called ‘bound’ components which propagate with the phase velocities of their carrying waves and lie at the branches approximated by curves

$$\omega^2 = n|k|, \quad (4.2.2)$$

where  $n$  (number of branch) is a positive integer. Some energy is concentrated near a straight line passing through the origin. The nature of these modes is unclear, so a further investigation is required for explanation of these features. Strictly speaking, not all of the component (4.2.1) with  $n > 1$  can be called ‘bound,’ since those with  $k$  which is not a multiple of  $n$  have no ‘carrier.’ However, they propagate as if they were ‘bound’ to a free wave with the wave number  $k/n$ . Note that separation of modes

into ‘bound’ and free is not determined well, since some free waves have definitely their own ‘bound waves.’ So, the wave structure turns out to be quite complicated.

Another experiment was designed to approximate real ocean surface waves assigned by the amplitudes

$$a_k = \begin{cases} A_0 \left( \frac{k}{k_p} \right)^P & k_0 \leq k \leq k_0 + M_m - 1 \\ 0 & \text{otherwise} \end{cases} \quad (4.2.3)$$

where  $A_0$  is amplitude of  $k_0$ th mode, while power  $P < 0$  is the amplitude decrement. The Fourier coefficients were calculated as

$$\eta_k = a_k \begin{cases} \sin \phi_k & k \leq 0 \\ \cos \phi_k & k > 0 \end{cases}, \quad (4.2.4)$$

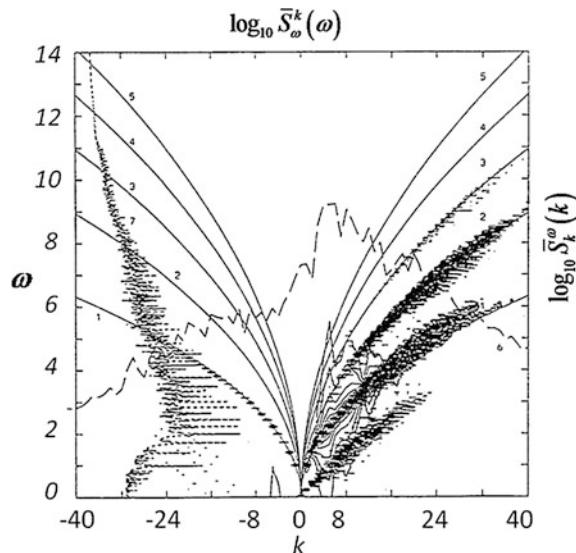
where  $\phi_k$  is the random phase.

The Fourier coefficients for the initial surface velocity potential were assigned in such a way that in linear approximation, all wave components propagated in positive directions:

$$\varphi_k = \text{sign}(k) \eta_{-k} \sqrt{\frac{1 + \sigma k^2}{k \tan h(kH)}}. \quad (4.2.5)$$

The values  $A_0 = 0.01$ ,  $k_p = 5$ ,  $P = -1.5$ , and  $\sigma = 0$  were chosen. The wave number–frequency spectrum calculated for this case is shown in Fig. 4.4. This picture is quite similar to that in Fig. 4.3. Again, most of the energy is concentrated along the ‘main’ branches (4.2.2), and ‘quasi-rectilinearity’ is again quite distinct. It is not excluded that the modes belonging to this branch are the artifacts of

**Fig. 4.4** The same characteristics as in Fig. 4.3 but for initial conditions approximating real spectrum (4.2.3)



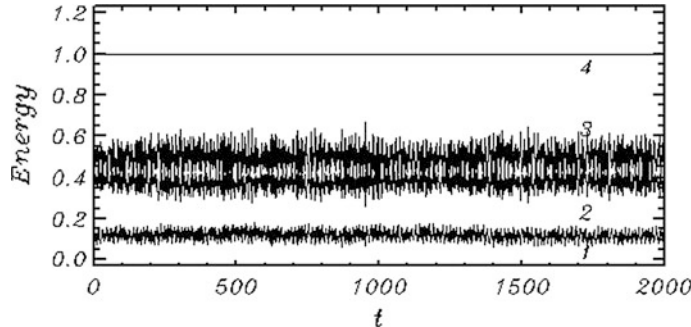


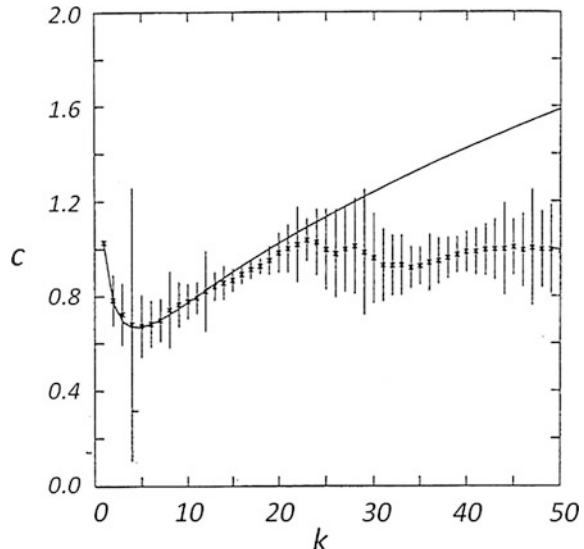
**Fig. 4.5** Simulation of gravity-capillary waves ( $\sigma = 0.05$ ). Time evolution of gravitational potential energy  $e_p$  (curve 1), potential energy of surface tension (2), kinetic energy (3), and their sum (4)

processing. The formula for calculation of phase velocity (4.2.1) was derived assuming that Fourier components for elevation  $\eta_k$  are constants. It is shown in Chap. 5 that such assumption is not always correct.

In the next experiment, the gravity-capillary waves were simulated with the non-dimensional parameters  $A_0 = 0.001$ ,  $k_p = 16$ ,  $P = -1.5$ , so the potential, kinetic, and kinetic capillary energies were of the same order. The integration was carried out with time step 0.001 up to  $t = 1000$ . The evolution of a different type of energy for this case is shown in Fig. 4.5.

The horizontal momentum  $M_h$  and the volume  $V$  are conserved with the relative error margins of the order of  $10^{-13}$  and  $10^{-11}$ , respectively. It is shown that while all the energy components show significant fluctuations, their sum (curve 3) is nearly constant, its slow decrease being due to damping at high wave numbers. The dependence of phase velocity on wave number for this case and its standard

**Fig. 4.6** Simulation of gravity-capillary waves ( $\sigma = 0.05$ ). Time-averaged phase velocity (asterisks) and its standard deviation (vertical bars) as function of wave number. Curve corresponds to linear dispersion relation



deviation are shown in Fig. 4.6. As in the runs with pure gravity waves, the phase velocity at low wave numbers follows the linear dispersion relation (4.2.2), though with considerable scattering.

### 4.3 Simulation of Steep Waves

The method developed was applied to simulation of nonlinear growth of deepwater gravity waves (with the external pressure  $p_e = 0$ ) and initial stages of their breaking. Obviously, a breaking wave, as a solution to the potential flow equations, exists only within a limited time interval. A potential flow model is thus unable to reproduce later stages of wave breaking which occur after the potential flow solution ‘blows up,’ and the actual flow becomes rotational and turbulent.

Two groups of model runs were carried out (Table 4.1): integrations starting from monochromatic waves of different amplitudes (runs 1–4) and the cases where the initial wave profiles represent amplitude (run 5) and phase (run 6) modulation. For cases 1–6, the period of wave was about  $2\pi$ , and for cases 5 and 6, the linear estimations for the group periods were 40.7 and 5, respectively.

The integration time  $T$  in the table can be considered in comparison with the periods of the simulated waves. In linear approximation, these periods are as follows:  $S_{k\omega}$  for runs 1–4,  $2\pi/\sqrt{10.5}$  for run 5, and  $2\pi/\sqrt{5}$  for run 6. For all the runs except run 4,  $T$  is the time of collapse of the numerical solution and can be closely identified with the time of existence of the potential flow solution (see discussion of convergence in the previous section). For the solution in run 4, the time of existence is apparently infinity. As a test of the model’s ability to simulate evolution of very large waves, we first chose the initial data that can be somewhat unrealistic, namely a monochromatic wave with the maximum slope (non-dimensional amplitude)  $a = \max(h_x) = 0.5$ .

The results are shown in Fig. 4.7 where the instantaneous surface height profiles as well as velocity fields and deviations of pressure from its generalized hydrostatic component (i.e.,  $p + \zeta$ , according to Sect. 4.2) are depicted for different moments of time. The initial conditions are shown in the upper panel; the middle panel corresponds to the moment when the maximum slope  $\max|h_x|$  first turns into infinity (the overturning begins); the lower panel represents the condition close to the collapse, with the overturning already in advanced stage. Note the pressure ‘bubble’ in the middle panel, which becomes somewhat less pronounced later, when ‘excessive mass’ of the overturning crest is about to be released. The results also illustrate one more advantage of the conformal mapping method, which is its ability to reproduce surface height profiles that are multi-valued functions of the horizontal coordinate  $x$ .

In Fig. 4.8, the same instantaneous fields are presented for the case of the initially monochromatic wave with  $a = 0.3$  (run 2). This wave, too, eventually breaks, but it is only a relatively small portion of mass in a close vicinity of the peak that overturns. Unlike the previous case, by the moment when overturning begins

**Table 4.1** Characteristics of numerical experiments;  $h$  is amplitude,  $M$  and  $N$  are the parameters of resolution,  $\Delta t$  is time step, and  $\delta$  is integration time

Run no.	1	2	3	4	5	6
Initial conditions, $h$	$0.5 \cos x$	$0.3 \sin x$	$0.28 \cos x$	$0.27 \cos x$	$0.01 (\cos 10x + \cos 11x)$	$0.04 \cos(5x + \sin x)$
Resolution, $M$	3072	6144	3072	1536	12288	3072
Resolution, $N$	13284	27648	13284	6912	55296	13284
Time step, $\Delta t$	$5 \cdot 10^{-4}$	$2.5 \cdot 10^{-4}$	$5 \cdot 10^{-4}$	$10^{-3}$	$5 \cdot 10^{-4}$	$10^{-3}$
Integration time, $\delta$	3.15	5.58	7.11	500	51.01	37.44
Comments	Breaking	Breaking	Breaking	No breaking	Breaking	Breaking

( $t = 5.45$ ), the crest sharpens dramatically, which accelerates overturning; simulation of this effect required a higher resolution than in run 1. The middle panel of Fig. 4.7 depicts the wave well before its overturning but with a high pressure area under the crest, already well developed, and other features of the nonlinear behavior, such as sharpening of the wave crest, increase of its height (more than 1.6 times of its initial value), and large velocities at crest—already strongly pronounced. The lower panel represents a moment during the short period between the beginning of overturning and collapse of the solution. At this stage, as well as

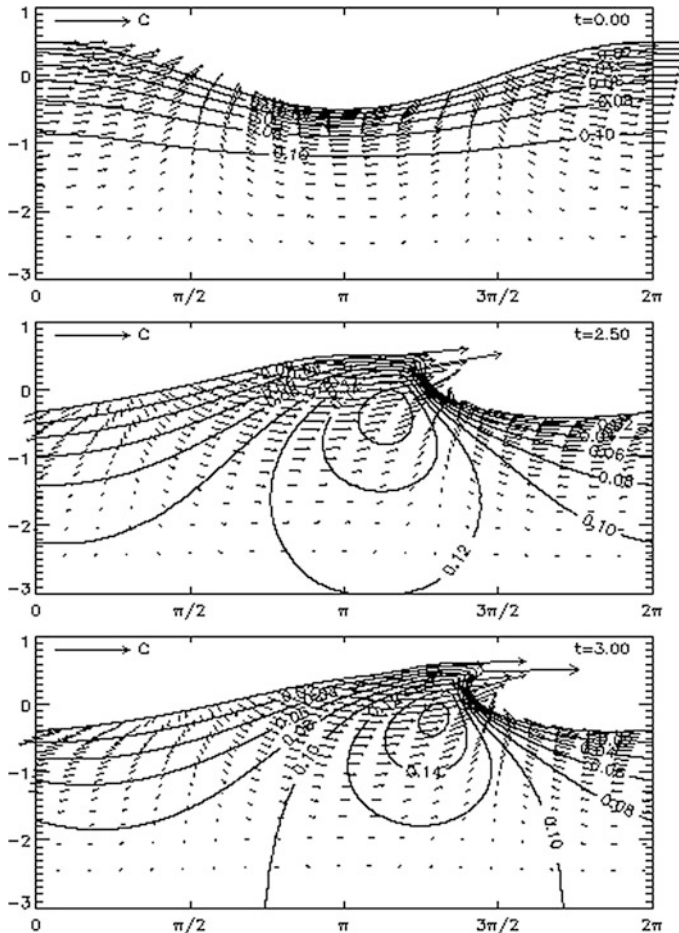


**Fig. 4.7** Surface profiles, velocity vector fields (scaled by the linear phase velocity of the base wave shown at the left upper corner of each panel), and deviations of pressure from its generalized hydrostatic component (contour lines) for the initially monochromatic wave with the maximum slope  $a = 0.5$  (run 1) at different times  $t$  (indicated at the right upper corner). (Chalikov and Sheinin 2005 © 2005 Elsevier Inc. with permission of Elsevier)

during the breaking stage in run 1, the velocities at the crest exceed the (linear) phase velocity by 1.1–1.3 times.

Time evolution of maximum slope  $\max|h_x|$ , maximum velocity  $\max|\vec{V}| = \max(\sqrt{\Phi_x^2 + \Phi_z^2})$ , maximum surface height  $\max(h)$ , and wave height  $\Delta h = \max(h) - \min(h)$  for the cases of initially monochromatic waves with  $a = 0.28$  (run 3) and  $a = 0.27$  (run 4) is shown in Figs. 4.7 and 4.8, respectively. Again, the

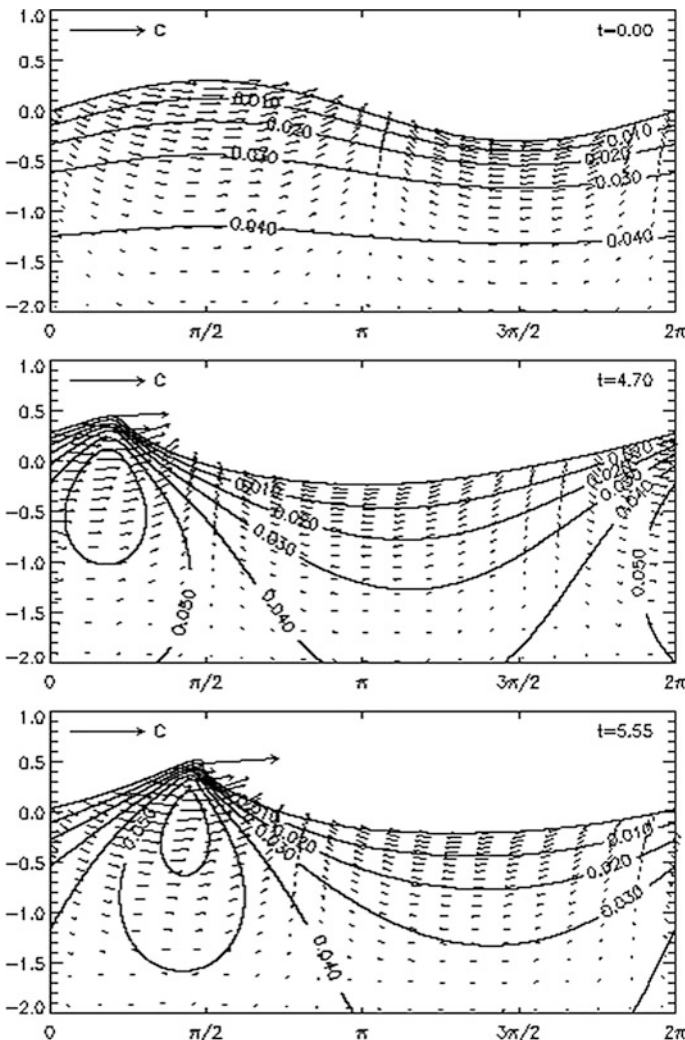


**Fig. 4.8** The same as shown in Fig. 4.7 but with  $a = 0.3$  (run 2). (Chalikov and Sheinin 2005 © 2005 Elsevier Inc. with permission of Elsevier)

behavior of both waves is highly nonlinear, and during the initial stage of about one wave period, the two waves exhibit quantitatively similar growth, steepening, and acceleration at the crest. However, while this initial evolution results in breaking for the former wave in a manner similar to run 2, the latter wave survives its climax, and its characteristics reverse their tendencies to reach their initial values and then continue to oscillate in a quasiperiodic manner. It suggests that for the initially monochromatic waves, the critical value  $a^*$  of the initial amplitude (the values at which the waves with  $a > a^*$  eventually break and the waves with  $a < a^*$  do not) is between 0.27 and 0.28. Note that these conclusions were obtained with a high-resolution scheme for which the influence of dissipation was shifted to very high frequencies.

Thus, the wave in run 4 is close to the highest non-breaking initially monochromatic wave. It is worth mentioning that the maxima of its height  $\Delta h$  (about 0.62, see the lowest panel in 4.13), let alone its initial height  $2a = 0.54$ , are considerably less than the height of the steepest Stokes wave (0.886) or the Stokes wave of the highest energy (0.858). Likewise, the total energy of the wave in run 4 is only about 0.50 of the maximum energy of Stokes waves. Thus, both the maximum height and energy of the non-breaking initially monochromatic waves are significantly less than those for the Stokes waves, so the latter characteristics cannot serve as the criteria of breaking.

It is noteworthy that for all the simulations with the initially monochromatic waves, the growth of the maximum surface height (the height of the crest)  $\max(h)$  significantly exceeded that of wave height  $\Delta h$  (see 2, 3; cf. 3rd and 4th panels in Figs. 4.9 and 4.10), and sharpening of the crest was accompanied by flattening of trough. Skewness was also increasing. For non-breaking waves, these processes turn out to be fully reversible (run 4, Fig. 4.10). It is interesting to note that the values of Jacobian less than  $J = 0.2$  were never observed. Hence, division by Jacobian in Eq. (2.2.35) did not play a significant role for instability. On the contrary, very large values of  $J$  in the vicinity of sharp crests (up to  $J = 100$ ) were typical. It did not influence the stability directly, but imposed additional restrictions to time step.

Runs 5 and 6 simulate a nonlinear evolution of the wave fields which have a relatively low initial maximum slope  $\max|h_x|$  (0.209 and 0.239, respectively). Runs 5 and 6 result in the development of steep breaking waves. In run 5, the initial condition is a superposition of two monochromatic waves with the same amplitude and close wave numbers. The elevation can be described by the expression  $h = 0.02 \cos 0.5x \cos 10.5x$ ; thus, it represents ‘single’ wave with slowly changing amplitude. The results are shown in Fig. 4.11 (instantaneous fields) and Fig. 4.12 (time evolution of the geometric characteristics). Note that while a monochromatic wave overturns in about one wave period or less (if ever), it takes some 26 wave periods for the modulated wave in run 5 to reach the breaking stage. In the former

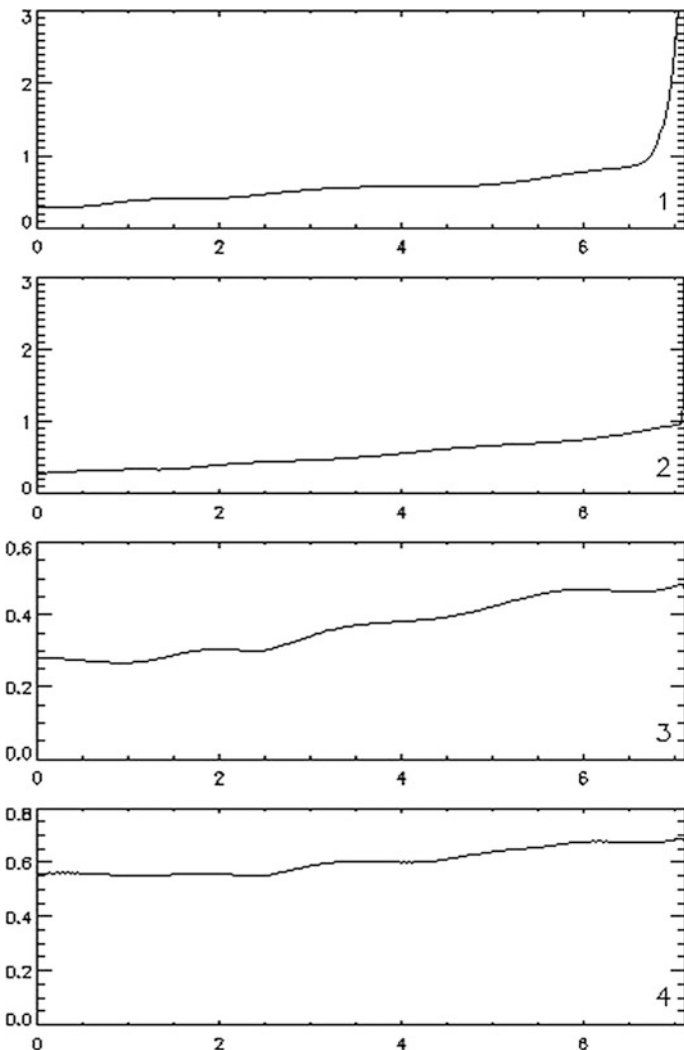


**Fig. 4.9** Temporal evolution of geometric characteristics of the initially monochromatic wave with  $a = 0.28$  (run 3): 1—maximum slope  $\max|h_x|$ ; 2—maximum velocity  $\max|\vec{V}|$ ; 3—maximum surface elevation  $\max(h)$ ; 4—wave height  $\Delta h = \max(h) - \min(h)$ . (Chalikov and Sheinin 2005 © 2005 Elsevier Inc. with permission of Elsevier)

case, an individual wave has initially sufficient energy to grow nonlinearly up to the breaking point, while in the latter case, an individual wave that eventually breaks does not have a ‘critical’ initial energy but grows as a result of a relatively slow process of energy redistribution along the wave train.

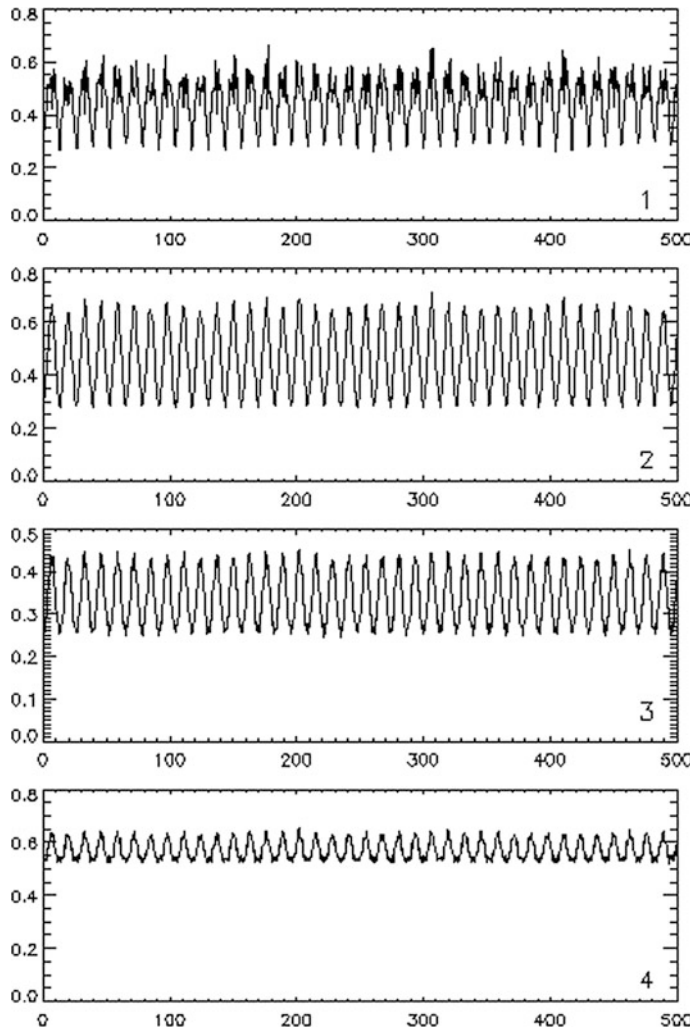


**Fig. 4.10** The same as shown in Fig. 4.9 but with  $\alpha = 0.27$  (run 4). (Chalikov and Sheinin 2005  
© 2005 Elsevier Inc. with permission of Elsevier)

In run 6, the initial condition represents phase (or frequency) modulation of the base wave with wave number  $k = 5$ . The results (Figs. 4.13 and 4.14) are basically similar to those for the case of the amplitude modulation (run 5): redistribution of energy along the wave train, which continues for many periods of the base wave (13 wave periods in run 6) and is clearly shown in Figs. 4.11 and 4.13, eventually results in the formation of a very high and steep breaking wave that has a sharp crest where the velocity exceeds the phase velocity. The crest is followed by a deep

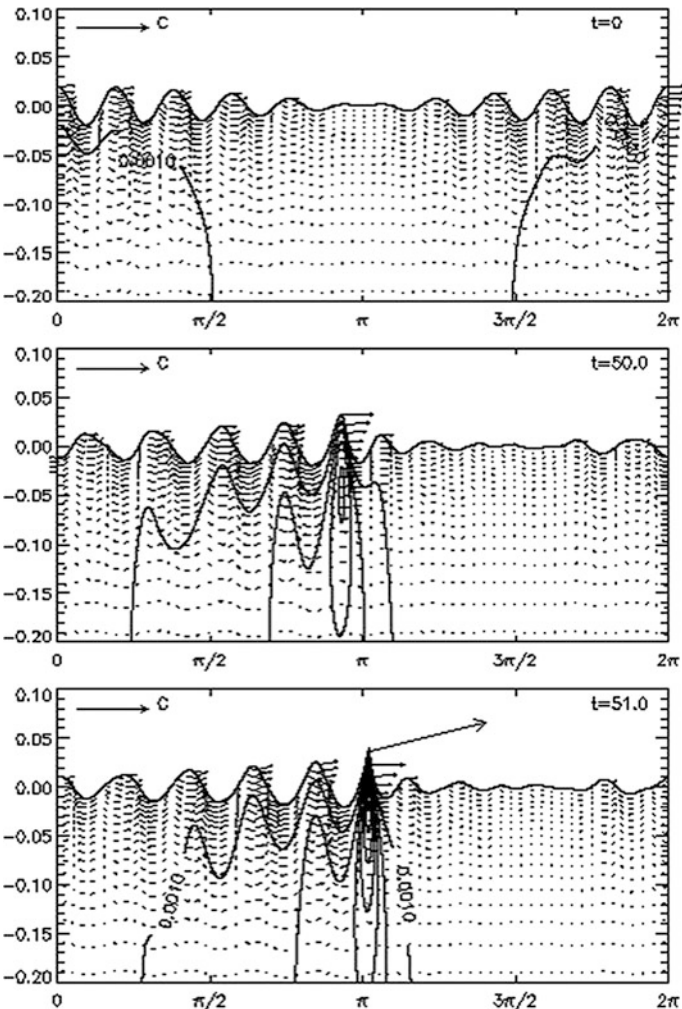


**Fig. 4.11** The same as shown in Fig. 4.7 but for the simulation starting from a base wave with an amplitude modulation (run 5). (Chalikov and Sheinin 2005 © 2005 Elsevier Inc. with permission of Elsevier)

trough; a high pressure area is formed under the crest; the maximum surface elevation becomes about twice as large as its initial value (Figs. 4.6 and 4.8, lower panel).

A special feature of run 6 is that the numerical simulation survives the first wave-breaking event (Fig. 4.13, 2nd panel; note the corresponding maxima of the geometric characteristics in Fig. 4.14). The critical stage begins at  $t \approx 32.5$ , and the

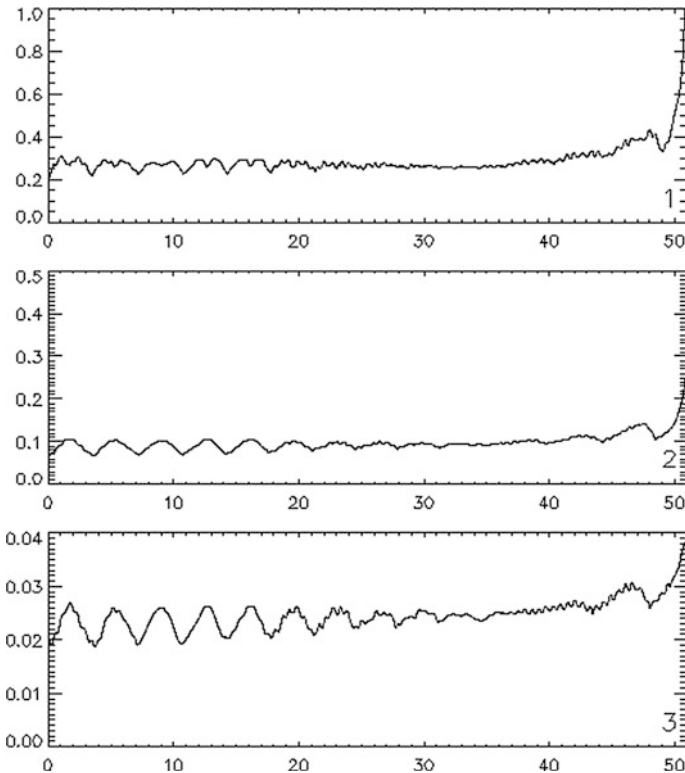


**Fig. 4.12** Temporal evolution of geometric characteristics for the simulation starting from a base wave with an amplitude modulation (run 5): 1—maximum slope  $\max|h_x|$ ; 2—maximum velocity  $\max|\vec{V}|$ ; 3—maximum surface elevation  $\max(h)$ . (Chalikov and Sheinin 2005 © 2005 Elsevier Inc. with permission of Elsevier)

exact solution (for which the numerical solution with  $M = 12288$  proves a close approximation) collapses at  $t = 33.16$ . However, this event turns out to be a ‘mini-breaking’ that affects only a very narrow vicinity of the top of the sharp crest. A coarser resolution  $M = 3072$  used in run 6 initiates a greater numerical dissipation and allows it to absorb this event, with the release of energy as small as  $4 \cdot 10^{-4}$  of its total value, before the critical stage the solution practically coincides with that obtained with a higher resolution. The artificially lowered resolution allowed us to follow the wave-train evolution beyond the first wave breaking, though, obviously, with a lower accuracy. In Fig. 4.13, 3rd panel, we see the wave that previously underwent breaking followed by subsiding, while the successive wave has become sharper and higher. In the lowest panel, this last wave exhibits a

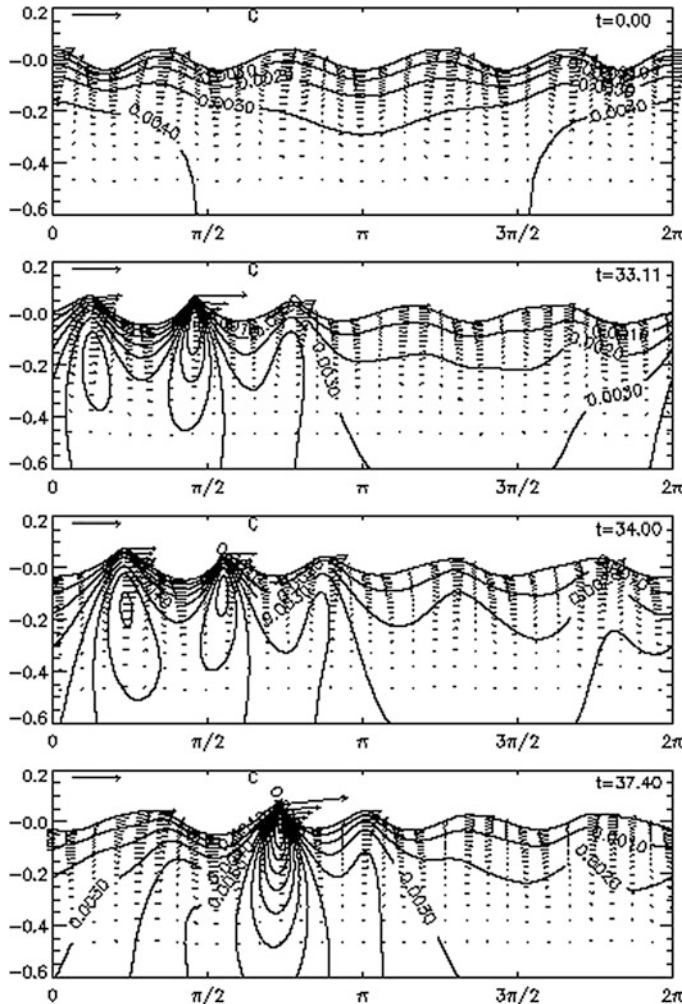


**Fig. 4.13** The same as shown in Fig. 4.7 but for the simulation starting from a base wave with a phase modulation (run 6). (Chalikov and Sheinin 2005 © 2005 Elsevier Inc. with permission of Elsevier)

surface height maximum that is significantly greater than that reached during the first breaking (see Fig. 4.6, lower panel), while the crest sharpens and accelerates dramatically. At this point ( $t = 37.40$ ), the wave is already in the breaking stage, and the numerical solution finally collapses at  $t = 37.44$ .

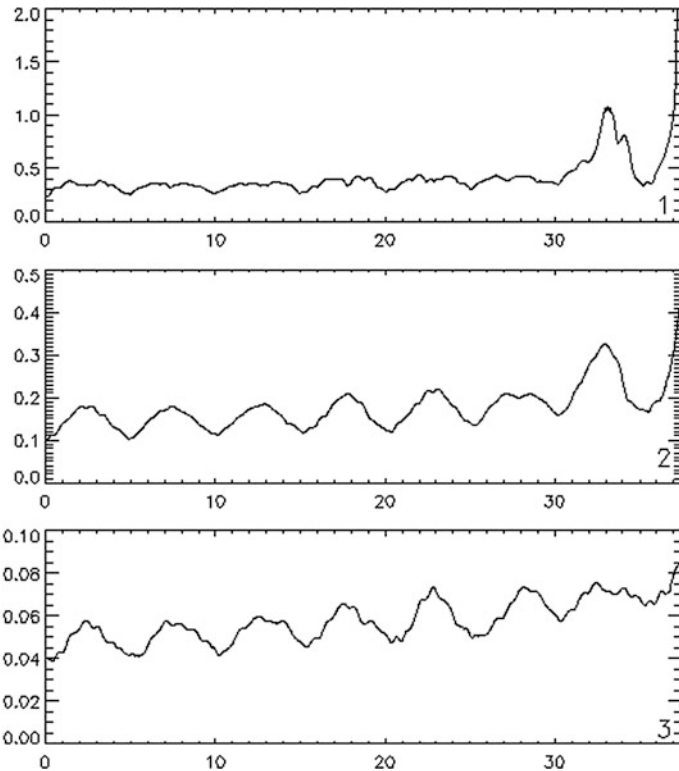


**Fig. 4.14** The same as shown in Fig. 4.12 but for the simulation starting from a base wave with a phase modulation (run 6). (Chalikov and Sheinin 2005 © 2005 Elsevier Inc. with permission of Elsevier)

#### 4.4 Interaction of Surface Waves at Very Close Wave Numbers

An evolution of bichromatic waves represents a substantial interest in the fluid mechanics, oceanography, and maritime engineering (e.g., Badlock et al. 2000; Trulsen and Stansberg 2001; Madsen and Furhman 2006; Chiang et al. 2007), as well as in the other fields of physics (e.g., Leibisch et al. 2012). In this section, the evolution of surface water waves is considered to make it clearer to what extent the bichromatic wave modes can be close in the frequency/wave number space before the dynamics of their interactions changes, if at all. In this regard, the topic may be relevant to various applications for nonlinear waves in dispersive media (see Babanin et al. 2014).

In this section, like in Chalikov (2012), the wave steepness was chosen in such a way that the waves do not break. In the case when breaking occurrence was detected (see Babanin et al. 2010), the simulation run was stopped and the results

were not used in this section. The breaking does not just lead to a decrease of the local energy; it also produces a new type of nonlinear interactions and redistribution of energy across the spectrum (e.g., Tulin and Waseda 1999). The wave breaking would need some parametric treatment, and at this stage, we intended to concentrate on the nonlinear evolution of waves which can be explicitly modeled on the basis of the fundamental equations.

In this study, initially, the energy of bichromatic waves is placed on the neighboring dimensionless wave numbers  $k_1$  and  $k_1 + 1$ , i.e., 10 and 11, 100, and 101, up to 1000 and 1001 (note that the dimensional wave number of primary wave can be regarded the same in every case). Thus, the relative separation of the modes  $dk/k_1$  decreases from 0.1 down to 0.001, respectively. The steepness of the individual modes is defined as  $\varepsilon/2 = a_k k_1 = a_{k+1} (k_q + 1)$  and prescribed, and therefore, the initial amplitude  $a$  is a bound parameter. Integration, unless specified otherwise, is over 1000 wave periods.

In Fig. 4.15, an evolution of the initially bichromatic spectra with  $k_1 = 800$  is shown. The overall steepness is  $\varepsilon = 0.2$  (i.e.,  $a_k = 0.1$ ). The initial spectrum is shown in black and is captured after the first 5 periods of the wave evolution (integration step is 1/1000 of a wave period). The yellow spectrum is the last in the computations, after 1000 wave periods of the evolution. The blue spectra correspond to the output every 5 periods.

In Fig. 4.15, even though the energy was initially placed at  $k_1 = 800$  and  $k_2 = 801$  linear harmonics only, it can be seen that already after 5 wave periods, it appears at a set of bound harmonics at  $k = 1600 (+2)$  and  $k = 2400 (+3)$ ; i.e., the initial sinusoidal waves immediately turn themselves into Stokes-like waves. Also, apparent is the subharmonic  $k = dk = k_2 - k_1$ . Both effects are expected (e.g., Agnon and Mey 1985; Toffoli et al. 2007; Osborne 2010; Chalikov 2012).

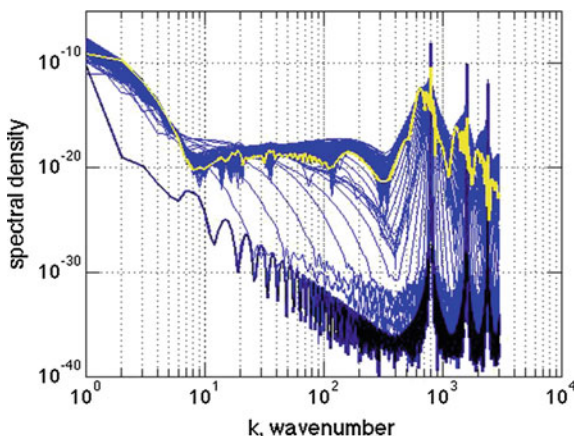


**Fig. 4.15** Evolution of bichromatic waves with initial wave numbers  $k_1 = 800$  and  $k_1 = k_1 + 1 = 801$ , steepness  $\varepsilon = 0.2$ . *Black* spectrum is initial, after 5 periods of wave evolution, and *yellow* spectrum is the last, after 1000 periods. *Blue* spectra are output every 5 periods. (Babanin et al. 2014 © 2014 Springer-Verlag Berlin Heidelberg, with permission of Springer)

The evolution of this train of Stokes waves over 1000 wave periods leads to reduction of the energy of the primary bichromatic set and its bound harmonics, downshifting of the energy of the main peak and growth of the subharmonics. The yellow spectrum, although the last in the evolution, is not the highest between the peaks, i.e., the spectral density fluctuates. This observation is consistent with the evolution of the nonlinear spectrum in Chalikov (2012).

Details of the evolution of the original spectral peak at  $k_1$  and of the newly growing peak at the first mode  $k = dk$  are shown in Fig. 4.16. The first subplot demonstrates downshift of the original peak  $k_{\text{shift}}/k_1$  where  $k_{\text{shift}}$  is the wave number of this peak after 1000 wave periods of evolution, as a function of the initial separation of the bichromatic waves in the Fourier space,  $dk/k_1 = 1/k_1$ . Panel *b*, below shows decay of the spectral density of the peak,  $S_{\text{shift}}/S_1$ , over this period of time.

For the low steepness of  $\varepsilon = 0.05$ , the original peak remains approximately where it was (Fig. 4.16a) and its energy does not significantly change (Fig. 4.16b). For steeper waves shown in Fig. 4.16b, the energy of the original peak progressively reduces as the steepness increases. As we can see in panels (c) and (d), a substantial part of this energy is passed on to the subharmonic at  $k = 1$ .

The pattern is different and more complicated with respect to the downshift  $k_{\text{shift}}/k_1$  as in Fig. 4.16a. For the waves steeper than  $\varepsilon = 0.05$ , downshifting for very close wave numbers, i.e., at  $1/k_1 = 0.001$ , ultimately reaches some 20 %. For  $\varepsilon = 0.1$ , such

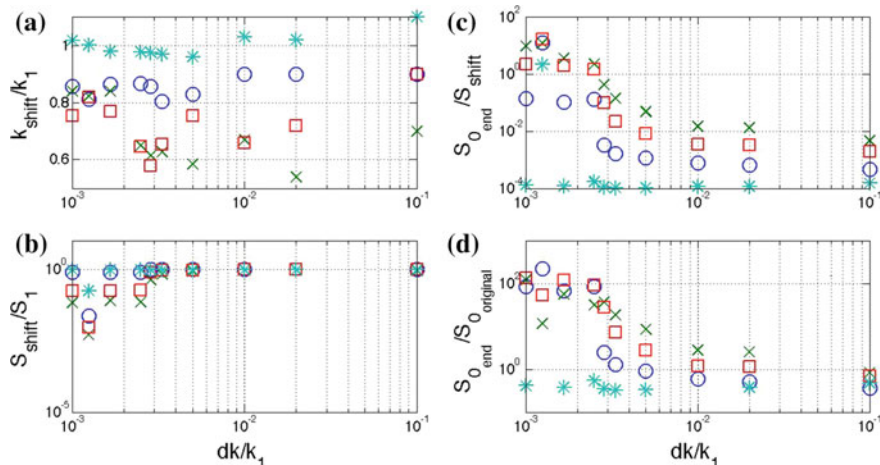


**Fig. 4.16** Behavior of the original spectral peak at  $k_1$  (spectral density  $S_1$ ) and the first mode at  $k = 1$  (spectral density  $S_0$ ).  $k_{\text{shift}}$  and  $S_{\text{shift}}$  are wave number and spectral density of the original peak shifted after 1000 periods of evolution, respectively.  $S_{0,\text{original}}$  and  $S_{0,\text{end}}$  are the initial and final spectral density of the first mode, respectively. In all panels, asterisks correspond to steepness  $\varepsilon = 0.05$ , circles to  $\varepsilon = 0.1$ , squares to  $\varepsilon = 0.15$ , and x-marks to  $\varepsilon = 0.2$ . Bottom scale is  $dk/k_1 = 1/k_1$ . **a** Peak shift,  $k_{\text{shift}}/k_1$ . **b** Decay of the spectral energy in the original peak,  $S_{\text{shift}}/S_1$ . **c** Ratio of spectral densities of the new peak at the first mode and the original peak, after 1000 periods,  $S_{0,\text{end}}/S_{\text{shift}}$ . **d** Growth of the spectral density of the new peak at the first mode  $S_{0,\text{end}}/S_{0,\text{original}}$ . (Babanin et al. 2014 © 2014 Springer-Verlag Berlin Heidelberg. with permission of Springer)

shift is achieved gradually as  $dk/k$  is reduced from 0.1 to 0.001. For  $\varepsilon = 0.15$  and  $\varepsilon = 0.2$ , the peak wave numbers drop to much lower values, below 60 % of the original peak between  $dk/k = 0.1$  and 0.0025, but for  $dk/k < 0.0025$ , the downshift bounces back up and levels around the same 80 % mark. It appears as if for such close wave numbers the peak shift is no longer dependent on the steepness.

The change of behavior of steep waves at  $dk/k \sim 0.0025$  mark is most noticeable in panels (c) and (d) on the right. These panels deal with the dynamics of the first-mode peak. Here,  $S_0$  is the spectral density of this peak in the beginning ('original') and after 1000 wave periods ('end') of simulations. In panel (c),  $S_{0\text{end}}/S_{\text{shift}}$  shows the growth of the first mode at the expense of the original peak at  $k_1$ . The ratio demonstrates a clear dependence on the mean steepness. The growth increases toward lower values of the wave number separation  $1/k_1$ , but at  $dk/k \sim 0.0025$ , there is a sudden jump in the growth, by two orders of magnitude for  $ak = 0.1 - 0.15$ . For the waves with steepness  $ak = 0.15 - 0.2$ , the new peak at  $k = 1$  exceeds the original peak after 1000 periods of evolution. A similar behavior is shown in Fig. 4.16d for the growth of the first mode  $S_{0\text{end}}/S_{0\text{original}}$ . For  $dk/k < 0.0025$ , this ratio depends on steepness, but for  $dk/k > 0.0025$ , it levels at approximately 100, independently of the steepness.

There is no apparent jump in the right panels for the wave trains with low steepness of  $\varepsilon = 0.05$ . Does this signify a threshold-like behavior of the observed instability in terms of steepness?

## 4.5 Conclusion

While the properties of stationary solutions suggest lots of intriguing problems, we use these results mainly as a tool to validate the non-stationary model. The validations were performed by using the solutions obtained in Sect. 4.2 as the initial conditions for the non-stationary problem. Since the coordinate system of the latter was attributed to the mean flow rather than to the wave profile, the model simulates the running Stokes and gravity-capillary waves. It should be emphasized that the validation was far from trivial, as the non-stationary model is based on the equations much more complicated than the stationary ones and on the numerical procedure of its own which 'does not know' that the simulated waves are supposed to retain their shape even for large amplitudes. The result proves that (1) Stokes and gravity-capillary waves are stable with respect to the truncation errors of the non-stationary model and that (2) these errors are small enough.

We use the non-stationary models for case studies of evolution of nonlinear wave fields (full description of the experiments is given in Chalikov and Sheinin, *Technical Note*. 1996, available on request). The cases chosen were somewhat arbitrary, as our aim was to provide a possibly broader variety of applications of the technique developed. The effect of 'bound waves' is most clearly seen in the simulation designed to approximate the laboratory experiment by Yuen and Lake

(1982). The most surprising feature of the multi-mode wave fields was a clear separation of wave number–frequency spectra into the regular curvilinear branches with most of the energy concentrated along what we call ‘main branches.’ This set of branches satisfies a dispersion relation which form is given by (4.2.1) where the number  $n$  of the branch is 1 for the branch containing free waves and is greater than 1 for the branches consisting of ‘bound waves.’ In this structure, the nonlinear effects were manifested both in the existence of multiple branches and in deviation of the parent curve ( $n = 1$ ) from the linear dispersion relation for relatively large wave numbers. In most cases, the deviation is clearly pronounced when the curve approaches a straight line and the group velocity tends to constant; however, this effect needs further analyses. The nonlinearity also produces other regular branches. The energy of the modes belonging to the additional branches is usually very small, sometimes with a remarkable exception of a peculiar pattern (or group of patterns) which, at least for the wave numbers that are not too small, could be roughly approximated by a straight line passing through the origin. The nonlinear behavior of small shortwaves was perhaps most strongly manifested in the case of a long Stokes wave with the superimposed small shortwaves where a free wave branch is poorly represented, while propagation of shortwaves is largely controlled by the interaction with the Stokes wave. On the other hand, the nonlinear energy flux to higher wave numbers was remarkably larger in the case of gravity-capillary waves than in all other runs which included the pure gravity and pure capillary wave simulation with the same initial surface height. This case also needs further investigation, as the structure of the wave number–frequency spectrum was partially obscured by apparent merging of the branches.

The evolution of an initially monochromatic wave is one of the simplest examples of nonlinear interaction. Our simulations showed that such waves exhibit growth of the wave height, an even greater growth of the crest height, sharpening, and acceleration of the crest and flattening of the trough. With the initial maximum slope  $a \leq 0.27$ , such waves do not break, and the behavior of their geometric characteristics is quasiperiodic in time, so the above-listed tendencies prove fully reversible. For  $a \geq 0.28$ , these tendencies result in wave breaking which occurs within approximately one wave period or less; the overturning is well reproduced in the simulations, the picture being especially impressive for larger waves reminiscent of a ‘wall of water,’ observed by many sailors. The quantitative estimate of the critical  $a$  may depend on definition of the velocity potential for initial monochromatic wave. In our case, the potential was represented by one Fourier component (such as surface height) whose phase was determined in such a way that the wave propagate in one direction.

We also considered two cases of the wave fields with more complex initial conditions. The first initial condition was the two Fourier components with close wave numbers, i.e., the base wave with the amplitude modulation. The other initial condition was the base wave with the phase modulation. Both simulations were characterized by redistribution of energy along the wave train, which continued for many periods of the base wave and resulted in formation of the large steep breaking

waves with sharp crests. The whole picture is qualitatively close to the extreme waves observed (Magnusson et al. 1999).

To summarize the above, we investigated an evolution of the bichromatic wave trains with close and very close wave numbers by means of a fully nonlinear wave model. We should emphasize that this is an academic study the physical implications of which should be further explored. In the academic model, although the subharmonic wavelengths become very large, we are still able to use the deepwater environment for wave propagation. In any experiment, very long waves would inevitably find themselves in finite depths, a complication which we decided to neglect at this stage. The academic model also gives us an advantage of keeping the wave energy constant, as the dissipation and wave breaking would be another complication.

Without such complications, we find that the interaction of two monochromatic waves at water surface enters a different dynamic regime, if their wave numbers become very close. While the downshifting of the initial wave energy and the growth of the first mode in the course of evolution of bichromatic waves can be expected, their apparent dependence on the wave steepness and  $dk/k$  appears new. A behavior of these features changes, if  $dk/k < 0.0025$ : Both the downshifting and the growth rate become independent of  $dk/k$ . The effect investigated here indicates that there probably exists a physical limit for approximation of the continuous spectrum.

Since two adjacent modes create more or less continuous spectrum, it is not surprising that the spectrum undergoes downshifting. However, it seems that this downshifting occurs too fast, as compared with the downshifting modeled by Chalikov (2012). It happens because two adjacent modes always create a mode with wave number  $k = 1$ . The interaction of other modes with the first mode definitely accelerates the downshifting. Such effect should be considered as artificial, since the energy cannot move outside the spectral domain. If the spectrum is very dense, a flux of energy can go to a very small wave number; i.e., the interaction of infinitely close modes creates outflux of energy to the infinitely long waves. It is unlikely that such mechanism of the ultra-long wave energy dissipation exists in reality.

# Chapter 5

## Statistical Properties of One-Dimensional Waves

**Abstract** A numerical model for long-term simulation of gravity surface waves is described. The model is designed as a component of a coupled wave boundary layer/sea waves model for investigation of a small-scale dynamic and thermodynamic interaction between ocean and atmosphere. The statistical properties of a nonlinear wave field are investigated on the basis of direct hydrodynamical modeling of the 1-D potential periodic surface waves. The high accuracy was confirmed by validation of the non-stationary model against known solutions and by comparison between the results obtained with different resolution in the horizontal. It is shown that the scheme allows to reproduce propagation of a steep Stokes wave for thousands of periods with a very high accuracy. The method developed is applied for simulation of the evolution of wave fields with a large number of modes for many periods of dominant waves. The statistical characteristics of a nonlinear wave field for the waves with different steepness have been investigated: spectra, curtosis and skewness, dispersion relation, and lifetime. The main result that wave field can be presented as a superposition of linear waves is valid just for small amplitudes. It is shown that a nonlinear wave field is rather a superposition of Stokes waves than that of the linear waves.

### 5.1 ‘Lifetime’ of Wave Components

The method of numerical simulation of surface waves, described in Chap. 2, is applied here to the investigation of statistical properties of a nonlinear wave field (Chalikov 2005, see also Agnon et al. 2005). In general, this investigation is complicated because of the specific wave instability, i.e., wave breaking. If the initial wave energy is large, the onset of wave breaking inevitably leads to termination of calculations. Such instability can be effectively eliminated with some algorithms of breaking parameterization. However, if such algorithms are applied, the statistics of free waves might be distorted. For example, such smoothing algorithm sometimes eliminates appearance of high sharp waves.

This is why we first investigated the dependence of time on the initial conditions, up to onset of wave breaking. The appropriate integral characteristics for a fixed length scale might be the initial energy of waves. Naturally, for different timescales, this characteristic is incomplete. The initial integral (effective) steepness of surface  $s$  turns out to be more convenient:

$$s \propto \left( \int_0^M k^2 S(k) dk \right)^{\frac{1}{2}} \quad (5.1.1)$$

The initial conditions were assigned as a superposition of the linear modes with amplitudes

$$a_k = \begin{cases} a_0 \left( \frac{k}{k_0} \right)^{-p} & k_0 \leq k \leq k_d \\ 0 & \text{otherwise.} \end{cases} \quad (5.1.2)$$

and random (different for each case) set of phases. The mode with wave number  $k_0$  has amplitude  $a_0$ , and amplitudes above  $k_0$  decrease as  $k^{-p}$  ( $p > 0$ ). The value of  $k_0$  defines resolution of spectrum, so it cannot be too small. In most calculations,  $k_0 = 10$  and  $p = 6$  were taken. Further increase of  $k_0$  did not change the results described below. The statistical results were also very close when  $p = 5$  was chosen. A large value of  $P$  was finally chosen to avoid the numerical instability leading to breaking. As the steepness  $s$  for steep (but still not breaking) waves slightly decreases during long-time simulations due to the tail dissipation (2.3.4)–(2.3.6), an effective steepness for each run was obtained by the averaging over time. The number of modes  $M$  was 400, the number of grid points  $N = 1600$ , and the time step  $\Delta\tau = 0.0025$ . The calculations were performed for 70 cases

$$a_l = 0.009 + 0.001 \cdot l, \quad l = 1, 2, 3 \dots 70 \quad (5.1.3)$$

The onset of breaking was recognized when the total energy started growing and exceeded its initial value at 1 %. This criterion indicates the time of breaking onset with high accuracy, because the fourth-order Runge–Kutta scheme develops instability very quickly. The onset of breaking depends not only on the total nonlinearity of an initial wave field, but also on the initial set of phases. This dependence is weaker than the dependence on steepness. To take into account the effect of the initial phases, the calculations (5.1.3) were repeated with different sets of phases. The total number of runs was equal to 980. The dependence of the time up to breaking  $T_l$  (time  $\tau$  normalized by a period of peak wave  $T_p = 2\pi/\sqrt{k_0}$ ) on the effective steepness is shown in Fig. 5.1. Each point is obtained by averaging over the sampling set. Each set includes 160,000 values (100 wave profiles).

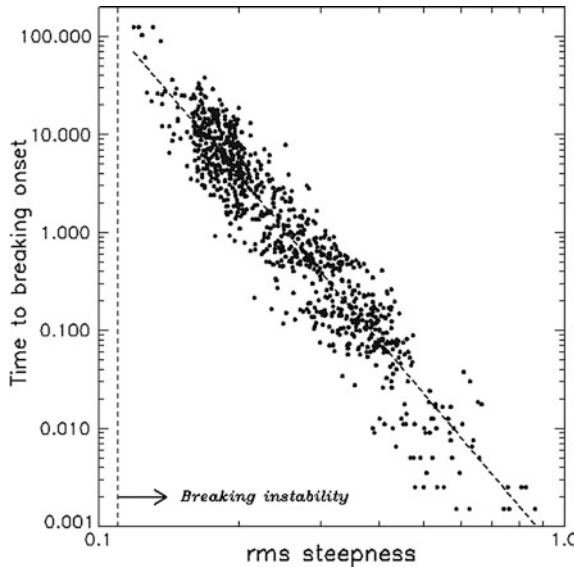


**Fig. 5.1** Dependence of time to onset of breaking instability on rms steepness. *Dotted line* is approximation (5.1.4) (Chalikov 2005)

As seen, the stability of wave field and its life without breaking decreases quickly with the increase of steepness. For large initial steepness the breaking occurs immediately, and the dependence on the initial phases becomes more significant. However, for the effective steepness  $s$  less than 0.11, the breaking was virtually absent. This statement cannot be considered as precise; we can just testify that we never observe the breaking onset below  $s = 0.10$  in the runs up to  $t = 2500$ . The dependence of  $T_k$  on  $s$  can be approximated by the formula

$$T_k = 4.6 \times 10^{-4} s^{-5.61}, \quad (5.1.4)$$

Approximation (5.1.4) has correct asymptotic behavior ( $T_k \rightarrow \infty$ , when  $s \rightarrow 0$ ), but it is unlikely that a specific form of this dependence is correct for the values of  $s$  smaller than it was explored. Note that the number of modes used in our calculations was much larger than that in the calculations made by Song and Banner (2002), but the threshold for onset of breaking  $s = 0.10$  obtained here is close to that in the cited paper.

## 5.2 Statistical Characteristics of a Multi-mode Wave Field

For calculations of statistical characteristics of wave, ten long-term runs were produced up to 1,000,000 time steps (790 periods of peak wave) with the initial peak steepness in the range of  $a_0 k_0 = 0.0001\text{--}0.09$  corresponding to the effective

**Table 5.1** Parameters of numerical experiments

#	1	2	3	4	5	6	7	8	9	10
$a_0$	0.00001	0.001	0.002	0.003	0.004	0.005	0.006	0.007	0.008	0.009
$s$	0.0001	0.013	0.026	0.029	0.039	0.052	0.079	0.089	0.099	0.106
$M$	400	400	400	400	400	400	400	1000	1000	1000

steepness in the range  $s = 0.0001\text{--}0.106$ . The number of modes  $M$  for the cases 1–7 was 400, the number of grid points  $N = 1600$ , and the time step  $\Delta\tau = 0.001$ . For the cases 8–10 corresponding to large steepness, the tail dissipation (2.3.4)–(2.3.6) for  $M = 400$  was large. To reduce this effect, the number of modes for these cases was increased to  $M = 1000$  ( $N = 4000$ ), while the time step and the number of steps were the same as for  $M = 400$ . The amplitudes  $a_k$  and a corresponding effective steepness for these cases are given in Table 5.1.

The wave spectra and a rate of dissipation are presented in Fig. 5.2. As seen, a high wave number part of the spectrum is fluctuating within the range of the order of its averaged values, while the amplitudes of these fluctuations grow with the increase of the initial steepness and wave number. Gray area in the right part of the frames corresponds to the tail dissipation function [see Eqs. (2.3.4)–(2.3.6)]

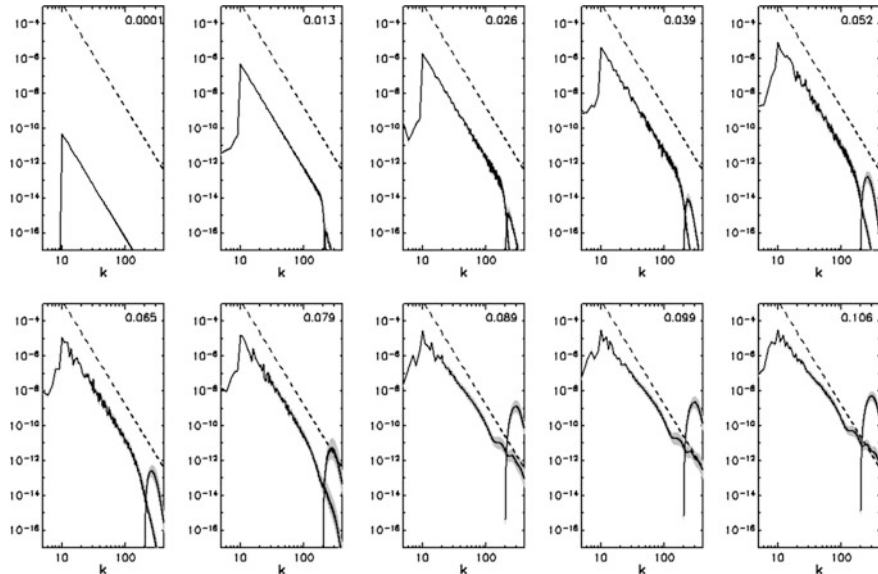


**Fig. 5.2** Averaged for  $t = 2500$  (790 peak wave periods) wave spectra, initially assigned by Eq. (5.1.2). The curves in the right side of each panel are the rate of dissipation of potential energy [see Eqs. (2.3.4)–(2.3.6)]. Straight line corresponds to  $S = k^{-6}$  function. The gray vertical bars correspond to the rms of the spectra and the rate of dissipation (Chalikov 2005)

$$D_k = \mu_k (z_k^2 + z_{-k}^2) \quad (5.2.1)$$

Tail dissipation is located in the high-frequency part of the spectrum. It removes effectively the fast growing but very small modes in the vicinity of the cut wave number  $M$ . This dissipation is so weak that it does not significantly influence conservation of the total energy. For the cases 1–7, the total energy decreased over the period of integration in the 10th decimal digits, and for the steepest initial conditions (case 10), the energy decreased at  $10^{-3}\%$ . In general, an accuracy of preservation of the total energy grows quickly with the increase of the spectral resolution (and shifting of the tail dissipation to the higher wave numbers). Straight line in Fig. 5.2 corresponds to the spectrum  $S \propto k^{-6}$ . As seen, the averaged spectrum follows closely this dependence. Note that this property is not connected to the form of the initial conditions (5.1.2). We used the value  $P = 6$  just because it corresponds to the spectrum developing in the process of integration. An initial spectrum can be assigned in an arbitrary form providing the rms steepness beyond the critical values  $s = 0.011$ . The same spectrum was obtained as in Fig. 5.2 when  $p = 5$  and  $k_d = 10$  were chosen. As we can see below, the main reason for fast adjustment of the spectrum to its quasi-equilibrium shape is a strong nonlinearity which makes the timescales for the individual high wave number components very short.

Fast modification of the wave field due to nonlinearity is clearly seen in Fig. 5.3 where a long-time evolution of the amplitudes of the first 6 components (with the wave numbers  $k = 10–15$ ) for different rms steepness is given. Only for extremely flat waves with the rms steepness of the order of  $10^{-4}$  (the steepness of peak wave  $a_0 k_0$  is also equal to  $10^{-4}$ ), wave amplitudes remain constant for a long time. For the rms steepness

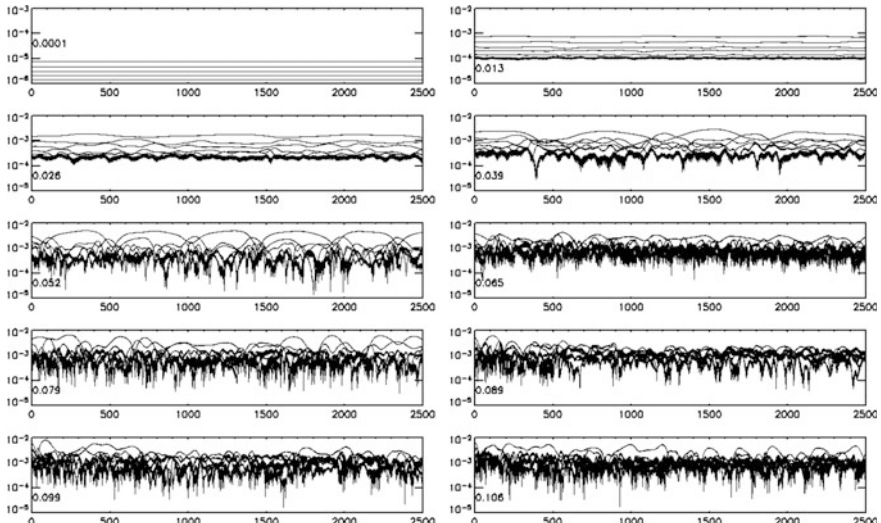


**Fig. 5.3** Evolution of five consequent amplitudes starting from peak wave number  $k = 10$  for different steepness during 790 peak periods (Chalikov 2005)

$ak = 0.013$ , the 15th amplitude fluctuates significantly. With the increase of steepness, these fluctuations spread between all the modes in spectral peak, and the amplitudes of fluctuations grow with the increase of steepness. A small part of these fluctuations can be attributed to the exchange between the potential and kinetic energies. However, since the fluctuations are much larger than the sum of the kinetic and potential energies for each component, an explanation of such behavior cannot be given without consideration of fast energy exchange between the wave modes. It is important that such strong variation of the energy of wave components occurs at very strict conservation of total energy (we remind that the cases with the development of breaking instability were excluded). Qualitatively, this process is similar to convergence of energy in a physical space which was studied by Song and Banner (2002).

It makes sense to consider the timescale  $T_l$  characterizing a typical ‘lifetime’ of wave components

$$T_k = E_p \frac{k^{\frac{1}{2}}}{2\pi} \left( \left( \frac{\partial E_p}{\partial t} \right)^2 \right)^{-\frac{1}{2}}, \quad (5.2.2)$$

where  $E_p = \frac{1}{2}(h_k^2 + h_{-k}^2)$  is the potential energy of  $k$ th wave component in the Cartesian coordinate system. Timescale  $T_k$  is normalized formally by period of the wave component following from the linear wave theory. Dependences of  $T_k$  on the wave numbers for different rms steepness are given in Fig. 5.4 together with their

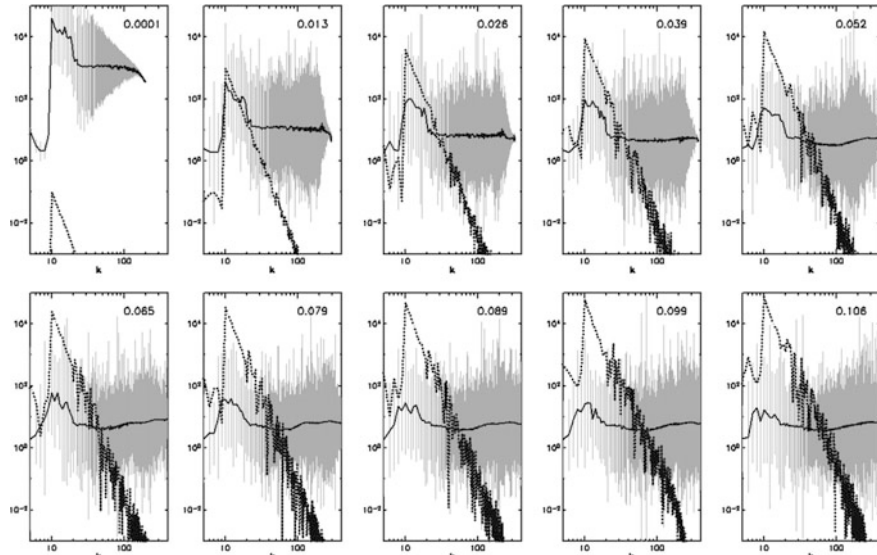


**Fig. 5.4** ‘Lifetime’ of the components of the wave field  $\tilde{T}_k$  expressed in periods for the every specific component (Eq. (5.2.2), solid lines). Gray lines indicate the scatter of  $\tilde{T}_k$ . Dotted lines are the averaged wave spectrum. The numbers in the upper right corner are the effective steepness (Chalikov 2005)

scatter. Again, all the wave components are stable for a very small steepness only, i.e., their amplitudes remain constant over hundreds and thousands of periods. With the increase of frequency  $T_k$  in the vicinity of the wave peak, the timescale decreases to 100 for  $s = 0.026$  and then to 10 for  $s = 0.106$ . For  $k > 20$ , the timescales are very small (of the order of one period of the linear wave with the same wave number) for any steepness considered, except for the case with  $s = 10^{-4}$ . The spectral energy of the wave components for  $k = 20$  is smaller by 3 decimal orders than that in wave peak. Evidently, such fast fluctuations cannot be attributed to free surface waves.

This statement becomes more evident after consideration of the phase velocities of waves calculated with formulas (2.7.4) and (2.7.5) and rms of phase velocity  $c_k$

$$c_{\text{rms}} = \left( \overline{(c_k - \bar{c}_k)^2} \right)^{\frac{1}{2}} \quad (5.2.3)$$

The dependencies of the phase velocities and their rms on wave number for different values of steepness are shown in Fig. 5.5. Each value of the phase velocity is calculated over an ensemble of 2500 wave records. Each record has length  $N = 1600$  (for cases 1–7) or  $N = 4000$  (for cases 8–10). As seen, a linear dispersion relation  $c_k = k^{-1/2}$  is perfectly correct only for  $s = 0.0001$ . For the waves with  $s = 0.013$ , fluctuations of the phase velocity for  $k = 20$  become noticeable. With further increase of steepness, the phase velocity of high modes increases and its fluctuations grow. A simple explanation of these phenomena was given in ChSh. In fact, at each wave number, several modes coexist, i.e., one mode is a free wave, while others are the so-called bound waves which correspond to the additional

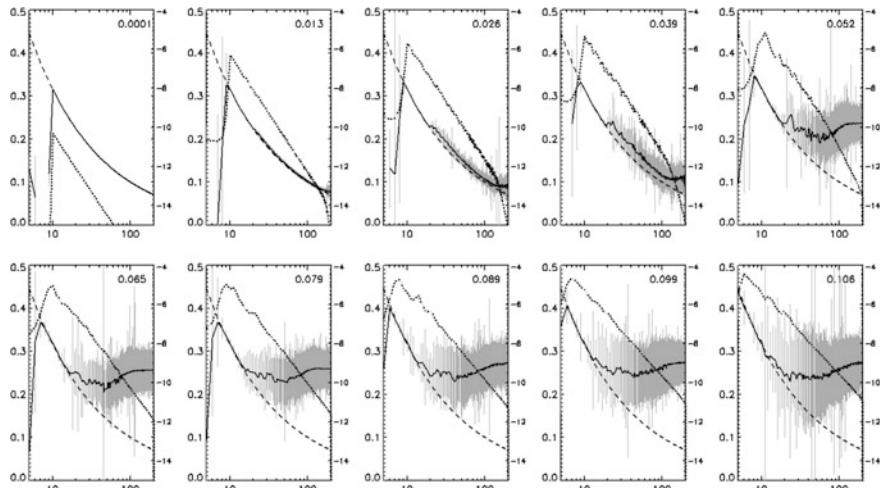


**Fig. 5.5** Phase velocities of wave components as function of wave number (see Eq. 4.2.7). Dashed line is a linear dispersion relation. Gray vertical bars correspond to the rms of phase velocities (Eq. 6.3.5). Dotted line is a wave spectrum (right axis) (Chalikov 2005)

modes attached for every steep enough wave. The calculation of the phase velocity based on (2.7.4) and (2.7.5) gives some weighted value between the velocities of free and bound modes. At present, it is unclear how to separate bound waves and free waves during processing. Since the bound modes attributed to different carrying waves may have the same wave numbers and the amplitude of carrying waves is changing in time due to the nonlinearity (see Fig. 5.3), the situation becomes quite complicated. To understand how the shape of wave differs from that assumed in the linear theory, the calculations of high-order moments for different value steepness were performed.

Function  $z(\xi)$  was transferred from the conformal coordinates to function  $\eta(x)$  in the Cartesian coordinates using the fourth-order periodic polynomial spline (providing accuracy of the order of  $10^{-11}$ ) and then recorded for processing. Every 100 of such records were linked in a single set with the length of  $L = 160,000$  which was used for calculation of the statistical characteristics such as mean  $\bar{\eta}$ , variance  $V$ , skewness  $S$ , and kurtosis  $K$ :

$$\begin{aligned}\bar{\eta} &= \frac{1}{L} \sum_{j=0}^{L-1} \eta_j, & V &= \frac{1}{L-1} \sum_{j=0}^{L-1} (\eta_j - \bar{\eta})^2, & S &= \frac{1}{L} \sum_{j=0}^{L-1} \left( \frac{\eta_j - \bar{\eta}}{\sqrt{V}} \right)^3, \\ K &= \frac{1}{L} \sum_{j=0}^{L-1} \left( \frac{\eta_j - \bar{\eta}}{\sqrt{V}} \right)^4 - 3,\end{aligned}\quad (5.2.4)$$

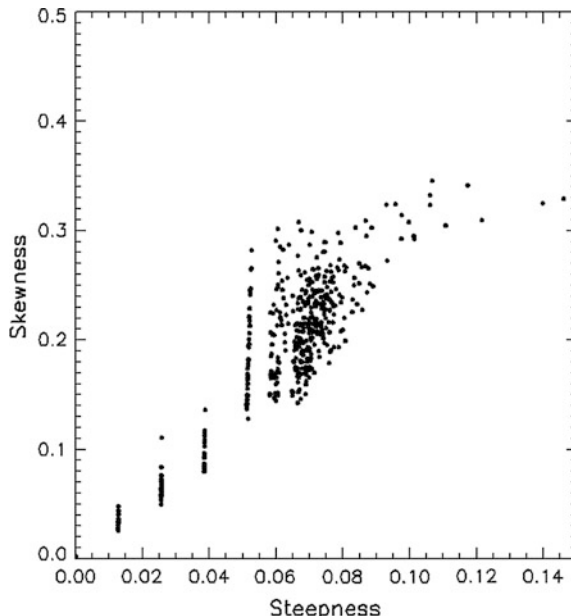


**Fig. 5.6** Skewness  $S$  of wave field as function of the effective steepness. Each point obtained by averaging over sampling set with total length of 160,000 values (100 wave profiles) (Chalikov 2005)

The value of  $\bar{\eta}$  is very small and remains constant (because of strict conservation of the volume), and  $V$  is a doubled potential energy. When wave field is a superposition of a large number of small-amplitude harmonic waves, both the skewness and kurtosis are equal to zero. Skewness  $S$  characterizes asymmetry of the distribution of probability. If the positive values of  $\eta$  are larger than the negative values, then  $S > 0$ . Kurtosis is positive if crests are sharper and troughs are smoother than those in the case of linear waves. As shown in Fig. 5.6, the skewness is really close to 0 for  $s = 0.001$  only, but with the increase of the nonlinearity, it grows fast and reaches the value as large as  $S = 0.35$ , which corresponds to a significant increase of the values of crest heights over the depth of troughs. Qualitatively, the same properties are supported by the data on the kurtosis (Fig. 5.7) which grow with the increase of nonlinearity, thus proving that wave crests become sharper, while troughs get gentler when nonlinearity grows.

The data on skewness and kurtosis in Figs. 5.6 and 5.7 and the analysis of wave height records and the results of simulations based on the principal wave equations always exhibit the fundamental properties of a nonlinear wave field, i.e., real waves tend to be sharper and higher than the harmonic waves.

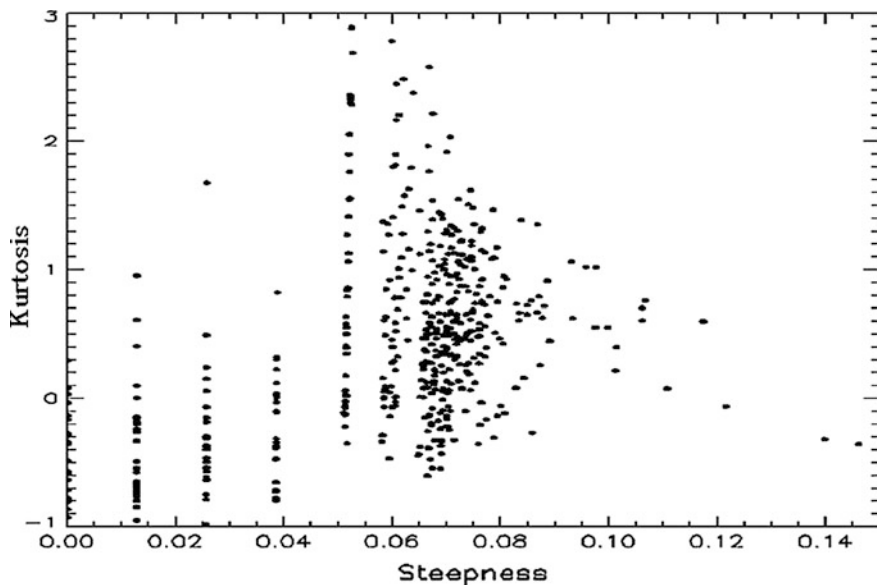


**Fig. 5.7** The same as in Fig. 5.6, but for kurtosis of wave field (Chalikov 2005)

### 5.3 Mysterious Properties of ‘Upper’ Conformal Coordinates

There are questions to be answered: Do the Stokes waves have any practical value or are they just a beautiful example of the analytical solution for the stationary gravity waves which are so unstable that they never exist? Probably, a routine Fourier presentation used in most of the theoretical and experimental investigations distorts the nonlinear nature of large waves.

Trying to answer these questions, we made an attempt of presentation of a nonlinear wave field as a superposition of Stokes waves. Naturally, the functions  $S_k$  corresponding to the Stokes waves are not orthogonal, so the calculation of the coefficients  $\sigma_k$  in expansion

$$h(x) = \sum_0^M \sigma_k S_k \quad (5.3.1)$$

becomes a minimization problem. Because the shape of Stokes waves  $S_k$  depends on its amplitude  $\sigma_k$ , it is a nonlinear problem. This problem is complicated but still resolvable. However, we found a much more elegant solution.

Let us consider the conformal coordinates for the upper domain  $z > \eta$ .

$$\begin{aligned} x &= \xi_u - \sum_{-M \leq k \leq M, k \neq 0} v_{-k}(\tau) \frac{\cosh k([H_u] - \zeta_u)}{\sinh kH} \vartheta_k(\xi_u) \\ z &= \zeta_u + \sum_{-M \leq k \leq M, k \neq 0} v_{-k}(\tau) \frac{\sinh k([H_u] - \zeta_a)}{\sinh kH} \vartheta_k(\xi_u), \end{aligned} \quad (5.3.2)$$

where  $v_k$  are the Fourier coefficients for interface, while  $\xi_u, \zeta_u$  are the conformal coordinates in the upper domain. The transformations (2.2.3) and (2.2.4) have a somewhat opposite behavior of ‘density.’ Where the Jacobean in the lower coordinate is small (in the crests), in the upper coordinate, it is large. The opposite situation is with the troughs. The system of coordinates (3.3.2) is used for modeling of the turbulent flow above waves and windwave interaction (Chalikov 1998, Chap. 9). In this work, we use the transformation (5.3.2) for the infinite height  $H_a$ . The advantage of this transformation is that for the same accuracy of approximation, the sharp waves in the lower coordinates need a significantly larger number of modes than those in the upper coordinates. The number of modes for the approximation with the same accuracy in the Cartesian coordinates is somewhere in between. The convergence of Fourier expansion is the fastest in the upper coordinates and the lowest in the lower coordinates. For  $k = 10$ , the value of Fourier mode in the upper coordinates is by 2 decimal orders smaller than that in the Cartesian coordinates and by 3 decimal orders smaller than that in the lower coordinates. This statement is illustrated in Fig. 5.8 representing the spectra of Stokes waves (thin curves) with the steepness  $ak = 0.05, 0.10, 0.15, 0.20, 0.25$

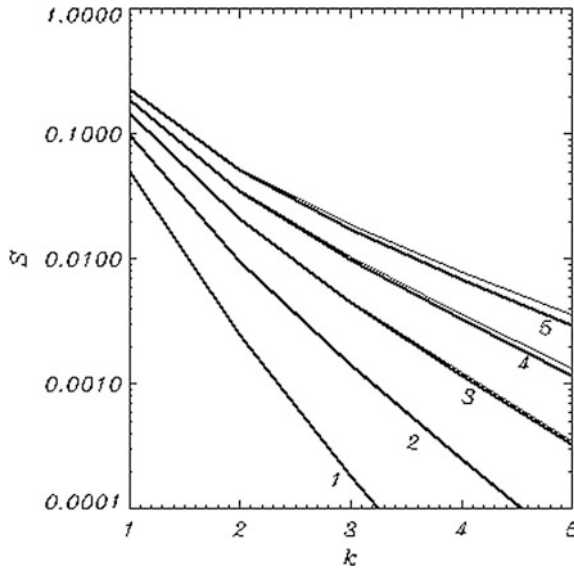


**Fig. 5.8** Thick curves correspond to Stokes wave spectrum in lower coordinates [Eqs. (2.2.3) and (2.2.4)], and thin curves correspond to  $a \cos(\xi_u)$  in upper coordinates (Eqs. 5.3.2) transferred to power coordinates by periodic spline interpolation. 1— $a = 0.05$ , 2— $a = 0.10$ , 3— $a = 0.15$ , 4— $a = 0.20$ , 5— $a = 0.25$  (Chalikov 2005)

(for infinite depths) calculated in the lower coordinates [Eqs. (2.2.3) and (2.2.4)] with the method described in Sect. (2.4.2). Thick curves represent the function  $a \cos(\xi_u)$  in the upper coordinates (Eq. 3.3.2), transferred to the lower coordinates by periodic spline interpolation with the accuracy of the order of  $10^{-11}$ .

In general, the steepness of sea waves rarely exceeds the value  $ak = 0.30$ , so the Fourier presentation of wave surface in the upper coordinate can be considered with high accuracy as the expansion over Stokes waves which are nearly orthogonal in the upper coordinate system and orthogonal in the Cartesian coordinate system with the weights corresponding to the inverse Jacobian. In Fig. 5.9, the left panel represents the averaged wave spectra calculated in the Cartesian coordinates for 10 cases (Table 3.1), while the right panel shows the difference between the averaged wave ‘spectrum’ in the upper coordinate and the spectrum in the Cartesian coordinates. As seen, the difference at low wave number is large and positive, while in high wave number, it is negative. It means that the presentation of surface as a superposition of Stokes waves is more compact than the routine presentation as a superposition of linear waves. It is well known that sea waves usually have sharp crests and gentle roughs. All quasi-linear theories ignore such evident property of real wave fields. This property explains qualitatively the increase of the skewness and kurtosis for steep waves shown in Figs. 5.6 and 5.7.

Visual observations of a long-wave evolution of surface show that a steep enough wave field exhibits the quasi-periodic behavior: A period of more or less

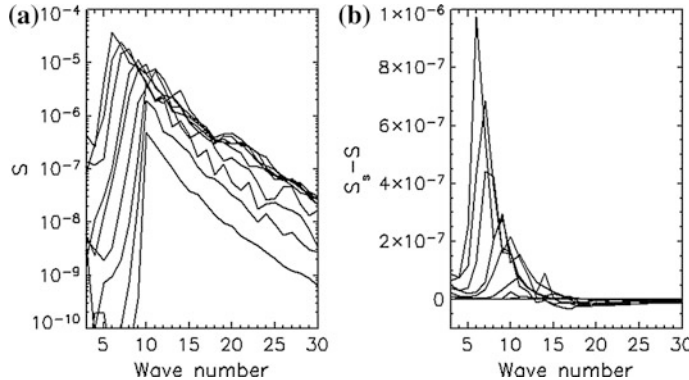


**Fig. 5.9** Left panel the same as in Fig. 5.2 spectra in linear  $k$ -scale; right difference between spectra and ‘spectrum’ over Stokes waves (Chalikov 2005)

smooth waves follows the period when large waves become sharper (the same effect was observed by Song and Banner 2002). In our calculations, the length of domain was equal to 10 lengths of peak wave. During the period of sharpening, several waves may become sharper simultaneously, though more often it happens with just one wave. In Fig. 5.10 (panel 1), an evolution of the kinetic and potential energies for  $s = 0.089$  is given. Both energies fluctuate with the amplitude up to 10 %, but their sum remains constant within many decimal digits. In panel 2, the top curve represents an evolution of the maximum wave height defined over the whole period for 2500 wave profiles separated by interval  $\Delta t = 1$ ; bottom curve corresponds to the evolution of the minimum value of the second derivative  $\partial^2\eta/\partial x^2$  for the same set. As seen, the periods of the wave height increase always coincide with the periods of the minimum of the second derivatives corresponding to the sharpening of crests. In panel 3, the ‘sharpest’ wave profile for time  $t = 815$  corresponding to the minimum of  $\partial^2\eta/\partial x^2$  is presented (dotted curve), while solid line is the smoothest wave profile (the minimum of absolute value of  $\partial^2\eta/\partial x^2$ ). It is evident that both profiles are equally smooth, except for the first of them which has a single high peak. The wave number spectra of these profiles are given in panel 4. The spectrum corresponding to the first case has large high wave number values. In fact, all these components were required for correct approximation of a single sharp peak in the domain. So, for most of the cases with a developed wave field, a considerable part of high-frequency spectrum does not correspond to real waves. It is just an artifact created due to the effort of the linear presentation of a strongly nonlinear process. In reality, concentration of energy occurs in a physical space making its Fourier presentation meaningless. This might also explain why the formally calculated timescales (Eq. 3.16 and Fig. 5.4) for high-frequency waves are so small.

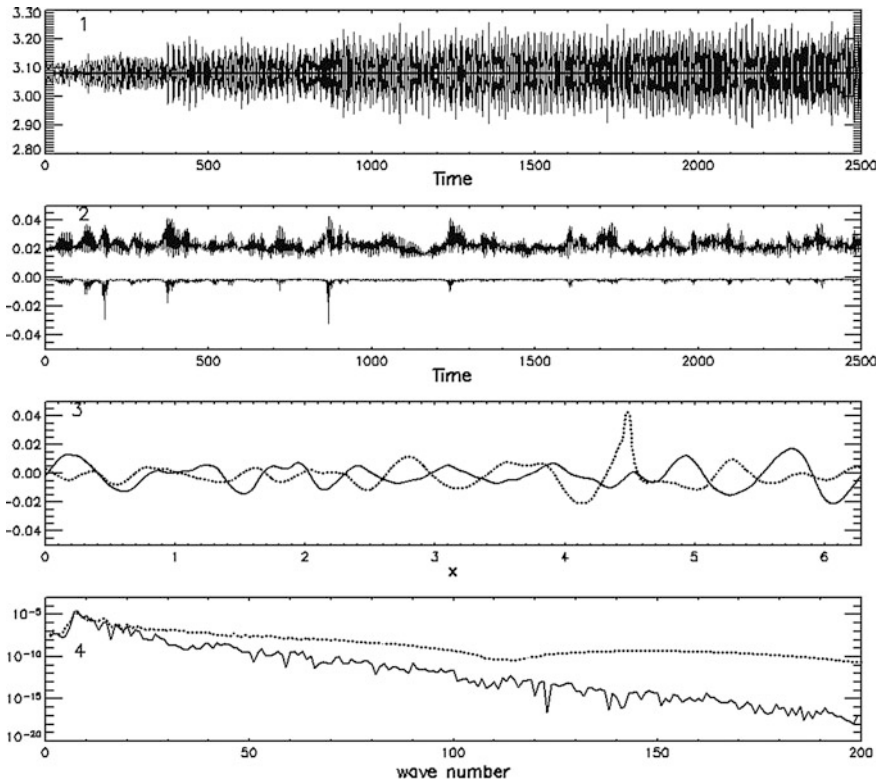


**Fig. 5.10** 1 The evolution of kinetic and potential energies (thin lines). Their sum (thick line) remains constant all over the time. 2 the top curve represents evolution of the maximum wave height defined over whole period for 2500 wave profiles separated by interval  $\Delta t = 1$ ; bottom curve—the evolution of the minimum value of the second derivative  $\partial^2\eta/\partial x^2$  for the same set. 3 the ‘sharpest’ wave profile for time  $t = 815$  corresponding to the minimum of  $\partial^2\eta/\partial x^2$  (dotted curve); the ‘smoothest’ wave profile for time  $= 2224$ , corresponding to the maximum (minimum of the absolute value) of the  $\partial^2\eta/\partial x^2$  (solid line). 4 the wave spectrum corresponding to the ‘sharpest’ wave profile (dotted line) and ‘smoothest’ wave profile (solid line) (Chalikov 2005)

## 5.4 Conclusions

Consideration of the timescales for a multi-mode wave field with initially random phases shows that the low-frequency waves preserve their individuality, but their ‘lifetime’ decreases with the increase of steepness. The total energy of each mode always fluctuates because of the quasi-periodic reversible energy exchange between the wave components. It is intriguing that the length of the period of such fluctuations on the average equals 9 wave peak periods. It reminds the famous sailor’s rule of ‘ninth wave.’ For high frequencies, the lifetime is of the order of one period, and these disturbances cannot be attributed to waves, rather to ‘wave turbulence.’

The applicability of 1-D approach and even of the potential assumption for high-frequency waves is highly questionable. This approach obviously cannot properly simulate the processes where 2D nonlinear interactions are of essence. However, from the results of this work, an important conclusion follows for 2-D waves as well. Naturally, all the nonlinear effects in a 2D case should be clearer pronounced. Such interactions are more intense in potential approximation formally because of an infinitely larger number of interacting modes. However, for the windwave interaction problem, the 1-D wave model is acceptable because it is able to produce a broad spectrum of waves and surface disturbances which generate rich statistics of nonlinear fluctuations in the airflow above waves.

It is well known that in real wave field, the dominant waves have more or less sharp crests and gentle troughs. Naturally, when a routine Fourier presentation is used, for approximation of such waves, additional modes are required which are sometimes called ‘bound waves.’ For some reason, the shape of dominant waves is close to Fourier modes in the ‘upper’ coordinate system. Naturally, these modes form an orthogonal basis in the ‘upper’ coordinate system, being also orthogonal in the Cartesian coordinate system with the weights equal to the inverse Jacobian of transformation to the ‘upper’ coordinate. It is remarkable that the Fourier expansion for stationary solutions for potential waves in the ‘upper’ coordinate system (Stokes waves) converges faster than those in the Cartesian coordinate system. For real wave field with the moderate steepness, the superposition of Fourier modes in the ‘upper’ coordinate is very close to the superposition of Stokes waves in the Cartesian coordinates.

The most important application of the scheme developed is the coupled modeling of waves and wave boundary layer (see Chalikov 1998, 9). The majority of works are actually based on the small-amplitude assumption. This oversimplified approach can be used for simple qualitative analysis only. The linear approaches are definitely inapplicable for giving recommendations on such complicated issues as a type of closure scheme for a full nonlinear problem. Lots of works use the nonlinear approach based on Reynolds equations, most of them considering the stationary flow above monochromatic waves (e.g., the simulations of Mastenbroek et al. 1996; Meirlink and Makin 2000, based both on the model created by Chalikov 1978). It is known that even small disturbances of such obstacles as sharpening of crest produce a dramatic change of the pressure field and form drag (this effect is well known in the engineering fluid mechanics). It is also known that just a simple group effect can produce high and steep waves (in physical space) with the deep minimum of pressure behind the crests. The nonlinearity enhances the effect of sharpening, thus strongly increasing the pressure difference. On the total, wave drag and energy exchange are the results of the ensemble effect of the essentially non-stationary fluctuations of pressure and surface stresses. It is clear that all these processes are completely absent in routine monochromatic stationary models.

It cannot be proved that the multi-mode wave field interacts with atmosphere as a set of independent waves and that true integral result could be obtained by simple superposition of monochromatic cases. It is well known that even a single wave produces a broad spectrum of pressure fluctuations which complicate the flow. The

atmospheric response to a strongly non-stationary wave field is also essentially non-stationary. The structure of the non-stationary flow (e.g., a distribution of surface pressure) can be completely different from the stationary one. The first attempt to take into account such nonlinearity and group effects was made using our old finite-difference model (see review Chalikov 1986) where wave surface was assigned as a superposition of running waves with different frequencies. Such approach is much closer to reality than that based on the stationary models, because it allows us to reproduce group structure of waves and its nonlinear consequences. However, it was found that such approach, being a lot better (and much more complicated) than the monochromatic stationary approach, turned out to be imperfect too, because the specifics of the real wave shapes and nonlinear group structure were not represented.

The main disadvantage of 1-D approach is weak nonlinearity. It is known that in 2-D case, the nonlinearity is much stronger formally, because of an infinite number of interacting waves. Weak nonlinearity results in the formation of a fast decreasing spectrum ( $s \propto k^{-6}$ ). Unfortunately, the 1-D model cannot provide a more saturated spectrum. However, the main conclusions of this work concerning inapplicability of the linear dispersive relation and a transient character of high-frequency waves are definitely true for 2-D waves.

# Chapter 6

## Nonlinear Interaction in One-Dimensional Wave Field

**Abstract** Full nonlinear equations for one-dimensional potential surface waves were used for investigation of evolution of the initially homogeneous train of exact Stokes waves with steepness  $AK = 0.01 - 0.42$ . The numerical algorithm for integration of non-stationary equations and calculation of exact Stokes waves is described. Since the instability of the exact Stokes waves develops very slowly, a random small-amplitude noise was introduced in the initial conditions. Development of instability occurs in two stages: In the first stage, the growth rate of disturbances was close to that established for small steepness by Benjamin and Feir in (1967) and for medium steepness—by McLean (1982). For any steepness, Stokes waves disintegrate and create a random superposition of waves. For  $AK < 0.13$ , waves do not show tendency for breaking which is recognized by surface approaching a non-single value shape. Sooner or later, if  $AK > 0.13$ , one of the waves increases its height and finally comes to a breaking point. For the large steepness  $AK > 0.35$ , the rate of growth is slower than for medium steepness, but it does not turn to zero, as it was predicted by McLean (J Fluid Mech 114:315–330, 1982) on the basis of linearized equations for disturbances. The data for spectral composition of disturbances and their frequencies are given. The model is used for investigation of evolution of the wave field initially assigned as a train of harmonic waves. It is shown that a harmonic wave of any amplitude quickly generates new modes which undergo complicated evolution. These modes cannot be referred to neither as bound waves nor as free waves. The results of numerical simulation of adiabatic evolution of the waves assigned in the initial condition with empirical spectrum are presented. It is shown that wave spectrum is subject to strong fluctuations. Most of such fluctuations are reversible; however, a residual effect of the fluctuations causes downshifting of the spectrum. The rate of downshifting depends on the nonlinearity.

## 6.1 Adiabatic Transformation of Stokes Waves

In this chapter, the investigation of nonlinear properties of 1-D surface wave is done for the wave train of Stokes waves. The stability of such an initially uniform wave train was a subject of many investigations. It was shown that for weakly nonlinear waves, it is unstable to low-frequency perturbations (Lighthill 1965), Benjamin and Feir (1967), (hereafter B.-F.). The numerical investigations (Longuet-Higgins 1978) extended those results to the large-amplitude waves and long-wave perturbations. The most detailed results were obtained by McLean (1982) who investigated numerically the stability of exact Stokes waves to two-dimensional small-amplitude disturbances. The evolution of disturbances was investigated using linearized equations. An experimental investigation of the 2-D instability of finite-amplitude waves was performed in (Melville 1982).

This work deals with the 1-D finite-amplitude Stokes waves disturbed by the small-amplitude initial noise, on the basis of the fully nonlinear equations. In this case, the development of disturbances and their interaction with the initial waves are simulated in a fully nonlinear manner, being regulated by conservation of the total energy and momentum.

Here, we applied the method for numerical simulation of the surface waves developed in ChSh, to the investigation of the evolution of Stokes waves with the wave number  $K$  and the amplitude  $A$  (capital letters  $A$  and  $K$  are used for description of the initial conditions at  $t = 0$ , while  $a$  and  $k$ —for variables).

Choosing the value of  $K$  is not a trivial problem. If  $K = 1$  is assigned, then a successive mode (not existing in the initial conditions) has a wave number  $k = 2$ , so it is twice shorter. Obviously, such a poor approximation imposes restriction upon the nonlinear interactions and generation of the additional modes. Assigning  $K = 1$  is convenient for validation of the model by comparison with the analytical stationary solution, because such a ‘dense’ presentation of waves (e.g., Stokes waves or Crapper waves) does not leave room in the Fourier space for development of the intermediate modes by instability. This is why the solution for running Stokes waves demonstrated in Chap. 4 was stable during thousands of periods. Putting  $K \geq 2$  (the analytical solution is described in this case by the modes with the wave numbers  $k = nK$ ,  $n$  is an integer) changes the situation dramatically, i.e., the potential possibility of development of waves at wave numbers  $(n - 1)K + 1 < k < (n + 1)K - 1$ ) arises. Theoretically, these waves cannot appear in a model, but like in nature, the noise (mostly the errors of time derivatives approximation) always creates the background. No matter how small the parasitic perturbations are, they do inevitably grow, resulting finally in a major transformation of wave surface. Increasing accuracy of the numerical scheme can delay this development, though for investigation of the geophysical fluid dynamics problems, it is not necessary, because the presence of noise and development of instability correspond to the physical reality. Even very small-amplitude waves with  $AK = 0.01$  are unstable, but because the time of development of B.-F. instability for small

$AK$  is proportional to  $(AK)^2$ , the integration should be performed over quite long periods.

All the calculations described below were initially performed for the monochromatic waves assigned by the linear theory in a range  $AK = 0.05 - 0.40$  with no initial disturbances. Since these waves are not a solution of steady equations, an initial wave train for  $AK > 0.28$  undergoes strong modification up to a clear tendency for overturning. The fast growth of modes with the wave numbers  $50n(n = 2, 3, 4\dots)$  was observed at the initial stage of run. Such evolution takes place at precise conservation of the invariants: The sum of the potential and kinetic energies is preserved with accuracy of the order of  $10^{-15}$  (the conservation of the horizontal momentum and volume is even better). The amplitudes of the newly emerging modes are not small, this evolution occurring for any steepness  $AK \geq 0.05$ . Strictly speaking, the pure small-amplitude monochromatic linear waves never exist. It is surprising that a new set of amplitudes was similar to a corresponding set of ‘bound’ waves for the Stokes wave with approximately the same amplitude as compared with the amplitude of the initial linear wave. It means that the wave crest tends to be sharper, while the trough becomes smoother. When the initial monochromatic waves turn into a complicated multi-mode wave field, the surface becomes much closer to the superposition of Stokes waves than to the superposition of linear waves, as it is usually assumed in the quasi-linear theories (Dold 1992). The same calculations performed for the initially assigned exact Stokes waves showed that the train of such waves is more stable. Contrary to the monochromatic waves, introducing of finite-amplitude initial disturbances is inevitable in this case. Otherwise, the growth of the computational noise turns out to be very slow, which makes the approach impractical.

Finally, we choose the value  $K = 50$  which provides a fair approximation for the growing components of the spectrum. Fourier modes for the initial Stokes wave have the wave numbers  $k = 50n$ , where  $n = 2, 3, 4\dots$ . The individual evolutions of the wave surface for different resolutions are different, so upon disintegration of the initially homogeneous wave train, the solutions can be compared by their statistical characteristics only, for example, for the averaged on time wave spectrum. The simulations of the evolution of Stokes waves calculated by the algorithm described in Part 2 were performed for the number of modes  $M = 2000$  and the number of grid points  $N = 8000$ , which provided sufficient resolution both in the Fourier and physical spaces even for the steepest waves. The initial small-amplitude noise for variable  $z$  is assigned as a random function of a number of points in grid space, uniformly distributed within the range  $[-10^{-6}A, 10^{-6}A]$ . The velocity potential for noise was calculated on the basis of the linear theory. The time step  $\Delta\tau$  was equal to 0.002. The application of a twice-shorter time step for the strongly nonlinear cases proves that the differences between the results are negligible. The calculations were done for 42 different values of initial steepness:  $AK = 0.42 - 0.01i$  where  $i = 0, 1, 2, 3\dots 41$ . Stokes waves were calculated in the  $(\xi, \zeta)$  coordinates with the algorithm described in Chap. 3. The post-processing was done for the data transferred back from the  $(\xi, \zeta)$  coordinates to the Cartesian coordinate by a periodic

spline interpolation providing the accuracy of the order of  $10^{-11}$  for very steep waves and  $10^{-30}$  for the small-amplitude waves. The maximum length of integration  $\tau_{\max}$  was chosen equal to 4000, which corresponds to 4500 periods of the initial wave. The runs for  $AK > 0.13$  were terminated upon approaching to overturning. A criteria for terminating the run was defined by the first appearance of a non-single value of surface  $\eta$ :

$$x(i+1) < x(i), \quad i = 1, 2, 3 \dots N-1 \quad (6.1.1)$$

It was possible to continue integration after that point; however, the details of that development are not the subject of this chapter. It is important to note that after the moment when the criterion (6.1.1) has been reached, the solution would never return to stability; the volume of the fluid crossing the vertical  $x(i)$  quickly increases. Up to this moment, conservation of the sum of the potential and kinetic energies of the horizontal momentum and the volume was excellent. The overturning always starts on the crest of the steepest wave. When the surface becomes a non-single value, at the initial stage of further evolution, the conservation of invariants remains good, but later, a sharp increase of energy occurs, and further integration becomes pointless. Usually, it happens just for one Runge–Kutta time step, so the primary cause of such numerical instability is probably the growth of the right-hand sides of Eqs. (2.2.34) and (2.2.35). Application of the dynamic time stepping (similar to that used by Zakharov et al. 2002) can prolong this agony, though for a very short time. The numerical instability connected with breaking has a physical nature. In reality, the falling volume of water becomes rotational and splits into small patterns (which manifests itself, e.g., as whitecapping). A well-pronounced long jet simulated in Dold (1992) was probably obtained by applying a severe smoothing in a physical space. We do not apply such smoothing.

According to the Benjamin and Feir instability theory for the first-order Stokes waves, the amplitudes of disturbances  $a_k$  in the vicinity of the main mode with the wave number  $k = K$  grow exponentially

$$a_k \propto \exp(\beta_k t), \quad (6.1.2)$$

In our notations, the explicit formula for  $\beta_k$  derived in B.-F. can be represented in the form

$$\beta_k = \gamma_k K^{1/2}, \quad \text{where } \gamma_k = 0.5 |d_k| \left( 2(AK)^2 - d_k^2 \right)^{1/2}, \quad (6.1.3)$$

where  $d_k$  characterizes a relative ‘distance’ in a Fourier space between the modes with the amplitude  $a_k$  and the main mode  $A_K$

$$d_k = \left( \left( \frac{k}{K} \right)^{1/2} - 1 \right). \quad (6.1.4)$$

Below, the function  $\gamma$  is represented as a function of two parameters:  $AK$  and  $\delta_k$  where

$$\delta_k = \frac{k}{K} - 1, \quad (6.1.5)$$

hence

$$d_k = (\delta_k + 1)^{1/2} - 1. \quad (6.1.6)$$

The numerical investigation of instability of exact Stokes waves based on the linearized equation for disturbances was done by McLean (1982). It was found that for small  $d_k$ , the results perfectly coincide with the predictions of B.-F. theory, but with increase of  $d_k$  (or  $\delta_k$ ), the rate of growth becomes considerably less than that predicted by B.-F. It was also found that with increasing steepness, the one-dimensional perturbations are stable and the three-dimensional perturbations become the most unstable.

Analysis of the results of our calculations showed that a simple scenario described by Eq. (6.1.2) and investigated in (McLean 1982) is not complete. The fully nonlinear equations predict two regimes of development of instability. The examples of evolution of amplitudes for different steepness and values of  $d_k$  are given in Figs. 6.1 and 6.2. In Fig. 6.1, the development precisely corresponds to (6.1.2). After a short initial period of fast fluctuations at  $t < 10$ , the modes  $k = 33(d = -0.34)$  (solid line) and  $k = 67(d = 0.34)$  (dashed line) for the steepness  $AK = 0.21 - 0.26$  grow exponentially until reaching the quasi-equilibrium regime, when all the modes fluctuate in time (see examples in Chalikov 2005). The newly emerging modes are nearly symmetrical relative to the central modes with wave number  $K = 50$ . The examples of the second type of evolution are represented in Fig. 6.2. As shown, the amplitudes of modes with wave numbers  $K = 10(d = -0.80)$  and  $k = 90(d = 0.80)$  undergo two stages, i.e., slow and fast development. Obviously, the B.-F. instability theory and the numerical results of McLean (1982) are valid for the first regime, while the second regime remains unexplained. The numerical model of McLean (1982) assumed one-way interaction between the unperturbed Stokes wave and small-amplitude disturbances. The values of  $\beta$  as a function of  $AK$  and  $d_k$  were calculated by the rms method approximating the equation

$$\log(a_k) = \log(a_0) + \beta(AK, d_k)t, \quad (6.1.7)$$

( $a_0$  is an initial value of  $a_k$ ) for the first and second stages separately. A formal definition of the point where the first regime is replaced by the second regime is difficult, so these values were chosen for each case manually. Duration of each regime expressed in periods of Stokes wave as a function of steepness  $AK$  is given in Fig. 6.3. A dotted line indicates duration of the first stage of development.

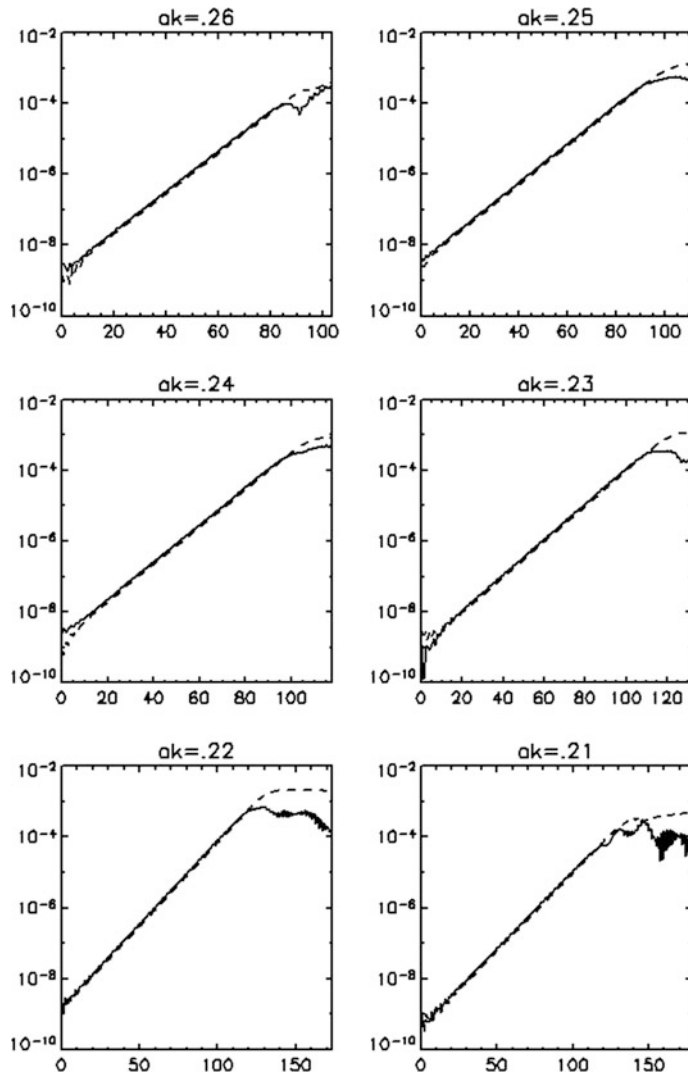


**Fig. 6.1** Examples of first type of development: initial evolution of the amplitude of the modes with wave numbers  $k = 33(d = -0.34)$ , solid line, and  $k = 67(d = 0.34)$  (dashed line) for steepness  $AK = 0.21-0.26$ . Horizontal axis corresponds to time and vertical axis to amplitude (Reproduced with permission from Chalikov 2007. © 2007 AIP Publishing LLC)

A thin dotted curve corresponds to the second period where the growth was considerably faster than in the first period. A solid line indicates the total duration of run up to the point of onset of breaking. For  $AK = 0.13$ , the waves survive over 1921 periods, while for  $AK = 0.12$ , the breaking does not happen at least within 4500 periods. Hence, the critical initial steepness falls in the interval

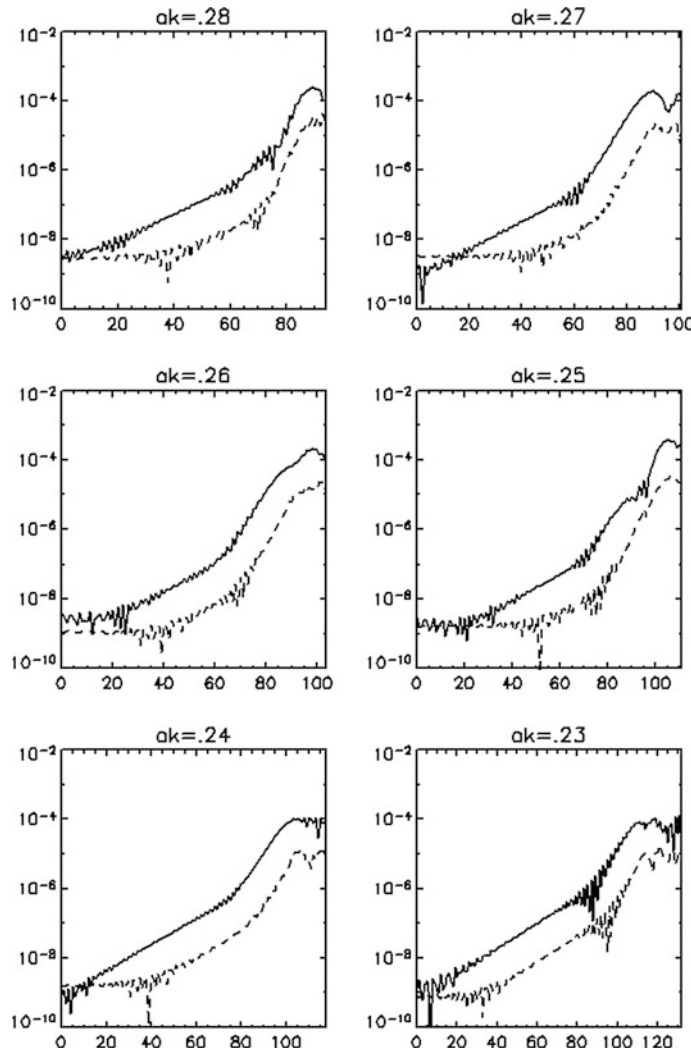
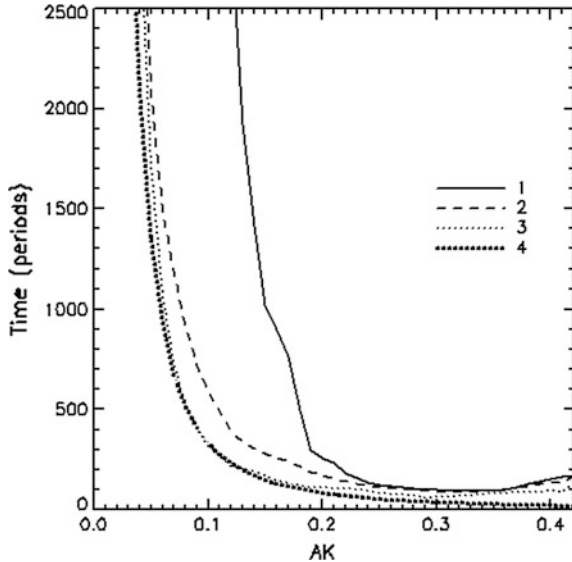


**Fig. 6.2** The same as in Fig. 6.1 but for second type of development: wave numbers  $k = 10(d = -0.80)$  and  $k = 90(d = 0.80)$  for steepness  $AK = 0.23-0.28$  (Reproduced with permission from Chalikov 2007 © 2007 AIP Publishing LLC)

(0.12 and 0.13). An attempt to define this value with a third digit was unsuccessful, because the precise evolution is sensitive to the choice of initial disturbances. In general, the data on initial development of disturbances in the first regime (curve 1) cannot be considered as absolute, because development can be stretched by decreasing the level of the initial noise. A thick dotted line corresponds to dependence  $t \propto (AK)^{-2}$  following from the B.-F. theory. It is remarkable that this dependence is valid at least for  $AK < 0.15$ .

**Fig. 6.3** Duration of the first regime (curve 3), the second regime (curve 2), and total time up to terminating of run due to breaking onset (solid line 1) as function of initial steepness  $AK$ . Curve 4 corresponds to dependence  $t \propto (AK)^{-2}$ . All times are expressed in periods of wave with wave number  $K = 50$  (Reproduced with permission from Chalikov 2007 © 2007 AIP Publishing LLC). (Reproduced with permission from Chalikov (2007). © 2007 AIP Publishing LLC)



The example of development of unstable modes for  $AK = 0.13$  is given in Fig. 6.4. The initial spectrum represents the modes of Stokes wave at wave numbers  $k = nK, n = 1, 2, 3, \dots$  and superimposed noise. As shown, disintegration of Stokes waves occurs in a more complicated manner than it was predicted by the B.-F. theory: The similar disturbances grow around all the modes with wave numbers  $k = nK, n = 2, 3, 4, \dots$ . This result proves the prediction of the McLean (1982) theory describing development of one-dimensional disturbances (Class 1 in McLean's notation) in a form

$$\eta' = \sum_{-\infty}^{\infty} a_j \exp(i((1 + \delta)jx - \sigma t)) \quad (6.1.8)$$

where  $a_j$  is the amplitudes.

The amplitudes of the modes emerging around the modes of Stokes wave are much smaller than the amplitude of the main mode ( $k = K = 50$ ). Obviously, the bound disturbances for these modes cannot result from the local interactions in the vicinity of the modes with the wave numbers  $k = nK$  for  $n > 1$ , because according to Eq. 4.3, the energy of these modes are too small to be able to support such a development simultaneously with developing around the first Stokes mode. Distributions of new modes growing around the modes of Stokes wave are similar to each other. It is most likely that these modes grow due to quadratic self-interactions which were demonstrated in Chap. 4.

The rate of growth  $\gamma$  for the disturbances around the first mode of Stokes wave in the first period, as function of  $\delta$  for different steepness, is shown in Fig. 6.5. For small steepness, the calculated data are in excellent agreement with the B.-F. theory,

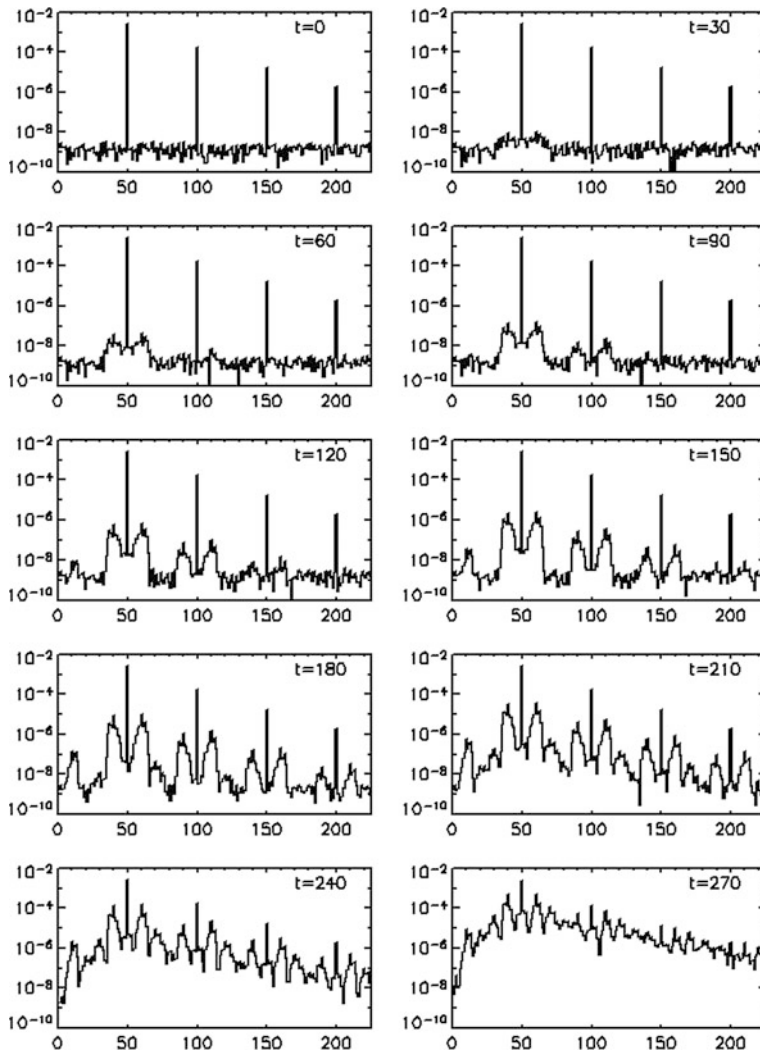


**Fig. 6.4** Example of evolution of spectrum due to development of unstable modes for  $AK = 0.13$ . Vertical axis corresponds to wave numbers and horizontal axis to amplitudes (Chalikov 2005) (Reproduced with permission from Chalikov 2007 © 2007 AIP Publishing LLC)

but with increasing of steepness, the numerical model gives smaller values of  $\gamma$ . The same results were obtained with the linearized equations integrated in a strongly nonlinear environment (see McLean 1982). For  $AK = 0.40$ , the linear B.-F. theory for the first-order Stokes wave overestimates  $\gamma$  by one decimal order. The numerical experiments predict also additional areas of fast growth with the maximum in the vicinity of  $\delta = +0.7$ . For  $\delta = 0.7$ , this area can be referred to the area of influence of the second Stokes mode at  $K = 100$ . These maxima are repeated around each

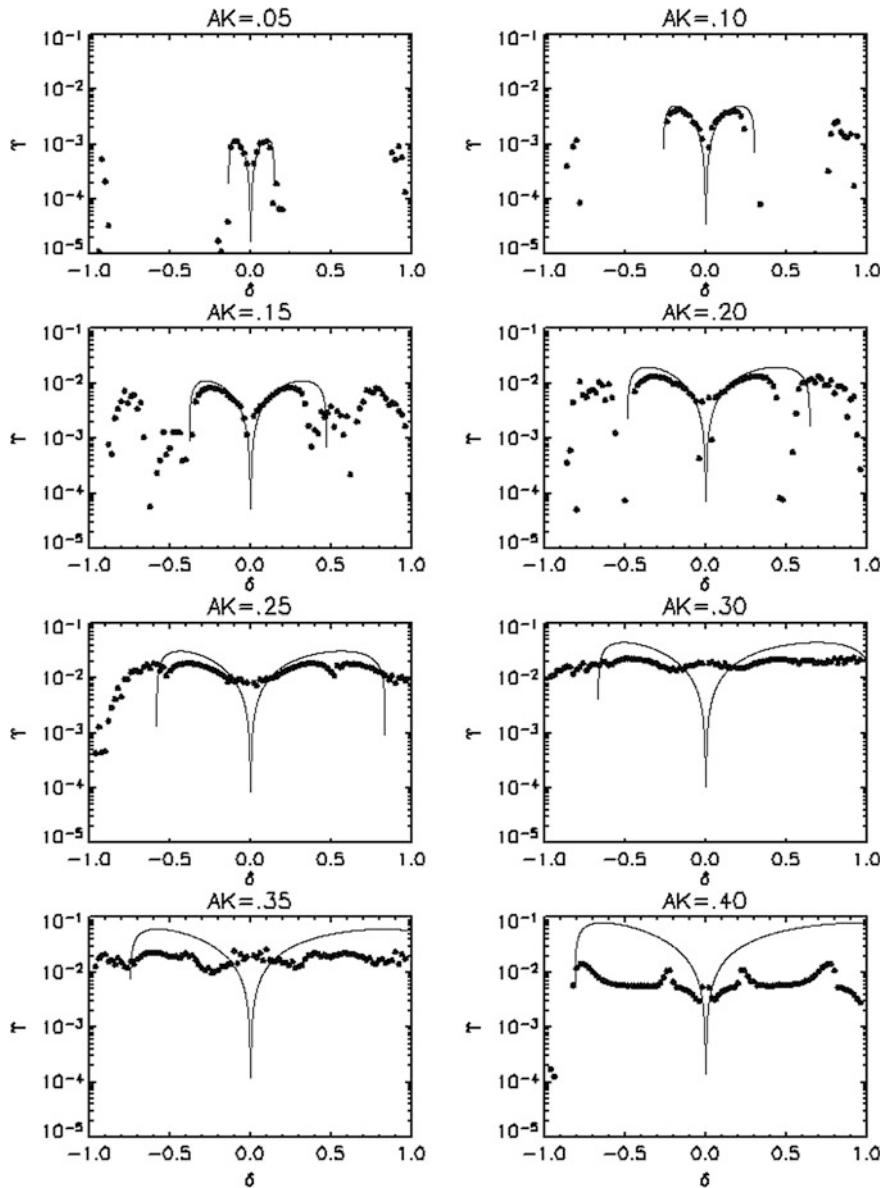
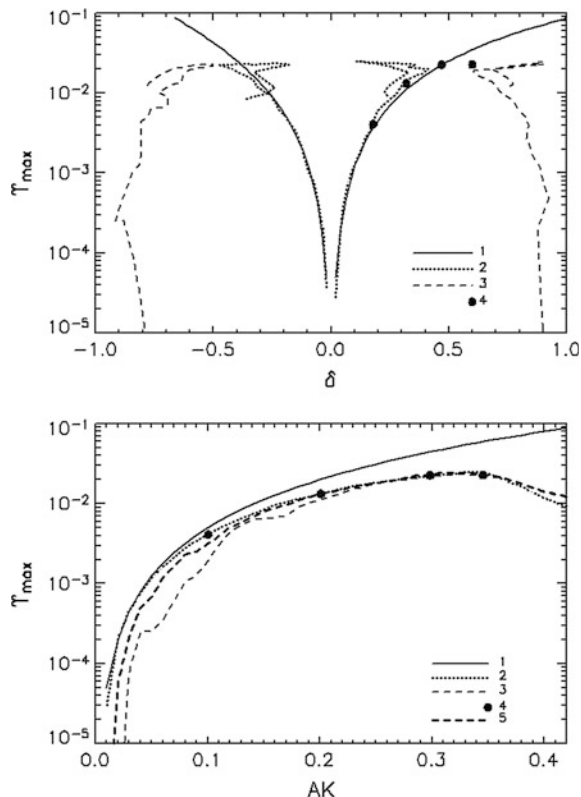


**Fig. 6.5** Non-dimensional growth rate  $\gamma$  in the first stage of development as function of  $\delta$  and  $AK$ . Solid lines correspond to B.-F. analytical results and the dots are estimations obtained with Eq. (6.1.7) (Reproduced with permission from Chalikov 2007 © 2007 AIP Publishing LLC)

Stokes mode. The cause of growth of the super-harmonics of Stokes wave around  $\gamma = -0.7$  is unclear. For the large steepness  $AK > 0.25$ , the rate of growth becomes nearly constant for all  $\delta$ . The calculations (McLean 1982) predicted decrease of  $\gamma$  at  $AK > 0.35$ . Our calculations do not confirm this behavior, rather supporting the results obtained by Kharif and Ramamonjisoa (1988). McLean predicted appearance of two-dimensional disturbances for large  $AK$  initially identified by Longuet-Higgins (1978). The current model, being essentially one-dimensional, predicts unstable regime in the entire  $\delta$  domain. The three-dimensional problem is discussed in Chap. 12.

The data on maximum growth rate  $\gamma_{\max}$  in the interval  $(-1 < \gamma < 1)$  for the first period is given in Fig. 6.6 (solid lines). The location of this point relatively to the main mode ( $\delta = 0, k = 50$ ) is given in the top panel. As shown, for  $|\delta| < 0.2$ , the location of maximum growth coincides precisely with the predictions of B.-F. theory. In the interval  $0.2 < \delta < 0.4$ , the results are very close to the data obtained by McLean (1982). For  $\delta > 0.4$ , an agreement with the McLean calculations is poor, because the location of the point of maximum is difficult to define (see panel for  $AK = 0.30$  in Fig. 6.5). The second maxima of growth are located around  $\delta = +0.8$  (dotted lines). At large  $AK$ , their position is also unstable. The dependence of  $\gamma_{\max}$  on steepness  $AK$  is given in the bottom panel (Fig. 6.6). Again,  $\gamma_{\max}$  at small

**Fig. 6.6** Results of estimations of the growth rate for first stage. *Upper panel*—maximum rate of development disturbances as function of  $\delta$  (Eq. 6.1.5): 1 B.-F. theory; 2 estimations with Eq. (6.1.7) for primary maxima; 3 the same estimations for secondary maxima; 4 maximum rates calculated by McLean (1982). *Bottom panel*—1 B.-F. theory; 2 estimation with Eq. (6.1.7) for primary maxima (values for  $\delta > 0$  and  $\delta < 0$  are practically coincide); 3 ( $\delta < 0$ ) and 4 ( $\delta > 0$ ) are estimations with Eq. (6.1.7) for secondary maxima (Reproduced with permission from Chalikov 2007 © 2007 AIP Publishing LLC)



$AK$  agrees with the B.-F. theory; however, starting from  $AK = 0.2$ , the  $\gamma_{\max}$  becomes smaller: At  $AK = 0.35$ , it is 5 times smaller than in the B.-F. theory. The same data as in Fig. 6.6 but for the second stage of growth are given in Fig. 6.7. As shown, the rate of growth of disturbances at this stage is considerably higher than at the first stage, but for large steepness, the rate of growth is also decreasing.

The generalized data on the rate of growth  $\gamma$  as a function of steepness  $AK$  and  $\delta$  for the first stage are given in Fig. 6.8. The value  $\delta = 0$  corresponds to the zero mode of Stokes wave ( $K = 50$ ). The contours of  $\gamma$  are nearly symmetrical with regard to  $\delta = 0$ . The maximum value  $\gamma = 0.027$  was found in point  $\delta = 0.5, AK = 0.32$ . A close value  $\gamma = 0.025$  was obtained in symmetrical point  $\delta = -0.5, AK = 0.32$ .

The more specific data on disturbances at the first stage are given in Fig. 6.9 where the wave number spectrum  $S_k$ , frequency spectrum  $S_\omega$ , and wave number/frequency spectrum  $S_{k\omega}$  are presented. For these calculations, we used the records of the amplitudes of the Fourier components  $\eta_k(t)$  in the Cartesian coordinate system

**Fig. 6.7** The same as in Fig. 6.6 but for second stage  
(Reproduced with permission from Chalikov 2007 © 2007 AIP Publishing LLC)

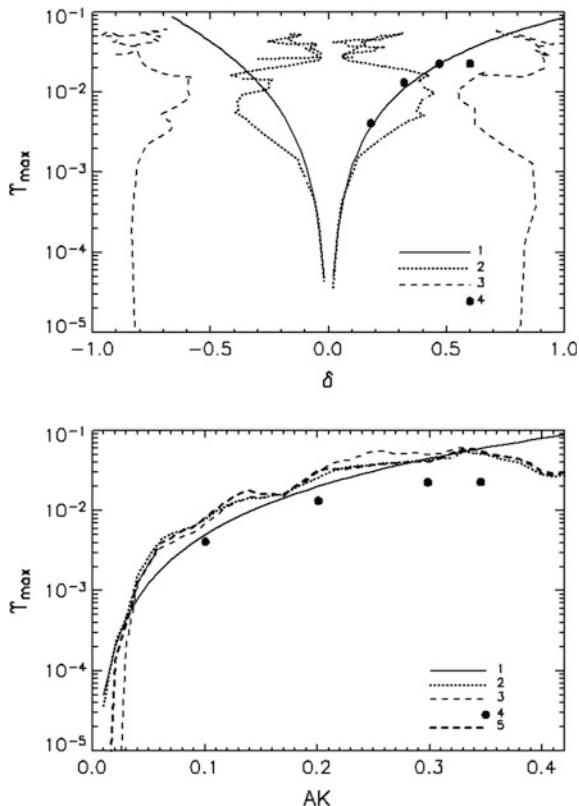
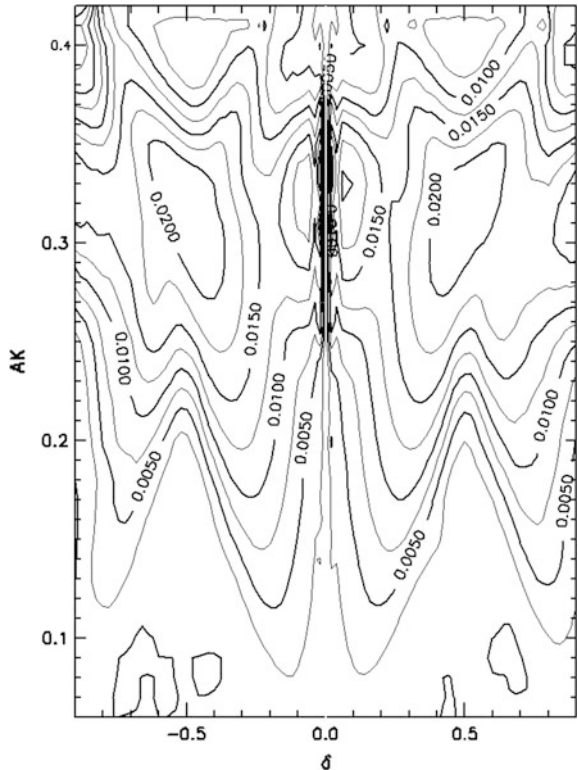


**Fig. 6.8** Rate of growth  $\gamma$  (contours) in a first stage as function of  $\delta$  and  $AK$  (Reproduced with permission from Chalikov 2007 © 2007 AIP Publishing LLC)



$$\eta(x, t) = \sum_{-M \leq k \leq M} \eta_k \vartheta_k(x), \quad (6.1.9)$$

(where functions  $\vartheta_k$  are defined by 2.2.6). Then,  $\eta_k(t)$  are represented by the Fourier series over time

$$\eta(x, t) = \sum_{-M \leq k \leq M} \sum_{0 < l < \Omega} h_{kl} \vartheta_l(t) \vartheta_k(x). \quad (6.1.10)$$

The density of spectrum  $S_{k\omega}$  can be calculated by the formula

$$S_{k\omega} = \frac{1}{2} \left( (h_{k,l} - h_{-k,-l})^2 + (h_{k,l} - h_{-k,l})^2 \right), \quad (6.1.11)$$

and frequency  $\omega$  is connected with index  $l$  by the relation

$$\omega = \frac{2\pi}{T_r} l, \quad (6.1.12)$$

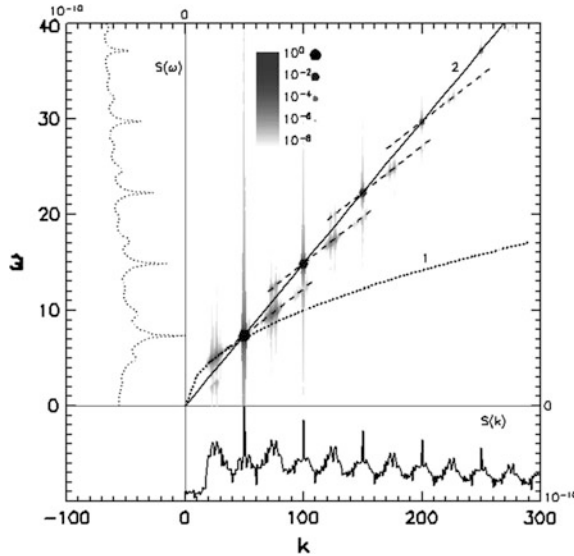


**Fig. 6.9** Wave spectrums for  $AK = 0.32$  obtained by averaging over first stage of instability development. Wave number/frequency spectrum is drawn by dots of different sizes and color (see legend and explanations in a text): 1 linear dispersive relation and 2 dispersive relations for modes of the Stokes wave. Wave number spectrum is drawn in a bottom right quadrant (*bottom horizontal axis* corresponds to wave numbers and *right vertical axis* to wave number spectrum). Frequency spectrum is drawn in left right quadrant (*left vertical axis* is a frequency, and *top horizontal axis* corresponds to frequency spectrum (Reproduced with permission from Chalikov 2007 © 2007 AIP Publishing LLC)

where  $T_r = 214.26$ , and  $l$  is length of period (consisting of 21,426 records including  $2M + 1 = 4001$  Fourier amplitudes  $\eta_k$  through the time interval  $\Delta t = 0.01$ ). The spectrum  $S_{k\omega}$  is defined in a range of the wave numbers  $(-M \leq k \leq M)$  and in a range of the frequencies  $(0 \leq \omega \leq \Omega)$  where  $\Omega$  is a maximum frequency  $\Omega = 2\pi/\Delta t = 200\pi$ .

The solid curve shown in Fig. 6.9 corresponds to the wave number spectrum  $S_k$  normalized to its maximum value (the lower part of the right axis) obtained by summation over  $\omega$

$$S_k = \sum_{i=0,J} S_{k\omega} \Delta \omega \quad (6.1.13)$$

where  $J = 0.5(T_r/\Delta t - 1)$  is dimension of  $S_{k\omega}$  over frequencies. Dotted curve corresponds to the wave number spectrum  $S_\omega(\omega)$  (left part of the top axis) normalized to its maximum value obtained by summation over  $k$

$$S_\omega = \sum_{k=-M,M} S_{k\omega} \Delta k. \quad (6.1.14)$$

Both spectra contain well-pronounced peaks at wave numbers of the Stokes wave modes. The structure of disturbances between the consequent modes of Stokes wave is the same. These disturbances are less pronounced in the frequency spectrum  $S_\omega$  because the amplitudes of disturbances fluctuate in time. Much more information is delivered by the wave number–frequency spectrum  $S_{k\omega}$ . Physically, the  $S_{k\omega}$  is the doubled density of the potential energy in a cell  $((k, k + \Delta k), (\omega, \omega + \Delta\omega))$  where  $\Delta k = 1$  and  $\Delta\omega = 2\pi/T_r$ . The negative values of  $k$  correspond to the waves running to opposite direction (these waves were not assigned in the boundary conditions). These waves are also generated, but their energy is small, so we neglect them. Actually, the spectrum  $S_{k\omega}$  decreases quickly with the growth of  $k$  and  $\omega$ , so we consider domain only for the relatively low- positive wave ( $k < 300$ ) numbers and low frequencies ( $\omega < 40$ ). The spectra  $S_{k\omega}$  are shown in Fig. 6.9 for the initial stage of run with  $AK = 0.32$ . The left axis corresponds to the frequency  $\omega$ , while the bottom axis shows the wave number  $k$ . The spectrum is drawn as the circles whose size and blackness depend linearly on  $\log_{10}(S_{k\omega})$  (see legend). Hence, the main components of Stokes waves correspond to the black circles, while small disturbances are shown by gray dots. All components of Stokes wave lie precisely on a straight line (2) corresponding to the theoretical seventh-order phase velocity of Stokes waves  $C_s = 0.1488$  with the accuracy up to 4 digits. The dotted line represents dependence  $\omega = k^{1/2}$  (linear phase velocity for  $k = 50$  equals to 0.1414). The disturbances are represented by their averaged values for the entire first stage of development, so their actual values up to the end of this period are larger than those represented in Fig. 6.9. The amplitudes of modes of Stokes wave in the presence of disturbances are not constants due to the fast (and obviously reversible) nonlinear interaction between the modes and disturbances. This is why each point corresponding to the Stokes wave modes is surrounded by a broad vertical halo (gray vertical lines, aggregated, in fact, from a large number of gray points). The additional modes growing due to B.-F. instability between the Stokes wave modes also have variable amplitudes. Each mode of Stokes wave is surrounded by two families of disturbances arising below and above the wave number of mode  $k_s$  of Stokes wave. The disturbances with  $k < k_s$  move faster than Stokes wave, while the disturbances at  $k > k_s$  move slower. Only the first group of waves which are the super-harmonics for Stokes wave satisfy well to the linear dispersive relation. All other growing modes can be attributed neither to free waves (because they lie far away from the dotted line corresponding to the linear dispersive relation) nor to the ‘bound waves’ of Stokes wave (because they do not fall to the solid straight line). The connection between frequency  $\omega$  and wave number  $k$  for disturbances can be approximated by formula:

$$\omega = \omega_s + c_k(k - k_s) \quad (6.1.15)$$

where  $\omega_s = C_s k_s$  are the frequencies of the Stokes modes. Dependences (4.1.15) are shown in Fig. 6.9 by dashed lines. Remarkably, those disturbances grow symmetrically relatively to the Stokes modes in a wave number space, an empirical coefficient  $c_k = 0.097$  preserving its value with good accuracy for all Stokes modes.

## 6.2 Quasi-Stationary Regime

The time of instability development (see Fig. 6.3) depends strongly on the initial nonlinearity characterized by steepness  $AK$ . An evolution of 25 modes with the wave numbers  $k = 25 + 2n$ ,  $n = 1, 2, 3 \dots 25$  for  $AK = 0.15$  is shown in Fig. 6.10.

It is shown that some of the modes are developing exponentially until reaching a quasi-stationary regime, and other modes are developing in two stages, slow and fast. By the end of this development, the disturbances absorb most of the energy of zero Stokes mode. Finally, the wave surface becomes a random superposition of running nonlinear waves with fluctuating amplitudes. This quasi-stationary regime

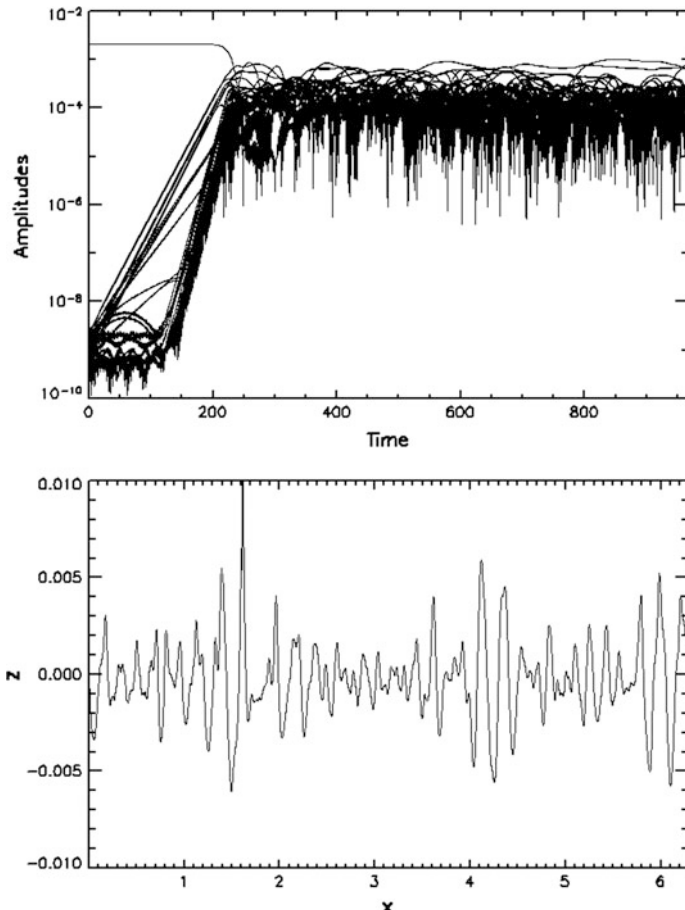


**Fig. 6.10** Top panel evolution of amplitudes of modes with wave numbers  $k = 25 + 2n$ ,  $n = 1, 2, 3 \dots 25$  adjacent to main mode of Stokes wave ( $K = 50$ ); bottom panel last recorded surface  $z$  before breaking (Reproduced with permission from Chalikov (2007). © 2007 AIP Publishing LLC)

was explicitly simulated for all the values of steepness  $AK > 0.04$ . Presumably, for smaller steepness, this regime can be reached too, but the time scale for development of the B.-F. instability increases as  $(AK)^{-2}$  (see Fig. 6.3, curve 4); hence, such development takes a very long time. The final surface on the way to breaking (bottom panel in Fig. 6.11) is a typical multi-mode wave surface. Note that the peak of spectrum in a quasi-stationary regime is shifted to the lower wave numbers as compared with its initial location.

The nature of the modes appearing due to the nonlinearity is fairly complicated. The simulated quasi-stationary regime for  $t > 250$  was used for calculating phase velocities and spectrum (top and bottom panels in Fig. 6.10). The calculation of an

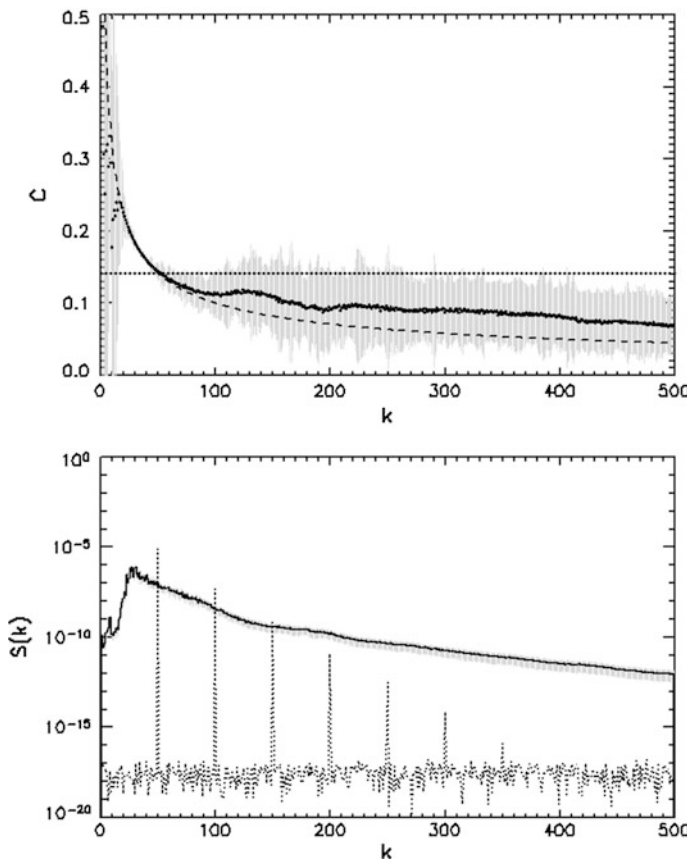


**Fig. 6.11** Characteristics of wave field in quasi-stationary regime for  $AK = 0.15$ ,  $250 < t < 950$ , top panel phase velocity  $c$  as function of wave number  $k$  calculated with Eq. (6.3.4). Dotted line corresponds to initial phase velocity of Stokes wave,  $c_s = 0.1488$  and dashed line is a linear dispersive relation  $c = k^{1/2}$ . Bottom panel is a wave spectrum in quasi-stationary regime. Gray vertical lines characterize the scatter of spectrum; gray dotted line corresponds to initial spectrum of Stokes wave. (Reproduced with permission from Chalikov 2007 © 2007 AIP Publishing LLC)

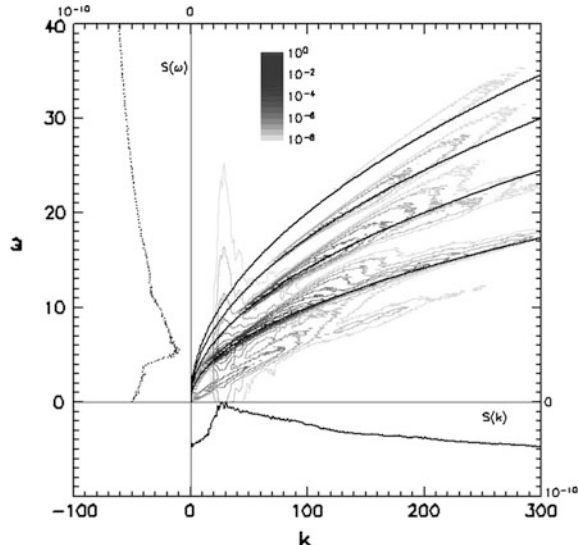
instantaneous value of the phase velocity of the  $k$ th wave component can be done with the relations (2.7.4) and 2.7.5).

For a developed spectrum, the lowest modes ( $k = 20–80$ ) obey dispersive relation, but the phase velocity for high wave numbers is larger than that for the linear waves. A simple explanation of such phenomenon was given in Chalikov and Sheinin (1998). In fact, at each wave number, several modes coexist: One is a free wave; all others are the so-called bound waves corresponding to the additional modes attached to every steep enough wave. Naturally, these ‘bound’ waves run with the phase velocity of carrying wave. The calculations of the phase velocity based on (5.2) give a weighted value between the velocities of free and several bound modes. Evidently, the nonlinear waves cannot obey a strict dispersion relation  $\omega = |k|^{1/2}$  because the calculation type of the relation (4.2.1) assumes that amplitude of any wave  $A_k = (a_k^2 + a_{-k}^2)^{1/2}$  remains constant. Figure 6.12 and the statistical data on ‘life time’ of waves given in Fig. 6.3 prove that only the low-wave number modes with large amplitudes remain more or less steady. For the high-wave number modes, a timescale of unsteadiness is of the order of one period, and such waves are rather a nonlinear object than the free waves. A scatter of the dispersion relation can be also increased by Doppler effects, i.e., the phase velocity of short waves is affected by orbital velocity fields produced by all waves.

Let us suppose that the wave field represented by a set of nonlinear waves, as well as the frequencies of main modes  $\omega_{i0}$ , satisfies the dispersive relation

$$\omega_{i0} = k_i^{1/2}(1+f(a_ik_i))^{1/2}, \quad (6.2.1)$$

**Fig. 6.12** The same as in Fig. 6.11, but for  $AK = 0.15$ ,  $250 < t < 950$ . Solid lines correspond to generalized dispersive relation (Eq. 6.2.3) for  $n = 0, 1, 2, 3$  (Reproduced with permission from Chalikov 2007 © 2007 AIP Publishing LLC)



where  $f$  is a function correcting the linear dispersive relation for the case of finite amplitude.

Let us define that Eq. (6.2.1) corresponds to the bound mode of 0th order and find a frequency of the  $n$ -order bound mode  $\omega_{kn}$  ( $n = 1, 2, 3, \dots$ ) at wave number  $k$ . The bound mode has the same phase velocity as its main carrying mode with the wave number  $k_m = k/(n+1)$  and frequency  $\omega_m = k_m^{1/2}$ . Hence, the frequency of the  $n$ -order bound mode  $\omega_{kn}$  can be found from the proportion

$$\frac{k_m}{\omega_m} = \frac{k}{\omega_{kn}}, \quad (6.2.2)$$

and the general dispersion relation for any order of bound modes obtains the form

$$\omega_{kn} = ((n+1)k)^{1/2}(1+f(a_m k_m))^{1/2}, \quad (6.2.3)$$

where  $k_m = k/(n+1)$  and  $\omega_m = k_m^{1/2}$  are the wave number and frequency of the carrying wave. Neglecting the correction  $f$ , Eq. (6.2.3) obtains a simple form

$$\omega_{kn} = ((n+1)k)^{1/2} \quad (6.2.4)$$

The branches for  $n = 0, 1, 2$  ( $k > 0$ ) and  $n = 0$  ( $k < 0$ ) are shown in Fig. 6.12 by thin lines. Three branches of the dispersive relation for  $n = 0, 1, 2$  ( $k > 0$ ) and for  $n = 0$  ( $k < 0$ ) are clearly pronounced. However, the spectrum reveals a lot of new features which are not so easy to explain. Firstly, all dependencies of frequency on wave numbers have a large scatter increasing with growth of wave numbers. Secondly, for all the branches, dependence of frequencies on wave numbers systematically declines off the dispersion relation (6.2.3) at high wave numbers. Probably, this effect can be explained by a high non-steadiness of these modes. Thirdly, there is a linear branch  $\omega = 0.14k$  which probably reflects the group effects. The contribution of different branches in the total energy is represented in Fig. 6.12 where  $S_{k\omega}$  is represented as a function of frequency  $\omega$  for different (only positive) wave numbers  $k = 25n, n = 1-8$ . Note that the results represented in Fig. 6.12 (bottom panel) are similar to the results obtained by Chalikov and Sheinin (1998, Fig. 10) where up to 14 branches of the dispersion relation were found.

Note that the calculations of a well-defined wave number-frequency spectrum even for 1-D waves require a very long time series. For calculation of spectrum in one panel in Fig. 6.12, a number of ‘measurements’ as large as 240,000,000 were used. These data can be considered as ‘precise.’ Similar calculations with the observational data need a significantly larger volume of the data. This is why just plain confirmation of linearity usually has been obtained.

### 6.3 Transformation of Harmonic Wave on Deep Water

Harmonic waves play an important role in the theory of surface waves and technical applications. It is often assumed that the real wave field can be represented as a superposition of such wave with randomly distributed phases. In many cases, such suggestion is exact enough if the exchange of energy between modes is not important. Such wave-to-wave interactions can depend on many details. For example, for investigation of the Benjamin–Feir instability, a development (Benjamin and Feir 1967) is necessary to take into account at least the first term of Stokes expansion. Hence, if carrying wave is assigned as a harmonic wave, the B.-F. instability should not arise. However, the exact modeling in the conformal coordinates shows that the B.-F. instability does arise and develops not slower than for Stokes waves. Such development manifests itself in appearance and development of the new wave components ('bound waves') due to quadratic interactions; then, the B.-F. instability starts to develop and finally the full stochasticization of wave field occurs (Chalikov 2007). It is followed by formation of irreversible fluxes of energy producing the high-wave number dissipation and shift of energy to the lower wave numbers (downshifting). The dissipation can be reduced by extension of domain in a Fourier space, but the downshifting remains in any case (Chalikov and Babanin 2014). Remarkably, this clearly pronounced and fast process cannot be reproduced on the basis of the Hasselmann's theory (Hasselmann 1962). Steep waves have two regimes of instability. The evolution of train of harmonic waves with steepness  $AK > 0.28$  is terminated by their simultaneous breaking. The waves with steepness  $AK < 0.28$  get transformed producing new modes. The rate of such transformation depends on the initial steepness, but the evolution is finally terminated by breaking if the initial steepness of carrying wave  $Ak > 0.12$  (Chalikov and Sheinin 2005). Here, the evolution of harmonic wave of small and medium steepness is investigated on the basis of the 2-D conformal model (Eqs. 2.2.34 and 2.2.35). The aim of this investigation was to prove that harmonic waves are unstable 'per se' in the absence of disturbances.

The initial condition for elevation  $\eta(\xi, \tau = 0)$  and surface velocity potential  $\phi(\xi, \zeta = 0, \tau = 0)$  for a train of harmonic waves were calculated with the formulas of the linear theory:

$$\eta(\xi) = A \cos(Kx), \quad \phi(\xi, \zeta = 0) = -AK^{1/2} \sin(Kx), \quad (6.3.1)$$

where  $A$  is an initial value of the wave amplitude with wave number  $K$ . In fact, the number  $K$  defines accuracy of approximation. Here, the value  $K = 20$  was chosen. The number of modes  $M$  was equal to 4000 and the number of knots  $N = 16,000$ . An accuracy of the numerical scheme was demonstrated earlier by simulation of a running Stokes wave. An additional proof of accuracy is the exact conservation of full energy:

$$E = (2\pi)^{-1} \int_0^{2\pi} (z^2 x_{\xi} - \varphi \varphi_{\xi}) J^{-1} d\xi \quad (6.3.2)$$

The value of  $E$  changed by less than  $10^{-7}E$  in all runs is described below. Since the subject of the investigation was an initial evolution of wave, the calculations were performed over 50 periods of carrying wave.

The linear theory prescribes that the kinetic energy of waves is equal to the potential energy. For nonlinear waves, this is incorrect: Between these two kinds of energy, a permanent quasiperiodic exchange occurs. The amplitude of such fluctuation grows quickly with the increase of steepness. An example of such fluctuations for the initial steepness  $AK = 0.255$  is given in Fig. 6.13 where an evolution of the potential and kinetic energy and their half sum is given. As seen, for this case, both components of the energy can change in the range  $\pm 5\%$ . The total energy remains strictly constant.

The main results for the waves with the initial steepness  $AK = 0.005, 0.105, 0.255$  are shown in Fig. (6.14) where the trajectories characterizing the evolution are given in space  $(f, a)$  ( $a$  is the amplitude of mode and  $f$  is a fetch for the given mode calculated by the formula

$$f_k = \int_0^{\tau} c_k dt, \quad (6.3.3)$$

where  $c_k$  is the phase velocity of  $k$ th mode calculated by the formula (4.2.7).

The derivatives on time are just the right-hand side of the Eq. (2.2.34) written for the Fourier components of  $z$ . It is convenient to use Eq. (6.3.4) for calculations by the rms method

$$\bar{c}_k = \frac{\overline{AD}}{\overline{D^2}}, \quad (6.3.4)$$

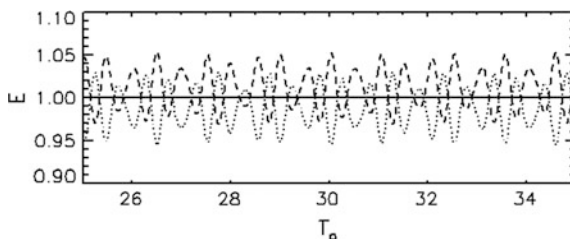
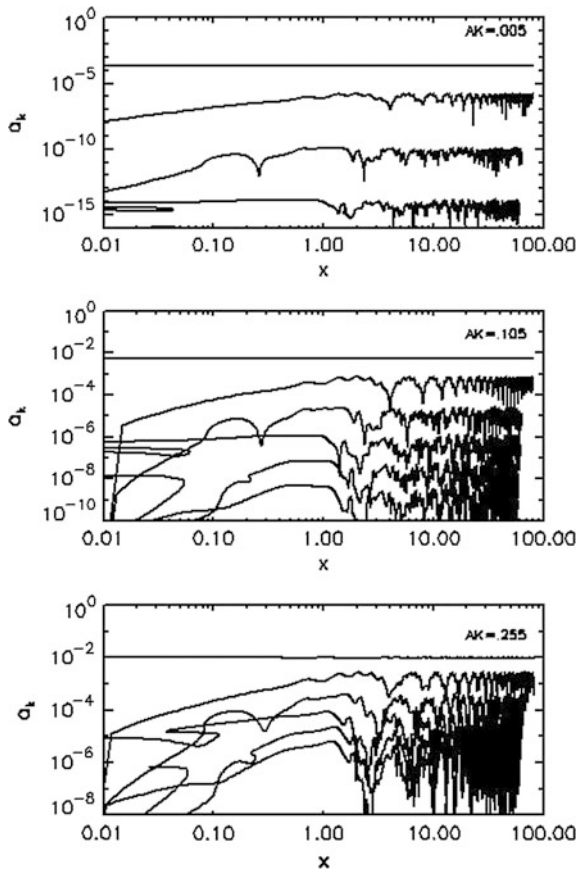


**Fig. 6.13** Example of evolution of kinetic energy (dotted curve), potential energy (dashed curve), and their half sum (solid curve) normalized by their initial values as function of time, expressed in periods of carrying wave (Chalikov 2005)

**Fig. 6.14** Evolution of amplitude of carrying mode with wave number  $K = 20$  (top, practically straight lines) and amplitudes of additional modes with wave numbers  $k = nK$  as functions of fetch expressed in lengths of carrying wave) (Chalikov 2005)

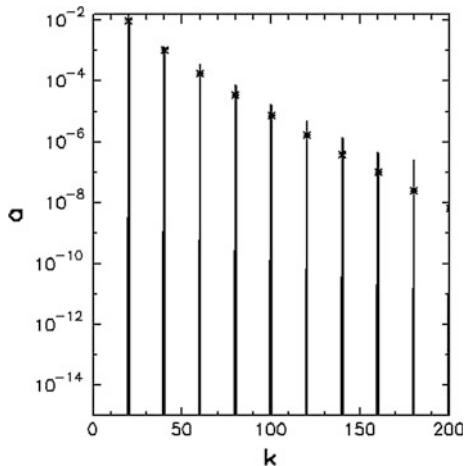


( $\overline{c_k}$  is the rms mean phase velocity,  $A$  is numerator, and  $D$  is denominator in (4.2.7)). The averaging was done over 100 consequent time steps.

The uppermost curve at each section shown in Fig. (6.14) corresponds to the amplitude of wave with wave number  $K = 20$ . Because of logarithmic scale only for the case  $AK = 0.255$ , the energy of carrying wave is not a constant. As shown, the harmonic wave immediately produces new modes at wave numbers  $k = nK$  ( $n = 2, 3, 4, \dots$ ) through the irreversible quadratic interactions. The new modes are not attached to carrying wave, and on the contrary, their phase velocities fluctuate within wide ranges. However, a fetch for each mode is comparable with that for the carrying wave. The modes with the wave numbers different from  $k = nK$  do not emerge even for a very long integration, which confirms high accuracy of the numerical scheme.

An evolution of amplitude of the carrying mode ( $K = 20$ ) and the amplitudes of the first three new modes is shown in Fig. 6.15. For convenience, not absolute

**Fig. 6.15** The averaged over time wave amplitudes as functions of wave numbers for initial steepness  $AK = 0.255$ . The stars correspond to amplitudes of modes for Stokes wave



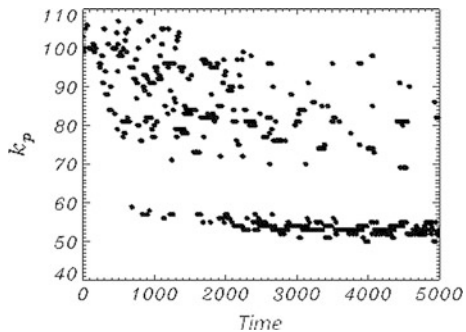
values of amplitude  $\bar{a}_k$  but their disturbances normalized by the averaged values are represented here.

$$b_k = \frac{a_k - \bar{a}_k}{\bar{a}_k}, \quad (6.3.5)$$

As shown, amplitude of the mode with wave number  $k = 40$  changes in counter-phase with the amplitude of carrying wave, the fluctuations of the modes with higher wave numbers being similar to the fluctuations of the first disturbances with wave number  $k = 2K$ .

It is most interesting that after the averaging of spectrum over time, the amplitudes of disturbances are qualitatively close to the amplitudes of Stokes wave for wave number  $K$  (see Fig. 6.16).

**Fig. 6.16** The wave number  $k_p$  in a maximum of spectrum as a function of time (Case 6)



## 6.4 On Nonlinear Energy Transfer in Unidirected Adiabatic Surface Waves

Here, the model was used for simulation of a deepwater wave evolution for very long periods (Chalikov 2012). The wave field in the initial condition was assigned as a superposition of linear waves with random phases and a spectral distribution described by the one-dimensional JONSWAP spectrum for different inverse wave ages  $\Omega = U/c_p$  ( $U$ —a wind velocity,  $c_p$  is a phase velocity of wave in the peak of spectrum), i.e., for different wave steepness. Since the equations were integrated over thousands of wave periods, the details of initial conditions as well as a specific set of phases were of no significance.

In the course of evolution, the wave spectrum was changing due to the nonlinear interactions. Opposite to the linear case, a value of the integral potential energy  $E_p$  in the nonlinear wave field is not a constant, since the potential  $E_p$  and kinetic  $E_k$  energies fluctuate. However, the total energy  $E = E_p + E_k$  is an adiabatic integral invariant. The total energy in the numerical model remains constant on condition that a spectral domain is very broad and a flux of energy into the high-wave number part of the spectrum is not restricted. For a finite size of the domain, a flux of energy into the truncated part of the spectrum occurs. A corresponding decrease of the total energy can be considered as dissipation. To make the process quasi-stationary, such a weak loss of energy was compensated by appropriate correction of the total energy  $E$ . The procedure of the high-wave number smoothing and maintaining of the total energy was described in Sects. 2.3 and 8.3 (see also Chalikov 2005).

The equations were integrated with the total number of modes  $M = 1000$  and the number of grid knots  $N = 4000$  with time step  $\Delta t = 0.001$  for 5,000,000 steps, which corresponds to 8000 initial peak wave periods  $T_p = 2\pi/\omega_p$ , where  $\omega_p$  is frequency in the maximum of the initial spectrum  $S(t = 0, \omega)$  connected with the peak wave number  $k_p$  by the dispersion relation  $\omega_p = \sqrt{k_p}$ . The initial value of  $k_p$  was always equal to  $k_0 = 100$ . The initial spectrum decreases fast for the wave numbers  $k < k_p$ , while for  $k > k_p$ , it was assigned in a wave number space up to the wave number  $k_p + 20$ . We do not give more details, because a specific shape of the initial spectrum is of no significance, and only the integral characteristics are important (see Table 6.1).

**Table 6.1** Integral characteristics of numerical runs (see text)

No	$U/c_p$	$s_1$	$s_2$	$\Delta_k$
1	1.0	0.064	0.029	12
2	1.5	0.078	0.036	19
3	2.0	0.092	0.042	30
4	2.25	0.097	0.044	33
5	2.5	0.103	0.047	34
6	3.0	0.113	0.051	42
7	3.5	0.123	0.055	50

The main parameter of JONSWAP spectrum is the so-called inverse wave age  $U/c_p$  ( $U$  is wind velocity,  $c_p = k_p^{-1/2}$  is phase velocity in the peak of spectrum) which characterizes the stage of the sea wave development. The value  $U/c_p = 3.5$  corresponds to the case of steep ('young') waves when wind velocity exceeds phase velocity 3.5 times. The value  $U/c_p = 1$  corresponds to the case of 'old sea,' when wind velocity is equal to the peak phase velocity. In this case, the waves do not obtain energy from wind. In our calculation, the parameter  $U/c_p$  is used as an index for the cases with different wave steepness. The wave steepness is characterized by the two integral parameters:

$$s_1 = \left( \sum_{k=1}^M k^2 S(k) \Delta k \right)^{1/2}, \quad (6.4.1)$$

$$s_2 = k_p \left( \sum_{k=1}^M S(k) \Delta k \right)^{1/2}. \quad (6.4.2)$$

where  $S(k)$  is the spectral density in the interval  $\Delta k = 1$ . The parameter  $s_2$  characterizes the steepness of a low-wave number part of spectrum, while parameter  $s_1$  characterizes the steepness created mostly by the high-wave number modes and the local steepness in a physical space. The calculations were made for 6 different values of  $U/c_p$ . As shown, the steepness  $s_2$  in our calculation varies from 0.064 to 0.123 (the values corresponding to a developed wave field and the so-called young sea, respectively). The runs with a larger initial steepness were terminated by breaking instability followed by the local steepness approaching infinity in a physical space. The breaking can be prevented by introduction of a breaking parameterization algorithm. However, such cases cannot be referred to the adiabatic cases, so they were excluded from consideration.

The aim of this work was the observation of the spectrum evolution. It was found that at the initial stage of development, the energy spreads quickly over a high-wave number part of the spectrum, forming a spectral 'tail.' The energy moves also to a low-wave number domain, but it is a slow process. At all stages of the development, the amplitudes of each mode quickly fluctuate in time even in the peak of spectrum. Such fluctuation can be recognized as manifestation of the reversible nonlinear interactions. However, an alternative explanation can be based on a purely geometrical consideration. When the spectral resolution is high, the Fourier series represents just an approximation of surface. Since each Fourier coefficient is a product of integration over the entire domain, the small disturbances of surface can misplace the energy from one mode to another (probably, the closest to the initial one). The interpretation of wave field as a superposition of the linear modes with fixed phases and phase velocities is too straightforward to be correct.

Fast fluctuations of amplitudes obscure a directed evolution of the spectrum, but the averaged over wave number spectrum obtains a two-peak structure in all of the runs: On the low-wave number slope of the spectrum, a new peak starts to grow,

while the initial peak weakens. Finally, the spectrum shifts to the lower wave numbers. Both of the spectral peaks fluctuate, which is why the largest amplitude can belong to either of the first or the second peak, alternatively.

It is well shown in Fig. 6.17 where the location of a spectral maximum is shown as a function of non-dimensional time. The top group of points belongs to the high-wave number peak, while the bottom group refers to a new peak (see Fig. 6.20).

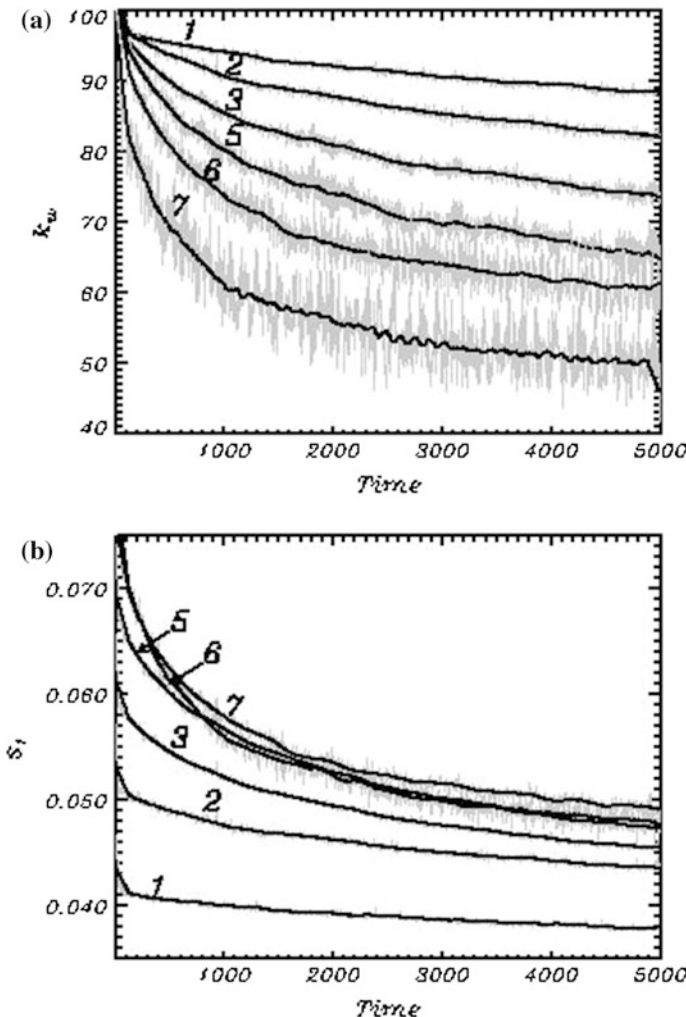


**Fig. 6.17** Results of calculations with a number of modes  $M = 1000$  and with correction of total energy: **a** dependence of a weighted wave number  $k_w$  (Eq. 6.4.3) on a time  $t$ ; **b** dependence of the integral steepness  $s_1$  on a time  $t$ . In both frames, fluctuating gray curves show actual dependence; solid curves are the product of the moving averaging with a window width equal to 41 (Chalikov 2012)

The bottom cloud of points becomes denser with time, since the low-wave number peak becomes the main one. The scatter reflects fluctuations of the amplitudes. Note that the smooth spectra demonstrated in various investigations are often obtained at low spectral resolution. Note also that contrary to the wave number spectra, the frequency spectra obtained over the long enough periods are always smooth, since the fluctuations of energy at the adjacent wave numbers cause the averaging of spectrum in a frequency space.

As shown in (6.1.7), the formally defined wave number  $k_p$  in a maximum of spectrum has a very large scatter due to the amplitude fluctuation. The mean spectrum-weighted wave number  $k_w$  defined by the following expression

$$k_w = \sum_{k=1}^M k S(k) \left( \sum_{k=1}^M S(k) \right)^{-1} \quad (6.4.3)$$

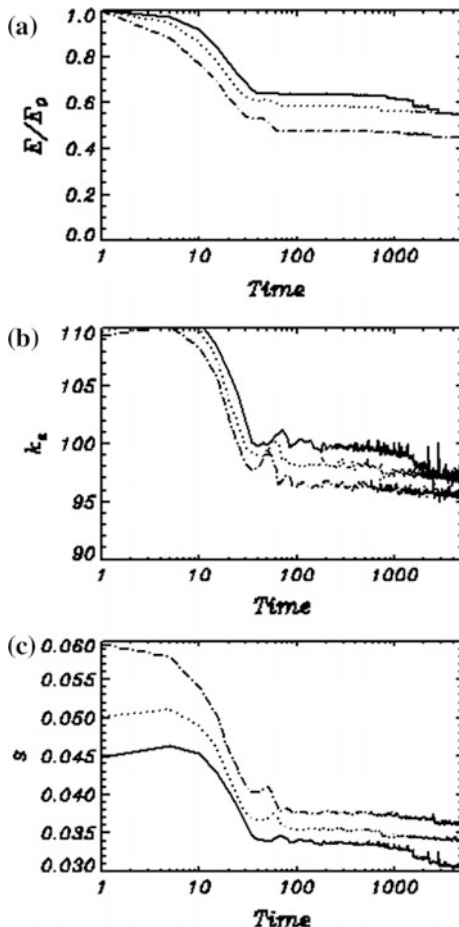
is more convenient.

In Fig. 6.18, the weighted wave number  $k_w$  is represented as a function of non-dimensional time  $t$ . For all the cases, the time was equal approximately to 8000 initial peak wave periods. As shown, all the spectra move monotonically to the low wave numbers. The rate of this downshifting increases with increase of the initial steepness (given in Table 6.1), while the steepness  $s_1$  decreases due to the spectrum broadening. It is particularly noticeable for the initial high steepness (cases 1 and 2).

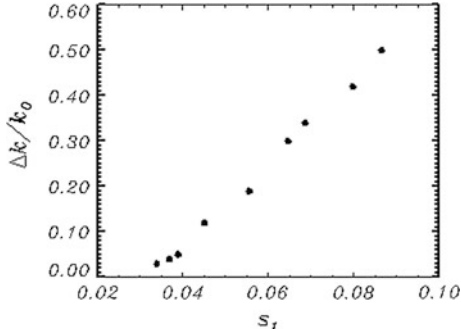
As shown in panel a, the total energy decreases up to 50-60 % from the initial value. Accordingly, the integral steepness decreases also two times (panel c). This is why the rate of downshifting became much lower than that for the same cases 1, 2 and 4 with the permanent level of energy. However, downshifting appears in these cases as well. A systematic downshifting was not reproduced in the one-dimensional wave field simulations carried out on the basis of the nonlinear Schrödinger's equation and Zakharov's equation (Janssen, 2003). Both of the approaches assume a weak nonlinearity of wave fields and use a number of simplifying hypotheses. Probably, the wave field simulated in this investigation was not steep enough to show the downshifting. It is also quite possible that the simplified 1-D equations in no way can reproduce the downshifting. The level of energy was maintained in all of the numerical experiments with an accuracy of 6 digits. The reviewer of paper (Chalikov 2012) suggested that downshifting can be produced by this input of energy. Such statement can be hardly correct, since the input of energy in every spectral bin is proportional to the energy contained in this bin. To validate this statement, three additional runs for cases 1, 2, and 4 (Table 6.1) were performed for  $M = 2048$  with no correction of energy. In this case, the truncation area was shifted far toward the high wave numbers. The results are shown in Fig. 6.19.

The total shift of the weighted frequency  $\Delta k_w/k_0$  over the entire period of integration as a function of the initial steepness  $s_1$  is shown in Fig. 6.20. As shown, downshifting in a unidirected adiabatic wave field can be quite significant. The three lowermost points shown in Fig. 6.4 were obtained with no correction of the

**Fig. 6.18** Results of the calculations with a number of modes  $M = 2048$  with no correction of the total energy:  
**a** dependence of the total wave energy on a time  $t$ ;  
**b** dependence of the spectrum-weighted wave number  $k_w$  (Eq. 6.4.3) integral steepness  $s_1$  on a time  $t$ ;  
**c** dependence of the integral steepness  $s_1$  on a time  $t$  (Chalikov 2012)



**Fig. 6.19** Dependence of the total change of the weighted wave number  $k_w$  for the entire period of integration (normalized by the initial wave number  $k_0$ ) on the initial integral steepness  $s_1$  (Chalikov 2012)



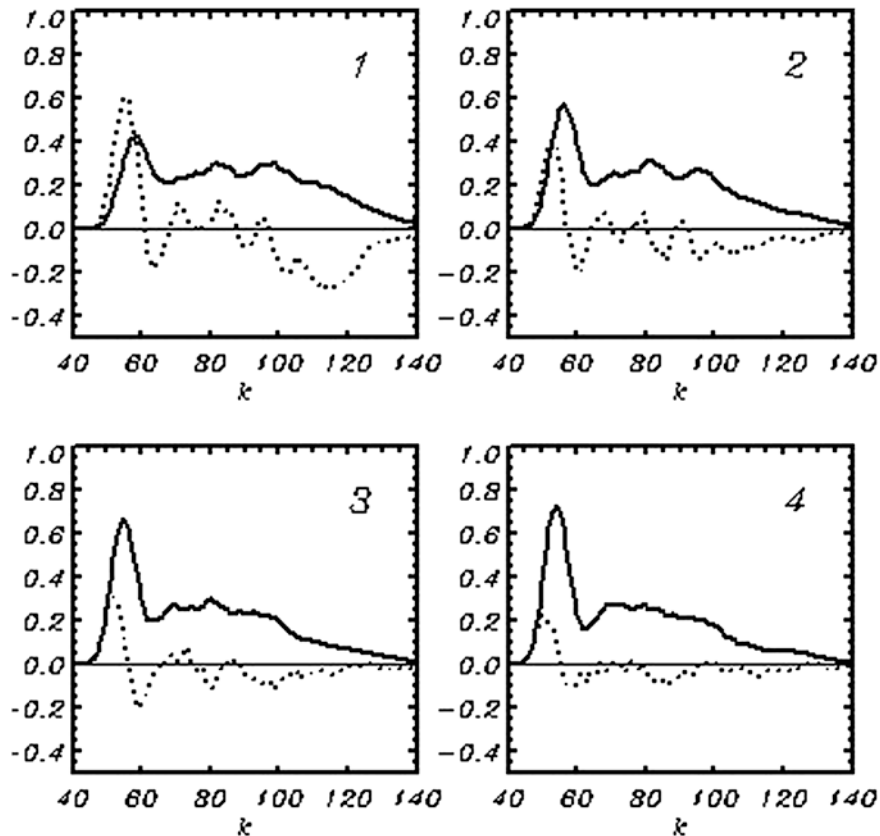


**Fig. 6.20** The averaged over the consecutive periods of length  $\delta t = 1000$  wave spectra,  $S(k)$  (solid curves) and the spectrum of the nonlinear interaction rate  $S_n(k)$  (dotted curves). The spectral density below  $k = 40$  is very close to 0

total energy. As shown, the rate of downshifting for these cases is much smaller than that for the cases with large steepness, because the wave energy dissipates due to the flux to a truncated part of the spectrum. As a result, the averaged steepness becomes small.

The wave spectrum  $S(k)$  and a rate of spectrum change due to the nonlinear interactions  $S_n(k)$  are shown in Fig. 6.20. The spectra  $S(k)$  are averaged over 5 successive intervals, while the spectra  $S_n(k)$  are just a simple difference between the successive averaged wave spectra

$$S_n(k) = (\Delta t)^{-1} (S(k, t + \Delta t) - S(k, t)) \quad (6.4.4)$$

The wave spectra have a multi-peak structure most of the time. It can be explained by the specific initial conditions, i.e., all the energy was assigned to the

unidirected modes with no angle spreading. The angle spreading lowers the energy of modes directed along the  $x$ -axis. The spectral peak in the initial condition was probably too high for 1-D simulations. Anyway, the presence of an additional peak does not change the results qualitatively. The spectrum of the nonlinear interactions rate  $S_n(k)$  reflects a tendency for the wave spectrum evolution. The spectrum  $S_n(k)$  is mostly positive on the low-wave number slopes of the wave spectrum and negative on the high-wave number slopes of the wave spectrum, which results in shifting of the spectral energy to the left.

## 6.5 Conclusions

In this chapter, we applied the method for numerical simulation of periodic surface waves, developed in ChSh, for a long-range simulation of the initially homogeneous Stokes wave train contaminated with small initial noise. The initial conditions representing the exact Stokes waves with steepness  $AK = 0.01–0.42$  are calculated with a simple and very fast algorithm developed for the stationary solution (Chapter 3). It is shown that an initial development of disturbances agrees with the B.-F. instability theory up to the steepness  $AK = 0.1$  and for the larger steepness with the results of McLean (1982). The unstable modes develop around each mode of Stokes waves. In most cases, the initial relatively slow growth is followed by the second stage of development (Fig. 6.2), when growth occurs several times faster than in the first stage. The development in the second stage is characterized by decrease of the zero-mode energy; hence, it occurs under the control of the conservations laws. The dependence of the rate of growth  $\gamma$  in the first stage is calculated in a broad range of wave numbers and steepness (see Fig. 6.8). The calculated wave number/frequency spectrum shows that the newly arising waves cannot be referred to the free linear waves or bound modes of Stokes waves. All Stokes waves (at least with  $AK \geq 0.04$ ) finally disintegrate and create a quasi-stationary multi-mode regime (Fig. 6.10). For steepness  $AK > 0.12$ , one of the waves comes to overturning, thus terminating the run. The wave fields born by Stokes waves with initial steepness  $AK \leq 0.12$  are virtually stable. The threshold  $0.12 < (AK)_c < 0.13$  is established accurately. It does not depend either on the resolution of the model or on the wave number of a zero mode of Stokes wave. The definition of a more precise value of  $(AK)_c$  is difficult because the development depends on the structure and amplitudes of the initial noise. The phase velocities of low-wave number waves at  $K < 20$  are difficult to calculate because of their low energy. In the energy-containing part of spectrum ( $20 < k < 60$ ), the waves in quasi-stationary regime agree strictly with the linear theory, but for the larger wave numbers, the phase velocity is systematically higher than that of the linear waves. It happens because the calculations of phase velocity based on (5.2) give a weighted by energy value between the velocities of free waves and several bound modes. The calculations of the wave number–frequency spectrum prove that the dispersive

relation consists of several branches. Each of them corresponds to a different order of bound waves. An explicit form of the dispersive relation was derived. The wave surface can be represented by a set of Stokes waves much more accurately than by superposition of the linear modes.

An applicability of the 1-D approach and a potential assumption of high frequency waves are questionable. Obviously, this approach cannot properly simulate the processes where irreversible 2-D nonlinear interactions are essential. The model developed can be applied for a broad range of the situations in which the 1-D approximation is acceptable. Fortunately, a lot of wave phenomena are largely controlled by strong nonlinear interactions which are relatively fast and for which the 1-D approximation is often adequate. The formation of extreme waves is one of such phenomena. As yet, the model simulations of very large waves are far from a merely academic interest. It has long been known that the nonlinear redistribution of energy can result in a sudden emerging of extremely large and steep waves, commonly known as *freak* or *rogue* waves.

The harmonic waves are not a solution of the exact equations of the potential wave theory. Hence, even in the absence of any disturbances, they undergo a complicated evolution creating the discrete spectrum of non-stationary waves. On the average, this spectrum is close to the spectrum of Stokes wave. When the initial steepness becomes larger, the rate of development of such instability increases. When the initial steepness exceeds 0.28, the instability results in the appearance of a non-single-value surface and wave breaking. Meanwhile, the Stokes wave in the absence of disturbances up to the critical steepness remains stable. In the long-term calculations, the B.-F. instability can arise due to the errors of approximation of time derivatives or to the not sufficient enough resolution in grid space, or to any details of the numerical scheme. Definitely, the harmonic waves represent a good basis for presentation of the wave field, but it is unlikely that the wave modes can be considered as the real physical objects, since the set of their amplitudes and phases depends on spectral resolution. The properties found in Sect. 2.7 show that nonlinear interactions of the linear modes can lead to unpredictable consequences.

In this chapter, the results of numerical modeling of the multi-mode unidirected adiabatic wave evolution were represented. It is shown that due to the nonlinearity, the irreversible nonlinear interactions and downshifting develop. The rate of downshifting increases with increase of the nonlinearity. This conclusion contradicts to the Hasselmann's results. The Hasselmann's theory is based on the numerous simplifying assumptions. Representing a wave field as a superposition of linear modes with random phases is most restricting assumption. In the Benjamin and Feir investigation, it was shown that keeping just the first Stokes correction for a harmonic wave resulted in the instability development. Later on, it was demonstrated that there was no need in assigning nonlinear modes because initially the 1-D harmonic waves took a Stokes-like shape. After that, the B.-F. instability developed, and a fully random wave field was generated at the nonlinear stage. Hence, the absence of the 1-D interactions is inherent to the linear waves only. It follows from the Hasselmann's integral that in a 2-dimensional wave field, all the

interactions between the modes running in the same direction are missing. Evidently, the inaccuracies of the nonlinear interaction calculations with Hasselmann's integral grow with narrowing of spectrum. Our calculations suggest that the unidirected wave interactions have probably the same intensity as those between the two-dimensional waves. This effect is important for many practical problems, especially for the wave forecasting problem.

# Chapter 7

## Modeling of Extreme Waves

**Abstract** This chapter describes the results of more than 4000 long-term (up to thousands of peak wave periods) numerical simulations of nonlinear gravity surface waves performed for the investigation of properties and estimation of statistics of extreme ('freak') waves. The method of solution of 2-D potential wave's equations based on conformal mapping is applied to the simulation of wave behavior assigned by different initial conditions, defined by JONSWAP and Pierson–Moskowitz spectra. It is shown that nonlinear wave evolution sometimes results in the appearance of very big waves. There are no predictors for appearance of extreme waves; however, a height of dimensional waves is proportional to a significant wave height. The initial generation of extreme waves can occur simply as a result of linear group effects, but in some cases, the largest wave suddenly starts to grow. It is followed sometimes by a strong concentration of wave energy around a peak vertical. It is taking place typically for one peak wave period. It happens to an individual wave in a physical space, no energy exchange with surrounding waves taking place. Probability function for steep waves has been constructed. Such type function can be used for the development of operational forecast of freak waves based on a standard forecast provided by the 3-D-generation wave prediction model (WAVEWATCH or WAM).

### 7.1 Extreme Wave Phenomenon

In sixties, the author of this manuscript was earning his living as a crewman on a fishing trawler. Dragnet fishing routes ran in North Atlantic as well as in the Barents and Norwegian seas. One day, when working on deck, we heard our sailing master's loud warning from the above porthole: 'Look out, guys!' And immediately after that our sailing master's head disappeared behind the porthole, the deadlights thoroughly closed up. We turned back and instead of a usual skyline saw a huge water mountain rapidly approaching our vessel. Normally, the skyline was clearly seen from the four meter height of our deck. All the crewmen working on deck, except of me, rushed to the tackle and got a tight hold of it. The boat was lying

athwart, but suddenly she slid violently to one side, a powerful flow of water immediately having swept over the deck. The wave was much taller than me, and in a moment, it washed overboard many tons of the fish we had caught. It also tried to throw me overboard, but fortunately, though standing fully in the cold water, I managed to reach up a shrine and was almost convulsively grasping it. Shortly after that, the wave was gone leaving behind just an empty deck. We had nothing to do but wait for another lift of our dragnet. Afterward, the crewmen having behind their shoulders many years of navigation in these waters told me that such wave has been appearing here almost every year.

The author did not know then that many years later, he would be studying this phenomenon on the professional basis. However, that experience of my youth had left such a deep impression in my soul that being already a scientist I could give a graphic description of that freak wave: (a) Its height had been somewhat around 5–7 m, while all other waves height had not exceeded three meters; (b) the wavelength along its crest had been no less than several hundred meters, while the wavelength along its movement direction had been significantly less; (c) before the wave front, a big trough had been formed, which had been the cause of such a steep roll of the boat; (e) upon wave approaching its upper slope had looked almost vertical.

The extreme waves called ‘*freak*’ or ‘*rogue*’ are formally defined as waves whose height exceeds the significant wave height  $H_s = 2$  (sometimes, 2.1 or 2.2). Sailors used call such waves ‘monster’ waves. So, if the significant wave height is equal to one meter, then all the waves with a trough-to-crest height exceeding two meters should be referred to the category of ‘freak’ waves. It is hard to imagine that such waves can be characterized as ‘monster’ waves even if they are observed from board of a small vessel. On the other side, if a steady west wind with a speed of 20 m/s in the South Ocean generates a wave with the height of around 20 m and length of around 0.5 km (according to the reports of oceanographers sailing in those areas, such waves are not rare), then such a wave would just lift and drop a vessel, the only damage incurred, being yet another attack of seasickness among the vessel crew. According to the marine folklore, freak waves appear as ‘*walls of water*’ with ‘*holes in the sea*’ around them. Quite naturally, no one would pay attention to the ‘walls’ or ‘holes’ of 1 m high. It is assumed that such ‘walls’ should be considerably higher than the elevation of observer above the peak of an incoming wave. For a small yacht, a breaking wave with a trough-to-crest height of four meters can appear as a ‘freak wave.’ The same wave, however, seems to be just a usual steep wave for a skipper of a huge tanker. Such a wave is definitely dangerous and can be obviously called ‘a monstrous wave’ by inhabitants of the land of Lilliputians.

Evidently, the current scientific definition of the term ‘*freak wave*’ is imperfect. Remarkably, the sea folklore provides a better description of freak wave properties, focusing on their shape, and assuming, of course, that they are very big. The term ‘*vertical walls*’ definitely indicates that the waves surge before observer and undergo the active phase of breaking. The linear velocities of water in breaking waves approach the phase speed of wave, which for the developed sea is close to the wind speed. A ‘*vertical wall*’ does not lift a vessel, it hits it. Such waves at wind

40 m/s can develop the dynamic pressure about  $10^6$  Pa, which is too much even for a tanker. Obviously, the great energy releasing at breaking is not the only weapon carried by extreme waves. Another dangerous property of extreme waves is a high gradient of slope or a vertical acceleration: A big vessel can be just broken on a wave of great curvature. Definitely, other properties are also important. Big and long, though, non-breaking waves can be dangerous for sea platforms, while they are relatively safe for sea vessels.

Thus, the classification of dangerous waves must be different for different objects, floating or fixed, for deep sea or near-shore area, and it must consider not only the size of waves, but also their shape and mechanical properties.

Considering the practical application of the rare wave theory, we can also come to the conclusion that a strict unconditional ‘definition’ of freak waves is not required at all. For better use of research recommendations, it would be more efficient to define the categories of freak waves, as it has been done, for examples, for tropical storms. A reasonable warning on appearance of such waves should sound as follows: ‘from 6 am today until 6 am tomorrow in a specific area of  $100 \times 100$  km a breaking wave as high as 10 m (category three) will be one of  $1000 \pm 200$  waves; a breaking wave with a height of 15 m (category five) will be one of  $8000 \pm 1000$  waves,... etc.’ For unbreaking waves, the probability of such waves is somewhat higher. The probability of coming across a freak wave is convenient to express in terms of expectance time for the waves of different categories. A set of most important dynamic characteristics of such waves can be also provided. Potential customers can decide for themselves, whether it is a real ‘freak’ wave, and modify their route or degree of preparedness accordingly. Similar recommendations can be developed for the ship designing, sea constructions, and insurance purposes. Naturally, an extreme wave is the phenomenon which manifests itself in direct contact with an object. Such cases can be relatively frequent in uncomfortable areas with high winds and low intensity of navigation (e.g., in the middle and high latitudes of the South Ocean) and, therefore, remain unnoticed. On the contrary, in the areas of recommended routes (off the coast of South Africa), even a single catastrophic event may create a ‘freak wave’ of publications. If the probability of extreme waves could be connected with the more or less standard oceanographic characteristics (e.g., the data on wind and wave climate), the estimations of climatology of dangerous waves of different categories might be very useful for industry, navigation, ship design, and, of course, insurance purposes. The reliable data on direct registration of the freak wave events are few; thus, the operational monitoring of extreme waves from satellites is the most important, though, perhaps, not resolved problem.

The attempts to completely attribute generation of big waves to focusing of wave energy on a specific geometry of currents or topography, or certain wind conditions, cannot be taken seriously. Each of such mechanisms can increase an effect of wave growth, but it is unlikely that it plays an important role in general statistics (independent of the specific location) for open ocean. It is well known that the frequency of big wave occurrence greatly exceeds the values calculated with plain

extrapolation of regularities obtained on the basis of the linear theory. At present, the ‘scientific community’ is coming to the opinion that the main role in appearance of such a phenomenon is played by a strong nonlinearity of waves, which makes the process of ‘freaking’ much more frequent than it might be predicted on the basis of the linear theory. This statement is also true for other branches of the geophysical fluid dynamics: For example, the probability of a very strong wind also greatly exceeds the estimations based on the Gaussian distribution. For insurance purposes, it would be a great mistake to do estimations of tornado probability using the Gaussian extrapolation of the wind speed climatic probability.

At present, freak waves are the subject of intense research. Various theoretical investigations and laboratory experiments were conducted over the recent years (see reviews Kharif et al. 2003, 2009; Dysthe et al. 2008). As it usually happens at the initial stage of any studies, the generation of freak waves was explained by many different mechanisms. The linear theory is evidently unable to describe an extreme wave onset. That is why the linear theory additionally assumes the possibility of the wave energy geometry focusing on specific structures of surface currents or/and bathymetry. However, it is known that freak waves appear both in deep and shallow waters, in the presence or absence of appropriate current systems. Besides, it is unlikely that the focusing can provide such fast development. All the processes mentioned above have been investigated within the framework of weakly nonlinear models, such as the nonlinear Schrödinger equation, the Davey–Stewartson system, the Korteweg–de Vries equation, and the Kadomtsev–Petviashvili equation. These approaches considerably simplify principal equations, since they reduce them to the single equation for surface elevation. Janssen (2003) explained the freak wave occurrence as a consequence of a four-wave interaction. His suggestion is based on the Zakharov’s equation (Zakharov 1968) which predicts deviation of the Gaussian process resulting in the nonzero kurtosis, but still zero skewness. Real waves have always positive skewness. It is unlikely that the model which cannot simulate a simpler and a more important third-order moment (skewness) is able to correctly simulate a much more complicated fourth-order moment. There also exists a hypothesis that freak wave can arise due to the specific atmospheric forcing. This statement is evidently true. Homer (edition of 2000) had once noticed: ‘...it is the force of wind that makes the waves so great.’ However, the timescales of wind forcing are too great to explain a sudden rise of one out of many waves. The wind forcing creates high density of wave energy, but it is just a long prehistory of stochastic ‘freaking’ process, connected with the spontaneous transformation and release of huge amounts of energy. Benjamin–Feir instability (Benjamin and Feir 1967) is considered to be an important mechanism of developing the wave spectrum homogeneity due to slow growth of the new wave components; however, it is inapplicable for the finite-amplitude fast wave evolution controlled by conservation of energy and a strong nonlinearity (Chalikov 2007). The similarity between the B-F instability criteria, applicable to a discrete spectrum and the so-called BFI index (Janssen 2003) introduced for a developed spectrum, is doubtful.

The most popular tool for investigation of nonlinear waves is the nonlinear Schrödinger equation. This equation has been playing an important role in

investigation of a freak wave generation. The numerical calculations based on the Schrödinger equation show that some of the freak wave cases can appear as a result of modulation instability and the focusing of energy (Henderson 1999; Dysthe and Trulsen 1999; Osborne et al. 2000). Using the JONSWAP spectrum, Onorato et al. (2000) performed numerical experiments to investigate a freak wave generation and its statistics. In particular, it was shown that for a narrow spectrum (an increased value of ‘enhancement’ coefficient in the JONSWAP spectrum), the probability of the rogue wave occurrence is increasing. However, the numerical approach based on the Schrödinger equation can be referred to as a qualitative method, because the results of such simulation look strange sometimes: They make an impression that the waves simulated in this way seem unnaturally big. Some of the calculations (e.g., Slunyaev et al. 2002) show that an enhancement of amplitude can be 7 times as high. The simulations based on the equations of the fluid dynamics show that big waves always tend to a strong asymmetry before breaking (Chalikov and Sheinin 2005; Babanin et al. 2007). The simplest definition of asymmetry is a ratio of the distance between the forward trough and crest to the distance between the back trough and crest. This characteristic is most important as an indicator of the breaking onset. The breaking restricts growth of amplitude and makes the statistics of big waves more natural. The evident advantage of the numerical approach based on the Schrödinger equation is that it can be generalized for a qualitative investigation of 2-D waves (Osborne et al. 2000). In the numerical investigation of a one-dimensional wave evolution, a use of precise numerical models based on the fluid mechanics equations is evidently preferable.

The work is considering simulation of numerous cases of the nonlinear evolution of a 1-D wave field leading to breaking or/and formation of extreme waves. The results obtained are used for preliminary estimations of occurrence, statistics, and some mechanical properties of extreme waves. It is shown below that extreme waves are a relatively rare but quite a typical phenomenon which can be well simulated using full fluid mechanics equations. The limitations of two-dimensionality make the results less general than those which could be obtained with the use of the 3-D model. However, it would be premature to start the simulations using a highly complicated and expensive 3-D model before trying all the possibilities suggested by a fast and precise 2-D model. Most of the scientific communities keep to the opinion that the formation of freak waves (at least, in its last stage) is mainly a one-dimensional process, as the rate of strong nonlinear interactions between the unidirectional waves is probably higher than that for the directionally spread waves (Onorato et al. 2009).

## 7.2 Description of the Numerical Experiments

In this study, the method of approximation of wave surface by superposition of Stokes waves, described in Sect. 5.3, was used. Briefly, the method is based on the use of the ‘upper conformal coordinates’  $(\xi_u, \zeta_u)$  (Eq. 5.3.2) for domain  $z > \eta$ . It

was shown that the superposition of linear waves assigned in this coordinate system after interpolation to the Cartesian coordinates turns into the superposition of Stokes waves with high accuracy. Note that full equations at any reasonable initial conditions, after some accommodation period, reproduce this effect too, since harmonic waves tend to turn into Stokes-like waves. This chapter describes how the initial generation of Stokes waves was done to accelerate transition to the statistically homogeneous regime.

In this study, we applied the above-described method for the numerical simulation of surface waves for investigation of evolution of a wave train assigned by the one-dimensional version of JONSWAP spectrum  $S_f$  (Hasselmann et al. 1973) for finite fetches as a function of frequency  $\omega$ .

$$S_f(\omega) = \frac{\alpha g^2}{\omega^5} \exp\left(-\beta_1 \left(\frac{\omega_p}{\omega}\right)^4\right) \gamma^r, \quad (7.2.1)$$

where  $\beta_1 = 1.25$ ,  $\gamma = 3.3$ ,  $\omega_p$  is a parameter and whose value is close to the frequency of spectral peak  $S_p$ . Other parameters can be expressed through  $\omega_p$ :

$$r = \exp\left(-\frac{(\omega - \omega_p)^2}{2\sigma^2\omega_p^2}\right), \quad \alpha = 0.0099\Omega^{0.66}, \quad \sigma = \begin{cases} 0.07 & \omega \leq \omega_p \\ 0.09 & \omega > \omega_p \end{cases}; \quad (7.2.2)$$

where  $\Omega = \frac{\omega_p U_{10}}{g} = \frac{U_{10}}{c_p}$  is the non-dimensional frequency in spectral peak and  $c_p$  is phase velocity.

It is well known that an approximation (7.2.1) overestimates spectrum at low values of non-dimensional frequencies  $\Omega \leq 1.3$  (large fetches). To keep the right asymptotic behavior, the approximation (7.2.1) was combined with Pierson and Moskowitz spectrum (PM, Pierson and Moskowitz 1964) for fully developed waves

$$S_\infty(\omega) = \frac{\alpha g^2}{\omega^5} \exp\left(-\beta_2 \left(\frac{\omega_p}{\omega}\right)^4\right) \quad (7.2.3)$$

by the following relation:

$$S = S_\infty W + S_f (1 - W), \quad (7.2.4)$$

where  $W$  is weight which is convenient to represent as a function of  $\Omega$ . It is easy to calculate that  $\Omega_\infty = 0.855$  for PM spectrum. Since transition from spectrum  $S_\infty$  to  $S_f$  happens in a small interval of  $\Omega$ , function  $W$  quickly decays with growth of distance  $\Omega - \Omega_\infty$ . The function  $W(\Omega)$  was approximated by the formula:

$$W = \exp(-15(\Omega - \Omega_\infty)). \quad (7.2.5)$$

In the initial JONSWAP approximation, the enhancement parameter for spectrum  $\gamma$  was accepted as constant:  $\gamma = 3.3$ . Later, some investigators came to the

conclusion that this parameter can be a function of fetch or peak frequency  $\omega_p$ . According to (Babanin and Soloviev 1998),  $\gamma$  increases with  $\Omega$  as

$$\gamma = 1.224\Omega \quad (7.2.6)$$

Merging was done in a very narrow interval [0.855 – 1] (see 7.1). The number of cases falling in this interval is so small that it does not influence the statistics. Approximations (7.2.1) and (7.2.3) were rewritten in terms of wave numbers using the dispersion relation valid at least up to  $3\Omega_p$  (Chalikov 2005). The non-dimensional wave number  $k_p$  in spectral peak is a parameter of initial conditions. To describe the low wave number, the slope of spectrum,  $k_p$ , should exceed 1, and for good approximation of the entire spectrum (as well as its spreading due to the nonlinearity),  $k_p$  should be considerably smaller than the total number of modes  $M$ . Actually,  $k_p$  is a parameter of accuracy of approximation. The initial conditions for Fourier coefficients of free surface  $\eta(x)$  were assigned in the following form:

$$|h_k| = (2S(k)\Delta k)^{1/2}, \quad \eta_k = |h_k|\sin(\varphi), \quad \eta_{-k} = |h_k|\cos(\varphi), \quad k = 1, 2, 3 \dots k_m \quad (7.2.7)$$

where  $|h_k|$  is an amplitude of  $k$ th mode;  $\eta_k, \eta_{-k}$  are Fourier coefficients in the Cartesian coordinates; and  $\varphi$  is the random (over  $k$  and over different runs) phases of modes uniformly distributed in the interval  $0$ – $2\pi$ . The Fourier coefficients  $f_k$  for surface potential  $f(x)$  were assigned by

$$f_k = -|k|^{1/2}a_{-k}, \quad k = -M_i, M_i, \quad (7.2.8)$$

where  $M_i$  is the number of modes assigned in the initial conditions. After inverse Fourier transform, functions  $\eta(x)$  and  $f(x)$  were transferred from the ‘upper coordinates’  $(\xi_u, \zeta_u)$  to the ‘lower coordinates’ by periodic spline interpolation, providing accuracy of the order of  $10^{-11}$  for very steep waves, and  $10^{-30}$ —for the medium amplitude waves. Post-processing was done for the data transferred back to the Cartesian coordinates by the same algorithm. Peak of spectrum was placed at  $k_p = 8$ ,  $\Omega = \sqrt{k} = 2.83$  or at  $k_p = 20$ ,  $\Omega = 4.47$ . The number of waves assigned in the initial conditions  $k_m$  was equal to 32, so the amplitude of the smallest assigned wave was by  $4^3$  smaller than the amplitude  $h_p$  in the peak of spectrum.

The spectral tail was developing during the first period of the peak wave at higher frequencies. This evolution occurs for any steepness. Simulation of the wave evolution assigned by (7.2.2)–(7.2.8) was performed for the number of modes  $M = 2000$  and the number of grid points  $N = 8000$ , which provided a sufficient resolution both in the Fourier and physical space. The control runs with resolution  $M = 4000$  and  $N = 16,000$  revealed the same statistical properties of the solution. The time step  $\Delta\tau$  was equal to 0.002 (and 0.001 for  $M = 4000$ ). An application of a twice shorter time step for strongly nonlinear cases proves that the difference

between the results is negligible, except for small variations at the last time steps before breaking. Many runs were terminated due to some wave tendency for overturning. Several dozens of runs for a relatively small steepness lasted up to 2000 periods with no breaking event. A criterion for terminating a run was defined by the first appearance of a non-single value of surface  $\eta$  (Eq. 6.1.1). It was possible to continue the integration shortly after that moment (see Chalikov and Sheinin 2005), but the details of this development are not the subject of this chapter. It is important to emphasize that after the moment when the criterion (7.2.9) has been reached, the solution would never return to stability: The volume of fluid crossing the vertical  $x(i)$  quickly increases. Up to this moment, conservation of both the sum of the potential and kinetic energies and the horizontal momentum and volume was excellent. When the surface becomes a non-single value (at the initial stage of breaking), conservation of the invariants still holds, though later, a sharp increase of energy occurs, and further integration becomes useless. Usually, it happens just for one Runge–Kutta time step, so probably, the primary cause of the numerical instability is the growth of the right-hand side of Eqs. (2.2.34) and (2.2.35). Disintegration of the solution happens mostly due to inapplicability of potential approximation and, in general, of fluid dynamic equations for the single-phase fluid.

Extreme waves are a rare phenomenon in nature. Therefore, they are seldom reproduced in the numerical simulations too. The statistical characteristics of wave field, as well as the probability of extreme waves, seem to depend on the inverse wave age  $\Omega$  and the initial set of phases, especially for young steep waves. Dependence on the preassigned set of phases can be excluded by repeated calculations for the same set of amplitudes with a random choice of phases. One cycle of the calculations includes 60–90 cases for different peak frequencies:

$$\Omega_n = \Omega_\infty + 0.0294n, \quad n = 1, 2, 3, \dots, 60 - 90, \quad (7.2.9)$$

where  $n$  is the number of runs in a cycle and  $\Omega_\infty = 0.855$  is a non-dimensional peak frequency for the Pierson–Moskowitz spectrum. The upper limit of  $\Omega$  is equal to 3.50, which corresponds to the young sea. The cycle was repeated 64 times. The cycles 1–48 were performed with the use of the fixed enhancement parameter  $\gamma = 3.3$  and the peak wave number  $k_p = 8$ , while cycles 49–64 were performed when  $\gamma$  was assigned by the formula (7.2.6) and  $k_p = 20$ . The total number of runs was equal to 4294. The calculations performed on a Dell workstation (speed is 3.1 MHz) took about three months. To trace the generation and evolution of extreme waves, the wave profiles containing waves with a trough-to-crest height greater than  $2H_s$  were recorded. Many statistical characteristics, including different moments, were calculated in the course of simulations. The total volume of data selected and recorded was around 100 Gbt.

The parameter  $\Omega = U_{10}/c_p$  (or non-dimensional fetch) is convenient for calculation of the explicit form of wave spectrum. However, the use of  $\Omega$  in the operational analysis of wave spectra (measured or calculated by a wave forecasting model) is not convenient, as wave spectrum can be a non-single-peak spectrum, or it can be blurred with a swell whose energy might be comparable to the energy of

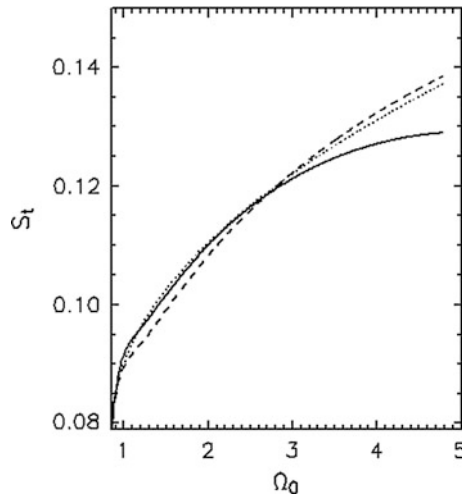


**Fig. 7.1** Dependence of steepness parameter  $S_t$  on wave age  $\Omega_0 = U_{10}/c_p$ . Solid line corresponds to the calculation with a combined JONSWAP/PM spectrum (Eq. 7.2.1) with  $\gamma = 3.3$ , dashed line corresponds to the same spectrum, but with  $\gamma$  defined by Eq. (7.2.6), and dotted line corresponds to approximation (7.2.11) (Reproduced with permission from Chalikov 2007 © 2007 AIP Publishing LLC; Reproduced with permission from Chalikov 2009 © 2009 AIP Publishing LLC)

wind waves produced by local wind. If the swell is strong, its interaction (e.g., through Benjamin–Feir–McLean instability) with the locally produced wind waves can result in generation of extreme waves. That is why we introduce more robust characteristics expressed as a product of significant wave height  $H_s$  and wave number  $k_s$  weighted by the spectrum:

$$S_t = k_s H_s, \quad \text{where } H_s = 4\sqrt{S} \text{ and } k_s = \frac{\sum_k^M k S_k}{\sum_o^M S_k} \quad (7.2.10)$$

For the JONSWAP-PM spectrum (Eq. 7.2.4), the dependence of  $S_t$  on  $\Omega$  is monotonic (Fig. 7.1). This function for parameter  $\gamma$  defined by (7.2.6) is approximated by the following relation:

$$S_t = S_0 + A_0(\Omega - \Omega_0)^{1/2}, \quad (7.2.11)$$

where  $S_0 = 0.316$ ,  $\Omega_0 = 0.855$ ,  $A_0 = 0.118$  (dotted line). Point  $\Omega_0$  corresponds to PM spectrum for the developed sea. Parameter  $S_t$  characterizes the non-dimensional density of wave energy. For young waves, the parameter  $S_t$  is larger than for the old waves, because the energy is concentrated in small wavelengths (large wave numbers).

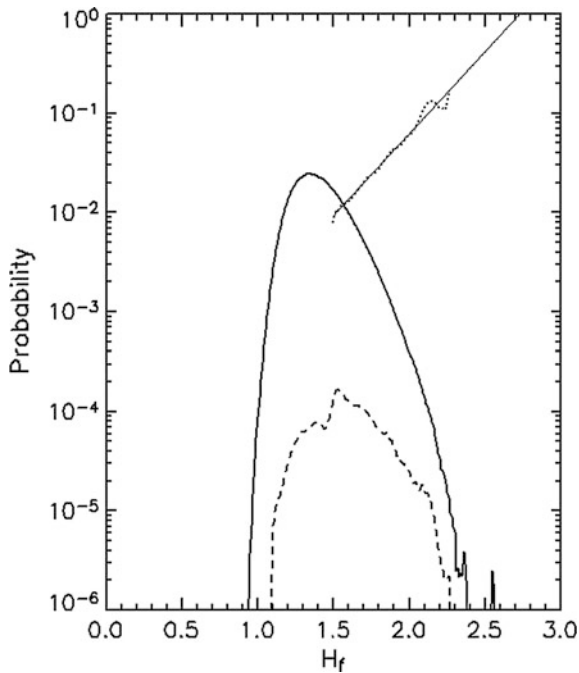
### 7.3 The Breaking and Surviving Extreme Waves

For practical needs, consideration of wave crest height above mean level  $z = 0$  does not make any sense, because the destructive wave power depends on the overall wave height from its trough to crest. It is not easy to detect this height formally. The calculation of a vertical distance between the maximum and its nearest minimum does not give the right answer, because there can be some local extremes there; hence, the wave height might be underestimated. Hence, the trough-to-crest height is essentially a non-spectral concept and this characteristic should be detected in physical space. Obviously, an extreme wave should be found between large waves. That is why the height of extreme waves  $H_{tc}$  in each record  $\eta(x)$  was defined here as a difference between the absolute maximum and absolute minimum in a moving window of length  $L_e$ . It would be reasonable to define  $L_e = 1.5L_p$  where  $L_p$  is the wavelength in peak of spectrum,  $L_p = 2\pi/k_p$ , and  $k_p$  is the actual wave number in the spectral peak. The extreme waves with the length exceeding  $1.5L_p$  were practically absent. Generalization of this algorithm for 2-D wave field is discussed in Chap. 12. It will be demonstrated below that development of freak waves happens very quickly, i.e., normally, within one or two wave periods. Let us define the single event as a run of wave over its single period. This suggestion allows estimating the total number of events used for statistical processing as equal to about 15 million. In this chapter, the main attention will be focused on the statistical properties of a non-dimensional trough-to-crest wave height  $H_f = H_{tc}/H_s$ .

If extreme waves were always breaking, the number of such waves would be close to the number of runs (there are few cases when a run reaches the designated end without breaking). In fact, the recorded ensemble of large waves was much greater, since development of extreme waves was not always interrupted by breaking. This conclusion is opposite to the results obtained by Dyachenko and Zakharov (2005) who concluded that all freak waves are breaking waves. Many waves return to medium sizes again after they have gone through intense enhancement. The probability distribution for breaking and non-breaking waves (normalized by the total number of waves) is shown in Fig. 7.2 by dashed and solid lines, respectively.

A fast decrease of probability for small  $H_f$  simply shows that there are no small waves in the selected window, while a decrease of probability for large  $H_f$  reflects scarcity of freak waves. An estimation of probability for a smaller window (up to  $0.5L_p$ ) shows that even short waves can break; however, this phenomenon is outside the scope of the subject covered by the current chapter. The ratio of the total number of non-breaking waves to that of breaking waves  $R_{nb}$  (showed by dotted curve in Fig. 7.2) equals 140 for the selected window. However, for each wave height, this ratio  $r_{nb}(H_f)$  is different: For freak waves  $H_f > 2$ , the ratio  $r_{nb}$  approaches 10. The exponential extrapolation of  $r_{nb}$  (thin line)

**Fig. 7.2** Distribution of probability of trough-to-crest height  $H_f$  for breaking (dashed line) and non-breaking (solid line) waves defined with the use of window length  $1.5L_p$ . Dotted line is a ratio of number of breaking wave and the number of non-breaking waves; thin line represents approximation (7.3.1) (Reproduced with permission from Chalikov 2009 © 2009 AIP Publishing LLC)



$$r_{nb} = 10^{-4.51 + 1.65H_f} \quad (7.3.1)$$

to high values of  $H_f$  shows that all waves exceeding  $H_f = 2.7$  do break. This limit value looks reasonable, though the critical value of  $H_f$  cannot be considered as well-estimated.

It would be quite useful to find connection between the trough-to-crest wave height and certain integral properties of wave field. For these purposes, we plot the value of the biggest trough-to-crest height defined for every record of surface against integral characteristics of the wave field calculated for the same wave profile. The dependence of the biggest trough-to-crest wave height on the statistical characteristics calculated over the entire instantaneous wave profile is given in Figs. 7.3, 7.4, and 7.5. In Fig. 7.3, the dependence of the largest trough-to-crest wave on parameter  $S_t$  is given. The parameter  $S_t$  characterizes wave age, and in general—the density of potential energy. Note that the parameter  $S_t$  is not invariant, but, being a low-order moment, it remains relatively stable.

It could be expected that a high energy wave field typical for young waves and strong nonlinearity can generate non-dimensional large waves (normalized by  $H_s$ ) more frequently than the waves of low energy and weak nonlinearity. However, as shown in Fig. 7.3, such suggestion proves to be incorrect: Large waves rather have a tendency to appear in the old wave field with low steepness. It becomes even more evident for freak waves ( $H_f \geq 2$ ) which are generated according to our data

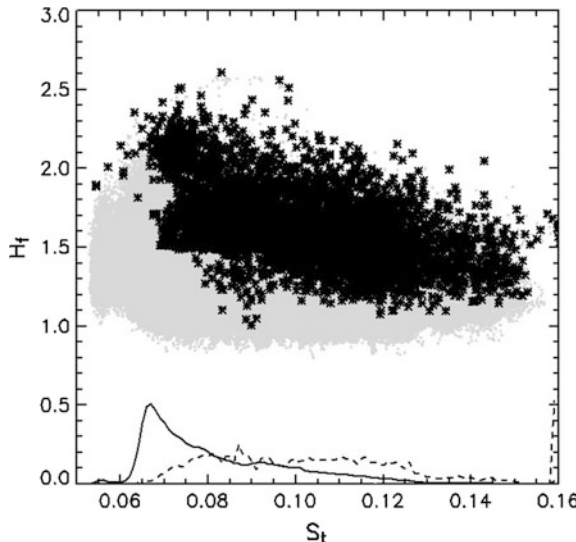


**Fig. 7.3** Dependence of extreme wave height  $H_f$  on parameter  $S_t$  (Eq. 7.2.12). Aggregated gray dots correspond to non-breaking waves (1,637,316 cases), while asterisks correspond to breaking waves (4742 cases). Solid line represents distribution of the number of cases for non-breaking waves, and dashed line shows the same distribution for breaking waves, both of them normalized by the corresponding number of events (Reproduced with permission from Chalikov 2009 © 2009 AIP Publishing LLC)

only in a developed wave field ( $U_{10}/c_p \equiv \Omega < 1.4$ ). The tendency for a freak wave population increase with decrease of  $S_t$  is well traced for the cases of breaking waves (indicated by asterisks in Fig. 7.3). However, it is shown that some of the freak waves (gray dots in the upper part of the panel) do not break at all.

Thus, the nonlinearity seems to be working opposite to what it was expected. It is a paradox; however, this result can be still explained by the influence of nonlinearity. If a wave–wave interaction is quite energetic, the waves come to a breaking point earlier than in the case of weak interactions, before the process of ‘freaking’ (considered below) takes place. This effect is clearly demonstrated in Fig. 7.4, where the time period up to the breaking point is plotted against parameter  $S_t$  characterizing a degree of nonlinearity. The waves with  $H_f > 2$  are indicated in the plot by asterisks, while all other waves are shown by gray dots. As shown, large waves appear mostly in the wave field with low steepness, and steep wave height seldom exceeds the value  $H_f = 2$ . To express it in terms of metaphor, active waves become *jealous* of the excessive growth of their neighbors.

An investigation of connection between the extreme wave probability and the integral characteristics was continued for the high-order moments, i.e., skewness  $Sk$  and kurtosis  $Ku$  (5.2.4). The maximum values of trough-to-crest height in a single record  $H_f$  are plotted in Fig. 7.5 against skewness  $Sk$  calculated over this record. Skewness reflects the vertical asymmetry of disturbances. As shown, the skewness

**Fig. 7.4** Time of wave evolution up to onset of breaking (expressed in peak wave periods) versus parameter  $S_t$  (Eq. 7.2.12). In the *upper panel*, a linear scale for time is used, while in the *bottom panel*, a logarithmic scale is used. Gray dots correspond to the case when values of  $H_f$  before breaking were less than  $H_f = 2$ , and asterisks represent the cases with  $H_f > 2$  (Reproduced with permission from Chalikov 2009 © 2009 AIP Publishing LLC)

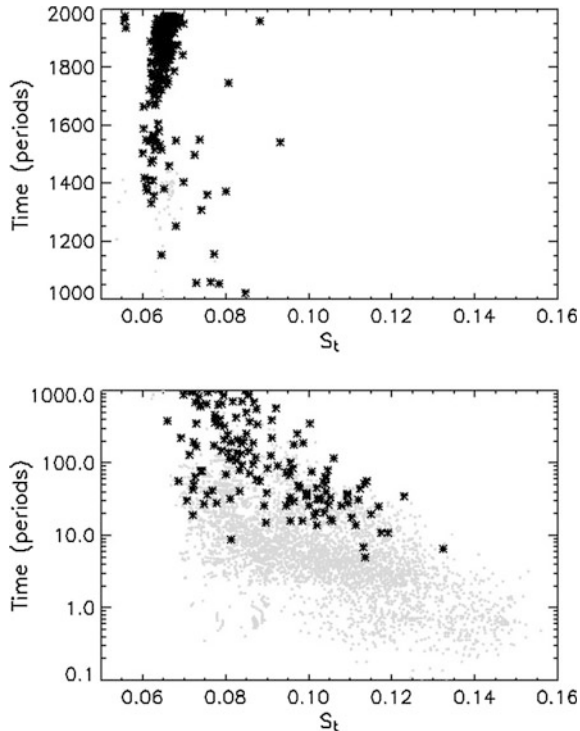


**Fig. 7.5** Extreme wave height  $H_f$  versus skewness  $Sk$ . Gray point, black asterisks, and lines are the same as in Fig. 7.3. The number of points is the same as in Fig. 7.3 (Reproduced with permission from Chalikov 2009 © 2009 AIP Publishing LLC)

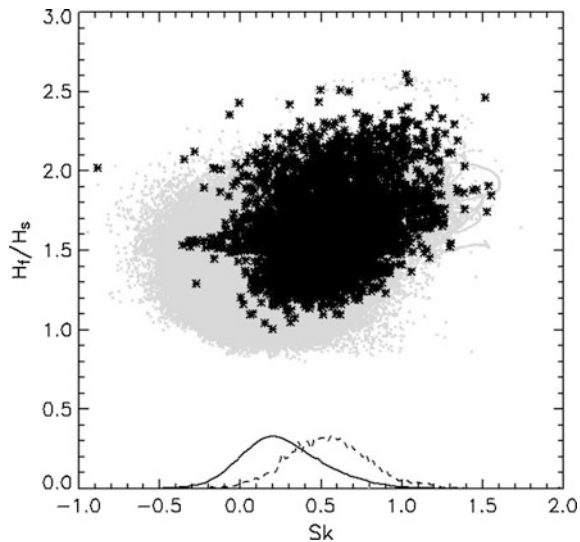
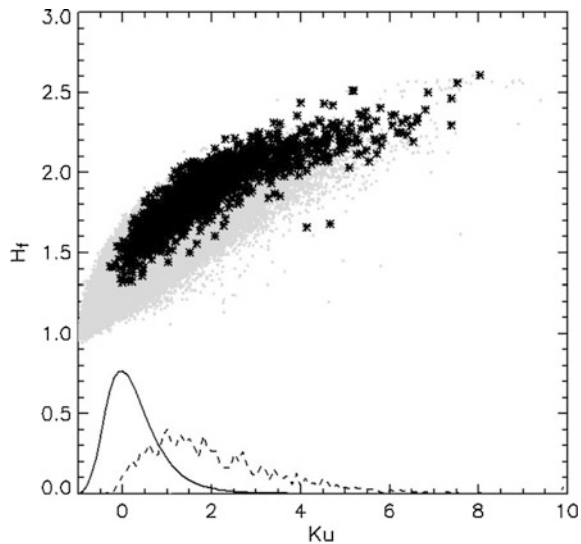


**Fig. 7.6** The same as in Fig. 7.5, but for kurtosis  $Ku$ . The plot includes 501,365 cases of unbreaking waves and 1165 cases of breaking waves (Reproduced with permission from Chalikov 2009 © 2009 AIP Publishing LLC)

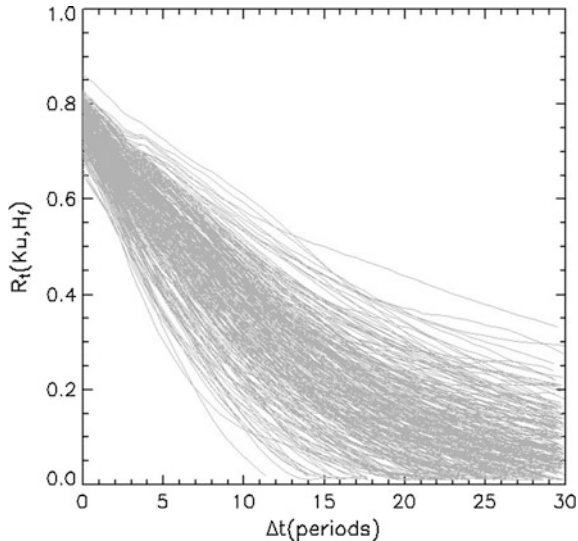


values considerably exceed zero. It indicates that the wave field is closer to the superposition of sharp-crested modes than to that of linear waves. In fact, a skewness value of wave profiles corresponding to the events of breaking is somewhat higher than that for non-breaking cases. The asterisks are shifted up compared to gray dots, and the maximum of probability for breaking cases (dotted line) is shifted to higher values of skewness for non-breaking cases. However, there is no evident connection between the height of extreme waves and their corresponding skewness.

It is remarkable that the connection of  $H_f$  with kurtosis  $Ku$  (Fig. 7.6) looks a lot more pronounced, i.e., the growth of  $H_f$  is distinctly succeeded by higher values of  $Ku$  both for breaking and non-breaking waves. (The number of cases included in Fig. 7.6 is smaller than that for Figs. 7.3 and 7.5, as recording of  $Ku$  was implemented starting from case #49.) This connection seems to have proved Janssen's hypothesis (Janssen 2003) that kurtosis can serve as *predictor* for freak waves. To clarify the nature of this dependence, the cross correlation functions  $R_t$  between variables  $Ku$  and  $H_f$  were calculated for 288 randomly chosen (and long enough) runs (Fig. 7.7). Time lag  $\Delta t$  is expressed in peak wave periods. As shown, the simultaneous values of  $Ku$  and  $H_f$  are well correlated at  $\Delta t = 0$  (where  $R_t = 0.7 - 0.8$ ), though the correlation quickly decreases with growing  $\Delta t$ . At  $\Delta t \cong 10 - 20$  peak wave periods, the correlation becomes insignificant. For a real large wave with the period of order of 20 s, this time is equal to 6 min. Hence, kurtosis and an extreme wave are interconnected at the distances up to several hundreds meters. The experiments described in (Onorato et al. 2009) have proved that kurtosis is a good indicator of big wave appearance in a wave tunnel.

It means that kurtosis cannot serve as a *predictor* for practical applications, but it is rather an *indicator* of local conditions. It is not surprising, as both high kurtosis

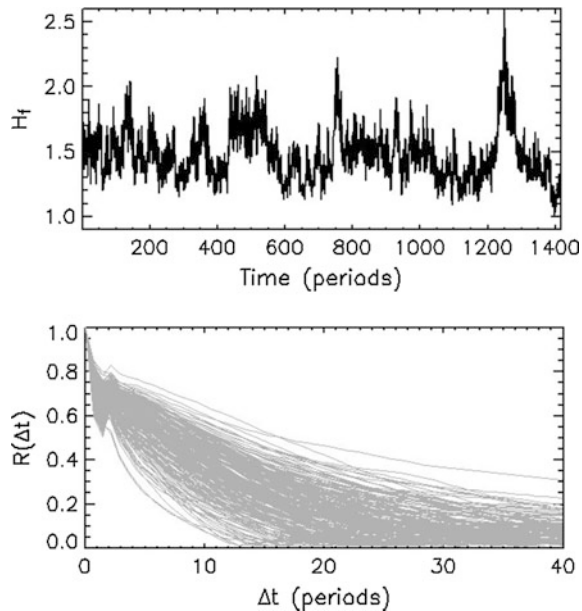
**Fig. 7.7** Cross-correlation functions  $R_t(K_u, H_f)$  for kurtosis  $K_u$  and extreme trough-to-crest wave heights  $H_f$ , calculated for 288 randomly chosen runs. Lag time expressed in periods of peak wave (Reproduced with permission from Chalikov 2009 © 2009 AIP Publishing LLC)



and the presence of large wave(s) reflect the same geometrical properties of wave profile, i.e., sharpness and heights of crests. An explanation of this effect is quite simple: Since the moment has 4th order, the contribution of high elevation is big. For the 6th, 8th, and any other even moments of higher order the connection should be closer. Note that our conclusion is obtained using relatively short wave profiles containing 10–20 peak waves, so that the weight of the extreme wave turns out to be comparatively high. Consequently, the connection of kurtosis and the extreme wave height is overestimated in our example. For far larger wave ensembles, an impact of rare extreme waves on the values of kurtosis evidently becomes negligibly small. It completely eliminates any possibility of using kurtosis not only as a *predictor*, but also as an *indicator* of freak waves. The wave spectrum predicted by the wave forecasting models reflects conditions averaged over elementary cell of a numerical scheme. The cell can include many thousands of waves. Just several of them during very short periods of ‘freaking’ can get very large. It is known that high-order moments are very sensitive to perturbations. Definitely, any calculations of the fourth-order moment on the basis of the averaged wave spectrum predicted with low accuracy are quite impossible. It is not surprising that such scheme for freak wave forecast implemented in the operational practice of ECMWF turned out to be unsuccessful.

An example of the extreme wave evolution is given in Fig. 7.8 (top panel). Each value of  $H_f$  is defined for a single record including 18–22 peak waves. The time interval  $\Delta t$  between the records was equal to 0.71 of the peak wave period. It can be seen that high values of  $H_f$  appear sporadically and that life of such wave is very short. To illustrate this statement, the autocorrelation functions  $R(\Delta t)$  for the cases of Fig. 7.7 are plotted in the bottom panel. As shown,  $R$  decreases quickly with the lag increase, and throughout dozens of the periods, the correlation becomes

**Fig. 7.8** Top panel is an example of extreme wave height  $H_f$  evolution, while bottom panel represents the autocorrelation function calculated for the cases of Fig. 7.7 (Reproduced with permission from Chalikov 2009 © 2009 AIP Publishing LLC)



insignificant. The timescale of the correlation  $T_R = \int_0^T R dt$  ( $T$  is a period that is long enough for the accuracy of estimation) averaged for all 288 cases is equal to 5.5 periods of wave peak.

Note that the run of Fig. 7.8 reproduces the largest extreme wave ( $H_f = 2.59$  at  $t = 1250$ ) ever recorded in our numerical experiments.

## 7.4 The Properties of Extreme Waves

The densities of potential  $E_p$  and kinetic  $E_k$  energies averaged over  $x$  (or  $\xi$ ) can be calculated by the formulas:

$$E_p = (2\pi)^{-1} \int_0^{2\pi} z^2 x_\xi d\xi, \quad E_k = (2\pi)^{-1} \int_0^{2\pi} \varphi \varphi_\xi d\xi, \quad E_c = E_p + E_k \quad (7.4.1)$$

The energy of a unit water column  $e_c$  was calculated by the formulas derived in the conformal coordinates:

$$e_p = \frac{1}{2} z^2, \quad e_k = \frac{1}{2} \int_{-\infty}^0 \left( \Phi_\xi^2 + \Phi_\zeta^2 \right) J^{-1} d\xi, \quad e_c = e_p + e_k, \quad (7.4.2)$$

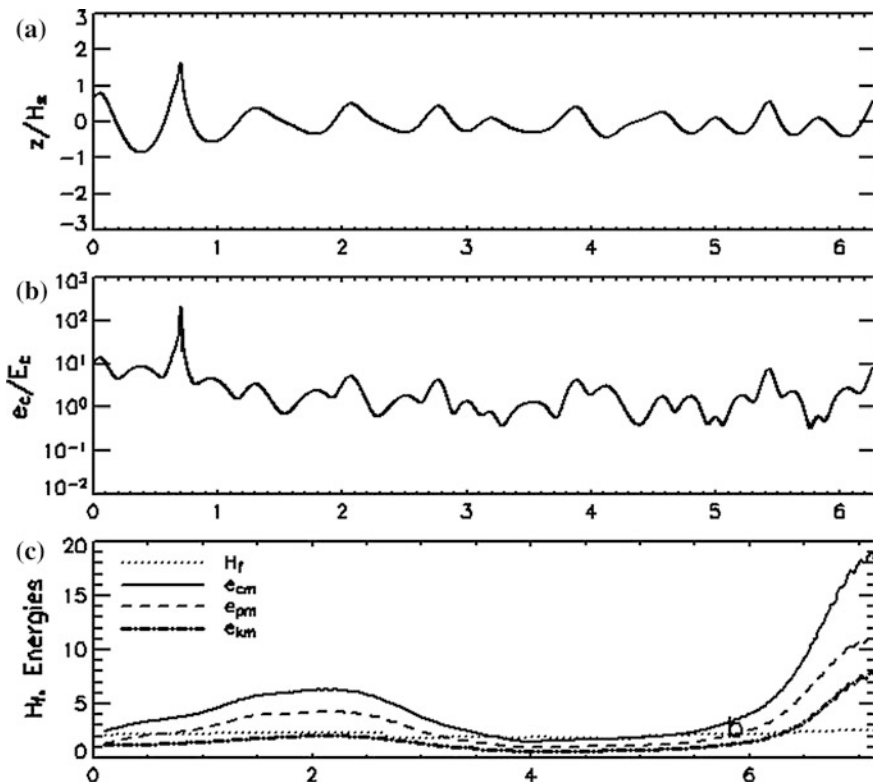
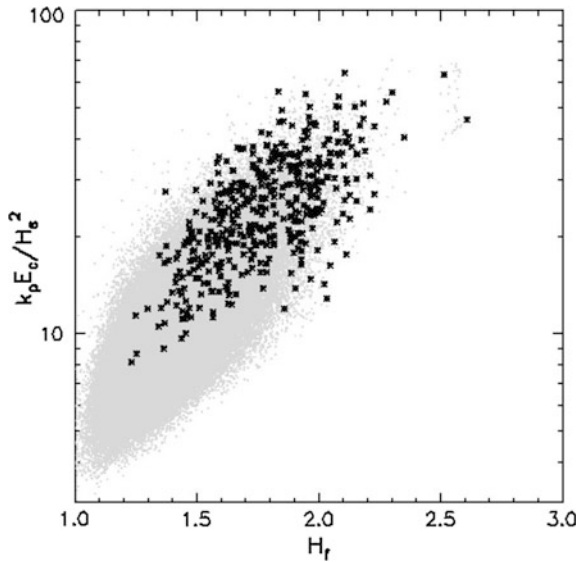


**Fig. 7.9** The non-dimensional columnar energy  $k_p e_c / H_s^2$  versus trough-to-crest height of extreme waves. **a** Example of a wave surface containing a freak wave with  $H_f = 2.5$  before its breaking; **b** is a profile of total columnar energy, normalized by the averaged columnar energy (in panels **a** and **b** abscissa corresponds to horizontal distance); **c** is a temporal evolution of extreme wave heights  $H_f$ , and maximum values of  $e_{km}$ , potential  $e_{pm}$ , and total  $e_{cm}$  columnar energy prior breaking. Abscissa corresponds to time (Reproduced with permission from Chalikov 2009 © 2009 AIP Publishing LLC)

where the integral over depth was calculated with high accuracy in a stretched vertical grid, assuming that  $\Delta\zeta_{j+1} = \varepsilon\Delta\zeta_j$ , where  $j$  grows downward, and the stretching parameter  $\varepsilon$  equals to 1.10. A typical wave profile including a freak wave with  $H_f = 2.5$  at  $x = 0.7$  is given in Fig. 7.9, panel (a). The corresponding profile of the overall columnar energy normalized by  $E_c$  is given in panel (b). The difference between the energy of usual waves and that of freak waves is so great that we had to plot the energy  $E = e_c/E_t$  in the logarithmic scale. The energy at peak of freak wave exceeds the averaged energy  $E_t$  by 150 times! It happens due to the concentration of energy in the vicinity of the freak wave crest. The evolution of the normalized trough-to-crest height  $H_f$  of the largest wave for the period (0 – 7.1) is

**Fig. 7.10** Non-dimensional columnar energy  $k_p E_c / H_s^2$  versus trough-to-crest height of extreme waves  
 (Reproduced with permission from Chalikov 2009 © 2009 AIP Publishing LLC)



shown in panel *c* of Fig. 7.9. As shown, an extreme wave height was increasing from  $H_f = 2.1$  to  $H_f = 2.5$  over this period, but its energy has grown up to 10 times of the initial value. At the final stage, before breaking, the columnar kinetic energy exceeds the potential energy by 1.5 times at the peak of spectrum. The connection between the columnar energy  $e_c$  and wave height  $H_f$  is shown in Fig. 7.10. As shown, this dependence is close to the exponential one.

Details of the extreme wave development from  $t = 5.06$  to  $t = 7.15$  are given in Fig. 7.11. As shown, a freak wave is developing just over two wave periods. The energy in peak column amplifies over this period of time by approximately 10 times. Fast growth of the maximum value of surface velocity normalized by the phase velocity  $v_m$  of the extreme wave is shown in panel *c* of Fig. 7.11. It is shown that the fluid velocity approaches the phase velocity before wave breaking. The evolution of energy  $E_f$  averaged throughout the trough-to-trough interval (which is assumed to be the overall energy of the chosen wave) as well as the maximum of energy at wave peak is given in panel *d* of Fig. 7.11. The most surprising feature of this picture is that the total energy of a developing wave remains nearly constant (it cannot be an exact constant as the domain has open boundaries), while its peak value grows dramatically. In some other cases, the total energy of certain waves is even decreasing. It proves that the freak wave goes through a self-amplification phase with no substantial exchange of energy with other waves. Therefore, any considerations of the freak wave generation in Fourier space are pointless: Just one wave in a wide set of similar waves unpredictably starts developing fast, accompanied by the powerful concentration of energy in the vicinity of wave peak. Evidently, it is the main property of the extreme wave, which makes the largest of

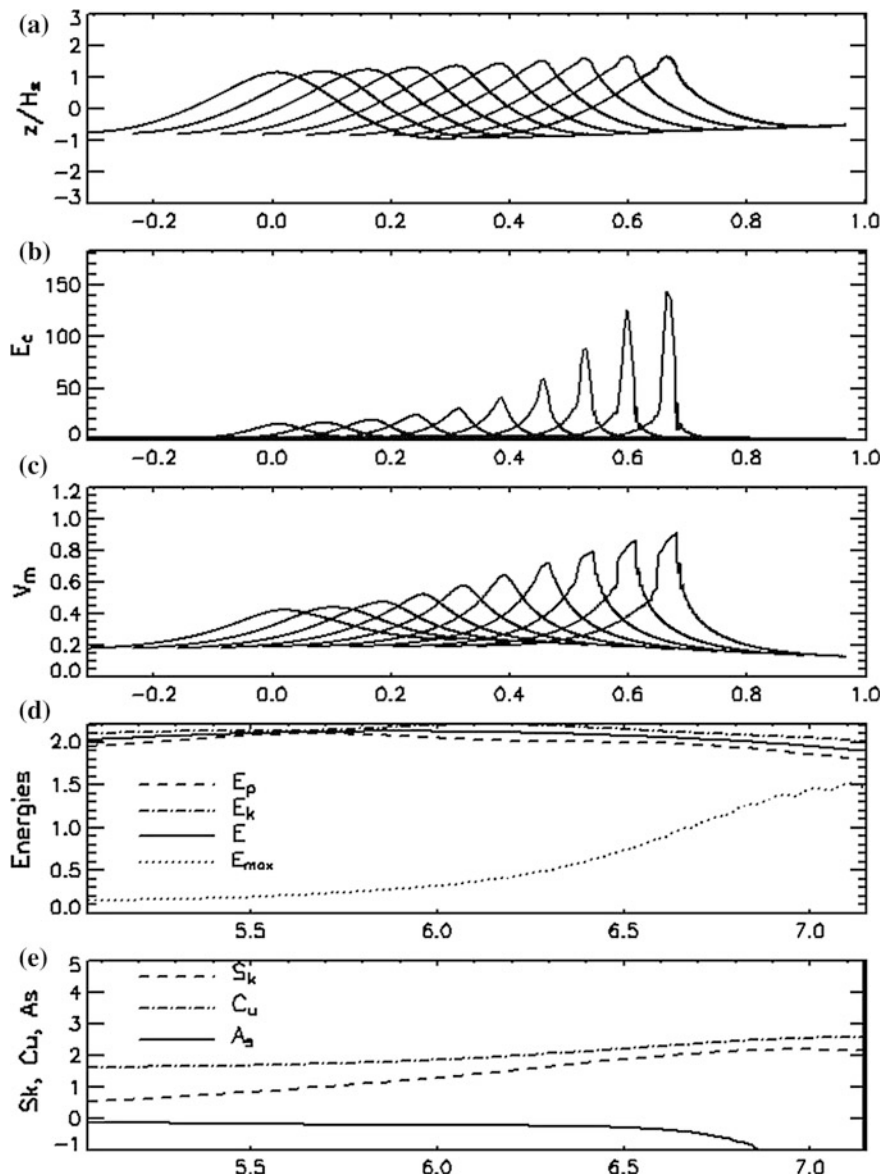


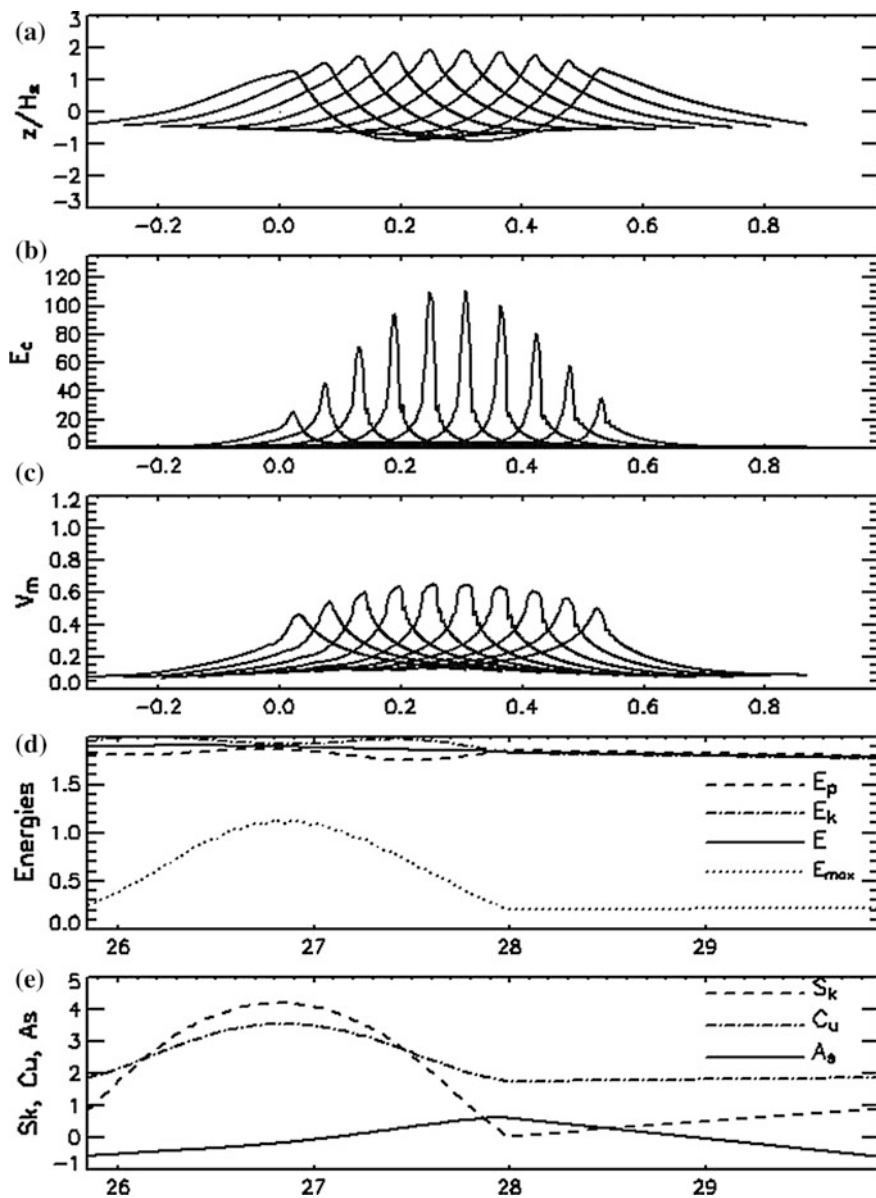
**Fig. 7.11** Example of a run for  $U_{10}/c_p = 1.6$  ( $S_t = 0.105$ ). In the panels **a**, **b**, and **c**, the horizontal axis is a distance: Panel **a** represents successive profiles (separated by interval  $\Delta t = 0.02$ ) of the largest wave within the time range from  $t = 5.06$  ( $H_f = 2.10$  at  $t = 2.28$  periods) up to the overturning moment at  $t = 7.15$  (3.22 periods); **b** corresponding to (a) evolution of columnar energy  $e_c$ ; **c** corresponding to (a) evolution of the absolute value of surface velocity normalized by phase velocity of peak wave  $V_m$ . In panels **d** and **e**, the horizontal axis corresponds to time: **d** shows temporal evolution of maximum values of total  $E_m$ , columnar kinetic ( $E_k$ ), potential ( $E_p$ ), and total ( $E$ ) energy; **e** represents temporal evolution of skewness ( $Sk$ ), kurtosis ( $0.1Ku$ ), and asymmetry ( $0.1As$ ) (Reproduced with permission from Chalikov 2009 © 2009 AIP Publishing LLC)

those waves a freak one. The mechanisms of this evolution are still unknown, and prediction of time and location of the wave development ('freaking') are impossible even in a numerical experiment. Fortunately enough, such knowledge would not make any sense for practical use. Much more important is the statistics of such events and mechanical characteristics of freak waves. The above problem is similar to that of the numerical forecast of thunderstorms: the atmospherics model can predict the possibility of storm generation in a cell of a numerical model, but not an exact location and time of such events.

Another type of wave evolution which was not terminated by breaking is shown in Fig. 7.12. In this case, the columnar energy  $e_c$  is also concentrating around the crest and reaching very high values, but upon passing the maximum values it starts to decrease, quickly returning to the normal level. It is impossible to explain why one wave comes to breaking while another one, being even higher, can survive. Obviously, each individual development depends on the details of current environment in a physical space: In some cases, group effects can initiate breaking which can start due to a very small disturbance. The final stage of this development, i.e., breaking, is characterized by a higher concentration of energy as compared to the energy accumulated for the case of a surviving wave. It is clearly shown in Fig. 7.13 where distribution of a surface energy probability for extreme waves with a trough-to-crest height  $H_f > 2.1$  is shown.

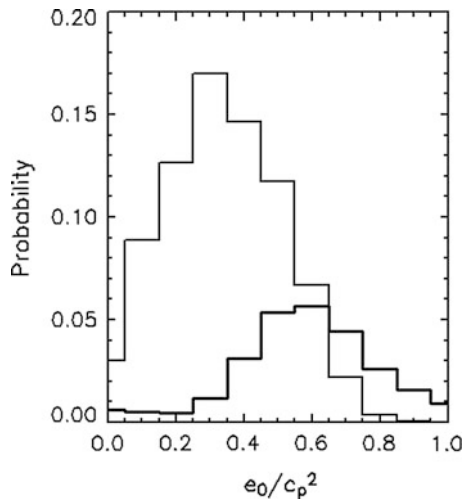
The probability is normalized by the total number of breaking and non-breaking waves. The probability of non-breaking waves is higher than that of breaking waves, but the maximum of surface energy is considerably shifted to higher values of extreme waves. This conclusion is also proved to be correct by the data shown in Fig. 7.14 where the maximum columnar energy  $E_{cm}$  and the surface velocity  $V_m$  (normalized by peak phase velocity  $c_p$ ) for each case of an extreme wave development are shown as a function of  $H_{fn}$ . Dots in this figure correspond to non-breaking waves, while asterisks show breaking waves. It is seen that most of the asterisks (but not all of them) fall mostly on the upper part of the figure. It means that large breaking waves generate a higher surface velocity and dynamic pressure on the surface of either floating or fixed objects; hence, they are more dangerous than non-breaking waves. The distribution of velocity on top of breaking wave is represented in Fig. 7.15.

It is shown that velocity reaches the value of phase velocity (which is the actual cause of the overturning). Being observed from the upfront trough, the top of wave looks exactly like a 'wall of water.' The topmost part of wave has height  $0.2H_f$ , and it is really vertical. The dimensional parameters of such wave look quite impressive. Let us assume that waves and wind have reached the state of equilibrium, and wave spectrum is described by the Pierson–Moskowitz formula. In this case, the phase velocity  $c_p$  of peak waves equals  $1.17U_{10}$ , and the significant wave height  $H_s$  equals  $0.22U_{10}^2/g$ . It follows that for  $U = 20$  m/s, the trough-to-crest extreme wave height  $H_f$  is equal to 23 m, for  $U = 25$  m/s—35 m and for  $U = 30$  m/s—50 m. The dynamic pressure  $P = \rho_w U^2$  ( $\rho_w$  is water density) created by a moving water can

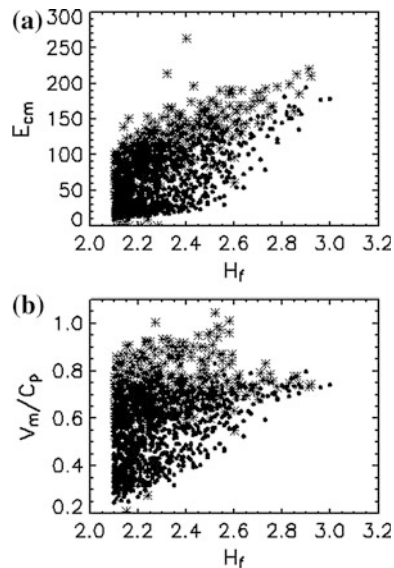


**Fig. 7.12** The same as in Fig. 7.11 but for non-breaking wave: **a** shows successive profiles (separated by interval  $\Delta t = 0.08$ ) of the largest wave within the time range from  $t = 25.84$  ( $H_f/H_s = 2.10$  at  $t = 11.63$  periods) up to the moment of wave height fall to the value  $2.1H_s$  at  $t = 29.88$  (3.22 periods). The maximum value  $H_f/H_s = 2.51$  was observed at  $t = 27.04$ . All other panels for this case are the same as in Fig. 7.11 (Reproduced with permission from Chalikov 2009 © 2009 AIP Publishing LLC)

**Fig. 7.13** Probability distribution of the surface kinetic energy (normalized by squared phase velocity  $c_p^2$ ) of extreme waves with trough-to-crest height  $H_f > 2.1$ : *Thin line* represents non-breaking waves (1092 cases) and *thick line* shows breaking waves (379 cases) (Reproduced with permission from Chalikov 2009 © 2009 AIP Publishing LLC)



**Fig. 7.14** All of the events when the value of trough-to-crest height is higher than  $2.1H_s$ : **a** is the maximum value of columnar energy  $E_{cm}$  (Eq. 7.4.1); **b** is the maximum value of surface velocity (normalized by phase velocity  $c_p$ ). In both panels, the horizontal axis is the maximum value of extreme trough-to-crest height  $H_f$ . Dots correspond to non-breaking extreme waves and asterisks show breaking extreme waves (Reproduced with permission from Chalikov 2009 © 2009 AIP Publishing LLC)



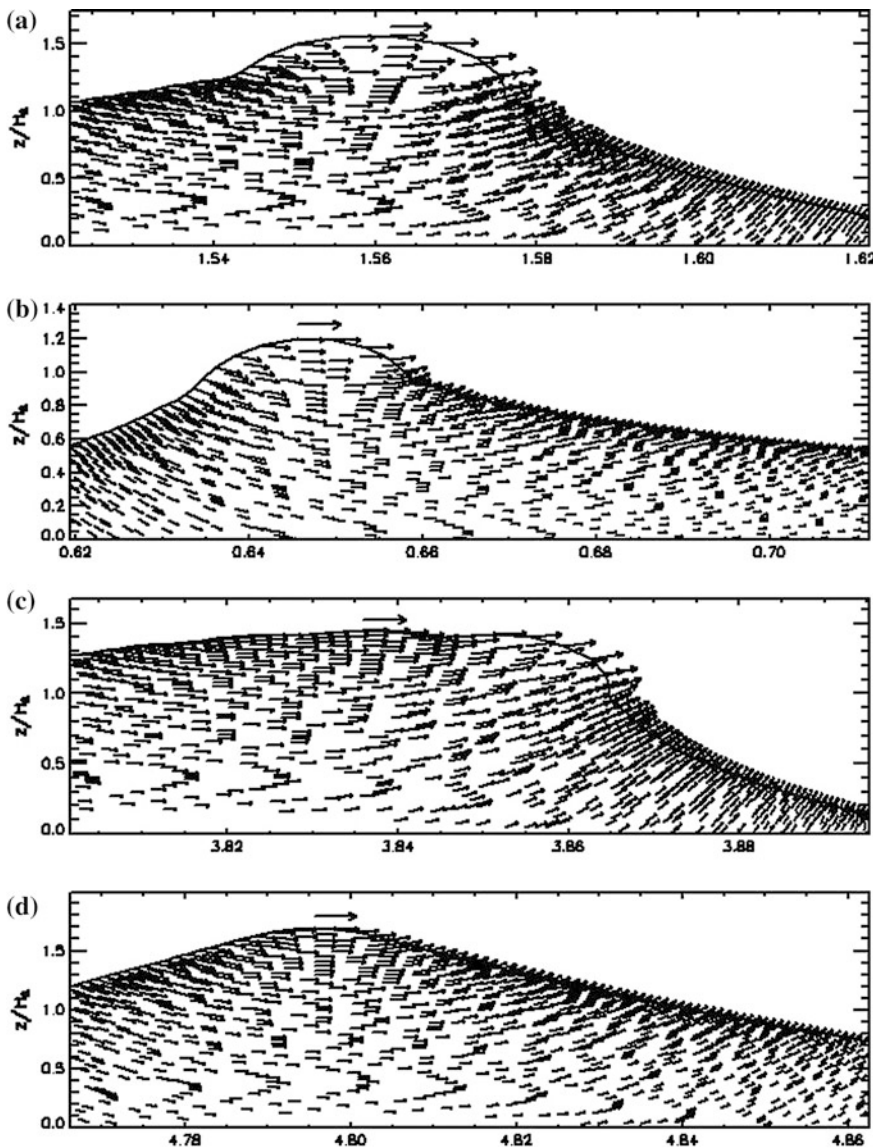


**Fig. 7.15** Examples of extreme wave shapes and velocity fields in the top part of waves: **a** is a sharp-crested breaking wave with high asymmetry  $As$  and skewness  $Sk$ : ( $H_s = 0.045$ ,  $H_f = 2.36$ ,  $Sk = 0.84$ ,  $As = 4.07$ ); **b** is a sharp-crested breaking wave with small asymmetry  $As$  and skewness  $Sk$ : ( $H_s = 0.038$ ,  $H_f = 2.10$ ,  $Sk = 0.08$ ,  $As = 0.55$ ); **c** is a flat-crested breaking wave with high asymmetry  $As$  and skewness  $Sk$ : ( $H_f = 0.039$ ,  $H_f = 2.16$ ,  $Sk = 1.06$ ,  $As = 4.28$ ); **d** is a sharp-crested non-breaking wave with medium asymmetry  $As$  and high skewness  $Sk$ : ( $H_s = 0.031$ ,  $H_f = 2.62$ ,  $Sk = 0.88$ ,  $As = 0.49$ ). The arrow on top indicates phase velocity (Reproduced with permission from Chalikov 2009 © 2009 AIP Publishing LLC)

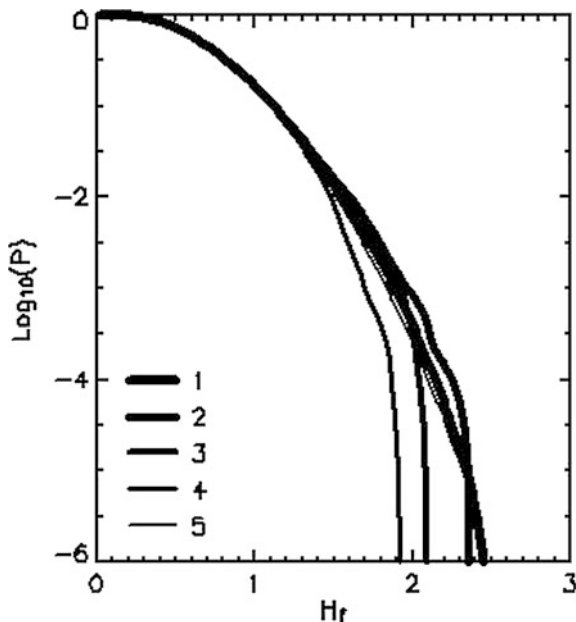
reach  $5.5 \cdot 10^5$ ,  $8.6 \cdot 10^5$  and  $1.2 \cdot 10^6$  Pa, respectively. If a wave does not break, the estimations for velocity should be reduced by 1.5–2 times, while for pressure—by 2–4 times.

## 7.5 Statistics of Extreme Waves

Figure 7.3 shows a slight tendency of an extreme wave height increase with decrease of steepness (wave age). Probably, a very energetic wave field destroys the growing waves before they reach large heights. However, it is reasonable to expect that with a further decrease of steepness, the generation of extreme waves should be less intense. To check up this statement, very long runs for different wave age of the combined JONSWAP/PM spectrum were performed. Because of the presence of a slow flux of energy to the high wave number range of spectrum, the wave field can gradually lose energy. To make a long run uniform, an imitation of energy flux from wind was added by multiplying all the Fourier components  $\eta_k$  and  $\phi_k$  ( $k = -M, M$ ) at each time step by coefficient  $\delta = (E_c^0/E_c)^{1/2}$ , where  $E_c$  is the total energy and  $E_c^0$  is the total energy at the initial conditions. A typical value of the coefficient  $\delta$  was 1.000001. Since this operation changes only the integral energy, it evidently does not influence the structure of spectrum and shapes of individual waves. The calculations were done for 5 cases starting from a very young sea ( $\Omega = U/c_p = 3$ ) up to the artificially ‘old’ sea whose wave spectrum was assigned by the PM spectrum multiplied by coefficient 0.1. The integral probability distributions for trough-to-crest heights calculated with moving window with length  $1.5L_p$  are given in Fig. 7.16 (each curve was interpolated from  $H_f = 0$  to  $H_f = 1$  with Raleigh formula).

The results of these calculations were unexpected: the largest extreme wave with the maximum value  $H_f = 2.65$  was simulated for the youngest wave field with  $\Omega = 3$ , but a considerably larger number of waves with  $H_f > 2.5$  were found for the case  $\Omega = 2$ . The cases  $\Omega = 0.855$  (PM spectrum for the developed sea) and the cases with reduced by factor 0.5 PM spectrum gave a reasonably smaller number of extreme waves, though a very gentle wave field with spectrum  $0.1S_\infty$  (the thin curve nearly coinciding with the thick one) showed the same statistics of extreme waves as the steepest wave field (the thickest curve). These results convince us that the frequency of freak waves is not directly connected with the energy of wave field; thus for obtaining the representative statistics, it is necessary to perform a long series of calculations for a broad range of the initial conditions characterized by wave spectrum and a set of initial phases. This approach was described in Sect. 7.2. It is remarkable that the statistical properties calculated for each run were dependent not only on the shape of the initial spectrum (which is understandable), but also on the phases of modes. For the same spectrum and different phases, the statistics of rare cases can be different: One run reproduces several extreme waves, while another one does not reproduce them at all. Extreme waves can appear either in the beginning of the run or after continuous integration. It means that the generation of extreme wave is an essentially random process which is initiated by very delicate

**Fig. 7.16** Probability distribution of trough-to-crest heights, calculated throughout long runs up to 2000 peak periods for initially assigned JONSWAP/PM spectrum:  
 1 –  $\Omega = 3$  (very young sea);  
 2 –  $\Omega = 2$  (young sea);  
 3 –  $\Omega = 0.855$  (developed sea); 4 –  $\Omega = 0.855$ ,  $S = 0.5S_\infty$  (PM spectrum multiplied by 0.5); 5 –  $\Omega = 0.855$ ,  $S = 0.1S_\infty$   
 (Reproduced with permission from Chalikov 2009 © 2009 AIP Publishing LLC)



and unpredictable properties of a local wave field in physical space. Later (see Chap. 12), we came to the conclusion that the reliable statistical characteristics of wave field can be obtained only with use of the ensemble modeling.

The data on the integral probability  $P$  of waves (probability of the waves whose crest-to-trough height exceeds  $H_f$ ) in the interval  $1 < H_f < 2.5$  calculated over all 4294 runs are represented in Fig. 7.17 where contours  $P_p(P, H_f)$  correspond to the number of cases falling in the cells with sizes  $\Delta H_f = 0.02$  and  $\Delta \log_{10} P = 0.1$  (the initial distribution of the points is also shown in Fig. 7.18).

The total number of points used for Fig. 7.17 is 190,337, and the number of trough-to-crest heights exceeding  $H_f = 2$  is 11,955. As shown, the data on the integral probability of trough-to-crest heights have a very large scatter, which is a reflection of a random nature of the extreme wave generation. This scatter excludes the possibility of use of the averaged integral probability, since distribution of the data inside the cloud of points should be taken into account. The attempts to stratify the data in Fig. 7.17 over parameter  $St$  (Eq. 3.9) characterizing the energy of waves were unsuccessful: The points corresponding to different runs obey the Gauss-like random distribution inside the cloud of data. Surely, it does not mean that statistics of the dimensional extreme waves does not depend on wave energy. It proves that normalizing of wave heights with the significant wave height is so effective that the statistics of non-dimensional extreme waves tends to be independent of wave energy. Figure 7.18 represents probability  $P_t$ , i.e., the integrated over  $P$  number of cases  $N_p$  by  $H_f$  bins and normalized by the total number of cases in bins

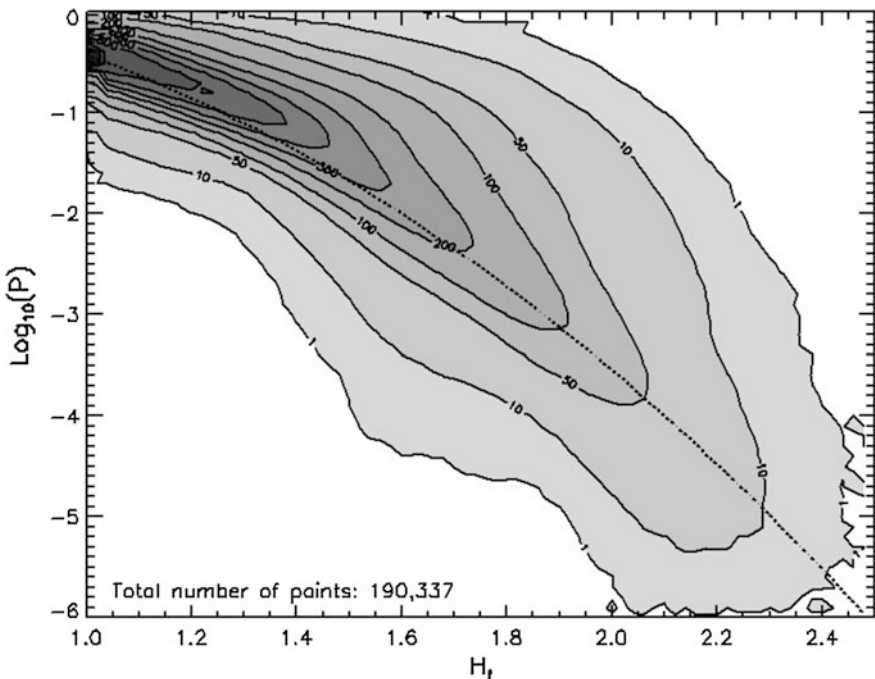


**Fig. 7.17** Contours  $P_p(P, H_f)$  corresponding to number of cases falling into cells of the following sizes  $\Delta H_f = 0.02$  and  $\Delta \log_{10} P = 0.1$ . Dotted line is an averaged value for each bin (Reproduced with permission from Chalikov 2009 © 2009 AIP Publishing LLC)

$$P_i(P, H_f) = \frac{\sum_0^P N_p(P, H_f)}{\sum_0^{P_\infty} N_p(P, H_f)}, \quad (7.5.1)$$

where  $P_\infty = 10^{-6}$  was chosen. The contours of  $P_i$  are plotted in Fig. 7.18 together with the initial data on the integral probability  $P$ . As shown, the data on  $P_i$  demonstrate a regular behavior, which gives the possibility to estimate the distribution of probability for the waves exceeding a specific value  $H_f$ . It is convenient to introduce the time expectance  $T_f$  of extreme wave instead of the probability (frequency) of wave

$$\tau_f = T_p(P P_i)^{-1} \quad (7.5.2)$$

The examples of estimation of the time expectance for extreme waves exceeding the values  $fH_s$ , ( $f = 2.1, 2.2, 2.3, 2.4, 2.5$ ) for different significant wave heights  $H_s$  from 2 to 12 m are given in Fig. 7.19. The connection between  $H_s$  and  $T_p$  was

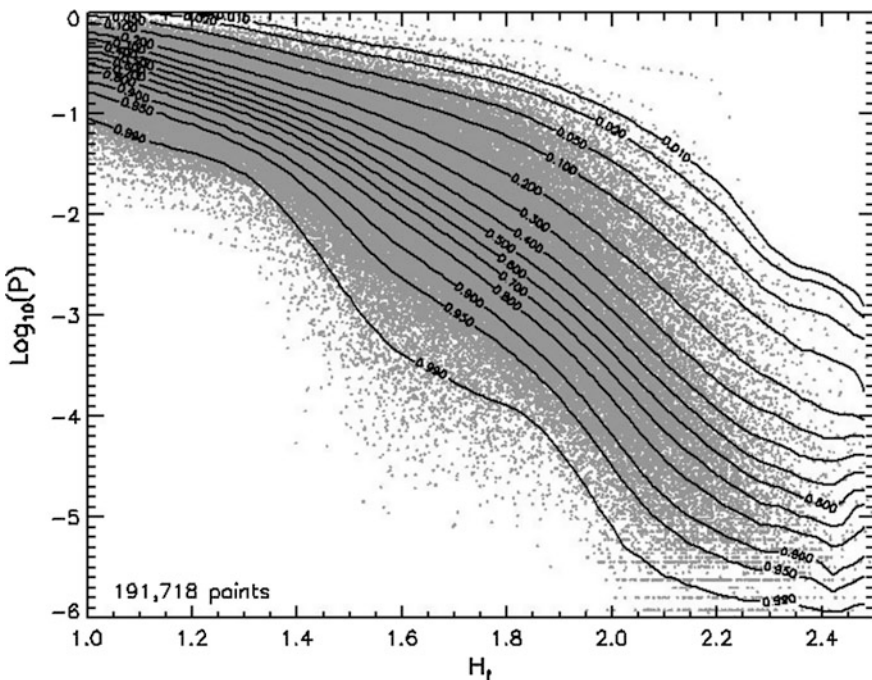


**Fig. 7.18** Probability  $P_t$  integrated over  $P$  number of cases by  $H_f$  bins and normalized by the total number of cases in the bins. Examples of estimations of time expectancy for extreme wave values exceeding  $H_f$ , ( $f = 2.1, 2.2, 2.3, 2.4, 2.5$ ) for different significant wave heights  $H_s$  in the range from 2 to 12 m (Reproduced with permission from Chalikov 2009 © 2009 AIP Publishing LLC)

established with the Pierson–Moskowitz spectrum; however, for this purpose, any wave spectrum can be used.

The vertical axes correspond to time expectancy  $\tau_f$  in days (logarithmic scale). The horizontal axis corresponds to the probability of meeting coming across the wave with height  $H_f$  and expectance  $\tau_f$  (logarithmic scale). Different curves correspond to different  $H_f$  (indicated in the legend in every frame). The thin vertical lines correspond to the probability  $P_t = 0.5$ . To make clear the use of this graph, let us give some examples. If the significant wave height  $H_s$  equals 4 m (top middle frame), then, with the probability 0.5, the time expectancy of wave with trough-to-crest height  $H_f = 8.2$  m will be 0.4 day; and for  $H_f = 10$  m, the time expectancy  $\tau_f = 10$  days. For  $H_s = 10$  m and  $H_f = 22$  m with probability 0.5, the expectancy time  $\tau_f = 0.6$  days, and for  $H_f = 25$  m  $\tau_f = 20$  days. The curves in different frames shown in Fig. 7.19 look very similar due to the logarithmic scales. It is a direct consequence of universality of the probability functions for non-dimensional wave heights. If the time expectancy were expressed in terms of the periods of peak wave  $T_p$ , then these frames would be identical. The dimensional period  $T_p$  grows as  $H_s^{1/2}$ , and  $\tau_f$  increases, correspondingly.

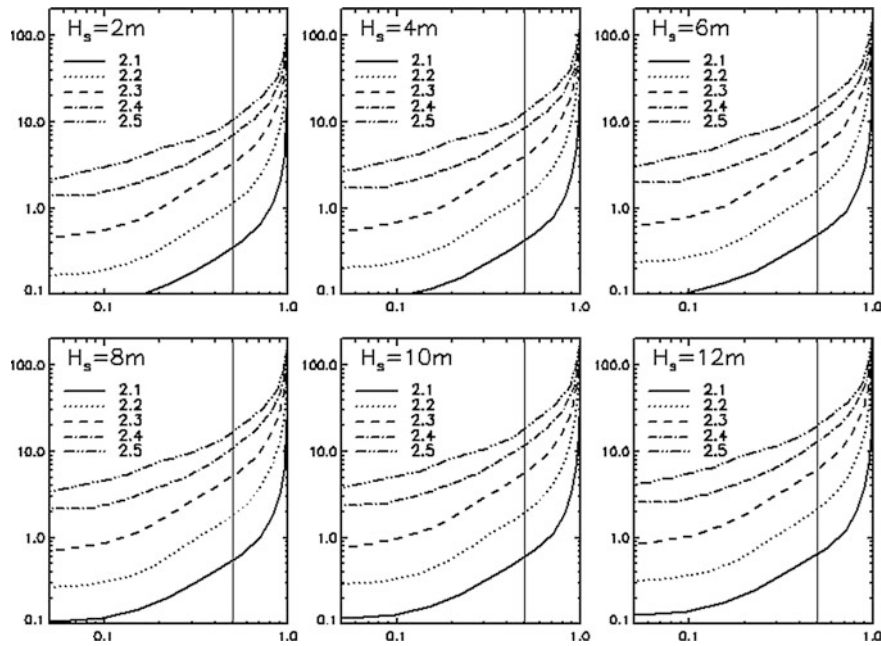


**Fig. 7.19** Examples of estimations of time expectance for extreme wave values exceeding  $H_f$ , ( $f = 2.1, 2.2, 2.3, 2.4, 2.5$ ) for different significant wave heights  $H_s$  in the range from 2 to 12 m (Reproduced with permission from Chalikov 2009 © 2009 AIP Publishing LLC)

## 7.6 Conclusion

In this chapter, the results of over four thousand numerical experiments were analyzed to investigate some properties of freak waves and calculate the probability of their appearance. Because of the self-similarity of governing equations, they can be used in a non-dimensional form; hence, the statistical results of long-term numerical simulations depend on the following initial conditions only: profiles of elevation  $\eta(x)$ , surface velocity potential  $\varphi(x)$ , and a set of initial phases. Considering the practical application of the theory of rare waves, we came to the conclusion that a strict ‘definition’ of freak waves in a non-dimensional form is not required at all. Instead, it makes sense to introduce the categories of dimensional extreme waves, like it was done, for example, for classification of hurricanes. For example, the  $n$ th category of freak wave can be defined as a wave with the trough-to-crest height equal to  $3n$  m.

The attempts were undertaken to stratify the wave statistics over some general integral characteristics, such as skewness, kurtosis, and initial density of energy or an enhancing parameter for spectrum. The results of the above efforts turned out to be quite unexpected at first sight: In a broad range of parameters for wind wave,

spectrum integral probability of freak waves was found to be virtually independent of spectrum shape.

Finally, we arrived at the conclusion that it is naive to expect that the high-order moments such as skewness and kurtosis can serve as predictors for freak waves. Firstly, the above characteristics cannot be calculated with the use of spectrum, usually determined with low accuracy. Such calculations are definitely unstable to a slight perturbation of spectrum. Secondly, even if spectrum is determined with high accuracy (e.g., calculated with the use of an exact model), the high-order moments cannot serve as predictors, since they change synchronically with variations of extreme wave heights. Appearance of freak waves occurs simultaneously with increase of the local kurtosis; hence, kurtosis is simply a passive indicator of the same local geometrical properties of wave field. This effect disappears completely, if spectrum is calculated over a very wide ensemble of waves (see Chap. 12). In this case, an existence of freak wave is just disguised by other waves, not freak ones. It is quite evident that kurtosis is not a predictor but an extreme wave indicator that is representative for such a small area that it can be observed as easily as a freak wave itself. Freak wave is even better recognizable than kurtosis. Thirdly, all the high-order moments are dependent on the spectral presentation; i.e., they increase with increase of the spectral resolution and cut-off frequency.

The statistics of non-dimensional waves as well as emergence of extreme waves is the innate property of a nonlinear wave field. The most pronounced indicator of freak wave is the freak wave itself.

The most surprising result was discovery that the probability of non-dimensional freak waves (normalized by the significant wave height) is virtually independent of the wave energy density. It just proves that normalization of wave heights by the significant wave height is so effective that the statistics of non-dimensional extreme waves tends to be independent of wave energy. The independence of freak wave probability on wave energy can be an indicator of the linear mechanism of ‘freaking’ (see Chap. 12). For superposition of linear modes, the significant wave height is a universal characteristic, so the probability of the non-dimensional wave height does not depend on energy of waves. The wave energy is not an indicator of the wave field steepness. Note that defining the integral steepness is actually not so easy, as any definition turns out to be dependent on the spectrum resolution, i.e., the value of wave number for spectrum peak and the total number of modes assigned for description of spectrum. This statement remains valid for routine presentation of wave field as a random superposition of linear modes. For true nonlinear waves, a dependence on resolution (if it is sufficiently high) should be insignificant. Firstly, spectrum should decrease with increase of wave number quickly enough for convergence of any important moments. Secondly, the waves with very close wave numbers cannot run as independent waves, they would probably interact, quickly forming a single nonlinear mode. The spectrum assigned with an excessively high resolution turns into a discrete spectrum (Zakharov et al. 2005; Chalikov et al. 2014). The wave field is rather a superposition of finite number of the nonlinear modes distorted with the random small-scale quasi-turbulent noise.

The shape of freak waves varies within a wide range: Some of them are sharp-crested and others are asymmetric, with a strong forward inclination. The investigations show that only the breaking and large waves can be referred to as freak waves. Some of them can be very big, but not steep enough to create dangerous conditions for vessels (not for fixed objects). An initial concentration of energy can occur merely as a result of group effects, but in some cases, the largest wave suddenly starts to grow. The growth is followed sometimes by strong concentration of wave energy around the peak vertical. It is taking place in the course of a few peak wave periods.

The results of this chapter can be considered as preliminary. To obtain more representative statistics of extreme waves, it is necessary to perform a significantly greater number of the numerical experiments using a 2-D model, probably, with a better resolution. The disadvantage of the current approach is the termination of run after it has reached the infinite slope (in the conformal coordinates, the slope is always finite). This effect can be avoided by introduction of the breaking parameterization. This algorithm performs local smoothing of surface, followed by loss of the excessive potential and kinetic energy (Chalikov and Sheinin 2005). In this chapter, the breaking parameterization was not introduced intentionally to avoid distortion of the statistics of extreme waves.

# **Chapter 8**

## **Numerical Investigation of Wave Breaking**

**Abstract** Results of numerical investigations, based on full dynamic equations, are presented for wave breaking in one-dimensional environment with wave spectrum. The breaking is defined as a process of irreversible collapse of an individual wave in physical space, and the incipient breaker is a wave which reached a dynamic condition of the limiting stability where the collapse has not started yet, but is inevitable. Main attention is paid to documenting the evolution of different wave characteristics before the breaking commences. It is shown that the breaking is a localized process which rapidly develops in space and time. No characteristics such as wave steepness, wave height, and asymmetry can serve as a predictor of the incipient breaking. Process of breaking is intermittent; it happens spontaneously and is individually unpredictable. Evolution of geometric, kinematic, and dynamic characteristics of the breaking wave describes the process of breaking itself rather than indicating an imminent breaking. It is shown that the criterion of breaking, valid for the breaking due to modulation instability in one-dimensional wave trains, is not universal if applied to the conditions of spectral environment. In this context, more important is development of algorithms for parameterization of breaking for wave prediction models and for direct wave simulations. Prototype of such algorithm is proposed on the basis of the diffusion-type highly selective operator. It is suggested that the main parameter is differential steepness calculated over entire spectrum. Thousands of exact short-term simulations of evolution of two superposed wave trains with different steepness and wave numbers were performed to investigate the effect of wave crests' merging. Nonlinear sharpening of the merging crests is demonstrated. It is suggested that such effect may be responsible for the appearance of the typical sharp crests of surface waves, as well as for wave breaking.

### **8.1 Wave-Breaking Phenomenon**

The wave breaking is important among a great variety of geophysical and engineering applications. In the geophysical system of air–sea interactions, the breaking controls the whitecapping dissipation of surface waves and, thus, the wave growth

(e.g., The WISE Group 2007). The breaking modifies the drag coefficient in the atmospheric boundary layer and, therefore, momentum and energy exchange between wind and waves; it produces turbulence for the upper-ocean mixing (e.g., Chalikov and Belevich 1993), and it also determines to a great extent the gas, heat, and moisture exchanges across the interface (e.g., Bortkovskii 1987). In the hydroacoustics, it is a primary source of the underwater sound (Kerman 1992); in remote sensing, it produces sea spikes (e.g., Melville et al. 1988) and whitecapping which then serve either as a proxy of wanted properties or an unwanted noise which needs to be dealt with (e.g., Sharkov 2007). In engineering, it is responsible for impacts on structures and vessels, may directly affect the bottom boundary layer in shallow areas, or may limit the maximum in probability distributions of wave height, among many other contributions and influences (see, e.g., Babanin (2011) for a review).

For many years, the breaking was regarded as a poorly understood phenomenon which is hard if not impossible to approach by the theoretical, numerical, and even experimental means. Indeed, it is a strongly nonlinear process where a wave (or rather a wave group which includes a breaking wave) suddenly, within a fraction of wave period, losses the energy accumulated from the wind over hundreds of wave periods. These events are sporadic; i.e., they do not cover the entire wavy surface, and this is in the wave system where all the other processes responsible for the wave evolution are presented. There are even accounts that the breaking distribution on the ocean surface is fractal (Zaslavskii and Sharkov 1987). Such features are difficult to explain in the analytical theories, difficult to reproduce in the numerical models, and difficult to measure.

In the past decade, however, an essential progress has been made in understanding the causes of wave breaking and quantifying the breaking probability as a function of environmental properties, first of all, those of the wave field itself. For monochromatic wave trains (or quasi-monochromatic, i.e., a combination of a carrier wave and small sideband perturbations), the breaking onset was identified with a limiting steepness of  $Hk/2 \approx 0.44$ , where  $H$  is a breaking-wave crest-to-trough height and  $k$  is its wave number (Brown and Jensen 2001 for linear-superposition breaking, Babanin et al. 2007, for modulational-instability breaking, Toffoli et al. 2010 for oceanic waves). Parameterizations of the breaking probability were suggested, based on the laboratory (Babanin et al. 2007) and field (Banner et al. 2000; Babanin et al. 2001) observations. Both revealed a threshold for the breaking onset, in terms of the background mean steepness of wave trains/fields. For the spectral environments, such an important feature as cumulative effect of the breaking at small scales was found (Babanin and Young 2005; Manasseh et al. 2006; Young and Babanin 2006).

It should be mentioned that a majority of investigations of the wave breaking in the laboratory and field were conducted for the breaking stage after the breaking onset (e.g., Holthuijsen and Herbers 1986; Xu et al. 1986; Jessup et al. 1997; Gemmrich and Farmer 1999; Melville and Matusov 2002; Kleiss and Melville 2011, among many others), whereas a majority of analytical and numerical research for the incipient-breaking stage (Longuet-Higgins 1969; Srokosz 1986; Yuan et al.

1986; Papadimitrakis 2005, among others for probability models, Banner and Tiang 1998; Song and Banner 2002; Irisov and Voronovich 2011 for numerical models). In the experiment, whitecapping signature or its derivatives such as underwater sound, void fraction, infrared surface trace, and radar reflection are typically used to detect the breaking events, and otherwise, it is difficult to judge on whether the wave is going to break or not. The theory, on the contrary, cannot describe the complicated nature of the multi-phase fluid mechanics of rapid wave collapse and concentrates either on the dynamics of a nonlinear wave evolution to the point where the collapse starts, or on interpreting the statistical properties of such point. We should note, however, that the physics of the prebreaking and post-breaking evolution is essentially different: The former is the nonlinear wave dynamics, and the latter is the water surface collapse. This chapter will be only considering the prebreaking stage and analyzing a wave evolution to the breaking onset and the onset itself, but not the breaking past this onset when the wave starts exhibiting the whitecapping.

Since the conclusion was drawn that a wave is to reach the limiting steepness in order to break, then any physical mechanism which can lead to such steepness will result in breaking. There can be lots of such mechanisms, i.e., the wave focusing or just superposition, modulational instability, modulation of short waves by longer waves in the spectral environments, strong wind forcing, and interactions of waves with currents or with the bottom. The latter four are specific to the wave scales or environmental conditions, and the former two are general and can occur in deep-water no-forcing circumstances.

If so, the question was which of the two would be more frequent in field conditions? Babanin et al. (2011) argued that the superposition of waves, with the typical field-wave steepness of the order of  $Hk/2 \approx 0.1$ , is possible, but its probability is very low in the field. Besides, signatures of breaking allow us to distinguish between the focusing- and instability-breaking types. For example, the above-mentioned mean-steepness threshold cannot be a feature of the superposition-caused breaking. This argument is indirect, but many other signatures point to the modulational instability more directly. These are double-breaking (Donelan et al. 1972), upshift of the spectral energy prior to breaking, oscillations of wave skewness/asymmetry, cumulative effect, which were observed in the field, but in the laboratory-simulated breaking, they clearly associate with the modulational instability (Babanin et al. 2010).

The modulational instability, however, is expected to be impaired or even suppressed in directional wave fields, as opposed to the unidirectional wave trains typically used in wave flumes (Onorato et al. 2009a, b; Waseda et al. 2009). In order to investigate this issue, a dedicated experiment was conducted in a three-dimensional wave tank, with the waves quasi-monochromatic in frequency domain, but with a broad range of wave-steepness and directional-distribution values (Babanin et al. 2011). In author's opinion, the result was encouraging: For wave trains with steepness and directional spread typical of those in the ocean, the modulational instability can be still active.

The present study is the first attempt to investigate the evolution of waves prior to breaking and the breaking onset in the environment with full wave spectrum, based on full nonlinear equations (Babanin and Chalikov 2012, see also Agnon et al. 2005; Babanin et al. 2010). The study is conducted by means of fully nonlinear one-dimensional potential model ChSh. This model is based on first principles, and it proved stable and energy conserving over thousand of wave periods of integration and does not have limitations in terms of wave steepness. It has been extensively used for numerical simulations of evolution prior to breaking in monochromatic and quasi-monochromatic wave trains and demonstrated excellent agreement with the laboratory experiments.

The contradiction between the results of simulations and experiments can be attributed to the presence of different types of deviations of ideal conditions in experiments. For example, the wave generation in laboratory deals with generation of surface only. However, the distribution of velocity (the second fundamental variable) is usually out of control. In Song and Banner (2002, hereinafter SB), for example, it was mentioned that the measured velocity field agrees with the calculations with accuracy 2 %. In fact, such disagreement is quite rough, since the imposing of disturbances of such magnitude would affect the numerical solution significantly. The wave dynamics is organized so well that comparison of 1-D numerical modeling with an ideal 1-D laboratory modeling can highlight applicability of the potential assumption only, but all other discrepancies should be attributed to imperfection of the laboratory data.

## 8.2 Description of the Numerical Experiments

Previously, the breaking was investigated with numerical models for the cases when wave field was represented by a small number of modes (Banner and Tian 1998; Song and Banner 2002). Irisov and Voronovich (2011) investigated breaking in the presence of continuous spectrum tail. Here, the investigation of breaking will be done for the multi-mode wave field corresponding to real wave spectrum.

In this study, we applied the above-mentioned method for numerical simulation of surface waves for investigation of a wave field evolution assigned by the one-dimensional version of JONSWAP spectrum  $S_f$  (Hasselmann et al. 1973) for finite fetch as a function of frequency  $\omega$  (Eq. 7.2.1).

In the initial JONSWAP approximation, an enhancement parameter for spectrum  $\gamma$  was accepted as constant:  $\gamma = 3.3$ . Later, some investigators came to the conclusion that the above parameter can be a function of fetch or peak frequency  $\omega_p$ . According to Babanin and Soloviev (1998),  $\gamma$  increases with  $\Omega_p$ :  $\gamma = 1.22\Omega_p$ .

The approximations (8.2.1), (8.2.2) were rewritten in terms of wave numbers using a dispersion relation that is precise at least up to  $3\Omega_p$  (Chalikov 2005).

The initial conditions for Fourier coefficients of free surface  $\eta(x)$  were assigned in the following form:

$$|h_k| = (2S(k)\Delta k)^{1/2}, \quad \eta_k = |h_k|\cos(\varphi_k), \quad \eta_{-k} = |h_k|\sin(\varphi_k), \quad k = 1, 2, 3 \dots M_i \quad (8.2.1)$$

where  $|h_k|$  is amplitude of  $k$ th mode;  $M_i$  is the number of modes assigned for the initial conditions;  $\eta_k$ ,  $\eta_{-k}$  are Fourier coefficients in the Cartesian coordinates, and  $\varphi_k$  is a random (over  $k$  and over different runs) phase distributed uniformly over the interval  $(0 \div 2\pi)$ . The Fourier coefficients  $f_k$  for the surface potential  $f(x)$  were assigned through:

$$f_k = \text{sign}(k)|k|^{-1/2}a_{-k}, \quad k = -M_i, M_i, \quad (8.2.2)$$

In this study, the model was applied for investigation of the breaking waves' onset. More details of the model, numerical scheme, and model validation can be found in Chap. 2. The peak wave number was equal to 16. The number of modes  $M$  was equal to 1000 and the number of knots  $N = 4000$ . Since the peak wave number was equal to 16, this resolution was even excessive.

An increase of the local steepness often results in development of instability and even in the overturning of sharp crests. Formally, the conformal mapping exists up to the moment when the overturning volume of water touches the surface. In such imaginary evolution, the number of the Fourier modes required increases up to infinity. If some special measures are not taken, the calculations normally terminate much earlier due to the strong crest instability (Longuet-Higgins and Tanaka 1997) followed by splitting of the falling volume into two phases. This phenomenon is obviously non-potential.

### 8.3 Results of the Numerical Experiments

The problem of breaking has recently been a subject of extensive theoretical and experimental research (see review in Babanin 2011). The ChSh model, as a precise and fully nonlinear model which can describe the wave-train evolution from any set of the initial conditions all the way to the breaking start, was lately extensively employed in this kind of research. Babanin et al. (2007) used it to predict the breaking onset, the prediction of which was then checked in a laboratory study of wave breaking. In Babanin et al. (2010), the model was used for a detailed research of the nonlinear properties of waves evolving to breaking, of the characteristics of the imminent breaker, and, coupled with the atmospheric boundary layer model of Chalikov and Rainchik (2011), for investigations of the wind influence on this evolution and the onset. In Babanin et al. (2010), the initial conditions were uniform wave trains. Galchenko et al. (2010, 2012) employed ChSh model to set up a variety of combinations of carrier wave and seeded perturbations to achieve different instability rates. It was presumed that such different rates would lead to different breaking severity, which was confirmed in an accompanying laboratory

experiment. Thus, in all these studies, the simulations with ChSh model were combined with the laboratory tests, and in all the cases, the agreement was excellent.

The results of the numerical investigations of the breaking onset on the basis of the Dold–Peregrine (DP) model were published in several papers of Banner with co-authors (Banner and Tian 1998; Song and Banner 2002, 2004; Banner and Song 2002; Banner and Pierson 2007). All these works considered evolution of the single wave with two superimposed disturbances. The onset of breaking was recognized by development of the numerical instability of the solution. Such criterion is evidently imperfect, since the numerical instability can develop long before the physical instability.

In our model, the onset of breaking was defined by the first appearance of non-single value of surface (Eq. 6.1.1). The details of this development are not the subject of this investigation. Once the criterion (8.3.1) has been reached, the solution never returns to stability: The volume of fluid crossing the vertical  $x$  ( $i$ ) increases rapidly. Up to this moment, the conservation of the sum of the potential and kinetic energy, horizontal momentum, and volume was excellent. Opposite to the criterion used in the works mentioned above, the criterion (8.3.1) is exact. In all the cases simulated here, the formation of ‘vertical wall’ occurred in the vicinity of wave crest. When the surface approaches non-single value (at the initial stage of breaking), the conservation of invariants still holds, though later, a sharp increase of energy occurs, and further, integration becomes useless. Usually, it happens just for one Runge–Kutta time step, so, probably, the primary cause of the numerical instability is growth of the right-hand side of Eqs. (2.3.4) and (2.3.6) and, particularly, the growth of the first and second derivatives. Disintegration of solution happens mostly due to inapplicability of the potential approximation and, generally, of the fluid dynamics equations for single-phase fluid.

When the model is set for simulation of a long-time development of spectrum, the termination of run due to the breaking can be prevented by the introduction of the breaking parameterization algorithm based on the selective high-frequency smoothing of the interface and surface potential profile in physical space (Chalikov 2005; Chalikov and Rainchik 2010). Since the current work is devoted to investigation of the breaking itself, this smoothing was disabled, and each model run was terminated using criterion (8.3.1).

It was found that, unlike the breaking in idealized conditions, in a multi-mode wave field, the breaking is an essentially random phenomenon. An onset of the breaking depends on many poorly controlled factors. Even if wave spectrum in the initial conditions is fixed, the time up to the onset of breaking is different for a different initial set of phases  $\vartheta_k$ . This effect is also clearly pronounced in the process of freak wave formation. Therefore, the statistics of breaking should be investigated by means of ensemble modeling.

To accelerate the breaking, the initial conditions were generated for JONSWAP spectrum at  $\Omega_p = 2$ . Hence, the phase velocity at wave peak was twice less than wind speed, what corresponds to the case of developing waves. Time step  $\Delta t$  was

equal to 0.0001. As many as 5000 runs with random set of phases were performed up to the termination due to breaking. Limiting time  $t = 1000$  (503 periods of peak wave) was reached just in several runs, and these cases were excluded from consideration. For detailed study of breaking, it is necessary to record a large volume of data with a very small time interval. Such recording was not possible to provide over the entire period of integration, since it takes too much of the computer memory. This is why the simulations were performed in two stages. In the first stage, the calculations were done up to the point of breaking; the recording of all data including restart was done with the interval  $\delta t = 5$ . In the second stage, the last record of restart was taken as the initial conditions for continuation of runs up to the point of breaking. In the course of these calculations, the records were stored with the interval  $\delta t = 0.1$ , which provided a good description of breaking development. These runs will be called ‘final runs.’ Each instantaneous record includes the following fields: surface elevation  $z$ , surface potential  $\Phi$ , surface velocity components  $u_0$  and  $w_0$  and their individual derivatives on time (accelerations)  $(du/dt)_0$  and  $(dw/dt)_0$ , local surface inclination  $\partial z/\partial x$ , curvature  $\partial^2 z/\partial x^2$ , local columnar potential  $e_p$ , kinetic  $e_k$  energy, and total  $e_t$  energies, which is defined as

$$e_k = \frac{1}{2} z^2, \quad (8.3.1)$$

$$e_k = \frac{1}{2} \int_{-\infty}^0 (\Phi_z^2 + \Phi_\zeta^2) J^{-1} d\zeta, \quad (8.3.2)$$

$$e_t = e_p + e_k. \quad (8.3.3)$$

For recognition of breaking the height of wave crest above a mean level  $z = 0$  does not make any sense, because wave stability depends on the overall wave height from its trough to crest. It is not easy to detect this height formally. Calculation of the vertical distance between the maximum and its nearest minimum does not give the right answer, because there can be some local extremes; hence, the wave height can be underestimated. Obviously, an extreme wave must be found between large waves. That is why the height of extreme waves  $H_{tc}$  in each record  $\eta(x)$  was defined here as a difference between the absolute maximum  $z_{\max} = H_m$  and the absolute minimum  $z_{\min} = \min\{D_d, D_u\}$  in the moving window of length  $L_e$ . The upwind trough depth  $D_u$  and downwind trough depth  $D_d$  were usually different before breaking (see fragment of wave surface in Fig. 8.1).

It is reasonable to define  $L_e = 1.5L_p$  where  $L_p$  is length of wave in peak of spectrum,  $L_p = 2\pi/k_p$  and  $k_p$  is the actual wave number in the spectral peak. Large waves with the length exceeding  $1.5L_p$  were practically absent. In each record, the length of the largest wave  $L_m$  can be defined as a distance between  $x$ -coordinates of right  $X_{td}$  and left  $X_{tu}$  minimums:  $L_m = X_{td} - X_{tu}$  (see 8.1). The lengths of upwind  $L_{mu}$  and downwind  $L_{md}$  slopes are defined as  $L_{mu} = X_m - X_{tu}$  and  $L_{md} = X_{td} - X_m$ , correspondingly, where  $X_m$  is  $x$ -coordinate of the crest of largest wave. Note that

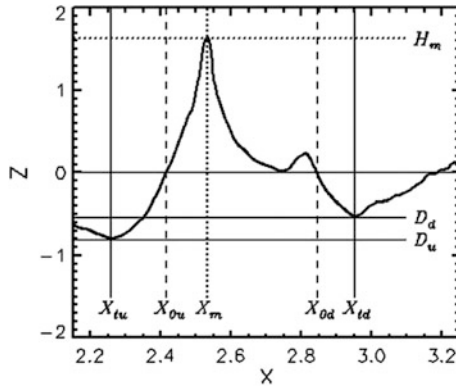
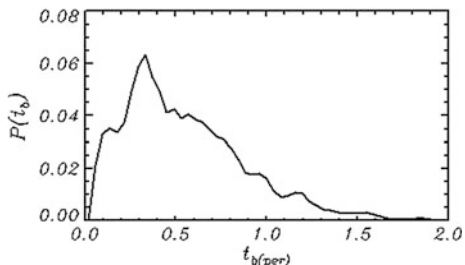


**Fig. 8.1** Scheme used for processing of wave surface records.  $H_m$  is the maximum wave height;  $X_m$  is the  $x$ -coordinate of peak of such wave;  $D_d$  is the maximum depths of front trough;  $X_{td}$  is the  $x$ -coordinate of this point;  $D_u$   $X_{tu}$  are the same characteristics for back trough;  $X_{0d}$  and  $X_{0u}$  are the zero downcrossing and upcrossing points correspondingly. Chalikov and Babanin 2012 © American Meteorological Society. Used with permission

small-scale waves add some uncertainty to the definition of geometrical characteristics of the selected wave.

The main difficulty of the breaking analysis is that the largest wave during the *final run* (the duration is less than 2.5 peak wave periods) can preserve its individuality only within a short period, so that the waves in different locations can play the role of the largest wave in the record at different moments. However, in most cases, it is the largest wave in the record that finally comes to breaking. The cases when the breaking occurred with not the largest waves were excluded from the consideration. To investigate a wave evolution, the tracing of the horizontal coordinate  $x_p$  of the largest wave peak was introduced, the waves with a continuous evolution of  $x_p$  up to the point of breaking being only selected. Remarkably, duration of the breaking development  $t_b$  is very short. The probability distribution for  $t_b$  expressed in peak wave period  $T_p$  is shown in Fig. 8.2. As shown, the maximum of the probability falls on the period  $0.35T_p$ . It suggests that the breaking is an impulsive phenomenon developing very fast upon reaching the appropriate conditions. These conditions can be formed by reversible interactions which are

**Fig. 8.2** Probability distribution  $P(t_b)$  for the period of breaking development  $t_b$ . Chalikov and Babanin 2012 © American Meteorological Society. Used with permission



much stronger and faster than the irreversible ones. If the breaking happens, then, obviously, the reversible interactions become irreversible. The breaking can be an efficient mechanism of nonlinear interactions, manifesting itself in downshifting (Melville and Matusov 2002; Donelan et al. 2012).

All the results presented below were obtained for the final time period of the single largest wave evolution preceded by breaking. The runs not terminated by breaking, as well as the cases when duration of a final run was less than  $0.2T_p$ , were excluded (in calculation of probability  $t_b$  shown in Fig. 8.2 they are accounted though).

An additional criterion of data quality was introduced by control of total energy  $E_t$

$$E_p = (2\pi)^{-1} \int_0^{2\pi} z^2 x_z d\xi, \quad (8.3.4)$$

$$E_k = (2\pi)^{-1} \int_0^{2\pi} \vartheta \vartheta_\zeta d\xi \quad (8.3.5)$$

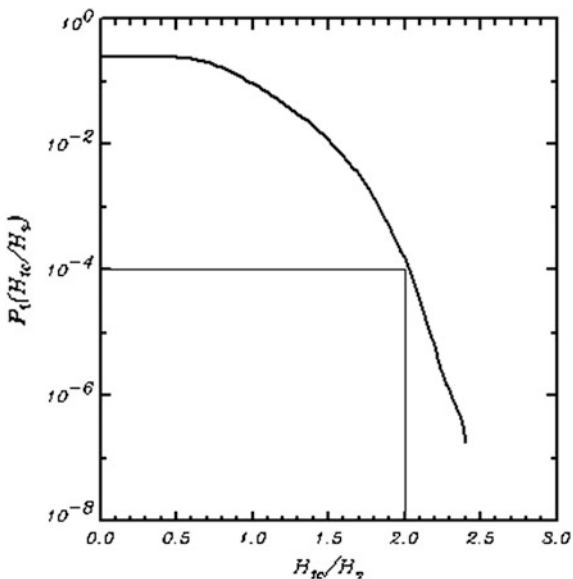
$$E_t = E_p + E_k, \quad (8.3.6)$$

where  $E_k$  is the kinetic energy and  $E_p$  is the potential wave energy. In the absence of the wind input and dissipation, the waves are adiabatic, but due to a slow flux of energy in the subgrid part of spectrum, the total energy can decrease. The variation of energy due to this effect is much slower than an increase of energy through the wind input. However, if wave surface approaches overturning, the local large gradients of elevation and surface potential cause the numerical instability which results in fast change of the total energy. In all the cases, this phenomenon took place very close to the moment when condition (8.3.1) is reached. For eliminating this effect, the cases when the energy change exceeded 0.01 % were excluded. Finally, only 2260 cases were used for further analysis.

The integral probability for the non-dimensional crest-to-trough height  $H_{tc}/H_s$  ( $H_s$  is the significant wave height,  $H_s = 4\sqrt{E_p}$ ) is given in Fig. 8.3.

The sampling interval was equal to 0.1, and for calculations of probability 670,764,710, the elementary events were used. As shown, large waves are not a rare phenomenon: The integral probability of waves exceeding significant wave height twice as much is equal to  $10^{-4}$ , i.e., one of ten thousand waves can be attributed to the so-called freak waves. Due to the self-similarity of the equations, this result for non-dimensional height is universal; however to be really ‘freak,’ the wave should be high enough indeed. Note that not all ‘freak’ waves break, but the portion of the breaking freak waves increases with its non-dimensional height  $H_{tc}/H_s$  (Chalikov 2009), and depending on  $H_s$  and a dominant wavelength, the breaking limits the maximum possible ratio  $H_{tc}/H_s$  in the field.

**Fig. 8.3** Integral probability  $P_i(H_{tc}/H_s)$  for trough-to-crest wave height  $H_{tc}$ , normalized by significant wave height  $H_s$ . Chalikov and Babanin 2012  
© American Meteorological Society. Used with permission



A typical example of a wave evolution terminated by breaking is shown in Fig. 8.4a. As shown, the wave increases its crest height twice from  $0.7 H_s$  to  $1.5 H_s$ . The depth of back trough remains more or less the same, while the depth of front trough decreases (see also Babanin et al. 2007, 2010). In panel *b*, an evolution of columnar energy  $e_c$  is presented. It is seen that the maximum columnar energy prior to breaking exceeds the average energy 8 times. This effect is demonstrated more clearly in Fig. 8.5 where the time evolution of the averaged over distance  $L_m$  energy  $E_m$  is represented together with the evolution of maximum value of the columnar energy  $E_{\max}$ . The averaged wave energy  $E_m$  changes insignificantly, mostly because of some uncertainty in definition of  $L_m$  caused by the presence of local extremes. However, the maximum of columnar energy  $E_{\max}$  changes several times. It will be shown below that such growth is provided by the concentration of the energy around crest vertical. It was found that this effect was the primary cause of the freak wave generation (Chalikov 2009). Evidently, the breaking waves and freak waves have a similar nature. However, large wave height is not a necessary condition of breaking, since smaller waves also break. This fact suggests that in the spectral environment, the breaking is not necessarily connected with the overall wave characteristics, but rather with a rapidly changing local condition in the vicinity of wave crest.

The results presented below are obtained by the processing of all the 2260 final runs. Evolution of the total energy of wave averaged over its length  $L_e$  and normalized by the total energy  $E_t$  as a function of time (expressed in peak wave periods) prior to breaking

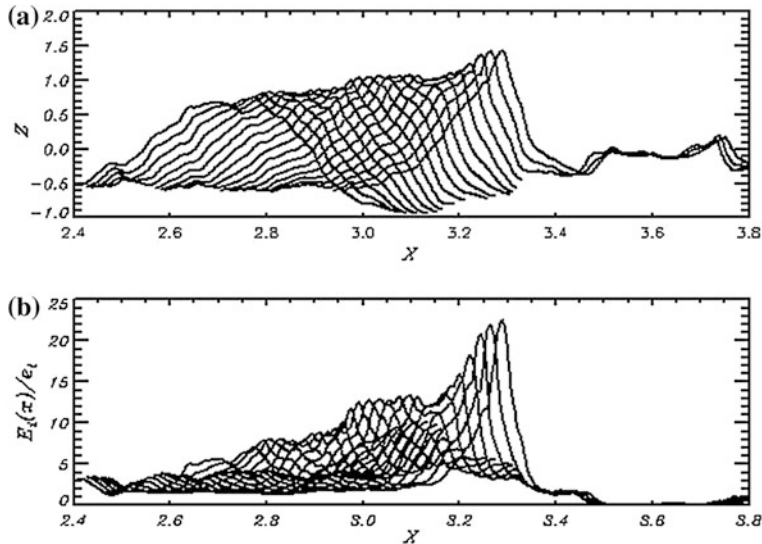


**Fig. 8.4** **a** Example of evolution of selected wave profile  $z$  up to onset of breaking. **b** Evolution of columnar energy  $e_t(x)$  normalized by mean energy  $e_t$  for the same period

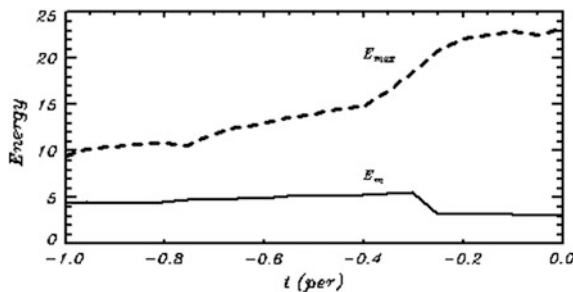


**Fig. 8.5** Evolution of averaged over wavelength columnar energy  $E_m$  and maximum of columnar energy  $E_{\max}$  for the development shown in Fig. 8.4. Chalikov and Babanin 2012 © American Meteorological Society. Used with permission

$$E_m = \frac{1}{E_t L_e} \int_{L_e} e_t dx \quad (8.3.7)$$

is shown in Fig. 8.6a. The solid thick curve is averaged over all cases' evolution of  $E_m$ , while the distance between the dotted lines indicates the dispersion. As shown, wave energy before breaking is close to the doubled averaged energy  $E_m$ , but it can be also several times larger or smaller than  $E_m$ . The dispersion shown in Fig. 8.6a is very stable and small, just of the order of 0.1. It is most interesting that on the average, the approaching of breaking does not manifest itself by the growth of wave

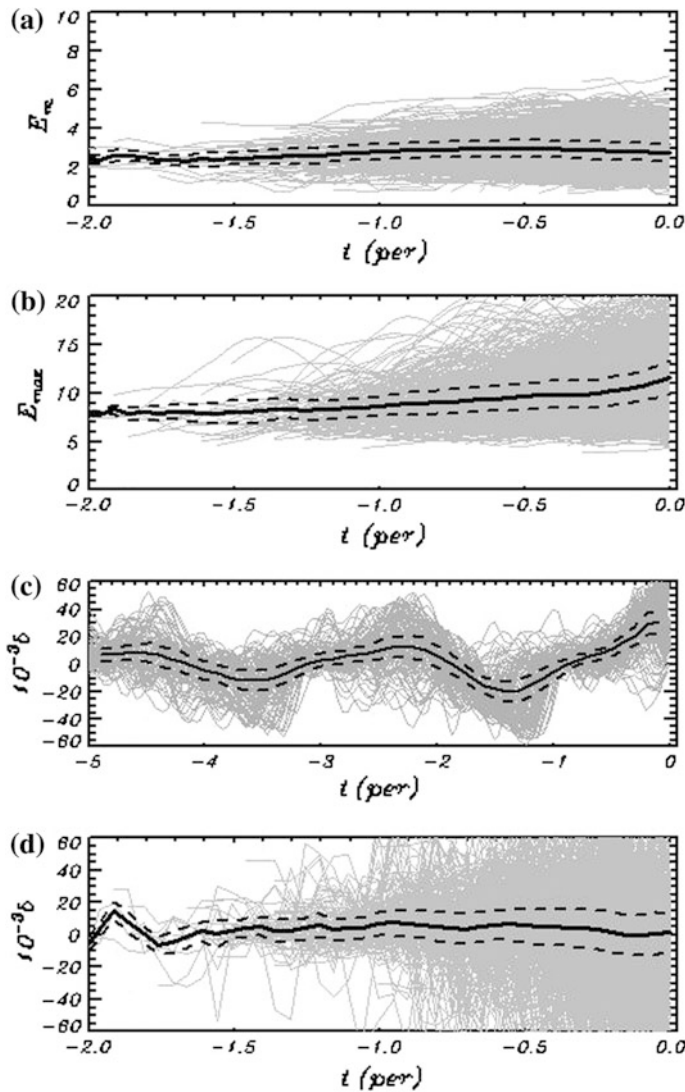


**Fig. 8.6** **a** Evolution of the energy of selected wave  $E_m$  (Eq. 8.3.6) averaged over wavelength  $L_m$  prior to breaking as function of time  $t$ , expressed in peak wave periods. Aggregated gray lines correspond to single cases, solid line represents the averaged over all cases' evolution, and dotted lines correspond to dispersion. Moment of breaking corresponds to time  $t = 0$ ; **b** the same as in panel a, but for maximum value  $E_{\max}$  of columnar energy  $E_t$  in selected window; **c** evolution of  $\delta$  (Eq. 8.3.9) for idealized initial conditions; **d** evolution of  $\delta$  in spectral environment. The style of curves in panels b and c is the same as in panel a. Chalikov and Babanin 2012 © American Meteorological Society. Used with permission

energy. This fact proves that a breaking wave in the spectral environment does not necessarily take energy from other waves. In the events simulated here, development of the breaking instability occurs because of modification of its shape; i.e., the wave becomes more sharp-crested with concentration of its energy around its peak; the crest itself becomes unstable, and the wave breaking starts. It is demonstrated clearly in Fig. 8.6b where an evolution of maximum columnar energy  $\max(e_t)$  is shown. As shown, the maximum energy increases on the average 1.5 times, though an individual growth can reach the value 3. Note that in the developing extreme (freak) waves, an amplification of maximum energy can reach a value as high as 10. Thus, the level of energy is not an indicator of breaking. In paper by Banner and Tian (1998), it was suggested that the onset of breaking can be recognized by the rate of growth of the energy averaged over wavelength  $E_m$ .

$$\beta_E = \frac{1}{\omega E_m} \frac{dE_m}{dt} \quad (8.3.8)$$

The behavior of this parameter was investigated with a numerical model of Dold (1992) based on the surface integral method. In the initial condition, one harmonic carrying wave and two small-amplitude disturbances were assigned; an evolution of energy of carrying wave was investigated. It was assumed that upon development of the modulation instability, the approaching of breaking can be recognized by parameter  $\beta_E$  exceeding some critical value. In fact, even for such highly idealized situation, Song and Banner (2002) found that ‘parameter  $\beta_E$  did not provide a robust indicator for resolving the onset of breaking.’ This is why they introduced an alternative parameter based on the maximum value of wave energy  $(E_m)_{\max}$

$$\delta = \frac{1}{\omega(E_m)_{\max}} \frac{d(E_m)_{\max}}{dt} \quad (8.3.9)$$

In fact, replacing  $\beta_E$  by  $(\beta_E)_{\max}$  cancels the role of the modulation instability, since the growth of maximum columnar energy can occur without the growth of overall wave energy (see Fig. 8.6a, b). Finally, authors came to the conclusion that the ‘calculations indicate that breaking or recurrence may be determined by a common threshold  $\delta_{\text{th}}$  in the range  $(1.3 \times 10^{-3}, 1.5 \times 10^{-3})$  for the non-dimensional growth rate.’

A practical role of the criterion similar to (8.3.9) is doubtful. Firstly, the authors’ primary idea was an explanation of the breaking on the basis of modulation instability when one wave grows at the expense of the others. Criterion  $\delta$  cannot describe such process, because it is based on the maximum energy of waves, which depends essentially on a shape of wave and can change without modification of the selected wave energy. This effect is clearly demonstrated in Fig. 8.5: The average wave energy slightly decreases, while the peak energy increases nearly three times. Secondly, this criterion is offered for the idealized situation of single harmonic wave with two superimposed disturbances, and it is unclear how to apply it for

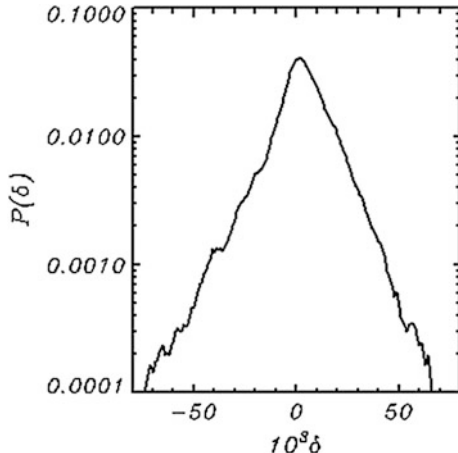
parameterization of breaking in the spectral models or in direct modeling of multimode wave field.

For investigation of breaking in idealized conditions, a series of experiments similar to those performed by SB were repeated with ChSh model. The carrying wave mode with amplitude  $a_p$  was placed at wave number  $k = k_p$ , where  $k_p$  was changing in a range of 3–10, while steepness  $k_p a_p$  was changing in a range of 0.085–0.185. A total of 160 long-term simulations were done up to the point of breaking or up to the non-dimensional time  $t = 500$  which corresponds to 138–252 periods of carrying waves. The disturbances with amplitudes  $0.1a_p$  were assigned at wave numbers  $k_p + 1$  and  $k_p - 1$ , which, for the given resolution, provided fast enough growth of disturbances (see Chalikov 2007). The number of modes was  $M = 2000$ , while the number of grid points was  $N = 8000$ ; i.e., a sufficient accuracy of approximation was maintained. This series of the numerical experiments was initially intended for investigation of breaking, but then, we focused on the simulation of breaking in spectral environments. A criterion for terminating a run was defined by Eq. (8.3.1).

The evolution of  $\delta$  (Eq. 8.3.9) prior to the wave breaking for such idealized wave field is shown in 8.6c. Gray curves correspond to the evolution of  $\delta$  in individual runs, while solid line shows an averaged evolution, and dashed lines indicate variance. Time  $t$  is normalized by a period of carrying waves. As shown, for the less-steep waves, DP model performs reasonably well and behavior of  $\delta$  in idealized conditions reminds somewhat a quasiperiodic regime obtained by SB. The evolution of  $\delta$ , however, is less regular than it was demonstrated in SB, since the simulated wave field has been modified due to appearance of new modes. The current calculation shows that criterion  $\delta$  can exceed the recommended values  $\delta_{\text{th}} = (0.7 - 2.8) \times 10^{-3}$  at least for one decimal order. It means that an exact model based on conformal transformation is much more stable, so the recurrence occurs upon reaching large values of  $\delta$ . Note that breaking can also occur at very small values of  $\delta$ .

The data on  $\delta$  obtained in a similar simulation of breaking in the spectral environment are shown in Fig. 8.6d. As shown, the data on evolution of  $\delta$  exhibit a great scatter. It is not surprising, since  $\delta$  is an overall characteristic, and for a complicated wave surface, its value is very sensitive to the definition of wavelength  $L_m$ . Besides, the height of a sharp-crested wave approaching the breaking point in the spectral environment can change very quickly; thus, the criterion (8.3.9) demonstrates irregular fluctuations. The parameter  $\delta$  can obtain both negative and positive values exceeding many times the above-mentioned limit  $\delta_{\text{th}}$ . These results suggest that even a modified formulation of the breaking criterion (8.3.9) cannot describe a variety of the situations. Note that the data in 8.6d describe the period just prior to breaking. However, large values of criterion  $\delta$  occur very often when growth of wave energy is reversible. The probability distribution of  $\delta$  obtained for all the runs over the entire period of integration is shown in Fig. 8.7. As shown, the probability of both negative and positive values of  $\delta$  is approximately the same, its absolute value greatly exceeding  $\delta_{\text{th}}$ . Note that a part of breaking cases shown in Fig. 8.7 is less than 0.001 %.

**Fig. 8.7** Probability distribution for criterion  $\delta$  (Eq. 8.3.9). Chalikov and Babanin 2012 © American Meteorological Society. Used with permission



Thus, we come to the conclusion that criterion  $\delta$  does not signify the breaking; the waves are much more stable than those reproduced by the model used in the papers cited. Hence, an investigation of a role of the energy input to waves, as well as the vertical gradient of mean velocity, performed by SB on the basis of criterion (8.3.8), was premature. Actually, the Dold's model is an excellent tool for investigation of wave dynamics when steepness is not too large; however, it is inapplicable for investigation of extreme conditions of breaking. Hence, it is most likely that the papers cited above discussed not the breaking instability, but the limits of the numerical stability of the model used. The model ChSh used in our calculation is able to precisely reproduce the dynamics of extremely steep waves (see long-term simulations of Stokes waves in Chalikov and Sheinin 2005; Chalikov 2005). The criterion (8.3.1) is exact, since up to the moment of the ‘vertical wall’ appearance an accuracy of solution is very high.

Some investigators (see, e.g., Zakharov et al. 2006) suggested that the breaking occurs due to reaching the limit form of Stokes waves  $H_{lc}/2L_m = 0.43$ , where  $L_m$  is the length of wave. An evolution of the largest trough-to-crest wave height  $H_{lc}$  normalized by the significant wave height is shown in Fig. 8.8a. Growth of the averaged height occurs only in the last stage, and it has the order of  $0.2 H_s$ . As shown, the breaking occurs in a wide range of  $H_{lc}/H_s$  between the values 1.0 and 2.5, so the trough-to-crest height of wave cannot serve as indicator for the wave breaking, though an increase of  $H_{lc}/H_s$  is always followed by growth of a breaking probability (Chalikov 2007). In multimode wave field, length  $L$  cannot be defined straightly, since the largest peak wave is distorted by smaller waves. An evolution of  $L_m$ , normalized by the spectral peak wavelength  $L_p = 2\pi/k_p$  is shown in Fig. 8.8b, which proves that on the average, wavelength changes insignificantly with a weak tendency to decrease by 10 %. This effect was confirmed by SB. However, the scatter of these data is very large. The data on the overall steepness  $S_{lc} = H_{lc}/2L_m$  of the largest wave prior to breaking is given in Fig. 8.8c. It is seen that just several waves break at high overall steepness  $S_{lc} = 0.4$ , but the breaking also occurs at such

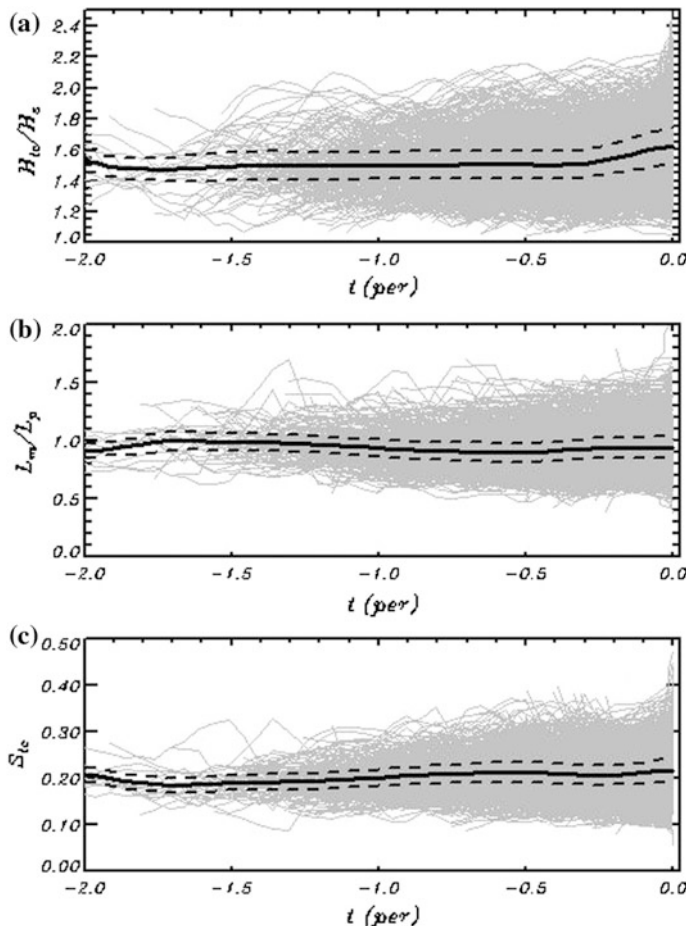
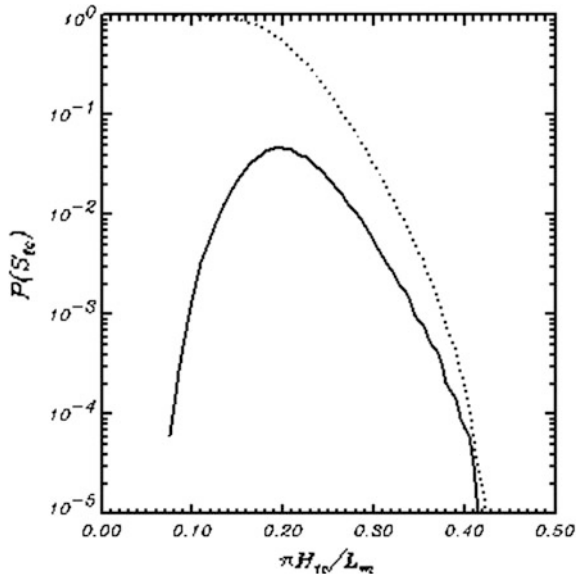


**Fig. 8.8** **a** Evolution of trough-to-crest wave height  $H_{lc}$  normalized by  $H_s$  prior breaking as function of time  $t$ ; **b** Evolution of ratio of actual wavelength  $L_m$  to spectral wavelength of peak wave  $L_p$ ; **c** Evolution of overall steepness  $S_{lc}$ . The styles of curves are the same as in Fig. 8.6. Chalikov and Babanin 2012 © American Meteorological Society. Used with permission

small steepness as  $S_{lc} = 0.1$ . The averaged steepness of breaking waves is not too small, and it is equal to 0.2, but it is twice smaller than the critical steepness for Stokes waves. The gray curves, corresponding to the individual cases are concentrated very close to the averaged curve, while very small dispersion of the results (shown by dotted curves) proves that scatter of wave steepness prior to breaking is very small. So, the overall steepness of waves is also not a criterion of wave breaking. The probability distribution of overall steepness shown in Fig. 8.9 proves that waves in the spectral environment break well in advance before they become very steep. It can be concluded that in multimode wave field, the parameter of overall steepness  $S_{lc}$  is not a reliable criterion for recognizing of breaking.

**Fig. 8.9** Probability distribution for criterion overall steepness  $S_M$ .  
 Chalikov and Babanin 2012  
 © American Meteorological Society. Used with permission



The important characteristics of wave shape closely connected with wave breaking are wave asymmetry  $A_s$  defined as (see Fig. 8.1) (Tulin and Landrini 2001; Cailliez 2002; Young and Babanin 2006; Babanin et al. 2007, 2010)

$$A_s = \frac{X_{0d} - X_m}{X_m - X_{0u}} \quad (8.3.10)$$

The negative asymmetry  $A_s < 0$  corresponds to the wave tilted forward in the direction of propagation. In Fig. 8.1, the wave has a large positive asymmetry due to the secondary peak at a downwind wave slope. This example proves that an estimation of overall wave characteristics is often complicated due to some uncertainty. An evolution of asymmetry prior to breaking is shown in Fig. 8.10a for small number of modes. These calculations prove that in the idealized calculations with a wave field, the waves have a negative asymmetry. Similar analysis of the data obtained in the spectral environment is given in Fig. 8.10b. As shown, the asymmetry has a very large scatter varying from  $-0.9$  waves to the values exceeding 1. On the average, the waves have a slight negative asymmetry, but just before the breaking the asymmetry changes the sign and becomes positive. This effect can be explained by a sharp modification of wave shape before breaking (similar to that shown in Fig. 8.1).

Kjeldsen and Myrhaug (1980) found that the front trough of the incipient breaker is shallower as compared with the rear trough, which is a persistent feature of the wave breaking observed in laboratory (Babanin et al. 2010). This was proved by the calculations with the idealized wave field, but the data obtained in the spectral environment rather contradict this conclusion; i.e., the front trough  $D_f$  of the

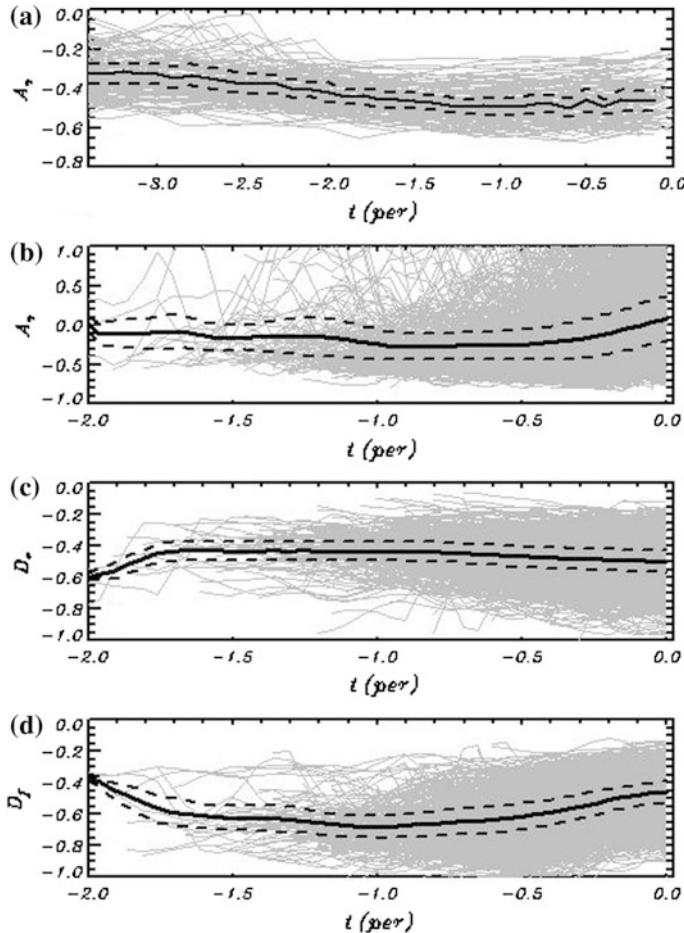


**Fig. 8.10** **a** The evolution of asymmetry  $A_s$  (Eq. 8.3.10); prior of breaking as function of time  $t$ , expressed in peak wave periods; **b** the same characteristics obtained in the calculation of spectral environment; **c** evolution of upwind rear depth  $D_u$  normalized by  $H_s$ ; **d** evolution of front trough depth  $D_f$  normalized by  $H_s$ . The styles of curves are the same as in Fig. 8.6. Chalikov and Babanin 2012 © American Meteorological Society. Used with permission.

breaking waves (Fig. 8.10b) is on the average deeper than the rear trough  $D_r$  (Fig. 8.10c). Note that both of the characteristics have a large scatter.

The theoretical analysis of breaking is usually based on presentation of wave field as a superposition of harmonic waves. Such restriction leads to the assumption that one mode grows taking the energy from other modes. If the number of modes is small, such transformation occurs within the length of a wave group. For the case of wind sea spectrum, such interval does not exist, so we should suppose that the growth of energy leading to breaking occurs everywhere in the area represented by wave spectrum. In reality, just few waves grow and break in physical space, this

process being represented in wave spectrum in a highly distorted form. A shape of wave approaching the point of breaking is very far off the harmonic function. It is illustrated in Fig. 8.11 where the ratio of wave height above a mean level to the rear trough (Fig. 8.11a) and to the front trough (Fig. 8.11b) is represented. As shown,

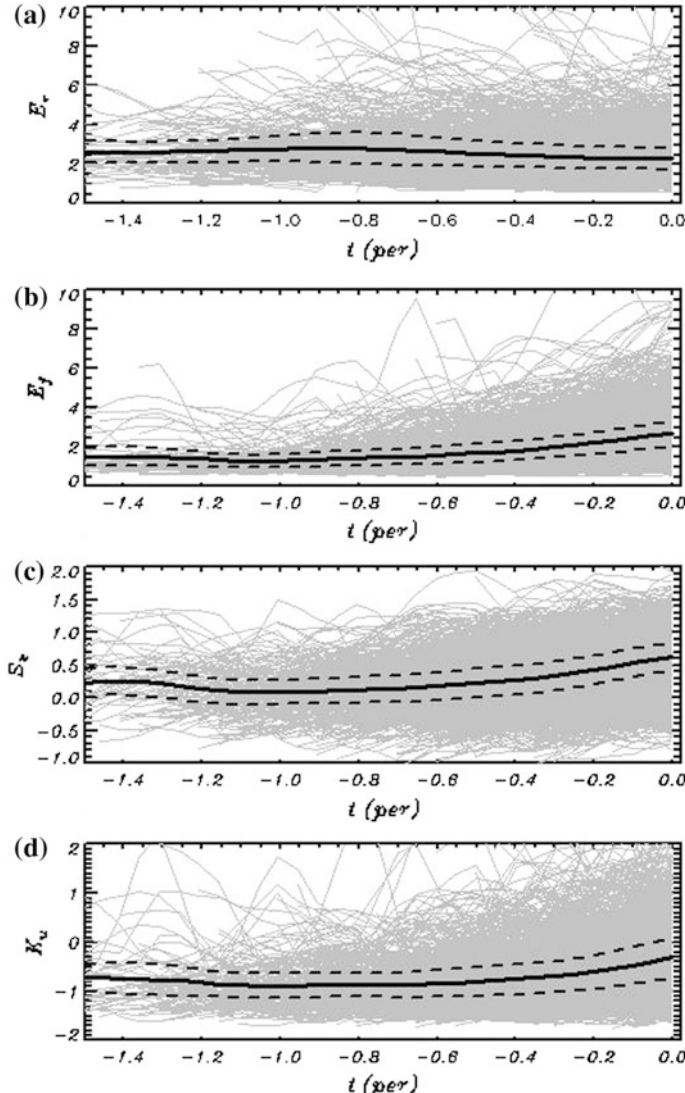


**Fig. 8.11** The evolution of geometrical characteristics prior breaking; **a** the ratio of wave height above mean level to depth of rear trough  $D_r$ ; **b** the ratio of wave height above mean level to depth of rear trough  $D_f$ ; **c** skewness  $S_k$  of waves; **d** the kurtosis  $K_u$  of waves. The styles of curves are the same as in Fig. 8.6. Chalikov and Babanin 2012 © American Meteorological Society. Used with permission

the wave height is twice as large as compared with the depth of troughs, while the depth of the front trough is on the average slightly deeper than the depth of the rear trough (see also Babanin et al. 2007, 2010). This effect is illustrated by Fig. 8.11c and d where the skewness  $S_k$  and kurtosis  $K_u$  calculated over the wavelength  $L_m$  are represented. As shown, the skewness of waves is on the average positive; hence, the crests are considerably higher than the depth of troughs. The kurtosis is on the average negative, which means that the areas of positive elevation are less extended than those of the negative elevation.

In fact, we came to the conclusion that not a single characteristic considered provides a reliable criterion for wave breaking in the spectral environment. Note also the scatter with respect to the mean. All the properties considered can be rather referred to the ‘overall’ characteristic whose definition is quite sensitive to real shapes of waves and strongly depends on the spectral resolution and shape of spectrum. Neither of these characteristics (including non-dimensional rate of wave height growth (Eq. 8.3.8) cannot be considered as a reliable criterion of the breaking onset. It is rather a local slope near the crest, as indicated below.

Considering Figs. 8.6a, b, and d, 8.8a–c, and 8.10a–c, we can conclude that opposite to the idealized conditions (see 8.6c), simple geometrical characteristics are very unstable. The shape of peak waves can be distorted by smaller waves; therefore, the values of wave height and wavelength as well as the overall steepness  $S_{tc}$  and asymmetry  $A_s$  can depend on small details. It explains the large scatter of these characteristics.

Now, we consider an evolution of the *local* characteristics of wave approaching the point of breaking, i.e., maximum  $s_{\max}$  and minimum  $s_{\min}$  slopes in the interval  $L_m = X_{td} - X_{tu}$  (Fig. 8.12a, b). As shown, the positive steepness (i.e., the steepness at rear slope) changes insignificantly, while the steepness at front slope can reach quite large negative values. Even a clearer is the characteristic of wave peak sharpness defined by a maximum value of the second derivative (Fig. 8.12c). Note that the value of the second derivative is multiplied by  $H_s$  for making this characteristic independent on the model parameters. In the numerical model, the value of the second derivative could reach several thousands, which forced us to modify the time step. However, all the differential characteristics reveal a large scatter; i.e., the breaking could occur both at large and small steepness and at large and small negative peak sharpness. The attempts to find a threshold value for the negative steepness were unsuccessful, since the process can be reversible up to very large values of  $s_{\min}$ , and only appearance of a non-unique surface (in fact, the onset of breaking itself) can be for sure accepted as a criterion of breaking. The same conclusion can be made for kinematic characteristics of surface: the maximum and minimum values of the surface orbital velocity components (Fig. 8.13a–d) and the components of acceleration (individual derivatives of velocity)  $dU/dt$  and  $dW/dt$  (Fig. 8.14). Deceleration of the horizontal velocity (Fig. 8.14b) and acceleration of the negative vertical velocity (8.14c) are pronounced most clearly. Again, the scatter of these characteristics is very large.

Finally, we come to the conclusion that all the characteristics considered cannot serve as a criterion of the breaking development. Some of them exhibit a tendency

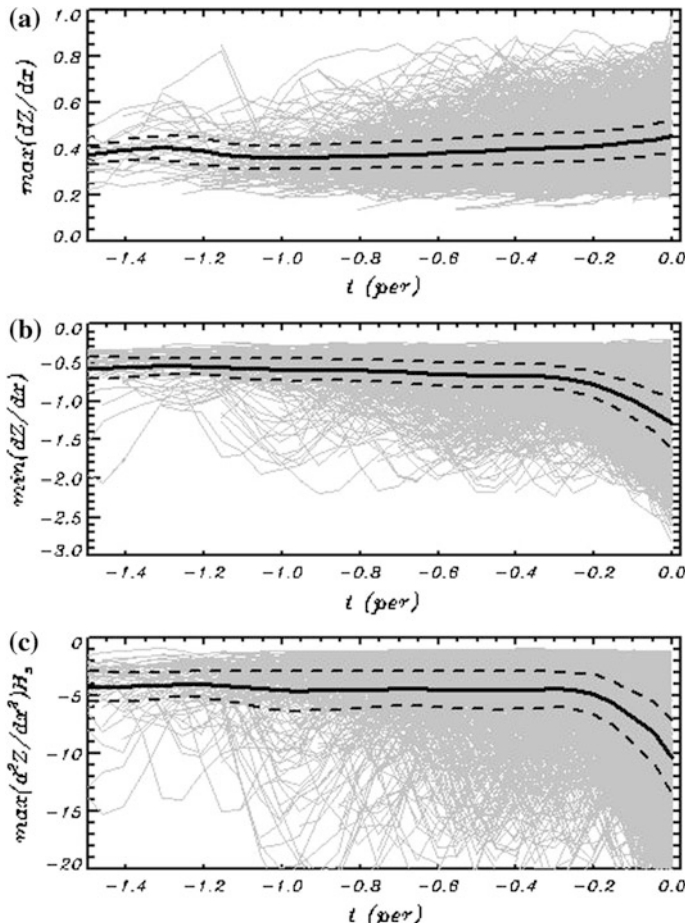


**Fig. 8.12** Differential characteristics of surface: **a** The evolution of maximum value of steepness  $\max(\partial z / \partial x)$ ; **b** the evolution of minimum value of steepness  $\min(\partial z / \partial x)$ ; **c** the evolution of minimum value of curvature  $\min(\partial^2 z / \partial x^2)H_s$  taken with opposite sign. The styles of curves are the same as in Fig. 8.6. Chalikov and Babanin 2012 © American Meteorological Society. Used with permission

for instability, but these features are developing during a very short period preceding the breaking, so they correspond to the process of breaking itself, rather than to the prescribing of an imminent breaking.

Such a detailed consideration of the breaking process allows us to formulate the question: ‘How is it possible to use a predictor for the breaking in the spectral environment?’ Definitely, the instability of interface leading to the breaking is an important problem of the fluid mechanics. This process is strongly nonlinear; therefore, the theory of breaking is expected to be highly complicated. The onset of

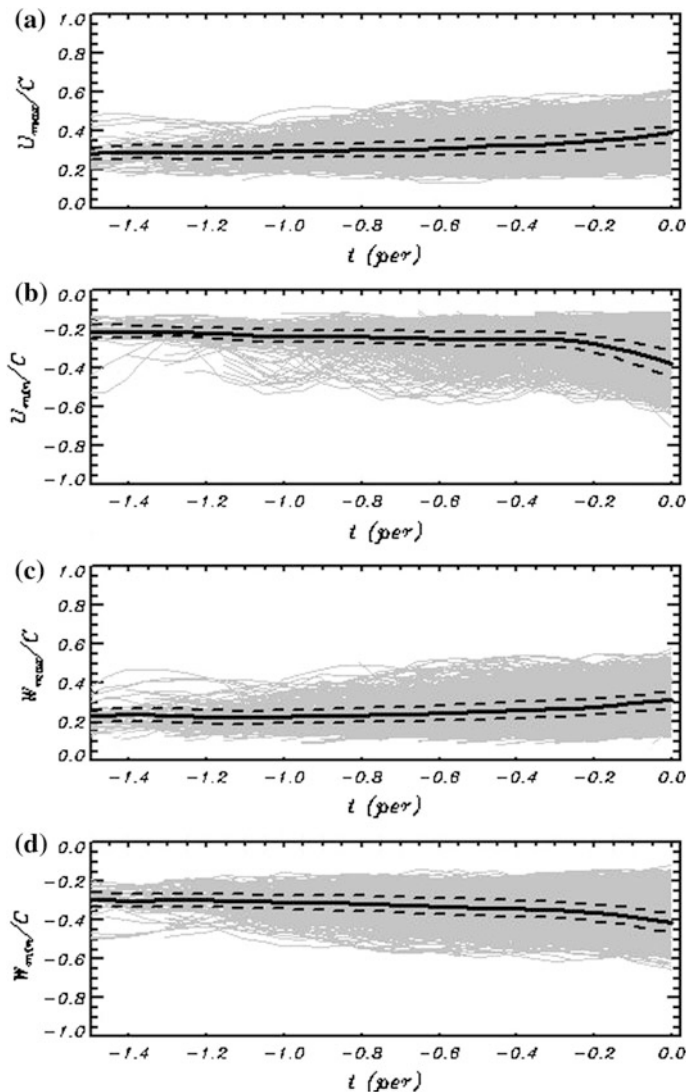


**Fig. 8.13** The evolution of surface kinematic characteristics: **a** the evolution of maximum value of horizontal velocity  $U_{\max}/c_p$ ; **b** the evolution of minimum value of horizontal velocity  $U_{\min}/c_p$ ; **c** the evolution of maximum value of vertical velocity  $W_{\max}/c_p$ ; **d** the evolution of minimum value of vertical velocity  $W_{\min}/c_p$ . All velocities are normalized by peak phase velocity  $c_p$ . The styles of curves are the same as in Fig. 8.6. Chalikov, Babanin 2012 © American Meteorological Society. Used with permission

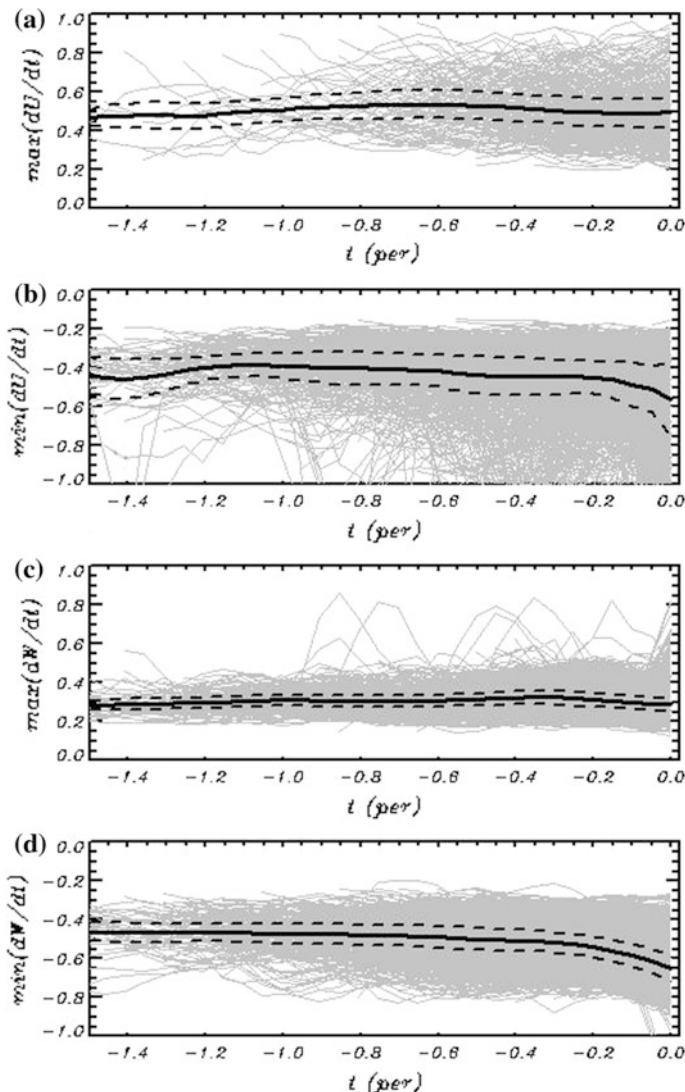


**Fig. 8.14** The evolution of surface dynamic characteristics (accelerations normalized by acceleration of gravity): **a** the evolution of maximum value of horizontal particle acceleration  $\max(dU/dt)g^{-1}$ ; **b** the evolution of minimum value of horizontal particle acceleration  $\min(dU/dt)g^{-1}$ ; **c** the evolution of maximum value of vertical particle acceleration. The styles of curves are the same as in Fig. 8.6. Chalikov and Babanin 2012 © American Meteorological Society. Used with permission

breaking is similar to the onset of free convection in liquid at unstable stratification. The criterion of convection instability is just appearance of unstable stratification in some part of liquid. It can result from different processes producing redistribution of density. Similarly, we can define as criterion of instability the appearance of a non-unique part of surface, when some volume of fluid becomes non-supported by pressure from the surrounding liquid and starts to move independently under the action of inertia and gravitation forces. The breaking can start under the influence of many factors producing the non-uniqueness of surface. Probably, the main of them is an appearance of the horizontal velocity exceeding the velocity of the shape propagation. It was proved by special numerical experiments with very high time and space resolution, performed by Chalikov and Sheinin (2005). It was shown that the horizontal velocity in the peak of wave before breaking always exceeded the phase velocity.

The breaking is a dissipative process leading to the loss of the kinetic and potential wave energy and to transition of energy to the horizontal flow and turbulence, so this process should be taken into account in different types of models designed for simulation of wave evolution. The most important models of such type are wave forecasting models [e.g., WAVEWATCH model (Tolman 2008)]. Evidently, no criterion of breaking can be used in such models, because they operate with wave spectrum; hence, the information on real wave surface is absent. In such models, the dissipation process is presented in a distorted form. Since the breaking occurs in the relatively narrow space intervals separated by broad parts with no breaking, the spectrum of the dissipation rate is distributed mostly in a high-frequency part of the spectrum, while in reality, the breaking reduces the height of the largest wave represented in spectral peak. The cause of this contradiction is that in the spectral model, the wave field is assumed to be a superposition of linear modes, while the breaking (and growth of freak waves) occurs due to transformation of a specific wave shape; i.e., the wave before breaking, as a rule, becomes sharp-crested. Therefore, the breaking reduces the height and energy of a nonlinear mode.

Appearance of a non-single-value surface in direct simulation is always followed by the numerical instability and termination of run. Since the termination can happen at a relatively low integral frequency, the long-term simulations, especially with the input energy from wind, are impossible. This is why an algorithm of the breaking parameterization based on the local elimination of breaking was developed. The algorithm (the basic concept of such algorithms is very close to that used for parameterization of free convection in atmospheric models) is designed to prevent the breaking instability by the highly selective high-frequency smoothing of the interface profile. Many schemes to parameterize such phenomenon were tested, the most efficient of them being based on a simple diffusion-type algorithm:

$$\eta_\tau = E_\eta + J^{-1} \frac{\partial}{\partial \xi} B \frac{\partial \eta}{\partial \xi}, \quad (8.3.11)$$

$$\varphi_\tau = F_\varphi + J^{-1} \frac{\partial}{\partial \xi} B \frac{\partial \varphi}{\partial \xi}, \quad (8.3.12)$$

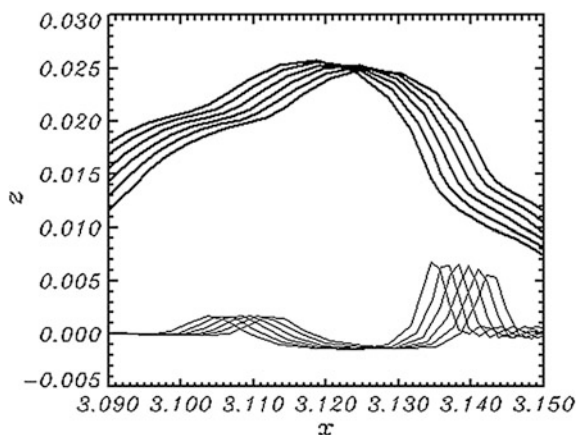
where  $E$  and  $F_\Phi$  are the right-hand sides of Eqs. (2.2.34) and (2.2.35), while the coefficient of diffusion  $B$  depends on the second derivative of the interface:

$$B = \begin{cases} C_b \left( \Delta \xi \frac{\partial^2 z}{\partial \xi^2} \right)^2 & \frac{\partial^2 z}{\partial \xi^2} > s \\ 0 & \frac{\partial^2 z}{\partial \xi^2} \leq s \end{cases}, \quad (8.3.13)$$

where the coefficient  $C_b$  is of the order of 0.1, while the critical value of the second derivative  $s$  is of the order of 300. The algorithm of the ‘tail dissipation’ (8.3.11)–(8.3.13) does not change the volume but reduces the local energy and momentum of waves. It is assumed that some portion of the energy (and momentum) loss is transferred to the horizontal flow, while another portion is transferred to turbulence (such transformations can be considered separately, see Chalikov and Belevich 1993). Note that the intensity of breaking in the presence of input energy does not depend much on parameters  $C_b$  and  $s$ : The waves can become on the average a little more sharp-crested, but the integral energy lost in the process of breaking finally remains approximately the same. An example of the local evolution of the surface affected by breaking is shown in Fig. 8.15.

Solid line corresponds to wave surface, while thin line shows a change of wave surface  $\Delta z_b$  due to the breaking described by the algorithm (8.3.11)–(8.3.13). As shown, the height of wave in the vicinity of crest decreases ( $\Delta z_b < 0$ ), since water is transferred to the front slope. A smaller volume of water falls also to the rear wave slope. The algorithm (8.3.11)–(8.3.13) is currently used in a long-term simulation of the wave field evolution. It effectively prevents development of the numerical instability arising as the surface gets closer to a non-single value profile and describes well (at least qualitatively) dissipation of wave energy. Such scheme does

**Fig. 8.15** Local evolution of surface in a course of breaking simulated by algorithm (8.3.11)–(8.3.13). Solid curve represents the top of breaking wave, and thin curves correspond to change of surface  $100\Delta z_b$  at consequent time steps with interval  $\Delta t = 0.01$ . Chalikov and Babanin 2012 © American Meteorological Society. Used with permission



not influence solution in the absence of breaking. We do not consider this algorithm as a final solution of the problem, since it cannot prevent collapse in cases of a very high initial steepness or high energy. However, for normal steepness of sea waves, as well as for the cases of a typical growth rate of the local energy, it works well. After implementation of the algorithm (8.3.11)–(8.3.13) with  $C_b = 0.1$  and  $s = 300$  in the ChSh model, the termination of run happened quite seldom. The results of a long-term simulation of the wave field evolution were demonstrated in Chalikov and Rainchik (2010) on the basis of the air/water coupled model. It was shown that the wave breaking is a highly intermittent process correlated with steepness. Of course, the rate of dissipation and the intermittence index depend on the stage of wave development and the magnitude of energy input.

The spectrum of breaking can be easily determined by a special post-processing of the results based on recorded fields of surface elevations and surface potential and different terms of the dynamic equations, including all dissipation terms. This algorithm has been generalized for 2-D wave field and implemented in the exact 3-D wave model constructed on the same basic principles as the 2-D model used in the current work. For investigation of energy balance and spectral decomposition of the dissipation term, a special series of numerical experiments for the inverse wave age  $U/c_p = 1, 2, 3, 4$  were performed. Each run was repeated 100 times for different random sets of phases. Unlike in the calculations performed for investigation of breaking, the algorithm (8.3.11)–(8.3.13) in this series was activated.

The spectral energy balance equations can be represented in the following form

$$\frac{ds_k}{dt} = \begin{matrix} 1 & \left(\frac{ds_k}{dt}\right)_{NL} \\ 2 & + \left(\frac{ds_k}{dt}\right)_{INP} \\ 3 & + \left(\frac{ds_k}{dt}\right)_{BR} \\ 4 & + \left(\frac{ds_k}{dt}\right)_{TL} \\ 5 & + \left(\frac{ds_k}{dt}\right)_{NU} \\ 6 & \end{matrix} \quad (8.3.14)$$

where term 1 corresponds to the rate of total change of the spectral energy  $S_k$  equal to the sum of the potential and kinetic energy in a wave number interval  $\Delta k = 1$ ; term 2 is a rate of nonlinear transformations (due to the nonlinear terms in the equations); term 3 is an increase of energy due to the wind input; term 4 is a change of spectrum due to the wave breaking; term 5 is the tail dissipation due to a flux of energy to the subgrid waves; and term 6 is a change of energy due to the errors of the numerical scheme. The last term 6 originates mostly from approximation in time, because errors of space approximation are practically absent. Since the fourth-order Runge–Kutta scheme for time stepping was used, error 6 is negligible. The change of spectrum due to the nonlinear interaction can be calculated on the time substep based on Eqs. (2.2.34) and (2.2.35) before calculating the input and dissipation. The potential energy and kinetic energy fluctuate, but their sum conserves with high accuracy, the calculation of term 2 being exact. The input energy (term 3) should be calculated with use of  $\beta$ -function (Chalikov and Rainchik 2010), but in the current work, this effect was taken into account by including an additional term in the right-hand side of Eqs. (2.2.34) and (2.2.35)

$$\begin{aligned}\frac{\partial h_k}{\partial \tau} &= \dots + h_k(\Delta\tau)^{-1}\rho, \\ \frac{\partial f_k}{\partial \tau} &= \dots + f_k(\Delta\tau)^{-1}\rho,\end{aligned}\quad (8.3.15)$$

where the symbol ... denotes the rest of the terms in Eqs. (2.2.34) and (2.2.35);  $h_k$  and  $f_k$  are the Fourier coefficients for elevation and surface potential;  $\Delta\tau$  is time step;  $\rho$  is defined by a ratio of the initial energy  $E_0$  (at  $\tau = 0$ ); and the current total energy  $E$  (Eq. 8.3.6) is as follows:

$$\rho = (E_0/E)^{1/2} - 1, \quad (8.3.16)$$

where a typical value of  $\rho$  is  $10^{-10}$ . Since  $\rho$  is very small, the substep (8.3.15) was performed using an explicit scheme at the time substeps preceding the calculation of tail and breaking dissipation. The scheme (8.3.15) was introduced for maintaining the total energy without modification of the kinetic and potential energy spectra. For the periods considered in the current work, the effect of the numerical dissipation prevented by algorithm (8.3.15) was very small. Each of the terms in Eq. (8.3.14) was calculated using a split numerical scheme by changing the energy spectrum at every step.

Separation of numerical dissipation on the basis of the scheme (8.3.14) was done for investigation of dissipation caused by the breaking and tail terms 4 and 5, respectively. Evidently, the rate of total (i.e., integral over spectrum) dissipation should depend on the total energy of wave field  $E$  (Eq. 8.3.6) and on another parameter characterizing the integral steepness of surface. We found that the most important characteristic responsible for breaking is the differential steepness  $S_t$  defined by the expression

$$S_t = \left( \int_0^M k^2 S(k) dk \right)^{1/2}. \quad (8.3.17)$$

We call this steepness ‘differential’ opposite to ‘bulk’ steepness (sometimes called ‘global’ steepness) of the type of  $k_p H_s$  ( $k_p$  is peak wave number, and  $H_s$  is significant wave height). The bulk steepness does take into account the high-frequency modes with low weight, and it cannot serve as a governing parameter of dissipation. If the spectrum at high frequencies has an asymptotic behavior  $S \sim \omega^{-5}$ , the integral (Eq. 8.3.17) diverges. This fact indicates strong dependence of the differential steepness on a high-frequency region. The characteristic (8.3.17) cannot be used as an absolute measure of steepness, but it is convenient for the comparison of the results for the same spectral resolution. The dependence of integral dissipation  $D_u$

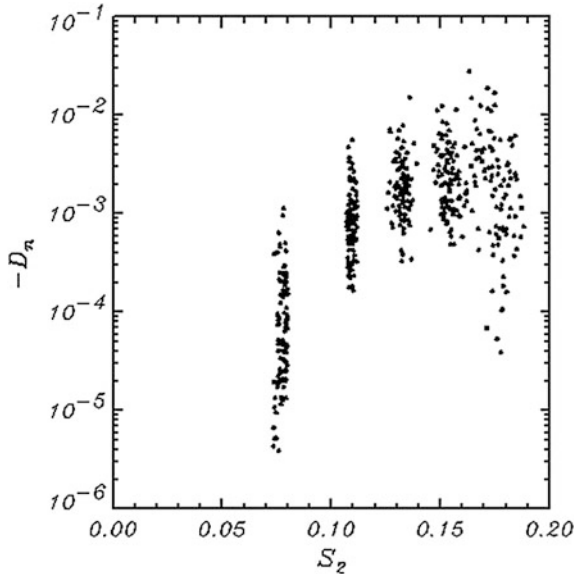


**Fig. 8.16** Dependence of the integral dissipation rate (terms 4 and 5 in Eq. 8.3.14) on overall wave steepness  $S_{13}$  ( $0.14 < S_2 < 0.16$ ), 4 ( $0.16 < S_2 < 0.18$ ), 5 ( $0.18 < S_2$ ) (Eq. 8.3.17). Chalikov and Babanin 2012 © American Meteorological Society. Used with permission

$$D_u = -\frac{T_p}{E} \int_0^M \left( \left( \frac{dS_k}{d\tau} \right)_{TL} + \left( \frac{dS_k}{d\tau} \right)_{TL} \right) dk \quad (8.3.18)$$

on parameters  $S_t$  is represented in Fig. 8.16, showing that the differential steepness in the presence of the energy input cannot exceed the value  $S_1 = 0.19$ . The tendency for decrease of the dissipation rate in the range  $0.16 < S_2 < 0.19$  results from the normalizing factors  $T_p/E$  in (8.3.18).

The spectra of breaking dissipation (terms 4) normalized by  $E^{3/2}\omega_p$  for five ranges of the non-dimensional differential steepness  $S_t$  are shown in Fig. 8.17. As shown, the normalized by  $E^{3/2}$  dissipation spectrum increases with growth of steepness. The maximum of dissipation falls on the peak of wave spectrum, but the dissipation spectrum is broad due to the nonlinear nature of this process. Note that unlike all the previous schemes, Fig. 8.17 represents the spectrum dissipation obtained in direct simulation of multi-mode wave field on the basis of full equations.

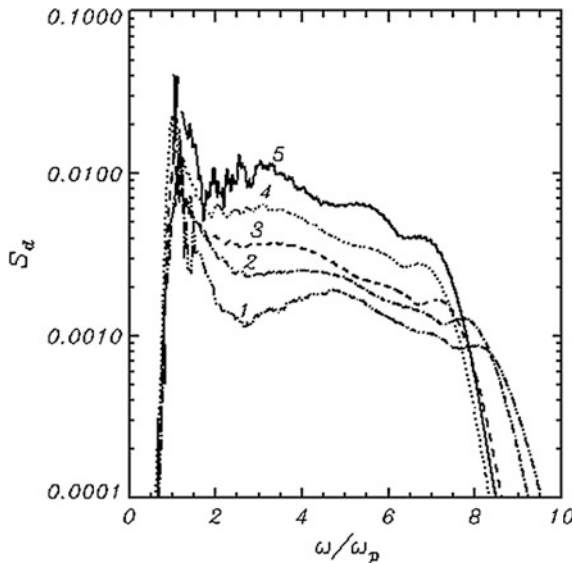


**Fig. 8.17** Spectrum of dissipation rate  $D_n$ : 1 ( $S_2 < 0.12$ ); 2 – ( $0.12 < S_2 < 0.14$ ); 3 ( $0.14 < S_2 < 0.16$ ), 4 ( $0.16 < S_2 < 0.18$ ), 5 ( $0.18 < S_2$ ), as function of  $\omega/\omega_p$ . Chalikov and Babanin 2012 © American Meteorological Society. Used with permission

## 8.4 Nonlinear Sharpening of Waves as a Possible Cause of Breaking

The main concept of this book suggests that the linear (sinusoidal) waves are not the physical objects. If produced, for example, by means of a mechanical wave maker, they turn themselves into Stokes waves before propagating, and this is the only nonlinear property and behavior among many others. One of the most evident manifestations of the nonlinearity of surface waves is the wave-breaking phenomenon (e.g., Babanin 2011). This process consists of several stages. At the first stage, a wave becomes sharp and tends to incline forward, so that the surface, in some places, can become a non-single value. Such transformation can be well described using exact models such as the conformal model or any version of the boundary integral model (e.g., the Dold and Peregrine (1984) model). At the second stage, the wave breaking itself takes place. This phenomenon is characterized by fast distortion of the wave shape; i.e., some volume of water moves forward and quickly loses its single-phase nature, becoming a mixture of water and air (whitecaps). This stage is characterized by formation of sprays in the air and bubbles in the water. Within the frames of the models mentioned above, the continuity of ‘jet’ can be artificially supported by using different smoothing procedures, while in general, simulation of this process should be based on some sort of the Lagrangian approach for two-phase liquid (see, e.g., Iafrati 2011). At the last stage

of wave breaking, the local smoothing of surface occurs. It is followed by the local decrease of the potential and kinetic energy. A part of the momentum is transferred to the waves and surface currents; the energy is transferred to turbulence (in the water and air), currents, and adjacent waves or even back to wind (Chalikov and Belevich 1992; Iafrati et al. 2013). Since the energy is partially distributed between the wave modes, the breaking initiates some sort of a fast nonlinear wave–wave interaction process [see discussions of this topic in Tulin and Waseda (1999); Donelan et al. (2012)]. Since such transformation does not cover all the waves in the train, the spectral image of the process becomes distorted.

A non-single-value surface in direct (phase-resolving) simulations is usually followed by the numerical instability and termination of run. Since it can happen at a relatively low mean steepness, the long-term simulations, especially those with the input of energy from wind, are impossible. This is why for our simulations an algorithm of the wave-breaking parameterization based on the local elimination of breaking was developed (Chalikov and Sheinin 2005). An algorithm is designed to prevent the breaking instability through a highly selective smoothing of the interface in physical space.

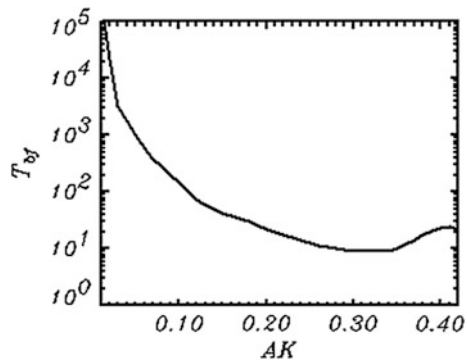
In this section, our attention is concentrated on the first stage of wave breaking. In other words, we are trying to understand the way the mechanism of the breaking onset works. This process is definitely connected with the local concentration of wave energy due to the fast nonlinear wave–wave interactions.

It is generally assumed that a relatively fast (compared with the Hasselmann resonance theory) transformation of the ocean wave spectrum is described by the so-called *modulation instability theory* originally known as ‘*Benjamin-Feir (B-F) instability theory*’ (Benjamin and Feir 1967). The concept of this theory is quite transparent; i.e., a one-dimensional nonlinear wave train in the presence of certain disturbances can enforce additional modes in the spectral vicinity of the main mode. Roughly speaking, the B-F theory explains redistribution of the wave energy in the frequency (wave number) space up to the final homogenization of an initially discrete spectrum. The original B-F results and numerical investigations of the B-F instability (Chalikov 2007) show that the timescale of a new mode growth for a typical ocean wave steepness exceeds hundreds or even thousands of the carrier wave period. The growth of the new mode amplitude  $a$  occurs exponentially

$$a(t) \sim \exp\left(\frac{2\pi t}{T_{bf}}\right), \quad (8.4.1)$$

where  $T_{bf}$  is the timescale which depends on the two parameters: steepness of the carrier mode  $AK$  ( $A$  in the amplitude of mode and  $K$  is its wave number) and quantity  $\delta = (k - K)/K$ , which is non-dimensional ‘distance’ in wave number space between the carrier wave and a new mode with wave number  $k$ . The dependence  $T_a(AK, \delta)$  was studied in the original work by Benjamin and Feir (1967); it was investigated in detail by using the numerical model based on conformal transformation of the coordinates (Chalikov 2007, Chap. 6). The numerical results confirmed the analytical results and considerably extended them. Values of

**Fig. 8.18** Dependence of the Benjamin–Feir timescale  $T_{bf}$  on steepness  $AK$  of the carrier wave



$T_{bf}$ , if expressed in periods of carrier waves, were calculated within the ranges  $0.01 \leq AK \leq 0.42$  and  $-1 \leq \delta \leq 1$ . The dependence of scale  $T_{bf}$  averaged over  $\delta$

$$T_{bf} = \int_{-1}^1 Td(AK) \quad (8.4.2)$$

is shown in Fig. 8.18.

As shown, the minimum values of  $T_{bf}$  are located at  $AK = 0.32$ . The B-F instability is theoretically efficient, provided that the carrier wave steepness is considerably larger than the typical steepness of sea waves. However, in this case, a steep wave is not isolated in the physical and spectral environments, and after a short interaction with the other modes, it inevitably approaches the breaking onset before a relatively slow B-F mechanism starts to act. For the typical steepness of sea waves  $AK < 0.1$ , the scale  $T_{bf}$  exceeds hundreds and thousands of the periods. Thus, a wave should undergo a long history of growth. It is quite obvious that the B-F instability mechanism cannot be considered as a leading mechanism of wave breaking.

Both the B-F and Hasselmann nonlinear interaction mechanisms refer to the so-called irreversible interaction producing slow transformation (or downshifting) of wave spectrum. However, it is well known that wave spectrum is very unsteady. The amplitude of every mode fluctuates in time (Chalikov 2005) with no change of the averaged spectrum, i.e., with no downshifting or angular spreading. It would be quite natural to assume that due to the reversible interaction, a random concentration of energy in physical space can be high enough to initiate the wave breaking. In some simplified approaches (e.g., in the models based on nonlinear Schrödinger equation (see Slunyaev et al. 2002), the breaking is missing; hence, the amplitudes of the simulated waves can be very large. In reality, the wave-breaking instability prevents an excessive growth of waves. This process is connected with the local decrease and redistribution of energy both in the physical and Fourier domains. As a result, in this case, the reversible interactions can finally become the irreversible ones.

The breaking is a continuous process of the local instability with a short timescale. We suggest that a trigger for breaking can be provided by reversible interactions which locally create a high concentration (focusing) of energy. An effect of one-dimensional and two-dimensional focusing has been investigated numerically and experimentally by Johannessen and Swan (1997, 2001, 2003). Another example of the same mechanism is investigated in the experimental work by Brown and Jensen (2001). The above-mentioned authors found that the merging of wave crests with different wave numbers gives a residual trough-to-crest height of the combined wave that is considerably larger than it follows from their linear superposition. All the works devoted to the focusing, however, can be referred to as the cases studies, i.e., when focusing occurs for the specifically selected configurations of the wave modes. In the current work, our attention is given to the investigation of statistics of focusing in connection with the wave breaking.

The effect can be easily reproduced with the exact 1-D conformal model (ChSh). The number of modes  $M$  was 256 and number of knots  $N = 1024$ . In the first series of the numerical experiments, two linear modes with different steepness and different wave numbers were assigned as initial conditions:

$$\eta(x) = a_1 \cos(k_1 x) + a_2 \cos(k_2 x + \varphi) \quad (8.4.3)$$

where  $a_1$  and  $a_2$  are amplitudes,  $k_1$  and  $k_2$  are wave numbers, and  $\varphi$  is phase. The surface velocity potential was calculated by means of the theory of small-amplitude waves. Integration was done with time step  $dt = 0.001$ . The steepness of both waves  $a_1 k_1$  and  $a_2 k_2$  was assigned within the range of  $0.01 - 0.30$  through the following relations:

$$a_1 k_1 = 0.01 + 0.3r, \quad a_2 k_2 = 0.01 + 0.3r \quad (8.4.4)$$

where  $0 \leq r \leq 1$  is a random number different for the two wave trains. The integer wave numbers are calculated by means of the following expressions:

$$k_1 = 1 + 2r, \quad k_2 = k_1 + 10r. \quad (8.4.5)$$

The trivial cases  $k_1 = k_2$  were excluded from consideration. The variable  $r$  in (8.4.4) and (8.4.5) is a random number function whose values within the range of  $0 \leq r \leq 1$  are different in all cases.

Setting the initial conditions in the form (8.4.3)–(8.4.5) allows us to investigate a very broad ensemble of situations which can be stratified through their integral steepness St calculated over the initial surface:

$$St = \left( \frac{1}{2\pi} \int_0^{2\pi} \eta_x^2(t=0) dx \right)^{1/2}. \quad (8.4.6)$$

The total number of runs is 1000. The aim of these calculations is estimating the difference between the linear and nonlinear solutions. A relatively short period of integrations  $t = 10$  was chosen on purpose, in order to exclude any possibility of the instability development according to the B-F scenario. A considerable part of the runs was terminated at  $t < 10$  because of breaking. The onset of breaking is defined by condition (8.3.1).

Differences between the linear and nonlinear solutions can be characterized by the *exceedance* criterion:

$$E = \frac{\max(\eta) - \min(\eta)}{2(a_1 + a_2)}, \quad (8.4.7)$$

Evidently, for the linear process  $E \leq 1$ , while the value  $E - 1$  characterizes the role of the nonlinearity in the process of crest sharpening. The characteristics of several runs with *exceedance*  $E > 1.2$  are given in Table 8.1 where  $T_m$  is the time of appearance of the maximum value of criterion (8.3.1) expressed in periods of the lower mode.

The wave profiles for the 12 cases calculated at moment  $t = T_m$  and included in Table 8.1 are shown in Fig. 8.19.

As shown, all these profiles contain sharp crests which result from the nonlinear focusing of energy. The focusing happens when two crests merge. Apparently, the focusing occurs both for the initially steep and not too steep wave trains, as well as for the breaking and non-breaking waves with different combinations of steepness and wave numbers. It appears that the effect of focusing certainly depends on the initial phase  $\varphi$ . All the *exceedance* data are compiled together in Fig. 8.20 where

**Table 8.1** Characteristics of the two initially assigned waves and their solutions

No	$T(\text{per})$	$k_1$	$k_2$	$a_1 k_1$	$a_2 k_2$	St	$\varphi$	$E$	$B$
0	1.172	1	4	0.284	0.052	0.085	2.200	1.20	0
1	1.179	2	10	0.304	0.049	0.097	1.980	1.21	1
2	2.154	2	6	0.048	0.242	0.062	2.486	1.22	0
3	1.226	2	3	0.046	0.294	0.091	1.192	1.21	1
4	2.180	2	7	0.011	0.287	0.084	0.980	1.21	0
5	1.421	2	3	0.297	0.018	0.091	0.757	1.22	1
6	1.154	2	11	0.306	0.020	0.096	0.666	1.22	1
7	2.204	2	5	0.053	0.229	0.056	3.078	1.20	0
8	1.145	2	11	0.310	0.041	0.100	0.409	1.21	1
9	1.892	2	9	0.022	0.299	0.092	2.642	1.22	0
10	1.628	2	6	0.041	0.262	0.071	0.011	1.21	0
11	1.167	2	8	0.309	0.018	0.098	2.647	1.22	1

$T_m(\text{per})$  is the time of appearance of maximum value of the criterion (8) expressed in periods of the lower mode;  $k_1$  and  $k_2$  are wave numbers;  $a_1 k_1$  and  $a_2 k_2$  are respective steepnesses imposed in the initial conditions; St is the initial integral steepness (Eq. 6,  $\eta_y = 0$ );  $\varphi$  is a phase;  $E$  is *exceedance* (Eq. 8);  $B$  is type of the termination ( $B = 0$  means no breaking;  $B = 1$  signifies breaking)

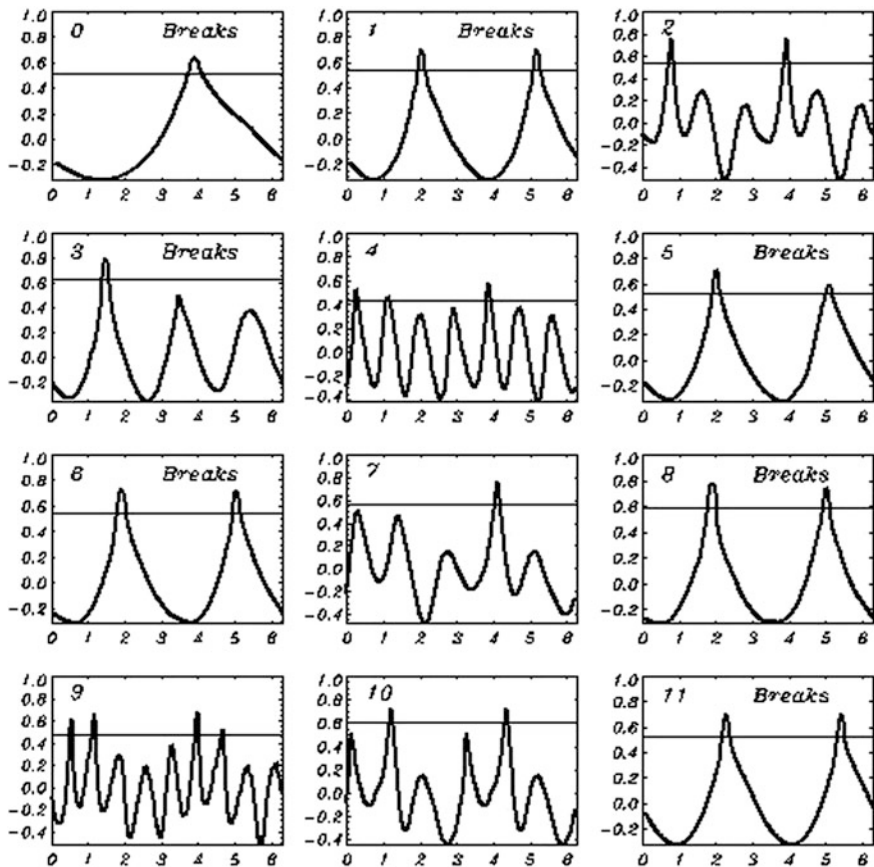


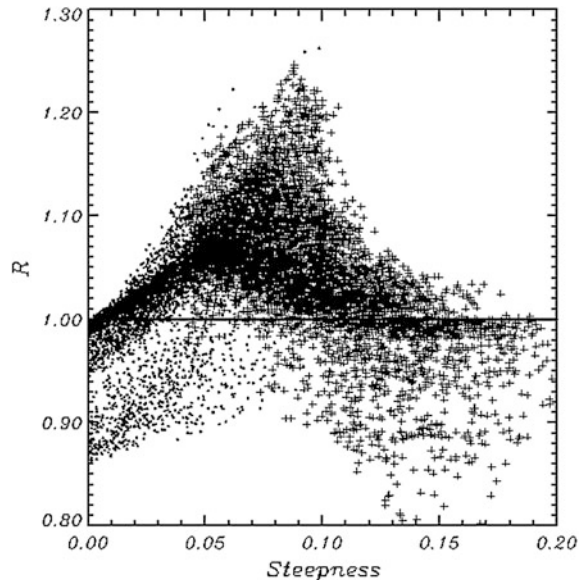
**Fig. 8.19** Examples of 1-D surface elevations with *exceedance*  $E > 1.2$  (see Table 8.1). The horizontal line corresponds to  $E = 1$

the parameter  $E$  is plotted as a function of the initial steepness (8.4.6). Exceedance  $E > 1$  is achieved in most of the runs (75 % of the total number of cases). It is interesting to note that the  $E > 1$  cases happen even at a very small steepness (of the order of 0.01).

The largest values of *exceedance* are obtained at  $\text{St} = 0.1$  above which the *exceedance* is decreasing. The decrease happens because at such mean steepness the wave breaks before getting high. The points shown in Fig. 8.20 correspond to the non-breaking cases, while the ‘plus’ signs correspond to the breaking cases. A fraction of breaking cases increases with growth of  $\text{St}$ , and at  $\text{St} = 0.1$ , it reaches the value 0.97. At  $\text{St} = 0.14$ , all runs are terminated by breaking.

It may appear that the effect of *exceedance* can be explained by the nonlinear transformation of each mode without nonlinear focusing. It is well known that due to the quadratic interactions, an initially linear wave quickly transforms into the

**Fig. 8.20** Dependence of exceedance  $E$  (Eq. 8.4.7) on the initial steepness (Eq. 8.4.6). Dots correspond to non-breaking waves, while the sign + marks breaking waves



nonlinear shape close to that of Stokes wave. Therefore, generally speaking, such transformation can indeed produce an *exceedance* effect. Simple estimations, however, show that such *exceedance* is much smaller. Even for Stokes wave with the steepness  $AK = 0.42$ , the correction given by all the ‘bound’ modes is about 5 %, while the exceedance shown in our computations can be as large as 20 %. For the waves with medium steepness considered in this paper, the Stokes correction is less than 1 %. So, it is unlikely that the focusing can be explained by the nonlinearity of separate waves. Nevertheless, in order to verify this conjecture, we performed an additional series of computations where the initial conditions were assigned as two superimposed Stokes waves with the steepness and phases calculated with Eqs. (8.4.4) and (8.4.5). The exact Stokes wave can be calculated with the algorithm described in Chalikov and Sheinin (1998) (see Chap. 3). Note that the superposition of two Stokes waves is not an exact solution of the stationary equations. Therefore, here, we use a simplified method of Stokes wave generation described in Chalikov (2005) (see Sect. 5.3). In this case, the criterion (8.4.7) characterizes the *exceedance* of the focused wave above the maximum trough-to-crest height of the wave train consisting of two superimposed Stokes waves.

As expected, the *exceedance* for the case of Stokes waves within the interval  $0.05 < St < 0.10$  turns out to be a little lower than that for the linear waves. On the contrary, for  $St > 0.10$ , the *exceedance* is bigger than for the linear waves. It can be explained by higher stability of Stokes waves as compared to the linear waves.

## 8.5 Conclusions

In this chapter, the exact two-dimensional model was used for investigation of the breaking onset recognized by the appearance of non-uniqueness of surface. This criterion is strict, since up to the moment of wave evolution, the conservation of integral is supported with high precision, and after that moment, the breaking is imminent. Due to the special strategy of the numerical experiments and archiving the results, an evolution of the wave close to breaking was registered with high accuracy. This last period prior to breaking was a subject of the investigation.

Opposite to the considerations based on a small number of modes, the definition of ‘wave’ in the spectral environment is less certain. In reality, such wave is a composition of many modes with more or less fixed phases. Due to dispersion wave, surface has a complicated shape. This is why the definition of an individual wave is also uncertain. The statistical characteristics of such wave usually have a large scatter. The spectral approach for investigation of breaking waves is misleading, since breaking occurs in a narrow interval of physical space, its spectral image being difficult to interpret. The mechanism of breaking in the spectral environment is quite different to that for the idealized situations when the wave field is represented by few modes.

The breaking develops very quickly, on the average, faster than for half of a peak wave period. To some extent, the breaking is similar to the development of freak waves which generally appear suddenly without any prehistory. Probably, the main cause of such development can be a reversible wave–wave interaction.

No reliable predictor was found for breaking in the spectral environment, such as threshold or limiting value of some global wave parameters which indicate an imminent breaking. The calculations with the exact model show that the criterion based on the rate of maximum energy can be exceeded many times. It means that a real process is much more stable than it was demonstrated in Song and Banner (2001) where the breaking onset was identified with the development of the numerical instability. The overall characteristics of breaking (such as overall steepness, asymmetry, overall kurtosis, and skewness) reveal weak connection with the breaking process.

The differential geometrical and kinematical characteristics such as the first and second derivatives of elevation, surface orbital velocity, and individual accelerations (as well as criterion  $\delta$ , as in Eq. 8.3.9) indicate development toward breaking clearer, but they rather describe the process of breaking itself than predict its onset. In another similar situation, the development does not necessarily result in breaking: At some moment prior to breaking, the process can become reversible.

The most striking property of the wave breaking in the spectral environment is the absence of any evident rules and criteria for breaking onset. We can only be sure that the breaking starts in most cases at the front slope of wave very close to its peak. The breaking occurs as a result of the local instability of flow in the areas with large negative steepness. As a rule, it is followed by deceleration of the horizontal component of surface orbital velocity and by the negative vertical acceleration.

The breaking process develops in the space intervals, much shorter than the dominant wavelength. For spectral description of such modification, high-frequency (wave numbers) modes are required. In reality, however, the breaking decreases energy of large wave by changing its shape. In general, the spectral approach is not fully applicable for the analysis of individual breaking cases which occur in physical space and cause a hardly interpretable transformation of wave spectrum.

The main difference is that in the spectral environment, wave surface can become unstable and collapse at a much lower global steepness than in a simple case with a small number of modes. This apparently happens due to the wave shape distortions which would trigger the breaking earlier. These distortions are most likely to happen in case of random superposition of waves of all scales.

An additional investigation of the fast wave transformation was undertaken, since some of the existing explanations of this phenomenon based on the B-F instability theory seem incomplete. The main contradiction of the B-F theory with the results of our numerical simulation and some other observations is a fast rate of the freak wave development and a short life of such wave. An additional motivation for search of the fast mechanism of wave transformation was provided by Brown and Jensen (2001) who discovered the effect of the nonlinear focusing experimentally. They noted: '*...conditions under which the Benjamin-Feir instability is able to act are expected to be satisfied only under extremely rare circumstances in deep water ocean waves.*' In fact, we have repeatedly simulated their experiment on the basis of exact 1-D model for a large number of cases and confirmed that the fast nonlinear focusing is a typical phenomenon that occurs at any steepness.

The question remains whether this effect can explain appearance of freak waves. We are inclined to think that the answer to this question is rather negative, though the effect of *exceedance* can make contribution to the freak wave formation. First of all, the effect of *exceedance* is not very significant, while a freak wave height can reach very large values. Secondly, the effect of *exceedance* is of high probability, and it evidently takes place, whenever the crests of two waves with different wave numbers merge. If this effect were indeed responsible for generation of freak waves, the probability of such waves would be much higher as compared to what we know now. It is still possible, however, that the effect of energy focusing is stronger for three or more waves or for the directionally spread waves; i.e., this phenomenon should be investigated on the basis of a more general formulation of the problem. The current investigation is only targeted at highlighting a possible mechanism of the breaking onset.

# Chapter 9

## Numerical Modeling of Wind–Wave Interaction

**Abstract** The description of a coupled wind and wave model in conformal coordinates is given. The wave model is based on potential equations for the flow with a free surface, extended with the algorithm of breaking dissipation. The wave boundary layer (WBL) model is based on the Reynolds equations with the  $K-\varepsilon$  closure scheme with the solutions for air and water matched through the interface. The structure of the WBL and vertical profiles of the wave-produced momentum flux (WPMF) in a long-term simulation of the coupled dynamics is investigated and parameterized. The shape of the  $\beta$  function connecting elevation and surface pressure is studied up to high non-dimensional wave frequencies. The errors of a linear presentation of the surface pressure are estimated.

### 9.1 Wave Boundary Layer (WBL)

The basic properties of the wind–wave interaction processes which are valid over a wide range of wind speeds and wave numbers are yet to be determined on a solid scientific basis. In the center of these investigations, there should be direct interactions of winds and waves. These processes have been most extensively investigated in the context of the processes describing growth and decay of the ocean wind waves, i.e., their so-called input and dissipation source terms in wave prediction models. Even for these processes, the conventional theories are either highly simplified (e.g., Miles' linear wind input theory) or actually nonexistent (wave energy dissipation due to whitecapping). Furthermore, direct observations of many characteristics are generally unavailable, as will be discussed below. In order to accurately describe this central interaction between winds and waves, it is necessary to obtain a detailed information about the following: (1) the physics of wave drag and exchange by the kinetic energy, heat, and passive substances; (2) the spectral shape of the wind–wave interaction parameter and its asymptotic behavior both at high frequencies (spectral tail) and low frequencies (long and fast waves); (3) its dependence on stratification and gustiness; (4) its directional distribution; (5) limits of applicability for the quasi-linear representation of wind input; and (6) the physics

and statistics of wave breaking and its dependence on wave spectrum and wind. More generally, modeling of the air–sea interaction processes also requires additional information on the following: (1) the influence of surface waves on the turbulent exchange of momentum, heat, mass, and passive substances between the air and water; (2) a role of surface waves in the dynamics of the wave boundary layer (WBL), the mixed layer (ML), and the upper thermocline (UT).

The main interaction mechanisms are active very close to the moving interface making it extremely difficult to carry out direct experimental measurements in the sea, especially at high winds. Most of the measurements are performed at the levels higher than the wave crests, in fact, at heights where the difference between WBL and conventional BL is not too large. The technical problems associated with conducting the measurements where they are actually required, i.e., very close to the surface, suggest that an adequate experimental solution can be beyond reality. At present, most of the measurement data available from the field experiments highlight only the consequences of the interaction but not its mechanics. Even the laboratory data have to be often considered as qualitative, because of the problems associated with the scaling and small sizes of the laboratory tanks. For example, the laboratory wind–wave tunnel measurements are carried out in a very thin layer that just starts to develop the WBL, while at sea, the WBL is formed at a great distance from the location of the measurements and is usually well adjusted to the wave field.

The modern technology developed in the geophysical fluid mechanics was not actually used for investigation of the WBL. The numerical hydrodynamic modeling is similar, to some extent, to the perfect laboratory modeling (no scale limitations, availability of simple ‘observations’ of arbitrary quantities in arbitrary locations), but its applicability surely depends on the applicability of many theoretical assumptions used. Being free from the restrictions arising from the scale difference, an approximation to reality can be sometimes closer than that obtained in physical simulations. Such situation is typical for many other branches of the fluid dynamics, especially in technical applications (see Fletcher 1988), and it is often proved that numerical methods do provide high-quality results which can be combined with experimental data and generate the results which are impossible to obtain just experimentally. In a more specific context of modeling of the wave growth under the action of wind, there are no significant theoretical extensions of the Miles’ theory, since most of the theoretical investigations are done in the framework of small-amplitude linear assumption (e.g., Belcher et al. 1994). However, it became clear years ago that successful development of the problem should be based on full nonlinear equations of turbulent flows.

The WBL is the lowest part of the constant flux atmospheric boundary layer (Chalikov 1976, 1978, 1980, 1986) where the fluctuations produced by waves are clearly pronounced. The height of the WBL is of the order of significant wave height  $H_s$ , normally—a few meters. At the bottom, it is in contact with the sea surface, while at the top, it merges with a surface layer widely known as the Monin-Obukhov layer (Monin and Yaglom 1971). In most cases, the height of WBL does not exceed that of a dynamic sublayer; hence, a direct influence of

stratification on wind–wave interaction is negligible. An indirect influence of stratification through a low-frequency part of the turbulent spectrum (gustiness) can be noticeable (Kahma and Calkoen 1992), and it can be included in the WBL model by use of variable upper boundary conditions. Within the WBL, the motion is profoundly influenced by the ocean surface waves. Since the WBL is responsible for wave drag, its structure changes dynamics of the entire constant flux atmospheric layer. The total momentum flux  $\tau$  splits in the WBL into two branches: wave-produced momentum flux  $\tau_w$  (WPMF) transferring energy and momentum to waves; shear turbulent flux generating currents. The contribution of the WPMF to the total flux is the biggest on wave surface, while WPMF quickly decreases with height within the WBL, eventually approaching zero at the top of the WBL where all of the momentum is transferred by shear turbulence.

The previous investigations of the boundary layer above waves were based mostly on the conventional theory of the boundary layer above infinite flat and rigid surface. In fact, the presence of waves was considered only as a sort of inconvenience, while the effect they produced was treated as modification of a roughness parameter. However, it seems to be still unexplained why the roughness parameter is normally about four orders of magnitude smaller than wave heights; moreover, no analysis of wind profile close to sea surface in the presence of finite-amplitude waves has been ever suggested.

A straightforward approach for the hydrodynamic theory of the WBL was first developed in the sixties (see Phillips 1977). However, only few studies accepted Phillips' concept that a lower part of the marine boundary layer has at least one distinct feature; i.e., its lower boundary is a curvilinear moving surface responsible for specific types of dynamic interactions. This effect was qualitatively studied in the linear small-amplitude theory (Miles 1957).

Development of the numerical WBL models began in mid-seventies when several papers covering this topic were published at the same time. Gent and Taylor (1976) investigated a stationary wind flow above one single wave for a broad range of the wave and airflow parameters. They were the first to find the theoretical dependence of the wind–wave energy exchange on wave frequency. The similar model, though based on the stream function, was developed by Simonov (1982). The most important Simonov's result accounted for the role of different turbulence closure schemes. It was concluded that for typical magnitudes of wave steepness, all closure schemes show similar results. The fully nonlinear modeling of wind–wave interaction (as well as the concept of the WBL) was first introduced by Chalikov in 1976 and 1978. The second paper considered a fundamental problem of deriving Reynolds equations for a boundary layer above the curvilinear moving surface. It was a 2-D WBL model based on the finite-difference approximations in both directions. In view of the limitations due to old computers, all the calculations were performed for monochromatic wave field or just for few wave modes (Chalikov 1986). The most difficult computational problem was development of an accurate numerical method for solution of a general elliptic equation for pressure above the nonstationary multimodal surface. The main results obtained with the use of the old version of the model are as follows:

- (1) derivation of the Reynolds equations in the surface-following coordinate system as well as general formulation of the WBL problem;
- (2) calculation of the spectral shape of a wind–wave interaction parameter ( $\beta$ -function) with the preassigned angular distribution based on ‘apparent’ frequency. Investigation of the statistical structure of the WBL (including profiles and spectral composition of the first, second, and some third moments of the wave-produced pressure, velocities, and turbulence);
- (3) one-dimensional theory of the WBL considering the spectral structure of the wave-produced momentum fluxes (Chalikov and Belevich 1993; Chalikov 1995);
- (4) implementation of the new energy input and dissipation schemes (Tolman and Chalikov 1994, 1996) in the NWS operational wave forecast WAVEWATCH model (see Web site <http://polar.wwb.noaa.gov/waves>). The energy input formulation is more accurate than that used in the family of WAM models. The extensive comparisons of wave forecasts produced by the WAVEWATCH III (Version 1.15) and WAM (Cycle 4) models using buoy and satellite data clearly showed that the WAVEWATCH model provided better forecasts of the observed wave characteristics, as compared with the WAM model. Certainly, this improvement was achieved not only due to implementation of new schemes for energy input and dissipation.

The results of further numerical modeling (Chalikov 2005) showed that it would be better to replace the term ‘*small amplitude*’ by the term ‘*very small amplitude*,’ as even for the steepness of the order of 0.05, the nonlinearity becomes an essential property of wave dynamics. Also note that applicability of the single-mode linear analysis for real finite-amplitude multi-modal wave fields has been never seriously discussed. What makes this problem special is the necessity to use the surface-following coordinate system for derivation of correct nonlinear equations. After transformation, the dynamic equations become highly complex and difficult to integrate; however, they allow describing the essence of the process, i.e., interaction of the turbulent wind with finite-amplitude waves.

The *wind–wave interaction* mechanism has been extensively investigated within the frame of the ocean wave evolution problem. All the studies were targeted at parameterization of the so-called *input and dissipation source terms* in wave prediction models. Even for such processes, the existing theories seem to be either highly simplified (e.g., Miles’ quasi-linear wind input theory) or purely speculative, as in case with the wave energy dissipation due to whitecapping. Moreover, it is a bare reality that the frequently cited Hasselmann’s approach with regard to calculation of the nonlinear interaction was never used in the wave forecasting models due to its high complexity. Furthermore, direct observations of a number of characteristics are hardly possible. An indirect analysis based on observations of the spectrum evolution is unable to separate the input, dissipation, and nonlinear interaction effects.

A standard spectral description of the energy input to waves is based on the concept of linear superposition of fluxes to the spectral components calculated

according to Miles' theory. For steep waves, this principle is incorrect. All the previous models considered the airflow above single harmonic wave and suggested the steadiness of flow. Actually, this assumption is acceptable only for small-amplitude waves. Due to the strong nonlinearity (leading to formation of bound waves, focusing of energy in physical space and wave breaking), wave field cannot be represented as a superposition of linear waves with random phases. The dynamic wind–wave interaction is highly complicated. For example, long waves modify the local flow which influences the energy input to short waves, while the short waves produce local drag that influences the flow over large waves. In general, all waves ‘spring, burgeon, and fall’ in the environment created by the entire spectrum. The energy input to waves, even with moderate steepness, is rather concentrated in physical space than in Fourier space. Hence, a Fourier image of the input is often difficult to interpret.

The more comprehensive theoretical formulation of the coupled problem became possible after introduction of the unsteady surface-following conformal mapping (ChSh). After transformation into the conformal coordinates, the 1-D wave equations obtain a very simple form. The approach is so precise that any comparison with observations allows to judge rather of the applicability of a 1-D potential approach with regard to real process than of the accuracy of the model itself.

The motivations for development of the new approach are quite evident. It is impossible to prove that the coexisting waves interact with atmosphere as a set of independent waves, so that the integral result can be obtained by a simple superposition of monochromatic cases. It is well known that even a single wave produces a broad spectrum of pressure fluctuations which modifies the flow. The first attempt to consider the nonlinearity and group effects was made using a finite-difference model (see review Chalikov 1986), where wave surface was assigned as a superposition of running waves with different frequencies. This approach is much closer to reality than that based on the stationary single-mode model. However, it was found that such an approach, being much better (and much more complicated) than the monochromatic stationary approach, was also imperfect due to two reasons: (1) the peculiar wave shapes and a nonlinear group structure are not represented in the above model; (2) the finite-difference model cannot provide the accuracy required.

The most reliable approach for investigation of the wind–wave interaction problem is modeling of the coupled wave and WBL dynamics (Chalikov 1998). The spectral approach to this problem is quite suitable; however, it should be used as a method for the numerical solution of equations and for representation of the results. The most complicated processes, such as group effects, wave breaking, bound waves, and development of extreme waves occur in physical space; hence, their spectral image is often not quite representative.

It is obvious that real waves have more or less sharp crests and smooth troughs. At the same time, Stokes waves are the exact solution of full equations. Stokes waves are stable in the absence of disturbances, while they slowly transform as a result of the Benjamin–Feir instability in the presence of disturbances. However, harmonic waves quickly disintegrate and obtain the shape of Stokes waves even in

the absence of disturbances. Wave field always includes the so-called bound waves moving with the phase speed of carrying wave. This expression is not quite adequate, since it obscures a genuine nature of the phenomenon. Actually, large waves are the more or less stable nonlinear objects consisting of a great number of linear modes with almost constant amplitudes and fixed phases. As a result, a multi-mode wave field is approximated rather by a superposition of nonlinear modes (Stokes waves) than by a superposition of the linear modes with random phases. The analysis of wave field in terms of Stokes waves was simplified due to an incidentally discovered property. It was found (Chalikov 2005) that the nonlinear (in the Cartesian coordinates) Stokes modes turn into the single Fourier modes with high accuracy after transformation to the ‘upper’ conformal coordinates. For obtaining the same accuracy of approximation of wave surface, the required number of such modes is small as compared with that of the Fourier modes in the Cartesian coordinate system.

The nonlinear properties of real waves are closely connected with the problem of wind and wave interaction. This problem of the geophysical fluid dynamics has always been the object of extensive investigations; however, the most of the theoretical works were based on a small-amplitude assumption. It was never discussed, to what extent the amplitudes might be small. The numerous analytical investigations (based on the simplified equations) that followed after the famous Miles’ (1957) work actually did not lead to deep insight into the problem. The structure of flow and the wave-produced drag above sharp-crested waves differ from those for harmonic waves. A more realistic approach is based on the numerical modeling of a stationary flow above the wavy surface (represented by one mode). Such models based on Reynolds equations and the turbulent closure schemes (Gent and Taylor 1976, Chalikov 1976, 1978) were used for investigation of a boundary layer structure above the finite-amplitude harmonic waves (see Chalikov 1986). The results obtained with use of such models are definitely closer to reality than the results of analytical exercises, though the above models are also imperfect. Despite the fact that the Chalikov’s model has undergone numerous modifications (see, e.g., Mastenbroek et al. 1996), it remains hardly suitable for investigation of real processes. Moreover, this scheme was based on a finite-difference approach, while for the periodic wave problem, it would be more appropriate to use the Fourier transform method. The pressure field was calculated through solution of the finite-difference Poisson equation, which imposes tough limitations on the wave steepness. The first attempts to consider more than one harmonic mode were not quite successful either.

The current approach to the problem (Chalikov 1998; Chalikov and Rainchik 2010) is based on the new principles. (1) The model is formulated as a high-resolution spectral problem in the nonstationary surface-following coordinate system. (2) Waves are the object of modeling; i.e., the full potential wave equations are solved along with the equations for boundary layer with matching of the solutions on the interface. (3) The well-developed and powerful Fourier transform method is used.

It is obvious that even minor obstacles (such as sharpening of crest) produce a dramatic change of pressure field and form drag (this effect is well known in the engineering fluid mechanics). It is also well known that just a simple group effect may produce high and steep waves (in physical space) with a deep minimum of pressure behind the crests. The nonlinearity enhances the effect of sharpening, thus strongly increasing the pressure anomalies. On the whole, the wave drag and energy exchange is the result of an ensemble effect of the nonstationary fluctuations of pressure and surface stresses. It is clear that all those processes are completely absent in routine monochromatic stationary models.

## 9.2 Equations of WBL

It is impossible to provide an exact formulation of a 2-D wind–wave interaction problem without the introduction of the surface-following conformal coordinates. A consistent development of the approach to the problem of wind–wave interaction began with Chalikov (1976, 1978).

Let us consider a boundary layer above a curved periodic surface  $\eta = (x, t)$  whose shape is represented by Fourier expansion:

$$\eta(x, t) = \sum_{-M}^M h_k(t) \vartheta_k(x). \quad (9.2.1)$$

Here,  $h_k$  are amplitudes and  $M$  is truncation number, while  $\vartheta_k(x)$  denotes the following function:

$$\vartheta_k(\xi) = \begin{cases} \cos(k\xi) & k \geq 0 \\ \sin(k\xi) & k < 0 \end{cases} \quad (9.2.2)$$

(note that  $(\vartheta_k)_{\xi} = k\vartheta_{-k}$ , and  $\sum (A_k \vartheta_k)_{\xi} = -\sum (kA_{-k} \vartheta_k)$ ). Let us introduce the conformal surface-following coordinate transformation for domain ( $0 < x \leq 2\pi$ ,  $H_w < z < H_a$ ):

$$\begin{aligned} x &= \xi \mp \sum_{-M \leq k \leq M, k \neq 0} \eta_{-k}(\tau) \frac{\cosh k([H_a, H_w] \mp \xi)}{\sinh kH} \vartheta_k(\xi) \\ z &= \zeta \mp \sum_{-M \leq k \leq M, k \neq 0} \eta_{-k}(\tau) \frac{\sinh k([H_a, H_w] \mp \zeta)}{\sinh kH} \vartheta_k(\xi) \end{aligned} \quad (9.2.3)$$

$$t = \tau$$

where  $H_a$  is WBL height and  $H_w$  is the water domain depth. The top signs in (9.2.3) refer to the air domain, while the bottom signs refer to the water domain. Note that transformation (9.2.3) is nonlinear, since  $\vartheta_k(\xi)$  are the functions of a new coordinate  $\xi$ . At  $\xi = 0$ , the function  $z(\xi)$  describes wave surface:

$$z(\xi, 0, \tau) = \eta(\xi, \tau) = \sum_{-M}^M \eta_k(\tau) \vartheta_k(\xi), \quad (9.2.4)$$

where  $M$  is the assigned number of modes, while  $\eta_k$  are Fourier coefficients in the curvilinear coordinate system. These coefficients differ from the Fourier coefficients  $h_k$  for water surface in the Cartesian coordinate system. To obtain the same accuracy of approximation of surface  $\eta$ , the number of modes in the Cartesian coordinates should be less than in the lower coordinates and more than in the upper coordinates.

The governing equations should be obtained by averaging Navier–Stokes equations. In the presence of a moving 2-D interface, the averaging is not a trivial problem. Phillips (1977) had discussed this problem in detail (see also Chalikov 1978). However, it should be pointed out that the averaging of equations for a 3-D case is always connected with some ‘apriori’ simplifications, so it cannot be done formally in the way it was done for a quasi-stationary flow in a simple domain (Monin and Yaglom 1971). Obviously, the best way to avoid some of the simplifications is to use the LES technique. Above the 1-D surface, the averaging can be understood as the averaging along  $y = \text{const}$ . (Phillips 1977).

After transformation into a new coordinate system and averaging, Euler equations can be written as follows (the sign of averaging for the first-order moments is omitted):

$$\begin{aligned} \frac{dJu}{d\tau} &= -\frac{\partial p x_\xi}{\partial \xi} + \frac{\partial p z_\xi}{\partial \zeta} - \frac{\partial(x_\xi \bar{u'} u' + z_\xi \bar{u'} w')}{\partial \xi} - \frac{\partial(-z_\xi \bar{u'} u' + x_\xi \bar{u'} w')}{\partial \zeta}, \\ \frac{dJw}{d\tau} &= -\frac{\partial p z_\xi}{\partial \xi} + \frac{\partial p x_\xi}{\partial \zeta} - \frac{\partial(z_\xi \bar{u'} w' + x_\xi \bar{w'} w')}{\partial \xi} - \frac{\partial(-z_\xi \bar{u'} w' + x_\xi \bar{w'} w')}{\partial \zeta}, \end{aligned} \quad (9.2.5)$$

where  $p$  is a deviation from hydrostatic pressure divided by air density;  $x_\xi$  and  $z_\xi$  are metric coefficients; and  $J$  is the Jacobian of mapping

$$J = x_\xi^2 + z_\xi^2, \quad (9.2.6)$$

$d/d\tau$  denotes full derivative on time

$$\frac{dJ()}{d\tau} = \frac{\partial J()}{\partial \tau} + \frac{\partial Ju()}{\partial \xi} + \frac{\partial Jw()}{\partial \zeta}, \quad (9.2.7)$$

$U$  and  $W$  are contravariant velocity components

$$U = J^{-1}((u - x_\tau)x_\xi + (w - z_\tau)z_\xi), \quad W = J^{-1}(-(u - x_\tau)x_\xi + (w - z_\tau)z_\xi). \quad (9.2.8)$$

The continuity equation takes the form:

$$\frac{\partial \tilde{u}}{\partial \xi} + \frac{\partial \tilde{w}}{\partial \zeta} = 0, \quad (9.2.9)$$

where  $\tilde{u}$  and  $\tilde{w}$  are covariant velocity components.

$$\tilde{u} = ux_\xi + wz_\xi, \quad \tilde{w} = -uz_\xi + wx_\xi \quad (9.2.10)$$

Approaching the surface ‘vertical’ velocity  $W$  goes to zero, and kinematic condition  $W = 0$  becomes valid with an increasing accuracy. On the surface itself  $W = 0$  strictly; hence,  $u = u_0, w = w_0$  where  $u_0$  and  $w_0$  are the surface velocity components. Equality  $W = 0$  means that momentum and any substance are not transferred by velocity through interface. To derive Eqs. (9.2.2)–(9.2.9), the next properties of conformal mapping were used:

$$x_\xi = z_\zeta, \quad x_\zeta = -z_\xi, \quad x_\xi = J^{-1}\xi_x, \quad x_\zeta = -J^{-1}\xi_z. \quad (9.2.11)$$

The second- and third-order moments containing fluctuations of metric coefficients and fluctuations of Jacobian are omitted, as the subgrid moments of such type quickly attenuate with increase of distance from the surface (see discussion of this problem in Chalikov 1978). The second-order turbulence moments are represented as a product of the turbulent viscosity coefficient  $K_m$  and a corresponding component of the velocity strain tensor  $\Phi_{ij}$  (Monin and Yaglom 1971). The coefficient  $K_m$  is taken in a form:

$$K_m = c_k e^2 / \varepsilon, \quad (9.2.12)$$

( $K$ - $\varepsilon$  model), where  $e$  is the kinetic energy of turbulence,  $\varepsilon$  is a rate of  $e$  dissipation (Launder and Spalding 1974),  $c_k = 0.0073$ , and

$$\begin{aligned} \overline{u' u'} &= 2K_m J^{-1} \Phi_{11} = 2K_m J^{-1} \left( \frac{\partial ux_\xi}{\partial \xi} - \frac{\partial uz_\xi}{\partial \zeta} \right) + \frac{2}{3}e \\ \overline{u' w'} &= K_m J^{-1} \Phi_{12} = K_m J^{-1} \left( \frac{\partial (uz_\xi + wx_\xi)}{\partial \xi} - \frac{\partial (ux_\xi + wz_\xi)}{\partial \zeta} \right) \\ \overline{w' w'} &= 2K_m J^{-1} \Phi_{22} = 2K_m J^{-1} \left( \frac{\partial wz_\xi}{\partial \xi} + \frac{\partial wx_\xi}{\partial \zeta} \right) + \frac{2}{3}e \end{aligned} \quad (9.2.13)$$

At the upper boundary, the metric coefficients obtain the values:  $z_\xi = 0$  and  $x_\xi = 1$ ; hence, the boundary conditions take the following form:

$$z = \zeta = H_a : \overline{u' w'} = \tau, \quad w = 0, \quad (9.2.14)$$

where  $\tau$  is a vertical flux of the horizontal momentum. The tangent turbulent stress on the surface  $\tau_0$  is calculated with the use of the quadratic law:

$$\tau_0 = C_l |\tilde{u}_1 - \tilde{u}_0| (\tilde{u}_1 - \tilde{u}_0). \quad (9.2.15)$$

Here,  $\tilde{u}_1$  and  $\tilde{u}_0$  are the covariant components of velocity in the lowest level and on the interface, respectively;  $C_l$  is a local drag coefficient the definition of which is given below.

Evolution of  $e$  and  $\varepsilon$  is described with the following equations:

$$\begin{aligned} \frac{dJe}{d\tau} &= \frac{\partial}{\partial \xi} K_e \frac{\partial e}{\partial \xi} + \frac{\partial}{\partial \zeta} K_e \frac{\partial e}{\partial \zeta} + P - \varepsilon \\ \frac{dJ\varepsilon}{d\tau} &= \frac{\partial}{\partial \xi} K_\varepsilon \frac{\partial \varepsilon}{\partial \xi} + \frac{\partial}{\partial \zeta} K_\varepsilon \frac{\partial \varepsilon}{\partial \zeta} + \frac{\varepsilon}{e} (c_2 P - c_4 \varepsilon) \end{aligned} \quad (9.2.16)$$

where the diffusion coefficients  $K_e$  and  $K_\varepsilon$  are proportional to the coefficient of turbulent viscosity  $K_e = K_m/c_e$ ,  $K_\varepsilon = K_m/c_\varepsilon$ , while  $P$  is the rate of turbulent energy production:

$$P = 0.5 J K_m (\Phi_{11}^2 + 2\Phi_{12}^2 + \Phi_{22}^2). \quad (9.2.17)$$

The rate of production  $P_H$  at the upper boundary of domain  $z = \zeta = H_a$  is calculated through the formula:

$$P_H = \frac{v_*^3}{\kappa H_a} \quad (9.2.18)$$

( $v_* = \tau^{1/2}$  is friction velocity at  $z = H_a$ ), and energy of turbulence  $e$  and the rate of  $e$  dissipation  $\varepsilon$  are equal to:

$$e_H = c_1 v_*^2, \quad \varepsilon_H = \frac{v_*^3}{\kappa H_a}. \quad (9.2.19)$$

The normal to surface  $\zeta = 0$  vertical diffusion of turbulent energy and diffusion  $K_e \frac{\partial e}{\partial \zeta}$  at the upper boundary  $\zeta = H_a$  are both equal to zero. A vertical diffusion of dissipation rate by the normal to the surface  $\zeta = 0$  and at the upper boundary  $\zeta = H_a$  is equal to:

$$K_\varepsilon \frac{\partial \varepsilon}{\partial \zeta}(\zeta = 0) = -v_{s0}^4 z_1^{-1} c_3^{-1}, \quad K_\varepsilon \frac{\partial \varepsilon}{\partial \zeta}(\zeta = H_a) = -v_*^4 H_a^{-1} c_3^{-1}, \quad (9.2.20)$$

respectively, where  $v_{s0} = \tau_0^{1/2}$  is the local tangent friction velocity defined by the local turbulent tangent stress  $\tau_0$  on the interface. The closure scheme based on

Eqs. (9.2.16)–(9.2.20) uses a set of empirical constants:  $\kappa \approx 0.41$  (Karman constant),  $c_1 = 3.7$ ,  $c_e = 1$ ,  $c_2 = 1.92$ , and  $c_3 = 1.3$ . In the absence of waves, as it follows from the self-similarity of logarithmic boundary layer, the constant  $c_4$  is connected with other constants:

$$c_4 = (c_1 - c_2)\kappa^{-2}c_3^{-1}. \quad (9.2.21)$$

All of the equations have been written in a non-dimensional form based on the following scales: length  $L(2\pi L$ —a horizontal scale of domain) and  $g$ —acceleration of gravity. All other scales have been constructed with the use of  $g$  and  $L$ .

### 9.3 The Numerical Scheme for WBL Equations

The numerical scheme is based on the Fourier transform method (Orszag 1970) and the fast Fourier transform (FFT) subroutine for an arbitrary number of modes. A detailed description of the method applied to the wave modeling problem is given by Chalikov and Sheinin (1998). The core of the method is that the linear part of equation is approximated directly, while the products of variables are calculated on the uniform over  $\xi$ -coordinate grid with the number of knots  $N = 4M$  ( $M$ —number of the Fourier modes). Then, the Fourier coefficients of the products are used for integration on time or for calculation of derivatives over the ‘vertical’ coordinate  $\zeta$ . The derivatives over  $\xi$  are calculated through analytical differentiation of the Fourier series. The vertical operators are approximated on a stretched grid where the intervals between the knots  $\Delta\zeta_j$  are calculated with the use of formula  $\Delta\zeta_{j+1} = \gamma\Delta\zeta_j$  ( $\gamma$  is a stretching coefficient; index  $j$  is going up), while the first value of  $\Delta\zeta$  ( $j = 1$ ) is defined from the following condition:

$$\sum_{j=1}^K \Delta\zeta_k = H_a, \quad (9.3.1)$$

where  $K$  is the total number of levels in WBL. To improve accuracy of the finite-difference approximation for the zero-number modes of  $u$  and  $\varepsilon$ , it was taken into account that

$$u \propto \ln(\zeta) + \text{const}, \quad \varepsilon \propto \zeta^{-1}, \quad (9.3.2)$$

The Fourier transform method is well developed and widely used for numerical solution of nonlinear equations. That is why we are not going into further description of the numerical scheme. For integration on time, the fourth-order Runge–Kutta scheme was used.

The most difficult problem arising at solution of the fluid mechanics equations in the curvilinear coordinates is the calculation of a pressure field that provides continuity condition (9.2.9). It is well known that the solution quickly becomes unstable if the equation of continuity is not valid with a high accuracy. The dynamic equations for covariant components of velocity (9.2.10) take the following form:

$$\begin{aligned}\frac{\partial \tilde{u}}{\partial \tau} &= -\frac{\partial p}{\partial \xi} + \tilde{F}_u \\ \frac{\partial \tilde{w}}{\partial \tau} &= -\frac{\partial p}{\partial \zeta} + \tilde{F}_w,\end{aligned}\quad (9.3.3)$$

where  $F_u$  and  $F_w$  are straightforward designations for the sum of turbulent and convective terms calculated as a combination of the right-hand sides of Eq. (9.2.5) at each substep of the Runge–Kutta scheme. Eq. (9.3.3) gives a possibility to derive a standard form of the Poisson equation for the updated pressure  $p^l$

$$\frac{\partial^2 p^l}{\partial \xi^2} + \frac{\partial^2 p^l}{\partial \zeta^2} = \frac{1}{\Delta t} \left( \frac{\partial \tilde{u}}{\partial \xi} + \frac{\partial \tilde{w}}{\partial \zeta} + \frac{\partial \tilde{F}_u}{\partial \xi} + \frac{\partial \tilde{F}_w}{\partial \zeta} \right)^{l-1}, \quad (9.3.4)$$

that can be solved through a tridiagonal matrix algorithm (TDMA, Thomas 1949) for the pressure Fourier components  $p_k$

$$k^2 p_k + \frac{\partial^2 p_k}{\partial \zeta^2} = R_k, \quad (9.3.5)$$

[ $R_k$  is a Fourier component for the right-hand side in (9.3.4)]. Approximation of a vertical derivative of  $p_k$  considers that the vertical profile of Fourier components for pressure can be approximated through the following function:

$$p_k(\zeta) = P_k(\zeta) \exp(-2|k|\zeta), \quad (9.3.6)$$

where coefficients  $p_k(\zeta)$  are a slowly changing function of  $\zeta$ . To provide the continuity equation to be valid up to the surface  $\zeta = 0$ , the boundary conditions for pressure are derived on the basis of the boundary conditions for a ‘vertical’ component of the surface covariant velocity  $\tilde{w}_0$ :

$$\begin{aligned}\tilde{w}_0 &= -u_0 z_\xi + w_0 x_\xi & \zeta = 0 \\ \tilde{w}_H &= 0 & \zeta = H_a,\end{aligned}\quad (9.3.7)$$

where  $u_0$  and  $w_0$  are Cartesian components of surface velocity. The calculated pressure is used for correction of the velocity field as presented in Eq. (9.2.5).

This method generalizes a standard approach for solution of the Navier–Stokes equations for a case of the curvilinear coordinates.

## 9.4 The Coupling of Wave Models with the Model of WBL

The coupled model consists of the two main components: wave model (WM) and WBL model. The models must be integrated simultaneously. However, there is a small parameter in the coupled problem, i.e., a ratio of density for air and water  $\rho_a/\rho_w \sim 10^{-3}$ . That is why the coupled modeling can be carried out as a separate stepping in time for both models with exchange of the matching information at each time step. The WBL model calculates the boundary conditions for the WM model: the surface pressure  $p_0$  and normal turbulent stress providing exchange by momentum and energy between air and water. The WM model calculates a shape of interface  $\eta(\xi)$ , a rate of ‘vertical’ displacement  $\eta_t$  required for calculation of the metric coefficients for the WBL model, as well as the surface velocity components  $u_0$  and  $w_0$  as a boundary condition for the Poisson equation for pressure and for calculation of tangent stress  $\tau_t$  on the interface. Along with surface pressure  $p_0$ , tangent stress  $\tau_t$  is responsible for formation of a constant stress layer in the WBL.  $\tau_t$  cannot be assimilated in a wave model due to potentiality.

Over the last years, a great attention has been given to the effect of breaking (Babanin 2011). In our opinion, a role of breaking for the air boundary layer is overestimated. A nonlinear dependence of pressure extremes on wave steepness plays a more important role, while the influence of breaking on WBL is just a consequence of that dependence. The breaking is much more important for water; moreover, we were lucky to find that a scheme based on conformal mapping allows a very close approaching to a breaking point. Finally, integration is always terminated in such a case; however, due to high accuracy of the scheme, such modeling of instability represents an example of a unique case in the fluid dynamics when the numerical and physical instabilities follow each other in a very close succession. We use two ways of interpretation of the breaking process. When the breaking process is a subject of investigation per se, it is simulated directly up to the point of instability. The last unrealistic phase of breaking can be easily detected by means of energy conservation control. The final stage of breaking is evidently non-potential. Such direct method is inapplicable when the wave model is used for a long-term coupled simulation in investigation of the WBL structure, wave drag, and energy exchange. For integral *rms* steepness less than 0.09, the breaking instability never occurs. For *rms* steepness of the order of 0.15, the breaking instability occurs immediately—within one peak wave period.

In long-term coupled simulations, the termination is certainly not desirable. This is why an algorithm of the breaking parameterization based on smoothing of the interface was developed. The algorithm (i.e., genetically similar to parameterization of free convection in the atmospheric models) designed to prevent the breaking instability by a highly selective high-frequency smoothing of the interface profile. Plenty of schemes to parameterize that phenomenon were tested, the best of them being based on a simple algorithm (8.3.12)–(8.3.14)

Parameterization of rotational breaking in a potential model allows us to effectively prevent development of real breaking. This scheme does not influence the

solution if the breaking does not develop. We do not consider this algorithm as a final solution of the problem, as it cannot prevent collapse in the cases when the initial steepness or energy is very high. However, for normal steepness of sea waves and for the cases when the growth of local energy occurs relatively slowly, it works well.

## 9.5 The Structure of Surface Pressure Above Solid Waves

The model formulated above was designed for simulation of the periodic regime. Strictly speaking, periodicity is never observed in natural conditions, because the characteristics of wave fields change in time and space under the action of input, dissipation, nonlinear interactions, and due to other causes. A development of waves in sea occurs over large distance of the order of

$$x_e = \beta^{-1} L_p \left( \frac{U^2}{2\pi L_p g} \right)^{1/2} \quad (9.5.1)$$

Here,  $x_e$  is a distance of saturation,  $\beta \propto 10^{-4}$  is a typical value of the wave growth parameter,  $\omega_p$  and  $L_p$  are frequency and wave length in peak of spectrum, and  $U$  is wind velocity. It follows from (9.5.1) that for typical values of  $L_p$ , a quasi-equilibrium regime can be reached over hundreds or thousands of wave lengths. Naturally, a small part of this distance can be considered as quasiperiodic. For longer periods and greater space, we can use a traditional approximate assumption connecting distance  $x_f$  (fetch) and time  $t_f$

$$x_f = t_f U \quad (9.5.2)$$

This assumption was used for simulating a horizontally inhomogeneous flow with the numerical model which is based on periodicity.

The experimental data on distribution of surface pressure above solid (wooden) waves were kindly provided by M. Donelan. The length of waves was equal to 8 cm; the number of waves was 11; the steepness of waves varied from 0.07 to 0.25, while the wind speed was in the range of 1–12 m/s. The surface pressure was recorded through the holes in the wavy plate. The experiment, which we simulate at present, was in fact devoted to the initial development of a boundary layer above the solid wavy surface. In this case, the structure of the boundary layer depends on distance from the initial points or on time—in the periodic mode.

$$\tau_{fin} = n \frac{2\pi L}{U}, \quad (9.5.3)$$

where  $n$  is the number of waves.

It is remarkable that the structure of the boundary layer changed very quickly just above the first wave, and the solutions reached by the end of the integration period  $T_{\text{fin}}$  were not too sensitive to the values of the initial boundary layer height  $H_i$  if it was taken not too small. At values  $H_i = 0$  (which means an absence of internal boundary layer in the initial conditions), a deep minimum of pressure was formed just behind the wave peak. This feature was not observed in a physical experiment. It means that the initial height of the boundary layer should be finite. Finally, we choose 0.5 cm. Because the surface stress (9.2.15) and production of the turbulent energy (9.2.16) were calculated in the same way as for the turbulent flow, the initial growth of internal boundary layer was very fast.

The major uncertainty in reproduction of this experiment was horizontal inhomogeneity. The height of inner  $h_i$  boundary layer was developing according to the law  $h_i \sim v_*$  (with the proportionality coefficient of the order of 1); hence, the value of  $h_i$  reached just several centimeters by 11th wave. During this time, the profile of surface pressure is changing. The simulation of flow was done with the model described in Sect. 9.2. Since the size of waves and the height of boundary layer were small, the parameterization of the turbulence and boundary condition on the surface were modified by taking into account the structure of flow in the viscous sublayer (Monin and Yaglom 1971). These lengthy descriptions are omitted. The calculations show that for complete adjustment of surface pressure to the airflow, the number of waves should be at least ten times as large. This is why we can expect just a qualitative agreement between the measured  $p_{\text{exp}}(x)$  and calculated with model surface pressure  $p_{\text{mod}}(x)$ .

The comparison of  $p_{\text{mod}}$  and  $p_{\text{exp}}$  is given in Fig. 9.1 for different values of wave steepness and wind speed. As shown, a clear qualitative agreement between the simulations and measurements is obvious. Note that such agreement is observed in a broad range of steepness and wind velocity values. A comparison with the experimental data for the range of surface pressure variations characterized by

$$\Delta P = \max(P_s) - \min(P_s) \quad (9.5.4)$$

(where  $P_s$  is surface pressure) is given for 7th and 8th waves (Fig. 9.2). The value of  $\Delta P$  for different experiments varies within the range of 3 decimal orders. As shown, the agreement between the experimental and calculated data is reasonable.

The structure of flow above wave essentially depends on shape of wave. The energy of the wave-produced component of velocity above Stokes wave is larger than that above the harmonic wave of the same amplitude. The trough of Stokes wave is smoother than that of harmonic wave. This is why the positive anomalies of pressure for Stokes wave are much weaker than those above harmonic wave as in Fig. 9.3.

On the contrary, above sharp crests of Stokes wave, the deep negative anomalies are well developed. What is even more important that the minimum of pressure above Stokes wave is more shifted to a downwind slope, which provides higher correlation of pressure with slope, i.e., larger values of momentum and energy fluxes. To illustrate this dependence, 24 versions of runs were made for six values

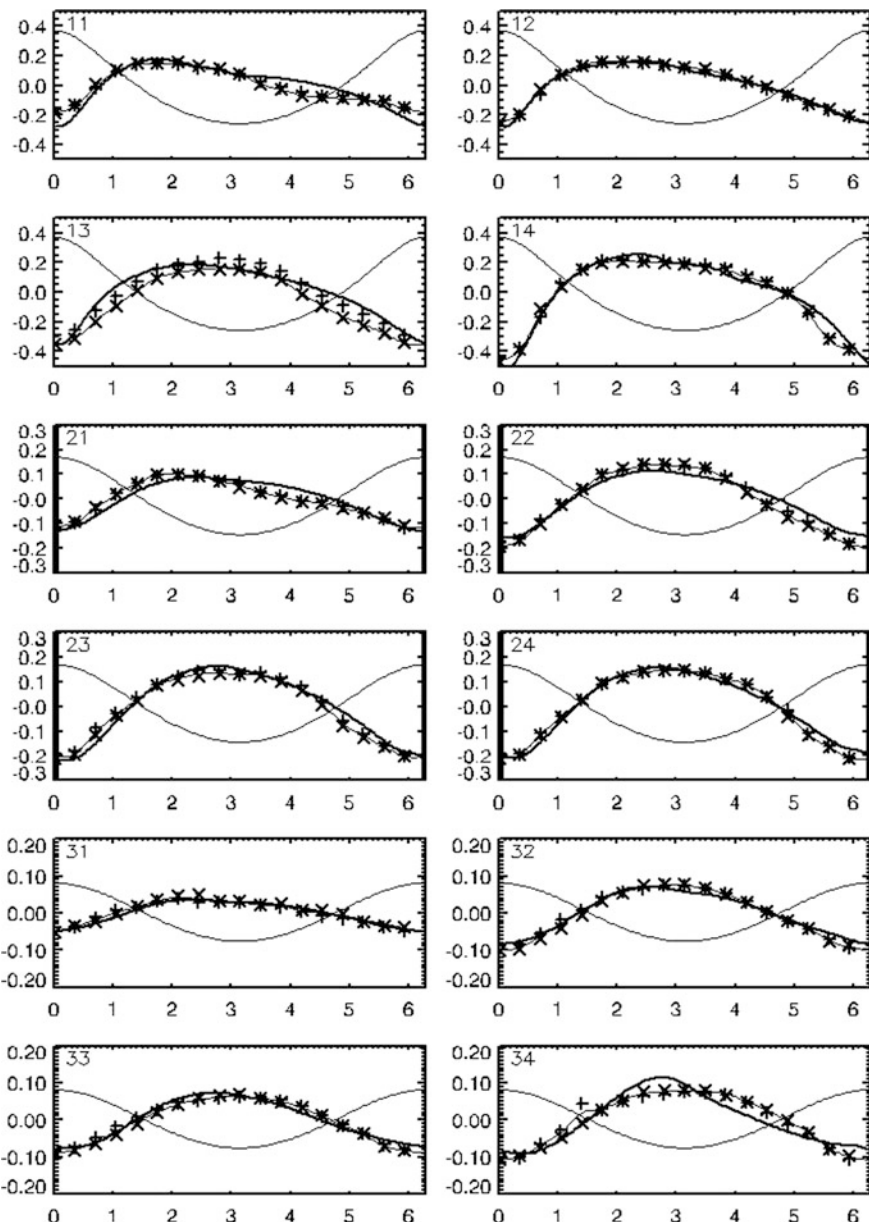


**Fig. 9.1** Comparison of pressure on surface if solid waves: thin curve corresponds the shape of surface, thick curve is pressure calculated with model, and stars correspond to measurements. The panels 11–14 correspond to steepness  $ak = 0.25$  for different wind velocity  $U$ : (11)— $U \approx 1.2$ ; (12)— $U = 5$ ; (13)— $U \approx 8$ ; and (14)— $U \approx 12 \text{ m s}^{-1}$ ; the panels 21–24 correspond to steepness  $ak = 0.14$ ; the panels 31–34 correspond to steepness  $ak = 0.07$ . The wind velocities for panels 21–24 and 31–34 are the same as for panel 11–14. The wind directed from right to left (Chalikov and Rainchik 2014 © 2010 Springer-Verlag Berlin Heidelberg. With permission of Springer)

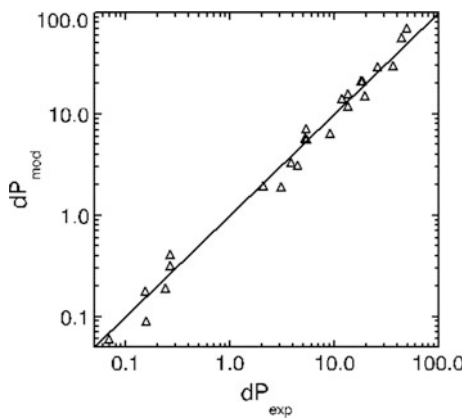


**Fig. 9.2** Comparison of experimental  $dP_{\text{exp}}$  and calculated  $dP_{\text{mod}}$  values of the surface pressure on solid waves (Chalikov and Rainchik 2014 © 2010 Springer-Verlag Berlin Heidelberg. With permission of Springer)

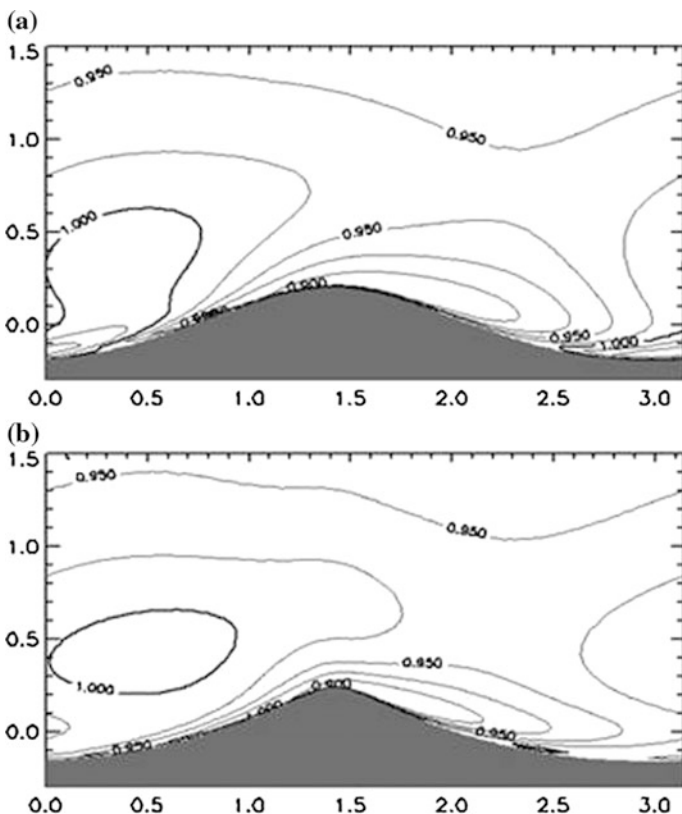
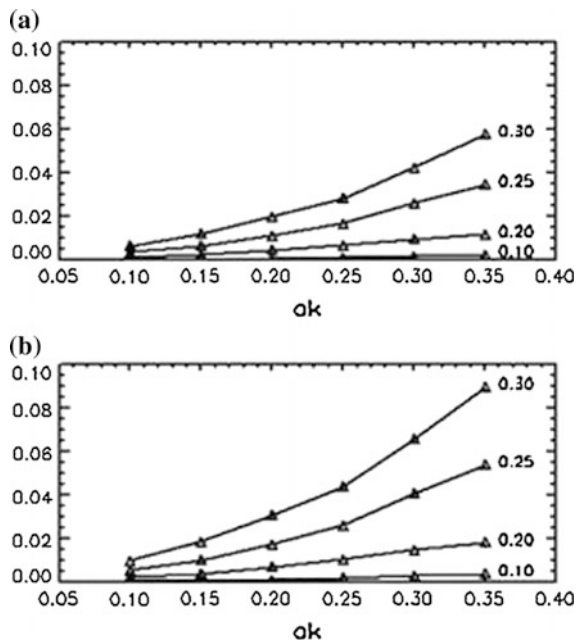


**Fig. 9.3** The distribution of pressure above harmonic wave (a) and Stokes wave (b) (Chalikov and Rainchik 2014 © 2010 Springer-Verlag Berlin Heidelberg. With permission of Springer)

**Fig. 9.4** Averaged over period flux of momentum to wave as function of steepness  $ak$  and friction velocity  $v_*$  (labels on curves).

a Harmonic waves; b Stokes waves (Chalikov and Rainchik 2014 © 2010 Springer-Verlag Berlin Heidelberg. With permission of Springer)



of steepness in the range of 0.10–0.35 for different friction velocities  $v_*(Lg)^{-1/2}$ . The averaged over period momentum flux as a function of steepness and friction velocities for harmonic (panel a) and Stokes (panel b) waves is shown in Fig. 9.4. As shown, the flux energy to Stokes wave exceeds that for the harmonic wave of the same amplitudes 1.5 times.

## 9.6 Description of the Numerical Experiments with the Coupled Model

In this study, the method of approximation of initial conditions by superposition of Stokes waves developed in (Chalikov 2005; see Sect. 5.3) was used. Briefly, the method is based on use of the ‘upper conformal coordinates’ (see Eq. 5.3.2) where  $\zeta > 0(\xi_u, \zeta_u)$ . It was shown that the superposition of linear waves assigned in this coordinate system turns into the superposition of Stokes waves with high accuracy after interpolation to the Cartesian coordinates. Note that full equations at any reasonable initial conditions (after some accommodation period) reproduce this effect too, since harmonic waves tend to turn into Stokes-like waves (see Sect. 6.3). In this chapter, the initial generation of Stokes waves was used to accelerate transition to the statistically homogeneous regime.

In this study, we have applied the above method for numerical simulation of surface waves for investigation of evolution of a wave field assigned with the one-dimensional version of JONSWAP spectrum  $S_f$  (7.2.1) for finite fetches as a function of frequency  $\omega$ .

The best way of modeling of the WBL might be based on a very high spectral resolution for reproduction of large and very small waves including capillary waves. It can be estimated that for such calculations, the number of modes should not be less than 10,000. A high horizontal resolution suggests a high vertical resolution, so the number of levels in the WBL should be about 100, so that the total number of knots would be of the order of 1,000,000. Such calculations are possible to perform but for few cases. This is why a moderate resolution for obtaining rich statistical data on the WBL structure was accepted (see below the description of the numerical experiments). If wave spectrum is not resolved up to a high wave number, the problem of parameterization of subgrid waves is encountered. By analogy with a solid rough surface, we assume that the local roughness parameter  $z_l$  is proportional to *rms*  $h_r$  of ‘rough elements,’ i.e., all subgrid waves:

$$z_l = 0.03 \left( \alpha \int_M^{\infty} k^{-3} dk \right)^{1/2} = 0.0027 k_r^{-1} \quad (9.6.1)$$

Finally, the local drag coefficient in Eq. (9.2.15) can be calculated as follows:

$$C_l = \kappa^2 \left( \ln \frac{z_1}{z_l} \right)^{-2}, \quad (9.6.2)$$

where  $z_1$  is the height of the lowest level.

## 9.7 Evolution of Waves

Figure 9.5 clearly illustrates the essence of the problem being solved.

The above-mentioned figure represents an instantaneous image of interacting flows for the case when an initial wave field is assigned as a superposition of 1000 linear (in the upper coordinate system) wave modes corresponding to the JONSWAP spectrum for the non-dimensional peak frequency  $\Omega = U_{10}/c_p = 2$ . The number of knots over the ‘horizontal’ coordinate  $\zeta$  equals 4000; over the ‘vertical coordinate’  $\zeta$ , the number of levels equals 70; and a stretching parameter  $\gamma$  equals 1.07. In fact, the coupled model simulates a periodic process in a circular wind–wave tunnel, though, with neither wave reflection from the walls nor the centrifugal acceleration. The periodic domain includes 16 peak waves. It is impossible to show the entire domain with length  $L = 2\pi$  and height  $H_a = 0.7$ ;

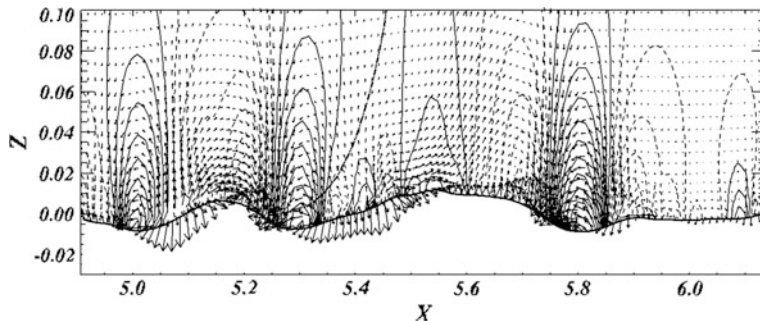


**Fig. 9.5** An example of 2-D flow structure above waves. The contours represent pressure distribution (solid lines correspond to positive values and dashed lines to negative values); arrows are vectors of wave-produced velocity. A small fragment of the reproduced field is drawn: the total height of domain is about 0.7; length equals  $2\pi$  (Chalikov and Rainchik 2010 © 2010 Springer-Verlag Berlin Heidelberg. With permission of Springer)

therefore, Fig. 9.5 shows just a small fragment with the height equal to 0.1 and the length equal to 1.2. The thick periodic curve corresponds to water elevation distorted with dispersing waves. The contours in the air domain represent distribution of pressure (solid lines correspond to positive anomalies, while the dashed ones—to negative anomalies). A smooth curve in the middle of the picture shows the averaged wind profile. The horizontal axis for this curve is  $x - 4.95$ . The wind and waves are directed from left to right. The wind speed at the top edge of the picture equals 0.5. The waves demonstrate a tendency for peak sharpening and trough smoothing. The vectors correspond to the wave-produced velocity field obtained by extraction of the averaged wind profile.

Figure 9.5 shows a wave-produced velocity field. The largest distortions of pressure and velocity fields occur behind wave crests of big waves. In general, the negative anomalies of pressure and high gradients of wave-produced velocities are concentrated in narrow intervals with a high negative steepness of wave surface. Such intervals appear more frequently than those with a high positive steepness; e.g., a wave has a tendency for inclining forward, while a flux of energy depends nonlinearly on the local steepness. The spectral presentation of such pressure becomes less meaningful, since the high-wave number Fourier modes do not correspond to real waves; they rather provide approximation of impulse-like negative anomalies of pressure. Positive anomalies of pressure are distributed more or less smoothly over the areas of positive steepness. On the whole, such pressure field generates a positive flux of momentum from wind to wave.

The main advantage of the mathematical ‘wind–wave channel’ is the possibility of generation of a full set of all kinematic and dynamic fields. It is easy to install any ‘sensor’ for registration and calculations of any statistical and spectral characteristics including high-order moments. The total kinetic and potential energy is defined through the following relations:

$$E_p = (2\pi)^{-1} \int_0^{2\pi} z^2 x_\xi d\xi, \quad E_k = (2\pi)^{-1} \int_0^{2\pi} \varphi \varphi_\xi d\xi, \quad E_t = E_p + E_k. \quad (9.7.1)$$

The rate of total energy exchange between air and waves can be calculated as follows:

$$F_t = \overline{p\eta_\tau} + \overline{\tau'_0 u'_0 x_\xi}, \quad (9.7.2)$$

where the first term describes the work of surface pressure, and the second term—that of tangent stress. In general, a flux of energy is directed from wind to waves; however, in some cases, when a wave spectrum includes a swell which phase velocity is higher than the wind speed, the energy is directed from waves to wind (e.g., waves accelerate wind). Such waves are always present in a wind–wave spectrum, though the effect of the inverse flux of energy in a low-frequency spectral range is insignificant.

An integral rate of dissipation of kinetic  $D_k$  and potential  $D_p$  energy is calculated with the use of:

$$D_k = \overline{\eta(\eta_\tau)_d}, \quad D_p = \overline{\varphi(\varphi_\tau)_d}, \quad D = D_k + D_p, \quad (9.7.3)$$

where  $(\eta_\tau)_d$  and  $(\varphi_\tau)_d$  are the sum of dissipation terms. Equation (9.7.3) includes ‘dissipation’ (2.3.4)–(2.3.6), describing a flux of energy into subgrid wave numbers, and a breaking dissipation described with the algorithm (8.3.14). Note that wave profiles often do not contain any intervals affected by breaking; however, dissipation due to breaking (when it does occur) is normally greater by orders comparing to the ‘tail dissipation.’

The evolution of wave energy, input and dissipation of energy for initial conditions assigned by JONSWAP spectrum at  $\Omega_p = 2$ , is shown in Fig. 9.6

The wave field in this run was initially represented by 100 wave modes with  $k_p = 16$  and  $M = 1000$ . The wave energy increases under the action of wind. In panel *a*, the evolution of potential  $E_p$  (a thin curve), kinetic  $E_k$  (a dotted curve) and total  $E_t = 0.5(E_p + E_k)$  (a thick curve) energy (see Eq. 9.7.1) for the last 30 peak wave periods is represented. The potential and kinetic energy averaged over the period  $(0, 2\pi)$  quickly fluctuates, but these fluctuations are not pronounced for the sum  $E_t$ . The energy input to waves (panel *b*, a solid curve) also fluctuates due to the variable wave steepness that is represented in frame *b* by the highest absolute value of steepness in every instantaneous wave profile. In most cases, the negative steepness is stronger than the positive one, as the waves are asymmetric. That is why the steepness in panel *c* is taken with an opposite sign. As shown, enhancing of input and dissipation correlates with steepness. Such fluctuations cannot be explained on the basis of the linear theory. Frame *d* shows the same evolution over

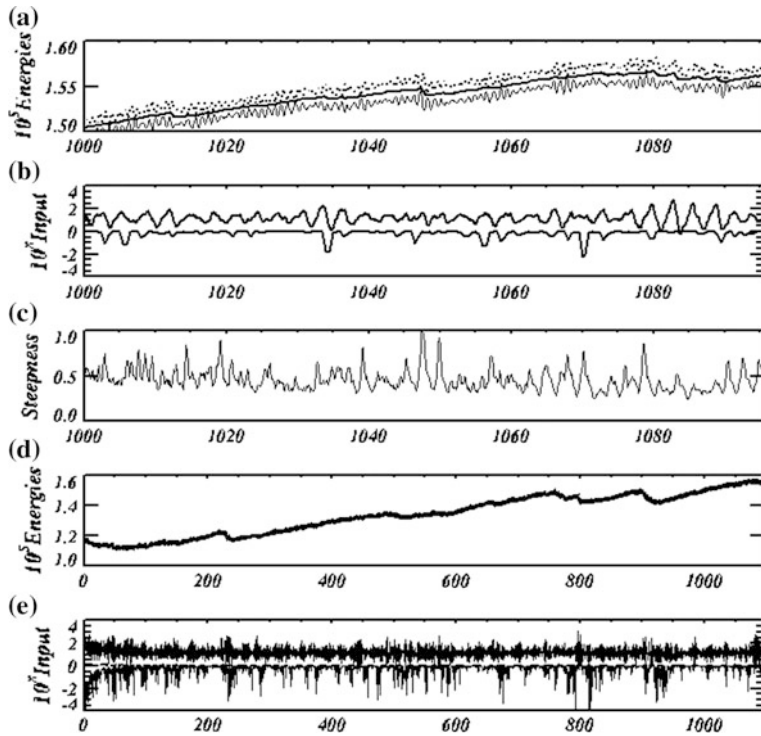


**Fig. 9.6** **a** Evolution of potential  $E_p$  (thin curve), kinetic  $E_k$  (dotted curve), and total  $E_t = 0.5(E_p + E_k)$  (thick curve) energies (Eq. 9.7.1) over the last 30 peak wave periods; **b** evolution of input (upper curve, Eq. 9.7.2) and dissipation  $D$  (lower curve, Eq. 9.7.3) of energy for the same period; **c** evolution of the highest steepness (with an opposite sign) in a wave profile; **d** evolution of energy over the total interval of integration (about 370 periods of peak wave periods). In this frame, the curves for  $E_p$ ,  $E_k$ , and  $E_t$  merge; **e** evolution of the total input (upper curve) and dissipation (lower curve) for the same period (Chalikov and Rainchik 2010 © 2010 Springer-Verlag Berlin Heidelberg. With permission of Springer)

the total interval of integration (about 370 periods of peak wave periods). In the above frame, the curves for  $E_p$ ,  $E_k$ , and  $E_t$  merge into one thick line. The bottom frame **d** shows evolution of the total input of energy (an upper quickly fluctuating curve) and its dissipation (a bottom curve). A dashed straight line close to a zero line corresponds to input of energy to waves through tangent stress that is much smaller than the input provided by the pressure field. The input of energy is strongly intermittent. Such intermittence occurs as the input depends not on the spectrum (that fluctuates slowly in the energy-containing part), but on geometry of surface in a physical space.

## 9.8 Wave-Produced Momentum Flux (WPMF)

The main difference between the WBL and a boundary layer above flat surface is the presence of a moving curvilinear interface between water and air. In linear theories, such finite-amplitude fluctuations of the interface are actually ignored; however, in mathematical simulations, such an approach is unacceptable. Numerical modeling of a boundary layer and waves is impossible to carry out in the Cartesian coordinate system, which is the main reason to introduce the surface-following coordinates. The dynamic equations in curvilinear coordinates are more complicated compared with those in a standard form. Anyway, in a 2-D case, it is possible to introduce the conformal coordinates. The equations written in those coordinates are not simple yet, however, they are much simpler comparing to those in general curvilinear coordinates. Moreover, the equations written in such coordinates can be easily interpreted. The main advantage of surface-following coordinates (9.2.3) is that water and air domains are separated by a coordinate surface  $\zeta = 0$ . The natural boundary condition above a flat surface is  $w = 0$  at  $z = 0$ . In conformal coordinates, the ‘vertical’ contravariant velocity acquires a role of the vertical velocity  $W$ . Since a kinematic condition on the surface is  $W = 0$ , it means that an exchange of finite volumes through the interface is absent.

Let us average the equation for horizontal momentum (5) over a coordinate  $\zeta = \text{const}$

$$\frac{\partial \langle Ju \rangle}{\partial t} = \frac{\partial}{\partial z} \left( -\langle uW \rangle + \langle pz_\zeta \rangle + \langle -z_\zeta \bar{u}' \bar{u}' + x_\zeta \bar{u}' \bar{w}' \rangle + \langle \bar{u}' \bar{w}' \rangle \right) \quad (9.8.1)$$

(I)	(II)	(III)	(IV)
-----	------	-------	------

This is the equation of a horizontal momentum balance. Since  $\langle \zeta \rangle = z$  and  $\langle \partial/\partial\zeta \rangle = \partial/\partial z$ , Eq. (9.8.1) can be considered as written in the Cartesian coordinate system.

A rate of change of momentum depends on the vertical divergence of a vertical momentum flux provided by: wave-produced velocities (I), pressure (II), fluctuations of stresses (III), and an averaged turbulent flux (IV). Equation (9.8.1) is similar to the standard equation of momentum balance above a flat surface:

$$\frac{\partial u}{\partial \tau} = \frac{\partial \langle u' w' \rangle}{\partial z}. \quad (9.8.2)$$

However, Eq. (9.8.1) takes into account additional mechanisms of a vertical momentum transport. Note that contrary to (9.8.2) averaging in (9.8.1) is performed along the curvilinear paths. Such type of averaging is suitable in the presence of a curvilinear surface, as a surface kinematic condition  $W = 0$  at  $\zeta = 0$ . Eq. (9.8.2) makes no sense for the case with a curvilinear boundary, since Eq. (9.8.2) can be obtained by averaging beyond the highest elevation in ensemble. Through the

interface, the momentum is transferred by pressure field and tangent stresses. As the wave model is potential, it cannot assimilate the tangent stress; therefore, waves obtain energy mostly through a surface pressure field.

At present, very large number of 1-D models are known. All of them are invented (not derived but just written ‘ad hoc’) in Cartesian coordinate system, so the main specifics of WBL (splitting of momentum flux into separate branches) cannot be represented (see, e.g., Belcher and Hunt 1993; Belcher et al. 1994; Kudryavtsev et al. 1999; Makin and Kudryavtsev 1999). As a whole, the equation used turns out to be too simple to be useful. It is surprisingly that these ‘equations’ are used then for investigation of very complicated problems: influence of wave breaking, sea swell, drops in air, and bubbles in sea. On our opinion, any attempts to derive the one-dimensional equation for WBL in Cartesian coordinate system are fruitless.

For investigation of a vertical structure of the WBL, the results of the long run described in the previous section were used. The instantaneous wave-produced fluctuations of pressure have an irregular structure; however, being averaged over time, they exhibit distinct regularities. The averaged vertical profiles of the spectral component for pressure  $P_k$  are shown in the upper panel of Fig. 9.7.

As shown, pressure spectrum decays exponentially with height. After normalizing of each profile by a surface value and introducing of a non-dimensional vertical coordinate  $k_z$ , the profiles of  $P_k$  become more or less universal and can be approximated through the following relation:

**Fig. 9.7** Spectral structure of pressure field. *Upper panel* vertical profiles of Fourier amplitudes for pressure  $P_k$ . *Bottom panel* vertical profiles of pressure Fourier amplitudes, normalized their surface value  $P_{0k}$  as a function of non-dimensional height  $k_z$  (Chalikov and Rainchik 2010 © 2010 Springer-Verlag Berlin Heidelberg. With permission of Springer)

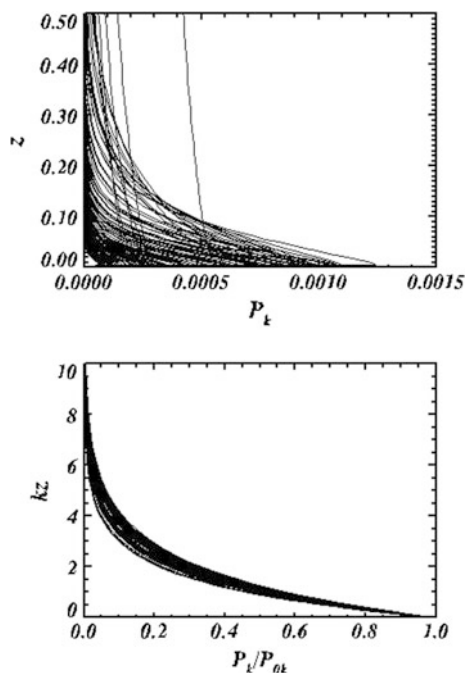
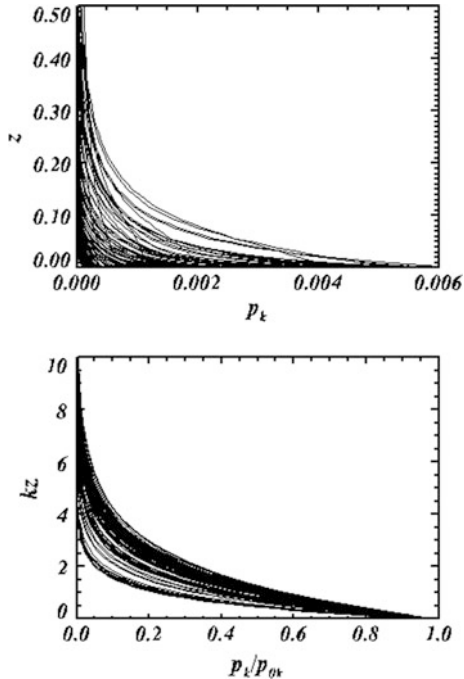


**Fig. 9.8** Spectral structure of a wave-produced velocity field. *Upper panel* vertical profiles of Fourier components for kinetic energy of the wave-produced velocity field. *Bottom panel* the same Fourier components normalized by surface value as a function of non-dimensional height  $kz$ .  
 (Chalikov and Rainchik 2010)  
 © 2010 Springer-Verlag Berlin Heidelberg. With permission of Springer)



$$P_k = P_{0k} \exp(-A_p kz), \quad (9.8.3)$$

where  $P_{0k}$  is a surface value of  $P_k$  and  $A_p$  is a decrement falling within a  $0.6 < A_p < 0.7$  range. Hence, pressure fluctuations in a turbulent flow attenuate slower, compared with those in potential waves. The spectrum of kinetic energy of wave-produced velocity fluctuations demonstrates similar behavior (see Fig. 9.8) with the decrement  $A_e$  varying in the range of  $0.6 < A_e < 1.0$ .

An example of surface pressure spectrum is shown in Fig. 9.9 (curve 2) where a spectrum of elevation (curve 1) and a spectrum of near-surface kinetic energy (curve 3) are also represented.

The spectrum of near-surface kinetic energy attenuates slower with increase of wave number than the wave spectrum. It is interesting to note that the maximum of surface pressure spectrum is shifted from the maximum of wave spectrum to higher wave numbers. It is located at the maximum of spectral steepness  $S_k$  (curve 4) defined by the following expression:

$$S_k = k \sqrt{S_k \Delta k}, \quad (9.8.4)$$

where  $k$  is a wave number,  $S_k$ —values of wave spectrum, and  $\Delta k = 1$ . Hence, the anomalies of surface pressure depend rather on steepness than on wave amplitudes.

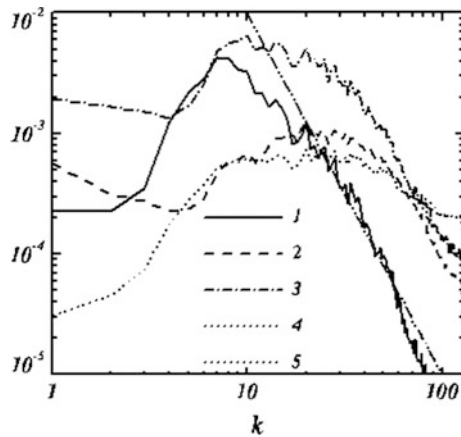


**Fig. 9.9** Typical spectra of: surface elevation—curve 1, surface pressure—curve 2, surface kinetic energy—curve 3, spectral steepness—curve 4, Eq. (9.8.4) (Chalikov and Rainchik 2010 © 2010 Springer-Verlag Berlin Heidelberg. With permission of Springer)

Different components of a vertical momentum flux (Eq. 9.8.1) normalized by an outer stress  $\tau$  are given in Fig. 9.10 as a function of  $z/L_p$  ( $L_p = 2\pi/K_p$ ).

The aggregated gray lines are instantaneous profiles, while the solid lines are the averaged profiles. As shown, all of the components of the WPMF are concentrated in the vicinity of surface in a layer with the thickness of the order of  $0.2L_p$ . The averaged turbulent momentum flux  $F_a$  (term IV in Eq. 9.8.1) transfers momentum

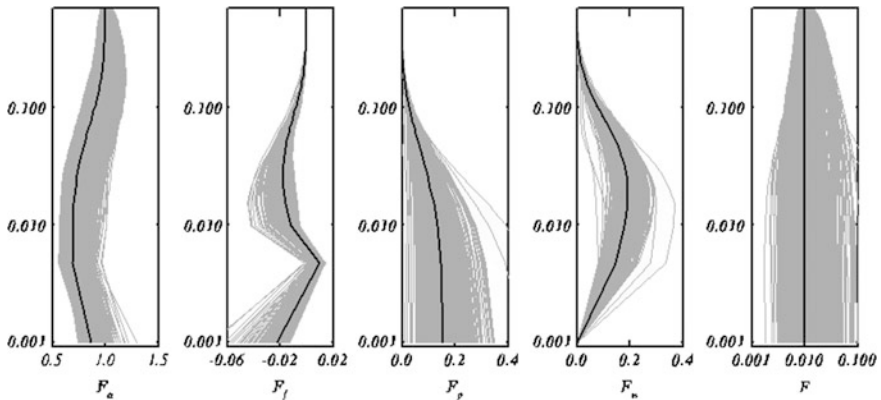


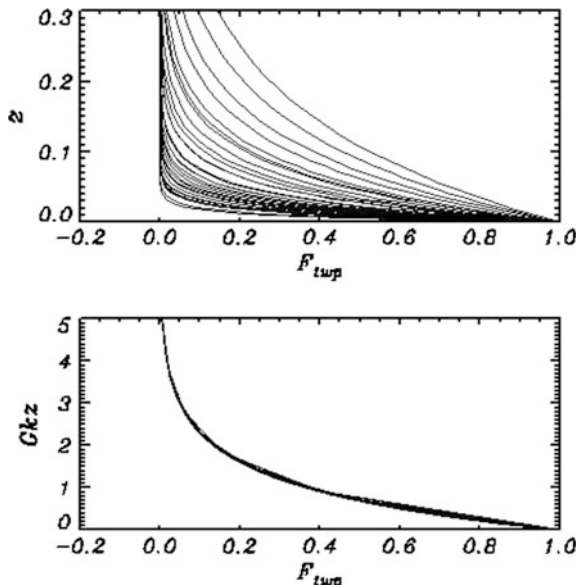
**Fig. 9.10** Different components of vertical momentum flux as a function of  $z/L_p$  normalized by the outer stress  $\tau$ . Aggregated gray lines are instantaneous profiles; solid lines are averaged profiles:  $F_a$ —an averaged turbulent momentum flux (0th mode);  $F_f$ —momentum flux provided by wave fluctuations of turbulent stresses;  $F_p$ —momentum flux provided by pressure field;  $F_w$ —momentum flux provided by velocity field;  $F$ —the total momentum flux (Chalikov and Rainchik 2010 © 2010 Springer-Verlag Berlin Heidelberg. With permission of Springer)

to the averaged flow in water (drift currents).  $F_a$  reaches the minimum value  $0.7\tau$  at height  $z = 0.01L_p$  and equals  $0.9\tau$  on the surface. Hence, in this case, only 10 % of the total stress is transferred to waves. A flux of momentum transferred by fluctuating turbulent stresses  $F_f$  (term III in Eq. 9.8.1) is quite insignificant, which means that correlation between a tangent surface stress and a tangent component of an orbital velocity is weak. Pressure transfers the main part of the momentum to waves  $F_p$  (term II in Eq. 9.8.1). In the case under consideration, this flux monotonically increases approaching the surface where it reaches the value of  $0.2\tau$ . However, it should be emphasized that the surface value of  $F_p$  depends on spectral resolution (see Sect. 9.10 below). With increase of cut frequency, this value grows approaching the total stress  $\tau$ . The flux of momentum transferred by the velocity field  $F_u$  (term I in Eq. 9.8.1) reaches the maximum at height  $z/L_p \approx 0.1$ , then decreases approaching the surface, and it is strictly equal to zero on the surface due to the surface kinematic condition.

Let us define the  $k$ th spectral component of a WPMF  $\tau_w^k$  as the Fourier component of the total momentum flux to waves, e.g., the sum of I, II, and III terms in Eq. (9.8.1). The averaged profiles of spectral components of the WPMF calculated over the entire run described above are shown as a function of  $z$  in Fig. 9.11.

As shown, the shapes of those profiles considerably depend on a wave number. These data can be regularized by normalizing with a surface value of  $\tau_w^k$  and by introducing a non-dimensional wave height  $Gk_z$  in the same way as it was done with the data shown in Figs. 9.7 and 9.8. After such transformation, profiles of the  $\tau_w^k$  look like the profiles in the bottom panel of Fig. 9.7. However, such regularization can be much more precise when introducing the following dependence:

**Fig. 9.11** The upper panel vertical profiles of the total WPMF as a function of  $z$ ; lower panel the same profiles but normalized by surface values as a function of  $Gk_z$  (Eq. 9.8.5) (Chalikov and Rainchik 2010 © 2010 Springer-Verlag Berlin Heidelberg. With permission of Springer)



$$\tau_w^k = \tau_{w0}^k \exp(Gkz), \quad (9.8.5)$$

where  $G$  is a weak function of  $\tilde{\omega} = \Omega/\Omega_p$ :

$$G = 0.985 + 0.4(\tilde{\omega})^{0.81}, \quad (9.8.6)$$

Note that  $\tilde{\omega}$  is also equal to the ratio of dimensional frequencies  $\omega$  and  $\omega_p$ .

Spectral components of the profiles of  $\tau_w/\tau_{w0}$  as a function of  $Gkz$  are shown in the lower panel in Fig. 9.11. As shown, Formula (9.8.5) provides satisfactory parameterization of a vertical profile of the WPMF spectral components. Note that the results discussed below do not change significantly, when function  $G(\tilde{\omega})$  is replaced by a constant.

## 9.9 Evaluation of $\beta$ -Function

According to the linear theory, the Fourier components of surface pressure  $p_0$  are connected with a surface elevation through the following expression:

$$p_k + ip_{-k} = (\beta_k + i\beta_{-k})(h_k + ih_{-k}), \quad (9.9.1)$$

where  $\beta_k$  and  $\beta_{-k}$  are the so-called real and imaginary parts of  $\beta$ -function (e.g., Fourier coefficients at COS and SIN respectively). It is traditional suggestion that both coefficients of  $\beta$  are functions of non-dimensional frequency  $\Omega = \omega_k U$  (where  $U$  is a non-dimensional wind velocity). It would be reasonable to suggest that a wind velocity value might be different for different frequencies; hence, the non-dimensional frequency  $\Omega$  could be defined in the following way:

$$\Omega = \omega_k U(\lambda_k/2) = U(\lambda_k/2)/c_k \quad (9.9.2)$$

where  $\omega_k = |k|^{1/2}$  is a non-dimensional frequency,  $c_k$  is a phase velocity of  $k$ th mode and  $U$  is a non-dimensional wind velocity at height  $\zeta = \lambda_k/2$ , where  $\lambda_k = 2\pi/k$  is a length of  $k$ th mode.

One of the main goals of this paper was evaluation of function  $\beta$  in a wide range of non-dimensional frequency  $\Omega$ . For such purposes, forty-seven long-term (up to several hundred peak wave periods) numerical runs with a different wind velocity and spectral resolution were performed using the coupled wind–wave model (see Table 9.1). The wind velocity was assigned through different values of wind stress  $\tau = v_*|v_*|$  at the upper level directed along and against the general direction of waves. The main characteristics of the runs are indicated in Table 9.1. A stretching coefficient for a vertical grid  $\gamma$  was chosen equal to 1.07 (for large wind), while some of the experiments were repeated with  $\gamma = 1.05$  and even with  $\gamma = 1.01$ . A peak of spectrum was usually placed at wave number  $k_p = 4$ ; however, the runs

**Table 9.1** Parameters of runs

No.	$v_*$	$\Omega_p$	$\Omega_{\min}$	$\Omega_{\max}$	$T_p$	$\gamma$	$k_p$
1	-0.50	-28.75	-48.97	-10.65	57.3	1.07	16
2	-0.40	-24.78	-43.64	-8.97	89.1	1.07	16
3	-0.30	-20.31	-37.04	-7.16	12.7	1.07	16
4	-0.30	-20.31	-37.04	-7.16	19.1	1.07	16
5	-0.20	-8.97	-28.75	-5.18	127.3	1.07	4
6	-0.15	-7.16	-23.72	-4.10	127.3	1.07	4
7	-0.10	-5.18	-17.84	-2.94	222.8	1.07	4
8	-0.10	-5.18	-17.84	-1.64	79.6	1.07	4
9	-0.05	-2.94	-10.65	-1.64	95.5	1.07	4
10	-0.0125	-0.91	-3.53	-0.50	95.5	1.07	4
11	-0.00625	-0.50	-1.98	-0.27	12.7	1.07	4
12	-0.00313	-0.27	-1.10	-0.15	87.5	1.07	4
13	0.00313	0.27	0.15	1.10	76.4	1.07	4
14	0.00625	0.50	0.27	1.98	103.5	1.07	4
15	0.0125	0.91	0.50	3.53	350.1	1.07	4
16	0.025	1.64	0.91	6.19	159.2	1.07	4
17	0.05	2.94	1.64	10.65	127.3	1.07	4
18	0.05	2.94	1.64	10.65	127.3	1.05	4
19	0.08	4.10	2.31	14.46	127.3	1.07	4
20	0.10	5.18	2.94	17.84	127.3	1.07	4
21	0.10	5.18	2.94	17.84	222.8	1.05	4
22	0.13	6.19	3.53	20.91	159.2	1.07	4
23	0.10	6.83	2.94	17.84	495.2	1.01	8
24	0.15	7.16	4.10	23.72	159.2	1.07	4
25	0.15	7.16	4.10	23.72	127.3	1.05	4
26	0.20	5.18	5.18	28.75	143.2	1.07	4
27	0.20	5.18	5.18	28.75	127.3	1.05	4
28	0.15	9.39	4.10	23.72	117.0	1.01	8
29	0.25	10.65	6.19	33.15	39.8	1.07	4
30	0.25	10.65	6.19	33.15	12.7	1.05	4
31	0.30	12.24	7.16	37.04	82.8	1.07	4
32	0.30	12.24	7.16	37.04	57.3	1.05	4
33	0.35	13.74	8.08	40.52	82.8	1.07	4
34	0.35	13.74	8.08	40.52	82.8	1.05	4
35	0.40	15.16	8.97	43.64	70.0	1.07	4
36	0.40	15.16	8.97	43.64	95.5	1.05	4
37	0.20	15.16	5.18	28.75	12.7	1.07	16
38	0.20	15.16	5.18	28.75	22.3	1.07	16
39	0.45	16.53	9.82	46.44	82.8	1.07	4
40	0.45	16.53	9.82	46.44	55.7	1.05	4

(continued)

**Table 9.1** (continued)

41	0.50	17.84	10.65	48.97	54.1	1.07	4
42	0.50	17.84	10.65	48.97	63.7	1.05	4
43	0.55	19.10	11.46	51.24	71.6	1.05	4
44	0.60	20.31	12.24	53.29	79.6	1.07	4
45	0.40	24.78	8.97	43.64	19.1	1.07	16
46	0.50	28.75	10.65	48.97	15.6	1.07	16
47	0.50	28.75	10.65	48.97	95.5	1.07	16

$v_*$ —friction velocity;  $\Omega_p = u(\lambda_k/2)/c_p$ ;  $(\Omega_{\min}, \Omega_{\max})$  is a range of  $\Omega_k$  covered by run,  $T_p$ —length of run (expressed in peak wave periods);  $\gamma$ —stretching coefficient for vertical grid; and  $k_p$ —peak wave number

29 and 30 were carried out with  $k_p = 8$ , and the runs 36–44—with  $k_p = 16$ . The total number of modes  $M$  was normally equal to 100, while some runs intended for validation of the results were repeated with  $M = 200$ ,  $M = 1000$ , and  $M = 2000$ .

It should be noted that though the algorithm of breaking parameterization (38) and (39) was activated, most of the runs lapsed due to a breaking instability that occurs following the approach of a downwind slope to vertical. To resume another run in the automatic mode, a criterion for run termination was defined as the first appearance of a non-single value of surface  $\eta$  in the Cartesian coordinates (see Eq. 6.1.1). It is important that after the moment when the criterion (6.1.1) has been reached, the solution never returns to stability: The volume of fluid crossing the vertical  $x(i)$  quickly increases. Overturning always started at the crest of the steepest wave. When a wave starts to overturn at the initial stage of the evolution, the conservation of invariants remains good; however, later, a sharp increase of energy occurs, and further integration becomes senseless. The numerical instability exhibiting itself in breaking has a physical origin: Actually, a falling water volume becomes rotational and splits into small patterns (i.e., a whitecapping phenomenon).

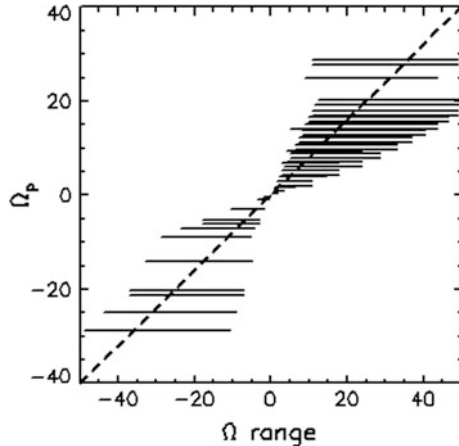
Strengthening of stability can be achieved by increase of  $C_b$  value and decrease of  $s$  value in Eq. (8.3.14); however, in this case, sharp wave crests become smoother, which weakens dynamic interaction between wind and waves. That is why a relatively soft smoothing is chosen. Note that local breaking occurs for some unpredictable reason, and duration of a run ( $T_p$  in Table 9.1, expressed in periods of peak wave) is found to be dependent even on a set of initial phases for waves.

Each run performed for different  $\Omega_p$  provided data required for the calculation of  $\beta(\Omega)$  within the interval  $[\Omega_{\min}, \Omega_{\max}]$  (see Table 9.1). The intervals are shown in Fig. 9.12 by straight lines. A vertical axis corresponds to  $\Omega_p$ , and the lines are stratified as rows in Table 9.1.

As shown, the data cover the interval  $-50 < \Omega < 50$ . Shortening of lines approaching  $\Omega = 0$  does not mean that the intervals contain less data. Such effect is caused by nonlinearity of dispersion relation  $k = \omega^2$ .

The total number of 1-D records of wave surface (each containing 400 points) was equal to 27,802. After the Fourier transform of each of those records, the first 50 complex Fourier coefficients for  $p_0$  and  $\eta$  were used for calculations of

**Fig. 9.12** Ranges of non-dimensional frequencies  $\Omega$  covered by the numerical experiments: the *lower line* corresponds to the *top line* in Table 9.1, while the *topmost line*—to the *last line* in Table 9.1 (Chalikov and Rainchik 2010 © 2010 Springer-Verlag Berlin Heidelberg. With permission of Springer)



$\beta$ -function. The total number of points falling within the interval  $-50 < \Omega < 50$  was equal to 1,390,100. For estimation of  $\beta$  values, the above interval was separated into 100 bins with the width of  $\delta\Omega = 0.1$ . The number of points falling within each interval was roughly the same—around 1400.

The generation of a great volume of data was necessary, since the  $\beta$ -function values have a considerable scatter. The one-point value of real  $\beta_k^i$  and imaginary  $\beta_{-k}^i$  parts of  $\beta$ -function can be calculated through the Fourier coefficients for  $p_0$  and  $\eta$ :

$$\beta_k^i = |\eta_k^i|^{-2} (p_k^i \eta_k^i + p_{-k}^i \eta_{-k}^i), \quad \beta_{-k}^i = |\eta_k^i|^{-2} (p_{-k}^i \eta_k^i + p_k^i \eta_{-k}^i), \quad (9.9.3)$$

while the averaged values of  $\beta_k$  and  $\beta_{-k}$  were calculated in each bin using *rms* method:

$$\beta_k = \sum_1^{N_i} \left( |\eta_k^i|^{-2} (p_k^i \eta_k^i - p_{-k}^i \eta_{-k}^i) \right) \left( \sum_1^{N_i} |\eta_k^i|^4 \right)^{-1}, \quad (9.9.4)$$

$$\beta_{-k} = \sum_1^{N_i} \left( |\eta_k^i|^{-2} (p_{-k}^i \eta_k^i - p_k^i \eta_{-k}^i) \right) \left( \sum_1^{N_i} |\eta_k^i|^4 \right)^{-1}, \quad (9.9.5)$$

where  $N_i$  is the number of points falling in each  $i$ th bin. Dispersion of coefficients for  $\beta$ -function is calculated as follows:

$$\sigma_k = \left( N_i^{-1} \sum_1^{N_i} (\beta_k^i)^2 - \beta_k^2 \right)^{1/2}, \quad \sigma_{-k} = \left( N_i^{-1} \sum_1^{N_i} (\beta_{-k}^i)^2 - \beta_{-k}^2 \right)^{1/2} \quad (9.9.6)$$

$\beta$  (a vertical axis) as a function of  $\Omega$  (horizontal axis) is drawn in Fig. 9.13 for three intervals  $-50 < \Omega < 50$ ,  $-10 < \Omega < 10$  and  $-2 < \Omega < 2$ . A thick line (white—

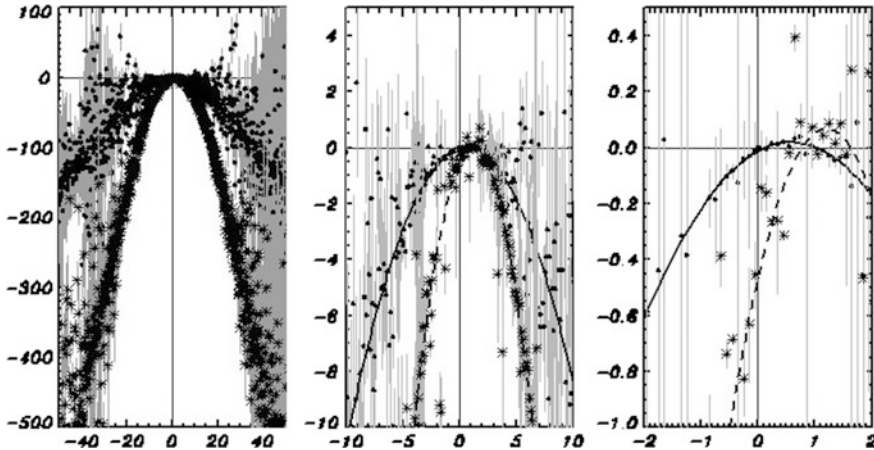


**Fig. 9.13** The left frame  $\beta$  as a function of  $\Omega$ . Thick lines (white in the left frame) correspond to  $\beta_i$  and dashed line  $\beta_r$ . The sign + indicates mean values in the bins, while gray lines are dispersion. The two other frames show the twice zoomed  $\beta$ -function (Chalikov and Rainchik 2010 © 2010 Springer-Verlag Berlin Heidelberg. With permission of Springer)

in the left frame) corresponds to  $\beta_i$ ; a dashed line corresponds to  $\beta_r$ . The sign + indicates mean values, while gray vertical lines show dispersion.

As shown, the data on  $\beta$  have a very wide scatter, as if they were obtained from the experimental data. It will be shown later that such a scatter has a deep physical nature. However, the volume of data is so big that the shape of  $\beta$ -function, especially for the range of  $-20 < \Omega < 20$ , can be determined with satisfactory accuracy. The function  $\beta$  can be approximated through the following expression:

$$\beta_{-k} = \begin{cases} b_1 + d_1(\Omega - \Omega_1) & \Omega < \Omega_1 \\ b_0 + a_0(\Omega - \Omega_0) + a_1(\Omega - \Omega_0)^2 & \Omega_1 \geq \Omega < \Omega_2 \\ b_2 + d_2(\Omega - \Omega_2) & \Omega \geq \Omega_2 \end{cases} \quad (9.9.7)$$

$$\beta_k = \begin{cases} b_3 + d_3(\Omega - \Omega_4) & \Omega < \Omega_4 \\ b_4 + a_2(\Omega - \Omega_3)^2 & \Omega_4 \geq \Omega < \Omega_5 \\ b_5 - d_3(\Omega - \Omega_5) & \Omega \geq \Omega_5 \end{cases}$$

where the numerical parameters are as follows:

$$\begin{aligned} \Omega_0 &= 0.7, \Omega_1 = -19.3, \Omega_2 = 20.7, \Omega_3 = 1.2, \Omega_4 = -18.8, \Omega_5 = 21.2, \\ a_0 &= 0.02277, a_1 = 0.09476, a_2 = -0.3718, b_0 = -0.02, b_1 = 37.43, b_2 = 38.34, \\ b_3 &= -141.0, b_4 = 0.07, d_1 = -3.768, d_2 = 3.813, d_3 = 14.80 \end{aligned} \quad (9.9.8)$$

The function  $\beta$  is used for calculation of momentum  $\mathbf{F}$  and energy  $E$  flux in the spectral interval  $\Delta\omega$ :

$$\mathbf{F}(\omega) = g\mathbf{k}\beta_{-k}(\Omega)S(\omega)\Delta\omega, \quad E(\omega) = g\omega\beta_{-k}(\Omega)S(\omega)\Delta\omega \quad (9.9.9)$$

Here  $\mathbf{k}$  and  $\omega$  are a *dimensional* wave number and frequency, respectively, and  $S$  is *dimensional* spectral density. The relations (9.9.9) were suggested in a small-amplitude theory. Applicability of Eq. (9.9.1) for finite-amplitude waves has never been discussed. Note that an equation for the spectral energy flux  $E(\omega)$  is obtained from the equation for the spectral momentum flux  $F(\omega)$  using dispersion relation  $\omega = \sqrt{gk}$ . For low wave numbers, the dispersion relation is valid, while for high-frequency waves, a connection between wave number and wave frequency is actually absent (Chalikov 2005); hence, the flux of energy to high-frequency waves should be the subject of special investigation.

For validation of function  $\beta$ , the data obtained in additional runs were used. The runs were carried out for different values of the initial steepness  $S_t$  defined in the following way:

$$S_t = \left( \sum_1^M k^2 |\eta_k|^2 \right)^{1/2} \quad (9.9.10)$$

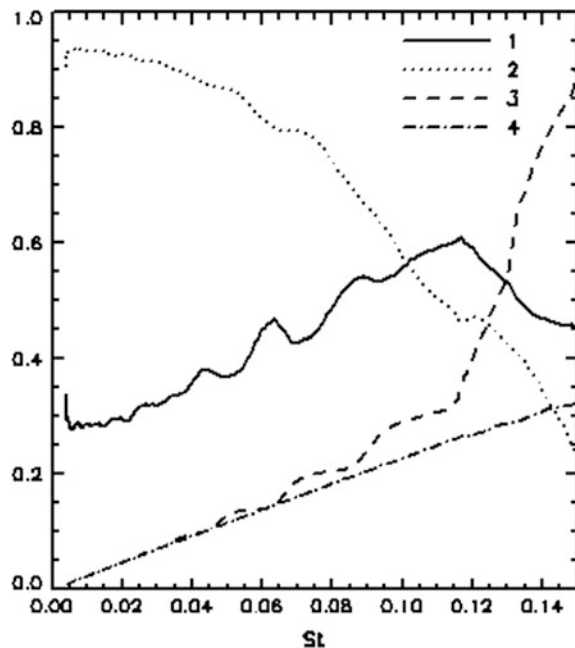
Note that in general,  $S_t$  cannot serve as an indicator of steepness, since the integral of  $k^2 S$  diverges at  $S \sim \omega^{-5}$ . Here, we use a parameter  $S_t$  only for comparison of different runs. For calculations, 396 runs with  $S_t$  changing within the range of 0.005–0.15 were used. The non-dimensional *rms* error of the pressure calculated through  $\beta$ -function  $p_b$ , as compared with the pressure calculated with the model, was obtained. The error is normalized by dispersion of anomalies of the ‘true’ (e.g.,  $p_0$ ) pressure:

$$e_1 = \frac{|p_0 - p_b|}{\left( \overline{p_0^2} \right)^{1/2}}. \quad (9.9.11)$$

The dependence of  $e_1$  on  $S_t$  is shown in Fig. 9.14 by curve 1. The error is growing until it reaches the value of  $S_t = 0.12$ ; then it decreases, since the dispersion of pressure grows faster than the error. It should be noted that approximation (9.9.7) is not intended for calculation of the energy flux (or input flux) to the individual wave modes up to high frequencies.

The dependence of the correlation coefficient  $r(p_0, p_b)$  on steepness  $S_t$  is shown in Fig. 9.14 by curve 2. Both of the characteristics show that a good agreement between the ‘true’ pressure and that restored with  $\beta$ -function exists only for small and medium steepness. For medium steepness  $S_t = 0.1$ , the correlation is about 0.7, which makes the method of flux calculation (9.9.9) still acceptable. For higher

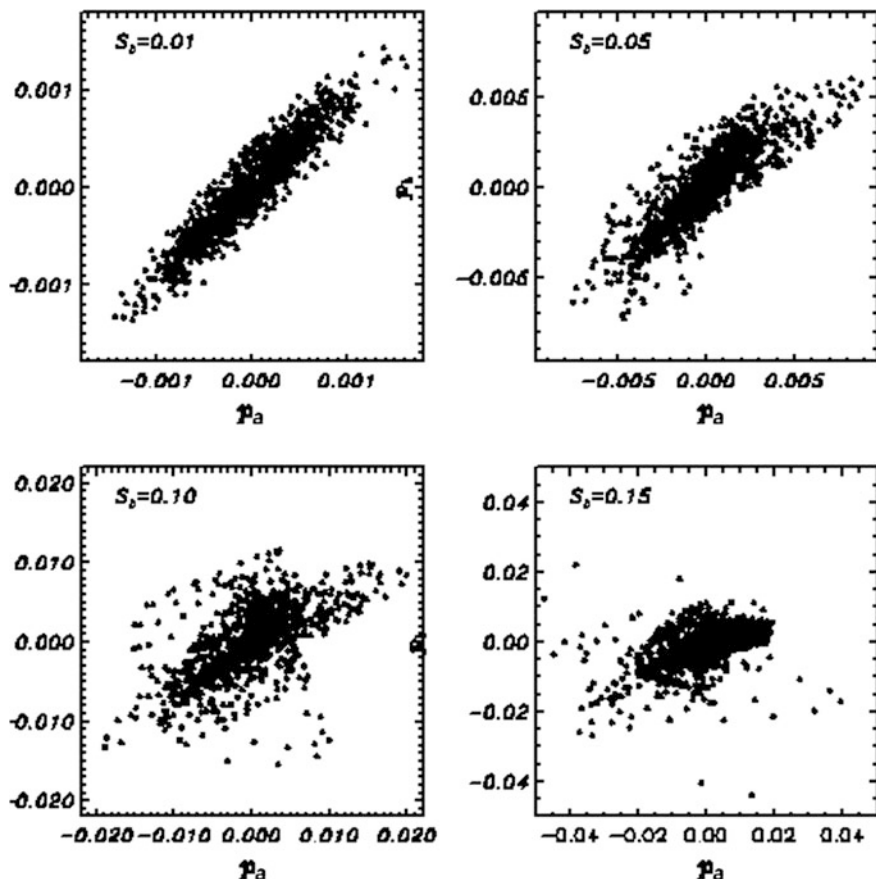
**Fig. 9.14** Comparison of surface pressure  $p_0$ , calculated using the coupled model, with surface pressure  $p_b$  calculated with the use of  $\beta$ -function (Eq. 9.9.9). *Curve 1* normalized difference between  $p_0$  and  $p_b$  (Eq. 9.9.11); *Curve 2* correlation coefficient for  $p_b$  and  $p_0$ ; *Curve 3* dispersion of  $p_0$ ; *Curve 4* dispersion of  $p_b$  (Chalikov and Rainchik 2010) © 2010 Springer-Verlag Berlin Heidelberg. With permission of Springer)



steepness, the connection between the ‘true’ and ‘restored’ pressure actually disappears. There exist a lot of reasons why the method based on  $\beta$ -function cannot provide good accuracy of calculations of surface pressure at higher steepness. The main reason is a nonlinear dependence of the pressure anomalies on the steepness. Dependence (9.9.1) suggests a linear connection between *rms* of the pressure and steepness of wave surface (curve 4 in Fig. 9.14), while the dispersion of pressure anomalies grows quickly (curve 3 in Fig. 9.14) at high steepness. This effect is clearly seen from the point-to-point comparison of  $p_0$  and  $p_b$  given in Fig. 9.15 for different values of steepness.

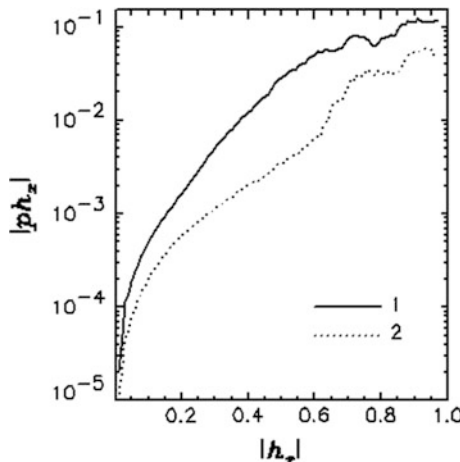
As shown, for steepness  $S_t$  of the order of 0.01, an agreement between  $p_0$  and  $p_b$  can be considered as good. For steepness  $S_t = 0.05$ , small anomalies of pressure are still reproduced well, while big anomalies are underestimated. With further increase of steepness, disagreement between big values of  $p_0$  and  $p_b$  becomes more significant. Such effect can be easily explained. Big pressure anomalies are usually concentrated in narrow zones in the vicinity of sharp peaks. Such distribution of pressure does not have a clear spectral analogy; hence, the linear dependence (9.9.1) becomes meaningless. As a result, steep and sharp waves provide the flux of momentum and energy significantly exceeding the values that can be obtained on the basis of the linear connection between elevation and pressure.

The dependence of the local flux of momentum  $|ph_x|$  on the local slope  $|h_x|$ , averaged over 396 wave records, is shown in Fig. 9.16.



**Fig. 9.15** The point-to-point comparison of surface pressure  $p_b$  calculated on the basis of  $\beta$ -function, with surface pressure  $p_0$  calculated with the use of the 2-D coupled model for different integral steepness  $S_b$  (Chalikov and Rainchik 2010 © 2010 Springer-Verlag Berlin Heidelberg. With permission of Springer)

**Fig. 9.16** The local momentum flux  $|ph_x|$  versus local steepness  $|h_x|$ . The averaged over 398 wave records. Curve 1 corresponds to calculations with model; 2 to calculations with  $\beta$ -function (Chalikov and Rainchik 2010 © 2010 Springer-Verlag Berlin Heidelberg. With permission of Springer)



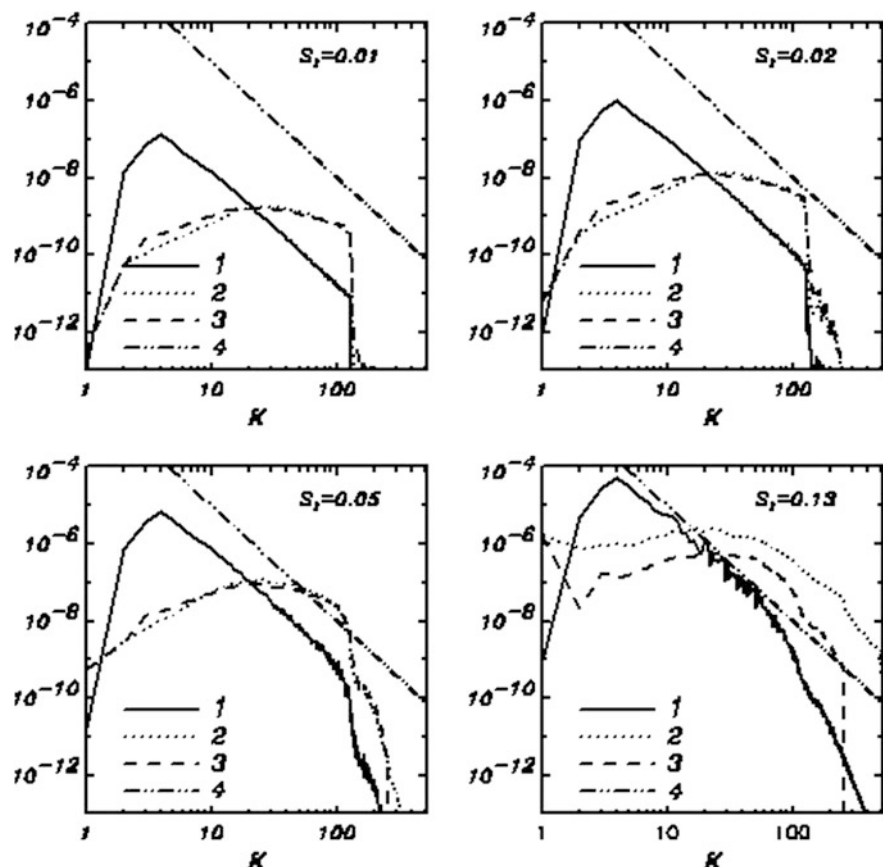


**Fig. 9.17** Curve 1 wave spectrum; curve 2 surface pressure spectrum calculated using the coupled model; curve 3 surface pressure calculated with the use of  $\beta$ -function for different integral steepness; curve 4 corresponds to  $k^{-3}$  dependence. Steepness is indicated in each frame (Chalikov and Rainchik 2010 © 2010 Springer-Verlag Berlin Heidelberg. With permission of Springer)

As shown, a simulated growth of flux of momentum occurs much faster with increase of slope, as compared with growth of the flux of momentum calculated on the basis of  $\beta$ -function. It means that the magnitude of wave drag depends on frequency of steep waves. Such properties are well pronounced in the spectrum of wave drag in Fig. 9.17.

As shown, for small and moderate steepness  $S_t = 0.01 - 0.05$ , the agreement between spectra for  $p_0 h_x$  and  $p_b h_x$  is good, while for high steepness  $S_t = 0.13$ , the spectrum for  $p_0 h_x$  is higher than that for  $p_b h_x$  over the entire spectral interval.

## 9.10 Conclusions

A coupled model based on full equations is used for simulation of evolution of a multi-mode wave field under the action of wind. Such calculations cannot be carried out without introduction of the new physics in the wave model. Firstly, the flux of energy in a subgrid part of spectrum was parameterized by permanent reduction of the potential and kinetic wave energy at high frequencies (Eqs. 2.3.4–2.3.6). Without such smoothing, the calculations quickly terminate due to the nonlinear instability. Secondly, it was necessary to prevent overturning of waves. This process was parameterized by introduction of the ‘breaking’ algorithm representing a highly selective local smoothing of the surface and surface potential in separate intervals of physical space where approaching a high curvature was observed (Eqs. 8.3.12–8.3.14). The ideas of such smoothing algorithms are widely used in the geophysical fluid dynamics. In particular, the breaking parameterization is very similar to resolving of static instability in the numerical atmospheric models.

A closure problem for Reynolds equations is a subject of numerous speculations. It is well known that the closed system of Keller–Friedmann equation (Keller and Friedmann 1924) cannot be derived formally (see Monin and Yaglom 1971). That is why lots of additional assumptions have been introduced ever since. An applicability of the closed equations can be proved by comparison with the experimental data only. A simple  $K-\varepsilon$  scheme was used in the model. Opposite to the conclusions of Belcher et al. (1994) made in the frame of the linear approach, we could hardly find solid arguments in favor of use of a more complicated scheme. It would be naive to expect that introducing more equations containing many poorly known constants could lead to improvement of the results. Moreover, our previous experience proves that a complicated approach, as a rule, turns out to be worse than a simple one. Normally, most authors prefer not to describe their ‘tricks’ introduced to provide ‘vitality’ of the model (e.g., preventing appearance of the negative energy). It was shown in the technical fluid dynamics (see, e.g., Breuer et al. 1996) that the  $K-\varepsilon$  scheme applied even for the flows with the complicated geometry is neither better nor worse, as compared with the more complicated schemes. Since the level of the kinetic energy of a wave-produced velocity is about the same as the energy of turbulence, a boundary layer above waves can be considered as a weakly distorted logarithmic boundary layer. That is why for small and medium wave steepness even the assumption  $K \sim ke^{1/2}\zeta$  could work well, though the  $K-\varepsilon$  scheme was introduced in hope to better simulate the flow separation.

The surface-following coordinates allow introducing explicit expressions for different mechanisms of momentum (and energy) fluxes produced by the averaged and fluctuating turbulence, as well as by velocity and pressure fields (Fig. 9.10). The sum of the above fluxes is the so-called WPMF that plays an important role in construction of a simplified 1-D model of the WBL (Fig. 9.11).

The vertical profiles of Fourier components for the WPMF normalized by its surface value can be represented as a function of non-dimensional height  $kz$ . This function is used in construction of the 1-D WBL model. If the number of wave

modes taken into account is great enough, the WPMF on the surface approaches the value of the total surface stress (which, due to the steadiness, is equal to the outer surface stress). However, the ultimate proportion of form and tangent stresses is meaningless, because the WPMF is a function of height and vertical resolution. When the number of wave modes is not large, the influence of form drag due to subgrid waves should be taken into account using an appropriate value of a local drag coefficient. Hence, when waves are described explicitly, the drag coefficient should be considered as a spectral concept.

The instantaneous boundary layer fields are highly chaotic; however, after appropriate averaging, they reveal some simple regularities. Vertical distribution of the Fourier modes for pressure, kinetic energy, and other variables are clearly stratified over wave numbers.

The obtained data allowed us to evaluate the so-called  $\beta$ -function, i.e., a complex coefficient in linear connection between the Fourier amplitudes for the elevation and surface pressure. The data on  $\beta$ -function exhibit wide scatter, but since the volume of data is huge (about 1,400,000 points), the shape of  $\beta$ -function was defined with satisfactory accuracy up to high non-dimensional frequencies (Eq. 9.9.7). The main reason for wide scatter is not the accuracy of modeling, and it rather results from the nonlinearity of flow: Interaction of wind and waves generates a much broader pressure spectrum, and then it can be predicted using the linear wave generation theory (Figs. 9.14, 9.15, and 9.16).

This chapter represents the results obtained with a 2-D coupled model. To obtain the results that would be more comprehensive, it is necessary to carry out another, more detailed investigation using a higher resolution and, probably, improved physics.

# Chapter 10

## One-Dimensional Modeling of the WBL

**Abstract** The  $\beta$  function and the universal shape of the WPMF profile obtained in coupled simulations allow a formulation of the one-dimensional theory of the WBL and the carrying out of a detailed study of the WBL structure including the dependence of the drag coefficient on the wind speed. It is shown that a wide scatter of the experimental data on the drag coefficient can be explained, taking into account the age of waves. It is suggested that a reduction of the drag coefficient at high wind speeds can be qualitatively explained by the high-frequency wave suppression. A direct wave model based on the one-dimensional nonlinear equations for potential waves is used for simulation of wave field development under the action of energy input, dissipation, and nonlinear wave–wave interaction. The equations are written in conformal surface-fitted non-stationary coordinate system. New schemes for calculating the input and dissipation of wave energy are implemented. The wind input is calculated on the basis of the parameterization developed through the coupled modeling of waves and turbulent boundary layer. The wave dissipation algorithm, introduced to prevent wave breaking instability, is based on highly selective smoothing of the wave surface and surface potential. The integration is performed in Fourier domain with the number of modes  $M = 2048$ , broad enough to reproduce the energy downshifting. As the initial conditions, the wave field is assigned as train of Stokes waves with steepness  $ak = 0.15$  at non-dimensional wave number  $k = 512$ . Under the action of nonlinearity and energy input, the spectrum starts to grow. This growth is followed by the down-shifting. The total time of integration is equal to 7203 initial wave periods. During this time, the energy increased by 1111 times. Peak of the spectrum gradually shifts from wave number non-dimensional  $k = 512$  down to  $k = 10$ . Significant wave height increases 33 times, while the peak period increases 51 times. Rates of the peak downshift and wave energy evolution are in good agreement with the JONSWAP formulation.

## 10.1 The One-Dimensional Model of WBL

The 2-D coupled modeling is a complicated problem requiring significant computer resources. In this connection, it would make sense to develop a 1-D model that could describe the main features of the WBL, suitable for different practical purposes. Such models have been developed in Chalikov and Belevich (1992) and Chalikov (1995). The new data obtained with the 2-D coupled model allow formulating this problem more precisely.

All variables in this section are assumed as dimensional. Neglecting the correlations of  $J$ ,  $\xi_x$  with any dynamic characteristics and taking into account that  $\langle \zeta \rangle = z$ , the one-dimensional equations of the WBL can be obtained by averaging Eqs. (9.2.5) and (9.2.16) along the coordinate  $\zeta$  (a sign of averaging  $\langle \rangle$  for all variables is omitted):

$$\frac{\partial u}{\partial t} = \frac{\partial}{\partial z} \left( K \frac{\partial u}{\partial z} + \tau_w \right), \quad (10.1.1)$$

$$\frac{\partial e}{\partial t} = \frac{\partial}{\partial z} K_e \frac{\partial e}{\partial z} + P - \varepsilon, \quad (10.1.2)$$

$$\frac{\partial \varepsilon}{\partial t} = \frac{\partial}{\partial z} K_e \frac{\partial \varepsilon}{\partial z} + \frac{\varepsilon}{e} (c_2 P - c_4 \varepsilon), \quad (10.1.3)$$

where  $K = c_k e / \varepsilon$  is coefficient of turbulent viscosity, and  $P$  is the rate of production of turbulent energy,

$$P = \frac{\partial u}{\partial z} \left( K \frac{\partial u}{\partial z} + \tau_w \right), \quad (10.1.4)$$

$\tau_w$  is the flux of momentum produced by the wave-produced fluctuations of velocity, stresses, and pressure [terms I, II, and III in Eq. (9.8.1)]. According to Eq. (9.8.5),  $\tau_w$  can be calculated by integration of the spectral WPMF constituencies:

$$\tau_w = \int_0^{\omega_r} \tau_w^k \exp(-G(\bar{\omega})kz) dk, \quad (10.1.5)$$

where  $G(\bar{\omega})$  is defined by Eq. (9.8.6), and the Fourier component of the WPMF on surface  $\tau_w^k$  is defined through the following expression:

$$\tau_w^k = kg \beta_{-k} \left( \tilde{\Omega}_k \right) S(k), \quad (10.1.6)$$

where  $\beta_{-k}$  was defined in (9.9.7);  $\tilde{\Omega}_k = \omega u (\lambda_k / 2) \cos \theta / g$  is an apparent frequency;  $S(k) = 0.5(h_k^2 + h_{-k}^2)$  is a wave number spectrum.

The stationary numerical solution for Eqs. (10.1.1)–(10.1.3) was obtained using the second-order scheme at stretched grid and an explicit time scheme. The whole scheme requires a very small time step  $\Delta t \sim 10^{-3}$  s estimated through the following relation:

$$\Delta t = 0.25 \min \left( \frac{(\Delta z)^2}{K} \right), \quad (10.1.7)$$

For the stationary solution, condition  $\tau_z = K \partial u / \partial z + \tau_w = \tau$  must be satisfied over the entire WBL. That is why the criterion for reaching the stationary solution was chosen in the following form:

$$(\max(\tau_z) - \min(\tau_z)) / \tau < 0.01 \quad (10.1.8)$$

Since a single run takes little of the computer time, a more efficient scheme was not used. However, for a regular use of the 1-D model (e.g., in the frame of a wave forecasting model), a better scheme should be semi-implicit, i.e., based on the TDMA algorithm (Thomas 1949) and iterations.

The boundary conditions for 1-D equations are similar to those for the 2-D equations (Eqs. 10.1.1–10.1.3). At the upper boundary  $z = H_a = 10H_s$  ( $H_s$  is a significant wave height), the tangent stress is assigned in the following way:

$$K \frac{\partial u}{\partial z} \Big|_{z=H_a} = \tau \quad (10.1.9)$$

The rate of production  $P_H$  at the upper boundary of domain  $z = H_a$  is calculated through the formula:

$$P_H = \frac{v_*^3}{\kappa H_a} \quad (10.1.10)$$

( $v_s = \tau^{1/2}$  is friction velocity at  $z = H_a$ ), while the energy of turbulence  $e$  and the rate of dissipation  $\varepsilon$  assume the following values:

$$e_H = c_1 v_*^2, \quad \varepsilon_H = \frac{v_*^3}{\kappa H_a}. \quad (10.1.11)$$

Vertical diffusion of the turbulent energy at  $K_e \frac{\partial e}{\partial z}$  at  $z = 0$  and that at the upper boundary of domain  $z = H_a$  are both equal to zero. The vertical diffusion of the dissipation rate at  $z = 0$  and that at  $z = H_a$  are accordingly equal to:

$$K_\varepsilon \frac{\partial \varepsilon}{\partial z} (\zeta = 0) = -v_{s0}^4 z_1^{-1} c_3^{-1}, \quad K_\varepsilon \frac{\partial \varepsilon}{\partial z} (\zeta = H_a) = -v_*^4 H_a^{-1} c_3^{-1}, \quad (10.1.12)$$

where  $v_{s0} = \tau_0^{1/2}$  is the local tangent friction velocity defined by the local turbulent tangent stress at the interface  $\tau_0$ . The constants  $\kappa, c_1, c_3$  as well as the relationship between  $K, K_e, K_\varepsilon$  are given in Sect. 9.2.

The 1-D WBL model is much simpler than the coupled model. This is why wave spectrum can be extended up to high wave numbers. The highest wave number  $\omega_r$  is limited by upper boundaries of the non-dimensional frequency  $\Omega = \pm 50$  in approximation (9.9.7). It was assumed that on the horizontal scales of the order of the limit resolution  $g/\omega_r^2$ , the sea surface is a smooth surface, and the local roughness parameter  $z_{0l}$  can be taken in the form:

$$z_{0l} = 0.1v/v_{0z}, \quad v_{0z} = \tau_0^{1/2}, \quad (10.1.13)$$

where  $v = 0.15 \times 10^{-4} \text{ m}^2/\text{s}$  is the molecular kinematic viscosity,  $v_{0z}$  is the local friction velocity, and  $\tau_0$  is the local tangent stress defined by Eq. (9.2.15) with the drag coefficient:

$$C_1 = (k / \log(z_v/z_{0l}))^2, \quad (10.1.14)$$

where  $z_v = 60v/v_{0z}$  is thickness of a viscous sublayer (Monin and Yaglom 1971). The thickness of the lowest level  $\Delta z_1$  was chosen to be equal to  $2z_v$ .

The initial 1-D wave spectrum was assigned in the form (7.2.1), and the 2-D spectrum  $S_2(\omega, \theta)$  was calculated as:

$$S_2(\omega, \theta) = S(\tilde{\omega})\psi(\theta), \quad (10.1.15)$$

where  $\tilde{\omega}$  is ‘apparent’ frequency:

$$\tilde{\omega} = \omega u(\lambda/2) \cos(\theta), \quad (10.1.16)$$

$\theta$  is an angle between the wind direction and direction of a wave mode;  $u(\lambda_\omega/2)$  is wind velocity defined at  $z = \lambda_\omega/2$ , where  $\lambda_\omega = 2\pi g/\omega^2$ . The values of  $u(\lambda_\omega/2)$  were calculated using a log-linear interpolation from  $u(z)$  profiles. For low-wave number modes,  $\lambda_\omega/2$  often exceeds  $H_a$ , while the value of  $u(\lambda_\omega/2)$  was calculated using a log-linear extrapolation which was used for  $\omega < \omega_p$  only. The function  $\psi$  was taken in the form (Donelan 1980):

$$\psi = 0.5 \operatorname{sech}(b), \quad b = \begin{cases} 2.16\Omega_p^{1/3}, & \Omega_p < 0.95 \\ 2.28\Omega_p^{1/3}, & \Omega_p > 0.95 \end{cases}. \quad (10.1.17)$$

The spectrum  $S_2(\omega, \theta)$  can be fixed; however, in our calculations, it was updated every 100 s with a new value of  $\Omega_{10}$  (Eq. 9.9.2) to obtain the fully adjusted WBL and wave field. The wave spectrum was approximated on a stretched over frequency grid  $\Delta\omega_{i+1} = \gamma\Delta\omega_i$  with a stretching coefficient  $\gamma = 1.03$ . The first frequency step  $\Delta\omega_1$  was equal to  $0.1\omega_p$  ( $\omega_p$  is dimensional peak frequency). The angle resolution  $\Delta\theta$  equals  $4^\circ$ .

## 10.2 Vertical Structure of WBL

The specific feature of the WBL is that a new mechanism of momentum transfer develops close to the surface (see Figs. 9.7 and 9.11). The main advantage of the 1-D approach is that wave drag can be considered in a wider range including high frequencies. Opposite to the purely turbulent stress, the WPMF emerges due to direct influence of waves, e.g., due to the curvilinearity of the underlying surface. Since the total momentum flux must be constant over height for a steady wind, the turbulent momentum flux decreases when approaching the surface. The WPMF modifies interconnection of the wind profile and stress. This is why the structure of the WBL becomes different from that of the boundary layer above flat surface. For investigation of the WBL structure on the basis of the 1-D model, a series of calculations was carried out for  $\Omega_p = (0.855, 1.0, 1.25, 1.5, 2.0, 3.0, 5.0)$  and for the initial value of  $u_{10}$  varying for each  $\Omega_p$  within the interval 8–40 m/s. The initial conditions for the WBL were assigned similar to those for the logarithmic boundary layer above flat surface. Due to the appearance of wave drag in the process of reaching the equilibrium solution, wind velocity  $u_{10}$  decreases and final values of  $u_{10}$  get lower as compared to those initially assigned.

Wind profiles above the waves of different age for two values of wind speed  $u_{10}$  (about 15 and 30 m/s) are shown in Fig. 10.1 as a function of dimension height  $z$  (m). The thin lines indicate a downward extrapolation of logarithmic wind profile from the levels where the WPMF equals zero, while the boundary layer preserves its standard structure.

As shown, in the lowest part of the WBL, the deviation of wind profile from the logarithmic profile can be as big as several meters for  $u_{10} \sim 14$  m/s and 10 m for

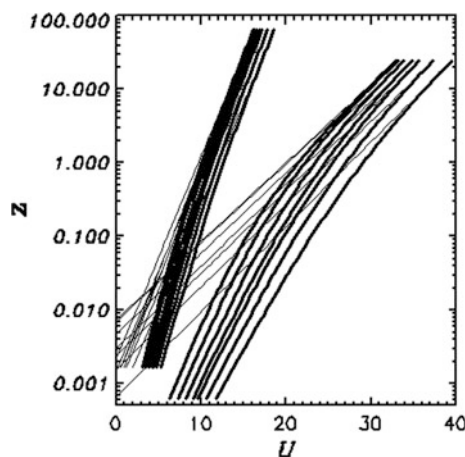
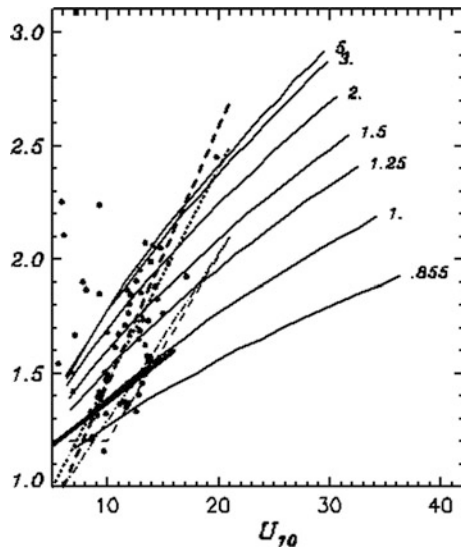


**Fig. 10.1** Wind profiles. In each group, thick curves correspond to the values  $U_{10}/c_p = 0.855, 1.0, 1.25, 1.5, 2.0, 3.0$ . For the left group,  $13.4 < U_{10} < 15.4$ , while for right group  $-29.5 < U_{10} < 36.3$ . Thin lines correspond to logarithmic wind profiles extrapolated downward from the outside part of the WBL. (Chalikov and Rainchik 2010 © 2010 Springer-Verlag Berlin Heidelberg. With permission of Springer.)

**Fig. 10.2** The drag coefficient  $C_{10}$  as a function of  $U_{10}$  and  $U_{10}/c_p$  (curves labeled). (Chalikov and Rainchik 2010 © 2010 Springer-Verlag Berlin Heidelberg. With permission of Springer.)



m/s  $u_{10} \sim 30$  m/s. It is important to note that such effect takes place in the vicinity of wave surface at heights of the order of the wave height. Such features can be investigated experimentally only using a surface-following measurement technique similar to that designed by Donelan et al. (2006).

The most obscure problem of wind–wave interaction is dependence of stress on wind velocity traditionally represented as dependence of the drag coefficient  $C_{10}$  on  $u_{10}$ . It is well known that the experimental data on  $C_{10}$  have large scatter just indicating that  $C_{10}$  grows with wind velocity at least up to  $u_{10} = 25\text{--}30$  m/s. The dependence of  $C_{10}$  on wind velocity and wave age calculated with the 1-D model is shown in Fig. 10.2. As shown, the drag coefficient depends on wave age even more than on wind velocity. This conclusion is in qualitative agreement with the observations (Shedman et al. 2003). It accounts for a wide scatter of experimental data on the drag coefficient as a function of  $u_{10}$  only.

The data on  $C_{10}$  and  $u_{10}$  can be interpreted in terms of the total roughness parameter  $z_0$  formed by all the drag mechanisms. The dependence of non-dimensional roughness  $z_0 g/v_*^2$  is given in Fig. 10.3. The data do not prove a universal character of the Charnock scale  $\text{Ch} = v_*^2/g$ . However, the real data in  $(u_{10}, \Omega_p)$  space are distributed in a more narrow area than the area covered in 9.12. For example, only few data can fall in the domain,  $u_{10} > 20, \Omega_p > 2$ . Such events occur, since the early stage of wave development at medium and strong wind does not last long. Hence, the value of  $z_0 g/v_*^2$  varies within the range of 0.01–0.02, which is in a good agreement with the values obtained by Smith and Banke (1975) and Garrat (1977) and Wu (1980).

Let us consider the integral fluxes of momentum and energy to waves:

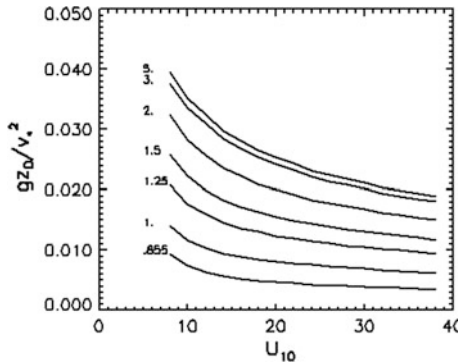


**Fig. 10.3** The non-dimensional roughness parameter  $z_0 g / v_*^2$  as a function of  $U_{10}$  and  $\Omega_p$ . (Chalikov and Rainchik 2014 © 2010 Springer-Verlag Berlin Heidelberg. With permission of Springer; Chalikov and Rainchik 2010 © 2010 Springer-Verlag Berlin Heidelberg. With permission of Springer.)

$$T(k) = \frac{g}{\tau} \int_0^k k \beta_{-k} S(k) dk \quad (10.2.1)$$

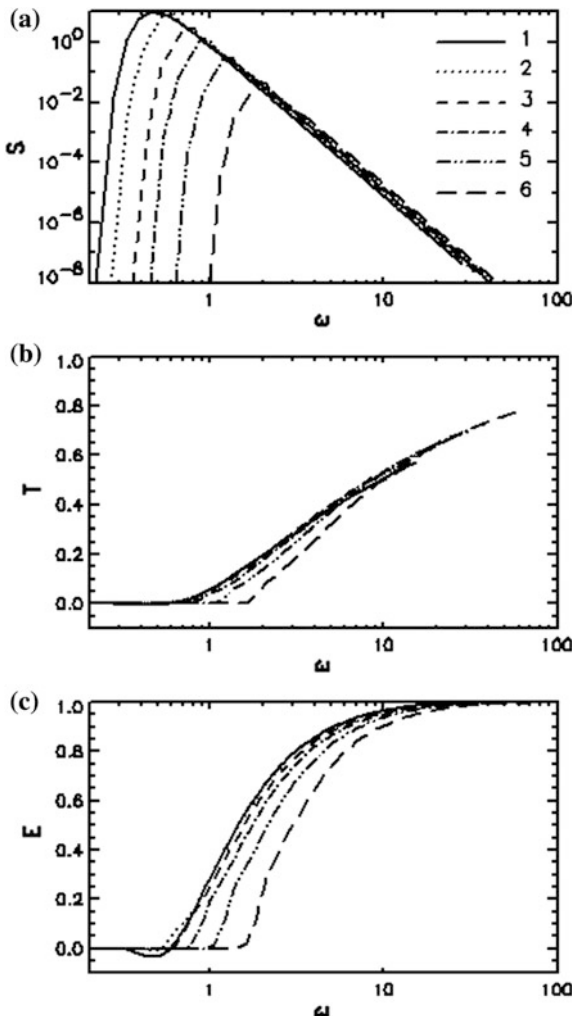
$$E(k) = \frac{g}{E_M} \int_0^k \omega \beta_{-k} S(k) dk, \quad E_M = E(M) \quad (10.2.2)$$

Functions (10.2.1) and (10.2.2) indicate which part of the total flux of momentum  $\tau$  and energy  $E_M$  is transferred to waves within the wave number range  $0-k$ . The integral spectra for  $T$  and  $E$  are shown in Fig. 10.4 (frames *b* and *c*) along with the wave spectrum (panel *a*).

As shown, with increase of wave number, the energy flux comes more or less quickly to the saturation level. It is quite different with the integral momentum flux, as it keeps on growing with increase of frequency for all the values of  $\Omega_p$ . It is impossible to extend the spectrum to higher frequencies, as  $\beta$ -function has been studied within the range of  $-50 < \Omega < 50$ . The data in panel *b* of Fig. 10.4 prove that the flux of momentum is accumulated mostly in a high-frequency (high wave number) range of the spectrum. The better the high-wave number structure of surface is described, the bigger part of the momentum flux can be reproduced explicitly. The ratio of the calculated momentum flux to waves and the total momentum flux is shown in Fig. 10.5, panel *a*.

As shown, the momentum  $\tau_w$  coming to waves can reach 80 % of the total momentum flux, while  $\tau_w$  decreases with growth of  $\Omega_p$ . It is interesting to note that the ratio of energy flux to waves and energy  $E = \tau_{10} u_{10}$  transferred downward through  $z = 10$  m exhibits quite an opposite behavior; i.e., it increases with growth of  $\Omega_p$ . Such properties of the momentum and energy exchange can be explained by

**Fig. 10.4** **a** Wave spectrum, **b** integral flux of momentum  $T(k)$  (Eq. 10.2.1), **c** integral flux of energy  $E$  ( $k$ ) (Eq. 10.2.2) as functions of  $\omega$  for different  $\Omega_p$ : curve 1— $\Omega_p = 0.855$ ; 2—1.0; 3—1.25; 4—2.0; 5—3.0; 6—5.0. (Chalikov and Rainchik 2010  
© 2010 Springer-Verlag Berlin Heidelberg. With permission of Springer.)

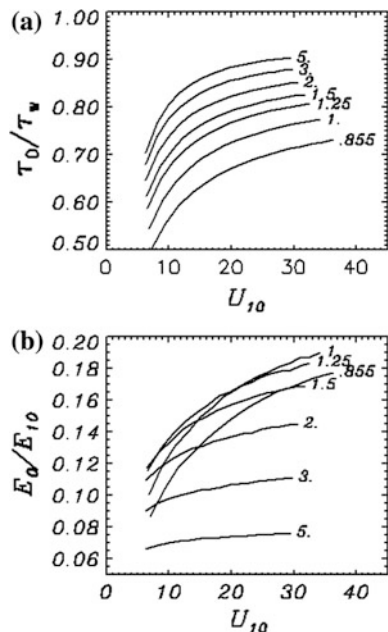


the properties of spectrum: The high-frequency spectral density responsible for the momentum flux is high for the young sea (an overshoot effect), while low-frequency waves that absorb the major part of the energy input are larger for the old sea.

There is a possibility that in smooth areas of water surface, some part of momentum is transferred by molecular viscosity, while in the areas with the high energy of short waves, the momentum is transferred to small waves.

Since the shape of spectrum and  $\beta$ -function are not known at high frequencies, it is impossible to investigate the ultimate ratio of the surface WPMF and the total surface stress. Fortunately enough, this problem has no practical importance. The high-frequency waves quickly disappear (Chalikov 2005) and transfer the momentum to currents, while the energy is given to currents and turbulence

**Fig. 10.5** **a** The ratio of surface WPMF and total stress  $\tau$  as a function of  $U_{10}$  and  $U_{10}/c_p$ , **b** ratio of energy flux to waves and total energy flux transferred downward at  $z = 10$  m. (Chalikov and Rainchik 2010 © 2010 Springer-Verlag Berlin Heidelberg. With permission of Springer.)



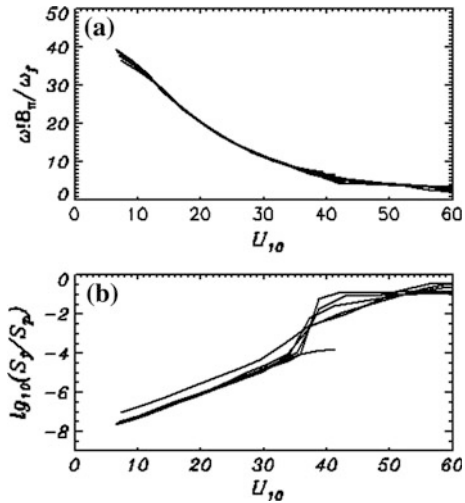
(Chalikov and Belevich 1992). The most important thing is that the total friction at wave surface depends significantly on the wave energy at high frequencies (see Fig. 10.4, panel *b*).

### 10.3 Drag Coefficient at High Wind Speed

As demonstrated in Fig. 10.2, the current theory predicts a monotonic growth of drag coefficient with the increase of wind speed. However, there exist some data showing that for the wind speed exceeding 25–30 m/s, the drag coefficient reaches the limit (Powell et al. 2003; Donelan et al. 2004), while for further increase of wind speed, the above coefficient can even decrease. Earlier, such effect was also noted in the analysis of the tropical cyclone development (Emanuel 1995). Currently, some attempts are made to explain such a behavior of drug coefficient on the basis of a ‘droplet theory’ (Kudryavtsev 2006). According to the theory, the drops generated by splitting of the falling water volume intensify dissipation of turbulence, which causes reduction of the drag coefficient. Such speculative scheme does not look worse than the others, though unfortunately, the model of drop generation (as well as the mechanism of interaction of drops with turbulence) uses too many arbitrary assumptions.

According to our data, the effect of wave drag reduction at high wind speed can be easily explained by the influence of high-frequency waves. It would be quite to

**Fig. 10.6** Parameters for high-frequency wave suppression: **a** ratio of peak frequency  $\omega_p$  and cutoff frequency  $\omega_f$ ; **b** ratio of spectral density  $S_f(\omega_f)$  and spectral density in a wave peak  $S_p$  (a logarithmic scale)

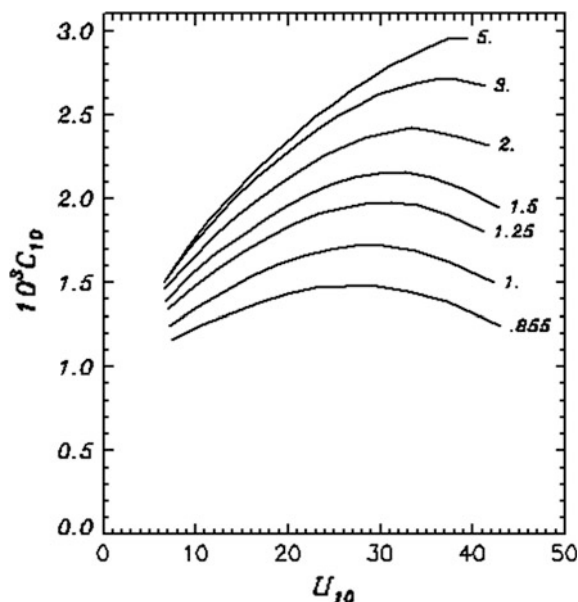


the point to suggest that the energy of short waves at high wind can be decreased due to two factors: the presence of foam suppressing short waves and wind speed deceleration in troughs due to flow separation. The last effect can be investigated using the coupled wind–wave model directly. The model must take into account a broad range of wave spectrum from peak waves to capillary waves. The high wind velocity and the necessity to use high vertical resolution in the WBL make this problem quite time-consuming; anyway, such calculations are quite possible to carry out from the technical point of view.

To prove that reduction of drag coefficient is caused by suppression of small waves, the calculations of drag coefficient with a modified JONSWAP spectrum were performed. It was suggested somewhat arbitrarily that the waves with the frequency above some frequency  $\omega_f$  are absent. The specific properties of the above modification are given in Fig. 10.6.

In the upper panel, the ratio of peak frequency and cut frequency  $\omega_f$  is shown as a function of wind speed. This ratio for  $u_{10} = 30 \text{ m/s}$  equals 10, so the length of the removed waves is 100 times shorter than the peak wave length. The ratio of energy  $S_f$  at frequency  $\omega_f$  and energy  $S_p$  in spectral peak is given in panel b. As shown, the waves with the spectral density above  $10^{-5}S_p$  are removed. Roughly speaking, the height of those waves is about 100 times smaller than the height of dominant wave. Hence, the modifications of the spectrum are quite insignificant. The above modifications were introduced into a new series of calculations using 1-D model (10.1.1)–(10.1.3). The dependence of drag coefficient (the small waves being removed) on wind velocity  $u_{10}$  is shown in Fig. 10.7. As shown, the drag coefficient significantly decreases at high wind speed. For developed sea ( $\Omega_p \sim 1$ ), the drag coefficient  $C_{10}$  has a maximum of  $C_{10} \approx 1.5 \times 10^{-3}$  at  $u_{10} = 30 \text{ m/s}$ , and for younger waves, the maximum is shifting to higher wind velocities.

**Fig. 10.7** The drag coefficient  $C_{10}$  as a function of  $U_{10}$  and  $\Omega = U_{10}/c_p$  (curves labeled), taking into account suppression of high-frequency modes. (Chaliko and Rainchik 2010 © 2010 Springer-Verlag Berlin Heidelberg. With permission of Springer.)



It should be emphasized that the result presented in Fig. 10.7 is purely qualitative, since the exact shape spectrum is unknown at high wind. Figure 10.7 just illustrates that a simple explanation of the drag coefficient reduction at high wind speed can be given on the basis of a high-frequency wave spectrum modification.

## 10.4 Evolution of Wave Field

In the JONSWAP experiment, the development of waves under the action of wind was studied for long fetches (Hasselmann et al. 1973). The main result of these investigations was the formulation of the non-dimensional empirical fetch laws (Battjes et al. 1987). These laws connect the local characteristics of waves, such as wave energy, steepness, and peak frequency with the external parameters, such as wave fetch and wind speed. Similar investigations were performed in the laboratory wind–wave channels. Unlike the experiments at sea, the laboratory experiments investigate growth of waves under the wind action for short fetches. It was found that at the initial stage of wave development, the fetch laws observed in laboratory are somewhat different from those obtained in the ocean. The causes of such differences are not clear, and we can suggest, among other potential reasons, that the boundary layer structure in the wind–wave channels might not be adjusted to the local wave conditions, and the boundary layer above waves is not developed, i.e., transient. In the sea, due to large horizontal distances, the boundary layer is close to the stationary and horizontally homogeneous conditions; hence, the

structure of wave boundary layer is fully formed. Consequently, it is quite possible that the input of energy in a wind-wave channel differs from that in natural conditions. The development of two-dimensional waves was simulated by Willemse (2001, 2002) on the basis of discrete Krasitskii (1994) equations for a nonlinear wave evolution, by taking into account the simplified input and dissipation terms. The results obtained did not demonstrate a realistic behavior of the wave energy.

In the current work, the process of wave development is simulated with one-dimensional fully nonlinear model. The one-dimensional version of the model was chosen intentionally, in order to investigate an evolution of unidirectional waves. Recently, it was shown that adiabatic waves (i.e., with no input and dissipation effects) can undergo downshifting with the rate depending on the initial wave steepness (Chalikov 2012). Note that a similar evolution of wave field was observed in wave channel (Shemer et al. 2001). Existence of non-resonant interactions which can be a cause of such effect was predicted on the basis of a narrowband approximation of Zakharov's (1968) equation (Janssen 2003) and then investigated in some details in (Annenkov and Shrira 2006). In the current work, the algorithms for parameterization of the energy input and wave breaking are added. When starting this work, we did not expect that the development of unidirectional waves would occur in accordance with the empirically observed fetch laws. The results of modeling, however, prove that there is no significant difference between the one-dimensional and two-dimensional wave evolution.

## 10.5 Wind Input

An exchange of energy and momentum between air and water occurs through dynamic surface pressure  $p_0$ . According to the linear theory (Miles 1957), the Fourier components of surface pressure  $p_0$  are connected with those of the surface elevation through the expression (9.9.1) where  $\beta_k$  and  $\beta_{-k}$  are real and imaginary parts of the so-called  $\beta$ -function (i.e., Fourier coefficients at COS and SIN, respectively;  $\rho_a/\rho_w$  is a ratio of the air and water densities, respectively). Hence, for derivation of shape of beta-function, it is necessary to measure simultaneously the wave surface elevation and non-static pressure on the surface. The experimental measurement of surface pressure is a very difficult problem, since the measurements should be done very close to a moving surface with a surface-following sensor. Such measurements are very few, particularly, in the field. They were carried out for the first time by a group of authors in laboratory and later in the field (Snyder et al. 1981; Hsiao et al. 1983; Hasselmann and Bosenberg 1991; Donelan et al. 2005, 2006). The data obtained in this way allowed us to construct the real part of beta-function which is used in some versions of the wave forecasting models (Rogers et al. 2012). The second way of beta-function evaluation is based on the results of numerical investigations of the statistical structure of the boundary layer above waves on the basis of Reynolds equations with a good closure scheme. In

general, this method works so well that many problems in the technical fluid mechanics are often solved using numerical models, not experimentally. This approach has been developed starting from Chalikov (1978, 1986) and followed by Chalikov (1995), Chalikov and Makin (1991), and Chalikov and Belevich (1992). The results were implemented in the third-generation wave forecast WAVEWATCH model (Tolman and Chalikov 1994, 1996) and thoroughly validated against the experimental data in the course of developing WAVEWATCH-III (Tolman 2008). This method was later improved on the basis of a more developed coupled modeling of waves and boundary layer (Chalikov and Rainchik 2010), while the beta-function used in WAVEWATCH-III was corrected and extended up to high frequencies. A direct calculation of the energy input to waves requires both the real and imaginary parts of beta-function. Note that in the range of relatively low virtual frequencies, the new method is very close to the scheme implemented in WAVEWATCH-III.

It is a traditional suggestion that both coefficients are a function of the virtual non-dimensional frequency  $\Omega = \omega_k U \cos \psi = U/c_k \cos \psi$  (where  $\omega_k$  and  $U$  are the non-dimensional radian frequency and wind speed, correspondingly;  $c_k$  is phase speed of the  $k$ th mode;  $\psi$  is the angle between the wind and wave mode directions). Most of the schemes for calculations of  $\beta$ -function consider a relatively narrow interval of non-dimensional frequencies  $\Omega$ . In the current work, the range of frequencies covers the interval  $(0 < \Omega_p < 10)$ , and occasionally, the values of  $\Omega > 10$  can appear. This is why the function derived in Chalikov and Rainchik (2010) through the coupled simulations of waves and the boundary layer is used here. The wave model is based on potential equations for the flow with free surface, extended with the algorithm for breaking dissipation (see below the description of the breaking dissipation parameterization). The wave boundary layer (WBL) model is based on the Reynolds equations closed with the  $K - \varepsilon$  scheme; the solutions for air and water are matched through the interface. The  $\beta$ -function obtained in CR was used for evaluation of accuracy of the surface pressure  $p_0$  simulations. The shape of  $\beta$ -function that connects surface elevation and surface pressure is studied up to high non-dimensional wave frequencies both in positive and in negative (i.e., for the wind adverse to waves) domains. The data on the  $\beta$ -function exhibit a wide scatter, but since the volume of the data was large enough (47 long-term numerical runs allowed generation of about 1,400,000 values), the shape of the  $\beta$ -function was defined with a satisfactory accuracy up to very high non-dimensional frequencies ( $-50 < \Omega < 50$ ). As a result, the knowledge of the  $\beta$ -function in such a broad range allows us to calculate wave drag up to very high frequencies and to explicitly divide the fluxes of energy and momentum transferred by pressure and tangent stress (see examples of such calculations in Chalikov and Rainchik (2010), Ting et al. (2012)). This method is free of arbitrary assumptions on the drag coefficient  $C_d$ , and on the contrary, such calculations allow us investigating the nature of wave drag.

The  $\beta$ -function (see Fig. 9.13) is approximated by expression (9.9.7), (9.9.8) where the non-dimensional virtual frequency  $\Omega_k$  is defined by Eq. (9.9.2).

The main parameter of the scheme for the energy input calculation is wind speed  $U_{10}$  at standard 10 m height and the inverse wave age  $U_{10}/c_p$  where  $c_p$  is dimensional phase speed at spectral peak. The wind speed is constant over the integration period, while  $U_{10}/c_p$  changes due to downshifting of the wave energy and changes of the form drag.

It was indicated above that the initial wave field is assigned as a train of Stokes waves with the main mode placed on wave number  $k_0 = 500$ . An initial value of  $\Omega_0 = 10$  was chosen; i.e., a ratio of non-dimensional wind speed at height  $\lambda_0/2 = \pi/500$  and phase speed  $c_{10} = k_0^{1/2}$  is equal to 10. Such a high ratio corresponds to the initial stages of wave development. The values of  $\Omega$  for other wave numbers are calculated by assuming that the wind profile is logarithmic:

$$\Omega_k = \Omega_0 \frac{c_0}{c_k} \ln \frac{\lambda_k}{2z_0} \left( \ln \frac{\lambda_0}{2z_{00}} \right)^{-1}, \quad (10.5.1)$$

where  $z_{00}$  is the effective non-dimensional roughness for the initial wind profile, while  $z_0$  is the actual roughness parameter that depends both on the energy in a high-frequency part of spectrum and on wind profile. We call it ‘effective,’ since very close to the surface, the wind profile is not logarithmic (Chalikov 1995; Chalikov and Rainchik 2010). The value of this parameter depends on the wind velocity and energy in a high-wave number interval of wave spectrum, as well as on the length scale of the problem. All these effects can be accounted by coupling the wave model with the one-dimensional WBL model (Ting et al. 2012). Here, a simplified scheme for the roughness parameter is chosen. It is well known that the roughness parameter (as well as the drag coefficient) decreases with decrease of an inverse wave age. In our case, wind speed is fixed, and the dependence for the non-dimensional roughness parameter is constructed on the basis of the results obtained by Chalikov and Rainchik (2010):

$$z_0 = 15z_{00}\Omega, \quad (10.5.2)$$

where  $z_{00} = 10^{-3}$  is the initial value of the roughness parameter. Equation (10.5.2) approximates dependence of the effective roughness on the stage of wave development. Note that the results are not sensitive to the variation of the roughness parameter within reasonable limits.

## 10.6 Wave Dissipation

Algorithms for calculation of wave energy dissipation are developed in spectral wave forecast modeling (see, e.g., review Babanin et al. 2011). One of such schemes was implemented in the WAVEWATCH-III model (Tolman and Chalikov 1996). However, most of the results obtained for spectral modeling are not applicable for direct modeling, since the spectral image of wave breaking in Fourier

space is completely different from the same image in physical space. Since breaking occurs in the relatively narrow space intervals separated by broad parts with no breaking (i.e., they are local in physical space), the spectrum of the dissipation rate based on Fourier transform of such signal is distributed mostly in a high-frequency part of the spectrum, whereas in reality, the breaking reduces the height of an actual breaking wave which can represent spectral scales in the vicinity of spectral peak.

This is why over the past several years, the method of parameterization of dissipation was developed (Chalikov and Sheinin 2005). The parameterization of dissipation in high-wave number domain is discussed in Sect. 2.3 (Eqs. 2.3.4–2.3.6). The algorithm was validated in (Chalikov and Sheinin 1968, 2005). The sensitivity of the results to reasonable variations of  $r$  in Eq. (2.3.6) is low. This sort of dissipation which we call ‘tail dissipation’ effectively absorbs energy if wave numbers are close to truncation number  $M$ , the longer waves being virtually intact. This is why the total effect of ‘tail dissipation’ is very small. However, this algorithm provides stability.

Another mechanism of dissipation exists due to the interaction of non-potential small-scale motion and orbital velocities (see Chap. 11). Theoretically, potential waves cannot generate vortex motion; however, the scale considerations prove that Reynolds number can exceed critical values if the steepness of waves is not too small. It means that in the presence of the initial non-potential disturbances, the orbital velocities can generate vortex motion and turbulence. Babanin and Chalikov (2012) investigated this problem numerically on the basis of full two-dimensional ( $x$ – $z$ ) equations of potential motion with free surface in the cylindrical conformal coordinates. The recommendations were developed on including the integral turbulent wave dissipation in wave prediction models and the models of upper ocean layers. However, the preliminary results are not currently included in the simulations described in this paper, since the qualitative algorithm has not been developed and checked yet. Anyway, the volume dissipation due to turbulence is relatively weaker than the dissipation due to white capping called here the ‘breaking dissipation.’

The breaking is a dissipative process leading to loss of the kinetic wave energy and potential wave energy as well as to transition of the energy to currents and turbulence; therefore, dissipation should be taken into account in different types of the models designed for simulation of wave evolution. The most important models of such type are wave forecasting models [e.g., the WAVEWATCH model (Tolman 2008)]. Evidently, no local criterion of breaking can be used in such models, as they are formulated for wave spectrum, while any information on the real wave surface is absent. In such models, the dissipation process is presented in a distorted form. Since the breaking occurs in the relatively narrow space intervals separated by broad parts with no breaking, the dissipation rate spectrum is artificially extended over a high-frequency part of the wave spectrum. In reality, the breaking mostly reduces the height of the largest wave represented in spectral peak. This contradiction occurs due to the fact that in the spectral model, a wave field is assumed to be a superposition of the linear modes, while the breaking (and appearance of freak waves) occurs due to transformation of a specific wave shape; i.e., as a rule, a wave

before breaking becomes sharp-crested. Therefore, the breaking decreases height and energy of large nonlinear waves and reduces their nonlinearity. It is important to stress that the spectral treatment of dissipation reduces energy in the whole domain, while in the real process of dissipation in physical space, the wave energy is reduced locally.

The instability of interface leading to breaking is an important problem of the fluid mechanics. This process is strongly nonlinear and generally includes two-phase liquid; hence, the full theory of breaking is expected to be highly complicated. The onset of breaking is similar to the onset of free convection in liquid at unstable stratification, in this case, an appearance of unstable stratification in some part of liquid curves as a criterion of the convection instability. It can result from the different processes producing redistribution of density. Similarly, we can define the criterion of instability as an appearance of the local non-single value of surface when some volume of fluid becomes unsupported by pressure from the surrounding fluid and starts to move independently under the action of inertia and gravitational forces. The breaking can start under the influence of many factors producing non-uniqueness of surface. Probably, the main factor is an appearance of the horizontal velocity exceeding the velocity of shape propagation. It was proved by the special numerical experiments with a very high time and space resolution performed by Chalikov and Sheinin (2005). It is shown that the horizontal velocity in wave peak before breaking always exceeds the phase velocity. However, the detailed numerical investigation of the process of approaching the onset of breaking (Chalikov and Babanin 2013) shows that a reliable criterion for predicting all the breaking events probably does not exist: The location of breaking is unpredictable; the breaking develops very fast. Hence, the only way to parameterize this process in direct modeling is to prevent the overturning of surface.

The appearance of non-single-value surface in direct simulation is always followed by the numerical instability and termination of run. Since it can happen at a relatively low integral frequency, the long-term simulations, especially those with the input of energy from wind, are impossible. This is why an algorithm of the breaking parameterization based on the local elimination of breaking was developed. The algorithm is designed to prevent the breaking instability through the highly selective high-wave number smoothing of interface. Many schemes to parameterize such phenomenon were tested, the most efficient of them being based on a simple diffusion-type algorithm described in Sect. 9.4.

Note that the intensity of breaking in the presence of the input energy does not depend much on parameters  $C_b$  and  $s$  in Eq. (2.4.2). If these parameters are reduced, the waves can become, on the average, a little more sharp-crested, while the integral energy lost in the breaking process remains approximately the same.

The algorithm (8.3.12)–(8.3.14) is currently used in a long-term simulation of wave field evolution. It effectively prevents development of the numerical instability due to the surface approaching a non-single-value shape, as well as properly describes (at least qualitatively) the dissipation of wave energy. Such scheme does not influence the solution in the absence of breaking. We do not consider this algorithm as a final solution of the problem, since it cannot prevent collapse in cases

of very high initial steepness or high energy. However, for normal steepness of sea waves as well as for the cases of typical growth rate of the local energy, it works well and always provides stability. After implementation of algorithm (8.3.12)–(8.3.14) (with  $C_b = 10^{-3}$  and  $s = 300$ ), termination of run never happened. The results of a long-term simulation of the wave field evolution were demonstrated by Chalikov and Rainchik (2010) on the basis of the air/water coupled model. It was shown that the wave breaking is a highly intermittent process correlated with steepness. Of course, a rate of dissipation and an intermittence index depend on the stage of wave development and on the magnitude of the energy input. Note that the large wave height is not an obligatory condition of breaking, since smaller waves can also break. It proves that the breaking is not directly connected with the overall wave characteristics, but rather with a quickly changing local condition in the vicinity of wave crest. The mechanism of breaking in the spectral environment differs from that for the idealized situation when a wave field is represented by few modes only. The breaking develops rapidly, on the average, taking less time than the peak wave period. To some degree, the breaking is similar to the development of freak waves which normally appear suddenly without any prehistory. Both of the processes are connected with the evolution of wave shape with the increase of horizontal asymmetry and concentration of energy in the vicinity of wave peak.

The simulations did not show any signs of the modulational instability, such as growth of the harmonic mode at the expense of others. The situation with wave breaking and wave ‘freaking’ is just opposite to the scheme that follows from the quasi-linear approach; i.e., an individual nonlinear wave preserves its total energy, while the columnar energy is concentrated around the wave crest vertical, which is why the wave becomes sharper and unstable.

An example of a local evolution of the surface affected by breaking is shown in Fig. 10.8.

The solid line corresponds to wave surface, while the thin curve marks the change of wave surface  $100\Delta z_b$  due to the breaking described by algorithm (8.3.12)–(8.3.14). It happens during the interval equal to 0.05 non-dimensional time units, which corresponds to 0.04 of this specific mode period. As shown, the wave height in the vicinity of crest decreases ( $\Delta z_b < 0$ ), since the water is transferred to the front slope. A smaller volume of water falls also to the rear wave slope. The wave is moving from left to right, its height decreasing because of redistribution of the mass mostly over the forward slope and partially over the back slope. At  $x > 3.17$ , the modification of surface due to breaking is completely absent. A divergent form of the diffusion operator in Eqs. (8.3.12)–(8.3.14) guarantees the exact volume conservation. An evolution of the first derivative  $\partial z / \partial x$  (tangent of the surface slope) is shown in panel *b*. As shown, the largest slope is observed in a forward side of the wave. While the wave is breaking, its forward inclination is decreasing. In panel *c*, an evolution of the second derivative  $s = \partial^2 z / \partial x^2$  (curvature of the surface) is shown. This quantity is selected as the most sensitive criterion of the breaking onset. As shown, the surface curvature is very large (up to  $s = 500$ ). When the curvature falls below the threshold

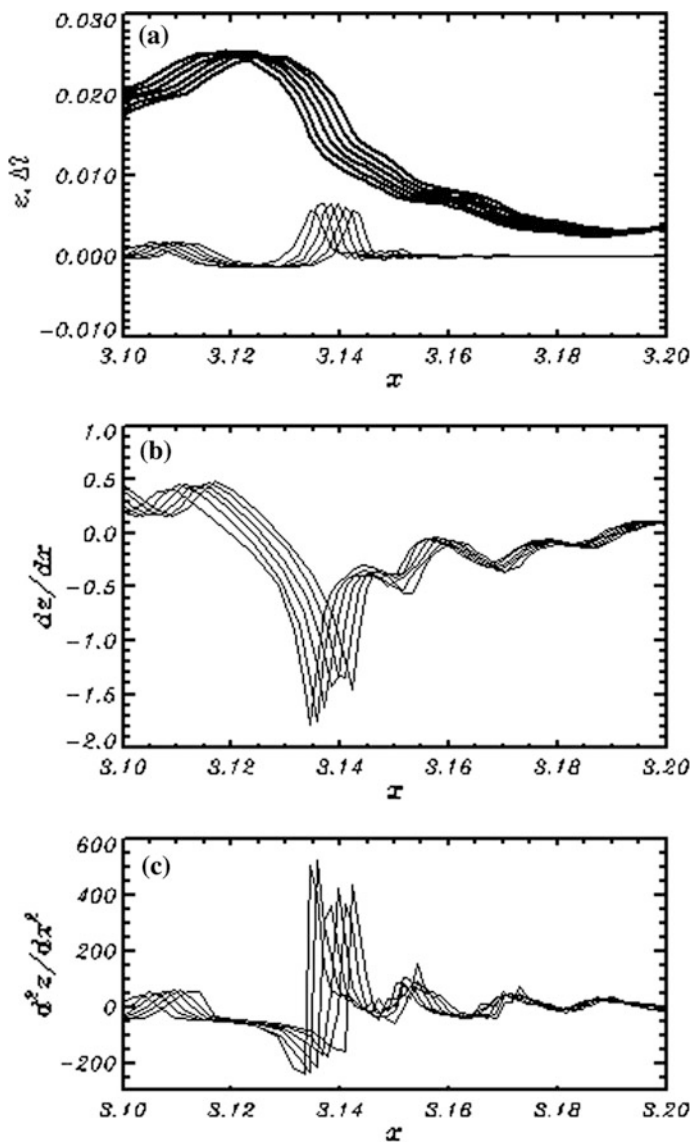


**Fig. 10.8** The local evolution of surface in the course of breaking simulated by algorithm (30, 32) over 0.05 non-dimensional time units, which corresponds to 0.04 period of this mode. The wave moves from left to right in all the three panels: **a** solid curve represents the top of breaking wave, and thin curves correspond to change of surface  $100\Delta z_b$  at consequent time steps with interval  $\Delta t = 0.01$ ; **b** is evolution of the first derivative  $\partial z / \partial x$  (tangent of surface slope); **c** is an evolution of the second derivative  $\partial^2 z / \partial x^2$  (curvature of the surface). (Chalikov and Babanin 2014 © 2014 Springer-Verlag Berlin Heidelberg. With permission of Springer.)

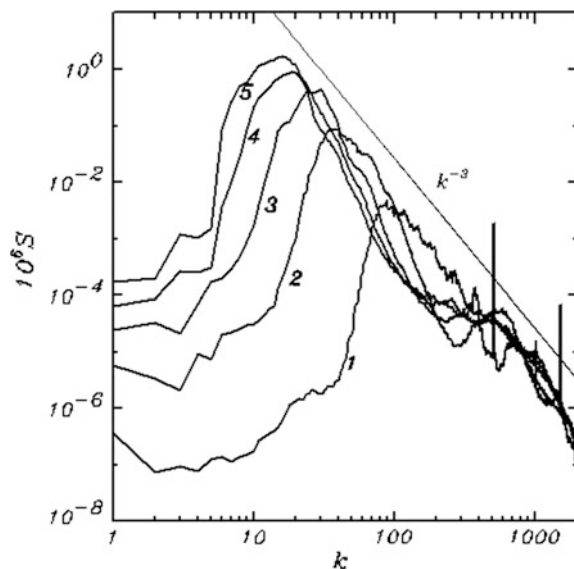
$s = 300$ , the breaking terminates. According to the suggested algorithm, the breaking always smoothes the narrow intervals with large positive curvature and does not affect other areas. The numerical parameters in (8.3.14) were chosen to compromise the closest approach to the point of breaking and numerical stability. The total dissipation rate does not depend significantly on these parameters.

## 10.7 Simulation of One-Dimensional Wave Field Evolution

The model (2.2.34)–(2.2.35) extended through the algorithms in Sects. 10.5 and 10.6 is used for simulation of the one-dimensional wave field evolution under the action of nonlinear interactions, wind input, ‘tail,’ and breaking dissipation. The number of modes  $M$  is equal to 2048 (4097 Fourier coefficients), while the number of grid points  $N = 8196$ . The initial wave field was assigned as a train of Stokes waves with the steepness  $ak = 0.15$ . The modes of Stokes wave are placed at  $k = 500, 1000, 1500, 2000$  (thus, 500 Stokes waves are assigned within the interval  $(0-2\pi)$ ). An algorithm for the Stokes wave calculations suggested by Chalikov and Sheinin (1996, 1998) is described in Sect. 3.2. The simulation with the time step  $\Delta t = 0.001$  is carried out for 2,000,000 steps, which corresponds to 20,000 non-dimensional time units or  $7117$  initial Stokes wave periods  $T_s \approx 2\pi/\sqrt{k_p}$ .

Under the action of wind, the wave energy starts to grow, while the spectral peak shifts to lower wave numbers. The spectrum is also transforming due to Benjamin–Feir instability. The spectra  $S_k$  obtained by averaging over 5 consecutive periods, each being equal to 4000 non-dimensional time units, are shown in Fig. 10.9.

**Fig. 10.9** Wave spectra  $S_k$  obtained by averaging over 5 consequent periods, each having the length of 4000 non-dimensional time units. Thin line shows the dependence  $S_k \sim k^{-3}$  or  $S_\omega \sim \omega^{-5}$ . (Chalikov and Babanin 2014 © 2014 Springer-Verlag Berlin Heidelberg. With permission of Springer.)



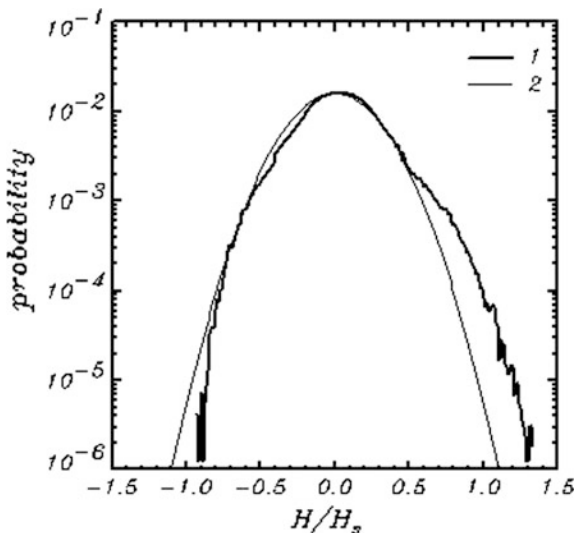
The first spectrum still contains peaks at  $k = 500$  and  $k = 1500$  of the Stokes modes. The mode at  $k = 1000$ , however, has already disappeared. The thin line shows dependence  $S_k \sim k^{-3}$  which corresponds to the  $S_\omega \sim \omega^{-5}$  law. The tendency to follow this dependence is getting clearer for the high-wave number part of the spectrum ( $k > 500$ ), but for the intermediate wave numbers, the slope is larger than for  $S_\omega \sim \omega^{-5}$  law. Note that we did not intend to reproduce a high-wave number part of spectrum with a 1-D model, because it is definitely formed by the 2-D interactions. We do not state that a two-dimensional model has the same properties as a three-dimensional model.

The initial wave number  $k$  was taken equal to 512 to leave a sufficient spectral space for developing of waves. Let us, for example, suggest that the length of Stokes wave  $\tilde{L}_s$  is equal to 0.5 m. Hence, the length of domain is 256 m, while the length scale  $L = 40.7$  m. The amplitude  $\tilde{a}$  of the initial waves is 0.012 m. The dimensional wave number  $\tilde{k}$  is  $12.6 \text{ m}^{-1}$ , dimensional frequency  $\tilde{\omega}$  is  $11.1 \text{ s}^{-1}$ , and phase velocity  $\tilde{c}$  is  $0.88 \text{ ms}^{-1}$ . The initial inverse wave age  $\Omega_p$  was taken 12; hence, the wind velocity  $\tilde{U}$  equals to  $0.88 \text{ ms}^{-1}$ . A significant wave height at the initial condition equals 0.038 m. By the end of development, the wave peak falls down to  $k = 14$ , which corresponds to  $\tilde{k} = 0.34 \text{ m}^{-1}$  and to the wave length  $\tilde{L}_s = 18.5$  m; the frequency decreases down to  $1.8 \text{ s}^{-1}$ , while the peak phase velocity grows up to  $5.3 \text{ ms}^{-1}$ . The significant wave height increases 65 times and approaches 0.975 m.

The waves simulated acquire quite distinct nonlinear features. The probability distribution of surface elevation normalized by the significant wave height  $\tilde{H} = H/H_s$  is shown in Fig. 10.10.

These data are obtained over the last 1/3 part of the entire period, when the wave field is not so non-stationary as during the initial period. As shown, the probability differs significantly from the Gaussian distribution; i.e., it is non-symmetric with

**Fig. 10.10** 1 Probability of surface elevation; 2 a normal distribution. (Chalikov and Babanin 2014 © 2014 Springer-Verlag Berlin Heidelberg. With permission of Springer.)



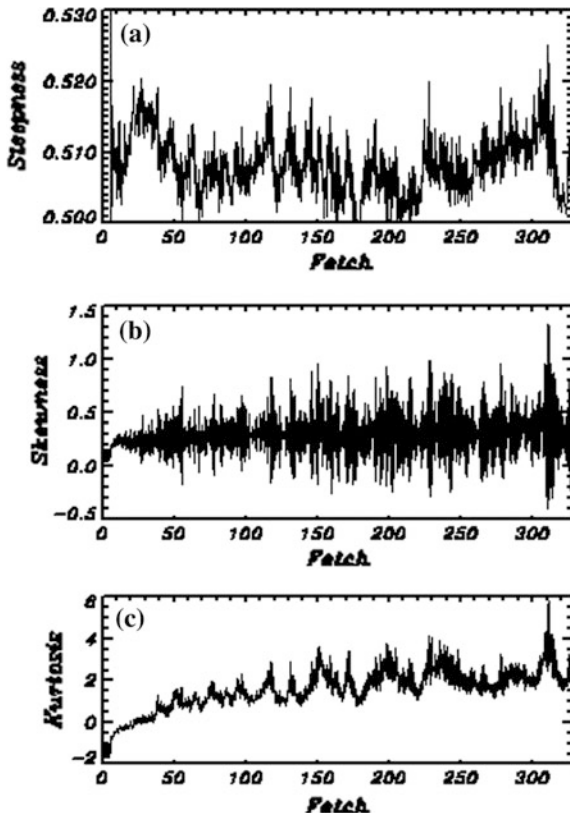


**Fig. 10.11** Statistical characteristics of waves: **a** rms steepness; **b** skewness; **c** kurtosis (Eqs. 10.7.1). (Chalikov and Babanin 2014 © 2014 Springer-Verlag Berlin Heidelberg. With permission of Springer.)

respect to  $\tilde{H} = 0$ . The distribution shows that the probability of large waves is much higher than the normal distribution predicts. The extreme waves have similar properties (Chalikov 2009).

The statistical characteristics of wave field are shown in Fig. 10.11.

As shown in panel *a*, the wave field has large overall steepness  $St$ , skewness  $Sk$ , and kurtosis  $Ku$  (Eq. 5.2.4). For superposition of linear waves, skewness and kurtosis are equal to zero. The positive skewness here indicates that the top of the probability curve is sharp; the tail on the right-hand side is longer than that on the left one, while the bulk of the values lie to the right of zero. It means that large values are more frequent than the normal distribution prescribes. The most evident manifestation of this property is the freak wave phenomenon. For linear waves, kurtosis  $Ku$  is equal to 0. The actual value of kurtosis fluctuates and can reach a value as large as 8. Large values of kurtosis mean that the distribution is narrower than the Gaussian one, and the extremes are large (in our case, the extremes are positive) while the

intervals of small elevation are smooth. The experimental data on skewness and kurtosis vary in broad limits and quite often show the values close to 0.5 and 1.0, correspondingly (Onorato et al. 2009). The developing and young waves are sharper than the developed waves, and this is why the high-order moments for such waves are larger. There is another effect that can be a cause of large values of the high-order moments. Opposite to energy (the second-order moment), the values of skewness and kurtosis depend significantly on the length of domain. At the initial stage, the number of peak waves is large, while the ensemble is broad. While waves are developing, the number of waves in domain decreases. By the end of the calculation, the domain contains just fifteen peak waves. Even if one of them becomes high and sharp, the values of kurtosis and skewness can become large.

An evolution of the integral characteristics of wave field is shown in Fig. 10.12 as a function of the non-dimensional fetch  $F$  defined as:

$$F(t) = \frac{1}{\lambda_0} \int_0^t c_p dt, \quad (10.7.1)$$

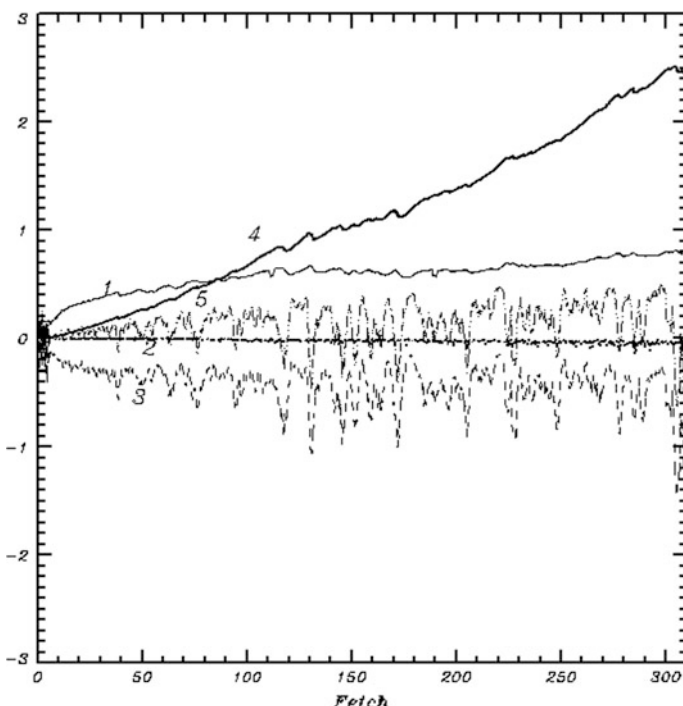


**Fig. 10.12** Evolution of the integral characteristics as function of fetch  $F$  (Eq. 10.7.2): 1 rate of energy input; 2 rate of ‘tail dissipation’; 3 rate of breaking dissipation; 4 evolution of the total energy; 5 the sum of input and dissipation terms. (Chalikov and Babanin 2014 © 20104 Springer-Verlag Berlin Heidelberg. With permission of Springer)

where  $c_p$  is a phase speed at peak of spectrum, while  $\lambda_0$  is an initial wavelength of Stokes wave.

Curve 4 corresponds to the growing total energy of waves. Curve 5 shows evolution of the wind-to-wave energy input. Curve 2 demonstrates a rate of ‘tail dissipation’ described by algorithm (2.3.4)–(2.3.6), while curve 3 shows a rate of ‘breaking dissipation’ (Eqs. 8.3.12–8.3.14). As shown, the ‘tail dissipation’ is steady and quite weak, while the ‘breaking dissipation’ is strong and intermittent. The sum of all the terms for the input and dissipation is presented by curve 5. On the average, the sum is positive (otherwise, the waves would not grow), but within the brief intense breaking events, the total input can be negative.

An evolution of the integral characteristics as a function of fetch  $F$  (Eq. 10.7.1) is shown in Fig 10.13. As shown, the values of all the components of the energy input and energy sink increase, while the wave energy grows (curves 1). Spectral distributions of different sources of the energy are seen most clearly in panel *d*. Thick curve 1 corresponds to the wave spectrum normalized by its maximum. Dashed curve 3 describes the energy input. As shown, it is positive and its shape is similar to the spectrum shape. Dotted curve 2 shows the spectral distribution of a nonlinear interaction rate. This term is very sensitive to the shape of spectrum, which explains a complicated character of the nonlinear interaction spectrum. However, at a low-frequency slope of wave spectrum, the nonlinear interactions are positive, while at the opposite slope, they are negative. It means that the nonlinear interactions in the energy-containing part of spectrum transfer energy to the longer wave components and produce downshifting. It is interesting to note that the breaking dissipation (curve 4) also works for downshifting; i.e., it is positive at a low-wave number slope of spectrum and in peak of spectrum; it is negative at a high-wave number slope. The same property can be observed in other panels of Fig. 10.13.

Firstly, such property can be explained by an incorrect spectral interpretation of a strongly nonlinear process. Since breaking occurs in the relatively narrow space intervals (in the vicinity of wave crests) separated by broad paths with no breaking, the spectrum of dissipation rate is extended toward its high-frequency end. In reality, the breaking mostly reduces height of the largest nonlinear waves not fully represented in wave spectrum.

Secondly, an existence of the spectral energy input due to the breaking does not contradict to the physical constraints. The breaking can be considered as a sort of irreversible nonlinear interaction. The diffusion-like algorithm (8.3.12–8.3.14) does not only lower the local potential and kinetic energy but also redistributes the energy in space; i.e., some parts in the vicinity of breaking obtain the energy, while others lose it. In the spectral space, the energy is distributed between the higher and lower wave numbers around the peak wave number. This concept has been previously formulated in the course of experimental and theoretical investigations. It was clearly expressed by Tulin and Waseda (1999): ‘...recurrence was prevented by the spreading of discretized energy to higher frequencies. Strong breaking was

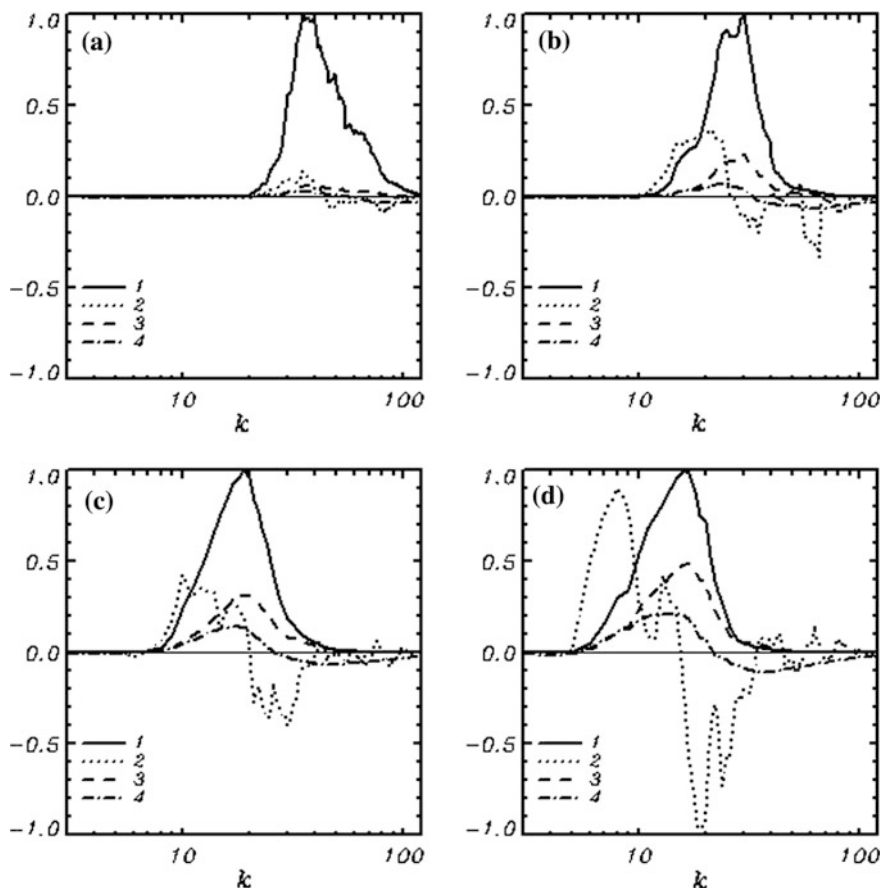


**Fig. 10.13** Spectra obtained by averaging over the last four consequent periods, length of each being equal to  $t = 400$ : 1 wave spectrum normalized by its maximum value; 2 rate of nonlinear interactions; 3 rate of energy; 4 rate of dissipation. (Chalikov and Babanin 2014 © 2014 Springer-Verlag Berlin Heidelberg. With permission of Springer.)

found to increase the transfer of energy from the higher to the lower sideband and to render that transfer irreversible. The end state of the evolution following strong breaking is an effective downshifting of the spectral energy.<sup>7</sup> The process of breaking simulated directly (Tulin and Waseda 1999) is described parametrically in the current work (see also Gramstad and Stiassnie (2013) on the role of breaking in nonlinear interactions and wave energy downshifting). Opposite to the usual nonlinear interactions, the breaking works at very small timescales, but both processes can be treated as the nonlinear energy transfer.

According to the JONSWAP experimental data (Hasselmann et al. 1973; Battjes et al. 1987), the non-dimensional wave energy  $E$  is a linear function of fetch  $F$ .

$$E = c_E UF, \quad (10.7.2)$$

where  $c_E \approx 1.7 \times 10^{-7}$  is an empirical constant;  $U = \frac{U_{10}^2}{gL}$  is a single non-dimensional parameter of the problem with the wind forcing. Dependence (10.7.2) can be represented in the following form:

$$E = \frac{E_0}{F_0} F, \quad (10.7.3)$$

where  $F_0$  and  $E_0$  are the reference fetch and wave energy (accordingly) introduced to eliminate uncertainty of the initial fetch, corresponding to the initial conditions for the spectrum. The total energy is calculated through the integral:

$$E = (2\pi)^{-1} \int_0^{2\pi} (z^2 x_\xi - \varphi \varphi_\zeta) d\xi, \quad (10.7.4)$$

where the first term corresponds to the potential energy; the second one—to the kinetic energy;  $x$  and  $z$  are the Cartesian coordinates of surface;  $\xi$  and  $\zeta$  are the conformal coordinates; and  $\varphi$  is the velocity potential. The dependence of  $E$  on  $F$  (Eq. 10.7.2) is shown in Fig. 10.13a (curve 1). Dependence (10.7.2) calculated with the use of the reference values  $E_0 = 7 \times 10^{-1}$  and  $F_0 = 30$  is represented by curve 2. As shown, an agreement between the empirical relation (10.7.2) and the dependence obtained in the course of the numerical simulation is very good.

According to the JONSWAP approximation, the dependence of the non-dimensional peak wave number on the fetch can be represented in the following form:

$$k_p = c_k U^{-1/3} F^{-2/3}, \quad (10.7.5)$$

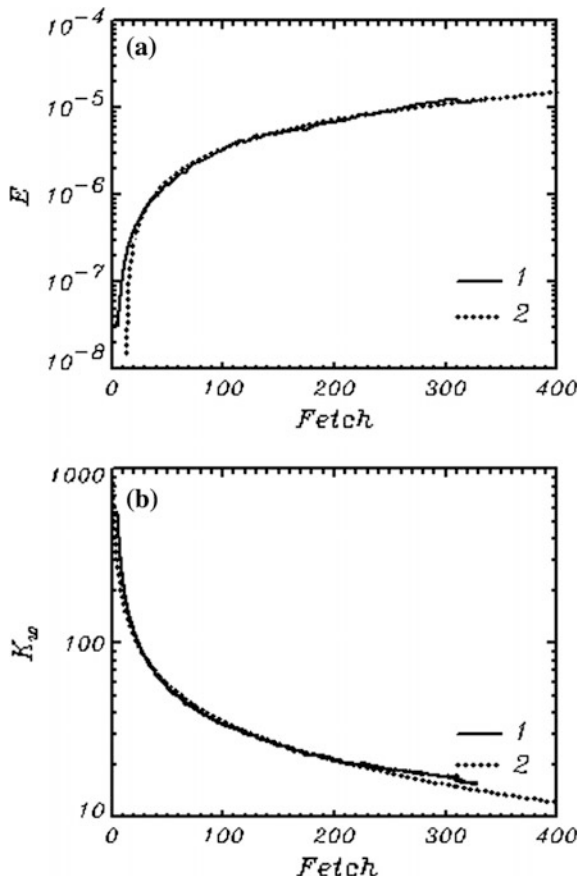
where  $c_k = 22^2$ . Since the parameter  $U$  is not defined, dependence (10.7.4) can be further represented as follows:

$$k_p = \bar{c} F^{-2/3}, \quad (10.7.6)$$

where parameter  $\bar{c}$  can be defined by the rms method, its value being not essential. Dependence  $k_p(F)$  calculated with the model (curve 1) and dependence (10.7.5) (curve 2) are shown in Fig. 10.14b.

Thus, we can come to the conclusion that the empirical laws  $E \sim F$  and  $k_p \sim F^{-2/3}$  are well reproduced with a one-dimensional model extended with the theoretical input and dissipation terms. It should be emphasized that no ‘tuning’ of

**Fig. 10.14** Comparison of the simulated evolution with that given by JONSWAP spectrum as the functions of fetch  $F$  (Eq. 10.7.2):  
**a** evolution of the total energy; **b** evolution of the weighted frequency.  
(Chalikov and Babanin 2014  
© 2014 Springer-Verlag  
Berlin Heidelberg. With  
permission of Springer.)



the model, i.e., variation of the coefficients in Eqs. (2.3.6) and (8.3.14), for obtaining a better agreement with the empirical laws, was used.

## 10.8 Conclusions

Unlike turbulent friction, the WPMF is not an internal property of a turbulent boundary layer, since it is created by external forcing, i.e., by waves. The presence of the WPMF brings forward the specific features of the WBL. The wind profile in the lowest part of the WBL deviates considerably from the logarithmic profile (Fig. 10.1). The 1-D theory of the WBL allows investigating the dependence of a drag coefficient  $C_{10}$  on wind velocity  $u_{10}$  (Fig. 10.2). It is proved that a wide scatter of the experimental data on  $C_{10}$  can be explained by additional dependence on a

wave spectrum shape. The same effect is clearly pronounced in the roughness parameter normalized by the Charnock scale (Fig. 10.3).

As demonstrated in Fig. 10.2, the current theory predicts a monotonic growth of the drag coefficient with the increase of wind speed. However, there exist some data showing that for the wind speed exceeding  $25\text{--}30 \text{ ms}^{-1}$ , the drag coefficient reaches the upper limit (Powell et al. 2003; Donelan et al. 2004), while at further increase of wind speed, the drag coefficient can even decrease. Earlier, such an effect was also noted when analyzing the tropical cyclone development (Emanuel 1995). Currently, some attempts are made to explain such behavior of drag coefficient on the basis of the ‘droplet theory’ (Andreas 2004; Kudryavtsev 2006). According to the theory, the drops generated as a result of splitting of the falling water volumes intensify dissipation of turbulence, which causes reduction of drag coefficient. Such scheme looks reasonable, although the model of drop generation (as well as the mechanism of drop–turbulence interaction) uses too many arbitrary assumptions.

According to our data, an effect of wave drag reduction at high wind speeds can be easily explained through the influence of high-frequency waves. It would be appropriate to suggest that the energy of short waves at high winds decreases due to two factors: the presence of foam that suppresses short waves and the flow deceleration in troughs due to flow separation. The latter can be investigated using the coupled wind–wave model directly, though the model must take into account a broad range of wave spectrum from peak waves to capillary waves. A high wind speed and the necessity to use high vertical resolution in the WBL make this problem quite time-consuming; anyway, such calculations are possible from the technical point of view.

Note that the reduction of drag can also be caused by ‘blowing away’ sharp crests: High winds can smooth the surface and remove the elements responsible for stress. This effect was directly observed in wind–wave tunnel (Troitskaya—private communication 2010).

To prove that the reduction of drag coefficient is caused by suppression of small waves, additional calculations of drag coefficient were performed with use of a modified JONSWAP spectrum. The somewhat arbitrary assumption suggests that waves, whose frequency exceeds some value  $\omega_f$ , are absent. In our calculations, the longest removed wave is 100 times shorter than the peak wavelength. The spectral density at  $\omega = \omega_f$  equals  $10^{-5} S_p$  ( $S_p$  is the spectral density in wave peak). The amplitudes of such waves are about 100 times smaller than the amplitude of a dominant wave. Hence, the modifications of spectrum are quite insignificant. The above modifications were introduced in a new series of calculations with use of the 1-D model, Eqs. (10.1.1)–(10.1.3). The dependence of the drag coefficient on wind speed  $u_{10}$  for such case is shown in Fig. 10.7. As shown, the drag coefficient significantly decreases at high wind speed; for the developed sea ( $\Omega_p \sim 1$ ), the drag coefficient  $C_{10}$  has the maximum of  $C_{10} \approx 1.5 \times 10^{-3}$  at  $u_{10} \approx 30 \text{ ms}^{-1}$ , while for younger waves, the maximum is shifted to higher wind speeds.

It should be emphasized that the result presented in Fig. 10.7 is purely qualitative, since the exact shape of spectrum is unknown at high wind speeds.

Figure 10.7 just illustrates a simple explanation of the drag coefficient reduction at high wind speeds on the basis of high-frequency wave spectrum modification.

Our construction of the 1-D approach developed in this chapter allows repeating the calculations of the coupled wave WBL dynamics on the basis of a wave model and a one-dimensional WBL model. These calculations are very efficient, since the 1-D WBL model is much faster than the 2-D model based on Reynolds equations.

The problem solved above can be also formulated for the wave spectrum  $S(k)$  rather than for the fundamental variables  $\eta$  and  $\varphi$ . In this case, it is possible to use parameterization for the wind input (9.9.7) and adopt any available spectral parameterization of breaking dissipation, for example (Tolman and Chalikov 1996). A traditional scheme for the nonlinear interactions based on Hasselmann's integral, in such case, is not required, since it is known that the non-reversible effect of the nonlinear interaction for unidirectional waves is equal to zero. Thus, it is straightforward to predict the way of spectral behavior that can be observed in the course of integration. The initial spectrum will grow until the dissipation remains less than the input energy, and upon reaching the balance, the stationary solution can be obtained. Because of the absence of the nonlinear interaction, no downshifting can be expected.

The calculations discussed in this paper demonstrate a completely different picture. It is shown that growth of the wave energy is accompanied by downshifting.

The aim of this investigation is to find a reasonable compromise between the 2-D ( $x/z$ ) and 3-D ( $x, y, z$ ) direct modeling of wind waves. The fundamental problem of wave modeling is reproducing of the observed 2-D wave field evolution under the action of wind, dissipation, and nonlinear interactions. Note that nonlinear interactions do not need to be ‘included’ in any direct model since the nonlinearity is the essential property of the fluid mechanics equations.

Real waves are always two-dimensional, and their development should be investigated with the three-dimensional wave model based on full equations and extended with the appropriate algorithms for the energy input and dissipation. Such model has been recently completed (Chalikov et al. 2014). In the current paper, we demonstrate that one-dimensional waves can develop under the strong influence of 1-D nonlinear interactions which, according to (Chalikov 2012), also work in one-dimensional wave fields. It is shown that the growth of energy and its rate of downshifting are in close agreement with the observational data obtained in the JONSWAP experiment. It means that the model with the suggested physics can describe the observed evolution of wave fields. The downshifting occurs due to both the one-dimensional nonlinear interactions and the effects of breaking. The integral of the breaking term over wave numbers is naturally negative; however, the rate of redistribution of energy over spectrum is more intensive than the dissipation and loss of energy due to such breaking. Note that spectral distribution of the breaking input is similar to the spectrum of nonlinear interactions. The breaking transfers energy from a high-wave number part of spectrum to low wave numbers. It means that the breaking is a process of irreversible wave–wave interaction, when some part of the energy is redistributed over the spectral space, while the remaining

part is transferred to the energy of turbulence and currents, as well as to the work against buoyancy forces and other mechanisms outside the wave system. Opposite to Donelan et al. (2012), here we do not deny an existence of the wave–wave interactions, which has been considered a major source term in the wave system since the publication by Hasselmann (1962). We are sure that these interactions play a significant role in the development of wave field. However, the Hasselmann's theory cannot be universal, since it is based on many simplifying assumptions, such as follows: (1) Wave field is assumed to be the superposition of weakly nonlinear modes with random phases and a linear dispersion relation, slowly interacting at timescales of thousands of wave periods. The term ‘weakly’ was never clearly specified. In reality, the local inclination of wave surface can be of the order of 1. The linear dispersion relation is valid only for a low-frequency part of spectrum. (2) Only the forth-order interactions are considered, mostly because the next orders present too many analytical difficulties. (3) The Hasselmann's theory only describes slow exact resonances and does not describe fast quasi-resonant interactions which, in particular, lead to the 1-D Benjamin–Feir instability and also produce redistribution of the spectral energy and, finally,—the downshifting (Chalikov 2012). (4) The convergence of Hasselmann's integral with the increase of the spectral resolution was never proved and may not be the case.

All the points stated above do not mean that the wave–wave resonances do not exist. The true and full set of nonlinear interactions is much more complicated as they occur among all the nonlinear objects and are not limited to the resonant quadruplets. In particular, the nonlinear interactions do occur among the unidirectional modes, which is not presented in the Hasselmann's equation; however, this effect is predicted by Benjamin–Feir theory (see also Annenkov and Shrira, 2006<sup>1</sup> on the role of the latter in 2-D wave fields).

The current work proves that there is no substantial difference between the 1-D and 3-D waves in the presence of input and dissipation. Such conclusion opens wide prospects for investigation of many important processes, such as dissipation (including breaking), energy input, and generation of extreme waves. Such prospects are quite important, since the 3-D modeling requires about 1000 times more extensive computing, and then, there is no well-tuned physics until now. Most of the important local phenomena are mostly one-dimensional, so it would be reasonable to investigate them with 1-D model, leaving 3-D modeling for the problems whose nature is essentially three-dimensional, for example, the problem of angular spreading of sea waves and its role in the processes of energy supply, wave breaking, and generation of extreme waves. Such investigations should be based on the well-established regularities obtained for unidirectional waves.

# **Chapter 11**

## **Numerical Investigation of Turbulence Generation in Non-breaking Potential Waves**

**Abstract** Theoretically, potential waves cannot generate the vortex motion, but the scale considerations (Babanin 2006) indicate that if the steepness of waves is not too small, the Reynolds number can exceed the critical values. This means that in presence of initial non-potential disturbances, the orbital velocities can generate the vortex motion and turbulence. This problem has been investigated by means of linear instability theory (Benilov et al. 1993). It was shown that pure two-dimensional motion always remains potential because one-dimensional vortex (in vertical plane) does not interact with the orbital motion. The waves can generate the vortex in horizontal plane, and further development of vorticity occurs due to exchange of energy between the components of vorticity. Then, due to nonlinearity, motion at smaller scales and more or less developed turbulent regime arise. This problem was investigated numerically on basis of full two-dimensional ( $x-z$ ) equations of potential motion with the free surface in cylindrical conformal coordinates. It was assumed that all variables are a sum of the 2-D potential orbital velocities and 3-D non-potential disturbances. Because the energy of waves is much larger than energy of turbulence, currently it was assumed that only one-way interaction exists: Non-potential motion takes the energy from potential waves. The non-potential motion is described directly with 3-D Euler equations, with very high resolution. The interaction between potential orbital velocities and non-potential components is accounted through additional terms which include the components of vorticity. The effects of turbulence are incorporated with a use of subgrid turbulent energy evolution equation. The turbulent scale is assumed to be proportional to grid resolution (LES technique). For small waves, the approach turns into a direct simulation method. Numerical scheme is based on 2-D Fourier transform method in ‘horizontal’ (in conformal coordinates) plane and on second-order approximation in the ‘vertical’. The pressure is calculated by means of Poisson equation in cylindrical conformal coordinates derived through covariant components of velocity. Poisson equation was solved with three-diagonal matrix algorithm (TDMA). Initial conditions for the elevations and the surface potential for waves were assigned according to the linear theory, and 3-D non-potential velocity components were inserted as a small-amplitude noise. Long-term numerical integration of the system of equations was done for different wave steepness. The vorticity and turbulence usually

occurred in vicinity of wave crests (where the velocity gradients reach their maximum) and then spreads over upwind slope and downward. Specific feature of the wave turbulence is its strong intermittency: The turbulent patches are mostly isolated, and intermittency grows with the decrease of the wave amplitude. The maximum values of energy of turbulence are in qualitative agreement with experimental data. The results suggest that even non-breaking potential waves can generate the turbulence, which thus enhance the turbulence created by the shear current. Further investigation of this process will include the effect of tangential stress on a sea surface and flux of turbulent energy from the surface generated by breaking waves.

## 11.1 Turbulence Generation by Potential Waves. Theoretical Background

The concept of the wave-induced non-breaking turbulence was recently proposed by Qiao et al. (2004) and Babanin (2006) and then proved by laboratory measurements (Babanin and Haus 2009; Dai et al. 2010) and in the field (Toffoli et al. 2012). Dai et al. (2010), for example, showed that, in the presence of gently sloped non-breaking waves, the initially stratified fluid became uniform by two orders of magnitude faster than in the absence of waves, i.e., in case of pure molecular diffusion.

Lately, an essential importance of this turbulence for the dynamics of the upper ocean and for the air-sea interactions has been also clearly demonstrated. In finite depth environment and at shelves, this turbulence produces mixing through to the bottom in response to a single storm, this contribution being critical for accurate modeling of the sediment suspension (e.g., Pleskachevski et al. 2011). When employed in the ocean-circulation and general-circulation models, an agreement between the data and the calculated sea surface temperature and the upper-ocean temperature profiles improved by up to 35 %, depending on the wave climate at a particular location, as well as on latitude (Qiao et al. 2004, 2010; Huang et al. 2008). In modeling of the current climate, an account for such turbulence might lead to the increase of the magnitudes of seasonal variation of the main hydrometeorological properties such as temperature, pressure, and other characteristics (Babanin et al. 2009) (Table 11.1).

While the concept appears new and the wave-induced turbulence is missing from most of the ocean-mixing schemes, because the waves are routinely treated as irrotational and, therefore, non-generating turbulence, the idea was in fact well-familiar to oceanographers over 50 years ago. The book of Kinsman (1965) includes a chapter on rotational wave motion, i.e., the linear and nonlinear wave theory in the presence of viscosity, with references to Stokes (1847), Longuet-Higgins (1953), and Phillips (1977); the book also contains a section on the wave-induced turbulence in non-breaking waves. We should add Kitaigorodskii (1961) to this early list of papers.

**Table 11.1** Characteristics of numerical models used for the generation of the ensembles of surfaces

	Spectral resolution	Grid resolution	Peak wave number	Time step	Number of time steps	Integration time ( $t_p$ )
3-D model 1st run	$256 \times 128$	$1024 \times 512$	16	0.005	200,000	636
3-D model 2nd run	$512 \times 128$	$2048 \times 512$	64	0.0025	100,000	318
2-D model	1000	4000	16	0.001	2,000,000	1273

It was the success of the potential theories of nonlinear waves, introduced in the 1960s, that made the non-potential wave theories seem redundant and, eventually, nearly forgotten. Such theories certainly provide a rich range of useful physics, both deterministic and stochastic. In other respects, however, irrotational theories are inadequate. Kinsman (1965) noted while giving comments on one of such applications: ‘Careful measurements of the mass-transport velocity associated with waves... all suggest that the Stokes wave is unsatisfactory model so far as the mass-transport velocity associated with water waves is concerned. It would seem that the argument on which Stokes chose irrotationality was crucially unsound, if a study of water waves was his object. You do not arrive at the same place by setting the viscous terms to zero to begin with as you do if you retain them and then let the viscosity tend to zero at the end of your analysis.’

Another reason for the disrepute of the old rotational wave theories was a relatively small rate of production of vorticity within these approaches. Such low rates, however, were a consequence of the two-dimensionality of the old analytical solutions, and this issue was well-appreciated by the old school of oceanographers: ‘Unfortunately, the analysis of turbulence is very difficult, since the process is essentially three-dimensional. This means that nothing remotely useful will result from a two-dimensional analysis of the sort we have used with infinitely long-crested waves’ (Kinsman 1965).

This problem was later investigated by means of a linear instability theory, and it was shown that this is not the long crestedness of waves, but the two-dimensionality which is the setback in 2-D approaches. This instability problem was formulated first by Benilov and Losovatskii (1977). Later, the idea was further developed by Kitaigorodskii and Lumley (1983) and Benilov et al. (1993). Within such theory, it was shown that pure two-dimensional motion remains potential because one-dimensional vortex (in vertical plane) does not interact with the wave orbital motion. If turbulence is treated in a three-dimensional sense, however, and the real turbulence is nearly always three-dimensional, the waves can generate the vortex in horizontal plane. Such vortex is unstable, and further development of vorticity occurs due to the exchange of energy between the components of vorticity. Then, due to the nonlinearity, motion at smaller scales and more or less developed turbulent regime arise on behalf of the wave energy.

Other theoretical and experimental studies should also be highlighted in this context, even if briefly. Jacobs (1978) introduced additional turbulent viscosity which remains after the mean orbital wave motion is averaged out, what Pleskachevski et al. (2011) called the ‘symmetric effect.’ Anis and Moum (1995) employed both the symmetric and ‘asymmetric’ effects, the latter being production of the turbulence due to waves being irrotational. In the field, the wave turbulence, unrelated to the breaking, was explicitly observed and even parameterized by Efimov and Khristoforov (1971).

The significance of such wave-induced turbulence, in the meantime, is hard to overestimate. Waves produce turbulence for the upper ocean in a number of ways, i.e., by breaking (e.g., Chalikov and Belevich 1992) and by interacting with background turbulence through the Stokes current (e.g., Ardhuin and Jenkins 2006), through triggering Langmuir circulation (e.g., Langmuir 1938; McWilliams and Sullivan 2000), and through the shear stresses within vertical gradients of the orbital velocities (see, e.g., Babanin 2011 for a review of these issues). While the former three mechanisms rely on the downward diffusion or advection of the near-surface turbulence, the last one generates turbulence directly through the water column at the scale of the wavelength (100 m) if the associated Reynolds numbers (wave heights) are large enough.

Thus, as it was mentioned above, the role of this turbulence in the upper-ocean mixing is essential. It is interesting, however, to quote Kinsman (1965) again with regard to: ‘... while the vorticity field induced by wave motion is of the second order and affects the mean motion to the second order, its effect on the fluctuating motion is of the third order...’

In the present chapter, a new wave-turbulence model is discussed; the results of its application are demonstrated and compared with experiment (Babanin and Chalikov 2012). This wave-turbulence model is based on full two-dimensional ( $x-z$ ) equations of potential motion with free surface in the cylindrical conformal coordinates. These equations constitute a fully nonlinear model of 2-D waves which is coupled with a 3-D model for turbulence. This latter non-potential motion is described directly with 3-D Euler equations with very high resolution. The interaction between potential orbital velocities and non-potential components is accounted through the additional terms which include the components of vorticity. The effects of turbulence are incorporated with a use of subgrid turbulent energy evolution equation. The turbulent scale is assumed to be proportional to grid resolution (LES technique). The results suggest that even non-breaking potential waves can generate the turbulence which thus enhances the turbulence created by the shear currents.

In this chapter, Sects. 11.2 through 11.5 contain description of different aspects of the model. The surface-following coordinates are introduced in Sect. 11.2, followed by the equations for vortical motion in Sect. 11.3. Section 11.4 describes the LES approach employed for simulation of turbulence, while Sect. 11.5 describes the fully nonlinear wave model. Section 11.6 demonstrates the computational results, while the conclusions are formulated in the final Sect. 11.7.

## 11.2 Cylindrical Conformal Coordinates

Let us introduce the curvilinear surface-following conformal in plane ( $x = x_1, y = x_2$ ) cylindrical coordinates  $(\xi, \vartheta, \zeta)$  connected with the Cartesian coordinates  $(x, y, z)$  by the relations ( $z$ -axis is directed upward):

$$x = \xi + x_0(\tau) + \sum_{-M \leq k \leq M, k \neq 0} \text{sign}(k) \eta_{-k}(\tau) \frac{\cosh|k|(\xi + H)}{\sinh|k|H} \theta_k(\xi), \quad (11.2.1)$$

$$z = \zeta + \eta_0(\tau) + \sum_{-M \leq k \leq M, k \neq 0} \eta_k(\tau) \frac{\sinh|k|(\xi + H)}{\sinh|k|H} \theta_k(\xi), \quad (11.2.2)$$

$$y = \vartheta, \quad (11.2.3)$$

$$t = \tau, \quad (11.2.4)$$

where the factors containing hyperbolic functions allow us to introduce finite depth  $z = H$ ,  $k$  is wave number,  $M$  is truncation parameter,  $t$  is time,  $\eta_k$  are Fourier amplitudes of two-dimensional surface  $\eta(\xi, \vartheta)$  (Eq. 2.2.5), and  $\theta_k(\xi)$  denotes function (2.2.6).

The metric coefficients for transformation (11.2.1)–(11.2.4) take the form

$$x_\xi = 1 + \sum_{-M \leq k \leq M} |k| h_k \frac{\cosh|k|(\xi + H)}{\sinh|k|H} \vartheta_k(\xi), \quad (11.2.5)$$

$$z_\xi = - \sum_{-M \leq k \leq M} kh_{-k} \frac{\sinh|k|(\xi + H)}{\sinh|k|H} \vartheta_k(\xi), \quad (11.2.6)$$

$$x_\tau = \sum_{-M \leq k \leq M} (h_\tau)_{-k} \frac{\cosh|k|(\xi + H)}{\sinh|k|H} \vartheta_k(\xi), \quad (11.2.7)$$

$$z_\tau = \sum_{-M \leq k \leq M} \text{sign}(k) (h_\tau)_k \frac{\sinh|k|(\xi + H)}{\sinh|k|H} \vartheta_k(\xi). \quad (11.2.8)$$

Conformal coordinates satisfy conditions (2.2.13) and (2.2.23) and

$$\frac{\partial J}{\partial \tau} + \frac{\partial J_{\xi t}}{\partial \xi} + \frac{\partial J_{\zeta t}}{\partial \zeta} = 0, \quad (11.2.9)$$

$$\frac{\partial J}{\partial \tau} + \frac{\partial}{\partial \xi} (-z_\xi z_\tau - x_\xi x_\tau) + \frac{\partial}{\partial \zeta} (z_\xi x_\tau - x_\xi z_\tau) = 0 \quad (11.2.10)$$

where  $J$  is a Jacobian of transformation (2.2.14).

Note that all the metric coefficients do not depend on coordinate  $\vartheta$ . Below, the rules of transformations are written out:

$$\frac{\partial(\cdot)}{\partial x} = \xi_x \frac{\partial(\cdot)}{\partial \xi} + \zeta_x \frac{\partial(\cdot)}{\partial \zeta} = J^{-1} \left( x_\xi \frac{\partial(\cdot)}{\partial \xi} - z_\xi \frac{\partial(\cdot)}{\partial \zeta} \right) = J^{-1} \left( \frac{\partial(\cdot)x_\xi}{\partial \xi} - \frac{\partial(\cdot)z_\xi}{\partial \zeta} \right), \quad (11.2.11)$$

$$\frac{\partial(\cdot)}{\partial z} = \xi_z \frac{\partial(\cdot)}{\partial \xi} + \zeta_z \frac{\partial(\cdot)}{\partial \zeta} = J^{-1} \left( z_\xi \frac{\partial(\cdot)}{\partial \xi} + x_\xi \frac{\partial(\cdot)}{\partial \zeta} \right) = J^{-1} \left( \frac{\partial(\cdot)z_\xi}{\partial \xi} + \frac{\partial(\cdot)x_\xi}{\partial \zeta} \right), \quad (11.2.12)$$

$$\frac{\partial(\cdot)}{\partial t} = \frac{\partial(\cdot)}{\partial \tau} + \xi_t \frac{\partial(\cdot)}{\partial \xi} + \zeta_t \frac{\partial(\cdot)}{\partial \zeta}. \quad (11.2.13)$$

### 11.3 Equation for Vortical Motion

Now, let us consider the Euler equation in the Gromeko–Lamb form

$$\frac{\partial \bar{u}}{\partial t} = - \frac{\partial}{\partial x} (\bar{p} + \bar{E} + z) + \bar{\omega}^y \bar{w} - \bar{\omega}^z \bar{v}, \quad (11.3.1)$$

$$\frac{\partial \bar{v}}{\partial t} = - \frac{\partial}{\partial x} (\bar{p} + \bar{E} + z) + \bar{\omega}^z \bar{u} - \bar{\omega}^x \bar{w}, \quad (11.3.2)$$

$$\frac{\partial \bar{w}}{\partial t} = - \frac{\partial}{\partial x} (\bar{p} + \bar{E} + z) + \bar{\omega}^x \bar{v} - \bar{\omega}^y \bar{u}, \quad (11.3.3)$$

where  $(\bar{u}, \bar{v}, \bar{w})$  are the full components of velocity,  $(\bar{\omega}^x, \bar{\omega}^y, \bar{\omega}^z)$  are the components of vorticity,  $\bar{p}$  is the deviation of pressure off the hydrostatic pressure, and  $\bar{E} = 1/2 \cdot (\bar{u}^2 + \bar{v}^2 + \bar{w}^2)$  is the kinetic energy. Since vorticity  $\bar{\Omega}_i$  of the potential flow is zero, a similar equation for potential motion described by variables  $(U, V, W, P)$  has the form

$$\frac{\partial \bar{U}}{\partial t} = - \frac{\partial}{\partial x} (\bar{p} + \bar{E} + z), \quad (11.3.4)$$

$$\frac{\partial \bar{V}}{\partial t} = - \frac{\partial}{\partial y} (\bar{p} + \bar{E} + z), \quad (11.3.5)$$

$$\frac{\partial \bar{W}}{\partial t} = - \frac{\partial}{\partial z} (\bar{p} + \bar{E} + z). \quad (11.3.6)$$

Full variables can be represented as a sum of the vortical  $(u, v, w, p)$  and potential  $(U, V, W, P)$  components:

$$\begin{aligned}\bar{u} &= u + U, \quad \bar{v} = v, \quad \bar{w} = w + W, \\ \bar{p} &= p + P, \quad \bar{\omega}^i = \omega^i + \Omega^i \quad \Omega^i = 0\end{aligned}\quad (11.3.7)$$

Hence, from (11.3.1)–(11.3.3), it follows that

$$\frac{\partial u}{\partial t} = -\frac{\partial}{\partial x}(p + E + uU + wW + z) + \omega^y(w + W) - \omega^z v, \quad (11.3.8)$$

$$\frac{\partial v}{\partial t} = -\frac{\partial}{\partial x}(p + E + uU + wW) + \omega^z(u + U) - \omega^x(w + W), \quad (11.3.9)$$

$$\frac{\partial w}{\partial t} = -\frac{\partial}{\partial x}(p + E + uU + wW) + \omega^x v - \omega^y(u + U). \quad (11.3.10)$$

Converting (11.3.8)–(11.3.10) to the standard form, we obtain

$$\frac{\partial u}{\partial t} + \frac{\partial uu}{\partial x} + \frac{\partial vu}{\partial y} + \frac{\partial wu}{\partial x} = -\frac{\partial}{\partial x}(p + uU + wW) + \omega^y W, \quad (11.3.11)$$

$$\frac{\partial v}{\partial t} + \frac{\partial uv}{\partial x} + \frac{\partial vv}{\partial y} + \frac{\partial wv}{\partial x} = -\frac{\partial}{\partial y}(p + uU + wW) + \omega^z U - \omega^x W, \quad (11.3.12)$$

$$\frac{\partial w}{\partial t} + \frac{\partial uw}{\partial x} + \frac{\partial vw}{\partial y} + \frac{\partial ww}{\partial x} = -\frac{\partial}{\partial z}(p + uU + wW) - \omega^y U. \quad (11.3.13)$$

Equations (11.3.11)–(11.3.13), together with the continuity equation

$$\frac{\partial u}{\partial x} + \frac{\partial v}{\partial y} + \frac{\partial w}{\partial z} = 0, \quad (11.3.14)$$

describe the fluid motion at low Reynolds numbers, on condition that the velocity components  $(U, W)$  of the potential motion are known. Solving these equations in the presence of curvilinear interface is generally impossible, so these equations should be rewritten in the surface-following coordinate system; in our case, these are the cylindrical conformal coordinates. After such transformation, Eqs. (11.3.11)–(11.3.13) take the form

$$\frac{dJu}{d\tau} = \omega^y W - x_\xi \Pi_\xi + z_\xi \Pi_\xi + F_\xi, \quad (11.3.15)$$

$$\frac{dJv}{d\tau} = \omega^z U - \omega^x W - J\Pi_\vartheta + F_\vartheta, \quad (11.3.16)$$

$$\frac{dJw}{dt} = -\omega^\vartheta U - z_\xi \Pi_\xi - x_\xi \Pi_\zeta + F_\zeta. \quad (11.3.17)$$

Here,  $\omega^\xi, \omega^\vartheta, \omega^\zeta$  are the vorticity components  $\omega^x, \omega^y, \omega^z$  multiplied by Jacobian  $J$ , while  $\Pi$  is the generalized pressure

$$\Pi = p + uU + wW + \frac{2}{3}e. \quad (11.3.18)$$

Operator  $\frac{d}{dt}$  in (11.3.15)–(11.3.17) denotes full-time derivative

$$\frac{d(\cdot)}{dt} = \frac{\partial(\cdot)}{\partial t} + \frac{\partial(\cdot)\hat{u}}{\partial\xi} + \frac{\partial(\cdot)\hat{v}}{\partial\vartheta} + \frac{\partial(\cdot)\hat{w}}{\partial\zeta}, \quad (11.3.19)$$

where  $v$  is a lateral component of velocity, and  $(\hat{u}, \hat{w})$  are the contravariant components of velocity defined by the equations:

$$\hat{u} = \xi_t + J^{-1}\tilde{u}, \quad \hat{w} = \zeta_t + J^{-1}\tilde{w}. \quad (11.3.20)$$

Here,  $(\hat{u}, \hat{v})$  are the covariant velocity components

$$\tilde{u} = ux_\xi + wz_\xi, \quad \tilde{w} = -uz_\xi + wx_\xi, \quad (11.3.21)$$

connected with the Cartesian velocity components  $(u, v)$  by relations:

$$u = J^{-1}(\hat{u}x_\xi - \hat{w}z_\xi), \quad w = J^{-1}(\hat{u}z_\xi + \hat{w}x_\xi). \quad (11.3.22)$$

Components of vector  $(\omega^\xi, \omega^\vartheta, \omega^\zeta)$  in the curvilinear coordinates take the form

$$\omega^\xi = J \left( \frac{\partial w}{\partial y} - \frac{\partial v}{\partial z} \right) = J \frac{\partial w}{\partial y} - \frac{\partial z_\xi v}{\partial\xi} + \frac{\partial x_\xi v}{\partial\zeta}, \quad (11.3.23)$$

$$\omega^\vartheta = J \left( \frac{\partial u}{\partial z} - \frac{\partial w}{\partial x} \right) = \frac{\partial z_\xi u}{\partial\xi} + \frac{\partial x_\xi u}{\partial\zeta} - \frac{\partial x_\xi w}{\partial\xi} + \frac{\partial z_\xi w}{\partial\zeta}, \quad (11.3.24)$$

$$\omega^\zeta = J \left( \frac{\partial v}{\partial x} - \frac{\partial u}{\partial y} \right) = \frac{\partial x_\xi v}{\partial\zeta} - \frac{\partial z_\xi v}{\partial\xi} - J \frac{\partial u}{\partial y}. \quad (11.3.25)$$

Equation of continuity (11.3.14) can be represented through the contravariant velocity components such as

$$\frac{\partial J}{\partial t} + \frac{\partial J\hat{u}}{\partial\xi} + \frac{\partial Jv}{\partial\vartheta} + \frac{\partial J\hat{w}}{\partial\zeta} = 0 \quad (11.3.26)$$

and through the covariant velocity components as follows

$$\frac{\partial \tilde{u}}{\partial \xi} + \frac{\partial v}{\partial \vartheta} + \frac{\partial \tilde{w}}{\partial \zeta} = 0. \quad (11.3.27)$$

Equation (11.3.26) provides accurate approximation of advection terms in (11.3.19), and the continuity equation in the form (11.3.27) served for the derivation of the Poisson equation for pressure. Let us represent Eqs. (11.3.15)–(11.3.17) in the following form

$$\frac{\partial Ju}{\partial \tau} = -(x_\xi \Pi_\xi - z_\xi \Pi_\zeta) + F^\zeta, \quad (11.3.28)$$

$$\frac{\partial Jv}{\partial \tau} = -J \frac{\partial \Pi}{\partial \vartheta} + F^\vartheta, \quad (11.3.29)$$

$$\frac{\partial Jw}{\partial \tau} = -(z_\xi \Pi_\xi + x_\xi \Pi_\zeta) + F^\xi, \quad (11.3.30)$$

where  $(F^\xi, F^\vartheta, F^\zeta)$  are

$$F^\xi = -\frac{\partial Ju \tilde{u}}{\partial \xi} - \frac{\partial Ju v}{\partial \vartheta} - \frac{\partial Ju \tilde{w}}{\partial \zeta} + J \omega^\vartheta W + T^\xi, \quad (11.3.31)$$

$$F^\vartheta = -\frac{\partial Jv \tilde{u}}{\partial \xi} - \frac{\partial Jv v}{\partial \vartheta} - \frac{\partial Jv \tilde{w}}{\partial \zeta} + J \omega^\zeta U - J \omega^\xi W + T^\vartheta, \quad (11.3.32)$$

$$F^\zeta = -\frac{\partial Jw \tilde{u}}{\partial \xi} - \frac{\partial Jw v}{\partial \vartheta} - \frac{\partial Jw \tilde{w}}{\partial \zeta} - J \omega^\vartheta U + T^\zeta, \quad (11.3.33)$$

and  $(T^\xi, T^\vartheta, T^\zeta)$  are the terms describing the subgrid turbulence

$$T^\xi = -\frac{\partial J(x_\xi \bar{u}' u' + z_\xi \bar{u}' w')} {\partial \xi} - \frac{\partial \bar{u}' v'} {\partial \vartheta} - \frac{\partial J(-z_\xi \bar{u}' u' + x_\xi \bar{u}' w')} {\partial \zeta}, \quad (11.3.34)$$

$$T^\vartheta = -\frac{\partial J(x_\xi \bar{v}' u' + z_\xi \bar{v}' w')} {\partial \xi} - \frac{\partial \bar{v}' v'} {\partial \vartheta} - \frac{\partial J(-z_\xi \bar{v}' u' + x_\xi \bar{v}' w')} {\partial \zeta}, \quad (11.3.35)$$

$$T^\zeta = -\frac{\partial J(x_\xi \bar{w}' w' + z_\xi \bar{w}' w')} {\partial \xi} - \frac{\partial \bar{v}' w'} {\partial \vartheta} - \frac{\partial J(-z_\xi \bar{u}' w' + x_\xi \bar{w}' w')} {\partial \zeta}. \quad (11.3.36)$$

The second-order turbulent moments are represented as follows

$$-\overline{u'u'} = 2K_m J^{-1} \Phi_{11} = 2K_m J^{-1} \left( \frac{\partial x_\xi u}{\partial \xi} - \frac{\partial z_\xi u}{\partial \zeta} \right). \quad (11.3.37)$$

$$-\overline{u'v'} = K_m J^{-1} \Phi_{12} = K_m \left( \frac{\partial u}{\partial y} + J^{-1} \left( \frac{\partial x_\xi v}{\partial \xi} - \frac{\partial z_\xi v}{\partial \zeta} \right) \right), \quad (11.3.38)$$

$$-\overline{u'w'} = K_m J^{-1} \Phi_{13} = K_m J^{-1} \left( \frac{\partial (uz_\xi + wx_\xi)}{\partial \xi} + \frac{\partial (ux_\xi - wz_\xi)}{\partial \zeta} \right), \quad (11.3.39)$$

$$-\overline{v'v'} = 2K_m J^{-1} \Phi_{22} = 2K_m J^{-1} \frac{\partial v}{\partial y}, \quad (11.3.40)$$

$$-\overline{v'w'} = K_m J^{-1} \Phi_{23} = K_m \left( \frac{\partial w}{\partial y} + J^{-1} \left( \frac{\partial z_\xi v}{\partial \xi} + \frac{\partial x_\xi v}{\partial \zeta} \right) \right), \quad (11.3.41)$$

$$-\overline{w'w'} = 2K_m J^{-1} \Phi_{33} = 2K_m J^{-1} \left( \frac{\partial z_\xi w}{\partial \xi} + \frac{\partial x_\xi w}{\partial \zeta} \right). \quad (11.3.42)$$

Let us approximate the time derivative by the forward difference. Then, new values of velocities  $(u^{t+1}, v^{t+1}, w^{t+1})$  are defined by the expressions

$$u^{t+1} = -\Delta\tau \left( J'^{t+1} \right)^{-1} (x_\xi \Pi_\xi - z_\xi \Pi_\zeta) + \left( J'^{t+1} \right)^{-1} (J^t u^t + \Delta\tau F^\xi), \quad (11.3.43)$$

$$v^{t+1} = -\frac{\partial \Pi}{\partial \vartheta} + \left( J'^{t+1} \right)^{-1} (J^t v^t + \Delta\tau F^\vartheta), \quad (11.3.44)$$

$$w^{t+1} = -\Delta\tau \left( J'^{t+1} \right)^{-1} (z_\xi \Pi_\xi + x_\xi \Pi_\zeta) + \left( J'^{t+1} \right)^{-1} (J^t w^t + \Delta\tau F^\zeta) \quad (11.3.45)$$

where  $J^t$  and  $J'^{t+1}$  are the previous and new values of Jacobian. Equations (11.3.43) and (11.3.45) both contain gradients of pressure. For derivation of Poisson equation in the curvilinear coordinates, we transform the Cartesian velocity components into the covariant velocity components using (11.3.21):

$$\tilde{u}^{t+1} = -\Delta\tau \Pi_\xi + \Phi^\xi, \quad (11.3.46)$$

$$v^{t+1} = -\Delta\tau \Pi_\vartheta + \Phi^\vartheta, \quad (11.3.47)$$

$$\tilde{w}^{t+1} = -\Delta\tau \Pi_\zeta + \Phi^\zeta, \quad (11.3.48)$$

where  $(\Phi^\xi, \Phi^\vartheta, \Phi^\zeta)$  are the combinations of the right-hand sides of Eqs. (11.3.43)–(11.3.45).

Now,

$$\frac{\partial \tilde{u}^{t+1}}{\partial \xi} + \frac{\partial v^{t+1}}{\partial \vartheta} + \frac{\partial \tilde{w}^{t+1}}{\partial \zeta} = 0. \quad (11.3.49)$$

and after introducing (11.3.46)–(11.3.48) into (11.3.48), we obtain Poisson equation for the diagnostic calculation of pressure

$$\Delta \Pi = (\Delta \tau)^{-1} ((\Phi_u)_\xi + (\Phi_v)_\vartheta + (\Phi_w)_\vartheta). \quad (11.3.50)$$

Hence, usage of the cylindrical conformal mapping allows us to obtain a standard scheme for the calculation of the generalized pressure (11.3.18). Equation (11.3.49) is solved in Fourier space with three-diagonal matrix algorithm (TDMA, Thomas 1949). Equations (11.3.28) and (11.3.30) are solved by a standard Fourier transform method. For approximation of vertical operators, the second-order scheme was used. Equations (11.3.28)–(11.3.30) are solved with high resolution which allows us to reproduce directly the large-scale part of the turbulence by means of the large-eddy simulations technique.

## 11.4 Large-Eddy Simulation Approach

The LES approach imposes spatial filtering on instantaneous fields; i.e., all the flow structures bigger than the imposed filter scales are resolved, and the smaller ones are filtered out. Now, in order to compensate these filtered-out scales, a subgrid turbulence model must be imposed to have a correct description of the original turbulent field. As for the LES approach with regard to the near-wall modeling, different versions of modeling of the subgrid turbulence are applied. They include the classical (Smagorinsky 1963) and dynamic (Germano et al. 1991) approaches. Smagorinsky models as well as the recently proposed coherent-structure scheme (Kobayashi 2005) are the schemes based on minimization of the theoretical subgrid dissipation (Vreman 2004). The turbulent boundary layer over flat plate (with the zero pressure gradient) was simulated by Spalart (1988) by employing DNS techniques over the range of Reynolds numbers  $225 < Re < 1410$ . For this particular case, a numerical database is provided (ERCOFTAC database) which makes it possible to perform a very detailed comparison for the first and second moments, as well as for the budgets of the second moments. In addition, the effects of different numerical grid resolutions can be easily estimated, and validation of the LES results can be performed. Porte-Agel et al. (2000) proposed a scale-dependent dynamic subgrid-scale LES model. Opposite to the standard dynamic model, it is not based on the assumption that the model coefficient is scale-variant. The new model introduces a secondary test filter which, in addition to the standard test filter, is used to determine the model coefficient. The new model showed improvements of the spectral slopes in the near-surface region where a standard Smagorinsky model and

a standard dynamic model are either too dissipative or not dissipative enough, respectively. In order to demonstrate applicability of the presented method for the flows in non-orthogonal geometries, then the configurations with a wavy horizontal wall are selected. This investigation is compared with the DNS and LES results of Kretenauer and Schumann (1992), Tseng and Ferziger (2004), and Choi and Suzuki (2005), as well as with the experimental results of Guenther and von Rohr (2003) and Kruse et al. (2003).

In the present work, the effects of the subgrid turbulence are taken into account through coefficient of the subgrid turbulent viscosity, which is used for calculations of the second-order moments (11.3.37)–(11.3.42). The coefficient of turbulent viscosity is estimated with formula

$$K_{x,y} = C_s (J^{-1} \Delta \xi \Delta \vartheta \Delta \zeta)^{1/3} e^{1/2}, \quad C_s = 0.1, \quad (11.4.1)$$

where  $l_t = (J^{-1} \Delta \xi \Delta \vartheta \Delta \zeta)^{1/3}$  is a turbulent length scale, and  $e$  is the kinetic energy of the subgrid turbulence. Evolution of  $e$  is calculated with equation

$$\frac{dJe}{d\tau} = \frac{\partial}{\partial \xi} K_e \frac{\partial e}{\partial \xi} + \frac{\partial}{\partial \zeta} K_e \frac{\partial e}{\partial \zeta} + P - \varepsilon \quad (11.4.2)$$

where  $P$  is a rate of production of  $e$ , while  $\varepsilon$  is a dissipation rate defined by the relation

$$\varepsilon = C_D e^{3/2} l_t^{-1}. \quad (11.4.3)$$

Expression for  $P$  is obtained from Eqs. (11.3.37)–(11.3.42).

## 11.5 Modeling of Waves

The details of the numerical scheme can be found in Chalikov and Sheinin (1998, 2005), Chalikov (2005, 2007, 2009), and Chalikov and Rainchik (2011). Equations (11.3.15)–(11.3.17) were integrated here together with the equations for vortical motion (11.3.28)–(11.3.10). The components of the potential velocity  $U$  and  $W$  were calculated through the following relations:

$$U = J^{-1} (x_\xi \Phi_\xi + z_\xi \Phi_\zeta) \quad (11.5.1)$$

$$W = J^{-1} (z_\xi \Phi_\xi + x_\xi \Phi_\zeta) \quad (11.5.2)$$

A current formulation of the problem suggests that the kinetic energy can be transferred from the orbital velocities of wave motion to the turbulence. Since the energy of turbulence is by 2–3 orders smaller than the energy of wave motion, then

the attenuation of wave due to generation of turbulence is very slow and can be neglected. In a more general approach, the direct and inverse interactions should be taken into account. Note that Eqs. (11.3.15)–(11.3.17) do not guarantee that energy can be transferred only from waves to turbulence; in some places, the opposite flux from turbulence to waves can be initiated. However, being averaged for a wave period or short intervals of time, the opposite flux of energy disappears; hence, waves always transfer energy to turbulence. Consideration of this effect is difficult due to the contradictions between the potential and non-potential formulation of the problems for waves and turbulence. The local input of energy to the orbital motion can contradict the potentiality assumption. This is why the only way to take into account an influence of turbulence on waves is the modification of the kinetic energy of the orbital velocities in terms of the surface velocity potential.

## 11.6 Results of Simulations

The coupled waves/turbulence model was first used for simulation of generation of turbulence in a train of monochromatic waves with steepness  $ak = 0.03\text{--}0.24$ . The simulations were initially performed with a 2-D version of the model, when lateral disturbances were absent. In this case, the imposed vortical motion quickly dissipated and the turbulence did not develop. These features follow directly from Eqs. (11.3.28)–(11.3.30), but such calculations were still conducted for validation of the entire model.

The figures in this section demonstrate outcomes of the 3-D version. The initial conditions were assigned on the basis of the linear theory as a train of harmonic waves with non-dimensional wave number  $k_p = 4$  (such setup corresponds to four waves in domain). To be sure that the model is correct, the first simulations were done for a purely potential flow in the absence of non-potential disturbances. As expected, the vortical motion and turbulence were not generated. Other numerical experiments were then conducted with the superimposed small random noise introduced as the initial vortical velocity field. The waves remain two-dimensional, i.e., long-crested and do not change in lateral  $y$ -direction. Note that monochromatic waves with the steepness larger than 0.12 create new modes which finally result in disintegration of the main modes and breaking. For the steepest wave with steepness  $ak = 0.24$ , the breaking happens at the periods which are still longer than those considered in the current work. Typical distribution of the sum  $E$  of the energy of explicitly simulated turbulent motion  $E_v$ .

$$E = \frac{1}{2} (u^2 + v^2 + w^2) \quad (11.6.1)$$

and the energy of subgrid turbulence  $E_t$  in a top layer with thickness of  $0.01L_p$  ( $L_p$  is peak wavelength) is shown in Fig. 11.1.

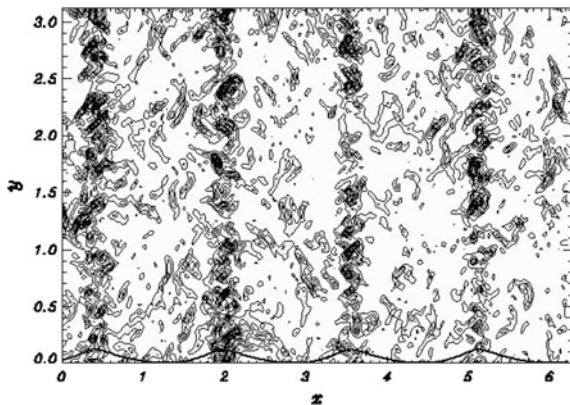
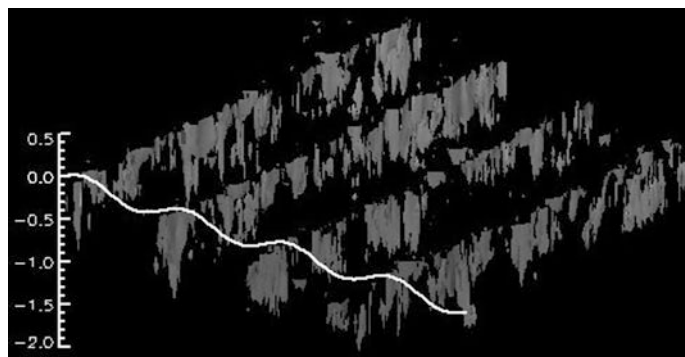


**Fig. 11.1** Distribution of energy  $E_k = E_v + E_t$  in near-surface layer in relative units (top view, the vertical scale is the lateral direction). The black areas correspond approximately to  $0.001gH_s$ . At the bottom, the wave profile is indicated (Chalikov and Babanin 2012)

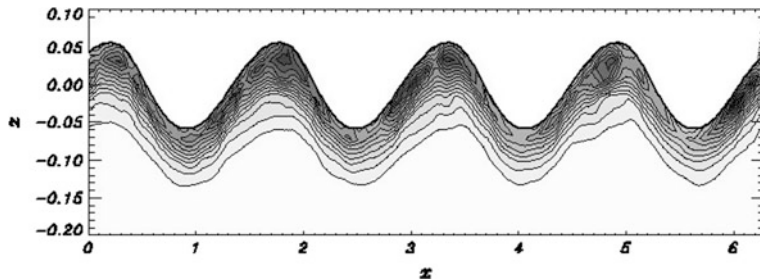
This is a view from above, and the curve at the bottom indicates shape of a long-crested wave. As shown, the largest disturbances are concentrated along the wave crests. These disturbances move with the phase velocity of carrying waves, which proves that the dissipation timescale is small, and the areas of increased vortical motion are tied with the zones of maximum gradients of orbital velocities.

Figure 11.2 outlines the shape of volume below water surface, which corresponds to the energy level of  $0.2\max(E_v)$ . This figure demonstrates the volume distribution of the total energy of disturbances for the case  $ak = 0.24$ . White curve indicates the surface elevation; i.e., the turbulent energy is concentrated along the long wave crests. For convenience, the vertical scales for energy and surface shape are different.

Distribution of the  $y$ -averaged energy of wave-produced disturbances  $\bar{E}^y$  is shown in Fig. 11.3.



**Fig. 11.2** Volume distribution of energy  $E_v = E_k + E_t$ . Volume which corresponds to the  $0.2\max(E_v)$  energy level is drawn. White curve indicates the shape of long-crested waves (Chalikov and Babanin 2012)



**Fig. 11.3** The distribution of energy  $\bar{E}_v^y$  averaged over  $y$ -axis for case of initially monochromatic waves with steepness  $ak = 0.24$  (Chalikov and Babanin 2012)

As shown, the disturbances are concentrated near surface and rapidly attenuate with depth. Such behavior is determined by the properties of orbital velocity field: The squared Fourier components of velocity deformations (which are responsible for generation of vorticity) have their maxima at the surface and attenuate as  $\exp(2kz)$  with depth  $z$  counted from surface. The time evolution of the volume-averaged energy of explicitly simulated vortex motion, as well as the energy of turbulence  $\bar{E}_v^{\xi\eta\xi}$ , is shown in Fig. 11.4 (solid and dashed curves, correspondingly) for different steepness. As shown, both quantities grow with time and to the end of the calculation reach more or less stationary conditions over time  $t = 6$  periods. Further integration was not performed, since we reproduced exact conditions of the laboratory experiments. The data on vertical distribution of the turbulent viscosity coefficient normalized by the molecular viscosity coefficient  $\tilde{K} = K/v$  are given for the waves with initial steepness  $ak = 0.24$  (dotted curves),  $ak = 0.18$  (dashed curves), and  $ak = 0.12$  (dashed-dotted curves) in Fig. 11.5.

Thin curves correspond to maximum values of  $\tilde{K}$  in domain at each level, while thick curves correspond to the averaged values of  $\bar{\tilde{K}}^\vartheta$ . Maximum values of viscosity for all the three cases are typically one decimal order of magnitude larger than the averaged values, which points to large intermittency of horizontal distribution of turbulent viscosity. Note that for the case  $ak = 0.08$ , the average viscosity is very close to molecular viscosity, which indicates that wave motion is laminar. However, even in this case, very narrow patches of turbulence in the vicinity of wave peaks are still generated.

In the absence of breaking [i.e., for the waves with small steepness and transitional Reynolds numbers, see also Babanin (2006)], the turbulence in the model is strongly intermittent, as shown in Figs. 11.5, and it concentrates at the rear face of the waves. This is what was also observed in laboratory experiments of Babanin and Haus (2009).

The intermittence of turbulence is confirmed by vertical profiles (in the Cartesian coordinates) of the averaged and instantaneous maximal total energy  $E_v^{xy}$  (i.e., sum of energy of the vortical motion and energy of the subgrid turbulence), as shown in Fig. 11.6.

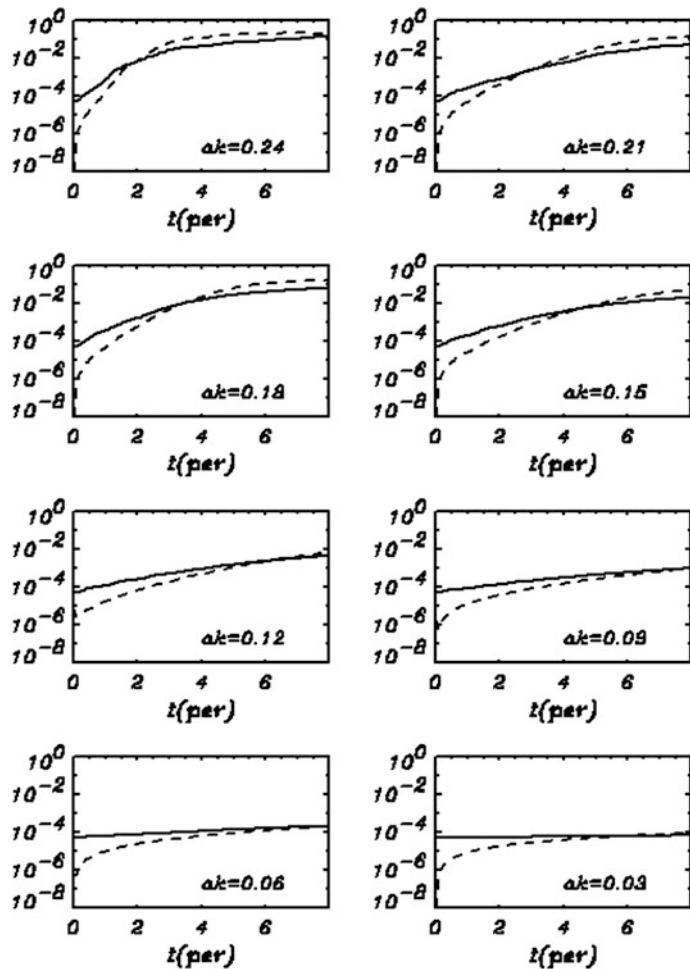


**Fig. 11.4** Evolution of volume-averaged kinetic energy of vortical motion  $\bar{E}_v^{-\xi\vartheta\xi}$  (dashed line) and kinetic energy of subgrid turbulence (solid line) for initially monochromatic wave of different steepness (indicated as legend in each subplot) (Chalikov and Babanin 2012)

The records used for calculations were obtained toward the end of the 6th period of integration. Thin horizontal lines in these subplots correspond to the depths of wave troughs  $z = \eta_{\min}$ . Above this level, the averaging was done over the area occupied by water. The dotted line indicates the maximum values observed at the 6th period of integration. Both curves suggest considerable growth of the energy above wave troughs. As shown, the average values of energy are lower at least by a decimal order than their maximum values (see also Fig. 11.1). For the largest wave steepness at the surface, the kinetic energy is equal to  $10^{-2}$  and it drops by two orders of magnitude at the vertical scale of  $\pi/8$  (i.e., at quarter of the wavelength)

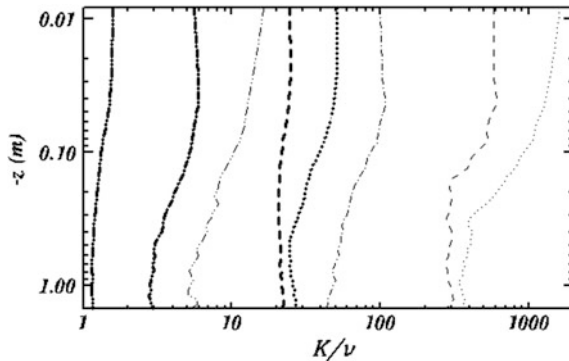


**Fig. 11.5** Vertical profiles of mixing coefficient  $\tilde{K} = K/v$  under initially monochromatic waves for initial steepness  $ak = 0.24$  (dotted curves),  $ak = 0.18$  (dashed curves),  $ak = 0.12$  (dashed-dotted curves), and  $ak = 0.08$  (dashed-double-dotted curves). Thin lines correspond to maximum values of  $\tilde{K}$  in the domain at each level, and thick lines correspond to averaged values of  $\tilde{K}$  (Chalikov and Babanin 2012)

and then remains approximately constant. At the lowest steepness, the surface energy is  $\sim 10^{-7}$ , and the two-order-of-magnitude drop occurs over 1/8th of the wavelength vertical distance too. Thus, in the range of the realistic water wave steepness, the intensity of the non-breaking wave-induced turbulence changes by 5 orders of magnitude. At  $ak \sim 0.1$ , the surface turbulence energy is  $\sim 10^{-5}$ . While such energy is apparently small as a dissipation source of surface waves, it plays a very essential role in the upper-ocean processes (Qiao et al. 2004, 2010; Huang et al. 2008; Babanin et al. 2009), as well as mixing in the stratified fluid (Dai et al. 2010), sediment suspension in finite depth seas (Pleskachevski et al. 2011), and swell attenuation (Babanin 2011), as described in Introduction.

Vertical profiles of the non-dimensional volumetric dissipation rate (solid curves) and its variance (dashed curves) obtained by averaging in the Cartesian coordinate system are shown in Fig. 11.7.

Here, wavelength corresponds to frequency  $f = 1.5$  Hz used in the laboratory experiment of Babanin and Haus (2009), and therefore, amplitude  $a$  shown in the legend is an indicator of steepness. The comparison of the volumetric dissipation rates produced by the model and the dissipation rates measured by Babanin and Haus (2009) is given in Fig. 11.8. Such dissipation rates  $\text{max}(\text{Diss})$  are plotted as a function of dimensional wave amplitude  $a(m)$ , like the volumetric dissipation rate  $\epsilon (\text{m}^2\text{s}^{-3})$  in Fig. 2 from Babanin and Haus (2009). Anyway, it is not exactly the same property as  $\epsilon$  in Babanin and Haus (2009). These dissipation rates were measured below troughs of the highest waves, i.e., always at some distance below the surface. The values of  $\text{max}(\text{Diss})$  in Fig. 11.8 indicate maximum dissipation in the wave-induced turbulence dissipation profile. In practice, this is an estimate of the volumetric dissipation rate near surface and above the mean water level.

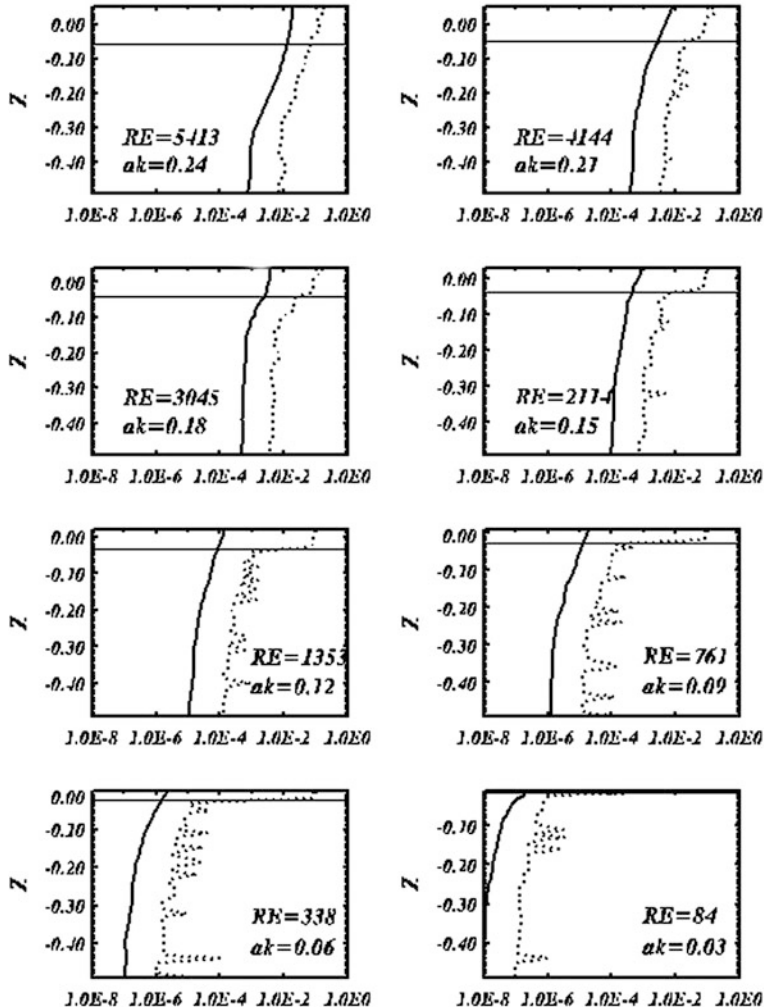


**Fig. 11.6** Vertical distribution of kinetic energy of the non-potential motion, average (*solid line*) and instantaneous maximal (*dotted line*), for a range of wave steepness from  $ak = 0.24$  (top left corner) down to  $ak = 0.03$  (bottom right corner), as shown in the legend of each subplot ( $RE$  is respective Reynolds numbers). The scales are dimensionless, the vertical scale is distance to the surface, and the horizontal scale is the turbulence energy (Chalikov and Babanin 2012)

Since it is known that the wave-induced turbulent energy concentrates within wave crests (Gemmrich 2010), such  $\text{max}(\text{Diss})$  is expected to be greater than  $\varepsilon$  in Babanin and Haus (2009). In the model, this happens because generation of turbulence has a maximum at the surface as mentioned above. In 11.8, the shaded area corresponds to the range of measurements and scatter of the observational data from

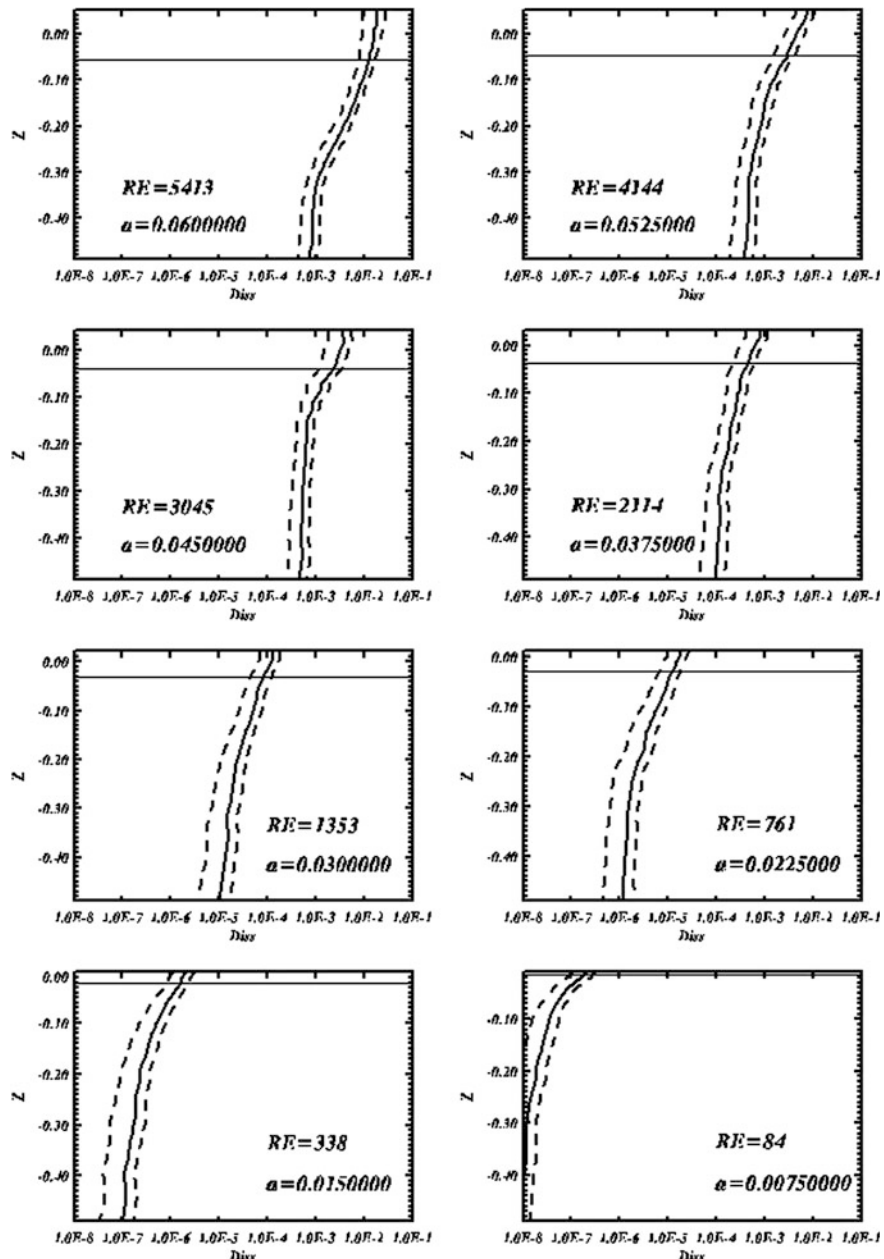
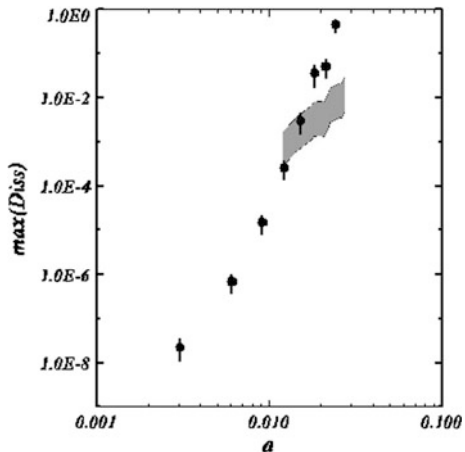


**Fig. 11.7** Vertical profiles of non-dimensional rates of volumetric dissipation rate ( $\text{m}^2\text{s}^{-3}$ ) for different steepness, as shown in the legend of each sub1.1plot ( $a$  is amplitude of 1.5 Hz waves, and  $Re$  is respective Reynolds numbers). Solid curves correspond to average profiles, and dashed curves indicate the dispersion (Chalikov and Babanin 2012)

**Fig. 11.8** Maximal volumetric dissipation rates  $\max(\text{Diss})$  versus wave amplitude  $a$ . The shaded area corresponds to the range of measurement and scatter of the observational data of Babanin and Haus (2009). Vertical segments indicate standard deviation of the dissipation estimates (Chalikov and Babanin 2012)



Babanin and Haus (2009). It was confirmed qualitatively that for wave amplitudes of  $\sim 1.5$  cm (the wavelength here, as in the experiment, corresponds to frequency 1.5 Hz), and for higher waves the maximum of dissipation within the crests is greater than that measured below the troughs. Different subplots show profiles for different wave amplitudes  $a$  and the corresponding wave Reynolds numbers (Babanin 2006):

$$Re_w = \frac{a^2 \omega}{\nu} \quad (11.16.1)$$

denoted as  $RE$  in panels. Here,  $a\omega$  denotes orbital velocity, i.e., the velocity scale in the Reynolds number ( $\omega$  is radian frequency), and  $\nu$  is the kinematic viscosity of water. It is quite obvious that due to intermittency, production of turbulence does not actually stop at low amplitudes/ $Re_w$ , but the magnitude of dissipation rates becomes so marginal ( $\varepsilon \sim 10^{-8} \text{ m}^2/\text{s}^3$  at  $Re_w = 84$ ) that it is hardly possible to measure. The lowest dissipation which Babanin and Haus (2009) were still able to detect above the noise level by their PIV method was of the order  $\varepsilon \sim 10^{-4} \text{ m}^2/\text{s}^3$ . If this is chosen as the reference, then  $Re_w \approx 2000$  can be regarded as the critical wave Reynolds number, close to the estimate  $Re_w \approx 3000$  of Babanin (2006).

The next set of the calculations was done for the initially assigned multi-mode wave field corresponding to Pierson–Moskowitz spectrum. The size of domain in  $x$ -,  $y$ -, and  $z$ -directions was  $1024 \times 128 \times 30$  knots. The rms steepness of this wave field was equal to 0.06, and explicit breaking events never happened. Some dissipation of wave energy occurs due to the flux of energy into the high wave number range, which was simulated through a special algorithm (see Chalikov and Sheinin 1998, 2005). In order to keep the energy in the wave system constant, the loss of energy was compensated by the energy input from wind [details of such simulations can be found, e.g., in Chalikov (2009)]. The initial modes were

assigned, again, by a small-amplitude theory, and the energy of random noise was about 1 % of the wave energy.

Temporal evolution of the volume-averaged kinetic energy  $E_k$  (solid curve) and the energy of the subgrid turbulence  $E_t$  (dashed curve) during the first 120 periods of integration are shown in Fig. 11.9. As shown, both energies are growing with a decreasing rate, and by the end of the integration period, the energy is close to some quasi-stationary level.

An example of  $y$ -averaged distribution of total energy  $\bar{E}_v^y$  is given in Fig. 11.10. Energy in Fig. 11.10 is represented in non-dimensional units. The turbulent kinetic energy and wave energy have different magnitudes, so to have an idea on absolute values of the energy generated by potential waves, it is reasonable to compare the integrated over depth total turbulent kinetic energy

$$E_v^{xyz} = \int_H^0 E_v^{xy} dz, \quad (11.6.2)$$

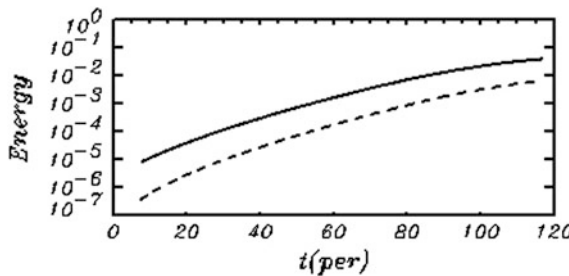


**Fig. 11.9** Evolution of volume-averaged turbulent kinetic energy  $E_k$  (solid curve) and energy of subgrid turbulence  $E_t$  (dashed curve). Both energies are normalized by the total wave energy and multiplied by length scale which is equal to 1 (Chalikov and Babanin 2012)

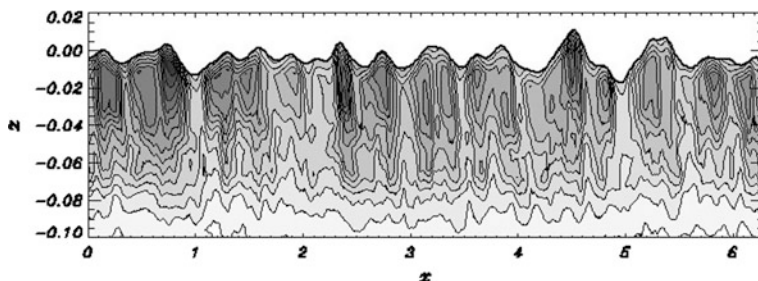


**Fig. 11.10** Distribution of averaged over  $y$ -axis energy  $\bar{E}_v^y$  (non-dimensional) for the case of waves with initially assigned Pierson–Moskowitz spectrum (Chalikov and Babanin 2012)

with the total energy of waves equal to the sum of the potential and kinetic energies  $E_w$  (see Chalikov and Sheinin 1998, 2005). According to the current calculations, the total turbulent kinetic energy  $E_v^{xyz}$  is within the range  $(0.03 - 0.04)E_w$ . Hence, the energy of non-potential motion in fully developed waves is not small.

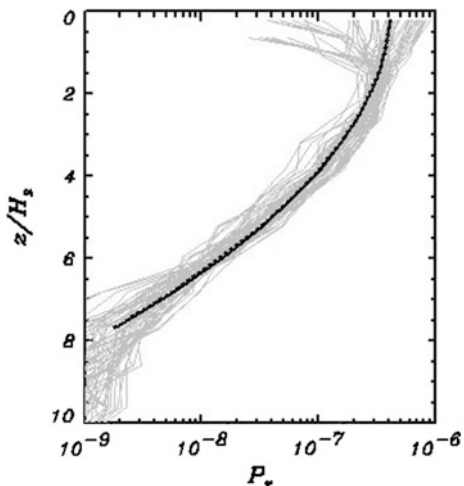
## 11.7 Coupling Between Waves and Upper-Ocean Layer

The most important problem of the wave-turbulence theory is the rate of wave energy dissipation (which on the average is equal to production of non-potential energy  $P_v$ ). The last numerical experiment with multi-mode wave field gives the possibility to calculate this production rate of non-potential motion energy  $P_v$  on the basis of the equation for energy evolution obtained directly from (11.3.28)–(11.3.30).

$$P_v = (\omega^\xi u - \omega^\vartheta v) W + (\omega^\xi v + \omega^\vartheta w) U \quad (11.7.1)$$

where  $(\omega^\xi, \omega^\vartheta, \omega^\varphi)$  are components of the vorticity in the cylindrical conformal coordinates,  $(u, v, w)$  are velocity components of the vortical motion, and  $(U, W)$  are components of the wave orbital velocity. Fortunately, when averaged over the horizontal coordinates,  $P_v$  turned out to be essentially positive; otherwise, the calculations could predict on the average inverse flux of energy from the turbulence to potential waves, which is hardly possible. The local profiles of the averaged over the horizontal coordinate production  $P_v^y$ , as a function of non-dimensional depth  $\bar{z} = z/H_s$  for the last period of integration, are shown in Fig. 11.11 ( $H_s$  is significant

**Fig. 11.11** Vertical distribution of non-dimensional dissipation rate  $P$  (see Eq. 11.7.1) of the vortical motion as function of non-dimensional depth  $\bar{z} = z/H_s$  (Chalikov and Babanin 2012)



wave height). These profiles are shown by gray lines, while solid curve corresponds to the mean profile  $\bar{P}_v^{xy}$ .

Any estimation of Reynolds number (11.16.1) gives here the values by the orders of magnitude exceeding the critical values of  $Re \approx 2000\text{--}3000$ . It means that real wave fields should generate the fully developed turbulence, while direct dependence of its intensity on  $Re$  number is negligible. This is why the dependence of non-dimensional variable  $P_v^{xy}$  on non-dimensional depth can be approximated by a simple relation

$$\bar{P}_v^{xy} = 6.60 \times 10^{-8} \exp(17.47z + 6.76z^2). \quad (11.7.2)$$

We should note that this parameterization is valid for Pierson–Moscowitz spectrum, i.e., for fully developed waves. For developing waves, which are steeper, relative production of turbulence will be larger, but here, such spectra were not modeled because steep waves also involve occasional breaking which was avoided in this study.

Taking into account the scaling accepted in the current work, the dimensional rate of production  $P(m^2 s^{-3})$  can be represented as follows

$$H_s^{-1/2} g^{-3/2} P = 3.87 \times 10^{-7} \exp(0.56\tilde{z} + 0.0057\tilde{z}^2), \quad (11.7.3)$$

and we should remind that the significant wave height  $H_s$  can be defined by integration over wave spectrum

$$H_s = 4 \cdot \left( \int_{\omega, \theta} S(\omega, \theta) d\omega d\theta \right)^{1/2} \quad (11.7.4)$$

where  $\omega$  is frequency, and  $\theta$  is angle.

The dependence of type of (11.7.2) can be used for the calculations of the volume input of energy from waves in equation of turbulent energy evolution. Being integrated over depth, the equation gives the rate of dissipation of wave energy due to the volume generation of turbulence. Note that the influence of waves in Eq. (11.7.2) is included through significant wave height only, which possibly makes this approach suitable for any kind of spectrum. The coefficients in (11.7.2) should be probably corrected.

## 11.8 Conclusion

A numerical model for the turbulence unrelated to wave breaking and produced by the orbital motion of potential waves is developed. The model consists of three parts: a fully nonlinear potential model of two-dimensional (i.e., long-crested)

waves, the LES three-dimensional model based on full Reynolds equations including parameterized subgrid turbulence, and a three-dimensional model of evolution of subgrid turbulence. The three-dimensionality of turbulence is of major importance, since the two-dimensional (in vertical plane) vortex does not interact with the wave orbital motion. The last two modules of the model are new and written in the cylindrical conformal coordinates. Small perturbations of potential motion are introduced and then allowed to develop as predicted by the theory.

A long-term numerical integration of the system of equations was done for different values of wave steepness. The vorticity and turbulence usually occur in the vicinity of wave crests (where the velocity gradients reach their maximum) and then spread over upwind slope and then downward. If modeled at low wave steepness, which is necessary to avoid breaking, a specific feature of such wave turbulence is its strong intermittency: The turbulent patches are mostly isolated, and intermittency grows with the decrease of the wave amplitude. The maximum values of the energy of turbulence are in qualitative agreement with the available experimental data.

The results suggest that even non-breaking potential waves can generate turbulence which thus enhances the turbulence created by shear current or by breaking. The importance of such turbulence has already been shown across a broad range of the upper-ocean processes, such as upper-ocean mixing and circulation, sediment suspension in finite depths, and swell attenuation. The new model can be used to investigate the phenomenon in a broad range of conditions and to produce parameterizations necessary for the simulations which cannot reproduce turbulence explicitly. The wave-turbulence model can be used for qualitative and even quantitative investigation of the phenomenon (if high resolution for the LES model can be provided).

# **Chapter 12**

## **Three-Dimensional Modeling of Potential Waves**

**Abstract** A simple and exact numerical scheme for long-term simulations of three-dimensional potential fully nonlinear periodic gravity waves is suggested. The scheme is based on the surface-following non-orthogonal curvilinear coordinate system. Velocity potential is represented as a sum of analytical and nonlinear components. The Poisson equation for the nonlinear component of velocity potential is solved iteratively. Fourier transform method, the second-order accuracy approximation of vertical derivatives on a stretched vertical grid, and the fourth-order Runge–Kutta time stepping are used. The scheme is validated by simulation of steep Stokes waves. A one-processor version of the model for PC allows us to simulate evolution of a wave field with thousands of degrees of freedom for hundreds of wave periods. The scheme is designed for investigation of nonlinear two-dimensional surface waves, generation of extreme waves, and direct calculations of nonlinear interactions.

### **12.1 Existing Approaches to Modeling of 3-D Waves, Their Advantages, and Disadvantages**

Currently, the most popular approach is the high-order scheme (HOS) model developed by Dommermuth and Yue (1987) and West et al. (1987). The HOS is based on Zakharov’s paper (1968), where a convenient form of the dynamic and kinematic surface conditions was suggested. The equations used by Zakharov were not intended for modeling, but rather for investigation of stability of finite amplitude waves. In that work, a system of coordinates where depth is counted from the surface was used, though the Laplace equation for the velocity potential was accepted in its traditional form. Zakharov’s (1968) followers, however, accepted this idea literally. They used two coordinate systems: a curvilinear surface-fitting system for surface conditions and the Cartesian system for calculation of the surface vertical velocity. The analytic solution for the velocity potential in the Cartesian coordinate system is known. It is based on the Fourier coefficients on a fixed level, while true variables are the Fourier coefficients for the potential on free surface.

Hence, the problem of transition from one coordinate system to another arises. This problem is solved by expansion of the surface potential into the Taylor series in the vicinity of surface. An accuracy of this method depends on the accuracy of estimation of exponential function  $\exp(k\eta)$  with finite order of Taylor expansion. For small-amplitude waves and for a narrow wave spectrum, such accuracy is evidently satisfactory. However, for a case of a broad wave spectrum which contains many wave modes, the order of the Taylor series should be high. Now, the problem is that the waves with high wave numbers are superposed over the surface of larger waves. Since the amplitudes of the surface potential attenuate exponentially, the amplitude of a small wave at positive elevation increases and, on the contrary, can approach zero at negative elevations.

Let us consider idealized Phillips spectrum  $a_k = a_1 \omega_k^{-5}$  assigned at frequencies  $\omega_k = k^{1/2}$ ,  $k = 1, 2, 3\dots$  with peak wave steepness  $a_1 k_1 = 0.1$  ( $k$  and  $\omega$  are non-dimensional wave number and frequency, correspondingly). It is easy to estimate that for the double peak frequency  $\omega/\omega_1 = 2$ , a relative accuracy  $10^{-4}$  of projection of the potential to level  $z = 0$  can be reached with 6 terms of the Taylor series; for  $\omega/\omega_1 = 3$  with 12 terms; and for  $\omega/\omega_1 = 4$  with 15 terms. A typical order of the Taylor expansion in the HOS model equals 3–5. It is clear that such setting of the HOS model cannot reproduce high-frequency waves, which reduces the nonlinearity of the model. This is why such model can be integrated for long periods using no high-frequency smoothing. Besides, the accuracy of the calculation of vertical velocity on surface depends on full elevation at each point. Hence, the accuracy is not uniform along wave profile. A substantial increase of the Taylor expansion order can definitely result in numerical instability due to the occasional amplification of modes with high wave numbers. A similar point of view was shared by the authors of the method based on the surface integral (Clamond et al. 2005). We should note, however, that comparison of the HOS method based on the West et al. (1987) approach with the method of the surface integral for the idealized wave field (Clamond et al. 2006) shows acceptable results. Still, applicability of the HOS method for simulation of waves with broad wave spectrum is unclear.

In this work, we develop a new approach specifically targeted at simulation of a long-term multi-mode wave field evolution in the deep ocean. The domain is considered as a small part of an infinitely large basin. In this case, it is possible to use substantial simplification of the problem, assuming periodicity over the horizontal coordinates. In many applications, a wave field in such domain can be presented as a superposition of running harmonic waves with random phases. Such linear approach becomes inapplicable for direct investigation of the wave field evolution resulting from nonlinear interactions of waves or from the development of wave field under the action of wind and dissipation.

It is well known that the nonlinear transformation and growth of waves occur over hundreds and thousands of wave periods. The slow rate of development imposes tough restrictions on the model because such modifications of waves should not be obscured with the numerical errors. It means that the model should be exact enough to reproduce a relatively slow spectrum evolution. This condition is

well satisfied with the 2-D model in the conformal coordinates considered above. The 3-D waves represent a far more difficult object because it is hardly possible to reduce the problem to the surface problem (in fact, the surface integral method cannot be referred to as a 2-D method, since it uses Green function); hence, the velocity potential should be calculated as a solution of elliptic equation.

## 12.2 Equations and Transformation of Coordinates

Let us consider a non-dimensional form of the principal 3-D equations for potential waves written in the Cartesian coordinates, i.e., Laplace equation for velocity potential,

$$\Phi_{xx} + \gamma^2 \Phi_{yy} + \Phi_{zz} = 0, \quad (12.2.1)$$

two boundary conditions at free surface  $\eta = \eta(x, y, t)$ , i.e., the kinematic condition

$$\eta_t + \eta_x \varphi_x + \gamma^2 \eta_y \varphi_y - \Phi_z = 0, \quad (12.2.2)$$

and Bernoulli integral:

$$\varphi_t + \frac{1}{2} (\varphi_x^2 + \gamma^2 \varphi_y^2 + \Phi_z^2) + \eta + p = 0, \quad (12.2.3)$$

where  $(x, y, z)$  are the Cartesian coordinate system,  $t$  is time;  $\eta(x, y, t)$  describes single-valued interface, i.e., free surface;  $\Phi$  is the 3-D velocity potential and  $\varphi$  is a value of  $\Phi$  at surface  $\eta$ ; and  $p$  is the external pressure created by the flow above surface and normalized using the density of water. The subscripts denote partial differentiation with respect to the corresponding coordinate. Taking into account the surface tension effect is quite straightforward. However, in this paper, we are focused on large waves, so the corresponding term in (12.2.3) is omitted.

Equations (12.2.1)–(12.2.3) are written in a non-dimensional form by using the following scales: length  $L$  where  $2\pi L$  is (dimensional) period in horizontal direction; time  $L^{1/2} g^{-1/2}$ ; and velocity potential  $L^{3/2} g^{1/2}$  ( $g$  is acceleration of gravity). The pressure is normalized by water density, so that the pressure scale is  $Lg$ . Equations (12.2.1)–(12.2.3) at  $p = 0$  are self-similar to transformation with respect to  $L$ . Wave spectrum is normally more or less narrow, that is why it is convenient to introduce different length scales  $L$  and  $L_y$  in directions  $x$  and  $y$ . Since the equations are solved in square domain ( $0 < \xi < 2\pi$ ,  $0 < \vartheta < 2\pi$ ), the ratio  $\gamma = L/L_y$  is included in the equations.

System (12.2.1)–(12.2.3) is solved as an initial value problem for unknown functions  $\Phi$  and  $\eta$  with the given initial conditions  $\Phi(x, y, z = \eta(x, y, t = 0), t = 0)$  and  $\eta(x, t = 0)$ . It should be noted that though Eqs. (12.2.2) and (12.2.3) are written for free surface, there are no straightforward ways to reduce the problem to a 2-D

problem, since for evaluation of  $\Phi_z$  Laplace Eq. (12.2.1) should be solved in the domain

$$\{0 < \xi \leq 2\pi, 0 < \vartheta < 2\pi, H < z \leq \eta\} \quad (12.2.4)$$

with a curvilinear upper boundary which is a function of  $\xi$  and  $\vartheta$ . Integration of the system in the Cartesian coordinates is either quite inaccurate or too expensive computationally and hardly efficient for the time intervals which are much greater than the chosen timescale. This is why the existing numerical models of waves are mostly based on the strongly simplified approaches.

Let us introduce the *non-stationary surface-following non-orthogonal* coordinate system:

$$\xi = x, \quad \vartheta = y, \quad \zeta = z - \eta(\xi, \vartheta, \tau), \quad \tau = t \quad (12.2.5)$$

The periodicity conditions over the ‘horizontal’ coordinates  $\xi$  and  $\vartheta$  are assumed:

$$\begin{aligned} x(\xi, \vartheta, \zeta, \tau) &= x(\xi + 2\pi, \vartheta, \zeta, \tau) + 2\pi, \\ y(\xi, \vartheta, \zeta, \tau) &= y(\xi, \vartheta + 2\pi, \zeta, \tau) + 2\pi, \\ z(\xi, \vartheta, \zeta, \tau) &= z(\xi + 2\pi, \vartheta, \zeta, \tau), \\ z(\xi, \vartheta, \zeta, \tau) &= z(\xi, \vartheta + 2\pi, \zeta, \tau). \end{aligned} \quad (12.2.6)$$

Variable  $\eta(x, y, t) = \eta(\xi, \vartheta, \tau)$  in (12.2.5) is the moving periodic wave surface given by Fourier series

$$\eta(\xi, \vartheta, \tau) = \sum_{-M < k < M} \sum_{-M_y < l < M_y} h_{k,l}(\tau) \Theta_{k,l} \quad (12.2.7)$$

and  $M$  and  $M_y$  are the numbers of modes in directions  $\xi$  and  $\vartheta$ , correspondingly, while  $\Theta_{k,l}$  is the function:

$$\Theta_{k,l} = \begin{cases} \cos(k\xi + l\vartheta) & -M_x \leq k \leq M_x, -M_y < l < 0 \\ \cos(k\xi) & -M_x \leq k \leq 0, l = 0 \\ \sin(k\xi) & 0 \leq k \leq M_y, l = 0 \\ \sin(k\xi + l\vartheta) & -M_x \leq k \leq M_x, 0 < l \leq M_y \end{cases}. \quad (12.2.8)$$

If the accuracy of Fourier approximation in both directions is the same, then  $\gamma = M_x/M_y$  is a ratio of the domain sides  $L/L_y$  in  $\xi$  and  $\vartheta$  directions. The formulation (12.2.8) that contains real coefficients of Fourier transform in the rectangular matrice allows us to present amplitudes in a form convenient for compact programming. Form (12.2.8) permits simple differentiation over  $\xi$  and  $\vartheta$  of any function  $F$  represented by the Fourier coefficients  $F_{k,l}$  in Fourier space:

$$\frac{\partial}{\partial \xi} \left( \sum_{-M < k < M} \sum_{-M_y < l < M_y} F_{k,l}(\tau) \Theta_{k,l} \right) = - \sum_{-M < k < M} \sum_{-M_y < l < M_y} k F_{-k,l}(\tau) \Theta_{k,l}, \quad (12.2.9)$$

$$\frac{\partial}{\partial \vartheta} \left( \sum_{-M < k < M} \sum_{-M_y < l < M_y} F_{k,l}(\tau) \Theta_{k,l} \right) = -\gamma \sum_{-M < k < M} \sum_{-M_y < l < M_y} l F_{k,-l}(\tau) \Theta_{k,l}. \quad (12.2.10)$$

Since the ratio of horizontal scales  $\gamma$  is taken into account in definition of derivative over  $\vartheta$ , it is not included in the equations given below.

The vertical coordinate (12.2.6) is constructed for a deepwater case. As shown, the vertical fluctuations of the ‘horizontal’ coordinates  $\xi$  and  $\vartheta$  do not attenuate with depth. Such fluctuations do not create any approximation problems. However, the lower boundary condition is applied at variable level  $H = \zeta + \eta$ . Since all the variables in wave motion attenuate with depth exponentially, the difference between the fixed and fluctuating levels for depth  $|H| \gg |\eta|$  becomes negligible. The possibility of using coordinates (12.2.6) for the finite depth case is mentioned in conclusion.

### 12.3 Three-Dimensional Deepwater Wave Model

The main advantage of the surface-following coordinate system is that the variable surface  $\eta$  is mapped onto the fixed plane  $\zeta = 0$ . The 3-D equations of potential waves in the system of coordinates (12.2.6) at  $\zeta < 0$  take the following form:

$$\eta_\tau = -\eta_\xi \varphi_\xi - \eta_\vartheta \varphi_\vartheta + (1 + \eta_\xi^2 + \eta_\vartheta^2) \Phi_\zeta, \quad (12.3.1)$$

$$\varphi_\tau = -\frac{1}{2} \left( \varphi_\xi^2 + \varphi_\vartheta^2 - (1 + \eta_\xi^2 + \eta_\vartheta^2) \Phi_\zeta^2 \right) - \eta - p, \quad (12.3.2)$$

$$\Phi_{\xi\xi} + \Phi_{\vartheta\vartheta} + \Phi_{\zeta\zeta} = \Upsilon(\Phi), \quad (12.3.3)$$

where  $\Phi$  is three-dimensional velocity potential;  $p$  is external pressure; and  $\varphi$  is a value of  $\Phi$  at surface  $\zeta = 0$ , while  $\Upsilon()$  is the operator:

$$\Upsilon() = 2\eta_\xi()_{\xi\xi} + 2\eta_\vartheta()_{\vartheta\vartheta} + (\eta_{\xi\xi} + \eta_{\vartheta\vartheta})()_\zeta - (\eta_\xi^2 + \eta_\vartheta^2)()_{\xi\xi} \quad (12.3.4)$$

Equations (12.3.1) and (12.3.2) are written at free surface the position of which in the surface-following coordinate system is fixed at  $\zeta = 0$ , as mentioned above. These equations formally look as two-dimensional; however, they include a vertical

derivative of potential  $\Phi_\zeta$  which should be derived from elliptical Eq. (12.3.3) with the following boundary conditions:

$$\Phi(\zeta = 0) = \varphi, \quad \frac{\partial \Phi}{\partial \zeta}(\zeta \rightarrow -\infty) = 0. \quad (12.3.4)$$

The second condition (12.3.4) in the numerical scheme is replaced by the condition at finite depth  $\frac{\partial \Phi}{\partial \zeta}(\zeta = H) = 0$  where depth  $H$  should be large enough to be considered as infinitely large. The previous calculations with 1-D model show that such  $H$  can be defined by the formula  $H = 2\pi n/k_p$  where  $k_p$  is the wave number of the mode with the largest amplitude, while  $1 < n \leq 2$ .

Equations (12.3.1) and (12.3.2) were suggested by Zakharov (1968) with no mention that they are derived formally with transformation (12.2.6). The approach has not been extended for the full system of the equations.

## 12.4 Linear (Analytic) and Nonlinear Components of Velocity Potential. Numerical Solution of 3-D Equation for Velocity Potential

The 2-D equations for potential waves written in the conformal coordinates have a remarkable property; i.e., Laplace equation remains the same. This is why the Fourier modes of the velocity potential can be represented through standard expansion. It means that the potential and any of its derivatives decrease exponentially from free surface. In a 3-D case in the Cartesian coordinates, as well as in the curvilinear coordinates, it cannot be precise. However, it would be quite reasonable to suggest that the exponential behavior remains dominant, while the potential can be represented as a sum of two components, i.e., analytic ('linear') component  $\bar{\Phi}$ , ( $\bar{\varphi} = \bar{\Phi}(\xi, \vartheta, 0)$ ) and arbitrary nonlinear component  $\tilde{\Phi}$ , ( $\tilde{\varphi} = \tilde{\Phi}(\xi, \vartheta, 0)$ )<sup>1</sup>:

$$\varphi = \bar{\varphi} + \tilde{\varphi}, \quad \Phi = \bar{\Phi} + \tilde{\Phi}. \quad (12.4.1)$$

The analytic component  $\bar{\Phi}$  satisfies Laplace equation:

$$\bar{\Phi}_{\xi\xi} + \bar{\Phi}_{\vartheta\vartheta} + \bar{\Phi}_{\zeta\zeta} = 0, \quad (12.4.2)$$

---

<sup>1</sup>Note that the term 'linear' is conventional, since this component is also influenced by the nonlinearity due to the curvature of surface.

with the known solution:

$$\bar{\Phi}(\xi, \vartheta, \zeta) = \sum_{k,l} \bar{\varphi}_{k,l} \exp(|k|\zeta) \Theta_{k,l}, \quad (12.4.3)$$

( $\bar{\varphi}_{k,l}$  are the Fourier coefficients of the surface analytical potential  $\bar{\varphi}$  at  $z = 0$ ). Solution satisfies the following boundary conditions:

$$\begin{aligned} \zeta = 0 : \quad \bar{\Phi} &= \bar{\varphi} \\ \zeta \rightarrow -\infty : \quad \tilde{\Phi}_\zeta &\rightarrow 0 \end{aligned} \quad (12.4.4)$$

The nonlinear component satisfies the equation:

$$\tilde{\Phi}_{\xi\xi} + \tilde{\Phi}_{\vartheta\vartheta} + \tilde{\Phi}_{\zeta\zeta} = Y(\tilde{\Phi}) + Y(\bar{\Phi}). \quad (12.4.5)$$

Equation (12.4.2) is solved with the boundary conditions:

$$\begin{aligned} \zeta = 0 : \quad \tilde{\Phi} &= 0 \\ \zeta \rightarrow -\infty : \quad \tilde{\Phi}_\zeta &\rightarrow 0 \end{aligned} \quad (12.4.6)$$

Derivatives of the linear component  $\bar{\Phi}$  are calculated directly with use of (12.2.9) and (12.2.10). The scheme combines the 2-D Fourier transform method in ‘horizontal surfaces’ and the second-order finite-difference approximation on the stretched staggered grid defined by relation  $\Delta\zeta_{j+1} = \chi\Delta\zeta_j$  ( $\Delta\zeta$  is a vertical step, and  $j = 1$  at the surface). The stretched grid provides an increase of accuracy of approximation for exponentially decaying modes. The values of the stretching coefficient  $\chi$  lie within the interval 1.05–1.20. The finite-difference second-order approximation of Eq. (12.4.5) on the non-uniform vertical grid is quite straightforward. The vertical derivatives of the first and second orders for  $\zeta < 0$  are approximated with the following formulas:

$$\begin{aligned} \frac{\partial^2 \Phi_{k,l,j}}{\partial \zeta^2} &\approx A^1(j)\Phi_{k,l,j-1} + A^2(j)\Phi_{k,l,j} + A^3(j)\Phi_{k,l,j+1} \\ \frac{\partial \Phi_{k,l,j}}{\partial \zeta} &\approx A^4(j)\Phi_{k,l,j-1} + A^5(j)\Phi_{k,l,j} + A^6(j)\Phi_{k,l,j+1} \end{aligned} \quad (12.4.7)$$

where

$$\begin{aligned} A^1(j) &= \frac{2\Delta\zeta_{j+1}}{D_j}, \quad A^3(j) = \frac{2\Delta\zeta_j}{D_j}, \quad A^2(j) = -A^1(j) - A^3(j) \\ A^4(j) &= \frac{2\Delta\zeta_{j+1}}{D_j}, \quad A^6(j) = \frac{2\Delta\zeta_j}{D_j}, \quad A^5(j) = -A^4(j) - A^6(j) \end{aligned} \quad (12.4.8)$$

and

$$D_j = \Delta\zeta_{j+1}(\Delta\zeta_j)^2 + \Delta\zeta_j(\Delta\zeta_{j+1})^2. \quad (12.4.9)$$

The number of levels  $L_w$  depends on shape of spectrum, and in the calculations represented below,  $L_w$  varies within the limits  $L_w = 15-100$ . Opposite to the HOS and surface integral methods, this numerical scheme for 3-D wave problem is written directly for the initial system of Eqs. (12.3.1)–(12.3.3).

The diagnostic Poisson-like Eq. (12.4.5) for the nonlinear component of the velocity potential  $\tilde{\Phi}$  is solved using tridiagonal matrix algorithm (TDMA, Thomas 1949) generalized for a 3-D case through the Fourier presentation over the ‘horizontal’ coordinates. The term  $\Upsilon(\tilde{\Phi})$  in the right-hand side of Eq. (12.4.5) is calculated at each iteration using the values of  $\tilde{\Phi}$  obtained at the previous iteration. The term  $\Upsilon(\bar{\Phi})$ , as well as the coefficients that include derivatives of  $\eta$  in the right-hand side of (12.4.5), is fixed inside the iterations. The initial  $\tilde{\Phi}$  is equal to zero, while in the process of calculations, this value is taken from the previous time step. Iterations continue until the residual error for Eq. (12.4.5) yields accuracy  $\varepsilon \sim 10^{-9} - 10^{-6}$ , depending on the parameters of the vertical grid. Typically, for all the calculations considered, error  $\varepsilon$  decreases exponentially during iterations. The speed of the calculations for a multi-mode wave field is reasonably high if the rms wave steepness does not exceed the value of 0.2. However, the model remains stable even if the local steepness considerably exceeds 1 at certain points.

The suggested scheme has obvious advantages if compared with the schemes that do not use splitting into nonlinear and linear parts, i.e., (1) Values of  $\tilde{\Phi}$  are by two orders less than the values of  $\bar{\Phi}$ ; (2) derivatives  $\tilde{\Phi}$  are calculated with analytical accuracy. This is why the number of levels and the prescribed relative accuracy of the solution for  $\tilde{\Phi}$  can be reduced; and (3) the number of iterations is reduced compared with the scheme for Eq. (12.3.3), so the calculation speed is higher. A typical number of iterations for Eq. (12.3.3) for  $\varepsilon = 10^{-7}$  are 5–10, while the number of iterations for Eq. (12.4.5) seldom exceeds 2. The 3-D solution being found, the Fourier coefficients for vertical velocity  $(\partial\Phi/\partial\zeta)_{k,l,0}$  on the surface are calculated as a sum of linear and nonlinear components:

$$\left( \frac{\partial\Phi}{\partial\zeta} \right)_{k,l,0} = \sum_{k,l} |k| \bar{\varphi}_{k,l} \Theta_{k,l} + A_j^1 \tilde{\Phi}_{k,l,1} - A_j^2 \tilde{\Phi}_{k,l,2}, \quad (12.4.10)$$

where  $A_j^1$  and  $A_j^2$  are the coefficients used for calculation of the vertical velocity at  $\zeta = 0$  with the second-order accuracy:

$$A^1 = \frac{\zeta_1}{\zeta_1\zeta_2 - \zeta_2^2}, \quad A^2 = \frac{\zeta_2}{\zeta_1^2 - \zeta_1\zeta_2}, \quad (12.4.11)$$

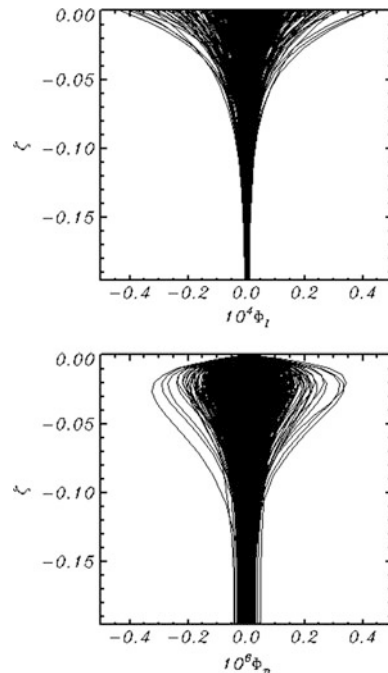
and  $\zeta_1 \zeta_2$  are vertical coordinates of  $\tilde{\Phi}_{k,l,1}$  and  $\tilde{\Phi}_{k,l,2}$ , respectively. Note that  $\tilde{\Phi}_{k,l,0} = 0$  and  $\zeta_0 = 0$ .

The Fourier transform method assumes that all the nonlinear terms are calculated on extended grid  $N \times N_y$  ( $N = 4M, N_y = 4M_y$ ) in physical space, the result being transformed into the Fourier space. The description of variables in terms of the Fourier components is more compact than that in terms of the grid values. That is why the Fourier components are considered as a basic presentation, while the grid fields are calculated and stored only when and where they are required.

The asymptotic behavior of  $\tilde{\Phi}_{k,l}$  in the vicinity of  $\zeta = 0$  is very close to the linear one, which provides high relative accuracy of the order of  $10^{-5}-10^{-4}$  for the second-order approximation for vertical derivative in Eq. (12.4.5) at  $\zeta < 0$  and for vertical velocity of the order of  $10^{-7}-10^{-8}$  on surface  $\zeta = 0$ . The profiles of the Fourier amplitudes of linear and nonlinear components are given in Fig. 12.1. The calculations were done for the initial wave field defined by Pierson and Moskowitz (1964) spectrum, with  $M_x = 256, M_y = 64, L_w = 15$  for  $t = 500$  (which corresponds to 100,000 time steps). As shown, the values of  $\tilde{\Phi}_{k,l}$  are by two decimal orders smaller than the values of  $\bar{\Phi}_{k,l}$ .

The model is mostly intended for simulation of the multi-mode long-term periodic wave field evolution with realistic spectrum. No matter how high the spectral resolution might be, for the long-term simulations of nonlinear waves, the energy flux into a truncated part of spectrum ( $\sqrt{k^2 + l^2} > M$ ) must be

**Fig. 12.1** *Upper panel* vertical profiles of Fourier coefficients for analytic components of velocity potential  $10^4 \bar{\Phi}_{k,l}(\zeta)$ ; *bottom panel* vertical profiles of Fourier coefficients for nonlinear component  $10^6 \tilde{\Phi}_{k,l}(\zeta)$  (Chalikov et al. 2014 © 2014 Springer-Verlag Berlin Heidelberg. With permission of Springer)



parameterized. Otherwise, sudden energy accumulation violating the energy conservation law at large wave numbers always corrupts the numerical solution. In numerical solutions of the fluid mechanics equations, this effect is suppressed by introducing different types of viscosity. Thus, the atmospheric models often include purely artificial operators formulated in the Fourier space. A similar scheme was described in the previous articles which considered the conformal method for direct wave modeling (Chalikov and Sheinin 1998, 2005). Following the scheme, simple dumping terms were added to the right-hand sides of the Fourier form of Eqs. (12.3.1) and (12.3.2):

$$\frac{\partial \eta_{k,l}}{\partial \tau} = E_{k,l} - \mu_{k,l} \eta_{k,l}, \quad (12.4.12)$$

$$\frac{\partial \varphi_{k,l}}{\partial \tau} = F_{k,l} - \mu_{k,l} \phi_{k,l} \quad (12.4.13)$$

where  $E_{k,l}$  and  $F_{k,l}$  are the Fourier coefficients for the right-hand sides of Eqs. (12.3.1) and (12.3.2), and

$$\mu_{k,l} = \begin{cases} rM \left( \frac{|k| - k_d}{M - k_d} \right)^2 & \text{if } |k| > k_d \\ 0 & \text{otherwise} \end{cases} \quad (12.4.14)$$

where  $|k| = \sqrt{k^2 + \gamma^2 l^2}$ , and  $k_d$  is radius of the domain which is not affected by smoothing. The value of  $k_d$  depends on the spectral resolution and position of spectrum in the Fourier domain. The value of  $k_d$  is chosen in the interval  $(0.5M, 0.9M)$  in different versions of the model. The value of  $r = 0.25$  is chosen for all of the runs discussed below, since it was found that the results were reasonably insensitive to the variations of  $r$ . Dissipation effectively absorbs energy at the wave numbers close to truncation number  $M$  and does not affect energy at wave numbers  $|k| \leq k_d$ . Note that increase of truncation number  $M$  shifts the dissipation area to higher wave numbers (if  $M \rightarrow \infty$ , the energy sink due to dissipation tends to be zero), so the scheme described above retains the approximation of the original (non-dissipative) system. Note also that the scheme (12.4.12)–(12.4.14) is introduced in order to describe real physical process, i.e., the dissipation of wave energy due to the flux of energy into a truncated part of spectrum. This process is usually very slow. The decay of total energy  $E$  at each time step is of the order of  $(10^{-7} - 10^{-6})E$ , but in the absence of such dissipation, the numerical instability growing exponentially in the vicinity of  $k = M$  occurs and finally terminates the solution. The fourth-order Runge–Kutta scheme was used for time integration of Eqs. (12.3.1) and (12.3.2). For any explicit time integration scheme, the stability criterion has the form  $\Delta\tau \leq C\omega_{\max}^{-1}$  (if dissipation does not play a significant role), where  $\Delta\tau$  is time step,  $\omega_{\max} = k_{\max}^{1/2}$  is maximum frequency of the system, and  $C$  is a

constant depending on the scheme; for the Runge–Kutta scheme,  $C = 2\sqrt{2}$ . We should note that such estimation does not always work in our case because of the strong nonlinear local effects. Finally, time step was chosen empirically. For example, for  $M = 256$ , the time step used was 0.005.

## 12.5 Validation of the 3-D Deepwater Model

No doubt that at sufficient number of modes, the Eqs. (12.3.1) and (12.3.2) can be integrated in time with the Fourier transform method and Runge–Kutta scheme with high accuracy. Thus, the critical point of the entire scheme is the accuracy of the solution of 3-D equations for the velocity potential (12.4.5) with the boundary condition (12.4.6). There are several methods of validation of the scheme for Eq. (12.4.5). The most straightforward method is based on the comparison of the vertical velocity on surface  $\Phi_\zeta$  for the 2-D problem obtained in the current scheme, with the vertical velocity calculated using the precise scheme based on conformal mapping. Such comparison was done for the Stokes wave with steepness  $ak = 0.40$ . Transferring the solution from the conformal coordinates to the uniform-over- $x$  grid was done using the fourth-order periodic spline interpolation. It was found that the solutions for vertical velocities obtained with 2-D and 3-D models have coincided, the accuracy being of the order of  $10^{-5}ak$ . Note that the two-dimensionality assumption used in such validation does not create a problem, since only the vertical operator is being checked.

The second method of validation is based on analytical solution for Eq. (12.3.3):

$$\Phi(\xi, \vartheta, \zeta) = \sum_{-M_x < k < M_x} \sum_{-M_y < l < M_y} \sum_{1 < i < N_x} \sum_{1 < j < N_y} \varphi_{k,l}^0 \exp(|k|(\zeta + \eta(\xi_i, \vartheta_j))) \Theta_{k,l}, \quad (12.5.1)$$

where  $N$  and  $N_y$  are the numbers of grid points in directions  $\xi$  and  $\vartheta$ , correspondingly;  $\varphi_{k,l}^0$  are Fourier coefficients of the velocity potential at the fixed level  $z = 0$ . Equation (12.5.1) defines the potential on surface  $\varphi = \Phi(\xi, \vartheta, 0)$  through the Fourier coefficients  $\varphi_{k,l}^0$  in the Cartesian coordinate system for  $z = 0$ . Since coefficients  $\varphi_{k,l}^0$  are unknown, then Eq. (12.5.1) cannot be used directly for integration of the system (12.3.1)–(12.3.3). However, Eq. (12.5.1) is useful for detailed validation of accuracy of its numerical solution. First, arbitrary Fourier coefficients  $\varphi_{k,l}^0$  for the velocity potential at level  $z = 0$  are chosen. Then, the velocity potential at free surface  $z = \eta$  is transferred using (12.5.1). The values of the velocity potential are used as surface boundary condition for Eq. (12.4.5). The calculated vertical velocity on the surface is then compared with the result calculated directly using Eq. (12.5.1)

$$\frac{\partial \Phi}{\partial \zeta}(\xi, \vartheta, 0) = \sum_{-M_x < k < M_x} \sum_{-M_y < l < M_y} \sum_{1 < i < N_x} \sum_{1 < j < N_y} |k| \varphi_{k,l}^0 \exp(|k|\eta(\xi_i, \vartheta_j)) \Theta_{k,l}$$
(12.5.2)

Such calculations prove that analytical solution (12.5.1) coincides with the results of the numerical solution of Eq. (12.3.3), the accuracy being equal to  $(10^{-5}-10^{-4})ak$ .

The second method of validation was applied for the wave field defined by JONSWAP spectrum at  $\Omega_p = U_{10}/c_p = 2$  with directional spreading proportional to  $(\operatorname{sech}(\theta))^4$ , ( $\theta$  is the direction of mode), which corresponds to steep waves. The exact calculations were made at resolution  $M = 128$ ,  $M_y = 32$ , with the number of levels  $L_w = 100$  and accuracy of the solution of Eq. (12.3.3) being equal to  $\varepsilon = 10^{-10}$ . Then, the solution at a lower resolution was compared with the high-accuracy solution. In Fig. 12.2, the dependence of rms error  $E_{\text{rms}}$

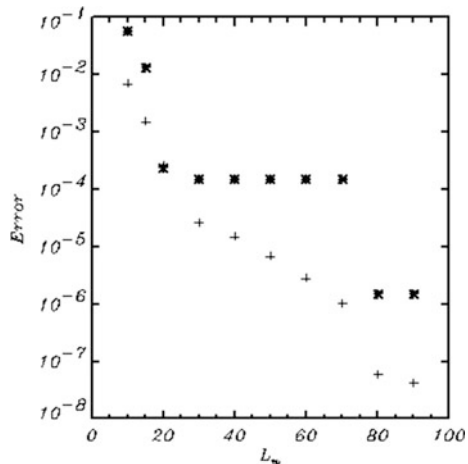
$$E_{\text{rms}} = \left( \overline{(w_{100} - w_L)^2} \right)^{1/2},$$
(12.5.3)

is given ( $w_{100}$  and  $w_L$  are the grid surface vertical velocities obtained at  $L_w = 100$  and at variable  $L_w$ ). As shown, rms accuracy  $E_{\text{rms}}$  monotonically decreases when approaching the number of levels  $L_w = 100$ .

The methods described above are targeted at validation of the numerical scheme for the elliptic Eq. (12.3.3) used at every time step. The most efficient method of validation of both the numerical scheme and codes for Eqs. (12.3.1)–(12.3.3) is the comparison of the results of integration of Eqs. (12.3.1)–(12.3.3) with exact steady solution of the equations obtained in a moving coordinate system. To obtain steady solutions with very high accuracy (crucial for the model validation), an iterative

**Fig. 12.2** Dependence of on the number of levels  $L_w$ .

Sign + corresponds to rms error  $E_{\text{rms}}$  (Eq. (12.5.3)), sign \* corresponds to maximum error (Chalikov et al. 2014 © 2014 Springer-Verlag Berlin Heidelberg. With permission of Springer)



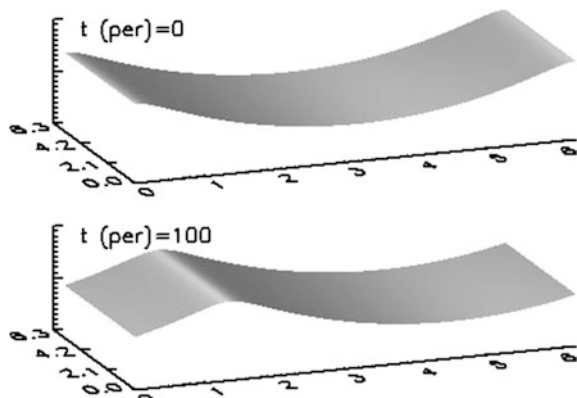
algorithm was developed on the basis of integration operators and Hilbert transform in the Fourier space (see Chap. 3). This method is also used in the current chapter. The calculations are performed for the Stokes waves propagating along the  $x$ -axis defined at wave numbers  $k = 1, 2, 3 \dots M, M_y = 0$ . This setting is most appropriate for validation of the numerical scheme, since there is no room for the development of the Benjamin–Feir instability (Benjamin and Feir 1967). Hence, all the modes with wave numbers  $k > 1$  represent the components ('bound waves') of Stokes wave. The similar calculations using the 2-D conformal model demonstrate the highest stability of the first 800 modes of Stokes wave over hundreds of wave periods (see Chalikov 2005). Note that Stokes waves can be also assigned at  $k = nk_0$  ( $n$  is a whole number); however, unavoidable numerical errors can finally play a role of disturbances initiating the development of the Benjamin–Feir instability.

The simulation of a very steep Stokes wave with steepness  $ak = 0.40$  (assigned in the initial condition) in the current work is performed with the parameters  $M = 128$ ,  $M_y = 16$ ,  $L_w = 30$ , and  $\varepsilon = 10^{-6}$ . Note that for simulation of the 2-D process, the number of lateral modes  $M_y$  can be chosen as 1. Value  $L_y = 16$  was used for a purely technical check of the codes, proving that lateral modes are not generated during integration. The wave surface assigned in the initial condition and the wave surface obtained after almost 100 periods of the calculations (about 10,000 time steps) are shown in Fig. 12.3.

As shown, the surface remains smooth without any signs of disturbances. The theoretical phase velocity of the Stokes wave with steepness  $ak = 0.40$  is equal to 1.0822. The phase velocity reproduced by the numerical model is 1.0820. The more detailed validations show the time evolution of the amplitudes of the first 13 Stokes wave modes (Fig. 12.4).

As shown, the first several modes of the Stokes wave with the amplitudes as small as  $10^{-4}$  remain practically unchanged, while the rest of the amplitudes fluctuate. The relative magnitude of fluctuation increases with growth of wave number. However, the average values of amplitudes for each mode do not change,

**Fig. 12.3** Shape of Stokes wave ( $ak = 0.40$ ) at  $t = 0$  and  $t = 100$  periods  
(Chalikov et al. 2014 © 2014 Springer-Verlag Berlin Heidelberg. With permission of Springer)



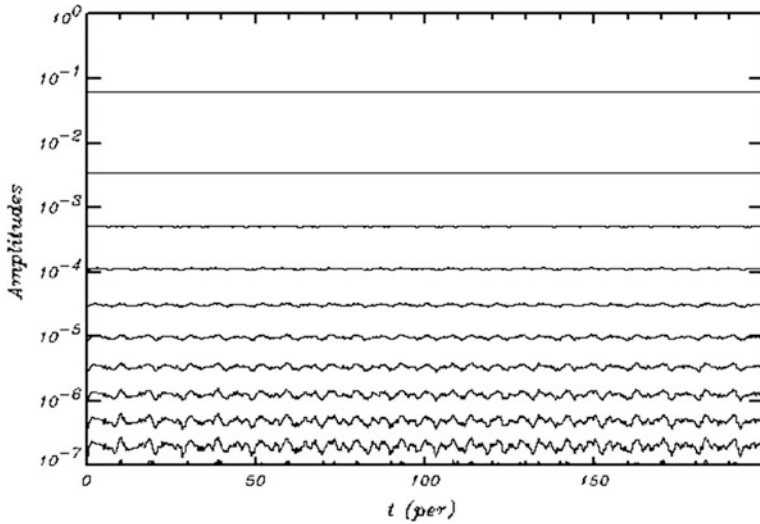


**Fig. 12.4** Evolution of amplitudes of steep ( $ak = 0.40$ ) Stokes wave  $A_s$  assigned initially at wave numbers  $k = 1, 2, 3, \dots, M$  (Chalikov et al. 2014 © 2014 Springer-Verlag Berlin Heidelberg. With permission of Springer)

their values decreasing monotonically with growth of wave number. There are no signs of instability which would indicate that high-order Stokes modes start growing. Evolution of the rms difference  $E_{\text{rms}}$  between the initial wave surface  $\eta_0$  and the surfaces  $\eta$  simulated in the course of integration

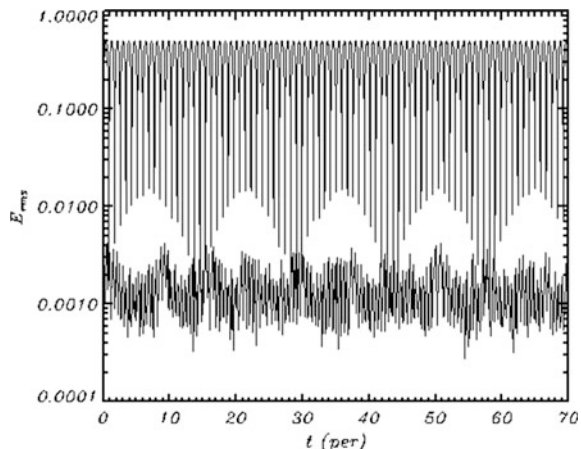
$$E_{\text{rms}} = \left( \overline{(\eta_0 - \eta(\tau))^2} \right)^{1/2} \quad (12.5.4)$$

is shown in Fig. 12.5 (top curve).

As shown,  $E_{\text{rms}}$  is a strictly periodic function of time. When phases become equalized, the rms difference decreases to  $10^{-3}ak$  with no tendency for growing. In reality, the error is smaller, because the accuracy of coincidence of surfaces depends on the frequency of sampling. The bottom curve represents a similar rms difference between the initial  $\eta_0$  and current waves  $\eta(\tau)$  calculated over the interval between two consequent peaks of the Stokes wave. Since domain  $0 < \xi < 2\pi$  contains only one wave peak, in order to calculate the rms difference, domain was periodically extended over the interval  $-2\pi < \xi < 4\pi$ . As shown, this error fluctuates around the value of  $10^{-3}$  with no tendency for growing.

Unlike the 2-D model, the 3-D model uses a finite-difference approximation for the velocity potential equation. This is why the solution for Stokes wave is not as exact as the same solution in the conformal coordinates. A higher vertical resolution results in higher accuracy of the solution for velocity potential, though such calculations certainly become more time consuming. Note that this method of

**Fig. 12.5** Top curve represents evolution of rms difference  $E_{\text{rms}}^1$  Eq. (12.5.4) between the initial wave surface  $\eta_0$  and the surfaces  $\eta$  simulated in the course of integration. Bottom curve corresponds to rms difference between the initial and superimposed wave profiles (Chalikov et al. 2014 © 2014 Springer-Verlag Berlin Heidelberg. With permission of Springer)



validation is full and non-trivial and the results being combined with the investigation of the numerical scheme for Eq. (12.3.3) prove high accuracy of the entire numerical model. For technical reasons, the similar validation was also done for the Stokes wave propagating along the  $y$ -axis.

In the following numerical experiment, the Stokes wave with steepness  $ak = 0.35$  was assigned at wave numbers  $k = 8, 16, 24 \dots M$ , while surface was initially distorted by random linear waves with the amplitudes by five decimal orders smaller, if compared with the amplitude of the Stokes first mode. The calculations were done in rectangular Fourier domain with dimensions  $M_x = 128$  and  $M_y = 32$ . Since the modes of the Stokes wave were set over the interval  $\Delta k = 8$ , the noise modes started to grow similar to the process simulated with the 2-D conformal model (Chalikov 2007). The medium steepness  $ak = 0.35$  was chosen here, because at larger steepness, the instability develops too fast.

Evolution of extreme values of steepness is shown in Fig. 12.6.

Absolute values of negative steepness are larger than those of the positive one, which indicates a forward inclination of the waves linked to the horizontal asymmetry. Wave field finally becomes too steep, while the waves tend to overturn. Unlike the 2-D conformal model which allows us to reproduce a non-single-valued

**Fig. 12.6** Evolution of maximum positive steepness (dashed curve) and minimum negative  $k = 8n$ , ( $n = 1, 2, 3 \dots$ ) with imposed disturbances (Chalikov et al. 2014 © 2014 Springer-Verlag Berlin Heidelberg. With permission of Springer)

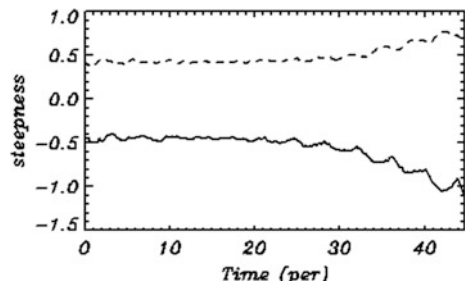
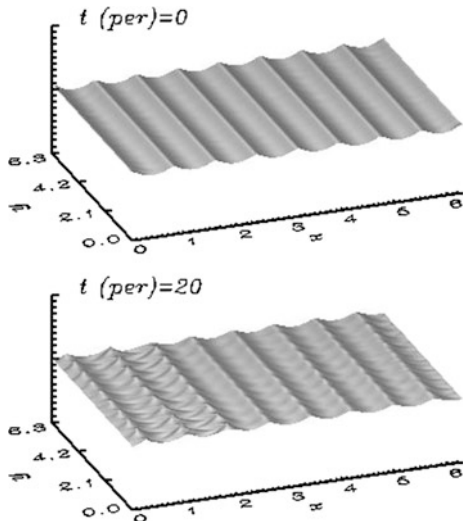


**Fig. 12.7** Train of Stokes waves ( $ak = 0.35$ ) at initial conditions ( $t = 0$ ) and a shape of surface just prior to the development of numerical instability ( $t = 20$  periods) (Chalikov et al. 2014 © 2014 Springer-Verlag Berlin Heidelberg. With permission of Springer)



shape of surface, the current model becomes unstable when the local steepness exceeds 1.1. Before this moment, the total wave energy is preserved with very high accuracy. A limiting value of steepness depends on the number of modes and magnitude of the time step.

The initial wave surface and the wave surface prior to breaking are shown in Fig. 12.7. As shown, the 2-D instability leads to the formation of a ‘horseshoe’ regular structure well known from the experiments (Su 1982) and numerical simulations based on surface integral (Fructus et al. 2005).

Evolution of amplitudes of the first seven modes of the Stokes wave is shown in Fig. 12.8. Solid lines correspond to the amplitudes of the Stokes modes, while aggregated gray lines show growing and fast-fluctuating intermediate modes. The main mode with the amplitude  $A_8 = 0.35$  does not show a visible change; the amplitudes of all other modes decrease, while the intermediate modes are developing by taking energy from all the modes of the Stokes wave. The total energy remains constant within the range of six decimal digits.

The 2-D wave spectrum prior to breaking (which corresponds to the developed ‘horseshoe’ quasi-regular structure of Fig. 12.7) is shown in Fig. 12.9 (top panel). Since all variables are non-dimensional, the spectrum is shown in conventional units, the darkest color corresponding to the maximum of spectral density  $S_m$ , while white color is showing the values less than  $10^{-12} S_m$ . The spectrum in Fig. 12.9 demonstrates that development of new modes in a 2-D case occurs in a more complicated way; i.e., the nearly discrete disturbances develop not at  $l = 0$  but rather at some angle to the main modes with wave numbers  $l = \pm 9, 18, 27$ . The main mode of the Stokes wave located at  $k = 8$  generates disturbances at the lateral wave number  $l = 9$ . The ratio of wave numbers is  $l/k = 1.125$  which is reasonably close to the value  $l/k = 1.15$  found with the linear 2-D instability theory of the Stokes wave

**Fig. 12.8** Evolution of amplitudes of Stokes wave ( $ak = 0.35$ , solid curves) assigned initially with superimposed noise. Aggregated gray lines correspond to new growing modes (Chalikov et al. 2014 © 2014 Springer-Verlag Berlin Heidelberg. With permission of Springer)

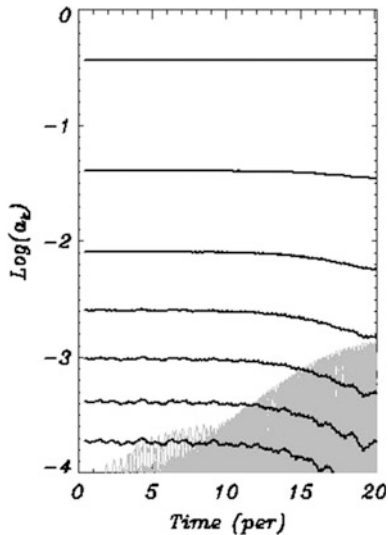
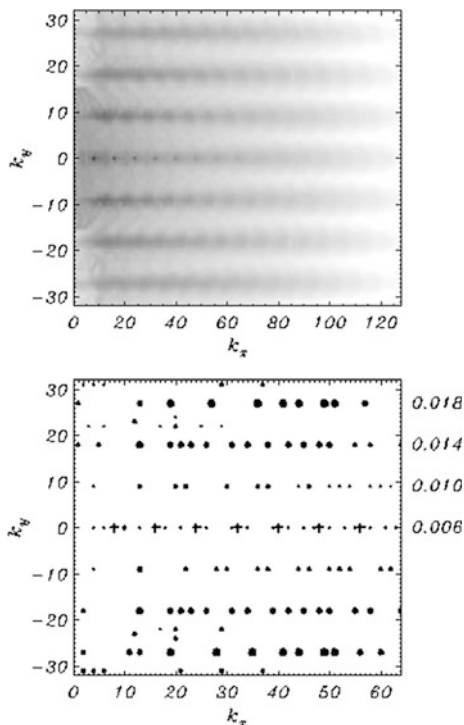


**Fig. 12.9** Top panel 2-D wave spectrum (conventional units) prior to the development of breaking (see Fig. 12.7). Bottom panel rate of development  $\beta$  of intermediate mode amplitudes (Eq. 12.5.5). The values of  $\beta$  are given outside the frame for each row. Crosses indicate the initial position of Stokes wave modes (Chalikov et al. 2014 © 2014 Springer-Verlag Berlin Heidelberg. With permission of Springer)



(McLean 1982). As shown, full equations also predict the development of new rows of modes at  $l = 9n$  ( $n = 1, 2, 3, \dots$ ), which corresponds to higher modes of the Stokes wave. Such evolution of growing modes can be approximated by the expression:

$$A_{k,l}(\tau) = A_{k,l}(0) \exp(\beta_{k,l}\omega\tau). \quad (12.5.5)$$

The values of  $\beta_{k,l}$  were calculated for  $A_{k,i}(\tau)$  using the rms method. In the bottom panel of Fig. 12.9, the local maxima of  $\beta$  are shown by dots whose sizes depend on the magnitude of  $\beta$ . The positions of the original Stokes wave modes are indicated by crosses. Figure 12.9 shows that disturbances are located symmetrically with respect to  $k$ -axis.

## 12.6 Simulation of a Multi-Mode Wave Field

The third series of calculations was performed to simulate a multi-mode wave field initially defined as a superposition of linear modes with random phases, corresponding to Pierson and Moskowitz (1964) spectrum with directional spreading in the energy-containing part of the spectrum proportional to  $(\operatorname{sech}(\theta))^4$ . The simulations were performed in rectangular domain with the number of modes different in  $x$ - and  $y$ -directions, i.e.,  $M_x = 256$ ,  $M_y = 64$ . In this case, the grid includes 564,288 knots (130,302 degrees of freedom). All the calculations were conducted on Dell workstation.

The peak of spectrum was initially placed at  $(k, l) = (64, 0)$ . Calculations with the time step  $\Delta\tau = 0.0025$  were performed up to non-dimensional time  $\tau = 250$  (10,000 time steps), which corresponds to 318 peak wave periods.

Over such a long period of integration, the energy of waves in the absence of any energy input decreases due to the flux of energy into the subgrid domain, as described above. Pierson–Moskowitz spectrum corresponds to the statistically steady wave regime, when the total energy input equals total energy dissipation. This balance can be introduced by using the energy input from wind, as formulated in Chalikov and Rainchik (2010), as well as the energy dissipation through the breaking adjustment as suggested in Chalikov and Sheinin (2005). In any case, at present stage, implementation of the complicated physics seems premature. This is why a quasi-stationary regime is reproduced on the basis of a simple scheme designed to preserve the total energy. It is done by the introduction of additional terms in the spectral form of Eqs. (12.3.1) and (12.3.2):

$$\frac{\partial \eta_{k,l}}{\partial \tau} = H_{k,l} + (1 - \gamma)\eta_{k,l}, \quad (12.6.1)$$

$$\frac{\partial \varphi_{k,l}}{\partial \tau} = F_{k,l} + (1 - \gamma)\varphi_{k,l}, \quad (12.6.2)$$

where  $\eta_{k,l}$  and  $\varphi_{k,l}$  are the Fourier amplitudes for  $\eta$ , while  $H_{k,l}$  and  $F_{k,l}$  are the Fourier amplitudes of the right-hand sides of Eqs. (12.3.1) and (12.3.2), including additional terms introduced by Eqs. (12.4.12) and (12.4.13);  $\gamma$  is coefficient:

$$\gamma = (E/E_0)^{1/2}, \quad (12.6.3)$$

and  $E_0$  is the initial total wave energy equal to the sum of the kinetic and potential energies;  $E$  is the total energy at the previous time step. Since the coefficient  $(1 - \gamma)$  is very small (of the order of  $10^{-6}$ ), algorithm (12.6.1)–(12.6.3) supports the total energy with the accuracy of the order of  $10^{-6}$ , which practically does not change the structure of the solution either in the Fourier space or in physical space. Note that algorithm (12.6.1)–(12.6.3) is designed to compensate attenuation of energy due to the flux to high wave number range.

For typical peak wavelength, corresponding to Pierson–Moscowitz spectrum, the horizontal size of domain is of the order of several kilometers. The domain includes too many waves that is why Fig. 12.10 shows a 1/64 part of the computed wave surface for  $\tau = 250$ . Visually, the surface closely reminds a natural ocean wave surface. The animations generated in the course of integration depict highly authentic wave field. Just after one peak wave period, the initially sinusoidal waves obtain a typical Stokes-like shape with sharp crests and flat troughs. The probability of surface elevation (normalized by significant wave height) is shown in Fig. 12.11. For the calculations, 655,360,000 values of  $\eta_{i,j}$  were used. Dashed line represents reflected branch of the probability distribution for negative  $z$ . As shown, the probability of positive elevation (wave crests) is considerably larger than that of the negative one (troughs), exactly as in the 2-D modeling. Thin line in Fig. 12.11 corresponds to the Gaussian distribution. As shown, the negative values of  $\eta$  have smaller probability than the Gaussian distribution predicts, while the probability of positive values  $\eta$  considerably exceeds the Gaussian probability. It can be explained by the tendency of waves to approach the Stokes-like shape. This feature also

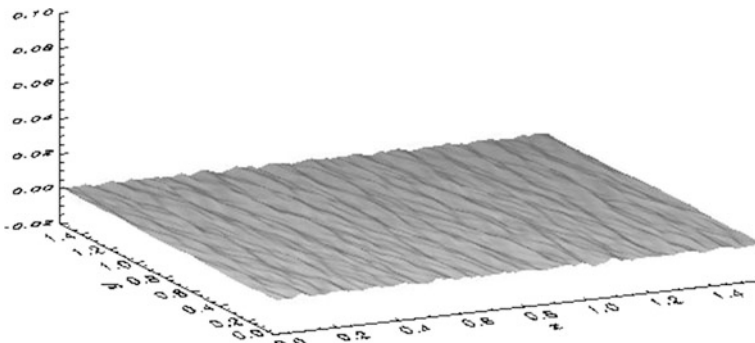
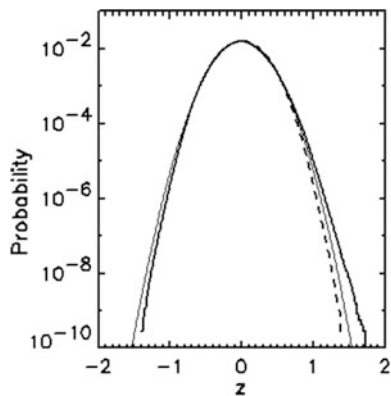


**Fig. 12.10** Example of the surface obtained at 318 periods of simulation of a wave field assigned initially with Pierson–Moscowitz spectrum. 1/64 part of the entire surface is shown (Chalikov et al. 2014 © 2014 Springer-Verlag Berlin Heidelberg. With permission of Springer)

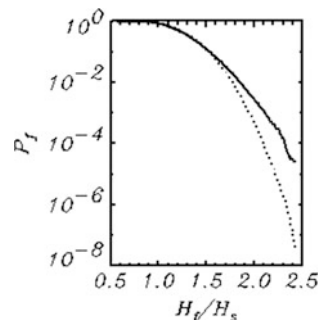
**Fig. 12.11** Probability of surface elevation. Thick curve corresponds to the model result, while dashed curve corresponds to the reversed probability distribution for negative values  $z$ ; thin curve represents Gauss distribution (Chalikov et al. 2014 © 2014 Springer-Verlag Berlin Heidelberg. With permission of Springer)



explains the mechanism of wave breaking and extreme wave generation. Some of the waves change their shape so significantly that they become unstable. It happens without a noticeable exchange between modes, with no sign of modulational instability found (see Chalikov 2009). The integral probability of the wave trough-to-crest height  $\tilde{H}_f = H_f/H_s$  ( $H_s$  is significant wave height) is shown in Fig. 12.12. As shown, a wave with non-dimensional height  $\tilde{H}_f > 2.1$  can emerge as frequently as one among one thousand waves. Naturally, to be really ‘freak,’ the wave should be large in physical space. The largest value of  $\tilde{H}_f$  was equal to 2.71.

Evolution of the kinetic (solid curve) and potential (dashed curve) energies is shown in the top panels of Fig. 12.13 as the percentage of the total energy divided into two. To make the figure clearer, only ten successive peak wave periods of the initial and final intervals are shown. The potential and kinetic energies fluctuate considerably (up to 1 %) over the period of adjustment of linear initial conditions to the nonlinearity. These fluctuations fall in the range of the order of 0.1 %, almost over the entire period of integration. The sum of the potential and kinetic energies is preserved with the accuracy of the order of  $10^{-5}$ . In the bottom panel of Fig. 12.13, evolution of skewness (solid line) and kurtosis (dashed line) is given. During the initial period, fast transformation of elevation and surface potential (initially

**Fig. 12.12** Thick curve shows the integral probability of trough-to-crest wave height  $H_f$  normalized by significant wave height  $H_s$ . Thin curve corresponds to Rayleigh distribution (Chalikov et al. 2014 © 2014 Springer-Verlag Berlin Heidelberg. With permission of Springer)



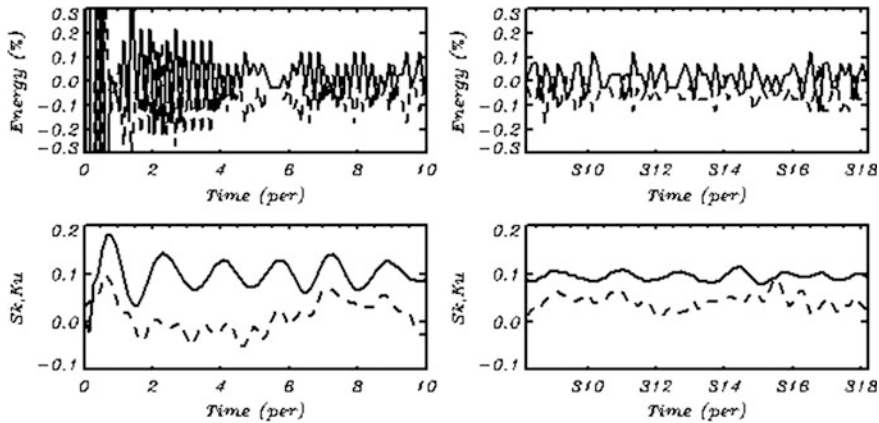


**Fig. 12.13** The top panels represent evolution of kinetic (solid curve) and potential (dashed curve) energies; the bottom frames show skewness (solid curve) and kurtosis (dashed curve) of wave surface. The left panels correspond to the first ten peak wave periods, and the right panels represent the last ten peak wave periods (Chalikov et al. 2014 © 2014 Springer-Verlag Berlin Heidelberg. With permission of Springer)

assigned according to the linear theory) occurs. Then, the system enters a quasi-stationary regime maintained for most of the integration time. Both skewness and kurtosis (exceeding 3) are positive, which is a particular feature of nonlinear waves.

It is generally accepted that the linear dispersion relation  $k = \omega^2$  ( $k$  and  $\omega$  are the non-dimensional wave number and frequency) is valid in a broad range of wave frequencies. The experimental data, however, confirm applicability of this formula to the relatively low frequencies. The numerical model gives us an opportunity to investigate this problem in more detail.

For the short time periods, when the rate of amplitude  $|h_{k,l}|$  change is small, i.e.,

$$\frac{\partial |h_{k,l}|}{\partial \tau} \ll \omega_{k,l} |h_{k,l}| \quad (12.6.4)$$

the mode evolution is described by the following relation:

$$\eta(\xi, \vartheta, \tau) = \sum_{k,l} h_{k,l} \theta_{k,l}(k\xi + l\vartheta - \omega_{k,l}\tau), \quad (12.6.5)$$

which gives

$$\frac{\partial \eta}{\partial \tau} = \sum_{k,l} \omega_{k,l} h_{-k,-l} \theta_{k,l}(k\xi + l\vartheta - \omega_{k,l}\tau); \quad (12.6.6)$$

and instantaneous value of frequency can be calculated as follows:

$$\omega_{k,l} = \frac{h_{k,l}^{\tau}}{h_{-k,-l}}, \quad (12.6.7)$$

where notation  $h_{k,l}^{\tau} = \frac{\partial h_{k,l}}{\partial \tau}$  is used. Calculations using (12.6.7) give large scatter. This is why the rms method for calculating the averaged values of frequency  $\bar{\omega}_{k,l}$  is used

$$\bar{\omega}_{k,l} = \frac{\overline{h_{k,l}^{\tau} h_{k,l}}}{\overline{h_{k,l}^2}}. \quad (12.6.8)$$

An accuracy of this method was verified with the  $h_{k,l}$  and  $h_{k,l}^{\tau}$  data, generated by the linear version of the model which was integrated over several tens of peak wave periods. It was found that for this case, the formula (12.6.8) satisfies the linear dispersion relation  $k = \omega^2$  with very high accuracy. Note that the waves with the same wave numbers running in opposite directions cannot be separated; i.e., the formula (12.6.8) gives absolute values of the frequency. In this particular case, it is not important, since the energy of opposite waves is very small. It was found that a deviation from the linear dispersion relation depends on the energy of mode, i.e., the less the energy, the stronger the deviation. These effects are demonstrated in Fig. 12.14 where the spectral density of energy is plotted in the coordinates  $(\omega_{\text{lin}}, \omega_{\text{mod}})$  where  $\omega_{\text{lin}} = k^{1/2}$  and  $\omega_{\text{mod}} = \bar{\omega}$ .

Different levels of energy (normalized by its maximum) are shown by gray tone of various densities. Solid curve shows the spectral energy distribution averaged over equal values of  $\omega_{\text{lin}}$ , i.e., over directions. As shown, the modes with large energy obey the linear dispersion relation; i.e., large energy is concentrated along the straight line  $\omega_{\text{lin}} = \omega_{\text{mod}}$ , while starting approximately from  $0.1S_p$  ( $S_p$  is a peak

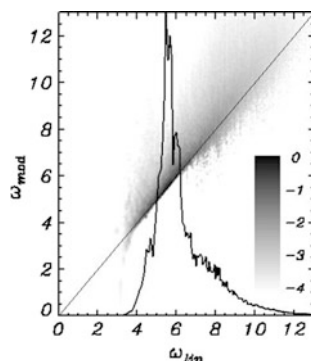


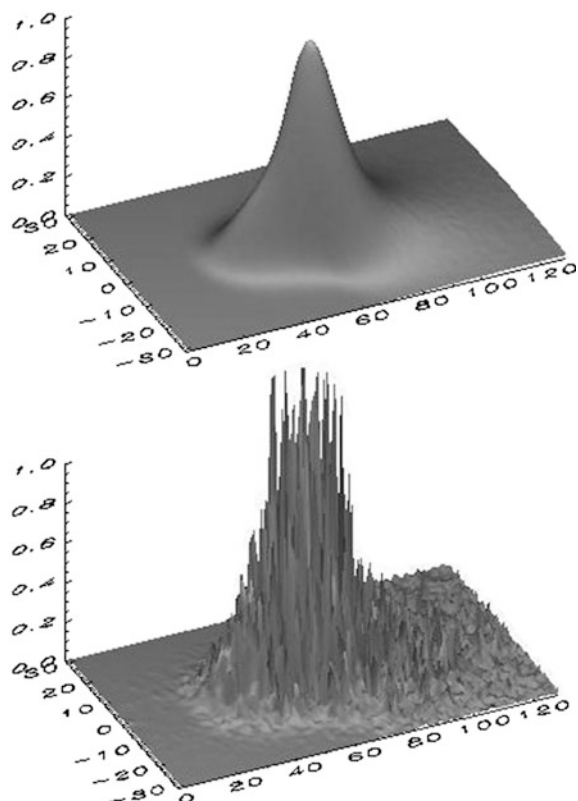
**Fig. 12.14** Distribution of spectral energy  $\log_{10} \bar{S}$  ( $\bar{S}$  is spectral density, normalized by its maximum) in the coordinates  $(\omega_{\text{lin}}, \omega_{\text{mod}})$ , where  $\omega_{\text{lin}} = k^{1/2}$  and  $\omega_{\text{mod}} = \bar{\omega}$  (Eq. 40). Solid curve shows the spectral density averaged over directions (Chalikov et al. 2014 © 2014 Springer-Verlag Berlin Heidelberg. With permission of Springer)

value of spectrum), the calculated frequency  $\omega_{\text{mod}}$  is mostly larger than the linear frequency  $\omega_{\text{lin}}$ . This effect was discovered experimentally and explained by Lake and Yuen (1978), later being reproduced in numerical models by Chalikov and Sheinin (1998). In reality, surface waves are nonlinear, each wave being constructed from a carrying mode and the so-called bound waves. These waves are not real waves; they are just shorter modes moving with the speed of the main mode. Besides, wave field contains free small-amplitude waves whose phase velocity is close to the linear phase velocity  $c = \omega/k$ . Consequently, at each wave number, free waves and bound waves coexist. Their averaged calculated frequency is larger than the linear frequency  $\omega_{\text{lin}}$ . This effect is pronounced more clearly if the total nonlinearity is large, while the energy of free waves remains small.

The most curious property of surface waves is demonstrated in Fig. 12.15.

The spectrum assigned in the initial conditions is smooth (top panel). However, after just several peak wave periods, the spectrum starts transforming; i.e., sharp peaks and deep holes appear. Finally, continuous spectrum transforms into the nearly discrete spectrum which consists of individual peaks. It is tempting to explain this phenomenon on the basis of the wave–wave resonance mechanism; i.e., the resolution is not high enough to cover all possible resonant combinations of

**Fig. 12.15** Top panel corresponds to the initial Pierson–Moskowitz 2-D wave spectrum  $\log_{10}(S)$ . Bottom panel corresponds to the final spectrum after integration over 318 peak wave periods (Chalikov et al. 2014 © 2014 Springer-Verlag Berlin Heidelberg. With permission of Springer)



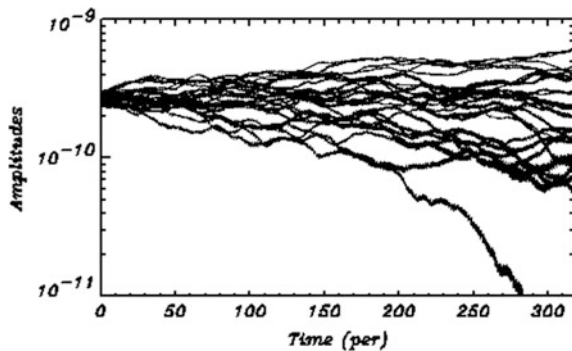
wave numbers and frequencies. This explanation, however, should be based on the assumption that exact dispersion relation is valid. In reality, the phase velocity of each wave mode is fluctuating due to many reasons, such as nonlinearity, Doppler effects, and the presence of bound waves. Consequently, the resonant conditions can get blurred over finite area, and therefore, such an explanation is not valid. If it were so, the spectrum would have been continuous. Moreover, if resolution were a problem, then following its increase, the spectrum would have been converging to the continuous spectrum similar to that in the top panel of Fig. 12.15, which actually never happens. Note that similar results were obtained using a simplified model based on the equations derived through expansion of the Hamiltonian up to the fourth order (Zakharov et al. 2002). The simplified approach allowed authors to use the resolution several times higher than that used in the current work. However, the simulation of evolution of the initially homogeneous spectrum resulted in the strictly discrete spectrum similar to that in Fig. 12.15. Authors of the paper cited above preferred to explain this effect by the appearance of ‘mesoscopic turbulence,’ which is certainly not an explanation. It should be noted that the discretization effect can be visible in the 2-D Fourier wave number space, while this effect manifests itself much weaker in single-point low-resolution frequency spectrum.

Another hypothesis of the wave spectrum tendency for discretization is based on consideration of a convergence problem. Actually, nonlinear interactions occur in the orbital velocity field. A change of the spectral resolution results in the modification of the statistical characteristics of elevation and velocity fields. It is quite obvious that with increase of the spectral resolution (provided that the total energy conservation is strictly valid), the statistical properties of velocity and elevation fields cannot formally come to any reasonable limit. It means that the physical mechanism that prevents homogenization of spectrum does exist. Probably, the modes with very close wave numbers cannot exist independently; hence, wave spectrum consists of finite number of nonlinear modes rather than infinite number of linear modes (see also Babanin et al. 2014). In other words, wave field probably has a ‘corpuscular nature.’ This can be an actual cause of the ‘Manhattan-like’ shape of the 2-D spectrum in Fig. 12.15.

It is interesting to note that the locations of peaks in spectrum are not fixed; peaks can slowly migrate in the Fourier space. This effect is illustrated in Fig. 12.16 where a temporal evolution of amplitudes of 25 modes in the vicinity of the initial peak  $(k_x, k_y) = (64, 0)$  is represented. The curve seems thick because of high-frequency fluctuations. Probably, these fluctuations are caused by fast exchange between the potential and kinetic energies for each single mode visible in Fig. 12.13 (top panel). Such fluctuations were also observed in the calculations with the exact 1-D conformal model (see Fig. 6.13). As shown, each mode in the process of evolution changes its location quasi-periodically up to several times. The total change of amplitudes over the entire period reflects the downshifting process.

Looking at the details of the consequent spectra, it is possible to see that each peak undergoes quasi-periodic fluctuations. The data on the spectrum evolution are used for the calculations of the nonlinear spectrum transformation rate  $N$

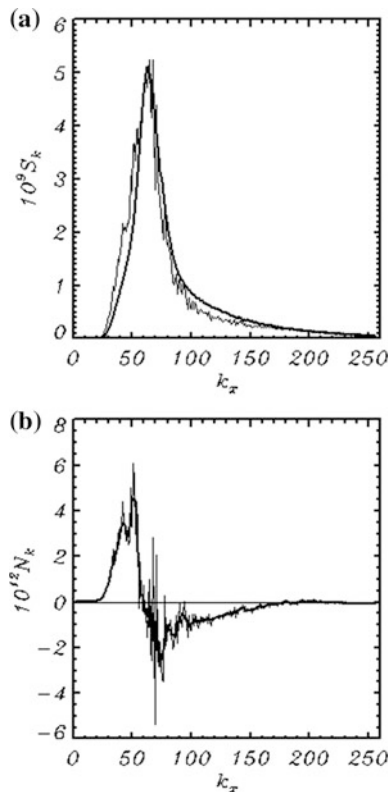
**Fig. 12.16** Time evolution of 25 Fourier amplitudes in the vicinity of the initial wave peak (Chalikov et al. 2014 © 2014 Springer-Verlag Berlin Heidelberg. With permission of Springer)



$$\frac{\Delta S_{k,l}}{\Delta t} = N_{k,l}, \quad (12.6.9)$$

where  $\Delta S_{k,l}$  is changing of the spectral density over time  $\Delta t$ , while  $N_{k,l}$  is the average rate of evolution of the spectral density due to nonlinear interactions. In Fig. 12.17, the spectrum  $\bar{N}_k^l$  integrated over the lateral wave numbers  $k_y$  is shown

**Fig. 12.17** **a** Wave spectrum integrated over lateral wave numbers  $k_y$ . Thick line shows the initial wave spectrum, and thin line shows the final wave spectrum obtained by 318th wave period. **b** Thin curve represents spectrum of a nonlinear interaction rate integrated over lateral wave numbers  $k_y$  [see Eq. (12.6.9)], and thick curve shows the same but smoothed spectrum (Chalikov et al. 2014 © 2014 Springer-Verlag Berlin Heidelberg. With permission of Springer)



(slightly smoothed over the  $k_y$  wave numbers). As shown, the shape of  $\bar{N}_k^l$  is qualitatively similar to the results of the calculations based on the Hasselmann integral. The energy at the front slope of spectrum increases, while the energy at the back slope of spectrum decreases, thus providing downshifting. Unfortunately, all the available schemes for the Hasselmann integral calculations do not allow us to perform any calculations for such a high resolution used in the present work. Note that the Hasselmann integral will probably never be checked by direct simulations, since the numerical models with low resolution are not exact, while high-resolution calculations of Hasselmann integral are impossible due to the fast growth of complexity of the algorithm with increase of resolution.

## 12.7 Ensemble Modeling of 3-D Waves

The instability of wave spectrum as well as its sensitivity to the details of the initial conditions is not the desirable, though, expected properties of the wave motion. Evidently, for obtaining stable results, it is necessary to perform multiple simulations of wave field evolution for the same initial wave spectrum, though for different sets of random wave phases. Such calculation is convenient to perform using multiprocessor computer (see Sanina 2014).

The non-uniformity of wave spectrum is convenient to estimate with parameter  $\Sigma$

$$\Sigma = \overline{\sum_{k,l} S_{k,l}^{-1} (\Delta S_{k,l}^2)^{1/2}} \quad (12.7.1)$$

which characterizes the ratio of the local dispersion of spectrum  $(\Delta S_{k,l}^2)^{1/2}$  (calculated over 4 adjacent points) and the central value of spectrum  $S_{k,l}$  averaged over the entire spectrum. When the spectrum is smooth, the value of  $\Sigma$  is small, and  $\Sigma$  approaches 1 when the local differences are of the order of the local values of spectrum.

Evolution of  $\Sigma$  calculated for 50 runs is shown in Fig. 12.18.

The initial spectra for all the runs were identical, but the wave fields were assigned with different random sets of phases. As shown, the rates of  $J$  growth in different runs were close to each other, while  $\Sigma$  increases from  $\Sigma = 0.1$  up to  $\Sigma = 0.48 - 0.55$  and preserves the tendency for further growth. Such high values of  $\Sigma$  indicate that the patchiness of spectrum is a typical phenomenon of a simulated wave field. The data obtained in different runs allow us to compare the spectra calculated with the use of the model to the end of each run at 94th peak wave period. The results of such comparison are given in Fig. 12.19.

Gray curves correspond to different runs, while solid curve corresponds to the averaged over ensemble spectrum, and dashed curves correspond to dispersion. As shown, the difference between the spectra is very large, which means that the

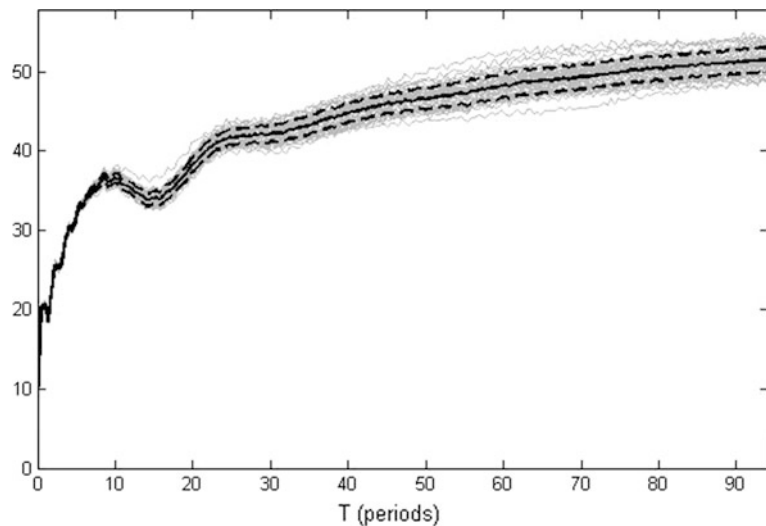


**Fig. 12.18** Temporal evolution of ‘patchiness’ index (Eq. 12.7.1). *Thin curves* correspond to the data obtained in parallel runs, *thick curve* shows the averaged over ensemble data, and *dashed curves* characterize dispersion of the data (Chalikov et al. 2014 © 2014 Springer-Verlag Berlin Heidelberg. With permission of Springer)

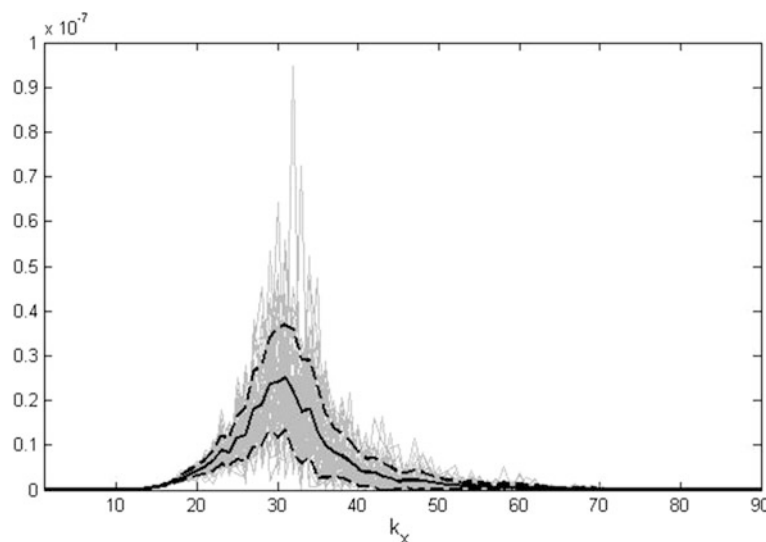
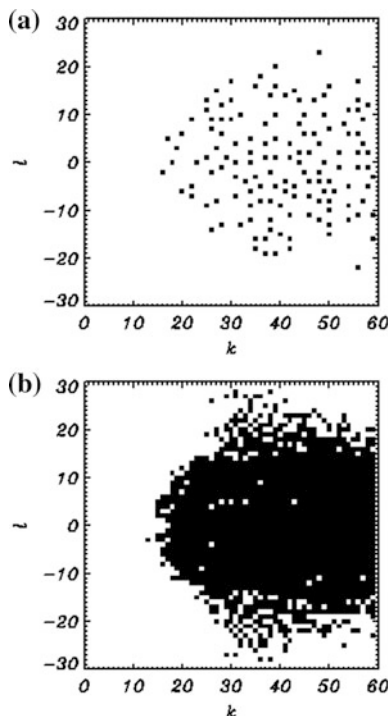


**Fig. 12.19** The wave spectra obtained by 94th peak wave period corresponding to the runs starting from the same wave spectrum but with a different random set of initial phases. *Thick curve* corresponds to the spectrum averaged over ensemble; *dashed curve* characterizes dispersion of the data (Chalikov et al. 2014 © 2014 Springer-Verlag Berlin Heidelberg. With permission of Springer)

evolution of spectrum depends on a set of the initial phases. The locations of peaks and holes are different in different runs. It is proved by Fig. 12.20 where in the top panel, the positions of local maxima in wave spectrum are shown. The local maxima are defined as the points where the value of spectrum exceeds the values in all eight surrounding points. To make the plot clearer, only the points where the spectral density in the central point exceeds  $0.01S_p$  ( $S_p$  is the peak spectral density) are included. The data in the top panel refer to a single spectrum, and the data in the bottom panel include the points for all of the 50 spectra. As shown, the points in the bottom panel are distributed over the wave number space more or less evenly. Note that the maxima can change their location also during a single long integration, but this process is very slow; i.e., the uniformity shown in the bottom panel of Fig. 12.20 can be probably reached only over thousands of peak wave periods. These results completely disregard the idea that peaks and holes can be explained by the resonance mechanisms.

The results of the calculations with the current model are interesting to compare with the results obtained with 3-D MNLS model (Dysthe et al. 2003) where the evolution of a narrow bandwidth spectrum assigned by the Gaussian distribution in the 2-D Fourier space was calculated using the nonlinear 2-D Dysthe equation (Dysthe 1979). The initial conditions for spectrum were assigned according to Eq. 7 in the work cited; i.e., the width of spectrum was 0.2 and the steepness was 0.1. The

**Fig. 12.20** Top panel shows positions of local maxima in a single spectrum. Bottom panel shows position of maxima in 50 parallel runs (Chalikov et al. 2014 © 2014 Springer-Verlag Berlin Heidelberg. With permission of Springer)



number of modes along  $x$ - and  $y$ -axes was equal to 128, and the total number of the Fourier modes was 66,049, while the number of grid points was 262,144. The first runs were done when a maximum of spectrum was initially located at  $k_p = 64, l_p = 0$ , but in this case, the spectrum showed unrealistic behavior at high wave numbers, since the energy was suppressed by dumping (12.6.1)–(12.6.3) introduced to support stability. In the next runs, a maximum of the spectrum was shifted to position  $k_p = 32, l_p = 0$ . Like in the work cited above, the results are obtained by averaging over ensemble of 20 runs for various sets of the initial random phase distribution. The spectrum simulated with our model is compared with the spectrum obtained with the Dysthe's model in Fig. 12.21.

As shown, both of the models identically reproduce the angle widening of spectrum. The asymmetry of this evolution can be explained by different wave steepness in high-frequency and low-frequency parts of spectrum; i.e., the root-mean-square steepness of the initial wave field is equal to 0.073, while the steepness formed by the modes with wave numbers  $k \leq k_p$  is equal to 0.042, and the steepness formed by the modes with wave numbers  $k \geq k_p$  is equal to 0.063. Crowding of contours at panel *a* in Fig. 12.21 can be probably explained by using filter outside the domain:

$$\left(\frac{k - k_p}{k_p}\right)^2 + \left(\frac{l}{k_p}\right)^2 = 1, k > k_p. \quad (12.7.1)$$

A qualitatively similar effect was observed in our calculations with  $k_p = 64$ . We found that the location of spectrum at  $k_p = 32$  provided room for smooth developing of spectrum toward high wave numbers. Hence, the computational domain in panel *b* has the size  $4 \times 4$ , while in panel *a*, it is  $2 \times 2$ . The spectrum obtained in Dysthe et al. shows downshifting. The same effect was obtained in our calculations.

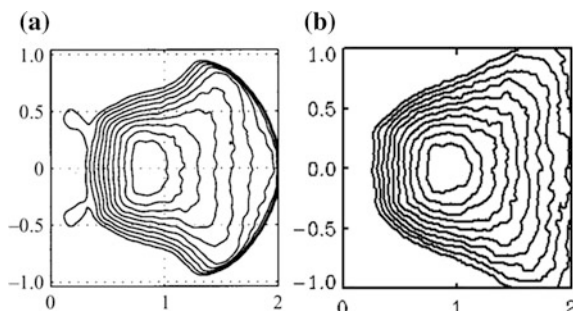


**Fig. 12.21** The wave spectrum  $\log_{10} S$  in coordinates  $(k/k_p, l/k_p)$ . Panel **a** represents the calculations of Dysthe et al. (2003) obtained after integration for  $T_p = 95$  wave peak periods, panel **b** calculation with model (11)–(13) obtained after integration for  $T_p = 67$ . Both spectra are normalized by their maximum value (Chalikov et al. 2014 © 2014 Springer-Verlag Berlin Heidelberg. With permission of Springer)

The low-energy ‘horns’ in a low-wave number part of spectrum  $b$  (Fig. 12.20) were not reproduced in the current calculations, but they were clearly pronounced in the calculations with higher accuracy (Sanina 2014). In general, it can be concluded that our results are in a reasonable qualitative agreement with the results of Dysthe et al. (2003).

## 12.8 Comparison of Linear and Nonlinear Extreme Wave Statistics

The most popular theory suggested for explanation of the freak wave phenomenon is the ‘*modulational instability theory*’ originally known as ‘*Benjamin–Feir (B.–F.) instability theory*’ (Benjamin and Feir 1967). The concept of this theory is quite transparent; i.e., the one-dimensional nonlinear wave in the presence of certain disturbances can produce additional modes arising in the vicinity of the main mode. Roughly speaking, the B.–F. theory explains redistribution of wave energy in the frequency (wave number) space up to the final homogenization of the initially discrete spectrum (Chalikov 2007). Most scientists believe that this mechanism can explain an abnormal growth of one wave mode. In case of broad spectrum typical for the wind-generated waves, such explanation is difficult to accept. First of all, it is unclear why one mode enjoys such preference and why this mode preserves its individuality in the course of its long development in a wave field with random phases. The original B.–F. results, as well as the numerical investigations of B.–F. (Chalikov 2007), showed that the period of new mode growth for typical sea wave steepness exceeds hundreds or thousands of carrying wave periods. Thus, freak wave should undergo a long course of development. Why do not interactions with other waves stop this growth, as if other waves do not exist?

The modulation instability theory of freak waves operates with such a poorly defined measure as the so-called Benjamin–Feir Index (BFI) parameter calculated as a ratio of the wave steepness  $AK_p$  ( $A$  is wave amplitude at spectral peak, and  $K_p$  is its wave number, both being dimensional), to the spectral bandwidth  $\Delta K/K_p$ ,  $\Delta K$  being the measure of width of the spectrum estimated as half-width at the half-maximum of spectrum (Onorato et al. 2009a,b). Actually, amplitude  $A$  at spectral peak essentially depends on the spectral resolution. The value of ‘width’ of spectrum is also uncertain since wave spectrum normally embraces a wide range of frequencies, so the value of BFI finally depends on somewhat arbitrary definitions.

Spectral analysis seems to be effective when it describes more or less uniform process like quadruplet interactions or energy input to waves, while it is rather pointless when applied to the analysis of extremely rare events represented by single- or multi-peak disturbances of the vast wave field. Such disturbances are evidently created locally in physical space, while they cannot manifest themselves in the wave spectrum which characterizes a large area.

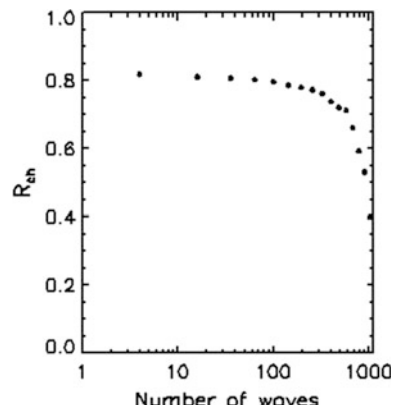
The role of ensemble size in relationship of kurtosis and extreme wave was investigated with the new exact model of potential waves. The initial conditions were assigned similar to those used in Sect. 12.5. Amplitudes of waves with random phases were calculated with the JONSWAP spectrum for the angle distribution proportional to  $(\operatorname{sech}(\theta))^4$ . Peak of spectrum was placed at wave number  $\mathbf{k} = (32, 10)$ . By now, the calculations have been done for about 100 periods of peak wave. The results recorded allowed to calculate dependence of the correlation coefficient of the highest wave in domain and kurtosis calculated for the same domain for different sizes of 2-D domains (expressed in squared length of peak wave). 990 wave surfaces containing  $512 \times 512$  knots were used for calculations of correlations. This dependence is shown in Fig. 12.22.

As shown, for the smallest domain the size of which is equal to 1/256 of the entire domain, the correlation coefficient is about 0.8. The coefficient decreases down to 0.4 with increase of domain size up to 1/4 of the entire domain. Obviously, with further increase of the domain size, the connection between kurtosis and the highest wave becomes insignificant. It proves that a clear relationship between kurtosis and extreme wave for the same ensemble disappears with ensemble extension.

No detailed data on time/space development of large waves are available; however, the results of the 2-D and 3-D mathematical modeling based on full equations show that the process of ‘freaking’ is very fast, while life of extreme waves is short. Such data do not prove an importance of the modulational instability theory for the explanation of the freak wave phenomenon. The aim of this chapter is to demonstrate new views on the freak wave problem.

The results presented below are obtained with the two-dimensional (2-D) and three-dimensional (3-D) wave models. Both models were used in a quasi-adiabatic mode. It means that a small output of energy due to the flux of energy to the subgrid domain is compensated by the input energy which is proportional to wave spectrum. Below, the non-dimensional variables are used.

**Fig. 12.22** Correlation coefficient between height of largest wave in ensemble and number of waves in ensemble (Chalikov et al. 2014 © 2014 Springer-Verlag Berlin Heidelberg. With permission of Springer)



The initial conditions in the models were assigned as a superposition of linear modes with random phases and amplitudes corresponding to the Pierson and Moskowitz (1964) spectrum. In the 3-D model, a symmetric directional distribution was assigned for the energy-containing part of the spectrum proportional to  $\cosh^n(\theta)$  where  $n = 4$  was taken. The fields of surface elevation with time interval of  $\delta t = 1$  were recorded.

The analysis of the results was done in terms of the non-dimensional trough-to-crest wave height  $H_{tc}$ . The value  $H_{tc}$  was defined as a difference between the maximum  $H_{\max}$  and minimum  $H_{\min}$  values of elevation normalized by the significant wave height:

$$H_{tc} = H_s^{-1}(H_{\max} - H_{\min}) \quad (12.8.1)$$

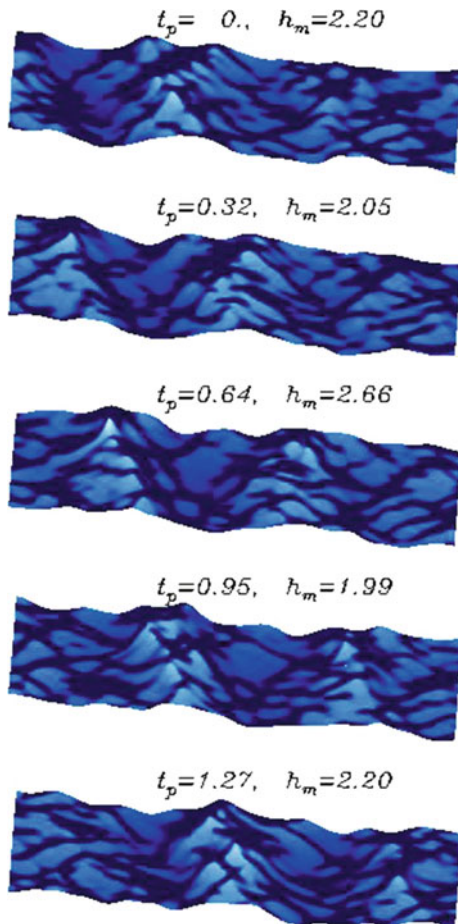
in the window with the size of  $1.5L_p \times 1.5L_p$  where  $L_p = 2\pi/k_p$  is non-dimensional peak wavelength. In 1-D case, the window turns into a linear segment. The window was moved discreetly in both directions by  $0.5L_p$  step. Such window parameters were chosen in order to take into account all the range of possible values of  $0 \leq H_{tc}$ . Actually, 99 % of  $H_{tc}$  exceeds 1. The shift was equal to  $0.5L_p$ ; however, just few values of  $H_{tc}$  were sometimes taken more than once; anyway, it does not influence the statistics.

Such type of processing needs some explanation. Actually, we do not see any other ways to construct true ensemble of  $H_{tc}$  values; however, there is a substantial difference between 1-D and 2-D cases. In 1-D case, the maximum and minimum of elevation fall on the same direction. In 2-D case, these values can fall on different y-positions. That can be the main reason why the probability of large waves in 1-D case is normally lower than that in 2-D case. Naturally, with narrowing of spectrum (i.e., at increase of power  $n$ ), the 2-D distribution should approach the 1-D distribution.

The probability of  $H_{tc}$  wave height in 2-D case can also be calculated with a unidirected algorithm, when each vector of elevations along  $x$  is processed as a result of the unidirected modeling. In this case, the maximum and the nearest minimum of elevation coincide with a general direction of wave propagation. Note, however, that the 2-D algorithm (based on square window) appears to be more practical.

A typical example of freak wave appearance is given in Fig. 12.23 where five consequent surfaces in a small fragment of the simulated domain are shown. The surfaces are reproduced through the interval of  $0.32t_p$  ( $t_p \approx 1.57$  is the period of one peak wave period varies in the range of  $1.90 < H_{tc} < 2.66$  (value  $H_{tc} = 2.66$  is the top value obtained in these simulations). In general, the shape of surface changes for such a short period significantly. The evolution of surface in Fig. 12.23 looks rather like an effect of dispersing superposition of different modes than appearance of modulation instability.

**Fig. 12.23** Example of a short-term evolution of elevation. The same fragment of the surface is given for a different moments, separated by the interval  $0.32t_p$ . The largest normalized trough-to-crest wave height in the fragment is indicated (Chalikov et al. 2014 © 2014 Springer-Verlag Berlin Heidelberg. With permission of Springer)



The ‘history’ of extreme waves in domain  $0 < y < 2$  for the period  $600 < t < 640$  is shown in Fig. 12.24 where the locations of large trough-to-crest waves (independent of their  $x$ -locations) are indicated: Blue dots correspond to the values of  $H_{tc} > 1.7$ , while red dots correspond to the values of  $H_{tc} > 2$ . As shown, the dots are concentrated in groups, thus proving their belonging to the same physical object. Many of the groups start with the blue dots and end also with the blue dots, while in the middle of the groups, red dots indicate freak waves. What is remarkable is that all these groups are short. Freak waves seem to arise suddenly with no prehistory, which also looks like as effect of superposition.

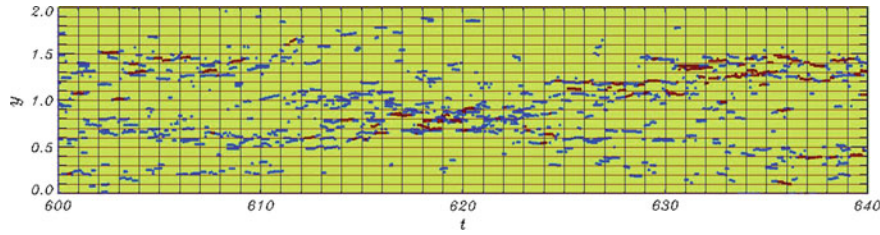


**Fig. 12.24** History of extreme wave appearance in coordinates  $(t, y)$  for the period  $600 < t < 640$  and the strip  $0 < y < 2$ . Blue points correspond to the values  $1.7 < H_{lc} < 2$ , and red points correspond to the values  $H_{lc} > 2$  (Chalikov et al. 2014 © 2014 Springer-Verlag Berlin Heidelberg. With permission of Springer)

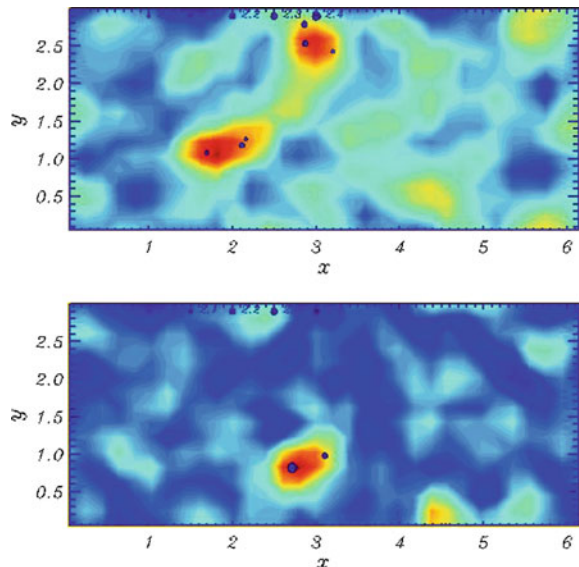
Let us consider local characteristics of wave fields, i.e., the steepness averaged over squared domain size  $1.5L_p \times 1.5L_p$  ‘jumping’ with the step  $0.5L_p$

$$\sigma = \left( (1.5L_p)^{-2} \sum_x \sum_y \eta_x^2 \right)^{1/2} \quad (12.8.2)$$

Examples of the instantaneous field of rms steepness calculated in this moving window are given in Fig. 12.25.

The upper panel refers to the data generated by the 3-D nonlinear model, while the bottom panel represents the data generated as a random superposition of linear waves.

**Fig. 12.25** Examples of the instantaneous field of rms steepness calculated in a moving window (see description of window in the text). The *upper panel* refers to the data generated by 3-D nonlinear model; the *bottom panel* represents the data generated as a random superposition of linear waves. The size of spots characterizes the height of freak waves (see legend) (Chalikov et al. 2014 © 2014 Springer-Verlag Berlin Heidelberg. With permission of Springer)



$$\eta = \sum_k \sum_l a_{k,l} \cos(kx + ly + \phi_{k,l}), \quad (12.8.3)$$

where  $k$  and  $l$  are wave numbers along the axes  $x$  and  $y$ , and  $0 < \varphi_{k,l} < \pi$  is a random phase; amplitudes  $a_{k,l}$  are calculated as follows:

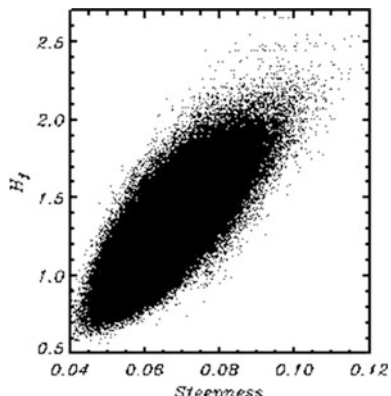
$$a_{k,l} = (2S_{k,l}\Delta k\Delta l)^{1/2} \quad (12.8.4)$$

( $\Delta k = \Delta l = 1$ ), and  $S_{k,l}$  is the energy density spectrum.

Different sizes of dots in Fig. 12.25 characterize height of freak wave. The field shown in the bottom panel of Fig. 12.25 looks like a typical member of the entire ensemble. Note that generating the fields with nonlinear models took about two months, while the same size of the ensemble of the fields calculated as a superposition of linear waves was generated for just 30 min. It can be expected that the wave fields obtained in such a different manner should be different as well. In particular, we expected that the averaged over window wave steepness of a random superposition of linear modes should be more or less uniform. To our surprise, the pictures and animations generated for both cases demonstrated very similar features; i.e., the more or less uniform fields always contained small areas with the highly increased steepness. The locations of freak waves (marked as black dots in Fig. 12.25) always fell into these areas. It is difficult to understand what primary cause of such collocations is as follows: Either freak waves themselves increase local steepness or the increased local steepness is followed by the appearance of freak waves (the ‘chicken-and-egg’ dilemma). Anyway, it is quite evident that the local steepness and height of an extreme wave in the window are connected with each other.

This connection is demonstrated in Fig. 12.26 where the extreme trough-to-crest wave height is plotted as a function of the local steepness. Note that the high-order moments, such as skewness and kurtosis, should demonstrate a much closer connection with the extreme wave height than steepness does. Of course, all these characteristics cannot serve as predictors of freak waves (see Janssen 2003), as well

**Fig. 12.26** The rms steepness of elevation calculated over the moving windows (see description of window in the text) versus  $H_{tc}$  found in that window (Chalikov et al. 2014 © 2014 Springer-Verlag Berlin Heidelberg. With permission of Springer)



as freak waves are not predictors for high-order moments. The connection between the high-order moments and wave height is essentially local, which restricts applicability of spectral analysis for the freak wave's phenomenon (see Fig. 12.22). The transient nature of freak waves demonstrated in Fig. 12.24 is well seen in the animations constructed from the pictures similar to Fig. 12.25. Both of the series demonstrate a very similar behavior.

The transitory character of extreme wave life can be also proved by Lagrangian tracing of the wave height represented in Fig. 12.27.

The more or less random choice of freak wave events demonstrates that freak wave develops rapidly and lasts approximately one peak wave period. Such behavior cannot be explained by the modulation instability theory; it looks rather like manifestation of a linear superposition of modes with different wave numbers and amplitudes.

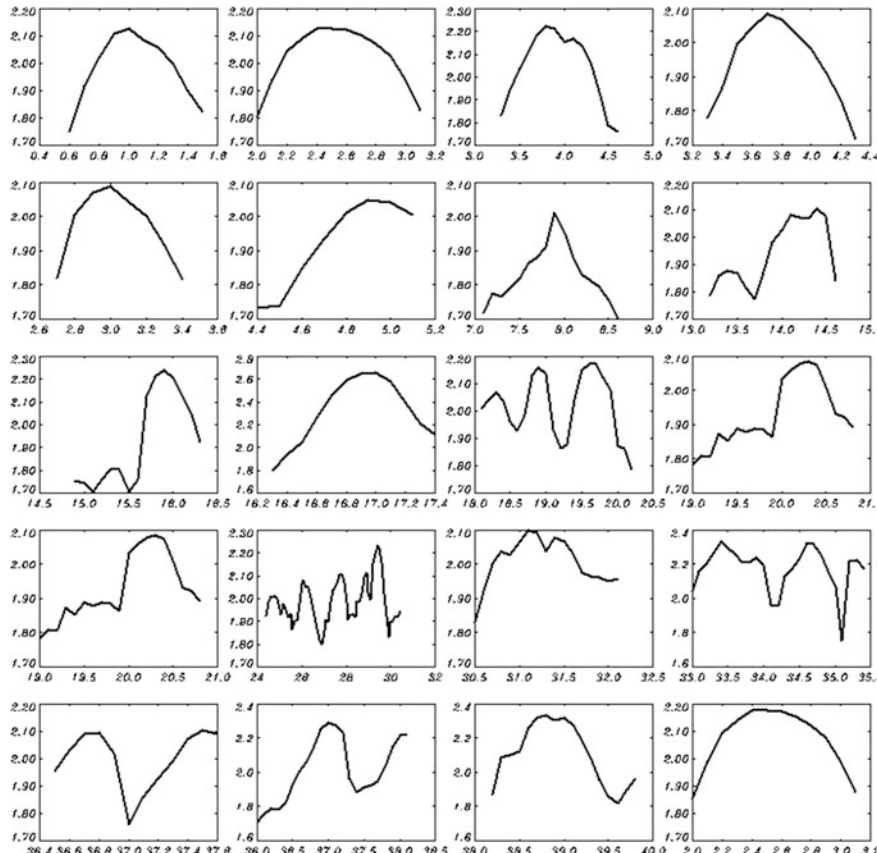


**Fig. 12.27** Lagrangian evolution of trough-to-crest height  $H_{lc}$ . The horizontal line indicates value  $H_{lc} = 2$  (Chalikov et al. 2014 © 2014 Springer-Verlag Berlin Heidelberg. With permission of Springer)

The most convincing demonstration of the linear nature of extreme waves is given in Figs. 12.28 and 12.29 showing integral probability of the trough-to-crest height  $H_{tc}$  of waves.

In Fig. 12.28, curves 1 and 3 are calculated using the results of the numerical simulation with the 3-D model (runs 1 and 3 refer to different resolutions); curves 2 and 4 are calculated over the same size ensembles of the fields composed as a superposition of linear waves. Surprisingly, linear calculations give the same high values of large trough-to-crest heights. Despite the fact that the data on the extremely high waves ( $H_{tc} > 2.5$ ) are not stable, they do not allow us to state that the probability of rare events is clearly different in all the cases considered. Note that the probability of  $H_{tc}$  shown in Fig. 12.28 is considerably larger than that obtained with 1-D models (see, e.g., Fig. 7.16). It can be explained by a more general definition of freak waves in 2-D case.

One-dimensional treatment of  $H_{tc}$  (when square matrix turns into 1-D vector directed along the wave propagation) gives the probability smaller by more than one decimal order as compared to the previous algorithm. Remarkably, the probability obtained over the similar ensemble of linear fields actually coincides with the nonlinear results (curves 5 and 6 in Fig. 12.28). Curve 7 represents the Raley distribution calculated by the following relation:

$$R = \exp\left(-\frac{(H_{tc} - \bar{H}_{tc})^2}{2\sigma_{tc}^2}\right), \quad (12.8.5)$$

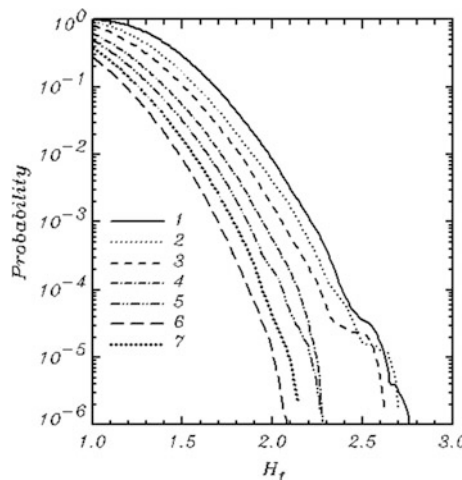


**Fig. 12.28** Integral probability of trough-to-crest height  $H_{tc}$ . (1, 2) resolution  $256 \times 128$ ; (3, 4) resolution  $512 \times 128$ ; (1, 3) full 3-D nonlinear model; (2, 4) 2-D superposition of linear modes; (5, 6) 1-D treatment of  $H_{tc}$ ; (5) full nonlinear 3-D model; (6) superposition of 2-D linear modes; (7) Raley distribution (Chalikov et al. 2014 © 2014 Springer-Verlag Berlin Heidelberg. With permission of Springer)

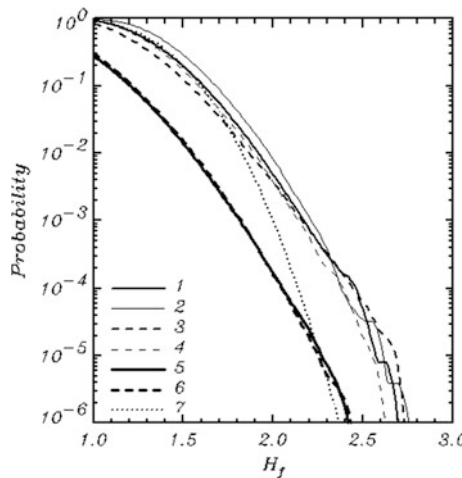


**Fig. 12.29** Integral probability of trough-to-crest height  $H_{tc}$  for different angular spreadings: (1)  $P = 4$ ; (2)  $P = 8$ ; (3)  $P = 16$ ; (4)  $P = 64$ ; (5)  $P = 256$ ; (6) 1-D full nonlinear model; (7) superposition of 1-D linear modes (Chalikov et al. 2014 © 2014 Springer-Verlag Berlin Heidelberg. With permission of Springer)

where  $\bar{H}_{tc} = 1.31$  and  $\sigma_{tc} = 0.22$  are the mean value and variance of  $H_{tc}$  obtained by averaging over the data used for calculation of the probabilities 1, 2, 3, and 4, as described above.

The effect of window narrowing in  $y$ -direction is quite similar to narrowing of wave spectrum (i.e., increasing  $n$ ). Such effect is demonstrated in Fig. 12.29 where the curves calculated for different values of  $n$  are represented. Curve 1 is the same as the curve 1 in Fig. 12.28. As shown, with narrowing of spectrum, the probability converges to that obtained with the 1-D model and the corresponding ensemble of 1-D linear surfaces.

## 12.9 Conclusions

In this paper, a straightforward method of numerical solution of the three-dimensional potential wave equations is suggested. The method uses the surface-following coordinate system. In the new coordinates, the kinematic and dynamic conditions on surface become more complicated, but if we consider them as the evolutionary equations for surface potential and elevation, we come to the conclusion that these conditions can be easily integrated in the same way as similar as one-dimensional equations in the conformal coordinates. However, calculations of vertical derivative of the potential on the surface become more complicated, since the Laplace equation for 3-D velocity potential turns into elliptic equation that should be solved at every time step, which requires the use of extensive computer resources. However, it should be noted that this problem is still a lot simpler than; for example, standard integration

of 3-D Navier–Stokes equations (or LES equations) in the curvilinear coordinates when a problem of solving the elliptic equation for pressure arises.

The potential wave problem gives a unique opportunity for validation of full nonlinear model in comparison with the exact stationary solution obtained in a moving coordinate system. This solution is obtained with a completely different algorithm; hence, such validation can be considered as full, non-trivial, and exact. Since the model uses finite-difference approximation in the vertical direction, we cannot expect a perfect agreement between the exact and approximate solutions, though the results of such comparison are quite convincing. The structure of Stokes wave was supported within a long interval of integration. If the numerical scheme was not accurate enough, the evolution of modes would exhibit chaotic behavior and the Stokes wave would quickly disintegrate due to the numerical instability. Such evolution was observed many times in the course of development of codes. The scheme is consistent, since with increase of resolution, its accuracy increases. Note that a highly efficient method by Clamond and Grue (2001) has been generalized for 3-D finite variable water depth by Fructus and Grue (2007). Currently, we investigate the possibility of application of the model for the finite depth problem. Such idea is based on presentation of the analytic component of surface potential in the following form:

$$\bar{\Phi}(\xi, \vartheta, \zeta) = \sum_{k,l} \bar{\phi}_{k,l} \frac{\cos(|k|(\zeta + H))}{\cos(|k|H)} \Theta_{k,l}, \quad (12.9.1)$$

where  $H$  is depth. Because the nonlinear component of the velocity potential attenuates with depth faster than the analytical one, the scheme of solution remains essentially the same.

The model was used here for simulation of evolution of a steep Stokes wave train with the superimposed initial noise. In case of directional wave fields, it was shown that evolution of wave field occurs in a different way, as compared to that of a unidirectional case; i.e., the new developing modes are oblique toward propagation of a carrier wave.

The most disappointing and unexpected property of the wave model is that the results depend essentially on the initial set of phases; hence, the most reliable results can be obtained using ensemble modeling. Such simulation can be effectively done in parallel processors. It is not excluded that the stable and smooth results can be obtained by introducing local viscosity in the Fourier space. Currently, it is unclear in what way this property can be brought into correlation with the natural process. However, we came to the conclusion that the primary physical variables are rather the fields of velocity (in the potential assumption, it is the velocity potential) and elevation. The Fourier modes are the result of formal presentation of wave fields, while they do not necessarily present real objects.

The numerical experiments are performed under quasi-adiabatic conditions. However, the model is designed for investigation of the nonlinear mechanics of two-dimensional surface waves, particularly, for investigation of extreme waves. After implementation of the energy input scheme and wave-breaking parameterization,

the model can be used for direct simulations of two-dimensional wave field evolution under the action of wind, nonlinear interactions, and dissipation.

All of the numerical results presented in the current work were obtained using a standard one-processor Dell computer with speed of 3.00 GHz. Since the model is based on the Fourier transform method, the parallel version of the model does not provide many advantages, while parallel processors are convenient to simultaneously run many versions of the same model, as well as to perform ensemble modeling.

Definition of freak wave is based on the concept of the trough-to-crest wave height, which is reasonable from the practical point of view. A natural wave field usually looks quite chaotic as a superposition of many dispersing modes which, in addition, are not conservative due to the fast reversible interactions. In our opinion, the only reasonable way to detect the instantaneous value of the trough-to-crest height is the detection of maximum difference of elevations in the prescribed window. Since freak waves should be most likely associated with the spectral peak, it would be reasonable to choose the window with the size of the order of peak wave length  $L_p$  and even somewhat bigger than that—for the elimination of uncertainty of real wave length. Our experience shows that the size of domain should be of the order of  $1.5L_p$ . In this case, we do not take into account all possible extremes (because the maximum and minimum can sometimes be at a distance exceeding  $1.5L_p$ ), but the same structures can be taken twice. Such rare events happen sometimes; however, their influence on the statistics is quite insignificant.

In one-dimensional wave field, such a trough-to-crest height definition gives quite definite results. However, in a two-dimensional wave field, some uncertainty arises because the positions of maxima and minima can be shifted with respect to the direction of wave propagation. The simplest way to avoid uncertainty is to give a definition of the trough-to-crest height as the difference between the maximum and minimum along the direction coinciding with that of peak wave propagation. Such treatment of freak wave does not seem to be quite adequate, as the wave power depends on full range of elevation.

The main result of the current investigation is comparison of the extreme wave statistics generated by full nonlinear models, and the statistics obtained over the ensemble of surfaces generated as a superposition of linear modes. In both cases, the integral energy is the same, and the spectra of surfaces are similar. The results obtained in this study are as follows: (1) Freak wave is a transient phenomenon; it develops and disappears approximately over a peak wave period. (2) The wave fields generated as a superposition of linear modes with random phases show the properties very similar to those of the wave fields generated by 1-D and 3-D nonlinear models. (3) Both methods of generation demonstrate high probability of freak waves. (4) Integral probability of large waves for nonlinear and linear waves is roughly the same. (5) 2-D treatment of freak waves results in a significantly higher probability of freak waves as compared with 1-D treatment or 1-D nonlinear simulations. (6) Probability of freak waves decreases with narrowing of spectrum and approaches the probability obtained with 1-D models and 1-D superposition of linear modes.

# Afterword: What Has Been Done

The work on mathematical modeling of sea waves started in 1970s, when a model for investigation of wind–wave interaction was completed (Chalikov 1976, 1978). Actually, it was an attempt to construct a coupled windwave model, but the wave counterpart was able to generate only monochromatic linear waves. The following numerous papers (see review in Chalikov 1986) considered the structure of the wave boundary layer (WBL) above 1-D wave surface assigned as a superposition of linear waves with random phases and a prescribed empirical spectrum. That model of WBL, as well as its modifications, was quite imperfect. The real progress in numerical wave modeling was achieved in 1989 when conformal transformation of 1-D potential equation was first applied. The construction of the first conformal numerical model was greatly accelerated by collaboration with Dmitry Sheinin. The extended results of the wave dynamics simulation were first presented at the conference organized by V. Zakharov (Chalikov and Sheinin 1994). It is funny that the authors of that work did not know that conformal mapping had been already used in many previous works (see references in Chap. 1), and initially, this approach had been suggested in the classical publications by Stokes (1947, 1980). The main difference between our approach and the previous approaches was that we used the advantages of conformal mapping for the construction of a numerical model for non-stationary equations. The initial highly complicated equations were transformed into the system of 1-D equations which can be solved with the highest accuracy by Fourier transform method (Chap. 2). The model is an example of most exact model in the geophysical fluid dynamics designed for simulation of the real process.

Being inspired by unlimited possibilities of the new approach, author of this book began to apply the model for investigation of some intriguing problems of the nonlinear wave physics. Opposite to the pure theoretical approaches, the motivations for investigation were provided by observations of the numerical results as if they were the observational data obtained at sea. Some of the most important results of numerical investigations are summarized below.

Employment of developed modern technologies in modeling of the WBL was far behind other branches of the geophysical fluid mechanics. The numerical hydrodynamic modeling is similar to perfect laboratory modeling. Being free of the

restrictions arising from the scale difference, an accuracy of description of the natural processes in numerical simulation can be often much higher than that which can be achieved in physical simulation. Such situation is typical for other branches of the fluid dynamics, perhaps better developed, especially in technical applications. It was proved that numerical methods really do provide high-quality results which can be combined with those obtained from experiments. A good illustration of this statement is the experiments in wave channels. Very often experiments in the channels are devoted to the nonlinear transformation of waves, but investigators never know exactly the characteristics of waves they generate, because they are able to control only one fundamental variable, i.e., surface shape, while another variable, i.e., the velocity potential, remains unknown. The uncertainty greatly increases when multi-mode or angle-distributed wave fields are investigated. A relatively small size of wave channels makes impossible the investigation of nonlinear processes usually developing over large time and space scales. This is why wave channels only allow simulation of artificially strong interactions of waves with specifically chosen amplitudes and phases.

The exact and fast numerical methods for solution of stationary equations for gravity and gravity-capillary waves have been developed (Chap. 3). The algorithms turned out to be much more efficient than any algorithms suggested before. It should be noted that two separate algorithms for pure gravity and gravity-capillary waves were developed. In the latter case, our algorithm fails to converge when the non-dimensional capillarity coefficient becomes small. It was shown that with decrease of values of the capillary coefficient, the phase velocities of gravity-capillary waves decrease rather than approach the values of the Stokes phase velocity. It means that the equations with no surface tension terms are not a limit form of the equations for capillary-gravity waves in the same way as the Euler equations are not a limit form of Navier–Stokes equations while the viscosity is tending to zero.

While the properties of stationary solutions suggest a lot of intriguing problems, we used these results mainly as a tool for validation of non-stationary model (Sect. 4.1). We used a unique possibility to validate the non-stationary solution by comparison with the stationary solutions obtained in a moving with the phase velocity system of coordinates. It should be emphasized that the validation was far from trivial, as non-stationary modes are based on the equations much more complicated than the stationary ones, and on a numerical procedure of its own which ‘does not know’ that the simulated waves are supposed to be well preserved even for large amplitudes. It was shown that stationary solution remained unmodified during hundreds of periods. This suggests that Stokes and gravity-capillary waves are stable with respect to the truncation errors of non-stationary model, these errors being small enough.

We use non-stationary models for the case studies of evolution of nonlinear wave fields for different initial conditions assigned as a superposition of linear waves (Chap. 4). The most surprising feature of multi-mode wave fields was clear separation of the wavenumber–frequency spectra into regular curvilinear branches with most of the energy concentrated along what we call the ‘main branches.’

An effect of ‘bound waves’ is most clearly seen in the simulation designed to approximate the laboratory experiment by Yuen and Lake (1982). Special processing of the data shows that in some cases the number of recognizable branches can reach the value as large as 14.

For any single-value elevation field, it is possible to calculate the corresponding wave spectrum. The opposite procedure of restoration of the wave surface corresponding to wave spectrum is impossible, because information on the phases is missing. However, if we suggest that phases are a random function of wave number, the surface corresponding to spectrum can be calculated. There is no guarantee that the surface restored would have the same statistical characteristics (for example, high-order moments) as the initial surface, since distribution of phases is not random in reality. The situation becomes more uncertain if we consider spectrum as a sufficiently smooth function of wave number for presentation of the surface with higher resolution. Evidently, for denser spectrum amplitude of each mode will be less than the initial amplitude. It means that the results of calculation of nonlinear evolution of spectrum can depend on the spectral and space resolution. The simplest way to estimate this effect is simulation of interaction of the two modes assigned in the initial condition at adjacent wave numbers. Such calculations were done by Babanin et al (2014) (see Sect. 4.4). The results were quite unexpected. Initially, at wave number  $k = 1$  a new mode was generated due to nonlinear interactions. This mode started to interact with the initially assigned modes, which resulted in the formation of a more or less dense spectrum slowly moving toward the lower wave numbers, i.e., the downshifting has occurred. As a whole, this result should be considered as abnormal, since wavenumber  $k = 1$  characterizes the resolution of the model and nothing else. The modes infinitely close to each other can send energy to infinitely large scales; that is, the dissipation of energy is formed. It is unlikely that this mechanism of the ultra-long wave energy dissipation does exist in reality. Fortunately, it was found that such effect occurs only if the initial modes are very close to each other, this effect being absent at medium resolution. It allows suggesting existence of a limit resolution of spectrum. The use of higher resolution can lead to the generation of artifacts.

The effect considered can be completely attributed to the approximation problem, such as presentation of real surface as a superposition of the finite number of Fourier modes. The high resolution of spectrum as well as an insufficient resolution can lead to the unpredicted effects. Since the set of modes, their amplitudes, and phases depend completely on the resolution, it would be incorrect to consider these modes as real physical objects. Naturally, the nonlinear properties of each set of modes (for example, high-order moments) should be highly unstable with regard to the resolution. It is very unlikely that Hasselmann’s integral for the same spectrum converges to any reasonable limit with increase of resolution.

The problem of nonlinear interactions is closely connected with the stability of wave spectrum. In most investigations, it is assumed that wave field can be represented as a superposition of linear wave modes with random phases. We have already seen that this assumption is not correct, since wave field is rather a superposition of the main modes and their ‘bound waves,’ i.e., a superposition of

nonlinear modes. It is also interesting to check how stable the spectrum in a quasi-stationary regime is. Such calculations were done in Chalikov 2005 (see Chap. 6). Consideration of the timescales for a multi-mode wave field with the initially random phases shows that low-frequency waves preserve their individuality, but their ‘lifetime’ decreases with increase of the steepness. The total energy of each mode always fluctuates because of the quasi-periodic energy exchange between the wave components. For high frequencies, the lifetime is of the order of one period, and these disturbances cannot be attributed to waves, but rather to ‘wave turbulence.’ Applicability of 1-D approach and even the potential assumption is very questionable for high-frequency waves. According to the general opinion, this approach obviously cannot simulate the processes properly where irreversible 2-D nonlinear interactions are of essence. However, from the results of this work an important conclusion follows for 2-D waves as well. Naturally, all the nonlinear effects in a 2-D case should be pronounced clearer. These effects should appear in potential approximation, formally, because of an infinitely larger number of the interacting modes, and physically, because of a more complicated orbital velocity field.

The conformal model can be applied for a broad range of processes where the 1-D approximation is acceptable. However, many wave phenomena are largely controlled by strong nonlinear interactions which are relatively fast and for which the 1-D approximation is often adequate. The formation of extreme waves is one of such phenomena, and the model simulations of these waves are far from being of a purely academic interest. It has long been known that the nonlinear redistribution of energy is the characteristic of wave trains and may result in a sudden emergence of very large and steep waves commonly known as freak or rogue waves.

It is well known that in real wave field the dominant waves have more or less sharp crests and gentle troughs. Naturally, when the routine Fourier presentation is used, for approximation of such waves the additional modes are required which are sometimes called ‘bound waves.’ This unfortunate expression obscures the essence of the phenomenon, because real big waves are evidently rather single nonlinear modes which preserve their individuality for long time. For some unknown reasons, the shape of such waves is close to the Fourier modes in the ‘upper’ coordinate system. Naturally, these modes form an orthogonal basis in the ‘upper’ coordinate system and they are also orthogonal in the Cartesian coordinate system with the weights equal to inverse Jacobian of transformation to the ‘upper’ coordinate. It is remarkable that the Fourier expansion for stationary solutions for potential waves in the ‘upper’ coordinate system (Stokes waves) converges faster than in the Cartesian coordinate system. For real wave field with moderate steepness, the superposition of Fourier modes in the ‘upper’ coordinate is very close to that of the Stokes waves in the Cartesian coordinates. Probably, the fast convergence for Stokes solution for the potential waves in the upper coordinate makes good sense. The nonlinear transformation, somehow, ‘absorbs’ the nonlinearity, and the single mode in the upper coordinate (opposite to that in the usual coordinates) is a good approximation of the solution of strongly nonlinear equations. Derivation of equations in the ‘upper’ coordinates is tricky, because ‘there is no fluid.’ However, this idea does

not look completely crazy, because potential 2-D wave equations are essentially the ‘surface’ equations. Besides, these coordinates correspond to the case of a two-layer flow with the interface, if the density of upper liquid approaches zero. An additional important advantage of the ‘upper’ coordinate system is that the singularities of the interface can disappear or at least become much weaker.

In Chap. 6, we applied the method for numerical simulation of periodic surface waves, developed in ChSh, particularly, for a long-range simulation of the initially homogeneous Stokes wave train contaminated with small initial noise. It is shown that an initial development of the disturbances agrees with B.-F. instability theory up to the steepness  $AK = 0.1$ , and for the larger steepness with McLean (1982) results. The unstable modes are developing around each mode of Stokes waves but not around the main mode only, as it was predicted by B.-F. theory. The phase velocities of low wave number waves are difficult to calculate because of their low energy. In the energy-containing part of spectrum, the waves in a quasi-stationary regime strictly agree with the linear theory, but for larger wave numbers the phase velocity is systematically higher than that of the linear waves. It happens because the routine calculations of phase velocity give a weighted by energy value between the velocities of free and several bound modes. Calculations of the wave number-frequency spectrum prove that the dispersive relation consists of several branches. Each of them corresponds to a different order of bound waves. Wave surface can be represented by a set of Stokes waves much more accurately than by superposition of linear modes.

Harmonic waves are not the solution of exact equations of the potential wave theory. Hence, even in the absence of disturbances they undergo the complicated evolution creating discrete spectrum of non-stationary waves. On the average, this spectrum is close to the spectrum of Stokes wave. When the initial steepness becomes larger, the rate of development of such instability increases. Meanwhile, Stokes wave in the absence of disturbances remains stable up to the critical steepness. The B.-F. instability can occur due to the errors of approximation of time derivatives or as a result of insufficient resolution in grid space, or due to any details of the numerical scheme. Definitely, harmonic waves represent a good basis for the presentation of wave field, but it is unlikely that Fourier modes can be considered as real physical objects, since the set of their amplitudes and phases depends on the spectral resolution. The properties considered in Sect. 4.4 prove that calculation of nonlinear interactions of linear modes can sometimes give quite unpredictable results.

The results of numerical modeling of the multi-mode unidirected adiabatic wave evolution performed with use of precise 1-D fully nonlinear model are presented in Chap. 6. It is shown that due to nonlinear interaction the irreversible nonlinear interactions and downshifting develop. The rate of downshifting increases with increase of the nonlinearity. This conclusion contradicts the Hasselmann’s results based on the numerous simplifying assumptions. Presenting wave field as a superposition of linear modes with random phases and a fixed linear dispersion relation is the most restricting assumption. It was shown in the Benjamin and Feir investigation that keeping just the first Stokes ‘correction of harmonic wave resulted

in the developing of instability. Later it was demonstrated that assigning the non-linear modes was unnecessary: The initial 1-D harmonic waves took a Stokes-like shape due to quadratic interactions. Then, the B.-F. instability develops, and fully random wave field is generated at the nonlinear stage Chalikov (2005). Hence, the absence of 1-D interactions is inherent to the artificially linear waves only. It follows from the Hasselmann's integral that in a two-dimensional wave field all the interactions between the modes running in the same direction are missing. Evidently, the inaccuracies of the nonlinear interaction calculations with Hasselmann's integral grow with narrowing of spectrum. Our calculations prove that the unidirected wave interactions have probably the same intensity as those between two-dimensional waves. This effect is important for many practical problems, especially for the wave forecasting problem.

Extreme wind waves are a rare, though regular, phenomenon in the World Ocean. Such waves hold a huge destruction power. Navigation, sea technologies, in particular, oil and gas production, as well as the recreation industry persistently require investigation of the origin and physics of extreme waves as well as development of some technique for their forecasting.

The mechanical properties of extreme waves, their probability, and geographical distribution are still unknown, and no reliable prediction techniques still exist. The observational data on such waves are scratchy, and the laboratory experiments are difficult due to the extremely rare occurrence of such waves and short fetches. Since freak waves are an extraordinary phenomenon, it is unlikely that their statistics, mechanics, and the number of other quite delicate questions concerning the above problem can be investigated on the basis of various substitute equations.

For some reasons, the above techniques were not used before in the statistical investigations of wave processes. The pure spectral approaches used in wave prediction models for solution of the given problem are not suitable.

Extreme waves are as infrequent in computer simulations as in the ocean. This is why the investigation should cover a great number of the numerical experiments to be subjected to thorough analysis. The numerical approach is based on a 2-D ( $x-z$ ) model of potential waves and allows obtaining rich statistical material. According to the recent simulations of 3-D waves carried out in (Onorato et al. 2009; Dyachenko and Zakharov 2005), the probability of large waves increases for long-crested waves. It means that 2-D simulations are a limit case of such waves. However, large waves in a stormy sea are often long-crested, and the 2-D approach for investigating their statistics is hardly acceptable. This opinion is supported by the authors of WAM model (Janssen 2003), who implemented the 1-D analysis for experimental forecast of freak waves. However, there are no solid evidences that this scheme works. Note that the above authors never described the procedure of freak identification (see discussion of this problem in Chaps. 7 and 12).

The results of over four thousand numerical experiments are analyzed in Chap. 7 to investigate some properties of freak waves and calculate the probability of their appearance. Because of self-similarity of the governing equations, they can be used in a non-dimensional form; hence, the statistical results of long-term numerical simulations depend on the following initial conditions only: profiles of elevation

$\eta(x)$ , surface velocity potential  $\varphi(x)$ , and the set of initial phases. Considering the practical application of the theory of rare waves, we came to the conclusion that a strict ‘definition’ of freak waves in a non-dimensional form is not required at all. Instead, it makes sense to introduce categories of dimensional extreme waves, as it was done, for example, for classifications of hurricanes.

The shape of freak waves varies within a wide range: Some of them are sharp-crested; others are asymmetric, with a strong forward inclination. The investigations show that only breaking and large waves can be referred to freak waves. Some of them can be very big, but not steep enough to create dangerous conditions for vessels (but not for fixed objects). The initial concentration of energy can occur merely as a result of group effects, but in some cases the largest wave suddenly starts to grow. The growth is sometimes followed by strong concentration of the wave energy around the peak vertical. It is taking place in the course of a few peak wave periods.

The attempts have been undertaken to stratify wave statistics over some general integral characteristics, such as skewness, kurtosis, and the initial density of energy or the enhancing parameter for spectrum. At the first sight, the results of the above efforts turned out to be quite unexpected. In a broad range of the parameters for the wind wave spectrum, the integral probability of freak waves was found to be virtually independent of the spectrum shape.

We arrived to the conclusion that it would be naive to expect that the high-order moments such as skewness and kurtosis can serve as predictors for freak waves. Firstly, the above characteristics cannot be calculated using the spectrum usually determined with low accuracy. Such calculations are definitely unstable with regard to a slight perturbation of spectrum. Secondly, even if the spectrum is determined with high accuracy (for example, calculated using the exact model), the high-order moments cannot serve as predictors, since they change synchronically with variations of extreme wave heights. Freak waves occur simultaneously with increase of the local kurtosis; hence, kurtosis is simply a passive indicator of the same local geometrical properties of wave field. This effect disappears completely if spectrum is calculated over a very wide ensemble of waves (see Chap. 12). In this case, an existence of freak wave is just disguised by other waves, not the freak ones. It is quite evident that kurtosis is not the predictor but the extreme wave indicator representative for such a small area that it can be observed as easily as a freak wave itself. Freak wave is even better recognizable than kurtosis. Thirdly, all the high-order moments depend on the spectral presentation; i.e., they increase with increase of the spectral resolution and cut-frequency.

One researcher of freak waves criticizing our results, noted: ‘... the wave starts to grow, hence, increases its potential energy and this must come from somewhere’ (from private correspondence). The author of this book replied that probably the wave always appears as *a sinus* for this scientist. The process starts with an individual wave in physical space with no significant exchange of energy with surrounding waves. Sometimes, the crest-to-trough wave height can be as large as nearly three significant wave heights. On the average, only one-third of all simulated freak waves come to breaking, creating extreme conditions, however, if the

wave height approaches the value of three significant wave heights, all of the freak waves break. Evidently, this process cannot be investigated on the basis of purely spectral equations. The phenomenon of freak waves is a manifestation of innate properties of the nonlinear wave field, and they appear inevitably on condition that the time of observations or numerical simulations is long enough. The individual prediction of freak waves is impossible; however, the probability of their generation can be estimated.

Our investigations do not give any answer as to why freak waves occur. The problem is interesting, though it has very little practical application. It can be illustrated by an example from a much more developed branch of the numerical geophysical fluid dynamics, i.e., the large-scale atmospheric dynamics. It is well known that cyclones result from the instability of baroclinic waves on frontal surfaces. It is quite difficult to predict which of the numerous waves running over the frontal surface starts to grow and finally loses stability becoming a ‘freak’ baroclinic wave, breaking and turning into the cyclone. Until now the problem of cyclogenesis remains a semi-resolved problem of the numerical weather forecast. Nevertheless, the well-developed high-resolution atmospheric models predict climate probability of cyclogenesis with good accuracy.

The unexpected results concerning the freak waves statistics were obtained with three-dimensional model (see Sect. 12.8), which demonstrated that the freak wave appearance can be also explained by superposition of linear modes with realistic spectrum. The integral probability of trough-to-crest waves is calculated by two methods: The first one is based on the results of the numerical simulation of wave field evolution, performed with the one-dimensional and two-dimensional nonlinear models. The second method is based on calculation of the same probability over the ensembles of wave fields constructed as a superposition of linear waves with random phases and the spectrum similar to that used in nonlinear simulations. It is shown that the integral probabilities for nonlinear and linear cases are of the same order of values. It is not excluded that freak waves do not require a special theoretical explanation; i.e., their nature can be explained in a straightforward way just using geometrical considerations. We should state that such results undermine all the previous cumbersome investigations based on numerical modeling as well as the numerous attempts to construct special theories of freak waves. It is not excluded that the nature of freak waves might be much simpler than it was thought before. At present, we have to admit that such uncertainty still remains.

The results of numerical investigation of wave breaking in spectral environment on the basis of full equations are given in Chap. 8. Most of the investigations on breaking mechanism done before were based on consideration of the wave field consisting of few modes. The process in real rich spectral environment is quite different from the process in such oversimplified situation. In our investigation, the main attention is paid to the documentation of evolution of different characteristics before breaking. It is shown that breaking is a local process developing in the narrow intervals in physical space over very short periods. Not a single criterion such as wave steepness, wave height, and asymmetry can serve as predictor of the incipient breaking. The process of breaking is intermittent; it happens

spontaneously and is individually unpredicted. The breaking process develops in intervals which are much shorter than the dominant wave length. For spectral description of such modification, high-frequency (wave numbers) modes are required. However, in reality, the breaking decreases energy of large wave by changing its shape. In general, the spectral approach is not fully applicable for the analysis of individual-breaking cases which occur in physical space and cause unclear transformation of wave spectrum.

Evolution of the geometric, kinematic, and dynamic characteristics of a breaking wave describes the process of breaking itself rather than indicates the imminent breaking. It is shown that the criterion of breaking based on modulation instability is not universal, if applied to the conditions of spectral environment. More important is the development of algorithms for parameterization of breaking for wave prediction models and direct wave simulations. The prototype of such algorithm is developed on the basis of a diffusion-type highly selective operator. The examples of dissipation spectrum are given.

The effect of one-dimensional and two-dimensional focusing has been investigated numerically and experimentally by Johannessen and Swan (1997a, b, 2003). Another example of the same mechanism is investigated in the experimental work by Brown and Jensen (2001). The above-mentioned authors found that merging of wave crests with different wavenumbers gave the residual trough-to-crest height of combined wave that is considerably larger than it follows from their linear superposition. All the works devoted to the focusing so far can be referred to the case studies, i.e., when focusing occurs for the specifically selected configurations of wave modes. In the current work, our attention is given to the investigation of statistics of focusing in connection with wave breaking.

Thousands of exact short-term simulations of evolution of two superposed wave trains with different steepness and wavenumbers were performed to investigate the effect of wave crests merging. The nonlinear sharpening of merging crests is demonstrated. It is suggested that such effect may be responsible for the appearance of typical sharp crests of surface waves, as well as for wave breaking.

The question remains whether this effect can explain appearance of freak waves. We are inclined to think that the answer to this question is rather negative, though the effect of *exceedance* can make contribution to the freak wave formation. First of all, the effect of *exceedance* is not great, while the freak wave height can reach very large values. Second, the effect of *exceedance* is of high probability, and it evidently takes place, whenever the crests of two waves with different wavenumbers merge. If this effect were indeed responsible for the generation of freak waves, the probability of such waves would be much higher as compared to what we know at present.

The effect of focusing certainly explains apparent sharpness of surface waves in a multi-mode wave field, and most likely is connected with the mechanics of wave-breaking onset. The computations proved that frequency of breaking occurrence grows as a function of mean steepness of sea waves. This fact explains why the breaking happens more frequently in young seas.

Chapter 9 describes first attempts to simulate the wind and wave interaction process on the basis of a coupled windwave model. Both of the models are written

in the conformal surface-following coordinates. The use of such coordinates is the only way to construct an efficient coupled model. The conformity allows doing considerable simplifications in formulation of the problem and numerical scheme. Opposite to all previous investigations, the problem of wind–wave interaction is formulated as a statistical fluid dynamics problem: A coupled model was used for simulation of statistical regime of flows; physical conclusions were obtained by processing huge data volumes.

The fundamental concept of Wave Produced Momentum Flux (WPMF) is introduced in Chap. 9 and analyzed. The presence of WPMF is the main factor which makes the marine boundary layer different from the boundary layer above flat surface. It is shown that WPMF consists of several components of different nature. The structure of WPMF and its dependence on wave spectrum is investigated with 2-D-coupled windwave model and then used for construction of 1-D WBL model (Chap. 10). This model being joined with 1-D wave model is used for long-term simulation of sea waves. These calculations are very efficient, since the 1-D WBL model is much more efficient than the 2-D model based on Reynolds equations. It is demonstrated in Chap. 9 that one-dimensional waves can develop under the strong influence of the 1-D nonlinear interactions which, according to Mellville (1982), also work in one-dimensional wave fields. It is shown that the growth of energy and its rate of downshifting are in close agreement with the observational data obtained in the JONSWAP experiment. It means that the model with the suggested physics can describe the observed evolution of wave fields. The downshifting occurs due to both the one-dimensional nonlinear interactions and the effects of breaking.

Of course, the best way to avoid the problem of turbulence parameterization would be implementation of the LES technique, assuming that the large-scale part of the turbulence is simulated explicitly, while the subgrid part of the turbulence is parameterized in a relatively simple form. Construction of such model in the surface-following coordinates is complicated, still, more or less straightforward. However, the use of the model is connected with considerable troubles. Firstly, such model should be three-dimensional. The surface-following coordinate system for 3-D case leads to 3-D general elliptic equation for pressure to be solved with iterations. Secondly, the LES modeling implies very high 3-D resolution, which suggests very large computational resources. Hence, the problem becomes computationally ineffective or at least cumbersome. The alternative way to make the task more realistic is assumption of the two-dimensionality for waves and use of the cylindrical conformal coordinates. Evidently, this assumption makes applicability of the results dramatically lower. In any case, this problem is a great challenge for young scientists who wish to obtain really advanced results.

The problem of coupled dynamics of the atmospheric boundary layer and sea waves is similar to the problem of turbulent boundary layer in the upper ocean. The presence of turbulence in the upper ocean is quite evident as it can be generated by the currents with vertical gradients of velocity. For a long time, it was believed that potential waves cannot generate vorticity, and hence, they cannot make contribution to turbulence. Indeed, the potential motion formally always remains potential.

However, it is correct if the background vorticity is completely absent. In reality, both types of motion are presented in the upper ocean, and the point is in what way they can interact with each other. This problem was first formulated by Benilov and Losovatskii (1977) and then developed in some subsequent works of Benilov and others. A detailed description of this problem is given in Chap. 10 where the mathematical model of coupled dynamics of waves and vortical motions is offered. Unfortunately, the formulation of this model is highly complicated.

Theoretically, potential waves cannot generate vortex motion, but the scale considerations indicate that if the steepness of waves is not too small, the Reynolds number can exceed critical values. It means that in the presence of initial non-potential disturbances orbital velocities can generate vortex motion and turbulence. This problem had been previously investigated by means of the linear-instability theory and within this theory it was shown that the pure two-dimensional motion remains potential because the one-dimensional vortex (in vertical plane) does not interact with the wave orbital motion. However, if the turbulence is considered as three-dimensional, waves can generate vortex in horizontal plane. Such vortex is unstable, and further development of vorticity occurs due to the exchange of energy between the components of vorticity. Then, due to the nonlinearity, the motion at smaller scales, as well as more or less developed turbulent regime arise on behalf of wave energy.

In Chap. 11, this problem was investigated numerically on the basis of full two-dimensional ( $x-z$ ) equations of potential motion with free surface in the cylindrical conformal coordinates. It was assumed that all variables are a sum of 2-D potential orbital velocities and 3-D non-potential disturbances. Because the energy of waves is much larger than the energy of turbulence, it was currently assumed that only one-way interaction exists: The non-potential motion takes energy from potential waves. The non-potential motion is described directly with 3-D Euler equations with very high resolution. The interaction between potential orbital velocities and non-potential components is accounted through additional terms which include components of vorticity. The effects of turbulence are included using the subgrid turbulent energy evolution equation. The turbulent scale is assumed to be proportional to the grid resolution (LES technique). The numerical scheme is based on 2-D Fourier Transform method in ‘horizontal’ (in the conformal coordinates) plane and on the second-order approximation in ‘vertical.’ The pressure is calculated by means of Poisson’s equation in the cylindrical conformal coordinates derived through the covariant components of velocity. Poisson’s equation was solved with Three Diagonal Matrix Algorithm (TDMA). The initial conditions for elevations and surface potential for waves were assigned according to the linear theory; 3-D non-potential velocity components were inserted as small-amplitude noise.

The long-term numerical integration of the system of equations was done for different wave steepness. Vorticity and turbulence usually occur in the vicinity of wave crests (where the velocity gradients reach their maximum) and then spread over the upwind slope and downwards. The specific feature of wave turbulence at low steepness (steepness was kept low in order to avoid wave breaking) is its strong

intermittency: The turbulent patches are mostly isolated and intermittency grows with decrease of wave amplitude. Maximum values of energy of turbulence are in agreement with the available experimental data.

Two-dimensional ( $x - z$ ) modeling considered in the book cannot be considered as the ultimate method since real waves are, no doubt, three-dimensional. However, one-dimensional waves can often be considered as a good approximation of real waves, as wave crest length is usually much longer than wave length. Nevertheless, many processes such as wave breaking or generation of freak waves and their interaction with wind can be successfully investigated with two-dimensional model. At least, such investigation is reasonable to start with two-dimensional conformal modeling, because this method is highly efficient and allows considering a large number of numerical experiments with different parameters. Any 3-D model is not able to deliver such possibility due to its complexity and high demands to computation resources (mainly, the speed of calculations).

Anyway, three-dimensional modeling allows reproducing an evolution of surface waves due to nonlinear interaction. Therefore, developing a 3-D modeling is highly desirable. Such straightforward method of numerical solution of three-dimensional potential wave equations is suggested (Chap. 12). The method uses the surface-following coordinate system. The kinematic and dynamic conditions on the surface in the new coordinates become more complicated, but if we consider them as the evolutionary equations for the surface potential and elevation, we come to the conclusion that these conditions can be easily integrated in the same way as the similar one-dimensional equations in the conformal coordinates. However, calculations of vertical derivative of potential on the surface become more complicated, since the Laplace equation for 3-D velocity potential turns into a general elliptic equation that should be solved at every time step, which requires the use of extensive computer resources. However, it should be noted that this problem is still much simpler than, for example, standard simulations of 3-D Navier–Stokes equations (or LES equations) in the curvilinear coordinates when the problem of solving of the elliptic equation for pressure arises.

The potential wave problem gives a unique opportunity for validation of full nonlinear model by comparison with the exact stationary solution obtained in the moving coordinate system. This solution is obtained with a completely different algorithm; hence, such validation can be considered as full, non-trivial and exact. Since the model uses a finite-difference approximation in the vertical direction, we cannot expect a perfect agreement between the exact and the approximate solutions, though the results of such comparison are quite convincing. However, the structure of Stokes wave was supported over a long interval of integration. If the numerical scheme were not accurate enough, the evolution of modes would exhibit chaotic behavior and Stokes wave would quickly disintegrate due to the numerical instability. Such evolution was observed many times in the course of development of codes. The scheme is consistent, since with increase of resolution its accuracy increases. Currently, the possibility of application of the model for the finite depth problem is considered.

The model was used here for the simulation of evolution of steep Stokes wave train with the superimposed initial noise. For the case of directional wave fields, it was shown that evolution of wave field occurs in a different way as compared to evolution of the unidirectional case; i.e., the new developing modes are oblique toward propagation of carrier wave.

The most disappointing and unexpected property of the wave model is that the results depend essentially on the initial set of phases; hence, the most reliable results can be obtained with the ensemble modeling. Such simulation can be effectively done in parallel processors. It is not excluded that the stable and smooth results can be obtained by introducing the local viscosity in the Fourier space. Currently, it is unclear in what way this property can be brought into correlation with the natural process. However, we came to the conclusion that the primary physical variables are rather the fields of velocity (in the potential assumption, it is the velocity potential) and elevation. The Fourier modes are the result of formal presentation of wave fields, while they do not necessarily present real objects.

The numerical experiments are performed under the quasi-adiabatic conditions. However, the model is designed for investigation of the nonlinear mechanics of two-dimensional surface waves, particularly, for investigation of extreme waves. After implementation of the energy input scheme and wave-breaking parameterization, the model can be used for direct simulations of the two-dimensional wave field evolution under the action of wind, nonlinear interactions, and dissipation. This model can be combined with the 3-D LES model for the atmospheric WBL, being formulated in the same coordinate system. Such approach can be considered as the ultimate solution of the wind-wave interaction problem.

All of the numerical results presented in the current work were obtained using standard one-processor Dell computer with speed of 3.00 GHz. Since the model is based on the Fourier transform method, a parallel version of the model does not provide many advantages, while parallel processors are convenient to simultaneously run many versions of the same model, as well as to perform ensemble modeling.

The definition of freak wave is based on the concept of trough-to crest wave height, which is reasonable from the practical point of view. A natural wave field usually looks quite chaotic as a superposition of many dispersing modes which, in addition, are not conservative due to the fast reversible interactions. In our opinion, the only reasonable way to detect the instantaneous value of trough-to-crest height is the detection of maximum difference of elevations in the prescribed window. Since freak waves should be most likely associated with spectral peak, it is reasonable to choose the window with the size of the order of peak wave length and even somewhat bigger than that—for elimination of uncertainty of real wave length.

In one-dimensional wave field such a trough-to-crest height formulation gives quite definite results. However, in two-dimensional wave field some uncertainty arises because the positions of maxima and minima can be shifted with respect to the direction of wave propagation. The simplest way to avoid uncertainty is to define the trough-to-crest height as the difference between the maximum and minimum along the direction coinciding with that of the peak wave propagation.

Such interpretation of freak wave does not seem to be quite adequate, as wave power depends on the full range of elevation.

The main result of the current investigation is comparison of the extreme wave statistics generated by full nonlinear models and the statistics obtained over the ensemble of surfaces generated as a superposition of linear modes. In both cases, the integral energy is the same, and the spectra of the surfaces are similar.

The main advantage of 2-D model is that conformal transformation reduces the initial system of equation to two simple evolutionary equations which can be effectively solved with the Fourier transform method. In 3-D case even the orthogonal transformation is impossible, so the problem remains essentially three-dimensional. The surface integral method cannot be referred to two-dimensional, since it is based on Green function. The HOS method relies on Taylor series, which accuracy is not uniform along surface; what is more important this method is potentially unstable for high-order Taylor series.

One of the possible versions of such new scheme is offered in Chap. 12. This scheme is used for calculation of 3-D nonlinear interactions. The unexpected surprise is that for the same initial spectrum the results depend on the initial set of phases; hence, for obtaining reliable statistical results, it is necessary to perform ensemble modeling for different sets of initial phases. Such calculation shows that 2-D wave spectrum is highly irregular; i.e., it consists of peaks and holes, and what is most surprising, these patterns fall on different locations in the 2-D wavenumber space. It probably means that the nonlinear interactions are not connected with the fixed combinations of wavenumbers and frequencies, which Hasselmann's theory suggests. This result requires further discussion and explanation.

# References

- Agnon YE, Mey CC (1985) Slow-drift motion of a two-dimensional block in beam seas. *J Fluid Mech* 151:279–294
- Agnon Y, Babanin AV, Young IR, Chalikov D (2005) Fine scale inhomogeneity of wind-wave energy input, skewness, and asymmetry. *Geophys Res Lett* 32, L12603
- Andreas EL (2004) Spray stress revised. *J Phys Oceanogr* 34:1429–1440
- Anis A, Moum JN (1995) Surface wave-turbulence interactions: scaling  $\varepsilon(z)$  near the surface. *J Phys Oceanogr* 25:2025–2045
- Annenkov SY, Shrira VI (2006) Role of non-resonant interactions in the evolution of nonlinear random water wave fields. *J Fluid Mech* 561:181–207. doi:10.1017/S0022112006000632
- Ardhuin F, Jenkins AD (2006) On the interaction of surface waves and upper ocean turbulence. *J Phys Oceanogr* 36:551–557
- Asaithambi NS (1987) Computation of free-surface flows. *J Comp Phys* 73:380–394
- Babanin AV (2006) On a wave induced turbulence and a wave-mixed upper ocean layer. *Geophys Res Lett* 33, L20605. doi: 10.1029/2006GL027308, 6p
- Babanin AV (2011) Breaking and dissipation of ocean surface waves. Cambridge University Press, Cambridge, 463p
- Babanin AV, Young IR (2005) Two-phase behavior of the spectral dissipation of wind waves. In: Edge B, Santas JC (eds) Proceedings of the ocean waves measurement and analysis, fifth international symposium WAVES2005, 3–7 July 2005, Madrid, Spain, Sponsors CEDEX (Spain) and CORPI of ASCI (USA), paper no 51, 11p
- Babanin AV, Haus BK (2009) On the existence of water turbulence induced by non-breaking surface waves. *J Phys Oceanogr* 39:2675–2679
- Babanin A, Chalikov D (2012) Numerical investigation of turbulence generation in non-breaking potential waves. *J Geophys Res* 117, C00J17, doi:10.1029/2012JC007929
- Babanin AV, Young IR, Banner ML (2001) Breaking probabilities for dominant surface waves on water of finite constant depth. *J Geophys Res* C106:11659–11676
- Babanin A, Chalikov D, Young I, Savelyev I (2007) Predicting the breaking onset of surface water waves. *Geophys Res Lett* 34, L07605, 1029/2006GL029135
- Babanin AV, Ganopolski A, Phillips WRC (2009) Wave-induced upper-ocean mixing in a climate modelling of intermediate complexity. *Ocean Model* 29:189–197
- Babanin AV, Chalikov D, Young IR, Savelyev I (2010) Numerical and laboratory investigation of breaking of steep two-dimensional waves in deep water. *J Fluid Mech* 644:433–463
- Babanin AV, Waseda T, Kinoshita T, Toffoli A (2011) Wave breaking in directional fields. *J Phys Oceanogr* 41:145–156
- Babanin AV, Babanina A, Chalikov D (2014) Interaction of surface waves at very close wavenumbers. *Ocean Dyn* 64(7):1019–1023
- Badlock TE, Huntley D, Bird PAD, O'Hare T, Bullock GN (2000) Breakpoint generated surf beat induced by bichromatic wave groups. *Coast Eng* 39:213–242

- Baker GR, Meiron D, Orszag SA (1982) Generalized vortex methods for free-surface flow problems. *J Fluid Mech* 123:477–501
- Banner ML, Tian X (1998) On the determination of the onset of breaking for modulating surface gravity waves. *J Fluid Mech* 367:107–137
- Banner ML, Babanin AV, Young IR (2000) Breaking probability for dominant waves on the sea surface. *J Phys Oceanogr* 30:3145–3160
- Battjes JA, Zitman TJ, Holthuijsen LH (1987) A reanalysis of the spectra observed in JONSWAP. *J Phys Oceanogr* 17:1288–1295
- Belcher SE, Hunt JCR (1993) Turbulent shear flow over slowly moving waves. *J Fluid Mech* 251:109–148
- Belcher SE, Harris JA, Street RL (1994) Linear dynamics of wind waves in coupled turbulent air-flow. Part 1. Theory. *J Fluid Mech* 271:119–151
- Benilov AY, Lozovatskiy Y (1977) Semi-empirical methods of the turbulence description in the ocean. In the turbulent diffusion of the ingredients in the sea, the coordination center of COMECON (SEV). Inf Bull 5:89–97
- Benilov AY, McKee TG, Safray AS (1993) On the vortex instability of the linear surface wave. In: Taylor C (ed) Numerical methods in laminar and turbulent flow, VIII, Part 2. Pineridge Press, UK, pp 1323–1334
- Benjamin TB, Feir JE (1967) The disintegration of wave trains in deep water. *J Fluid Mech* 27:417–430
- Bingham HB, Zhang H (2007) On the accuracy of finite-difference solutions for nonlinear water waves. *J Eng Math* 58:211–228
- Bortkowskii RS (1987) Air-sea exchange of heat and moisture during storms, D. Riedel, 1944p
- Breuer M, Lakehal D, Rodi W (1996) Flow around a surface mounted cubical obstacle: comparison of LES and RANS-results. In: Deville M, Gavrilakis S, Ryhming II (eds) Computations of three-dimensional complex flows. Notes on Numerical Fluid Dynamics, 53, Braunschweig/Wiesbaden
- Brown MG, Jensen A (2001) Experiments in focusing unidirectional water waves. *J Geophys Res* C106:16917–16928
- Cai X, Petter H, Langtangen HP, Nielse BF, Tveito A (1998) Finite element method for fully nonlinear water waves. *J Comp Phys* 143:544–568
- Chalikov DV (1976) A mathematical model of wind-induced waves. *Doklady Acad Sci USSR* 229:121–126 (in Russian)
- Chalikov DV (1978) Numerical simulation of wind-wave interaction. *J Fluid Mech* 87:561–582
- Chalikov DV (1980) Mathematical modeling of wind-induced waves. News and problems of sciences series, Gidrometeoizdat, 50 pp (in Russian)
- Chalikov DV (1986) Numerical simulation of the boundary layer above waves. *Bound Layer Met* 34:63–98
- Chalikov D (1995) The parameterization of the wave boundary layer. *J Phys Oceanogr* 25: 1335–1349
- Chalikov D (1998) Interactive modeling of surface waves and boundary layer. Ocean wave measurements and analysis. ASCE. In: Proceeding of the third international symposium WAVES 97, pp 1525–1540
- Chalikov D (2005) Statistical properties of nonlinear one-dimensional wave fields. *Nonlinear Process Geophys* 12:1–19
- Chalikov D (2007) Simulation of Benjamin-Feir instability and its consequences. *Phys Fluid* 19:016602–016615
- Chalikov D (2009) Freak waves: their occurrence and probability. *Phys Fluid* 21:076602. doi:[10.1063/1.3175713](https://doi.org/10.1063/1.3175713)
- Chalikov DV (2010) Transformation of harmonic waves on a deep water. *Fundam Appl Hydophys* 9(3):14–21 (in Russian)
- Chalikov D (2012) On the nonlinear energy transfer in the unidirected adiabatic surface waves. *Phys Lett* 376(44):2755–2816

- Chalikov DV, Liberman YM (1991a) Integration of primitive equations for potential waves. *Izv. Acad Sci USSR Atm Ocean Phys* 27:42–47
- Chalikov D, Makin V (1991b) Models of the wave boundary layer. *Bound Layer Met* 56:83–99
- Chalikov D, Belevich M (1993) One-dimensional theory of the wave boundary layer. *Bound-Lay Meteorol* 63:65–96
- Chalikov D, Sheinin D (1994a) Numerical simulation of surface waves based on equations of potential wave dynamics. In: Proceedings ONR, Ocean Waves Workshop, 1994, Tucson, Arizona
- Chalikov D, Sheinin D (1994b) The numerical investigation of wavenumber-frequency spectrum for 1-D nonlinear waves. WMO/ISCU, CAS/JSC Working Group on Numerical Experimentation, Report #19. WMO/TD-No. 592
- Chalikov D, Sheinin D (1994c) Numerical investigation of wavenumber-frequency spectrum for 1-D nonlinear waves. Ocean Sciences Meeting, Feb 21–25, San-Diego, CA. Abstract in: EOS, transactions (supplement), AGU, 75, #3, p 100, 1994b.
- Chalikov D, Sheinin D (1996) Numerical modeling of surface waves based on principal equations of potential wave dynamics. Technical Note. NOAA/NCEP/OMB, 54 pp
- Chalikov D, Sheinin D (1998) Direct modeling of one-dimensional nonlinear potential waves. Nonlinear ocean waves. In: Perrie W (ed) Advances in fluid mechanics, 2001, vol 17, pp 207–258
- Chalikov D, Sheinin D (2005) Modeling of extreme waves based on equations of potential flow with a free surface. *J Comp Phys* 210:247–273
- Chalikov D, Rainchik S (2010) Coupled numerical modelling of wind and waves and the theory of the wave boundary layer. *Boundary-Layer Meteorol* 138:1–41. doi:[10.1007/s10546-010-9543-7](https://doi.org/10.1007/s10546-010-9543-7)
- Chalikov DV, Bulgakov KY (2010) Stokes wave at finite depth. *Fundam Appl Hydophys* 7(4):3–15
- Chalikov DV, Bulgakov KY (2014) Stokes wave at finite depth. *Fundam Appl Hydophys* 7(4):3–15
- Chalikov D, Babanin AV (2012) Simulation of wave breaking in one-dimensional spectral environment. *J Phys Ocean* 42(11):1745–1761
- Chalikov D, Babanin AV (2013) Three-dimensional periodic fully-nonlinear potential waves. In: Proceedings of the ASME 2013 32nd international conference on ocean, offshore and arctic engineering OMAE2013, 9–14 July 2013, Nantes, France, 8p. doi:978-0-7918-5533-1
- Chalikov D, Babanin AV (2014) Simulation of one-dimensional evolution of wind waves in a deep water. *Phys Fluid* 26(9):096697
- Chalikov D, Babanin AV, Sanina E (2014) Numerical modeling of three-dimensional fully nonlinear potential periodic waves. *Ocean Dyn* 64(10):1469–1486
- Chiang WS, Hsia SC, Hwung HH (2007) Evolution of sidebands in deep-water bichromatic wave trains. *J Hydraul Res* 45:67–80
- Choi HS, Suzuki K (2005) Large eddy simulation of turbulent flow and heat transfer in a channel with one wavy wall. *Int J Heat Fluid Flow* 26:681–694
- Clamond D, Grue J (2001) A fast method for fully nonlinear water wave dynamics. *J Fluid Mech* 447:337–355
- Clamond D, Fructus D, Grue J, Krisitiansen O (2005) An efficient method for three-dimensional surface wave simulations. Part II: Generation and absorption. *J Comp Phys* 205:686–705
- Clamond D, Francius M, Grue J, Kharif C (2006) Long time interaction of envelope solitons and freak wave formations. *Eur J Mech B/Fluids* 25:536–553
- Crapper GD (1957) An exact solution for progressive capillary waves of arbitrary amplitude. *J Fluid Mech* 96:417–445
- Crapper GD (1984) Introduction to water waves. Wiley, Chichester 224 pp
- Dai D, Qiao F, Sulisz W, Han L, Babanin AV (2010) An experiment on the non-breaking surface-wave-induced vertical mixing. *J Phys Oceanogr* 40:2180–2188
- Dallaston MC, McCue SW (2010) Accurate series solution for gravity-driven Stokes waves. *Phys Fluids* 22:82104

- Dimas AA, Triantafyllou GS (1994) Nonlinear interaction of shear flow with a free surface. *J Fluid Mech* 260:211–246
- Dold JW (1992) An efficient surface-integral algorithm applied to unsteady gravity waves. *J Comp Phys* 103:90–115
- Dold JW, Peregrin DH (1986) A efficient boundary-integral method for steep unsteady water waves. In: Morton KW, Baines MJ (eds) *Numerical methods for fluid dynamics*. Oxford University Press, Oxford
- Dommermuth DG (1993) The laminar interactions of a pair of vortex tubes with a free surface. *J Fluid Mech* 246:91–115
- Dommermuth D, Yue D (1987) A high-order spectral method for the study of nonlinear gravity waves. *J Fluid Mech* 184:267–288
- Donelan MA (1990) Air-sea interaction. *Sea: Ocean Eng Sci* 9:239–292
- Donelan MA, Longuet-Higgins MS, Turner JS (1972) Periodicity in whitecaps. *Nature* 239: 449–451
- Donelan MA, Babanin AV, Young IR, Banner ML, McCormick C (2005) Wave follower field measurements of the wind input spectral function. Part I. Measurements and calibrations. *J Atmos Oceanic Tech* 22:799–813
- Donelan MA, Babanin AV, Young IR, Banner ML (2006) Wave follower field measurements of the wind input spectral function. Part II. Parameterization of the wind input. *J Phys Oceanogr* 36:1672–1688
- Donelan MA, Curcic M, Chen MS, Magnusson AK (2012) Modeling waves and wind stress. *J Geophys Res* 117:C00J23. doi:[10.1029/2011JC007787](https://doi.org/10.1029/2011JC007787)
- Drennan WM, Hui WH, Tenti G (1988) Accurate calculation of Stokes wave near breaking. In: Graham C, Malik SK (eds) *Continuum mechanics and its applications*. Hemisphere Publishing, Washington, DC
- Dyachenko AI, Zakharov VE (2005) Modulation instability of Stokes wave—freak wave. *Pis'ma v ZhETF* 81:318–322
- Dysthe KB (1979) Note on a modification to the nonlinear Schrödinger equation for application to deep water waves. *Proc R Soc Lond A* 369:105–114
- Dysthe KB, Trulsen K (1999) Note on breather type solutions of the NLS as a model for freak-waves. *Phys Scr* T82:48–52
- Dysthe KB, Krogstad HE, Soquet-Juglard H (2003) Evolution of a narrow-band spectrum of random surface gravity waves. *J Fluid Mech* 478:1–10
- Dysthe K, Krogstad H, Muller P (2008) Oceanic rogue waves. *Annu Rev Fluid Mech* 40:287–310
- Eliassen EB, Machenhauer B, Rasmussen E (1970) On a numerical method for integration of the hydro-dynamical equations with a spectral representation of the horizontal fields, Report 2, Institute for Teoretisk, Meteorologi, Kobenhavns Universitet, Copenhagen
- Efimov VV, Hristoforov GN (1971) Wave and turbulence components of the velocity spectrum in the upper layer of the ocean. *Izv Acad Sci USSR Atmos Oceanic Phys Engl Transl* 7(2): 200–211
- Engsig-Karup AP, Bingham HB, Lindberg O (2009) An efficient flexible-order model for 3D nonlinear water waves. *J Comp Phys* 228:2100–2118
- Farmer J, Martinelli L, Jameson A (1993) A Fourier method for solving nonlinear water-wave problems: application to solitary–wave interactions. *J Fluid Mech* 118:411–443
- Fletcher CAJ (1988) Computational techniques for fluid dynamics, vol 1, 2. Springer, Berlin, 401 pp.
- Floryan JM, Rasmussen H (1989) Numerical methods for viscous flows with moving boundaries. *Appl Mech Rev* 42:32341
- Fochesato C, Dias F, Grilli S (2006) Wave energy focusing in a three-dimensional numerical wave tank. *Proc R Soc A* 462:2715–2735
- Fornberg B (1980) A numerical method for conformal mapping. *SIAM. J Sci Comput* 1:386–400

- Fritts MJ, Meinhold MJ, von Kerczek CH (1988) The calculation of nonlinear bow waves. In: Proceedings of the 17th symposium on naval hydrodynamics, The Hague, Netherlands, pp 485–497
- Galchenko A, Babanin AV, Chalikov D, Young IR, Hsu TW (2010) Modulation depth and breaking strength for deep-water wave groups. *J Phys Oceanogr* 40:2313–2324
- Fructus D, Clamond D, Grue J, Kristiansen Ø (2005) An efficient model for three-dimensional surface wave simulations. Part I: free space problems. *J Comp Phys* 205:665–685
- Fructus D, Grue J (2007) An explicit method for the nonlinear interaction between water waves and variable and moving bottom topography by Fructus and Grue. *J Comp Phys* 2007 222: 720–739
- Galchenko A, Babanin AV, Chalikov D, Young IR, Haus BK (2011) Influence of wind forcing on modulation and breaking of deep-water groups. *J Phys Oceanogr* 42:928–939 2012
- Gemmrich J (2010) Strong turbulence in the wave crest region. *J Phys Oceanogr* 40:583–595. doi:[10.1175/2009JPO4179.1](https://doi.org/10.1175/2009JPO4179.1)
- Germano M, Piomelli U, Moin P, Cabot W (1991) A dynamic subgrid-scale eddy-viscosity model. *Phys Fluids A* 3:1760–1765
- Grilli S, Guyenne P, Dias F (2001) A fully nonlinear model for three-dimensional overturning waves over arbitrary bottom. *Int J Num Math Fluids* 35:829–867
- Harlow FH, Welch E (1965) Numerical calculation of time-dependent viscous incompressible flow of fluid with free surface. *Phys Fluids* 8:2182–2189
- Hasselmann K (1962) On the non-linear energy transfer in a gravity wave spectrum, Part 1. *J Fluid Mech* 12:481–500
- Hasselmann K (1967) Weak-interaction theory of ocean waves. University of Hamburg, Hamburg, 112p
- Hasselmann K, Barnett RP, Bouws E et al (1973) Measurements of wind-wave growth and swell decay during the Joint Sea Wave Project (JONSWAP). *Tsch Hydrogr Z Suppl A8(12)*:1–95
- Haussling HJ, Van Eseltine RT (1975) Finite-difference methods for transient potential flows with free surfaces. In: Proceedings of the international conference on numerical ship hydrodynamics, University Extension Publication, Berkely, pp 295–313
- Henderson KL, Peregrine DH, Dold JW (1999) Unsteady water wave modulations: fully nonlinear solutions and comparison with the nonlinear Schrödinger equation. *Wave Motion* 29:341–361
- Hirt CW, Nichols BD (1981) Volume of fluid method for the dynamics of free surface. *J Comput Phys* 39:201–225
- Holthuijsen LH, Herbers THC (1986) Statistics of breaking waves observed as whitecaps in the open sea. *J Phys Oceanogr* 16:290–297
- Homer (750BC–650BC), Iliad (2000) The Project Gutenberg Etext of The Iliad, by Homer translated by Samuel Butle
- Hsiao SV, Shemdin OH (1983) Measurements of wind velocity and pressure with a wave follower during MARSEN. *J Geophys Res* 88:9841–9849
- Huang C, Qiao F, Song Z (2008) The effect of the wave-induced mixing on the upper ocean temperature in a climate model. *Acta Oceanol Sin* 27:104–111
- Hyman JM (1984) Numerical methods for tracking interfaces. *Physica D* 12:396–407
- Gemmrich JR, Farmer DM (1999) Observations of the scale and occurrence of breaking surface waves. *J Phys Oceanogr* 29:2595–2606
- Gent PR, Taylor PA (1976) A numerical model of the air flow above water waves. *J Fluid Mech* 77:105–128
- Gramstad O, Stiassnie M (2013) Phase-averaged equation for water waves. *J Fluid Mech* 718: 280–303
- Guenther A, von Rohr R (2003) Large-scale structures in a developed flow over a wavy wall. *J Fluid Mech* 478:257–285
- Iafrati A (2009) Numerical study of the effects of the breaking intensity on wave breaking flows. *J Fluid Mech* 622:371–411

- Iafrati A, Babanin AV, Onorato (2013) Modulational instability, wave breaking and formation of large scale dipoles. *Phys Rev Lett* 110:184504:5p
- Irisov V, Voronovich A (2011) Numerical simulation of wave breaking. *J Phys Oceanogr* 41: 346–364
- Jacobs CA (1978) Numerical simulations of the natural variability in water temperature during BOMEX using alternative forms of the vertical eddy exchange coefficient. *J Phys Oceanogr* 8:119–141
- Janssen P (2003) Nonlinear four-wave interaction and freak waves. *J Phys Oceanogr* 33:2001–2018
- Jessup AT, Zappa CJ, Lowen MR, Hesany V (1997) Infrared remote sensing of breaking waves. *Nature* 385:52–55
- Johannessen TB, Swan C (1997a) A numerical transient water waves—part 1. A numerical method of computation with comparison to 2-D laboratory data. *Appl Ocean Res* 19:293–308
- Johannessen TB, Swan C (1997b) A laboratory study of the focusing of transient and directionally spread surface water waves. *Proc R Soc Lond* A457:971–1006
- Johannessen TB, Swan C (2003) On the nonlinear dynamics of wave groups produced by the focusing of surface-water waves. *Proc R Soc Lond* A459:1021–1052
- Kahma KK, Calkoen CJ (1992) Reconciling discrepancies in the observed Growth of wind generated waves. *J Phys Oceanogr* 22:52–78
- Kano T, Nishida T (1979) Sur le ondes de surface de l'eau avec une justification mathematique des equations des ondes en eau peu profonde. *J Math Kyoto Univ (JMKYAZ)* 19–2:335–370
- Keller LV, Friedmann AA (1924) Differentialgleichung für die turbulente Bewegung einer kompressiblen Flüssigkeit. *Proc 1st Intern Congr Appl Mech* 31(4):789–799
- Kerman BR (1992) Natural physical sources of underwater sound: sea surface sound. Kluwer academic, Berlin, 749p
- Kharif C, Pelinovsky E (2003) Physical mechanisms of the rogue wave phenomenon. *Euro J Mech B/Fluids* 22:603–634
- Kharif C, Ramamontjarisoa A (1988) On the stability of gravity waves on deep water. *Phys Fluids* 31:1286–1288
- Kinsman B (1965) Wind waves: their generation and propagation on the ocean surface. Prentice-Hall, Englewood Cliffs, N.J., p 676p
- Kitaigorodskii SA (1961) On the possibility of theoretical calculation of vertical temperature profile in upper layer of the sea. *Bull Acad Sci USSR Geophys Ser* 3:313–318
- Kitaigorodskii SA, Lumley JL (1983) Wave-turbulence interaction in the upper ocean. Part1: the energy balance of the interacting fields of surface wind waves and wind-induced three-dimensional turbulence. *J Phys Oceanogr* 13:1977–1987
- Kjeldsen SP, Myrhaug D (1980) Wave-wave interactions, current-wave interactions and resulting extreme waves and breaking waves. In: Proceedings of the 17th coastal engineering conference, pp 2277–2303
- Kleiss JM, Melville WK (2011) The analysis of sea surface imagery for white cap kinematics. *J Atmos Ocean Technol* 28:219–224
- Kobayashi H (2005) The subgrid-scale models based on coherent structures for rotating homogeneous turbulence and turbulent channel flow. *Phys Fluids* 17(045104):1–12
- Krasitskii VP (1994) On reduced equations in the Hamiltonian theory of weakly nonlinear surface waves. *J Fluid Mech* 272:1–20
- Kretzner K, Schumann U (1992) Numerical simulation of turbulent convection over wavy terrain. *J Fluid Mech* 237:261–299
- Kruse N, Guenther A, von Rohr R (2003) Dynamics of large-scale structures in turbulent flow over a wavy wall. *J Fluid Mech* 485:87–96
- Kudryavtsev VN (2006) On effect of sea drops on atmospheric boundary layer. *J Geophys Res* 111:C07020. doi:[10.1029/2005JC002970](https://doi.org/10.1029/2005JC002970)
- Kudryavtsev VN, Makin VK, Chapron B (1999) Coupled sea surface-atmosphere model. Part 2. Spectrum of short wind waves. *J Geophys Res* 104(C4):7625–7639

- Lake BM, Yuen HC (1978) A new model for nonlinear wind waves. Part 1. Physical model and experimental results. *J Fluid Mech* 88:33–62
- Lauder BE, Spalding DB (1974) The numerical computation of turbulent flows. *Computer Methods in Applied Mech and Eng* 3:269–289
- Langmuir I (1938) Surface motion of water induced by the wind. *Science* 87:119–123
- Liebisch TC, Blanshsan E, Donley EA, Kitching J (2012) Atom-number amplification in magneto-optical trap via stimulated light forces. *Phys Rev A* 85(013407):4p
- Lighthill MJ (1965) Contribution to the theory of waves of finite amplitude in nonlinear dispersive system. *J Inst Math Appl* 1:269–306
- Longuet-Higgins MS (1953) Mass transport in water waves. *Phil Trans R Soc A* 245:535–581
- Longuet-Higgins MS (1969) On wave breaking and the equilibrium spectrum of wind-generated waves. *Proc R Soc Lond A* 310:151–159
- Longuet-Higgins MS (1978) The instabilities of gravity waves of finite amplitude in deep water. II Subharmonics. *Proc R Soc Lond* 360:489–505.
- Longuet-Higgins MS, Cokelet ED (1976) The deformation of steep surface waves on water. I. A numerical method of computation. *Proc R Soc Lond* 350:1–26
- Longuet-Higgins MS, Tanaka M (1997) On the crest instabilities of steep surface waves. *J Fluid Mech* 336:51–68
- Madsen PA, Fuhrman DR (2006) Third-order theory for bichromatic bi-directional water waves. *J Fluid Mech* 557:369–397
- Makin VK, Kudryavtsev VN (1999) Coupled sea surface-atmosphere model. Part 1. Wind over waves coupling. *J Geophys Res* 104(C4):7613–7623
- Manasseh R, Babanin AV, Forbes C, Rickards K, Bobevski I, Ooi A (2006) Passive acoustic determination of wave-breaking events and their severity across the spectrum. *J Atmos Oceanic Tech* 23:599–618
- Mastenbroek C, Makin VK, Garat MH, Giovanangeli JP (1996) Experimental evidence of the rapid distortion of the turbulence in the air flow over water waves. *J Fluid Mech* 318:273–302
- McLean JW (1982) Instabilities of finite-amplitude water waves. *J Fluid Mech* 114:315–330
- McWilliams JC, Sullivan PP (2000) Vertical mixing by Langmuir circulations. *Spill Sci Technol Bull* 6:225–237
- Mei CC (1978) Numerical methods in water-wave diffraction and radiation. *Annu Rev Fluid Mech* 10:393–416
- Meirink JF, Makin VK (2000) Modelling low-Reynolds-number effects in the turbulent air flow over water waves. *J Fluid Mech* 415:155–174
- Melville WK (1982) The instability and breaking of deep-water waves. *J Fluid Mech* 115:165–183
- Melville WK, Matusov P (2002) Distribution of breaking waves at the ocean surface. *Nature* 417:58–63
- Melville WK, Loewen M, Felizardo F, Jessup A, Buckingham M (1988) Acoustic and microwave signatures of breaking waves. *Nature* 336:54–56
- Miles JW (1957) On the generation of surface waves by shear flows. *J Fluid Mech* 3:185
- Miyata H (1986) Finite-difference simulation of breaking waves. *J Comput Phys* 5:179–214
- Monin AS, Yaglom AM (1971) Statistical fluid mechanics: mechanics of turbulence, 1:1087
- Mori N, Onorato M, Janssen PAEM (2011) On the estimation of the kurtosis in directional sea states for freak wave forecasting. *J Phys Oceanogr* 41:1484–1497
- Noh WF, Woodward P (1976) SLIC (simple line interface calculation). In: *Lecture Notes in Physics*, vol 59. Springer, New York, pp 330–340
- Onorato M, Osborne AR, Serio M, Damiani MT (2000) Occurrence of freak waves from envelope equations in random ocean wave simulations. In: Olagnon M, Athanassoulis GA (eds) *Rogue waves 2000* (Brest, France, 2000), Ifremer, pp 181–191
- Onorato M, Osborne A, Serio M, Bertone S (2001) Freak wave in random oceanic sea states. *Phys Rev Lett* 86(25):5831–5834

- Onorato M, Waseda T, Toffoli A, Cavalieri L, Gramstad O, Janssen PAEM, Kinoshita T, Monbaliu J, Mori N, Osborne AR, Serio M, Stansberg CT, Tamura H, Trulsen K (2009a) Statistical properties of directional oceanwaves: the role of the modulational instability in the formation of extreme events. *Phys Rev Lett* 102(1–4):114502
- Onorato M, Cavalieri L, Fouques S, Gramstad O, Janssen PAEM, Monbaliu J, Osborne AR, Pakozdi C, Serio M, Stansberg CT, Toffoli A, Trulsen K (2009b) Statistical properties of mechanically generated surface gravity waves: a laboratory experiment in a three-dimensional wave basin. *J Fluid Mech* 637:235–257
- Onorato M, Waseda T, Toffoli A, Cavalieri L, Gramstad O, Janssen PAEM, Kinoshita T, Monbaliu J, Mori N, Osborne AR, Serio M, Stansberg CT, Tamura H, Trulsen K (2009c) On the statistical properties of directional ocean waves: the role of the modulational instability in the formation of extreme events. *Phys Rev Lett* 102. doi:10.1103/PhysRevLett.102.114502, 4p
- Orszag SA (1970) Transform method for calculation of vector coupled sums. Application to the spectral form of vorticity equation. *J Atmos Sci* 27:890–895
- Osborne AR (2010) Nonlinear ocean waves and the inverse scattering transform. Elsevier, Amsterdam, 994p
- Osborne AR, Onorato M, Serio M (2000) The nonlinear dynamics of rogue waves and holes in deep-water gravity wave train. *Phys Lett A* 275:386–393
- Ovsyannikov LV (1973) Dynamics of liquid continuum. Institute of Fluid Mechanics. Siberian Branch of Russian Academy of Science. 15:104–125
- Papadimitrakis YA (2005) On the probability of wave breaking in deep water. *Deep-Sea Res II* 52:1246–1269
- Phillips OM (1977) Dynamics of upper ocean, 2nd edn. Cambridge University Press, Cambridge, 336 pp
- Pierson WJ, Moscowitz L (1964) A proposed spectral form for fully developed wind seas based on the similarity theory of S A Kitaigorodskii. *J Geophys Res* 69(24):5181–5190
- Pleskachevsky A, Dobrynin M, Babanin AV, Gunther H, Stanev E (2011) Turbulent diffusion due to ocean surface waves indicated by suspended particulate matter. Implementation of satellite data into numerical modelling, *J Phys Oceanogr* 41:708–724. doi:10.1175/2010JPO4328.1
- Porte-Agel F, Meneveau C, Parlange MB (2000) A scale-dependent dynamic model for large eddy simulation: application to a neutral atmospheric boundary layer. *J Fluid Mech* 415:261–284
- Powell MD, Vickery PJ, Reinhold TA (2003) Reduced drag coefficient for high wind speeds in tropical cyclones. *Nature* 422:279–283
- Prosperetti A, Jacobs JW (1983) A numerical method for potential flow with free surface. *J Comp Phys* 51:365–386
- Qiao F, Yeli Y, Yang Y, Zheng Q, Xia C, Ma J (2004) Wave-induce mixing in the upper ocean: distribution and application to a global ocean circulation model. *Geophys Res Lett* 31:L11303. doi:10.1029/2004GL019824
- Qiao F, Yuan Y, Ezer T, Xia C, Yang Y, Lu X, Song Z (2010) A three-dimensional surface wave —ocean circulation coupled model and its initial testing. *Ocean Dyn* 60:1339–1355
- Roberts AJ (1983) A stable and accurate numerical method to calculate the motion of a sharp interface between fluids. *IMA J Appl Math* 1:293–316
- Rogers WE, Babanin AV, Wang DW (2012) Observation-consistent input and whitecapping-dissipation in a model for wind-generated surface waves: description and simple calculations. *J Atmos Oceanic Tech* 29(9):1329–1346
- Sanina E (2014) Statistics of wave kinematics in random directional wave fields. PhD dissertation. Department of Mathematics, Centre for Ocean Engineering, Science and Technology (COEST), Faculty of Science and Engineering, Swinburne University of Technology, Melbourne, Australia
- Sharkov EA (2007) Breaking ocean waves, geometry, structure and remote sensing. Springer, Berlin 278p

- Sheinin D, Chalikov D (2001) Hydrodynamical modeling of potential surface waves. In: Problems of hydrometeorology and environment on the eve of XXI century. Proceedings of international theoretical conference, St. Petersburg, 24–25 June 1999. St.-Petersburg, Hydrometeoizdat, pp 305–337
- Shemer L, Jiao H, Kit E, Agnon Y (2001) Evolution of a nonlinear wave field along a tank: experiments and numerical simulations based on the spatial Zakharov equation. *J Fluid Mech* 427:107–129
- Simonov VV (1982) On the calculation the drag of wavy surface. *Izv Atm Ocean Phy* 18:269–275 (in Russian)
- Slunyaev A, Kharif C, Pelinovsky E, Talipova T (2002) Nonlinear wave focusing on water of finite depth. *Physica D* 173(1–2):77–96
- Smagorinsky J (1963) General circulation experiments with the primitive equations. *Mon Weather Rev* 91:530–558
- Spalart PR (1988) Direct simulation of a turbulent boundary layer up to  $Re_\theta = 1410$ . *J Fluid Mech* 187:61–83
- Snyder RL, Dobson FW, Elliott JA, Long RB (1981) Array measurements of atmospheric pressure fluctuations above surface gravity waves. *J Fluid Mech* 102:1–59
- Song JB, Banner ML (2002) On determining the onset and strength of breaking for deep water waves. Part I. Unforced irrotational wave groups. *J Phys Oceanogr* 32:2541–2558
- Srokosz MA (1986) On the probability of breaking in deep water. *J Phys Oceanogr* 16:382–385
- Stokes GG (1847) On the theory of oscillatory waves. *Trans Cambridge Philos Soc* 8:441–445; *Math Phys Pap* 1:197–229
- Stokes GG (1880) Supplement to a paper on the theory of oscillatory waves. *Math Phys Pap* 1:314–326
- Su M-Y (1982) Three-dimensional deep-water waves. Part I. Experimental measurements of skew and symmetric wave patterns. *J Fluid Mech* 124:73–108
- Tanaka M, Dold JW, Lewy M, Peregrine DH (1987) Instability and breaking of a solitary wave. *J Fluid Mech* 187:235–248
- Tanveer S (1991) Singularities in water waves and Rayleigh-Taylor instability. *Proc R Soc Lond A* 435:137–158
- Tanveer S (1993) Singularities in the classical Rayleigh-Taylor flow: formation and subsequent motion. *Proc R Soc Lond A* 441:501–525
- The WISE Group (Cavaleri L, Alves JHGM, Arduini F, Babanin A, Banner M, Belibassakis K, Benoit M, Donelan M, Groeneweg J, Herbers THC, Hwang P, Janssen PAEM, Janssen T, Lavrenov IV, Magne R, Monbaliu J, Onorato M, Polnikov V, Resio D, Rogers WE, Sheremet A, McKee SJ, Tolman HL, van Vledder G, Wolf J, Young I) (2007) Wave modelling —the state of the art. *Prog Oceanogr* 75:603–674
- Thomas LH (1949) Elliptic problems in linear differential equations over a network. Columbia University, New York
- Thompson JF, Warsi ZUA (1982) Boundary-fitted coordinate systems for numerical solution of partial differential equations—a review. *J Comput Phys* 47:1–108
- Ting CH, Babanin AV, Chalikov D, Hsu TW (2012) Dependence of drag coefficient on the directional spreading of ocean waves. *J Geophys Res* 117: C00J14. doi:10.1029/2012JC007920
- Toffoli A, Onorato M, Babanin AV, Bitner-Gregersen E, Monbaliu J (2007) Second-order theory and set-up in surface gravity waves: a comparison with experimental data. *J Phys Oceanogr* 37:2726–2739
- Toffoli A, Babanin AV, Waseda T, Onorato M (2010) The maximum steepness of oceanic waves. *Geophys Res Lett* 37:L05603. doi:10.1029/2009GL041771, 4p
- Toffoli A, Babanin AV, McConochie J, (2012) The effect of turbulence induced by non-breaking waves on the ocean mixed layer: Field observations on the Australian North-West Shelf. *J Geophys Res* 117:C00J24. doi:10.1029/2011JC007780, 8p
- Tolman HL (2008) A mosaic approach to wind wave modeling. *Ocean Model* 25(1–2):35–47

- Tolman H, Chalikov D (1994) Development of a third-generation ocean wave model at NOAA–NMC. In: Isaacson M, Quick MC (eds) *Physical and numerical modeling*. Vancouver, pp 724–733
- Tolman H, Chalikov D (1996) On the source terms in a third-generation wind wave model. *J Phys Oceanogr* 11:2497–2518
- Trulsen K, Stansberg CT (2001) Spatial evolution of water surface waves: numerical simulation and experiment of bichromatic waves. In: *Proceedings of the ISOPE*, Stavanger, Norway, Norwegian Research Council and Norsk Hydro and Statoil, pp 71–77
- Tsai WT, Yue DKP (1996) Computation of nonlinear free-surface flows. *Annu Rev Fluid Mech* 28:249–278
- Tseng YH, Ferziger JH (2004) Large-eddy simulation of turbulent wavy boundary flow—illustration of vortex dynamics. *J Turbul* 5(34):034
- Tulin MP, Waseda T (1999) Laboratory observations of wave group evolution, including breaking effects. *J Fluid Mech* 378:197–223
- Tulin MP, Landrini M (2001) Breaking waves in the ocean and around ships. In: *Proceedings of the twenty-third symposium of naval hydrodynamics*, pp 713–745
- Vreman AW (2004) An eddy-viscosity subgrid-scale model for turbulent shear flow: algebraic theory and applications. *Phys Fluids* 16:3670–3681
- Waseda T, Kinoshita T, Tamura H (2009) Evolution of a random directional wave and freak wave occurrence. *J Phys Oceanogr* 39:621–639
- Watson KM, West BJ (1975) A new numerical method for surface hydrodynamics. *J Geophys Res* 92(C11):11803–11824
- West B, Brueckner K, Janda R, Milder D, Milton MR (1987) A new numerical method for surface hydrodynamics. *J Geophys Res* 92:11803–11824
- Whitney JC (1971) The numerical solution of unsteady free-surface flows by conformal mapping. In: Holt M (ed) *Proceedings of the second international conference on numerical methods of fluid dynamics*. Springer, Berlin, pp 458–462
- Willemse JF (2001) Deterministic modeling of driving and dissipation for ocean surface gravity waves. *J Geophys Res* 106(C11):27187–27204
- Willemse JF (2002) Deterministic modeling of driving and dissipation for ocean surface gravity waves in two horizontal dimensions. *J Geophys Res* 107(C8):3121
- Vinje T, Brevig P (1981) Numerical simulation of breaking waves. *Adv Water Resour* 4:77–82
- Xu D, Hwang PA, Wu J (1986) Breaking of wind-generated waves. *J Phys Oceanogr* 16:2172–2178
- Yeung RW (1982) Numerical methods in free-surface flows. *Annu Rev Fluid Mech* 14:395–442
- Young IR, Babanin AV (2006) Spectral distribution of energy dissipation of wind generated waves due to dominant wave breaking. *J Phys Oceanogr* 36:376–394
- Yuen HC, Lake BM (1982) Nonlinear dynamics of deep-water gravity waves. *Adv Appl Mech* 22:67–229
- Yuan Y, Tung CC, Huang NE (1986) Statistical characteristics of breaking waves. In: Phillips OM, Hasselmann K (eds) *Wave dynamics and radio probing of the ocean surface*. Plenum, New York, pp 265–272
- Zakharov VE (1968) Stability of periodic waves of finite amplitude on the surface of deep water. *J Appl Mech Tech Phys* 9:190–194
- Zaslavskii GM, Sharkov EA (1987) Fractal features in breaking wave areas on sea surface. *Doklady Akademii Nauk SSSR* (Transactions of USSR Academy of Sciences—English Translation), 294:1362–1366
- Zakharov VE, Dyachenko AI, Vasilyev OA (2002) New method for numerical simulation of a nonstationary potential flow of incompressible fluid with a free surface. *Euro J Mech B/Fluids* 21:283–291
- Zakharov VE, Korotkevich AO, Pushkarev AN, Dyachenko AI (2005) Mesoscopic wave turbulence. *JETP Lett* 82(8):487–491